THEORY
OF CRYSTAL STRUCTURES

Discrete Modeling of Homometric and Isovector Divisions

V. G. Rau and T. F. Rau

Vladimir State Pedagogical University, Vladimir, Russia

e-mail: laemail@mail.ru

Received April 24, 2001

Abstract—As a further development of the method of discrete modeling of packings, the uniqueness of the division of the packing spaces into homometric (isovector) polyominoes is studied on the basis of the relation between the basic and vector systems of points. The particular criterion of the packing-space division based on the concept of the isovector nature of polyominoes with different numbers of points is formulated. © *2003 MAIK "Nauka/Interperiodica".*

Earlier, we suggested a criterion of division of a two-dimensional space into arbitrarily shaped polyominoes within the framework of the method of discrete modeling of molecules–polyominoes in the periodic space of a crystal lattice [1]. The criterion based on the concept of a packing multispace (PMS) of the Nth order represented as a superposition of the sublattices with the sublattice index N is formulated as follows. A polyomino consisting of N points of the basic system does not divide the space translationally if, upon the superposition of the vector system of this polyomino onto the corresponding PMS, the points of the vector system occupy the sites at which the lines from the complete set of the packing spaces with the sublattice index N are intersected. Accordingly, if at least one line not occupied by the points of the vector system of polyominoes is among the lines passing through the PMS sites, then the space can be divided translationally. Obviously, the number of various variants of the space division into specifically shaped polyominoes depends on the number of straight lines of the PMS having no common points with the vector system of polyominoes.

Below, we present the results of the study of the uniqueness of the division of packing spaces into homometric (isovector) polyominoes based on the analysis of the relation between the basic and vector systems of the points. A particular criterion of the division is formulated on the basis of the concept of isovector polyominoes with different numbers of points.

As is well known from the theory of X-ray structure analysis (see, e.g., [2]), the basic system of points is understood as a set of points fixed by the ends of the radius-vectors ($\mathbf{r}_1, \ldots, \mathbf{r}_i, \ldots, \mathbf{r}_N$) for each ith nucleus of the structure atoms set either in an arbitrary coordinate system (nonperiodic basic system) or in a coordinate system determined by the basis vectors of the lattice of translations whose unit cell contains these atoms

(periodic basic system). In comparison with the nonperiodic basic system, the periodic basic system has some additional interpoint distances associated with the translation vectors. The complete set of the interpoint distances $\mathbf{r}_{ij} = \mathbf{r}_j - \mathbf{r}_i = \mathbf{r}_k$ transforms the vector system of points in both nonperiodic and periodic basic systems constructed on the lattice with the same basis vectors.

To the points of real crystal structures there correspond certain physical quantities. If each point of the basic and the vector systems is brought into correspondence with the "electron" density $\rho(\mathbf{r}_i)$ and the Patterson density $P(\mathbf{r}_k)$, then the unit-cell content of the periodic lattices can be written as

$$\rho(\mathbf{r}) = \sum_{i=1}^{N} \rho_i \delta(\mathbf{r} - \mathbf{r}_i), \qquad (1)$$

$$P(\mathbf{r}) = \sum_{k=1}^{N^2} P_k \delta(\mathbf{r} - \mathbf{r}_k), \qquad (2)$$

where

$$\delta(\mathbf{r} - \mathbf{r}_i) = \begin{cases} 0, & \text{for } \mathbf{r} \neq \mathbf{r}_i \\ 1, & \text{for } \mathbf{r} = \mathbf{r}_i. \end{cases}$$

Single-crystal X-ray diffraction data allow one to construct a continuous function of the Patterson density that is a self-convolution of the electron-density function. This can be demonstrated on the above models of functions (1) and (2) by determining the inverted solution for the electron-density function by replacing each
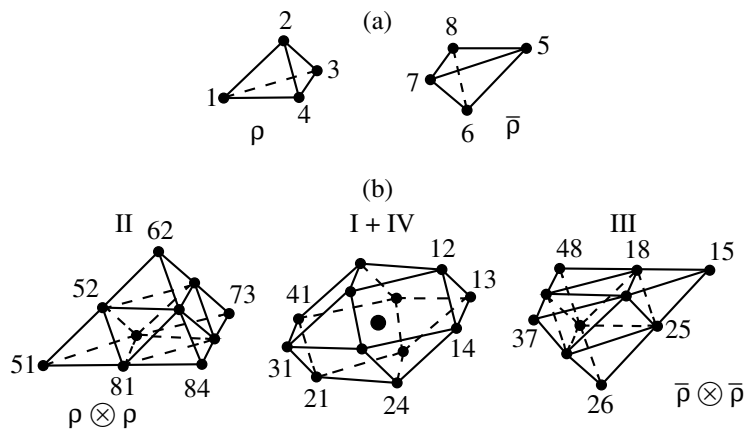
Fig. 1. Vector point system (b) as a self-convolution of the fragments of (a) the basic point system related by the center of inversion.

vector $\mathbf{r}_j$ by the vector $-\mathbf{r}_j$:

$$\rho \otimes \bar{\rho} = \left(\sum_{i=1}^{N} \rho_i \delta(\mathbf{r} - \mathbf{r}_i) \right) \otimes \left(\sum_{j=1}^{N} \rho_j \delta(\mathbf{r} + \mathbf{r}_j) \right)$$

$$= \sum_{i=1}^{N} \sum_{j=1}^{N} \{ \rho_i \rho_j [\delta(\mathbf{r} - \mathbf{r}_i) \otimes \delta(\mathbf{r} + \mathbf{r}_j)] \} \quad (3)$$

$$= \sum_{k=1}^{N^2} P_k \delta(\mathbf{r} - (\mathbf{r}_i - \mathbf{r}_j)) = \sum P_k \delta(\mathbf{r} - \mathbf{r}_k) = P(\mathbf{r}),$$

$$\text{where} \quad k \equiv ij.$$

Expression (3) is a particular case of the operation of convolution of two functions $\rho(\mathbf{r})$ and $\varphi(\mathbf{r})$, $\rho \otimes \varphi = \int_{\Omega} \rho(\mathbf{u}) \varphi(\mathbf{r} - \mathbf{u}) d\mathbf{u}$, where integration is taken over the domain of definition of functions Ω. The geometric sense of the convolution in the case of a discrete set of points can readily be understood from Fig. 1, where the basic system of points is represented by the function ρ and the inversion-related function $\bar{\rho}$, in the shape of a tetrahedron (Fig. 1a), whereas the vector system is constructed in accordance with the equality

$$(\rho + \bar{\rho}) \otimes (\bar{\rho} + \rho)$$
$$= \rho \otimes \bar{\rho}(\text{I}) + \rho \otimes \rho(\text{II}) + \bar{\rho} \otimes \bar{\rho}(\text{III}) + \bar{\rho} \otimes \rho(\text{IV}). \quad (4)$$

The result of the division of the vector system into four fragments is shown in Fig. 1b, where centrosymmetric fragments (I) and (IV) coincide and form a Galiulin cuboctahedron (for clarity, some points are identified).

The solution of the inverse problem of the construction of the basic system from the vector one was obtained by searching for the fragment that single out the image: triads of peaks, multiple peaks and fragments, "imaginary crosses," Wrinch hexagons, etc. In this case, the approach of the geometric simplex suggested by Galiulin encounters two serious difficulties

characteristic of all the geometric methods [3]. The first one is associated with the fact that even at the initial stage of the search for the solution by constructing, e.g., a Wrinch hexagon, not any arbitrary six points can form the star of a two-dimensional simplex (triangle of the basic system). The point is that the operation of difference, which acts onto a pair of vectors of the basic system, is an element of the sixth-order cyclic group with the generating matrix denoted by R_1 and called here a Wrinch matrix:

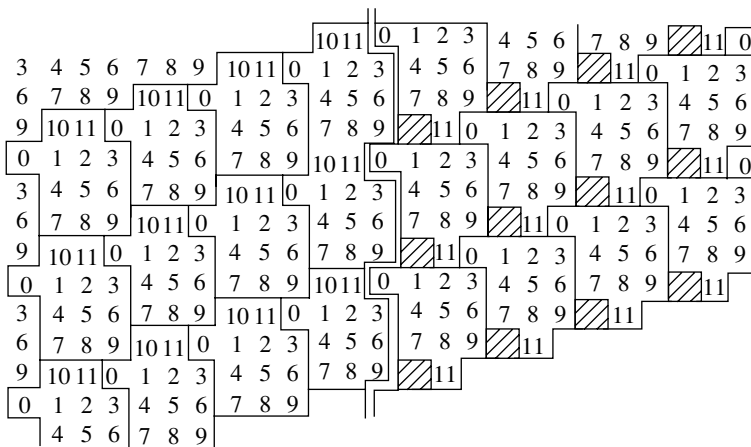$$R_1 = \begin{pmatrix} 0 & 1 \\ -1 & 1 \end{pmatrix}.$$

Then,

$$R_1 \begin{pmatrix} \mathbf{r}_i \\ \mathbf{r}_j \end{pmatrix} = \begin{pmatrix} \mathbf{r}_j \\ \mathbf{r}_j - \mathbf{r}_i \end{pmatrix};$$

$$R_2 = R_1^2 = \begin{pmatrix} -1 & 1 \\ -1 & 0 \end{pmatrix}, \quad R_2 \begin{pmatrix} \mathbf{r}_i \\ \mathbf{r}_j \end{pmatrix} = \begin{pmatrix} \mathbf{r}_j - \mathbf{r}_i \\ -\mathbf{r}_i \end{pmatrix};$$

$$R_3 = R_1^3 = \begin{pmatrix} -1 & 0 \\ 0 & -1 \end{pmatrix}, \quad R_3 \begin{pmatrix} \mathbf{r}_i \\ \mathbf{r}_j \end{pmatrix} = \begin{pmatrix} -\mathbf{r}_i \\ -\mathbf{r}_j \end{pmatrix};$$

$$R_4 = R_1^4 = \begin{pmatrix} 0 & -1 \\ 1 & -1 \end{pmatrix}, \quad R_4 \begin{pmatrix} \mathbf{r}_i \\ \mathbf{r}_j \end{pmatrix} = \begin{pmatrix} -\mathbf{r}_j \\ \mathbf{r}_i - \mathbf{r}_j \end{pmatrix}; \quad (5)$$

$$R_5 = R_1^5 = \begin{pmatrix} 1 & -1 \\ 1 & 0 \end{pmatrix}, \quad R_5 \begin{pmatrix} \mathbf{r}_i \\ \mathbf{r}_j \end{pmatrix} = \begin{pmatrix} \mathbf{r}_i - \mathbf{r}_j \\ \mathbf{r}_i \end{pmatrix};$$

$$R_6 = R_1^6 = \begin{pmatrix} 1 & 0 \\ 0 & 1 \end{pmatrix}, \quad R_6 \begin{pmatrix} \mathbf{r}_i \\ \mathbf{r}_j \end{pmatrix} = \begin{pmatrix} \mathbf{r}_i \\ \mathbf{r}_j \end{pmatrix}.$$

The corresponding characteristic matrix and equation allow one to calculate the eigenvalues $\lambda_{1,2}$. Indeed,

(a) (b) (c)

ρ φ $\rho \otimes \varphi = \sigma$

$\rho \otimes \bar{\varphi} = \omega$ $\omega \otimes \bar{\omega} = \sigma \otimes \bar{\sigma}$
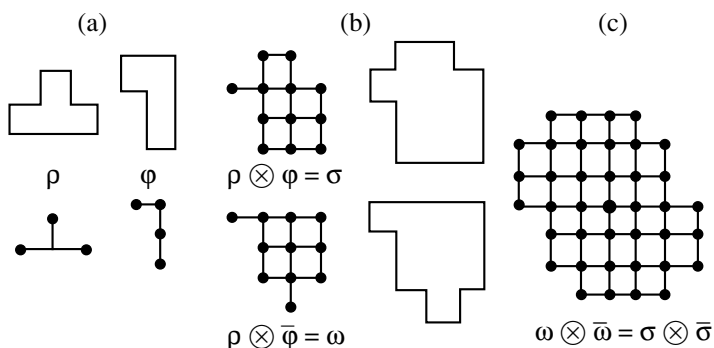
Fig. 2. Construction of homometric polyominoes by the convolution method: (a) initial polyominoes and their basic point systems, (b) convolution of the basic point systems and the corresponding homometric polyominoes, and (c) common vector point system of homometric polyominoes.

Fig. 3. Division (on the left) and packing (on the right) of the packing space $P\,12\,1_9$ into homometric polyominoes.

we have

$$\begin{pmatrix} \lambda & 0 \\ 0 & \lambda \end{pmatrix} - \begin{pmatrix} 0 & 1 \\ -1 & 1 \end{pmatrix} = \begin{pmatrix} \lambda & -1 \\ 1 & \lambda-1 \end{pmatrix} \Rightarrow \lambda^2 - \lambda + 1 = 0. \quad (6)$$

The above equation has the following solutions:

$$\lambda_{1,2} = \frac{1 \pm \sqrt{-3}}{2} = \frac{1}{2} \pm \frac{i\sqrt{3}}{2}$$

$$= \cos\frac{2\pi}{6} \pm i\sin\frac{2\pi}{6} = \exp\left(\pm i\frac{2\pi}{6}\right). \quad (7)$$

The rotation angles obtained determine a sixth-order cyclic group. Combining all the above operations into a sixfold axis, we finally obtain

$$\begin{pmatrix} 1 & 0 \\ 0 & 1 \\ -1 & 1 \\ -1 & 0 \\ 0 & -1 \\ 1 & -1 \end{pmatrix} \begin{pmatrix} \mathbf{r}_i \\ \mathbf{r}_j \end{pmatrix} = \begin{pmatrix} \mathbf{r}_i \\ \mathbf{r}_j \\ \mathbf{r}_j - \mathbf{r}_i \\ -\mathbf{r}_i \\ -\mathbf{r}_j \\ \mathbf{r}_i - \mathbf{r}_j \end{pmatrix}. \quad (8)$$

The second difficulty encountered in the deciphering is associated with homometry, i.e., the existence of various basic systems having the same vector systems or with the existence of the same sets of interpoint distances in different structures. Ignoring the multiplicities of the same vectors, which, in the general case, can be different, these structures can be called isovector structures [2]. In real structures solved based on diffraction data, isovector structures are very rare, but the possible existence of homometry deteriorates the suggested methods of finding the unique solution.

Isovector structures are more often encountered in the method of discrete modeling of packings. Indeed, at the packing coefficient $k \geq 0.5$, all the polyominoes are isovector ones. Moreover, the coordinates of the polyominoes and polycubes expressed in fractions of the unit cell are integral, whereas the figures themselves form a connected set of points. However, since the use of discrete modeling is aimed not at the deciphering vector systems but at the generation of new structures, the isovector nature of the structures does not hinder the method development. Moreover, in some instances, the use of the homometry concept allows one to simplify

the check of the ability of the structure to divide, because it is sufficient to choose for the test only one representative from the set of isovector figures. In order to construct a set of homometric polyominoes, we use the method suggested for the basic point system by Hoseman and Bagchi [4]: the convolutions of the point structures ρ, φ, δ, etc., are homometric if at least one of these structures is inverted. In other words, the following relationship is valid:

$$\rho \otimes \varphi \otimes \delta \ldots \sim \rho \otimes \bar{\varphi} \otimes \delta \ldots \sim \bar{\rho} \otimes \bar{\varphi} \otimes \delta \ldots \sim \ldots . \quad (9)$$

If the convolution is composed of two basic systems, then it represents a trivial homometric pair if at least one of the systems has a center of inversion, because, as a result, we obtain only the direct structure of points and the structure of points inverted with respect to the first one.

Now consider an example of the construction of a nontrivial homometric pair in the form of a convolution of two individual fragments.

With this aim, substitute each cell of the chosen polyominoes by a point, and, thus, transform these polyominoes into the basic point systems ρ and φ shown in Fig. 2a. The convolutions $\rho \otimes \varphi$ and $\rho \otimes \bar{\varphi}$ constructed by (9) form a homometric pair σ and ω (Fig. 2b) with the common vector point system (Fig. 2c). The corresponding σ- and ω-polyominoes constructed from the set of points of the basic systems σ and ω without allowance for their multiplicities (which transform them from homometric polyominoes into isovector ones) tile the packing space $P12\,1_9$ with the packing coefficients $k = 1$ for σ-polyominoes and $k = 11/12$ for ω-polyominoes (Fig. 3).

In the general case, the homometric basic systems obtained using the convolution operation have different numbers of the occupied points of the space, which allows us to formulate the *particular criterion* of the space division into polyominoes: if the basic point system of polyominoes consisting of N cells belongs to the nontrivial set of the isovector structures and if this set has at least one representative with the number of cells exceeding N, then the initial polyomino cannot translationally divide any of the packing spaces of the Nth order.

Indeed, if the initial polyomino divided at least one such space, then another representative of the isovector set should have also divided the same space, which is impossible, because the area of the latter representative exceeds the area of the cell. This discrepancy proves the validity of the suggested criterion.

All the above considered is also valid for the three-dimensional case of isovector polycubes (three-dimensional polyominoes). It is easy to perform the automated recalculation of the homometric polyominoes and, thus, create a database of isovector point sets that can be used for generation of various packings of the structures in the periodic space.

REFERENCES

1. V. G. Rau, Kristallografiya **45** (2), 231 (2000) [Crystallogr. Rep. **45**, 199 (2000)].
2. M. Buerger, *Vector Space and Its Application in Crystal-Structure Investigation* (Wiley, New York, 1959; Inostrannaya Literatura, Moscow, 1961).
3. R. V. Galiulin, M. I. Sirota, A. S. Naumov, and N. V. Belov, Kristallografiya **18** (1), 63 (1973) [Sov. Phys. Crystallogr. **18**, 39 (1973)].
4. R. Hoseman and S. Bagchi, *Direct Analysis of Diffraction by Matter* (North-Holland, Amsterdam, 1962).

Translated by L. Man

Cationic Motifs in Corundum, Spinel, and Amesite Homologous Structural Classes

N. L. Smirnova

Moscow State University, Vorob'evy gory, Moscow, 119899 Russia
Received February 1, 2002

Abstract—The coordinate spectra of the cationic motifs for 132 structural types in hexagonal and cubic crystal systems are analyzed. The homologous classes—polysome series of structural minals (modules)—are revealed. It is established that structural types of different compositions are characterized by similar structural cationic motifs and, hence, the growth and structure formation occur through the mechanism of ordered isomorphism. © 2003 MAIK "Nauka/Interperiodica".

Investigations into cationic motifs of different compounds date back to the advent of X-ray structure analysis. Even early experiments demonstrated that cations in structures of the sphalerite, halite, fluorite, cuprite, and other types are located at positions corresponding to the closest packings. The concept of the closest anionic packings whose holes are occupied by cations was developed by N.V. Belov [1]. Ordered isomorphs, i.e., superstructures of the closest packings, were revealed even in the first structures of chemical compounds, which were determined using X-ray diffraction analysis. A large number of superstructures were described in detail in [1].

In 1950–1964, superstructures of the closest packings revealed in chemical compounds of 90 structural types were modeled on the basis of the polarity and parsimony principles and a comparative crystal chemical analysis. The results obtained in this modeling allowed the conclusion that cationic–anionic, anionic, and cationic motifs involve a number of the simplest variants of the atomic arrangement in positions of the closest packing, body-centered cubic lattices, primitive cubic or hexagonal lattices, and their superstructures [2]. It was assumed that real structures represent a set of atomic partial structures that can also involve superstructures; in this case, atoms either can be displaced from their ideal positions or can be absent altogether, which corresponds to the formation of vacancies □. The structures of intermetallic and inorganic compounds and, especially, the cationic sublattices are composed of the same partial structures with identical superstructures. As is known, the positive charge in intermetallic compounds is compensated for by electrons. It seems likely that, in intermetallic compounds, the positive charge is compensated for by excess ions. Moreover, it was established that the frameworks characteristic of intermetallic structures can also exist in structures of inorganic compounds. In 1972–2000, the above inferences were confirmed by S.V. Borisov and other researchers, who investigated the cationic motifs (see, for example, [3]). It was demonstrated that, among the studied structures (belonging to more than one hundred structural types), almost half the structures are characterized by the distribution of cations over the *F*-type sublattices (the closest cubic packing) and approximately one-third of the structures have an *I*-type cationic sublattice (a body-centered cubic lattice). It turned out that there exist a large number of structures with a modified single-layer hexagonal packing of heavy atoms (a primitive hexagonal lattice). Variants with vacancies (□) make a particular contribution to the atomic motifs. In the 1980s, M. O'Keefe and B.G. Hyde [4] proposed an alternative approach to the interpretation of the cationic motifs. This approach was quite the opposite of that used traditionally; more precisely, they considered the cationic motifs with holes occupied by anions and confirmed the similarity between the structural motifs of intermetallic compounds and cationic sublattices of inorganic materials. Earlier, Belov [1] also noted that the cationic partial motifs represented by oxygen-centered tetrahedra (i.e., oxygen atoms in tetrahedra formed by cations) are observed in the La_2O_3 structure. Subsequent investigations of minerals, specifically with the use of combinatorial analysis, revealed a large number of similar structures with cationic partial motifs characterized by combinations of anion-centered tetrahedra [5].

From the foregoing, it is obvious that the formation of structures and, especially, cationic motifs due to zero-, one-, two-, or three-dimensional ordered isomorphism (combinatorics) has been the particular concern of many researchers engaged in crystallography.

A layer-by-layer representation of the structures under investigation is a widely accepted method. The structure image obtained by this method is referred to as the structural diagram. This diagram consist of a sequence of identical or different layers of polyhedra, projections, letters, chemical formulas, and planar nets.

All crystal structures, orbits, and lattice complexes can be represented as composed of 11 different Kepler–Shubnikov planar nets: 3^6, 6^3, 3636, 3^46, 3464, 3.12^2, 46.12, 4^4, 43^243, 48^2, and 3^34^2. The Kepler nets consist of regular polygons, whereas the Shubnikov nets are combinatorial topological Kepler nets and can be distorted [6].

Since the advent of structural analysis, the representation of solved structures in the form of nets, along with polyhedral and other representations, has been extensively used in crystallography. The net representation of structures has also found use in fundamental works. In [1], the majority of structures were described in terms of the closest anionic packings (i.e., the 3^6 nets), the spinel cationic motif was represented by the 3636 net, the corundum cationic motif was treated as the 6^3 net, and so on. According to Bokiĭ [7], most of existing structural motifs can be considered as the closest packings consisting of 3^6 nets and some structures are composed of 6^3 + 3636 nets. In 1956, we began to investigate the closest packings and to model the possible superstructures. In 1959, the results of these investigations were summarized in [2]. It was demonstrated that the superstructures of the closest packings and simple cubic structures are formed by sets of 3^6, 3636, 6^3, 3^46, 3^26^2, 4^4, and 43^243 nets and also by their combinations. Particular sets of these nets were used to model almost 90 structural types of intermetallic and inorganic compounds and their cationic, anionic, and cationic–anionic (one-, two-, and three-dimensional) motifs. Moreover, the cationic motifs were systematically studied in terms of Kepler–Shubnikov nets for the first time. In 1966, we developed a new technique for layer-by-layer analysis of the structures, which was referred to as the line diagram method [9]. With this method, all structural types in hexagonal, tetragonal, and cubic (hexagonal and tetragonal variants) crystal systems can be represented along the [001] axis as sets of Kepler–Shubnikov nets. Consideration was given to the structural types formed by the following nets: 3^6 [10]; 3636, 6^3, and 3^6 [11]; 3464, 3636, 6^3, and 3^6 [12]; and others. These nets make it possible to describe the majority of structural types and their cationic and anionic motifs. Cationic motifs of numerous structural types were systematically studied in [13] (1974) and [14] (1976). In particular, we considered a number of cationic motifs represented by the nets 3^6, 6^3, 4^4, and others (as well as by their more complicated combinations). The cationic motifs under consideration were described by different methods. The classification was performed with the use of particular nets, their sets (structural minals, i.e., units or modules), and composite structural minals with filling of all the possible positions and the separation of the invariant and variant parts. The number of different composite structural minals was found to be very small.

The Kepler–Shubnikov nets were widely used for describing the structural types in a number of monographs published in the 1970s. For example, in the monographs by Belov (1976) [15], Pearson (1972) [16], and Kripyakevich (1977) [17], the structural types of intermetallic and inorganic compounds were represented as projections of sets of the following nets: 3^6, 3636, 6^3, 3^46, 3^26^2, 4^4, 43^243, 48^2, and 3^34^2. A number of structural types presented in these monographs were not considered in the form of projections or line diagrams in our earlier works. For many structural types, the cationic motifs represented as nets were studied by Borisov and other researchers (see, for example, [18]). Analysis of the structural motifs with the use of software packages proved that planar densely filled cationic nets form the basis of many crystal structures. The advantage of the Borisov computer method resides in the fact that structures in any crystal systems can be analyzed along any directions. The advantage of the line diagram method is that the structures under investigation can be represented as spectra of atomic coordinates, which, in turn, makes it possible to use symmetry elements and to compare structures and their modules at any accuracy in the determination of the coordinates. Without description, structural motifs can be compared in much the same manner as X-ray powder diffraction patterns. The proposed method can be easily computerized. In recent years, our method of layer-by-layer modeling with the use of structural diagrams, specifically of the line diagrams in combination with nets, has been applied, together with the known techniques, to simulate crystal structures [19]. Thus, the representation of structures and their cationic motifs in the form of sequences of nets is an important problem.

We established that the hexagonal and cubic structures with threefold axes consist of seven nets, namely, 3^6, 6^3, 3636, 3^46, 3464, 3.12^2, and 46.12. Among them, three nets correspond to well-known motifs. These are the close-packed (3^6), corundum (6^3), and spinel (3636) nets composed of cations located in octahedra formed by anions [1]. The first net (a close-packed motif) is composed of edge-shared triangles. The corundum net consists of edge-shared hexagons. This net is also called the graphite or honeycomb net. The spinel net is composed of hexagons, but they are connected by corners. The centers of hexagons are not occupied. Recall that, according to [2], empty sites are treated as atoms (E) of a special type, which are commonly designated by an open square □. On this basis, the corundum and spinel nets can be considered superstructures with respect to the close-packed layer 3^6. The parameter of the close-packed layer is equal to 3 Å, and the parameters of the corundum and spinel nets are 5.2 and 6 Å, respectively. In our earlier work [9], we demonstrated that all structures with hexagonal basis parameters of 5–6 Å are built up only of these three nets and their combinations. All structural types with a basis parameter of 5 Å that consist of the 3^6 and 6^3 nets are assigned to the corundum homologous class [11]. Structural types with a basis parameter of 6 Å that involve the 3^6

and 3636 nets are attributed to the spinel homologous class. Structural types with a basis parameter of 5–6 Å that consist of nets of all three types belong to the amesite homologous class. The last class also includes all micas of different symmetries (for example, with orthorhombic basis parameters of 5.5 and 9.5 Å). Their silicon–oxygen layers (structural minals) consist of 6^3 and 3636 nets, and the corundum layers composed of octahedra (structural minals) are built up of 6^3 nets. Layers of both types form combined structural minals (joined as genes in genomes), which are encountered in many minerals.

As a rule, the data on the relation between the studied structures are represented by traditional methods of comparative crystal chemistry. These are projections in the form of points, polygons, polyhedra, sections, and axonometry. Moreover, it is possible to use the Schlegel and connectivity diagrams, sequences of letters, formulas, etc.

Since real structures are distorted to some extent, the atoms in a particular structure deviate from their ideal positions, specifically from the positions corresponding to the closest packing. The traditional methods of comparative crystal chemistry have failed to determine these deviations to sufficient accuracy. The line diagram method [9–14] turned out to be very convenient for revealing subtle differences between the related structures. The method is based on the representation of the studied structures in the form of spectra of lines corresponding to the coordinates of points in planar nets parallel to the basal plane of the unit cell. This method provides a layer-by-layer representation of the crystal structures with due regard for the symmetry and unit cell parameters.

Let us now consider a hexagonal or cubic (hexagonal variant) crystal system with threefold axes, in which an independent region is separated in the basal plane of the unit cell (Fig. 1). This region is divided into two equal parts. For each of these two parts, we introduce a particular coordinate system: (i) one coordinate system with the axes x, y, and u and the origin at the point 000 [initially, the point with the coordinates (1/3, 1/3)] and (ii) the other coordinate system with the axes $\hat{x}$, $\hat{y}$, and $\hat{u}$ and the origin at the point $\hat{0}\hat{0}\hat{0}$ [initially, the point with the coordinates (–1/3, –1/3)]. In the new coordinate systems, we choose pairs of significant coordinates, for example, ($xy0$, $x0u$, $0yu$) and ($\hat{x}\hat{y}\hat{0}$, $\hat{x}\hat{0}\hat{u}$, $\hat{0}\hat{y}\hat{u}$). The maximum sum of the coordinates is equal to 1/3. In the constructed spectra (Figs. 2–5), the net coordinates x, y, and u are depicted by crosses (×), dashes (–), and circles (○), respectively, in the vertical segment and at the end of this segment, which represents the spectral line (see, for example, spectrum 2.1 in Fig. 2). For each net (corresponding to a particular vertical segment), the distance along the z axis, which is equal to zc/a, is laid off on the horizontal axis, which makes it possible to
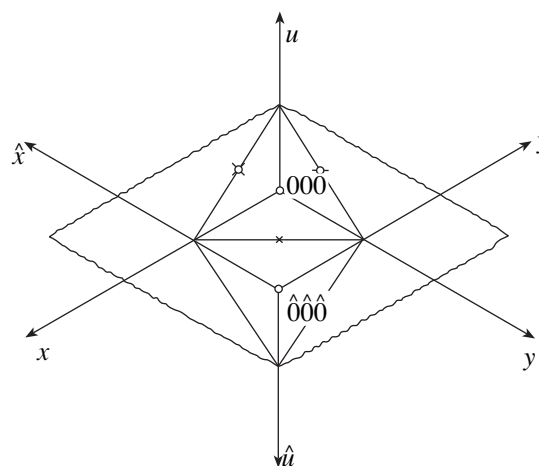

Fig. 1. Coordinate system used for constructing the spectra of structural types. Thin solid lines indicate the independent region.

compare all the structures on the same scale. The linear segments along the z axis are related by the symmetry elements. The atomic coordinates are specified accurate to within 0.01 along the x, y, and u axes and 0.001 along the z axis. Therefore, the line diagram is a spectrum in which the linear segments are determined by the coordinates of the points in nets perpendicular to the z axis. The coordinate equal to zero is presented only in the case when all three coordinates are equal to zero and is depicted by a circle (net 3^6) or a circle with a hat (net 3^6). In the spectra, the segments corresponding to coordinate 1/3 have a break (see, for example, spectrum 1.8 in Fig. 2) for the benefit of clarity. These segments end with a cross (coordinate 1/3 in the x axis), a dash (coordinate 1/3 in the y axis), or a circle (coordinate 1/3 in the u axis). A spinel perfect net is depicted by a segment ending with a cross and a dash, a circle and a dash, or a circle and a cross (Figs. 1, 3). These spinel nets are centered at atoms that are located along the threefold axes and whose coordinates are designated by a circle, a dash, and a cross, respectively. Earlier, it was shown that structural types and their spectra are characterized by structural minals with invariant (retained) lines and variant (appearing and disappearing) lines (i.e., the ordered implantation and subtraction). Two lines can correspond to either identical or different atoms (ordered substitution). The coordinates can deviate from their ideal values, and the separation between the lines can either decrease or increase (ordered deformation). The advantage of the spectral structural method over other techniques resides in its universality, accuracy, simplicity, and visualization. A comparison of the structures with the use of these spectra is performed in the same manner as X-ray diffraction patterns and IR, NMR, and NQR spectra. It is believed that the structural spectra correlate with other spectra.

In 1966–1986, we obtained the structural spectra of compounds and lattice complexes in more than ten
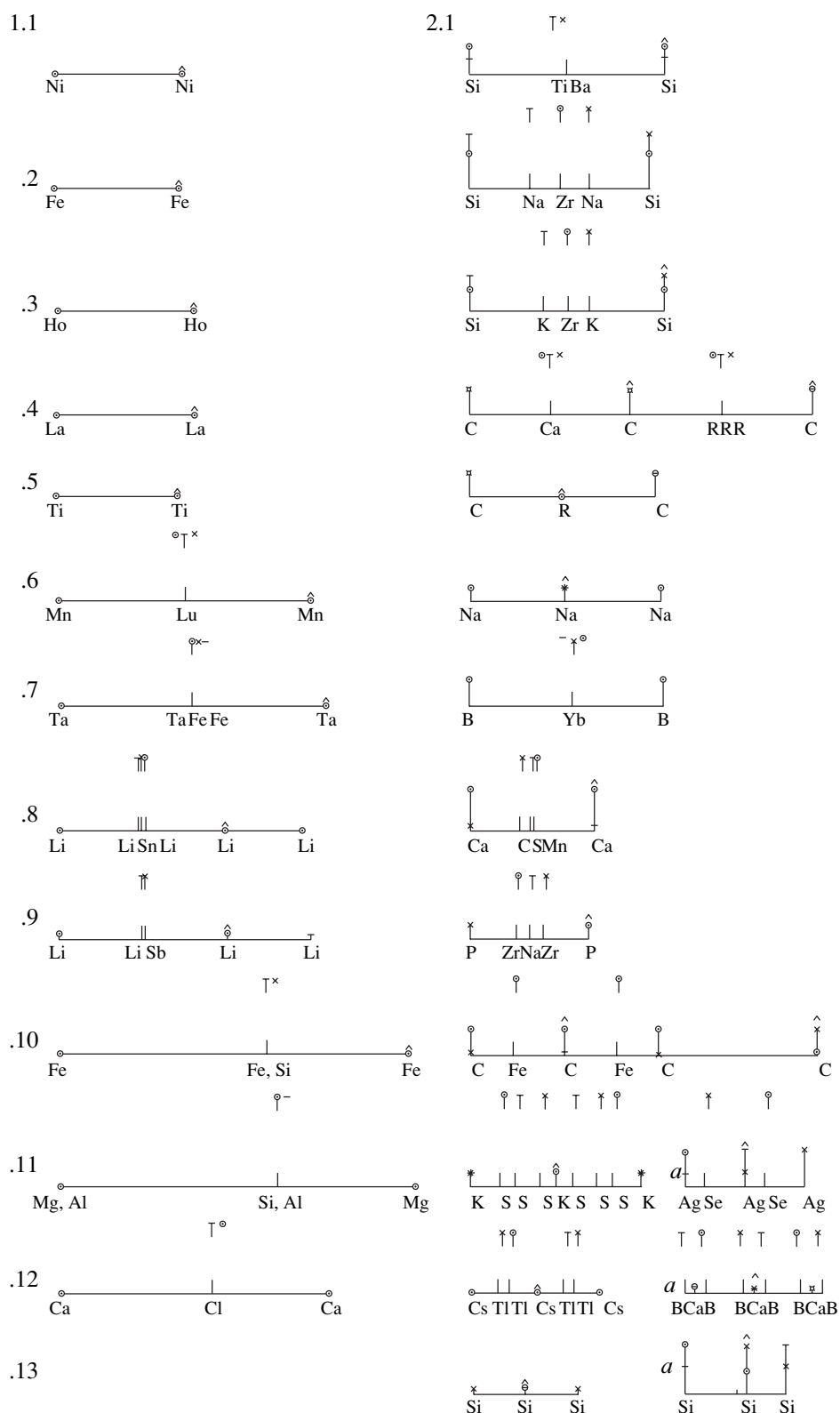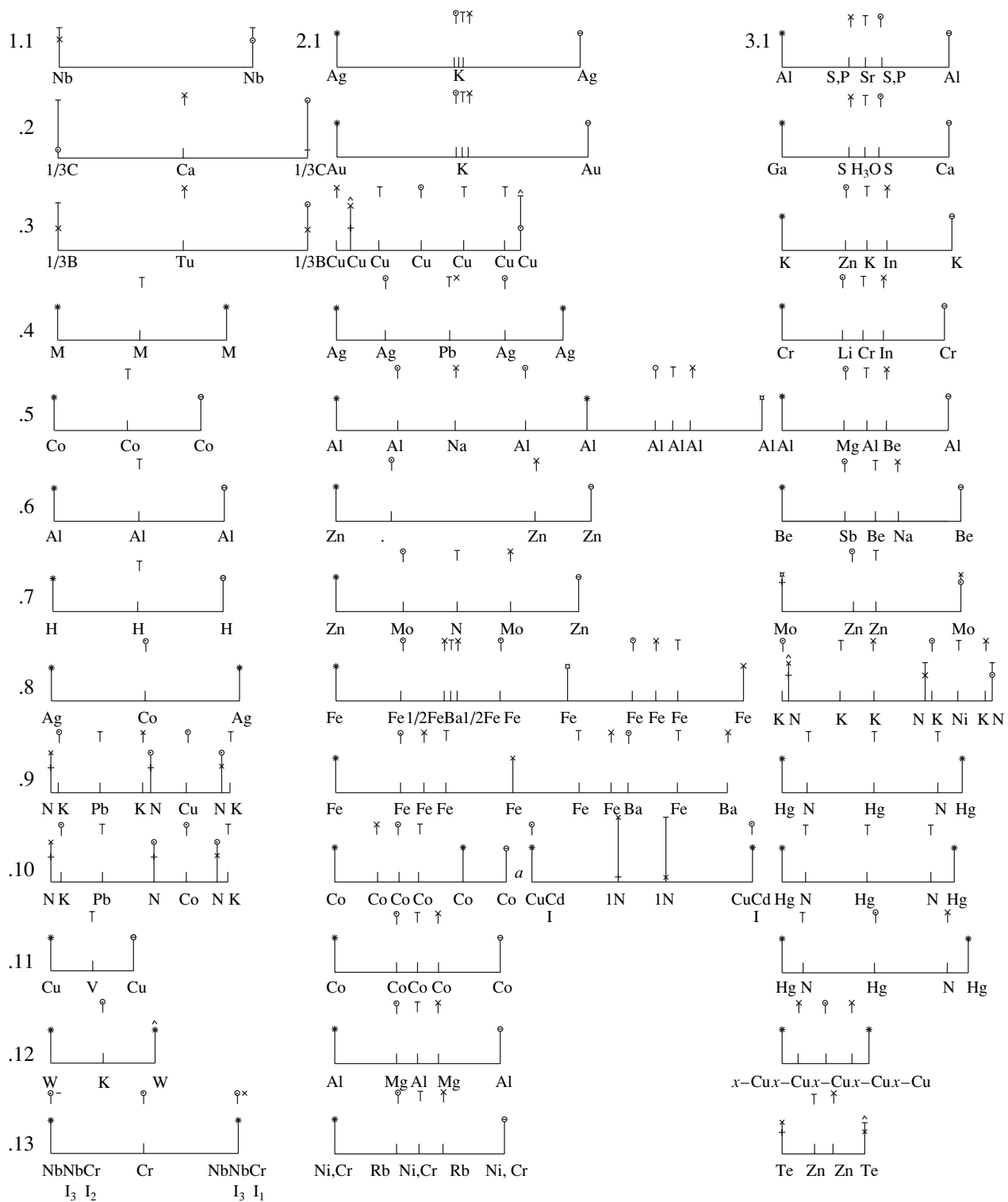
Fig. 2. Spectra of the cationic motifs in structural types of the corundum homologous class (each spectrum is denoted by the number of the column and the row): (1.1) Ni_3C, (1.2) Fe_3N, (1.3) HoD_3, (1.4) LaF_3, (1.5) Ti_3O, (1.6) $LuMnO_3$, (1.7) $Ta_2FeN_{2.5}$, (1.8) Li_8SnO_6, (1.9) Li_7SbO_6, (1.10) $Fe_3(Fe_1,Si_1)O_5(OH)_4$, (1.11) $(Mg_2,Al_1)(Si_1,Al_1)O_5(OH)_4$, and (1.12) $Ca(ClO)_2 \cdot 2Ca(OH)_2$; and (2.1) $BaTiSi_3O_9$, (2.2) $Na_2ZrSi_3O_9 \cdot 9H_2O$, (2.3) $K_2ZrSi_3O_9$, (2.4) $CaLn_2(CO_3)_3$, (2.5) $LnCO_3F$, (2.6) Na_2O_2, (2.7) $Yb(BO_3)$, (2.8) $Ca_3Mn(OH)_6SO_4CO_3 \cdot 12H_2O$, (2.9) $NaZr_2(PO_4)_3$, (2.10) $Fe_2(CO)_9$, (2.11) $K_2S_2O_6$, (2.12) $Cs_3Tl_2Cl_9$, (2.13) β-Si_3N_4, (2.11a) Ag_3NSeO_3, (2.12a) $Ca_3(BO_3)_2$, and (2.13a) α-Si_3N_4.
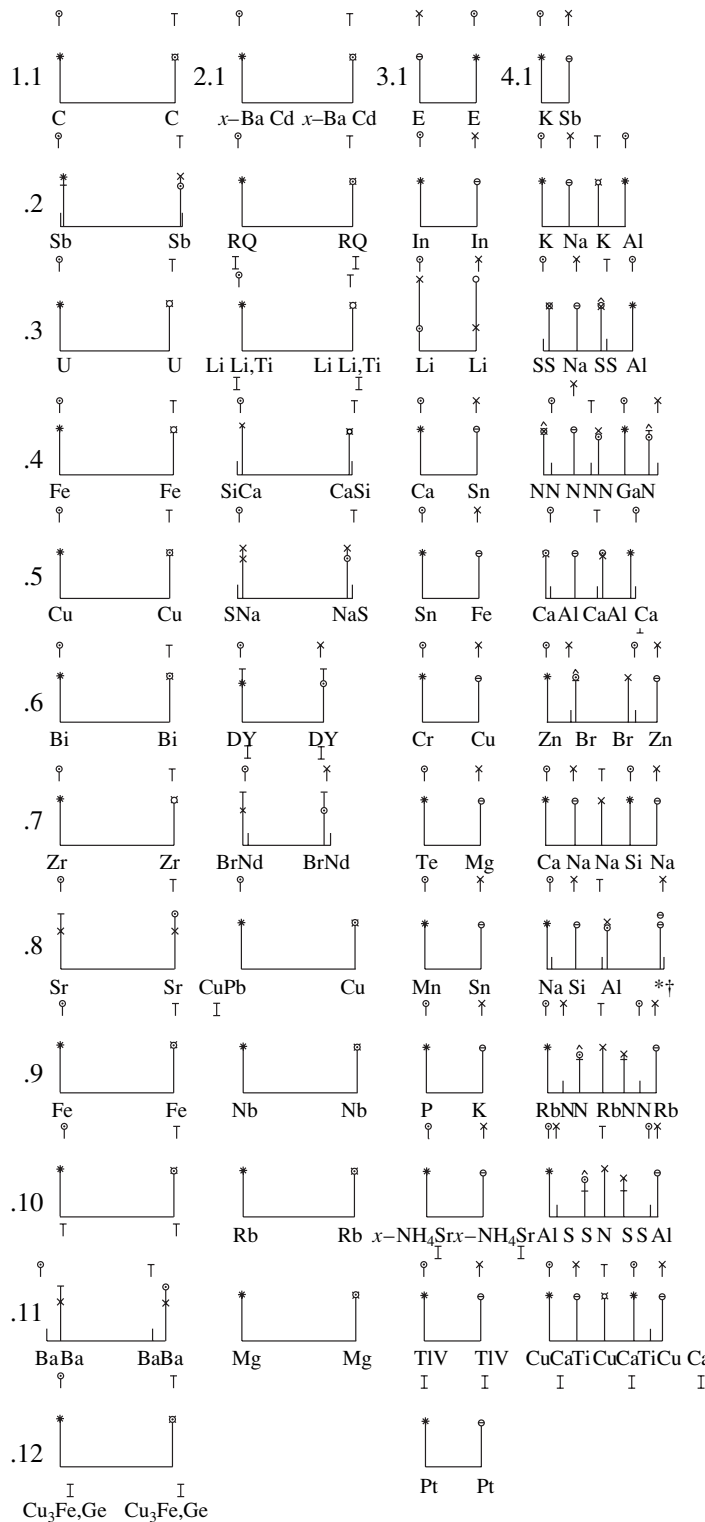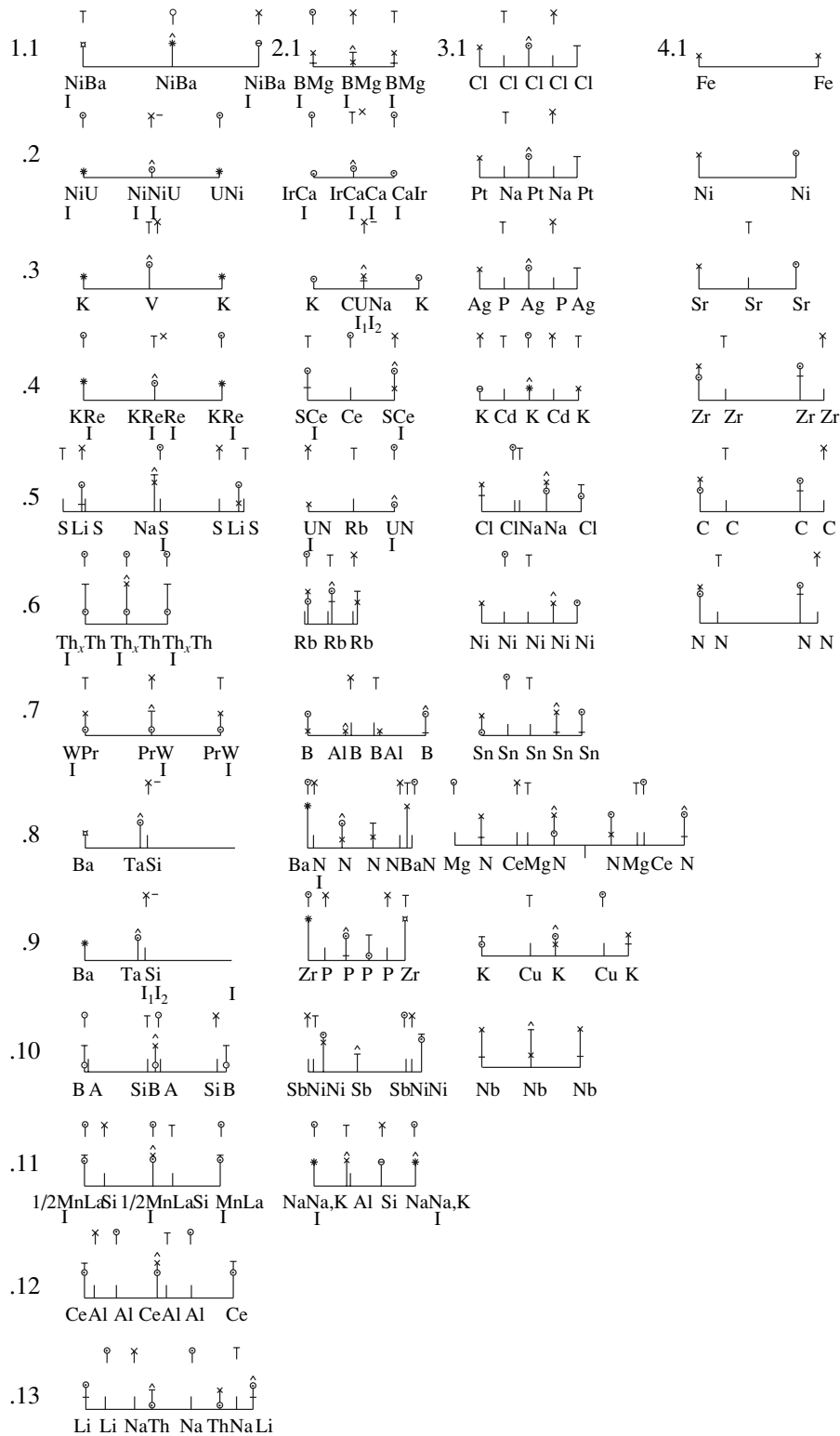
Fig. 3. Spectra of the cationic motifs in structural types of the spinel homologous class: (1.1) CO_2, (1.2) Sb_4O_6, (1.3) U_4S_3, (1.4) Fe_4N, (1.5) Cu_2O, (1.6) Bi_2O_3, (1.7) Zr_3Se_4, (1.8) $Sr(CN)_2$, (1.9) FeS_2, (1.10) M_8C_5 (M = T), (1.11) Ba_4OCl_6, and (1.12) $Cu_3(Fe,Ge)S_4$; (2.1) $Ba_{2x}Cd_2Cl_{6.3} \cdot H_2O$, (2.2) $R_2Q_2O_7$, (2.3) $Li(Li_1,Ti_1)O_3$, (2.4) Ca_3SiO_5, (2.5) $Na_6(SO_4)_2ClF$, (2.6) $Cr(NH_3)_6CuCl_5$, (2.7) $Nd(BrO_3)_3$, (2.8) $PbCu_6O_8$, (2.9) NbO, (2.10) Rb_3Se_8, and (2.11) Mg_3NF_3; (3.1) $8\Gamma.48H_2O$ ($\Gamma = E$), (3.2) $In(OH)_3$, (3.3) $LiCH_4$, (3.4) $CaSn(OH)_6$, (3.5) $FeSn(OH)_6$, (3.6) $Cr(NH_3)_6CuCl_5$, (3.7) $Mg(H_2O)_6TeI_6$, (3.8) $MnSnO_6$, (3.9) KPF_6, (3.10) $[(NH_4)_2,\square_1]SrCl_4$, (3.11) Tl_3VS_4, and (3.12) Pt_3O_4; and (4.1) $KSbF_6$, (4.2) K_2NaAlF_6, (4.3) $NaAl(SO_4)_2 \cdot 12H_2O$, (4.4) $(NH_4)_3GaF_6$, (4.5) $Ca_3Al_2O_6$, (4.6) $Zn(BrO_3)_2 \cdot 6H_2O$, (4.7) Na_2CaSiO_4, (4.8) $NaAlSiO_4$, (4.9) $RbNO_3$, (4.10) $NH_4Al(SO_4)_2 \cdot 12H_2O$, and (4.11) $CaCu_3Ti_4O_{12}$.

Fig. 4. Spectra of the cationic motifs in structural types of the amesite homologous class: (1.1) Nb_3Br_8, (1.2) $CaCO_3$, (1.3) $TuBO_3$, (1.4) M_8C_5, (1.5) $Co_2(OH)_3Cl$, (1.6) $Al[F,(OH)_3][\square,(H_2O)_6]$, (1.7) H_2O, (1.8) $Ag_3Co(CN)_6$, (1.9) $K_2PbCu(NO_2)_6$, (1.10) $KPbCo(NO_2)_6$, (1.11) Cu_3VS_4, (1.12) $(K_{0.27},\square_{0.06})WO_3$, and (1.13) $CrNb_2Se_4$; (2.1) $KAg(CN)_2$, (2.2) $KAu(CN)_2$, (2.3) $Cu_{2-x}Se$, (2.4) $Ag_5Pb_2O_6$, (2.5) $NaAl_{11}O_{17}$, (2.6) $Zn_5(OH)_8Cl_2 \cdot H_2O$, (2.7) $[(NH_4)_{1-x}(H_3O)_x]Zn_3Mo_2O_3OH$, (2.8) $BaFe_{12}O_{19}$, (2.9) $BaFe_6ZnO_{11}$, (2.10) Co_9S_8, (2.10a) $Cu_3Cd(OH)_6(NO_3)_2$, (2.11) Co_3S_4, (2.12) $MgAl_2O_4$, and (2.13) $Rb(Ni_1,Cr_1)F_6$; and (3.1) $SrAl_3(SO_4,PO_4)(OH)_6$, (3.2) $H_3OGa_3(SO_4)_2(OH)_6 \cdot H_2O$, (3.3) $K_2Zn(CN)_4$, (3.4) Cr_4LiInO_8, (3.5) $BeMgAl_4O_8$, (3.6) $NaSbBr_4O_7$, (3.7) $Zn_2Mo_3O_8$, (3.8) $K_4Ni(NO_2)_6$, (3.9) NHg_2Br, (3.10) $Hg_2NOH \cdot H_2O$, (3.11) $NHHg_2Br_2$, (3.12) Cu_2S, and (3.13) $(Zn,Fe)_2(TeO_3)_3Na_xH_{2-x} \cdot yH_2O$.

Fig. 5. Spectra of the cationic motifs in structural types of the gagarinite and pyrite homologous classes: (1.1) Ba_3NiO_4, (1.2) NiU_2O_6, (1.3) $K_3V_5O_{14}$, (1.4) K_2ReH_9, (1.5) $LiNaSO_4$, (1.6) $Th(Th_1,\square_1)S_{12}$, (1.7) $Pr_3WO_6Cl_3$, (1.8) $Ba_3Si_4Ta_6O_{26}$, (1.9) $Ba_3Si_4Ta_6O_{23}$, (1.10) $(Mn,W)_{1x}(Mn,W,Mg)_{3y}Si(O,OH)_7$, (1.11) $La_6(Mn_1,\square_1)Si_2S_{14}$, (1.12) $Ce_6(Al_{3.33},\square_{0.67})S_{14}$, and (1.13) $(Na_1,Li_2)Li_4Th_6F_{31}$; (2.1) $Mg_3BO_3(F,OH)_3$, (2.2) Ca_2IrO_4, (2.3) $K_3NaU(CO_3)_3$, (2.4) $Ce_2(SO_4)_3 \cdot 9H_2O$, (2.5) $RbUO_2(NO_3)_3$, (2.6) Rb_4O_6, (2.7) $Al_6B_5O_{15}(OH)_3$, (2.8) $Ba(NO_3)_2$, (2.9) ZrP_2O_7, (2.10) $NiSbS$, and (2.11) $Na(Na_2,K_1)Al_4Si_4O_{16}$; (3.1) $8\Gamma \cdot 46H_2O$ ($\Gamma = Cl$), (3.2) $NaPt_3O_4$, (3.3) Ag_3PO_4, (3.4) K_4CdCl_6, (3.5) $NaClO_3$, (3.6) $Ni(CO)_4$, (3.7) SnI_4, (3.8) $Ce_2Mg_3(NO_3)_{12} \cdot 24H_2O$, (3.9) $K_3Cu(CN)_4$, and (3.10) Nb_3Te_4; and (4.1) FeS, (4.2) Ni_3S_2, (4.3) $SrSi_2$, (4.4) $ZrOS$, (4.5) CO, and (4.6) NH_3.

homologous structural classes and developed the symmetry aspect of the problem. Moreover, the spectra of cationic motifs were described in [13, 14]. However, the structural diagrams of a large number of cationic motifs in corundum, spinel, and amesite structural classes were represented only in the form of letters and minal formulas. The purpose of the present work was to describe these cationic motifs in the form of spectra (Figs. 2–5). Note that the spectra shown in Figs. 2–5 also include cations of radical anions (N of NO_3, S of SO_4, etc.). Furthermore, we constructed the spectra of carbides free of C and nitrides free of N.

Cationic motifs of 132 structural types and the corresponding chemical compounds are represented in the form of spectra in Figs. 2–5. By analogy with X-ray diffraction patterns, our spectra are characterized by the separation between the lines; however, the role of their intensity is played by the coordinates of the vectors in the basal plane. In this case, we obtain not a variety of polyhedra and their combinations but nets of two types and, correspondingly, lines of two types: (i) lines I are associated with the atoms lying along the threefold axis (see, for example, spectrum 2.1 in Fig. 3), and (ii) lines X are attributed to the atoms lying off the threefold axis. There exist three types of lines I, namely, the lines I_1, I_2, and I_3, which correspond to the atoms lying along the axes x (3_1, cross), y (3_2, dash), and u (3_3, circle). Each net I and all the three nets taken together are close-packed nets (Fig. 1). Lines X can correspond to the two extreme coordinates $(0, 0)$ (a circle in the horizontal line of the spectrum) and $(1/6, 1/6)$. The coordinate symbols $(0, 0)$ and circles in the horizontal line can be both hatted and unhatted. The close-packed nets correspond to these coordinates. There are three types of $(1/6, 1/6)$ coordinates: $(1/6, 1/6, 0)$ (dash with a cross), $(1/6, 0, 1/6)$ (cross with a circle), and $(0, 1/6, 1/6)$ (dash with a circle). These coordinates indicate the spinel nets. The centers of their hexagons connected by corners are situated at the 3_3 (circle), 3_2 (dash), and 3_1 (cross) axes, respectively (Figs. 1, 3). The nets and lines X have intermediate coordinates. The sum of the coordinates does not exceed 1/3. The similarity and difference between the spectra are determined by the atomic coordinates and interatomic distances. A detailed analysis of the similarities and differences in all the spectra does not enter into the scope of this paper. Here, we only present a number of spectra and, as an example, consider the properties of particular spectra and their similarities to the spectra of the simplest structures of intermetallic compounds. The second stage of our investigation is aimed at revealing a correlation between the spectra and interatomic distances. The spectra consisting of lines I were described earlier in [14] and are not discussed in the present work.

Figures 2–5 show the spectra containing lines X in combination with lines I. Hereafter, the spectra in the text will be denoted by the numbers involving the respective numbers of the figure, the column, and the row. Spectrum 21.1 (Fig. 2) corresponds to a structural minal in the form of a layer bounded by two close-packed nets. Spectra 21.2–21.5 differ from spectrum 21.1 by small distortions. A set of lines I associated with the close-packed net is observed between lines X in spectrum 21.6. As a result, we have two structural minals or one combined structural minal composed of two structural minals. Consequently, the possibility exists of forming superstructures. Three lines are attributed to atoms of two sorts (spectra 21.7, 21.8). Vacancies can be in place of atoms of a particular sort. In the spectra, the vacancies are described by an imaginary line (spectra 21.10–21.12). The lines in spectrum 21.9 correspond to atoms of two different sorts and a vacancy. The decrease in the separation between the lines in spectra 21.8 and 21.9 is caused by the formation of flattened structural minals in a simple cubic structure. The deviation of the spectra in column 22. from an ideal spectrum is associated with the appearance of the structures with cations forming radical anions and the corresponding distortions of the nets and lines X.

In Fig. 3, we first consider an ideal spectrum of the spinel perfect centered (close-packed) nets 3636. In the closest packing, two nets form the structural minal represented by spectrum 31.1. The variety of the spectra presented in columns 31. and 32. stems from the line splitting, which is well known in the solution of crystal structures. Two networks corresponding to lines I and X can be filled with different atoms. However, no spectra involving four lines attributed to four different atoms are observed. In the spectra in columns 33. and 34., the separation between the lines and, consequently, between the nets is equal to the distance between the close-packed nets in the simple cubic and body-centered cubic structures along the threefold axis, respectively. Column 33. contains no spectra with four different atoms. The spectra in column 34. vary more significantly. Spectrum 34.8 exhibits four different lines corresponding to Na, Si, Al, and □ (vacancy with an imaginary line). Moreover, spectrum 34.11 in this column is similar to the spectra of the loparite cationic motifs $Ca_1Na_3Ti_2(Ti,Nb)_2O_3$ [12], ($Ca_1Na_3Ti_4$ · $Ca_1Na_3(Ti,Nb)_4$) [20] Bi_2O_3 ($□_1O_3Bi_4$ · $□_1O_3□_4$) [2], Cu_2O ($O_1□_3Cu_4$ · $O_1□_3□_4$) [2], and $LnAlO_3(Ln_4Al_4)$ [21].

The spectra depicted in Fig. 4 can be obtained from spectrum 31.1 by removing a number of lines: line I (spectrum 41.11) or lines I and X (spectrum 41.1). Spectra 41.2–41.8 are similar to spectrum 41.1. Among spectra 41.9–41.12, the last spectrum corresponds to tungsten bronze. Spectrum 42.12 represents the spinel structural type and the Laves–Friauf phase $MgCu_2$. Recall that, in a spinel structure, the cations occupy a number of tetrahedral holes (with an occupancy of 1/7) and octahedral holes (with an occupancy of 1/2) in an ordered manner. Therefore, the cationic component of the spinel structure is nothing more than an ordered subtraction isomorph. Spectrum 41.12 contains three

lines *I* between the lines of the *X*-type nets. Spectrum 42.12 is similar to many spectra, for example, spectra 42.11, 42.13, and 43.1–43.6. Furthermore, spectrum 42.12 is a constituent of the combined spectra of two structural minals (spectra 42.5, 42.8, and 42.9). It is also easy to trace the similarities and differences between other spectra.

In the spectra shown in Fig. 2, the lines of the *I*-type nets are located between the lines of the *X*-type nets. At the same time, the lines of the *I*-type nets in the spectra depicted in columns 51. and 52. (Fig. 5) coincide with those of the *X*-type nets. Although the spectra in Fig. 5 exhibit a wide variety of shapes, the spectra with a similar structure can be distinguished in this case, too. For example, spectra 53.1, 53.2, and 53.3 are similar to the spectrum of V_3Si; moreover, spectra 52.9, 51.2, 51.3, and 51.1 are similar to the spectra of FeS_2, Fe_2P, Th_3Pd_5, and $Y(OH)_3$, respectively.

The above analysis of the spectra has demonstrated that structural types of different compositions can exhibit similar structural cationic motifs. In [13], the cationic motifs were described by the diagram method using the appropriate letters and formulas. In the present work, the structural diagrams were represented in the form of spectra. Both methods offer a number of advantages and disadvantages. Additional information on the manifestation of ordered isomorphism can be extracted from the representation of the obtained results in the form of point projections, polyhedra, etc. The cationic spectra can be used in the identification of the structures of interest, because the cationic spectrum of the structure under investigation can be compared with the spectra presented in this work.

REFERENCES

1. N. V. Belov, *Structure of Ionic Crystals and Metal Phases* (Akad. Nauk SSSR, Moscow, 1947).

2. N. L. Smirnova, Kristallografiya **4** (1), 20 (1959) [Sov. Phys. Crystallogr. **4**, 17 (1959)].

3. S. V. Borisov, *Crystallography + Stereochemistry: XVI Scientific Readings in Honor of Academician N. V. Belov* (Nizhegorod. Gos. Univ., Nizhniĭ Novgorod, 1997), p. 22.

4. M. O'Keefe and B. G. Hyde, Struct. Bonding (Berlin) **61**, 77 (1985).

5. S. V. Krivovichev and S. K. Filatov, *Crystal Chemistry of Minerals and Inorganic Compounds with Complexes of Anion-Centered Octahedra* (Sankt-Peterb. Gos. Univ., St. Petersburg, 2001).

6. R. V. Galiulin, Usp. Fiz. Nauk **172** (2), 229 (2002).

7. G. B. Bokiĭ, *Introduction to Crystal Chemistry* (Mosk. Gos. Univ., Moscow, 1954).

8. N. L. Smirnova, Kristallografiya **1** (2), 165 (1956) [Sov. Phys. Crystallogr. **1**, 128 (1956)].

9. N. L. Smirnova and L. S. Mezhueva, Zh. Strukt. Khim. **7**, 566 (1966).

10. N. L. Smirnova, T. V. Mel'chakova, and R. E. Chigar'kova, Zh. Strukt. Khim. **10** (6), 1076 (1969).

11. N. L. Smirnova, Vestn. Mosk. Univ., Ser. Geol., No. 2, 100 (1967).

12. N. L. Smirnova, V. I. Artyushina, and M. P. Anisimova, Vestn. Mosk. Univ., Ser. Geol., No. 1, 73 (1969).

13. N. L. Smirnova, Vestn. Mosk. Univ., Ser. Geol., No. 3, 53 (1974).

14. N. L. Smirnova, *Crystal Chemistry of Inorganic Compounds* (Shtiintsa, Kishinev, 1976), p. 184.

15. N. V. Belov, *Essays on Structural Mineralogy* (Nedra, Moscow, 1976).

16. W. B. Pearson, *The Crystal Chemistry and Physics of Metals and Alloys* (Wiley, New York, 1972; Mir, Moscow, 1977), Parts 1, 2.

17. P. I. Kripyakevich, *Structural Types of Intermetallic Compounds* (Nauka, Moscow, 1977), p. 288.

18. S. V. Borisov, Kristallografiya **45** (5), 779 (2000) [Crystallogr. Rep. **45**, 709 (2000)].

19. V. S. Urusov, N. A. Dubrovinskaya, and L. S. Dubrovinskiĭ, *Design of Probable Crystal Structures of Minerals* (Mosk. Gos. Univ., Moscow, 1990).

20. N. V. Zubkova, A. V. Arakcheeva, D. Yu. Pushcharovskiĭ, and E. I. Semenov, Kristallografiya **45** (2), 242 (2000) [Crystallogr. Rep. **45**, 210 (2000)].

21. A. Rames-Gallarda and A. Vegar, Solid State Chem. **128** (1), 69 (1997).

Translated by O. Borovik-Romanova

X-ray Specular Reflection under Conditions of Extremely Asymmetric Noncoplanar Diffraction from a Bicrystal

V. A. Bushuev and A. P. Oreshko

Physics Department, Moscow State University, Vorob'evy gory, Moscow, 119899 Russia

e-mail: oreshko@mail.ru

Received March 21, 2002

Abstract—The angular dependence of the intensities of X-ray specular reflection has been rigorously analyzed under conditions of noncoplanar grazing Bragg diffraction in a crystal coated with a crystalline film (bicrystal). It is shown that the anomalous angular dependence of the specular-reflection intensity is extremely sensitive to the thickness (from fractions of a nanometer up to several nanometers), deformation, and the amorphization degree of the crystalline films. The optimum conditions for recording intensities are attained at grazing angles equal to 1.5–4.0 of the critical angle of the total external reflection. © 2003 MAIK "Nauka/Interperiodica".

INTRODUCTION

Recently, extremely asymmetric X-ray diffraction has been widely used in the diagnostics of the subsurface layers of semiconductor crystals [1–3]. For the first time, an extremely asymmetric diffraction scheme was used in the case where the reflecting atomic planes formed with the crystal surface an angle approximately equal to the Bragg angle, whereas an incident or a diffracted beam forms with the surface a small angle close to the angle of the total external reflection [4, 5]. In this case, X-ray specular reflection starts playing an important role, which considerably reduces the penetration depth of the field in the crystal and allows one to study ultrathin layers with thicknesses of the order of 10 nm. The shortcoming of the extremely asymmetric coplanar system is the requirement that the specimen surface have a special orientation, which hinders the use of these schemes in surface diagnostics.

In [6], a new scheme of noncoplanar diffraction from the reflecting planes normal to the crystal surface was suggested (the tilt angle with respect to the normal is $\psi = 0$). In this case, both incident and diffracted beams may simultaneously form small angles φ_0 and φ_h with the surface and experience strong specular reflection. Experimentally, this diffraction geometry was used in [7] for studying 7.5 to 200.0-nm-thick crystalline aluminum films grown on a GaAs substrate.

Unlike the conventionally used two-wave approximation [1–3], the analysis of diffraction in the grazing geometry requires a rigorous solution of the equations of the dynamical theory. This theory (in the case $\psi = 0$, based on the solution of a biquadratic dispersion equation) has been constructed for both ideal single crystals [8, 9] and crystals coated with an amorphous [10] or crystalline [11] film. It was shown that the diffraction reflection (rocking) curves are very sensitive to the

degree of perfection of the subsurface layers with the thicknesses of several nanometers or higher. The results of the corresponding experiments are considered elsewhere [1, 3].

In practice, cutting and the subsequent treatment of crystals do not allow one to obtain surfaces that are strictly parallel to the atomic planes. Therefore, the theory of the grazing X-ray diffraction from an ideal crystal whose planes form a small tilt angle $\psi \neq 0$ with the surface normal was developed [12, 13], and it was shown that even small tilt angles (several angular minutes) can considerably change the shape of the diffraction reflection curves.

In the most general case $\psi \neq 0$, one has to solve the fourth-degree dispersion equation, which can be solved only numerically. The problem is simplified at the grazing angles φ_0 or φ_h exceeding the critical angle of total external reflection, where the effect of the specularly reflected wave on diffraction drastically decreases. In this connection, the approximate modified dynamical theory of diffraction was developed [14–16], which allows one to solve the problem analytically in the whole range of the angles φ_0 and φ_h except for a narrow interval in the vicinity of the critical angle of the total external reflection for both ideal crystals [14, 15] and crystals coated with homogeneous amorphous films [16], and also for crystals with imperfect crystal structures in thin subsurface layers [14].

The theory of grazing diffraction was further developed in [17, 18], where the method for studying the curves of grazing X-ray diffraction from multilayer crystal structures and superlattices was considered on the basis of the solution of the problem of the dynamical diffraction in each layer. It was shown that the curves of the diffraction reflection are very sensitive to deformation $\Delta a/a \sim 10^{-3}$ of the 10-nm-thick layer of

crystalline germanium on the surface of a perfect Ge crystal [18].

In all the above studies, attention was focused on the analysis of the diffraction reflection, whereas the angular dependence of the intensities of specular reflection was ignored. At the same time, as was first indicated in [3] and then considered in detail theoretically in [19] and observed experimentally in [20], the angular behavior of grazing reflection in the diffraction region at fixed grazing angles is essentially dependent on the presence of ultrathin amorphous films on the surface and their thicknesses.

This study continues the investigation of the specular reflection of X-rays under the simultaneous fulfillment of the conditions of extremely asymmetric noncoplanar Bragg diffraction begun in [19]. Based on a rigorous solution of the fourth-degree dispersion equation, we performed a detailed analysis of the angular dependences of the specular and diffraction reflection from a bicrystal in the whole range of the grazing and tilt angles of the reflecting planes. It is shown that the specular-reflection curves are extremely sensitive to the parameters of homogeneous crystalline films on the crystal surface.

THEORY OF SPECULAR REFLECTION FROM A BICRYSTAL

Consider the formation of the curves of diffraction and specular reflection from a homogeneous plane-parallel film of arbitrary thickness d with interplanar spacings $a = a_0 + \Delta a$, the Fourier components of polarizability χ_{01} and χ_{h1}, and the reciprocal-lattice vector $\mathbf{h}_1$. The substrate is a single crystal with the reflecting planes forming an angle $\psi \ll 1$ with the surface normal $\mathbf{n}$ directed into the crystal along the z axis and characterized by the Fourier components of polarizability χ_0 and χ_h, the reciprocal-lattice vector $\mathbf{h}$, and the interplanar spacings a_0. The rigorous solution of the problem of dynamical diffraction can be obtained under the condition of equality of the tangential (along the crystal surface) components of the reciprocal-lattice vector, $h_{1t} = h_t$. In this case, the tilt angles of the film ψ_1 are determined from the condition $\cos\psi_1 = (1 + \delta)\cos\psi$, where $\delta = \Delta a/a_0$ is deformation. In the opposite case, one has to analyze the interference of the multiply scattered radiation which, in the film, consists of an infinite set of plane waves [21].

A plane monochromatic X-ray wave $\mathbf{E}_0\exp(i\mathbf{k}_0\mathbf{r})$ is incident from vacuum onto a bicrystal at a grazing angle φ_0 to the surface, so that, simultaneously, the diffraction reflection from the atomic planes of the substrate takes place. The fields in vacuum above the bicrystal surface and in the substrate have the form

$$\mathbf{E}_{\text{vac}}(\mathbf{r}) = \mathbf{E}_0\exp(i\mathbf{k}_0\mathbf{r}) + \mathbf{E}_s\exp(i\mathbf{k}_s\mathbf{r}) + \mathbf{E}_h\exp(i\mathbf{k}_h\mathbf{r}), \quad (1)$$

$$\mathbf{E}_{\text{cr}}(\mathbf{r}) = \sum_j \mathbf{D}_{0j}\exp(i\mathbf{q}_{0j}\mathbf{r}) + \sum_j \mathbf{D}_{hj}\exp(i\mathbf{q}_{hj}\mathbf{r}), \quad (2)$$

where E_0, E_s, and E_h are the amplitudes of the incident, specularly reflected, and diffracted waves, respectively; $|\mathbf{k}_0| = |\mathbf{k}_s| = |\mathbf{k}_h| = k_0 = 2\pi/\lambda$ is the length of the wave vector in vacuum and λ is the wavelength; $k_{sz} = -k_{0z}$; $\mathbf{q}_{0j} = \mathbf{k}_0 + k_0\varepsilon_{\text{cr}j}\mathbf{n}$ and $\mathbf{q}_{hj} = \mathbf{q}_{0j} + \mathbf{h}$ are the wave vectors; and D_{0j} and D_{hj} are the amplitudes of the transmitted and diffracted waves in the substrate ($j = 1, 2$). The values of $\varepsilon_{\text{cr}j}$ are determined from the solution of the general dispersion equation of the dynamical theory [1, 3]

$$(\varepsilon^2 + 2\gamma_0\varepsilon - \chi_0)(\varepsilon^2 + 2\gamma_{h0}\varepsilon - \chi_0 - \alpha) - C^2\chi_h\chi_{\bar{h}} = 0, (3)$$

where $\gamma_0 = \cos(\mathbf{k}_0, \mathbf{n})$ and $\gamma_{h0} = \cos(\mathbf{k}_0 + \mathbf{h}, \mathbf{n})$ are the directional cosines of the incident and diffracted waves, respectively; $C = 1$ and $C = \cos2\theta$ for the σ- and π-states of the radiation polarization and θ is the angle formed by the incident radiation and the reflecting planes of the substrate; and the parameter $\alpha = 2(\theta - \theta_B)\sin2\theta_B$ characterizes the deviation of the diffraction angle $\Delta\theta = \theta - \theta_B$ from the exact Bragg angle of the substrate θ_B, which is determined by the relationship $h = 2k_0\sin\theta_B$. If φ_0 is the grazing incidence angle, then

$$\gamma_0 = \sin\varphi_0, \quad \gamma_{h0} = \gamma_0 - \psi_B, \quad (4)$$

where $\psi_B = 2\sin\psi\sin\theta_B$ is the effective parameter of the tilt angle of the reflecting planes in the substrate. The diffraction reflection into the region $z < 0$ (Bragg geometry) is observed at such grazing angles φ_0 that $\gamma_0 < \psi_B$, i.e., $\gamma_{h0} < 0$ in (4).

In the general case, Eq. (3) is a fourth-degree equation with respect to ε and, therefore, has four roots ε_j. If the substrate is thick, the solutions should be chosen based on the condition $\text{Im}\,\varepsilon_j > 0$. In the Bragg geometry, this condition is met only by two roots (see [12]) denoted here as $\varepsilon_{\text{cr}1}$ and $\varepsilon_{\text{cr}2}$.

In the case of a crystalline film of a finite thickness, one has to take into account four roots in dispersion equation (3); therefore, the field in the film consists of four transmitted and four diffracted waves,

$$\mathbf{E}_f(\mathbf{r}) = \sum_j \mathbf{A}_{0j}\exp(i\mathbf{a}_{0j}\mathbf{r}) + \sum_j \mathbf{A}_{hj}\exp(i\mathbf{a}_{hj}\mathbf{r}), \quad (5)$$

where A_{0j} and A_{hj} are the amplitudes and $\mathbf{a}_{0j} = \mathbf{k}_0 + k_0\varepsilon_{fj}\mathbf{n}$ and $\mathbf{a}_{hj} = \mathbf{a}_{0j} + \mathbf{h}_1$ are the wave vectors of the transmitted and diffracted waves in the crystal film ($j = 1, 2, 3, 4$). The ε_{fj} values are determined from the solution of dispersion equations (3) in which the following replacements are made:

$$\chi_0 \longrightarrow \chi_{01}, \quad \chi_h \longrightarrow \chi_{h1}, \quad \chi_{\bar{h}} \longrightarrow \chi_{\bar{h}1},$$

$$\alpha \longrightarrow \alpha_1 = 2(\theta - \theta_B - \Delta\theta_f)\sin2\theta_B,$$

$$\gamma_{h0} \longrightarrow \gamma_{h01} = \gamma_0 - \psi_{B1},$$

where $\Delta\theta_f = -2\delta\tan\theta_B + \delta\sin\varphi_0/(\sin\psi\cos\theta_B)$ is the displacement of the maximum of the diffraction reflection curve of the film from the maximum of the diffraction reflection curve of the substrate, $\psi_{B1} = 2\sin\psi_1\sin\theta_{B1}$ is the effective parameter of the tilt angle of the reflecting planes of the film, and θ_{B1} is the Bragg angle of the film.

It follows from the basic system of dynamical equations [1] that the amplitudes of the diffracted and transmitted waves in the film and the substrate are related as $A_{hj} = R_{aj}A_{0j}$, $D_{hl} = R_{0l}D_{0l}$ ($j = 1$–4, $l = 1, 2$) where

$$R_{aj} = (\varepsilon_{fj}^2 + 2\gamma_0\varepsilon_{fj} - \chi_{01})/C\chi_{\bar{h}1},$$
$$R_{0l} = (\varepsilon_{crl}^2 + 2\gamma_0\varepsilon_{crl} - \chi_0)/C\chi_{\bar{h}}. \tag{6}$$

In order to determine the field amplitudes in Eqs. (1), (2), and (5), we write the continuity condition for the tangential components of the electric and magnetic fields at the upper and lower boundaries of the film. We also have to take into account that at grazing angles, the continuity of the magnetic field is equivalent to the continuity of the first derivative of the electric field with respect to the coordinate z. As a result, we arrive at the following system of eight equations. At the vacuum–film boundary, we have

$$E_0 + E_s = \sum_j A_{0j}, \quad \gamma_0(E_0 - E_s) = \sum_j \Gamma_{f0j}A_{0j},$$
$$E_h = \sum_j R_{aj}A_{0j}, \quad -\gamma_h E_h = \sum_j \Gamma_{fhj}R_{aj}A_{0j}. \tag{7.1}$$

At the film–substrate boundary, we have

$$\sum_j \Gamma_{f0j}A_{0j}g_{fj} = \sum_l \Gamma_{cr0l}D_{0l}g_{crl},$$
$$\sum_j R_{aj}A_{0j}g_{fj}\tau_f = \sum_l R_{0l}D_{0l}g_{crl}\tau_{cr}, \tag{7.2}$$
$$\sum_j \Gamma_{fhj}R_{aj}A_{0j}g_{fj}\tau_f = \sum_l \Gamma_{crhl}R_{0l}D_{0l}g_{crl}\tau_{cr},$$

where $j = 1$–4, $l = 1, 2$, $\gamma_h = \sin\varphi_h$ ($\varphi_h > 0$), and φ_h is the angle of the diffracted-radiation exit into vacuum with respect to the surface; at the given angles φ_0 and ψ, the exit angle φ_h is determined by equation $\gamma_h = (\gamma_{h0}^2 + \alpha)^{1/2}$ [12] and the condition $\alpha > -\gamma_{h0}^2$ sets the admissible deviations $\Delta\theta$ from the Bragg angles; and $g_{fj} = \exp(ik_0\varepsilon_{fj}d)$, $g_{crl} = \exp(ik_0\varepsilon_{crl}d)$, $\tau_f = \exp(-ik_0\psi_{B1}d)$, and $\tau_{cr} = \exp(-ik_0\psi_B d)$ are the coefficients that take into account the change in the phases of the waves and their absorption during their propagation in the film. We used the following notation:

$$\Gamma_{f0j} = \gamma_0 + \varepsilon_{fj}, \quad \Gamma_{fhj} = \Gamma_{f0j} - \psi_{B1},$$
$$\Gamma_{cr0l} = \gamma_0 + \varepsilon_{crl}, \quad \Gamma_{cr0l} - \psi_B. \tag{8}$$

The solution of system (7) for the amplitude coefficients $R_S = E_s/E_0$ of the specular reflection and $R_h = E_h/E_0$ of the Bragg reflection have the following form:

$$R_S = \sum_j (\gamma_0 - \Gamma_{f0j})Q_j / \sum_j (\gamma_0 + \Gamma_{f0j})Q_j,$$
$$R_h = (\gamma_0/\gamma_h)\sum_j R_{aj}(\gamma_h - \Gamma_{fhj})Q_j / \sum_j (\gamma_0 + \Gamma_{f0j})Q_j. \tag{9}$$

Here, Q_j are the coefficients relating the amplitudes of the transmitted waves in the field: $A_{0j} = Q_j A_{01}$. For a crystalline film, the coefficients take the form

$$Q_1 = 1,$$
$$Q_2 = -\sum_j R_{aj}(\gamma_h + \Gamma_{fhj})U_{1j} / \sum_j R_{aj}(\gamma_h + \Gamma_{fhj})U_{2j}, \tag{10}$$
$$Q_k = (-1)^{k+1}(U_{1k} + U_{2k}Q_2) \quad (k = 3, 4),$$

where the following notation was used

$$U_{j3, j4} = (g_{fj}/g_{f3, f4})(T_{1j}T_{24, 23} - T_{2j}T_{14, 13})/(T_{14}T_{23} - T_{24}T_{13}),$$
$$T_{1j, 2j} = R_{02, 01}(\Gamma_{cr01, 2} - \Gamma_{f0j})\tau_{cr} - R_{aj}(\Gamma_{crh1, 2} - \Gamma_{fhj})\tau_f. \tag{11}$$

Relationships (9)–(11) are the rigorous solution of the problem of the specular and diffraction reflection of X-rays from single crystals coated with homogeneous crystalline films. These relationships are valid for all the grazing angles φ_0 and the exit angles φ_h at $\gamma_0 < \psi_B$ and any admissible deviations $\Delta\theta$ from the exact Bragg angle.

Consider some limiting cases. If $d = 0$ (there is no film), then $g_{fj} = g_{crl} = \tau_f = \tau_{cr} = 1$ ($j = 1$–4, $l = 1, 2$), and general formulas (9) are reduced to the formulas that describe the specular and diffraction reflection from an ideal single crystal [19]. For a thick film, one has to select the solutions of the diffraction equation in the film proceeding from the condition $\text{Im}\varepsilon_{fj} > 0$. The absorption factor $g_{fj} \longrightarrow 0$ and $g_{crj} \longrightarrow 0$ and formulas (9) coincide with the corresponding formulas for a medium that has film parameters.

Now, consider a homogeneous amorphous film on the surface of a single crystal. Two waves (transmitted and specularly reflected) excited by the incident radiation, A_{01} and A_{02}, and two waves excited by the Bragg wave that enter the film from the crystal, A_{h2} and A_{h1}, propagate in the film. In this case, $\Gamma_{f01} = -\Gamma_{f02} = (\gamma_0^2 + \chi_{01})^{1/2}$ and $\Gamma_{fh1} = -\Gamma_{fh2} = (\gamma_h^2 + \chi_{01})^{1/2}$, $Q_{3, 4} = 0$, $R_{a3, 4} = 0$, and $R_{a1, 2}$ are the coefficients relating the amplitudes of the waves in the film; i.e., $A_{h1, 2} = R_{a1, 2}A_{01, 2}$. The coefficients $R_{a1, 2}$ are not determined by Eqs. (6) but from the solution of the system of the boundary equations. Thus, formulas (9) are reduced to the expressions

that describe the specular and diffraction reflection from a single crystal coated with an amorphous film [19].

In the range where the grazing angle φ_0 is much larger than the critical angle of the total external reflection $\varphi_c = \arcsin(|\chi_0|^{1/2})$, the roots of the dispersion equation (3) have considerably different values. With due regard for the smallness of polarizabilities χ_h and χ_{h1}, one can show that $\varepsilon_{f1,f2} \approx -\gamma_0 \pm (\gamma_0^2 + \chi_{01})^{1/2}$ and $\varepsilon_{f3,f4} \approx |\gamma_{h0}| \pm (\gamma_{h0}^2 + \alpha_1 + \chi_{01})^{1/2}$, and $\varepsilon_{cr1} \approx \chi_0/2\gamma_0$, $\varepsilon_{cr2} \approx 2|\gamma_{h0}| + (\alpha + \chi_0)/2|\gamma_{h0}|$. A rigorous numerical solution of Eq. (3) gives the same results, whence it follows that $R_{a1,2} \ll R_{a3,4}$ and $R_{01} \ll R_{02}$, i.e.,

$$U_{13} \approx 0, \quad Q_2 \approx 0, \quad Q_3 \approx 0,$$

$$Q_4 \approx -U_{14} \approx -(R_{a1}\tau_f - R_{01}\tau_{cr})g_{f1}/(R_{a4}\tau_f - R_{01}\tau_{cr})g_{f4}.$$

Since $\varepsilon_{f1}, \varepsilon_{f4}, \varepsilon_{cr1} \ll \gamma_0$, then $R_S \ll 1$; therefore, one can ignore the effect of specular reflection on the diffraction process. At the same time, the specific behavior of the total wave field in a crystal in the region of strong diffraction reflection from the substrate dramatically affects the angular dependence of the specular reflection. As a result, Eqs. (9) for the amplitude coefficients of the diffraction and specular reflection yield the following expressions:

$$R_h = \frac{R_{a1} + Q_4 R_{a4}}{1 + Q_4},$$

$$R_S = \frac{(\gamma_0 - \Gamma_{f01}) + Q_4(\gamma_0 - \Gamma_{f04})}{(\gamma_0 + \Gamma_{f01}) + Q_4(\gamma_0 + \Gamma_{f04})}, \quad (12)$$

which coincide with the corresponding expression obtained for a bicrystal in the two-wave approximation of large grazing angles in [22].

RESULTS AND DISCUSSION

Figure 1 and 2 show the curves of the diffraction $P_h = (\gamma_h/\gamma_0)|R_h|^2$ and specular $I_S = |R_S|^2 I_0$ reflection, where I_0 is the intensity of the X-ray beam incident onto a silicon single crystal coated with a film of crystalline silicon at different film thicknesses and grazing angles. As is seen from Fig. 1, the diffraction reflection curves are sensitive to the thicknesses of coating crystalline films, which is seen from the thickness oscillations. At large grazing angles and deviations from the exact Bragg condition, it follows from Eq. (12) that the oscillation period is determined by the expression $\Delta\theta = -4\pi\gamma_{h01}/(k_0 d \sin 2\vartheta_B)$; for the parameters that were used in the calculation of curve 5 in Fig. 2c, $\Delta\theta \approx 600''$. With an increase in the grazing angle, the oscillation period and the intensity of the reflected signal drastically decrease (cf. Figs. 1a, 1c). At the same time, the situation for the specular reflection curves (Fig. 2) is quite different. The angular dependences of specular reflection have extremely high sensitivity to the presence and

the thicknesses of the crystalline films: with an increase in the grazing angle, the sensitivity increases (cf. Figs. 2a, 2c), whereas the intensity of the useful signal increases by two to three orders of magnitude.

The most interesting situation is observed at the grazing angles $\varphi_{0,h} > \varphi_c$ for silicon $\varphi_c = 13.38'$. In this case, the specular reflection curves show very high sensitivity to the presence of a very thin disturbed layer on the surface, whose thickness can be of several nanometers (Figs. 2b, 2c).

As was first noted in [3] and then considered in detail for an ideal crystal and a crystal coated with an amorphous film in [19], the characteristic feature of specular reflection under the diffraction conditions is a pronounced anomaly in the angular dependence $I_S(\Delta\theta)$, which is of the dispersion type with the minimum and maximum in the vicinity of the diffraction angles $\Delta\theta_{1,2} = \Delta\theta_0 \mp \Delta\theta_B$ corresponding to the boundaries of the region of the total diffraction reflection:

$$\Delta\theta_0 = -\chi_0(1 + b)/(2b \sin 2\theta_B),$$

$$\Delta\theta_B = C|\chi_h|/(b^{1/2} \sin 2\theta_B),$$

where $b = -\gamma_0/\gamma_{h0}$ is the asymmetry coefficient of the Bragg reflection ($b > 0$).

It should be noted that the curves of the secondary-radiation yield $I_{SP} \sim 1 + |R_h|^2 + 2\sigma \mathrm{Re} R_h$ with a yield depth that is small in comparison with the extinction length $L_{ex} = \lambda(\gamma_0|\gamma_{h0}|)^{1/2}/\pi C|\chi_h|$, where $\sigma = C|\chi_{hi}|/\chi_{0i}$, $\chi_{gi} = \mathrm{Im}\chi_g$ [1, 3, 23], have approximately the same shape. The analogy becomes more obvious if the quantity Q_4 in (12) is expressed in terms of the amplitude coefficient of the diffraction reflection R_h. Then the amplitude of the specular reflection is

$$R_S \approx -(\chi_0/4\gamma_0^2)(1 + \sigma_s R_h), \quad (13)$$

where $\sigma_s = Cb_f^{1/2}(\chi_{h1}\chi_{\bar{h}1})^{1/2}/\chi_{01}$. Similar to the method of X-ray standing waves (XRSW) [1, 23], the second factor in (13) characterizes the amplitude of the total field on the bicrystal surface. However, the value of σ_s in (13) is not determined by the relative ratio of the imaginary parts of the Fourier components of the polarizabilities χ_h and χ_0 any more. Despite the fact that, at the grazing angles $\varphi_0 > \varphi_c$, the coefficient of specular reflections is very small, the intensity of this reflection can considerably (by several orders of magnitude, all other conditions being the same [20]) exceed the photoelectron or fluorescent quantum yield in the XRSW method.

The presence of the minimum and maximum on the specular-reflection curve $I_S(\Delta\theta)$ (13) is explained by the fact that, in the region of diffraction reflection, $P_h \approx 1$, and the phase R_h changes almost linearly from π at $\Delta\theta = \Delta\theta_1$ to zero at $\Delta\theta = \Delta\theta_2$. In this case, $R_h(\Delta\theta_{1,2}) \approx \mp b_f^{1/2}$, i.e., has different signs, which results in the formation
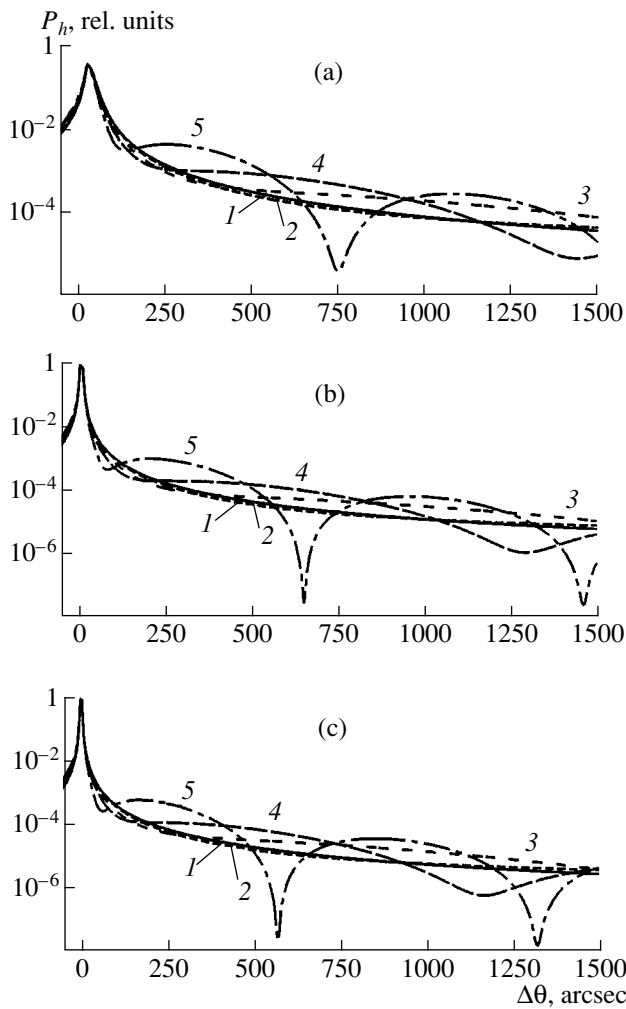
Fig. 1. Effect of the thickness of the surface crystalline silicon film on the shape of the diffraction-reflection curves depending on the angular deviation $\Delta\theta$ from the Bragg angle of the substrate (Si) at the grazing angles φ_0 = (a) 13′, (b) 25′, and (c) 45′. The film thickness d (nm) is (*1*) 0 (ideal crystal), (*2*) 1, (*3*) 2, (*4*) 3, (*5*) 5. CuK_α radiation, Si(220) reflection, ψ = 3°, the amorphization factor F_{am} = 1, deformation $\delta = -4 \times 10^{-4}$.

Fig. 2. Effect of the thickness of the surface crystalline silicon film on the shape of the angular curves of the specular-reflection intensities depending on the angular deviation $\Delta\theta$ from the Bragg angle at the grazing angles φ_0 = (a) 13′, (b) 25′, and (c) 45′. The film thickness d (nm): (*1*) 0 (ideal crystal), (*2*) 1, (*3*) 2, (*4*) 3, (*5*) 5, amorphization factor F_{am} = 1, deformation $\delta = -4 \times 10^{-4}$. The intensity of incident radiation I_0^5 pulse/s.

of the minimum and maximum on the specular-reflection curve I_S. At small grazing angles ($\gamma_0 \ll \psi_B$), the asymmetry coefficient of reflection $b_f \ll 1$. With an increase in the angle φ_0, at $\gamma_0 \approx \psi_B$, we have $b_f \gg 1$, and the contrast of the specular-reflection curve I_S increases.

The penetration depth of the field under conditions of specular reflection and large grazing angles obeys the inequality $L_s \gg L_{ex}$, where $L_s = \lambda/(2\pi \mathrm{Im}\gamma_s)$, and $\gamma_s = (\gamma_0^2 + \chi_0)^{1/2}$. Therefore, the formation of the refracted wave is determined by the coherent superposition of the transmitted and diffracted waves. Unlike this situation, in the region of small angles $\varphi_0 \leq \varphi_c$, the penetration depth of the field $L_s \leq L_{ex}$; i.e., it is determined mainly

by the total external reflection. Diffraction reflection occurs in a thinner layer, which results in a decrease in the amplitude of the maximum of the diffraction-reflection curve and, simultaneously, in its broadening (Fig. 1a). The specular-reflection curve in this case is pronouncedly smoothened and acquires the shape of a shallow minimum (Fig. 2a). For the parameters used in the calculation of the curves in Figs. 1 and 2, the penetration depths L_s = 1.9 μm, L_{ex} = 0.5 μm, and b_f = 0.69; L_s = 0.6 μm, L_{ex} = 0.2 μm, and b_f = 0.19; and L_s = 0.03 μm, L_{ex} = 0.13 μm, and b_f = 0.12 at the grazing angles φ_0 = 50″, 20″, and 13″, respectively.

At large grazing angles and pronounced angular deviation from the exact Bragg condition for the crystalline film, the amplitude coefficient of specular reflec-
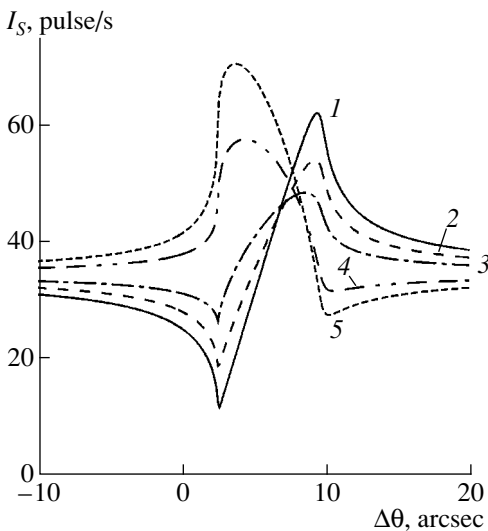
$I_S \times 10^{-3}$, pulse/s
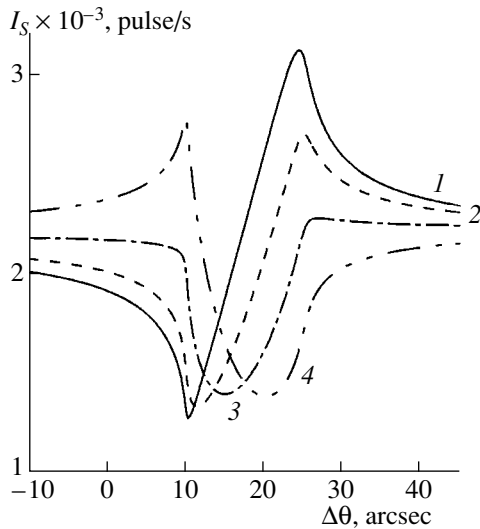
Fig. 3. Effect of deformation of the crystal film on the shape of the angular dependences of the intensities of specular reflection. Deformation $\delta \times 10^{-4}$: (*1*) 0 (ideal crystal), (*2*) 2, (*3*) 4, (*4*) 6. Grazing angle $\varphi_0 = 20'$. Thickness of the Si film $d = 5$ nm. Amorphization factor $F_{am} = 1$.

tion given by Eqs. (12) can be written in the convenient form

$$R_S \approx -(\chi_{01}/4\gamma_0^2)\{1 - R_{01}C_f(\tau_{cr}/\tau_f)\exp(i\omega)/\chi_{01}\}, (14)$$

where, in accordance to [23], the following notation is

introduced:

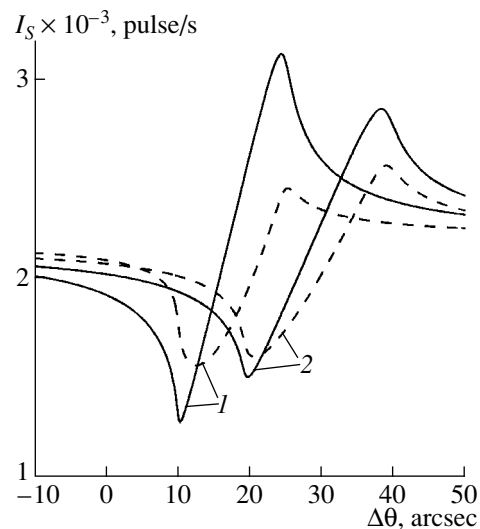$$y_1 = [\alpha_1 b_f + \chi_{01}(1 + b_f)]/2C_f, \quad y_{12} = (y_1^2 - 1)^{1/2},$$

$$C_f = Cb_f^{1/2}(\chi_{h1}\chi_{\bar{h}1})^{1/2}, \quad \omega = k_0 C_f d y_{12}/\gamma_0.$$

The quantity y_1 characterizes the deviation from the exact Bragg condition for the crystalline film.

The first term in (14) describes the behavior of the specular-reflection curve from the film far from the diffraction condition. The second term describes the dispersion behavior and the thickness oscillations (caused by the presence of the film) on the angular dependence of the specular reflection. A further increase in the film thickness results in a lower contrast of the specular-reflection curve in the region of diffraction reflection from the substrate and an increase in the contrast in the region of diffraction reflection from the film.

Figures 3 and 4 show the angular dependences of specular reflection from a bicrystal with various deformations δ and amorphization factors F_{am} of the film ($\chi_{h1} = F_{am}\chi_h$), respectively. As was indicated above, the diffraction-reflection curves of thin films are almost the same as those of the substrate. At the same time, even insignificant changes in the deformation and amorphization factor of the film lead to considerable changes in the shape of the specular-reflection curves in the region of diffraction reflection from the substrate.

Figure 5 shows the specular-reflection curves from a bicrystal at various tilt angles ψ of the reflecting planes of the substrate. It is seen that the sensitivity of the

I_S, pulse/s

Fig. 4. Effect of the amorphization factor of the crystalline film on the shape of the angular dependences of the specular-reflection intensity. Amorphization factor F_{am}: (*1*) 1 (ideal crystal, (*2*) 0.8, (*3*) 0.6, (*4*) 0.2, (*5*) 0 (amorphous film). Grazing angle $\varphi_0 = 50'$. Thickness of the Si film $d = 2$ nm. Deformation $\delta = 0$.

$I_S \times 10^{-3}$, pulse/s

Fig. 5. Effect of the tilt angle of the atomic planes ψ on the angular dependence of the specular-reflection intensity from a bicrystal (dash lines) and an ideal crystal (solid lines). The tilt angle (*1*) $\psi = 3°$ and (*2*) $\psi = 5°$. Grazing angles $\varphi_0 = 20'$. Thickness of the Si film $d = 4$ nm. Amorphization factor $F_{am} = 1$, deformation $\delta = 4 \times 10^{-4}$.

angular dependence of specular reflection increases with a decrease in the tilt angle.

CONCLUSIONS

The rigorous dynamical theory of specular reflection of X-rays from a bicrystal under conditions of extremely asymmetric diffraction and specular reflection are solved in the general form so that the results obtained are valid in the whole range of grazing angles of an incident beam and exit angles of diffracted radiation.

It is shown that the angular dependence of the specular-reflection intensity is very sensitive to the presence, thickness, deformation, and degree of amorphization of a thin (from fractions of a nanometer to several nanometers) crystalline film in the crystal surface. The problem can readily be generalized to the case of grazing and diffraction reflection from an arbitrary multilayer structure with any profiles of the variations in polarizability, deformation, and the amorphization factor.

The intensity of the specular reflection is sufficiently high and allows one to perform rapid analysis of thin subsurface and transient layers. The sensitivity of the method to the film thickness is about 0.5 nm and increases with an increase in the grazing angle; however, the intensity of the reflected signal simultaneously decreases. The optimum grazing angles range from one and a half to three to four critical angles of the total external reflection. At smaller grazing angles, the intensity of specular reflection increases; however, the sensitivity considerably decreases.

Thus, the results obtained show that it is possible to perform rapid nondestructive analysis of the structure of superthin subsurface layers and the interfaces using the specular-reflection data obtained under conditions of grazing Bragg diffraction.

REFERENCES

1. A. M. Afanas'ev, P. A. Aleksandrov, and R. M. Imamov, *X-ray Diffraction Diagnostics of Submicron Layers* (Nauka, Moscow, 1989).

2. M. A. Andreeva, S. F. Borisova, and S. A. Stepanov, Poverkhnost, No. 4, 5 (1985).

3. A. M. Afanas'ev and R. M. Imamov, Kristallografiya **40** (3), 446 (1995) [Crystallogr. Rep. **40**, 406 (1995)].

4. P. Farwig and H. W. Schurmann, Z. Phys. **204** (2), 489 (1967).

5. J. Hartwig, Phys. Status Solidi A **37** (2), 417 (1976).

6. V. G. Baryshevskiĭ, Pis'ma Zh. Tekh. Fiz. **2** (3), 112 (1976) [Sov. Tech. Phys. Lett. **2**, 43 (1976)].

7. W. C. Marra, P. Eisenberger, and A. Y. Cho, J. Appl. Phys. **50** (11), 6927 (1979).

8. A. M. Afanas'ev and M. K. Melkonyan, Acta Crystallogr., Sect. A: Found. Crystallogr. **39** (2), 207 (1983).

9. P. A. Aleksandrov, M. K. Melkonyan, and S. A. Stepanov, Kristallografiya **29** (2), 376 (1984) [Sov. Phys. Crystallogr. **29**, 226 (1984)].

10. P. A. Aleksandrov, A. M. Afanasiev, M. K. Melkonyan, and S. A. Stepanov, Phys. Status Solidi A **81** (1), 47 (1984).

11. P. A. Aleksandrov, A. M. Afanas'ev, and S. A. Stepanov, Poverkhnost, No. 8, 9 (1984).

12. P. A. Aleksandrov, A. M. Afanas'ev, and S. A. Stepanov, Kristallografiya **29** (2), 197 (1984) [Sov. Phys. Crystallogr. **29**, 119 (1984)].

13. P. A. Aleksandrov, A. M. Afanasiev, and S. A. Stepanov, Phys. Status Solidi A **86** (1), 143 (1984).

14. A. M. Afanas'ev, S. M. Afanas'ev, A. V. Esayan, and F. R. Khashimov, Poverkhnost, No. 12, 35 (1988).

15. A. M. Afanasev and O. G. Melikyan, Phys. Status Solidi A **122** (2), 459 (1990).

16. A. M. Afanasev and A. V. Esayan, Phys. Status Solidi A **126** (2), 303 (1991).

17. S. A. Stepanov, Kristallografiya **39** (2), 221 (1994) [Crystallogr. Rep. **39**, 182 (1994)].

18. S. Stepanov and R. Köhler, J. Phys. D **27** (7), 1922 (1994).

19. V. A. Bushuev and A. P. Oreshko, Fiz. Tverd. Tela (St. Petersburg) **43** (5), 906 (2001) [Phys. Solid State **43**, 941 (2001)].

20. V. A. Bushuev, R. M. Imamov, É. Kh. Mukhamedzhanov, and A. P. Oreshko, Kristallografiya **46** (6), 991 (2001) [Crystallogr. Rep. **46**, 909 (2001)].

21. P. A. Aleksandrov and S. A. Stepanov, Poverkhnost, No. 6, 117 (1986).

22. V. A. Bushuev and A. P. Oreshko, Poverkhnost, No. 1, 67 (2002).

23. V. A. Bushuev and R. N. Kuz'min, *Secondary Processes in X-ray Optics* (Mosk. Gos. Univ., Moscow, 1990).

Translated by L. Man

Influence of *in situ* Photoexcitation on Structure of Damaged Layer in GaAs (001) Substrates Implanted with Ar^{3+} Ions

K. D. Shcherbatchev*, V. T. Bublik*, Yu. F. Trush*, A. S. Markevich**, and V. N. Mordkovich**

* Moscow Institute of Steel and Alloys,
Leninskiĭ pr. 4, Moscow, 117936 Russia
e-mail: chterb@mail.girmet.ru
** Institute of Microelectronic Technology and Ultra-High-Purity Materials,
Russian Academy of Sciences, Chernogolovka, Moscow oblast, 142432 Russia
Received May 29, 2002

Abstract—The influence of photoexcitation on the formation of the defect structure in GaAs crystals implanted with 200 keV Ar^+ ions at doses of 1×10^{13}, 3×10^{13}, and 5×10^{13} cm^{-2} has been studied by high-resolution X-ray diffractometry. It was found that photoexcitation gives rise to annihilation of radiation-induced Frenkel pairs, and, thus, decreases the residual concentration of radiation-induced point defects. It is established that amorphization of the damaged layer proceeds via the formation and growth of clusters of radiation-induced point defects. The vacancy- and interstitial-type clusters are spatially separated—the former are located closer to the crystal surface than the latter. Photoexcitation hinders cluster growth and stimulates diffusion of interstitial defects into the substrate depth. © *2003 MAIK "Nauka/Interperiodica"*.

INTRODUCTION

The process of ion implantation into semiconductors is accompanied by the penetration of radiation-induced point defects into a semiconductor substrate. A cascade of collisions caused by an impinging ion forms within ~10^{-12} s a disordered region that is highly supersaturated with vacancies and intrinsic interstitial atoms [1]. This disordered region is unstable. Immediately after its formation, the processes of spatial separation of the vacancies and interstitial atoms begins, which is accompanied by the quasi-chemical reactions of these defects with one another and also with other imperfections of the crystal lattice. Since both vacancies and interstitial atoms can be in different charge states [2], photoexcitation of the electron subsystem of the target during ion bombardment accompanied by generation of nonequilibrium electrons and holes may influence the ensemble of the radiation-induced defects formed [3]. The influence of *in situ* photoexcitation on the shape of the X-ray rocking curve in GaAs crystals implanted with 200 keV Ar^+ ions at doses of $(1–5) \times 10^{13}$ cm^{-2} was revealed and described in [4]. Below, we describe the analysis of the strain profiles and static mean-square displacements constructed from the rocking curves [4].

OBJECTS AND EXPERIMENTAL METHODS

Semi-insulating GaAs (100) plates were implanted with 200 keV Ar^{3+} ions at doses of $(1–5) \times 10^{13}$ cm^{-2} on an HVEE-500 setup. The current density was 0.15 μA,

which excluded the heating of the substrate; the implantation temperature was ~298 K. To eliminate channeling, the angle formed by the beam with the surface normal was 7°. The implantation accompanied by photoexcitation was performed under the same conditions (simultaneous illumination of samples with a 25 mW cm^{-2} mercury lamp). Hereafter, the samples obtained under conditions of photoexcitation are referred to as "illuminated samples," while samples implanted without illumination are called "nonilluminated."

The imperfection of the implanted layers was studied by X-ray diffractometry in the dispersion-free triple-crystal scheme $(n, -n, n)$ with symmetric Bragg reflections. The slit monochromator and analyzer were perfect germanium crystals with a triple (400) reflection. In the triple-crystal scheme, the intensity distribution was measured in the vicinity of the [400] reciprocal lattice point. To separate the contributions that come from the coherent and noncoherent scattering components, the intensity was measured along the sections perpendicular to the diffraction vector which are located at different distances from the [400] reciprocal lattice point [5].

The rocking curves were modeled on the basis of the theory of dynamical diffraction using the formalism suggested in [6]. The strain profile $\varepsilon(z)$ was given by the set of basis points [7]. The curve corresponding to this profile was drawn by connecting the basis points using the cubic spline interpolation. The profile thus obtained was divided into 200 1 to 2-nm-thick lamellae. The

lamella thicknesses depend on the total thickness of the damaged layer. The rocking curves were simulated using the optimization program based on the genetic algorithm [7]. The positions of the basis points of the strain profile were varied to attain the best fit of the calculated and experimental curves, which was evaluated based on the χ^2 criterion [8].

The dependence of the shape of the rocking curves on the implantation dose observed in [4] was assumed to be caused by an increase in the amorphization degree of the layer at higher implantation doses. At low amorphization (low doses), the shape of the rocking curves is determined by the distribution of the vacancy and interstitial components of the Frenkel pairs in the depth of the damaged layer. To take into account amorphization, we introduced the static Debye–Waller factor into the description of the damaged-layer model. The amorphization degree (imperfection of the crystal lattice) was characterized by the distribution of the static Debye–Waller factor, $\exp(-L_H)$, over the layer depth, where L_H depends on the mean-square displacements $\langle u^2 \rangle$ of atoms from their sites in the deformed crystal lattice: $L_H = 8(\pi\sin\theta_B/\lambda)^2\langle u^2 \rangle$ (θ_B is the Bragg angle). Then the Fourier components of polarizability in a distorted crystal can be written as $\chi_h^* = \chi_h\exp(-L_H)$ [9]. Since $0 < \exp(-L_H) \leq 1$, the introduction of the static Debye–Waller factor into the computations leads to a decrease in the scattering power of the layer and, hence, to a decrease in the amplitude of the diffracted wave proportional to $|\chi_h^*|$. The profile of the Debye–Waller factor was also given by the set of the basis points connected by a spline. For the symmetric reflection, only the $\varepsilon_{zz}(z)$ and $\langle u^2 \rangle^{1/2}(z)$ components (the z axis is directed along the surface normal into the substrate) can be determined from the experiment. Knowing their values and taking into account that the value of the static mean-square displacements depends on the number of clusters and their dimensions, one can evaluate the concentration and clusters and their dimensions (volume) using the following expressions [9]:

$$L_H = \frac{8\pi\sqrt{2\pi}}{15V}h^{3/2}\left(\frac{1+\nu}{1-\nu}\right)^{3/2}c_{cl}(\Delta V)^{3/2},$$

$$\varepsilon_{zz} = \frac{1}{3}\left(\frac{1+\nu}{1-\nu}\right)c_{cl}\frac{\Delta V}{V}, \tag{1}$$

where h is the diffraction vector, V is the unit-cell volume, ν is the Poisson ratio, c_{cl} is the cluster concentration, ΔV is the variation of the unit-cell volume caused by the introduction of one cluster into the crystal lattice of the substrate. Equations (1) are written for spherical clusters; the formula for calculating L_H for dislocation loops is given in [10]. According to [11], dislocation loops are formed only after thermal treatment, because their formation requires overcoming a certain activation barrier. Since our samples were not subjected to

thermal treatment and the substrate was not heated during implantation, we consider here the spherical cluster model. Using the values of all the constants, we arrive at convenient expressions for profile analysis:

$$\frac{\Delta V}{V} \approx 5.53 \times 10^{-5}\frac{L_H^2}{\varepsilon_{zz}^2},$$

$$c_{cl} \approx 2.99 \times 10^5\frac{\varepsilon_{zz}^3}{L_H^2}. \tag{2}$$

Thus, the value of the mean-square displacements (the L_H parameter) can be considered as the characteristic of the degree of point defect agglomeration and cluster (microdefect) formation.

RESULTS AND DISCUSSION

The experimental rocking curves [4] are shown in Fig. 1. The initial analysis of these curves allowed us to draw the following conclusions. For illuminated samples, the maximum of the rocking curves corresponding to the average strain of the damaged layer is closer to the peak from the substrate than for nonilluminated samples. This means that illumination with a mercury lamp during implantation decreases the average strain in the damaged layer. Evaluation of the damaged-layer thickness (t) from the period ($\Delta\theta$) of the intensity oscillations on the rocking curves showed that the t value increases from 230 to 270 nm at higher doses. The thickness was evaluated using the formula of kinematical theory of scattering (see, for example, [19])

$$t = \frac{\lambda\sin\psi}{\Delta\theta\sin 2\theta_B} \tag{3}$$

(where λ is the wavelength of radiation used, ψ is the exit angle, and θ_B is the Bragg angle). No influence of photoexcitation on the damaged-layer thickness was revealed [4].
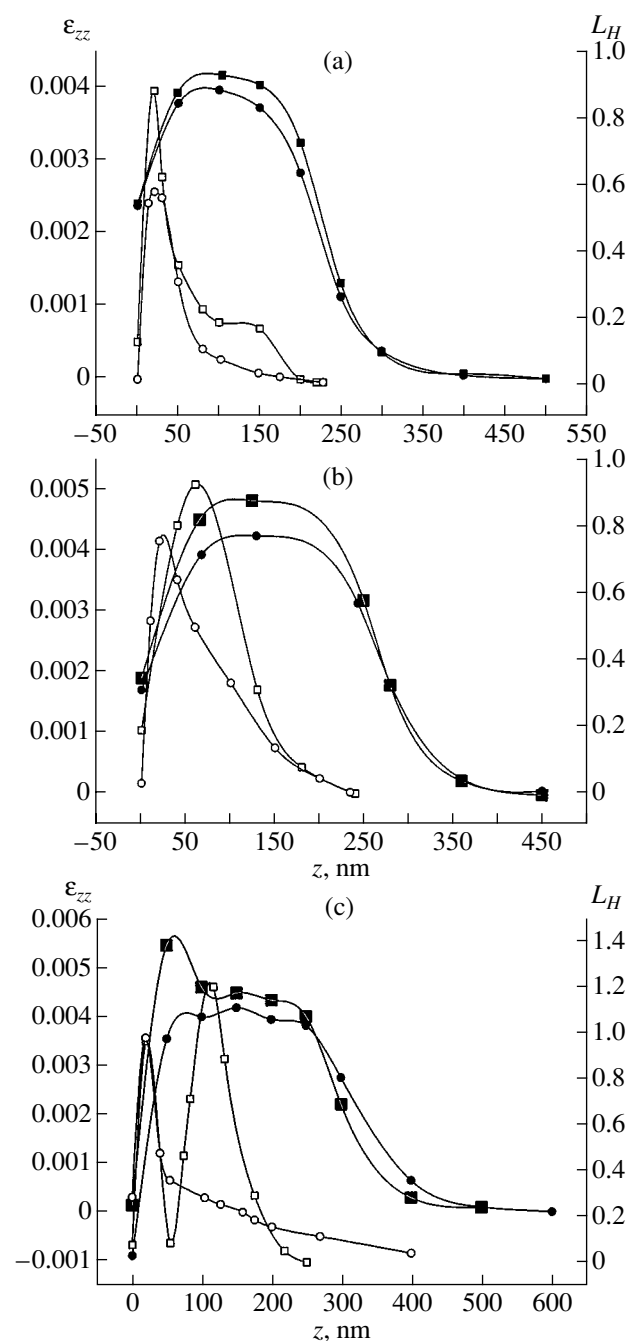
For a nonilluminated sample implanted at a dose of 5×10^{13} cm^{-2}, the shape of the rocking curve changed qualitatively (Fig. 1c, solid line): now the pronounced maximum that characterized the average strain in the damaged layer is absent. One can assume that the scattering power of a certain part of the damaged layer changed, most probably, because of its partial amorphization. These results required a more detailed analysis of the shape of rocking curves in order to better understand the processes taking place in the damaged layer under ion implantation.

Using the procedure described in [7], we determined the strain profiles ($\varepsilon_{zz}(z)$) and the $L_H(z)$ profiles for the samples (Fig. 2). The estimates of some characteristics of the strain profiles at the doses used are listed in the table. It is seen (Fig. 2a) that at a dose of 1×10^{13} cm^{-2}, the sample strain and the area below the curve of static displacements are somewhat less for the illuminated
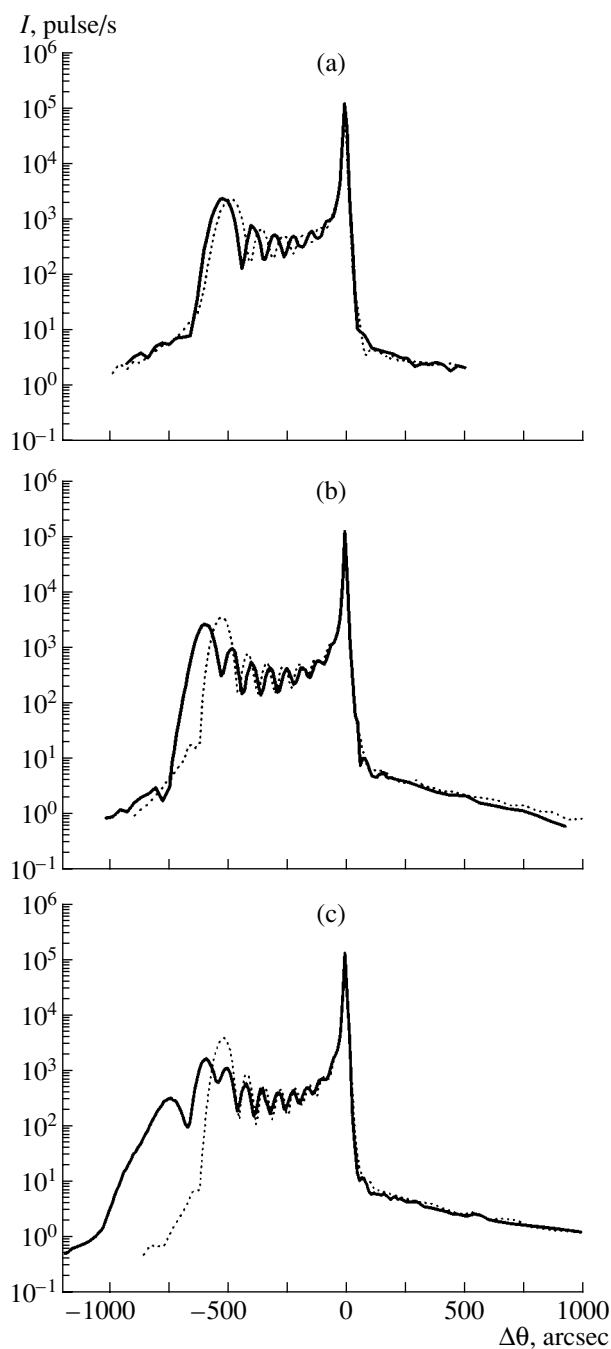
Fig. 1. Rocking curves of GaAs crystals implanted with 200-keV-Ar$^+$ ions under conditions of *in situ* photoexcitation (dashed line) and without photoexcitation (solid line) at different implantation doses D, cm^{-2}. (a) 1×10^{13}; (b) 3×10^{13}; (c) 5×10^{13}.

Fig. 2. Strain profiles $\varepsilon_{zz}(z)$ (filled squares and circles) and the exponents of statistical Debye–Waller factor $L_H(z)$ (open squares and circles) along the depth z for GaAs samples implanted with Ar$^+$ ions at different implantation doses D, cm^{-2}. (a) 1×10^{13}; (b) 3×10^{13}; (c) 5×10^{13}. ■ and □ indicate implantation in darkness; ● and ○ indicate implantation under conditions of *in situ* photoexcitation.

samples, which indicates that these samples are less imperfect. The most damaged layer is located at a depth of ~30 nm in both samples at a projective range of Ar^{3+} ions equal to about 145 nm.
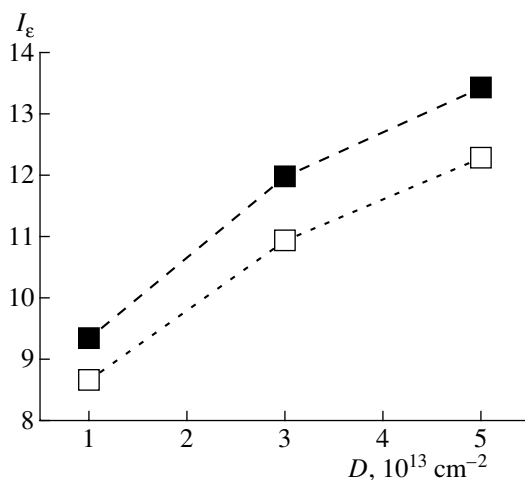
It is well known that the part of the damaged layer located close to the surface is enriched with vacancies [13] because of the high mobility of interstitial defects and their sink onto the surface. In this case, the

Quantitative characteristics of the strain profiles in the damaged layers of the GaAs (100) substrates implanted with Ar$^+$ ions under different conditions

Parameters	Irradiated in darkness			Irradiated under conditions of *in situ* photoexcitation		
	dose $\times 10^{-13}$, cm^{-2}					
	1	3	5	1	3	5
Strain maximum	4.19×10^{-3}	4.84×10^{-3}	5.60×10^{-3}	3.97×10^{-3}	4.30×10^{-3}	4.16×10^{-3}
Position of center of gravity, nm	128	147	164	126	151	192
Width, nm	237	251	262	229	259	305
Area	0.932	1.199	1.346	0.863	1.093	1.231

vacancy-type defects are located closer to the surface [14]. This should result in the enrichment of the part of the damaged layer located close to the surface with vacancies. The asymmetric shape of the strain profile indicates that the vacancies and the interstitial atoms are located at different depths. Therefore, the maximum of static mean-square displacements in the layers enriched with vacancies allows one to assume that the amorphization process proceeds via the formation of vacancy-type clusters (i.e., the clusters with a negative change of the specific volume $\Delta V/V$). In the illuminated samples, the structure distortion caused by such clusters is low, because the area of the peak of the static displacements is less. This allows one to assume that the total volume of the clusters in this sample at least does not have a lower value. The difference in the strain values is, evidently, associated with the fact that photoexcitation accelerates annihilation of vacancy-type and interstitial defects. It is difficult to evaluate the concentration and dimensions of the clusters of vacancy defects at this dose, because this requires the appropriate separation of the contributions that come to the total strain profile from the vacancies and interstitial defects. The latter defects are slightly associated and the degree of this association is lower in the illuminated samples.

Consider the influence of the implantation dose on the structure of the damaged layer. It follows from the table and Fig. 2b that the maximum strain increases by approximately 10% with an increase in the dose by a factor of 3. The profile width at the half height also increases. The center of gravity of the strain profile is also displaced into the depth. For the illuminated sample, the strain profile varies in a similar way. However, the amorphized layer in the nonilluminated sample is located deeper; the layer is wider and more amorphized. This difference increases in the samples implanted at a lower dose. In other words, an increase in the implantation dose results in an increase in the degree of association of vacancies into clusters and the degree of layer amorphization.

With an increase in the dose of implanted ions up to 5×10^{13} cm^{-2}, the rocking curve changes (Fig. 1c). For illuminated samples, the maximum strain is lower than for nonilluminated ones; however, the strain profile is noticeably broadened, and its center of gravity is displaced into the layer depth (Fig. 2c). For the nonilluminated sample, the evaluations by formulae (2) gave the following results: the concentration of vacancy clusters (300–500 vacancies per cluster) is 3×10^{-5}; the interstitial clusters are much smaller (~10–20 atoms), and their concentration is 2×10^{-3}. The vacancy clusters in the illuminated sample consist of ~500–1000 vacancies with their relative concentration being 4×10^{-6}, whereas interstitial defects form no clusters at all. Thus, photoexcitation affects the association of vacancies and interstitial defects differently.

The change in the profile shapes points to a further separation of the vacancies and interstitial defects in the depth and diffusion of the latter defects into the crystal bulk. Qualitatively, the profile shape has, in addition to the amorphization peak in the vacancy-enriched region, also a second peak in the region enriched with interstitial atoms. This is explained by the formation of clusters of interstitial defects in nonilluminated samples. In the illuminated sample, the layer containing slightly

Fig. 3. Dependence of the integrated strain I_ε on the dose D of implanted ions in the samples. Implantation in darkness is shown by filled squares; implantation under conditions of *in situ* photoexcitation is shown by open squares.

associated interstitial defects is smeared over a wide range of thicknesses. Apparently, photoexcitation prevents the formation of interstitial clusters at the given dose. Note that the layer amorphized by vacancy-type clusters at a dose of 5×10^{13} cm^{-2} is displaced toward the surface. With an increase in the dose, the integrated strain I_ε increases (Fig. 3). The absolute values of integrated strain are lower in the illuminated samples, which indicates a higher efficiency of annihilation of interstitial and vacancy defects in the samples implanted under conditions of *in situ* photoexcitation.

CONCLUSIONS

Thus, photoexcitation influences the secondary processes occurring with the participation of radiation-induced point defects in ion-implanted GaAs crystals. In particular, photoexcitation promotes annihilation of radiation-induced Frenkel pairs, thus increasing the residual concentration of the radiation-induced point defects. Since the degree of the structure distortion characterized by the Debye–Waller factor depends on the concentration of clusters of the radiation-induced point defects (of interstitial- and/or vacancy-type) and their dimensions, the amorphization of the damaged layer proceeds via the formation and growth of these clusters. It is established that the interstitial- and vacancy-type clusters are spatially separated, i.e., the vacancy-type clusters are located closer to the surface than the interstitial-type clusters. The clusters have smaller dimensions in the substrates implanted under conditions of *in situ* photoexcitation. Photoexcitation stimulates diffusion of interstitial defects into the substrate depth.

ACKNOWLEDGMENTS

REFERENCES

1. W. L. Brown and A. Ourmazd, MRS Bull. **17** (6), 30 (1992).
2. V. L. Vinetskiĭ and G. A. Kholodar', *Radiation Physics of Semiconductors* (Naukova Dumka, Kiev, 1979).
3. Yu. N. Erokhin, A. G. Ital'yantsev, and V. N. Mordkovich, Pis'ma Zh. Tekh. Fiz. **14**, 835 (1988) [Sov. Tech. Phys. Lett. **14**, 372 (1988)].
4. V. T. Bublik, K. D. Shcherbachev, and Yu. F. Trush, Izv. Vyssh. Uchebn. Zaved. Mater. Élektron. Tekh., No. 1, 73 (2002).
5. K. D. Chtcherbatchev and V. T. Bublik, Inst. Phys. Conf. Ser., No. 160, 187 (1997).
6. C. R. Wie, T. A. Tombrello, and T. Vreeland, J. Appl. Phys. **59** (11), 3743 (1986).
7. K. D. Shcherbachev, V. T. Bublik, and A. V. Kuripyatnik, Poverkhnost, No. 10, 74 (2001).
8. A. M. Afanas'ev, M. A. Chuev, R. M. Imamov, *et al.*, Kristallografiya **42** (3), 514 (1997) [Crystallogr. Rep. **42**, 467 (1997)].
9. M. A. Krivoglaz, *Theory of X-ray and Thermal Neutron Scattering by Real Crystals* (Naukova Dumka, Kiev, 1983, 2nd ed.; Plenum, New York, 1969).
10. M. Servidory and R. Fabri, J. Phys. B **26**, 22 (1993).
11. R. D. Goldberg, T. W. Simpson, I. V. Mitchell, *et al.*, Nucl. Instrum. Methods Phys. Res. B **106**, 216 (1995).
12. K. Bowen and B. Tanner, *High Resolution X-ray Diffractometry and Topography* (Taylor and Francis, London, 1998).
13. V. T. Bublik, K. D. Shcherbachev, E. A. Komarnitskaya, *et al.*, Kristallografiya **44** (6), 1106 (1998) [Crystallogr. Rep. **44**, 1035 (1998)].
14. L. Pelaz, G. H. Gilmer, M. Jaraiz, *et al.*, Appl. Phys. Lett. **73**, 1421 (1999).

Translated by T. Dmitrieva

DIFFRACTION AND SCATTERING
OF IONIZING RADIATIONS

Influence of Partial Replacement of Cu by Cd and Zn Atoms on Polymorphous Transformation in $Cu_{1.75}Te$ Crystal

Yu. G. Asadov, A. I. Movlamverdieva, and F. Yu. Asadov

Institute of Physics, Academy of Sciences of Azerbaijan,
pr. Dzhavida 33, Baku, 370143 Azerbaijan
e-mail: jusif@lan.ab.az
Received November 19, 2001; in final form, October 16, 2002

Abstract—A layer $Cu_{1.75-x}Te$ single crystal in which some Cu atoms were replaced by Cd and Zn atoms ($x = 0.05$) was studied by high-temperature X-ray diffractometry. It was established that this replacement substantially affects the number and temperature of polymorphous transformations. © 2003 MAIK "Nauka/Interperiodica".

The structure of the hexagonal $Cu_{1.75}Te$ phase was repeatedly studied by electron diffraction [1–3]. In [2], the crystal structure of the β^I-phase of the composition $Cu_{1.75}Te$ was determined, and it was shown that at room temperature it has a hexagonal structure with the lattice parameters $a = 8.28$ Å $\approx 2a_0$ and $c = 7.22$ Å $\approx c_0$, sp. gr. $P3m1–c_{3v}^1$ (where $a_0 = 4.237$ Å and $c_0 = 7.274$ Å are the parameters of the hexagonal phase Cu_2Te established in [4]). The second, β^{II}, phase was first found in the electron diffraction study of a Cu_7Te_4 thin film; it is hexagonal at room temperature and has the lattice parameters $a = 4.17$ Å $\sim a_0$, $c = 21.65$ Å $\sim 3c_0$, sp. gr. $P6m2–D_{3h}^1$ [3].

We studied the influence of partial replacement of copper by zinc and cadmium atoms on the mechanism and temperature of structural transformations in a $Cu_{1.75}Te$ crystal. With this aim, single crystals of the compositions $Cu_{1.75}Te$, $Cu_{1.70}Zn_{0.05}Te$, and $Cu_{1.70}Cd_{0.05}Te$ were grown by the Bridgman method.

$Cu_{1.75}Te$. Earlier [5, 6], we studied the structural phase transitions in layer $Cu_{1.75}Te$ single crystals. In the angular range $0° < 2\theta < 100°$, we managed to record at room temperature 12 diffraction reflections of the $(00l)$ type from layer $Cu_{1.75}Te$ single crystals, i.e., (002), (003), (004), (006, 100), (008), (009), (00.10), (00.12, 200), (00.14), (00.16) (00.18, 300), and (00.19). The parameters of the hexagonal unit cell calculated from these reflections are $a = 4.1753$ Å, $c = 21.6954$ Å and correspond to the parameters of the β^{II}-phase [3]. The number of reflections and their intensities are constant in the temperature range 290–593 K. As is seen from Fig. 1, the temperature dependences $a(T)$ and $c(T)$ of the hexagonal phase increase monotonically in this temperature range. At 593 K, of the above 12 diffraction reflections of the $(00l)$ type only the reflections with even l were recorded in this angular range, i.e., (002), (004), (006), (008), (00.12), (00.16), and

(00.18). Since the l indices are multiples of two, then, dividing into two, we obtain the following lattice parameters: $a = 8.4076$ Å, $c = 10.9216$ Å, which coincide with the lattice parameters indicated for the composition with 35 mol % Te [7]. At 653 K, the appearance of the reflection from the (III) plane of the fcc modification is accompanied by the appearance of only three reflections from the matrix crystal in the same angular range, these reflections have the indices (006, 100), (00.12, 200) and (00.18, 300). Dividing the reflection indices into three, we obtain the (002.100), (004.200), and (006.300) reflections. The lattice parameters calculated from these reflections are $a = 4.2402$ Å, $c = 7.3440$ Å and correspond to the lattice parameters of the hexagonal Cu_2Te phase [4]. In the temperature range 653–723 K, a $Cu_{1.75}Te$ crystal consists of the hexagonal and fcc phases. As is shown in Fig. 1, the hexagonal phase is transformed into the fcc phase at 723 K. The change of the lattice parameters of the hexagonal phase with temperature and its transformation into the fcc phase occur both on heating and cooling.

$Cu_{1.70}Zn_{0.05}Te$. In the angular range $10° < 2\theta < 80°$, we recorded nine diffraction reflections from the natural $(00l)$ surface of a layer $Cu_{1.70}Zn_{0.05}Te$ single crystal
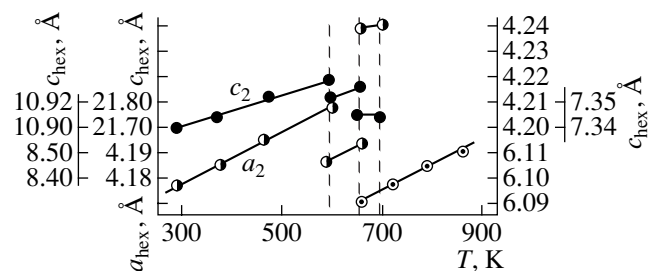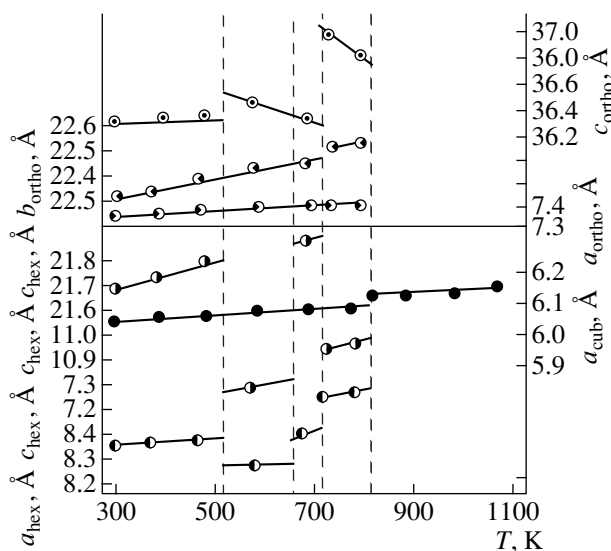

Fig. 1. Temperature dependence of the lattice parameters of a $Cu_{1.75}Te$ crystal; ◐ and ● are the a and c parameters of the hexagonal modification, respectively; ⊙ is the a parameter of the fcc modification.

at room temperature. Five of these reflections, (008), (009), (00.10), (00, 12.200), and (00.15), are due to the hexagonal phase with the lattice parameters $a = 4.1558$ Å, $c = 21.5926$ Å. All nine reflections are unambiguously indexed within the orthorhombic lattice (superstructure with respect to the hexagonal phase) with the parameters $a = 7.3383$ Å, $b = 22.1948$ Å, $c = 35.9863$ Å [8]. As is seen from Fig. 2, the lattice parameters of the hexagonal and orthorhombic phases increase monotonically with temperature up to 634 K. The (009) and (0015) reflections of the hexagonal phase disappear at 634 K. Similar to the case of $Cu_{1.75}Te$, the l indices of the remaining (008), (00.10), (00.12) reflections are multiples of two. Upon division by two, we obtain the reflections (004), (005), and (006,400), respectively. The parameters of the hexagonal lattice calculated from these reflections are $a = 8.357$ Å, $c = 10.852$ Å. The b and c parameters of the orthorhombic phase change in a jumpwise manner. At 873 K, all the diffraction reflections of the hexagonal and orthorhombic phases disappear, and the (311) reflection appears in the same angular range that is attributed to the high-temperature fcc phase with the lattice parameter $a = 6.0658$ Å.

$Cu_{1.70}Cd_{0.05}Te$. Indexing the diffraction pattern from the $Cu_{1.70}Cd_{0.05}Te$ sample confirmed the existence of three phases—the orthorhombic phase with the lattice parameters $a = 7.318$ Å, $b = 22.184$ Å, $c = 36.515$ Å; the hexagonal phase with the parameters $a = 8.290$ Å, $c = 21.655$ Å; and the metastable (at room temperature) primitive cubic phase with the lattice parameter $a = 5.978$ Å. The $Cu_{1.70}Cd_{0.05}Te$ single crystal showed ten diffraction reflections in the angular range $20° < 2\theta < 70°$ in a 10^{-3} Pa vacuum at room temperature. These reflections confirm the results obtained on a powder sample. It is important that in the temperature range 290–573 K, the number and intensities of reflections do not change, whereas the lattice parameters of the hexagonal, orthorhombic, and cubic phases increase monotonically (Fig. 3). Several (00l) reflections, namely, (008), (00.10), and (00.14), observed at room temperature disappear at 535 K, whereas the (009), (00.12), and (00, 15) reflections with l values that are multiples of three are observed. Dividing the l indices into three, we obtain from these reflections $c = 7.256$ Å, which corresponds to the c parameter of the hexagonal phase β^I-$Cu_{1.75}Te$. The a parameter calculated from the (203) and (321) reflections equals 8.280 Å [2]. As is seen from Fig. 3, the c parameter of the orthorhombic phase changes in a jumpwise manner at this temperature. At 673 K, all the reflections observed at room temperature are restored. At $T = 723$ K, the (009) and (00.15) reflections of the hexagonal phase disappear but (008), (00.10), (00.12) and (00.14) with odd l are preserved. Dividing their indices into two, we obtain (004), (005), (006), and (007) reflections; the lattice parameters calculated from these reflections are $a = 8.378$ Å, $c = 10.877$ Å [7]. It follows from Fig. 3, that at 723 K, the b and c parameters of the orthorhombic phase also
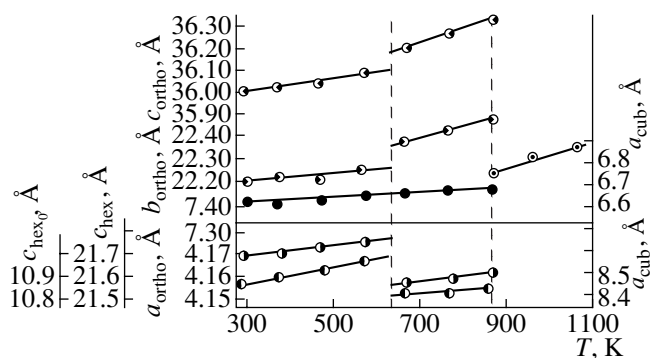
Fig. 2. Temperature dependence of the lattice parameters of a $Cu_{1.70}Zn_{0.05}Te$ crystal; ●, ◐, and ◔ are the a, b, and c parameters of the orthorhombic modification, respectively; ◓ and ◑ are the a and c parameters of the hexagonal modification, respectively; ⊗ is the a parameter of the fcc modification.

Fig. 3. Temperature dependence of the lattice parameters of a $Cu_{1.70}Cd_{0.05}Te$ crystal; ◓, ◔, and ⊙ are the a, b, and c parameters of the orthorhombic modification, respectively; ◓ and ◑ are the a and c parameters of the hexagonal modification, respectively; ● is the a parameter of the fcc modification.

change in a jumpwise manner. At 801 K, the hexagonal and orthorhombic phases are transformed into a high-temperature primitive cubic phase. As is seen from Fig. 3, at 801 K, the monotonically increasing lattice parameter of the cubic phase $a(T)$ changes in a jumpwise manner. Note that a deficit in copper is characteristic of copper chalcogenides $Cu_{2-x}S(Se, Te)$. In stoichiometric and nonstoichiometric compounds, S^{2-}, Se^{2-}, and Te^{2-} anions form the lattice framework, whereas Cu^{1+} and Cu^{2+} cations are statistically distributed over the tetrahedral and octahedral voids between two close-packed chalcogen layers irrespective of the crystal system. The lattice parameters of various crystalline modifications of the $Cu_{1.75-x}M_x$ crystals ($M =$ Zn, Cd; $X = 0$ and 0.05) are listed in the table.

Crystalline modifications of the $Cu_{1.75-x}M_x Te$ compound (M = Zn, Cd)

Composition	Modification	T, K	Lattice parameters, Å			Z	ρ_x, g cm^{-3}	Sp. gr.	References
			a	b	c				
$Cu_{1.75}Te$	Hexagonal	290	4.175		21.695	6	7.259	D_{3h}^1-P6m2	[3]
	Hexagonal	593	8.408		10.922	12	7.112		[7]
	Hexagonal	653	4.240		7.344	2	6.929	D_{6h}^1-P6/mmm	[4]
	Fcc	723	6.097			4	6.993	F$m3m$	
$Cu_{1.70}Zn_{0.05}Te$	Hexagonal	290	4.156	22.195	21.593	6	7.364	D_{3h}^1-P6m2	
	Orthorhombic		7.338		35.986	108	7.304		[3]
	Hexagonal	634	4.1704	22.364	10.852	12	7.247		[8]
	Orthorhombic		7.362		36.184	108	7.186		[7]
	Fcc	873	6.066			4	7.104	F$m3m$	[8]
$Cu_{1.70}Cd_{0.05}Te$	Hexagonal	290	8.335	22.305	21.654	24	7.374	C_{3v}^1-P3m1	
	Orthorhombic		7.315		36.202	108	7.319		
	Cubic		5.978			4	7.494		[3]
	Hexagonal	535	8.280	22.417	7.256	8	7.433		
	Orthorhombic		7.366		36.358	108	7.201		[2]
	Cubic		6.011			4	7.373		[8]
	Hexagonal	673	8.405	22.434	21.809	24	7.200	C_{3v}^1-P3m1	[3]
	Orthorhombic		7.384		36.279	108	7.194		
	Cubic		6.029			4	7.306		
	Hexagonal	723	8.378	22.518	10.877	24	7.265		[7]
	Orthorhombic		7.372		37.012	108	7.036		[8]
	Cubic		6.039			4	7.270		
	Cubic	801	6.092			4	7.082		

It is seen that at room temperature the $Cu_{1.75}Te$ compound has only one hexagonal phase. Copper atoms are in uni- (Cu^+–0.98) and divalent (Cu^{2+}–0.80) states. The Cu^+ ions are located in tetrahedral voids between two close-packed Te layers and the Cu^{2+} ions are located in octahedral voids. The structure type does not depend on temperature, the lattice parameters change at 593 and 653 K. At 723 K, the hexagonal modification is transformed into an fcc one. One can conclude that Zn^{2+} ions (0.83) isomorphously replace Cu^{2+} ions (0.80) in a $Cu_{1.70}Zn_{0.05}Te$ single crystal, whereas Cd^{2+} ions (0.99) replace Cu^+ ions (0.98) in $Cu_{1.70}Cd_{0.05}Te$. Naturally, the Zn–Te and Cd–Te chemical bonds differ from Cu–Te bonds, which seems to explain the fact that at room temperature the $Cu_{1.70}Zn_{0.05}Te$ compound consists of two phases, while the $Cu_{1.70}Cd_{0.05}Te$ compound consists of three phases. This also underlies the fact that the temperature and number of phase transformations in these compounds differ from the temperature and number of phase transformations in $Cu_{1.75}Te$.

REFERENCES

1. R. V. Baranova and Z. G. Pinsker, Kristallografiya **9** (1), 104 (1964) [Sov. Phys. Crystallogr. **9**, 83 (1964)].

2. R. V. Baranova, Kristallografiya **12** (2), 266 (1967) [Sov. Phys. Crystallogr. **12**, 221 (1967)].

3. R. V. Baranova, Kristallografiya **13** (5), 803 (1968) [Sov. Phys. Crystallogr. **13**, 695 (1968)].

4. H. Novotny, Z. Metallkd. **37**, 40 (1946).

5. Yu. G. Asadov, G. B. Gasymov, K. M. Dzhafarov, and L. V. Rustamova, Kristallografiya **36** (1), 147 (1991) [Sov. Phys. Crystallogr. **36**, 84 (1991)].

6. Yu. G. Asadov, L. V. Rustamova, G. B. Gasimov, *et al.*, Phase Transit. **38**, 247 (1991).

7. R. Blanchnik, M. Lasocka, and U. Walbrecht, J. Solid State Chem. **48**, 431 (1983).

8. L. Patzak, Z. Metallkd. **47**, 433 (1956).

Translated by T. Dmitrieva

REAL STRUCTURE
OF CRYSTALS

The Role of Structural Defects in Diffusion of Elements of Group VI in Semi-insulating Gallium Arsenide Crystals

M. B. Litvinova, S. V. Shutov, and O. N. Lebed'

Institute of Semiconductor Physics, National Academy of Sciences of Ukraine,
pr. Nauki 45, Kiev, 03028 Ukraine
e-mail: lmb@ist.com.ua
Received November 11, 2001; in final form, April 3, 2002

Abstract—The combined effect of the changes in the number and type of vacancies and dislocation density on selenium and sulfur diffusion in single crystals of undoped semi-insulating gallium arsenide has been studied. The differences in the diffusion mechanisms in the subsurface region of samples with an initial deficiency in gallium or arsenic are established as well as the dependence of the effective radius of arsenic trapping by dislocations on the ratio of the concentrations of gallium and arsenic vacancies. © 2003 MAIK "Nauka/Interperiodica".

INTRODUCTION

Gallium arsenide-based integral circuits have a higher operating speed in comparison with silicon-based ones. However, because of instability in reproducing their parameters, these circuits have certain limitations that hinder their widespread use. A decrease in the size of the working elements enhances the role of structural inhomogeneities during material doping and, thus, leads to a lower quality of the circuits. Despite the extensive fundamental studies of diffusion in GaAs [1–6], the character and mechanisms of the combined effect of different defects in the crystal lattice on the diffusion processes are still not quite clear.

It is well known that the elements of group VI substitute mainly arsenic in GaAs crystals and behave like donors [1–3]. Diffusion occurs by the dissociation mechanism [1–6]. At the impurity content $N < 10^{20}$ cm^{-3}, the diffusion zone is described by the Gaussian error function [1, 5]

$$N(x) = N_0 \operatorname{erfc} \frac{x}{2\sqrt{Dt}}, \qquad (1)$$

where $N(x)$ is the impurity concentration at the distance x from the sample surface, N_0 is the surface impurity concentration, t is the process duration, and D is the diffusion coefficient. In the framework of the mechanism under discussion, the effective diffusion coefficient for an n-fold donor impurity with due regard for the effect of electric field directed along the concentration gradient is determined by the following expression [1]:

$$D = (n+1)D_i N_S K_i P_{As}^{1/\alpha}, \qquad (2)$$

where D_i is the diffusion coefficient of interstitial atoms, N_S is the concentration of substitutional atoms, K_i is the parameter characterizing the mean lifetime of

interstitial atoms, and $P_{As}^{1/2}$ is the vapor pressure of the volatile component.

If the surface of the planar sample is a sink of arsenic atoms, we have

$$K_{i1} = (\pi/L)^2 D_i, \qquad (3)$$

where L is the length of the diffusion region. In the case where dislocations play the role of a sink, the following equations are valid:

$$K_{i2} = \frac{2\pi N_d D_i}{\log\left(\dfrac{r_d}{r}\right)}, \qquad (4)$$

$$r_d = \sqrt{\frac{1}{\pi N_d}} \qquad (5)$$

is the mean distance between the dislocations with the density N_d, and r is the effective radius of particle trapping by dislocations.

However, these relationships do not take into account the initial vacancy composition in GaAs crystals and its influence on the efficiency of the sinks of arsenic. In the present paper, we demonstrate the existence of such an influence and discuss the mechanisms underlying this phenomenon by considering the diffusion of selenium and sulfur atoms in GaAs.

EXPERIMENTAL TECHNIQUE

The starting material was Czochralski-grown undoped semi-insulating gallium arsenide single crystal, which allowed us to ignore the effect of impurity interactions on diffusion (the concentration of uncontrolled impurities in the material did not exceed 10^{16} cm^{-3} [2]) and to use the luminescence technique to
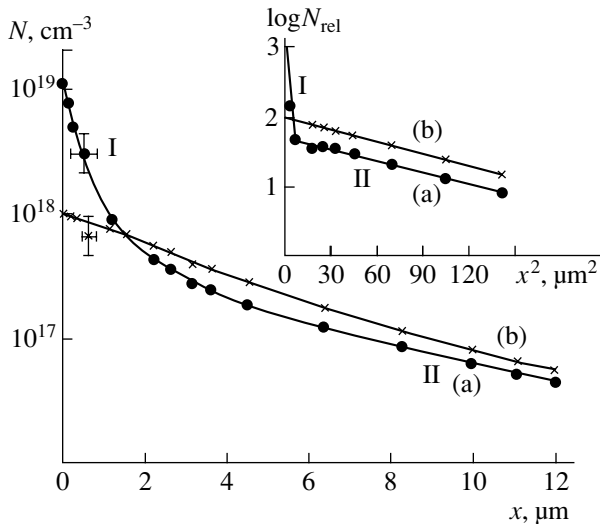
Fig. 1. Concentration profile of diffusion of Se atoms in GaAs in the cases (a) $[V_{Ga}] > [V_{As}]$ and (b) $[V_{Ga}] < [V_{As}]$. In the inset: the corresponding distributions for $N_{rel} = N(x)/N_0$ on the logarithmic scale in the cases (a) $[V_{Ga}] > [V_{As}]$ and (b) $[V_{Ga}] < [V_{As}]$.

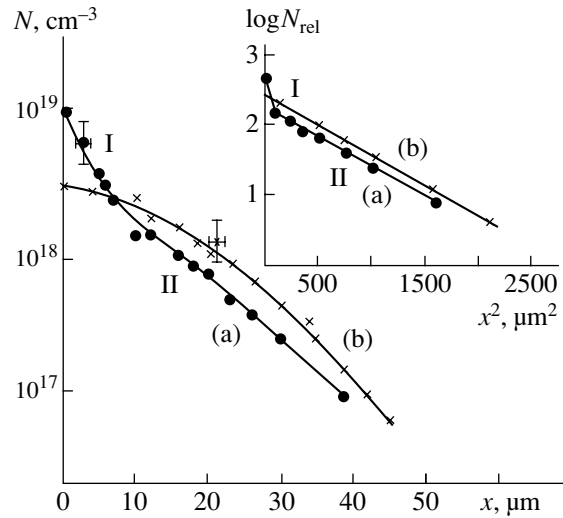**Fig. 2.** Concentration profile of diffusion of S atoms in GaAs in the cases (a) $[V_{Ga}] > [V_{As}]$ and (b) $[V_{Ga}] < [V_{As}]$. In the inset: the corresponding distributions for $N_{rel} = N(x)/N_0$ on the logarithmic scale for the cases (a) $[V_{Ga}] > [V_{As}]$ and (b) $[V_{Ga}] < [V_{As}]$.

evaluate the vacancy concentration in the initial crystals.

We studied diffusion in ~4-mm-thick samples (with a dislocation density of $N_d = 3 \times 10^4$–9×10^5 cm^{-2} and an electrical resistivity $\rho = 8 \times 10^7$–2×10^8 Ω cm) cut out normally to the growth axis from the (100)-oriented *n*-type single crystal. The chosen crystals had different initial concentration ratios of gallium $[V_{Ga}]$ and arsenic $[V_{As}]$ vacancies. Type-1 and type-2 crystals can be defined as those with $[V_{Ga}] > [V_{As}]$ and $[V_{Ga}] < [V_{As}]$, respectively. The diffusion process proceeded for six hours in quartz ampules evacuated to a pressure lower than 10^{-3} Pa at 850°C. Sulfur atoms diffused from the vapor phase obtained by vaporization of a piece of sulfur placed into a ~4-cm^3 ampule. Selenium diffused from a 1-μm-thick layer obtained by thermal deposition of Se onto the sample surface. This ensured the conditions necessary for diffusion from a stable source. After the diffusion of S and Se, the Ga_2S_3 and Ga_2Se_3 surface layers formed were etched away by acid.

In the course of sulfur and selenium diffusion, the impurity distribution at the plate surface was studied using the layer-by-layer etching and the anode oxidation technique with the additional illumination of the samples [7]. The charge-carrier density (at $n > 10^{16}$ cm^{-3}) was determined from the half-width of the photoluminescence edge band at 300 K [8]. At high impurity concentrations, a certain deviation of the charge-carrier concentration from the impurity concentration was observed. Therefore, we had to introduce the corresponding corrections to the N_{Se} and N_S values [2, 5].

In the initial GaAs samples, the $[V_{As}]/[V_{Ga}]$ ratio was determined from the intensity ratio of the photoluminescence edge band ($T = 77$ K) and of the band originating from the radiative transition from the conduction band to the acceptor level $C_{V_{As}}$. This corresponding technique and the method of recording the photoluminescence spectra at 300 K and 77 K are described in [9, 10] and [8], respectively. The density of growth dislocations was determined from the etching pits using a MIM-7 microscope.

EXPERIMENTAL

The selenium and sulfur diffusion profiles in the subsurface region of the samples differed for crystals with different values of the $[V_{As}]/[V_{Ga}]$ ratio. For type-1 samples, the concentration dependence has two regions (denoted as I and II) (see Figs. 1a, 2a). Region II is fitted by the erfc function, whereas region I significantly deviates from it and is better fitted by another function of the form

$$N(x) = N_0 \exp(-x/L), \qquad (6)$$

where x is the distance from the sample surface and L is the length of the diffusion region. In curve $\log N_{rel}$ versus x^2, these regions correspond to straight lines I and II (see insets in Figs. 1 and 2). The diffusion coefficients are determined by the slope of these lines as

$$D = 0.108 x^2/(t \log N). \qquad (7)$$

The diffusion coefficients D_1 (region I) and D_2 (region II) determined in such a way are indicated in the table. In the samples with the same initial vacancy concentra-

tion, D_1 for both elements increased with the dislocation density (Fig. 3).

The type-2 samples exhibited the same behavior of N (Figs. 1b, 2b) with a profile close to the erfc function. The diffusion coefficients for S and Se atoms found from the plots $\log N_{rel}$ versus (x^2) (see insets in Figs. 1 and 2) are equal to the values of D_{2Se} and D_{2S} and agree, by an order of magnitude, with the values reported in the literature ($D_{Se} = (1.6–6.3) \times 10^{-15}$ cm^2 s^{-1} and $D_S = 1.1 \times 10^{-14}– 2.5 \times 10^{-13}$ cm^2 s^{-1} [1–6]).

Figure 4 demonstrates the dependence of D_1/D_{10} on the ratio of vacancy concentration z for gallium and arsenic ($z = [V_{As}]/[V_{Ga}]$) in undoped crystals. The plots in Fig. 4 correspond to type-1 samples with close dislocation densities ($N_d = (4.3 \pm 0.5) \times 10^5$ cm^{-2}). As D_{10}(Se) and D_{10}(S) values, we chose the lowest values of the diffusion coefficient found in region I at $z \longrightarrow 1$.

DISCUSSION

Region I in Figs. 1a and 2a, whose existence in the diffusion zone of group-VI elements was not reported earlier [1, 3–6], is explained by the lower diffusion rate than that in region II. The deviation of the selenium and sulfur diffusion profiles from the erfc function in type-1 samples ($[V_{Ga}] > [V_{As}]$) indicates that the vacancy concentration influences diffusion, in contrast to type-2 samples ($[V_{As}] > [V_{Ga}]$), where no such a deviation was observed (see Figs. 1b, 2b). Moreover, the curve D_1 versus N_d (Fig. 3) proves the participation of dislocations in the diffusion process. Thus, the formation of the diffusion profiles of impurities in region I seems to be the result of the joint effect of vacancies and dislocations.

It should be assumed that in the crystals with gallium deficiency, where the arsenic flow to the surface sink is limited by the Ga$_2$S$_3$ or Ga$_2$Se$_3$ surface layers, the dislocations start playing a significant role (in

Diffusion coefficients (cm^2 s^{-1})

| Element	$D_1 \times 10^{16}$	$D_2 \times 10^{14}$
Se	0.61–3.12	0.34–0.46
S	0.92–2.68	61–64

accordance with Eqs. (2)–(4)). As a result, the secondary diffusion of impurities from the surface to the vacancies occurs due to dislocations. Such a process can take place if the diffusion coefficient of vacancies is much lower than the coefficient of impurity diffusion.

The self-diffusion coefficient for V_{As} ($T = 1123$ K) can be written as [1]

$$D_{V_{As}} = 7.9 \times 10^3 \exp(-4.0/kT) \qquad (8)$$

and equals 1×10^{-15} cm^2 s^{-1}. This value is lower by two orders of magnitude than D_{2S} and is of the same order of magnitude as D_{2Se} (see table). However, the diffusion coefficient that describes the arsenic flow to the sinks such as dislocations is determined not by the density gradient for defects but rather by the nature of their interactions with dislocations. This is confirmed by the dependence of D_1/D_{10} on the type of the vacancies in the crystals (Fig. 4). Therefore, in the case under discussion, $D_{V_{As}}$ seems to be lower than 10^{-15} cm^2 s^{-1} and, proceeding from the values of D_{1Se} and D_{1S}, is equal to about 10^{-16} cm^2 s^{-1}.

The As flow to the dislocation sinks affects the S and Se diffusion in the crystals with the initial deficiency in gallium but does not affect it in the crystals with the initial deficiency in arsenic. This also stems from the dependence of the efficiency of the dislocation sinks on the defect structure in the initial samples. In the atmospheres around dislocations (Cottrell atmospheres), the gallium vacancies are dominant in unannealed type-1
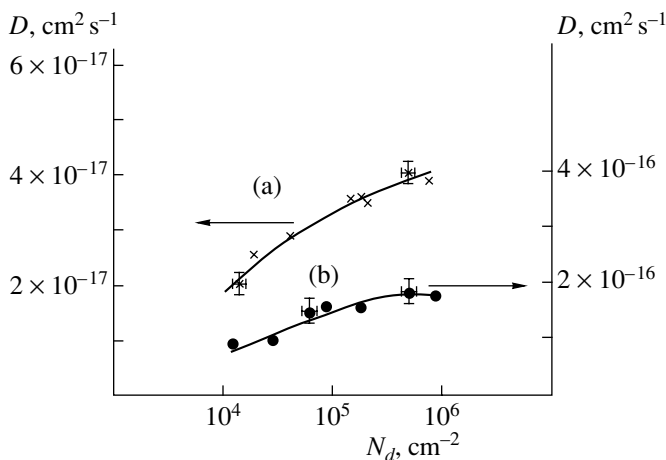
Fig. 3. Diffusion coefficient in region I versus dislocation density in type-1 samples: (a) GaAs (Se) and (b) GaAs (S).
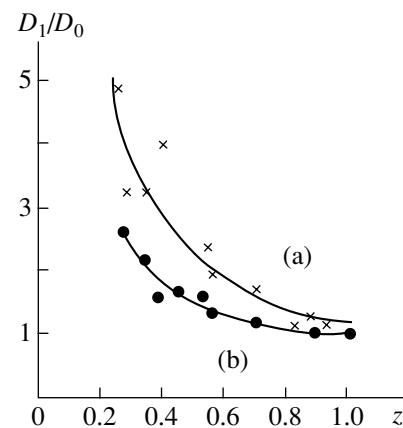
Fig. 4. Diffusion coefficient in type-1 samples in region I versus ratio $z = [V_{As}]/[V_{Ga}]$: (a) GaAs (Se) and (b) GaAs (S).

$r(z)$

$1/\sqrt{N_d}$

r_0

0   1   2   3   4   5 z

Fig. 5. The plot of the function $r(z)$ at N_d = const.

crystals, whereas in type-2 crystals, the arsenic vacancies are dominant. It is well known [1] that V_{Ga} have a negative charge at high temperatures, whereas V_{As} and interstitial arsenic atoms As_i have a positive charge. The electric field along the concentration gradient favors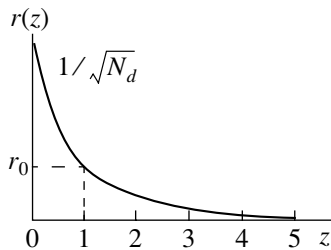 the motion of As_i^+ toward dislocations (As_i is the dominant point defect in the crystals where $[V_{Ga}] > [V_{As}]$ [11]) if V_{Ga}^- is the dominant constituent of the dislocation atmospheres and hinders this motion if V_{As}^+ dominates there. Hence, the effective radius characterizing the trapping of arsenic atoms by dislocations [see Eq. (4)] depends on the type of vacancies in the crystal. A formula for evaluating this dependence can be obtained in the following way.

The $D_1/D_{10}(z)$ profiles determined for selenium and sulfur in type-1 samples with close values of the dislocation density in the z range under study are approximated quite well (see solid curves in Fig. 4) by the relationship in the form

$$D_1/D_{10} = 1/z. \qquad (9)$$

If we assume that the existence of region II is determined by the dislocation sinks (parameter K_{i2}), it follows from Eqs. (2), (4), and (9) that

$$D_1/D_{10}K_1/K_{10}{}^2 = \log(r_d/r_0)/\log(rd/r) = 1/z, \quad (10)$$

where r is the effective radius of trapping of As by dislocations and r_0 is the same radius of trapping for the case where $z \longrightarrow 1$ (i.e., $[V_{Ga}] = [V_{As}]$).[1]

Using Eqs. (5) and (10), we find the dependence of the effective radius of trapping of As by dislocations on the concentration ratio of gallium and arsenic in an undoped gallium arsenide crystal

$$r = (\pi N_d)^{(z-1)/2} r_0^z. \qquad (11)$$

Thus, we obtained the exponential $r(z)$ function with the base $0 < (N_d^{1/2} r_0) < 1$. At N_d = const, this function is

---

[1] The variation in the other parameters in Eq. (2), in particular in D_i, resulting from the changes in the efficiency of the dislocation sinks, is assumed to be a secondary effect with respect to r and, therefore, is not taken into account in the approximation under study.

shown in Fig. 5. We see that the effective radius of trapping of arsenic by dislocations steeply grows with the gallium deficiency in the crystals where $[V_{Ga}] > [V_{As}]$ and only slightly depends on the vacancy composition if $[V_{Ga}] < [V_{As}]$.

CONCLUSIONS

Selenium and sulfur diffusion in undoped gallium arsenide single crystals depends on the joint effect of the vacancy composition and dislocation structure of the initial crystals.

In crystals with a deficiency in gallium, the diffusion profiles deviate from the erfc function. This deviation is caused by the secondary diffusion of an impurity from the surface to the vacancies formed due to the sink of arsenic to the dislocations.

The effective radius of the trapping of As by the dislocation sinks has a maximum value in crystals where the concentration of gallium vacancies is higher than the concentration of arsenic vacancies and decreases with an increase in arsenic deficiency. This is explained by the charge states of Ga and As vacancies and interstitial As atoms.

REFERENCES

1. F. S. Shishiyanu, *Diffusion and Degradation in Semiconductor Materials and Devices* (Shtiintsa, Kishinev, 1978).
2. M. G. Mil'vidskiĭ, O. V. Pelevin, and B. A. Sakharov, *Physicochemical Principles of Synthesis of Decomposing Semiconductor Compounds* (Metallurgiya, Moscow, 1974).
3. *Atomic Diffusion in Semiconductors*, Ed. by D. Shaw (Plenum, London, 1973; Mir, Moscow, 1975).
4. A. V. Young and L. G. Pearson, J. Phys. Chem. Solids **52**, 217 (1991).
5. A. V. Young and L. G. Pearson, J. Phys. Chem. Solids **31**, 517 (1970).
6. P. E. Childs, L. W. Laub, and J. B. Wagner, J. Br. Ceram. Soc., No. 19, 29 (1971).
7. I. N. Sorokin, V. Z. Petrova, Yu. D. Chistyakov, *et al.*, Zarubezhn. Élektron. Tekh., No. 14, 3 (1979).
8. G. P. Peka, V. F. Kovalenko, and V. N. Kutsenko, *Luminescence Methods of Control of the Parameters of Semiconductor Materials and Devices* (Tekhnika, Kiev, 1986).
9. K. D. Glinchuk, N. M. Litovchenko, A. V. Prokhorovich, *et al.*, Optoélektron. Poluprovodn. Tekh. **32**, 61 (1997).
10. V. F. Kovalenko, M. B. Litvinova, A. V. Prokhorovich, *et al.*, Optoélektron. Poluprovodn. Tekh. **31**, 129 (1996).
11. M. G. Mil'vidskiĭ and V. B. Osvenskiĭ, *Structural Defects in Semiconductor Single Crystals* (Metallurgiya, Moscow, 1984).

Translated by K. Kugel

Analysis of Chemical Bonding in the α and β Modifications of Zinc Diphosphide from X-ray Diffraction Data

I. E. Zanin*, K. B. Aleinikova*, and M. Yu. Antipin**

* Voronezh State University, Universitetskaya pl. 1, Voronezh, 394006 Russia
e-mail: zie@main.vsu.ru
** Nesmeyanov Institute of Organoelement Compounds, Russian Academy of Sciences,
ul. Vavilova 28, Moscow, 119991 Russia
Received January 15, 2002

Abstract—With the aim of studying the characteristic features of chemical interactions between atoms in the α (red tetragonal) and β (black monoclinic) modifications of zinc diphosphide, the maps of deformation electron-density distribution at the P–P and P–Zn bonds were constructed from precision X-ray diffraction data. The P–P bonds were demonstrated to be of a pronounced covalent nature. The maxima in the Zn–P bonds are shifted to the electronegative phosphorus atom, which is indicative of a mixed ionic–covalent nature of the bond, with the ionicity being higher in the α than in the β modification. Based on the dependence of the contribution of the metallic component on the delocalized electron density, it was concluded that the contribution of the metallic component is more pronounced in the black than in the red modification. An increase in the bond ionicity and the absence of delocalized electrons result in an increase in the forbidden gap in the red modification compared to its increase in the black modification. © 2003 MAIK "Nauka/Interperiodica".

INTRODUCTION

The formation of the tetragonal (α) [1] and monoclinic (β) modifications [2] of zinc diphosphide follows the rule of four electrons [3] implying the predominantly covalent character of chemical bonding. According to the bond scheme (Fig. 1), each zinc atom is surrounded by four phosphorus atoms, and each phosphorus atom is bound to two zinc and two phosphorus atoms. The atomic structures of both modifications of the ZnP_2 crystals are in complete agreement with this bond scheme. The atoms have a distorted tetrahedral coordination.

Both modifications have substantially different physical properties but have the same type of chemical bonding. The tetragonal modification is a high energy-gap semiconductor ($\Delta E = 2.25$ eV) characterized by a low carrier mobility, which allows one to use this modification as a dielectric in the MIS (metal-insulation–semiconductor) structures. In the monoclinic modification, the forbidden gap ($\Delta E = 1.33$ eV) is almost half as large as that in the tetragonal modification. It is commonly assumed that chemical bonding in complex semiconductors has a mixed ionic–covalent–metallic nature [4]. The predominance of the ionic component leads to a shift of the covalent bridge of the bond to the electronegative atom and an increase in the forbidden gap in comparison with the gap in isoelectron elemental semiconductors. An increase in the metallic component of the bond results in the "diffusion" of the covalent bridge, the appearance of delocalized electrons, and a decrease in the forbidden gap.

The construction of deformation electron-density (DED) maps based on precision X-ray diffraction data is the only direct way of obtaining information on the distribution of valence electrons and the nature of chemical bonding in crystals.

Our study was aimed at investigating the character of chemical bonding in two modifications of zinc diphosphide using DED maps constructed from precision X-ray diffraction data.

EXPERIMENTAL

Prismatic crystals of the α (**I**) and β (**II**) modifications of zinc diphosphide were prepared by deposition from the gas phase and then rolled into spheres 0.3–0.4 mm in diameter. The X-ray diffraction study of the α modification was performed on a Hilger–Watts diffractometer (λMoK_α radiation, graphite monochromator, $\theta/2\theta$ can, $\theta < 72°$). The X-ray diffraction study of the β modification was carried out on a Siemens P3 dif-

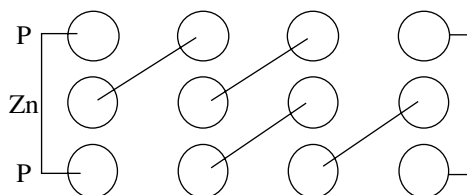**Fig. 1.** Scheme of the bonds in the α and β modifications of ZnP_2.

Table 1. Crystallographic characteristics, parameters of X-ray diffraction experiment, and details of structure refinement for modifications **I** and **II**

Structure, sp. gr.	α-ZnP$_2$ (**I**) $P4_32_12$	β-ZnP$_2$ (**II**) $P2_1/c$
T, K	293	293
a, Å	5.0661(5)	8.8632(7)
b, Å	5.0661(5)	7.2883(6)
c, Å	18.532(4)	7.5600(6)
β, deg	90	102.31(5)
V, Å^3	475.61(10)	477.10(80)
Number of observed reflections	7152	4312
Number of independent reflections with $F > 4\sigma(F)$	1958	2131
R	2.24	3.16
R_w	3.31	3.74
GOOF	1.13	1.3

Table 2. Atomic coordinates and equivalent isotropic thermal parameters (Å^2) in the crystal of modification **I**

Atom	x	y	z	U_{eq}
Zn	0.13554(4)	–0.34668(4)	0.05028(1)	0.00880(5)
P(1)	–0.19956(8)	0.31763(9)	0.05983(2)	0.00686(7)
P(2)	–0.01810(8)	0.00941(8)	0.12401(3)	0.00696(6)

Table 3. Atomic coordinates and equivalent isotropic thermal parameters (Å^2) in the crystal of modification **II**

Atom	x	y	z	U_{eq}
Zn(1)	0.0805(1)	0.7469(1)	0.3938(1)	0.003(1)
Zn(2)	0.3933(1)	0.0967(1)	0.2249(1)	0.003(1)
P(1)	0.3741(1)	0.4279(1)	0.2160(1)	0.001(1)
P(2)	0.2350(1)	0.0195(1)	0.4410(1)	0.001(1)
P(3)	0.2431(1)	0.4845(1)	0.4273(1)	0.002(1)
P(4)	0.0790(1)	0.2572(1)	0.3959(1)	0.002(1)

fractometer (λMoK_α radiation, graphite monochromator, $\theta/2\theta$ scan, $\theta < 75°$). The X-ray data for both modifications were collected within the full sphere of the reciprocal space at room temperature. The unit-cell parameters were refined using 24 reflections in the 2θ angular range from $22°$ to $25°$.

The structures were solved by the heavy-atom method and refined anisotropically by the full-matrix least-squares method (based on F_0) using the SHELXTL PLUS 4.2 program package [5]. The Ψ-scan empirical absorption corrections were applied to the X-ray data sets collected from both modifications. The absolute structure was confirmed by the refinement of the Flack parameter [6].

The crystallographic characteristics, parameters of X-ray diffraction study, and details of the structure refinement are given in Table 1. The atomic coordinates and thermal parameters U_{eq} for **I** and **II** are listed in Tables 2 and 3, respectively.

RESULTS AND DISCUSSION

A high-precision X-ray diffraction study of crystals **I** and **II** was carried out for the first time, which allowed us to determine more accurately the unit-cell parameters and interatomic distances and to compare the structures of these modifications. The refined P–P bond lengths in α-ZnP$_2$ (Table 4) are virtually equal to the P–P bond lengths in pure phosphorus (2.17 and 2.21 Å) [7]. The structure of α-ZnP$_2$ (Fig. 2) contains three crystallochemically independent atoms, namely, Zn, P(1), and P(2). All the atoms occupy eightfold positions. The P–P bonds form helical chains along the a and b axes. When projected, these chains resemble tetragonal wells. Three phosphorus chains are linked by zinc atoms. Two of these chains are extended along the same axis (either the a axis or the equivalent b axis), and the third chain is extended along another axis. The zinc atom forms two bonds with one of the equally directed chains and one bond with another chain. The maximum and minimum bond angles at the zinc atom are $124.17°$ and $99.39°$, respectively. These angles substantially differ from the ideal tetrahedral value ($109.5°$). Of the two crystallochemically independent phosphorus atoms, the P(2) atom is characterized by larger distortions of the tetrahedral angles (Table 4).

The structure of β-ZnP$_2$ (Fig. 3) contains six independent atoms in the fourfold positions. These are two zinc atoms [Zn(1) and Zn(2)] and four phosphorus atoms [P(1), P(2), P(3), and P(4)]. In the structure of **II**, the bond lengths and bond angles vary over wider ranges than the corresponding parameters in **I** (see Table 4). It was of interest to compare both structures and find the atoms in the structure of the β modification that can be considered as analogs of the zinc atom and both phosphorus atoms in the α modification. The bond angles appear to be the best parameters for this analysis. Thus, the maximum and minimum bond angles at the Zn(2) atom in the β modification are $125.7°$ and $101.3°$, respectively. These values are comparable with the bond angles at the zinc atom in the α modification (the maximum and minimum bond angles are $124.8°$ and $99.4°$, respectively). All six angles at the second crystallochemically independent zinc atom, namely, Zn(1) in β-ZnP$_2$, are close to the ideal tetrahedral value. Hence, we assumed that the Zn atoms in **I** are analogs of Zn(2) in **II**. Similarly, it was found that the P(1) atom in α-ZnP$_2$ is an analog of the P(1) atom in β-ZnP$_2$. The latter atom forms bonds only with the Zn(2) atom, which is an analog of the Zn atom in the

Table 4. Bond lengths d (Å) and bond angles ω (deg) for analogous atoms in the crystals of modifications **I** and **II**

I		II	
Analogous Zn and Zn(2) atoms			
Bond	d	Bond	d
Zn–P(2)	2.3931	Zn(2)–P(1)	2.420
Zn–P(1)	2.3601	Zn(2)–P(1)	2.360
Zn–P(1)	2.4064	Zn(2)–P(2)	2.435
Zn–P(2)	2.3932	Zn(2)–P(3)	2.431
Angle	ω	Angle	ω
P(1)–Zn–P(1)	124.18	P(1)–Zn(2)–P(1)	125.4
P(1)–Zn–P(2)	112.50	P(1)–Zn(2)–P(2)	110.9
P(2)–Zn–P(1)	105.12	P(2)–Zn(2)–P(3)	106.5
P(2)–Zn–P(2)	99.40	P(3)–Zn(2)–P(1)	101.3
P(2)–Zn–P(1)	103.32	P(1)–Zn(2)–P(3)	101.7
P(1)–Zn–P(2)	109.22	P(1)–Zn(2)–P(3)	109.4
Analogous P(1) and P(1) atoms			
Bond	d	Bond	d
P(1)–Zn	2.4094	P(1)–Zn(2)	2.420
P(1)–Zn	2.3601	P(1)–Zn(2)	2.360
P(1)–P(2)	2.2080	P(1)–P(2)	2.212
P(1)–P(2)	2.1673	P(1)–P(3)	2.205
Angle	ω	Angle	ω
Zn–P(1)–Zn	115.77	Zn(2)–P(1)–Zn(2)	117.5
P(2)–P(1)–Zn	113.85	P(2)–P(1)–P(3)	112.0
P(2)–P(1)–Zn	109.07	Zn(2)–P(1)–P(3)	112.1
P(2)–P(1)–(P2)	106.93	Zn(2)–P(1)–P(3)	109.8
P(2)–P(1)–Zn	106.00	Zn(2)–P(1)–P(3)	102.2
P(2)–P(1)–Zn	104.48	Zn(2)–P(1)–P(2)	102.7
Analogous P(2) and P(4) atoms			
Bond	d	Bond	d
P(2)–Zn	2.3932	P(4)–Zn(1)	2.342
P(2)–Zn	2.3931	P(4)–Zn(1)	2.341
P(2)–P(1)	2.2080	P(4)–P(2)	2.197
P(2)–P(1)	2.1673	P(4)–P(3)	2.184
Angle	ω	Angle	ω
P(1)–P(2)–Zn	112.24	P(3)–P(4)–Zn(1)	114.8
P(1)–P(2)–Zn	111.58	P(3)–P(4)–Zn(1)	112.4
P(1)–P(2)–Zn	110.3	P(2)–P(4)–Zn(1)	110.8
P(1)–P(2)–P(1)	109.2	P(2)–P(4)–Zn(1)	109.6
Zn–P(2)–Zn	108.27	Zn(1)–P(4)–Zn(1)	107.7
Zn–P(2)–P(1)	105.01	P(3)–P(4)–P(2)	101.4

II					
Bond	d	Bond	d	Bond	d
Zn(1)–P(2)	2.396	P(3)–Zn(2)	2.431	P(2)–Zn(2)	2.435
Zn(1)–P(3)	2.376	P(3)–Zn(1)	2.376	P(2)–Zn(1)	2.396
Zn(1)–P(4)	2.342	P(3)–P(1)	2.205	P(2)–P(1)	2.212
Zn(1)–P(4)	2.341	P(3)–P(4)	2.184	P(2)–P(4)	2.197
Angle	ω	Angle	ω	Angle	ω
P(2)–Zn(1)–P(3)	109.7	Zn(1)–P(3)–Zn(2)	119.7	Zn(1)–P(2)–Zn(2)	119.0
P(3)–Zn(1)–P(4)	110.9	Zn(1)–P(3)–P(1)	118.3	Zn(1)–P(2)–P(1)	118.0
P(4)–Zn(1)–P(2)	108.5	Zn(2)–P(3)–P(1)	110.9	Zn(1)–P(2)–P(4)	108.0
P(3)–Zn(1)–P(4)	110.9	Zn(1)–P(3)–P(4)	103.0	Zn(2)–P(2)–P(1)	107.8
P(2)–Zn(1)–P(4)	109.0	P(1)–P(3)–P(4)	102.8	P(4)–P(2)–P(1)	102.5
P(4)–Zn(1)–P(4)	107.7	P(4)–P(3)–Zn(2)	97.9	Zn(2)–P(2)–P(4)	98.5

Note: Errors in the bond lengths and bond angles are not higher than 0.0007 Å and 0.02°, respectively.
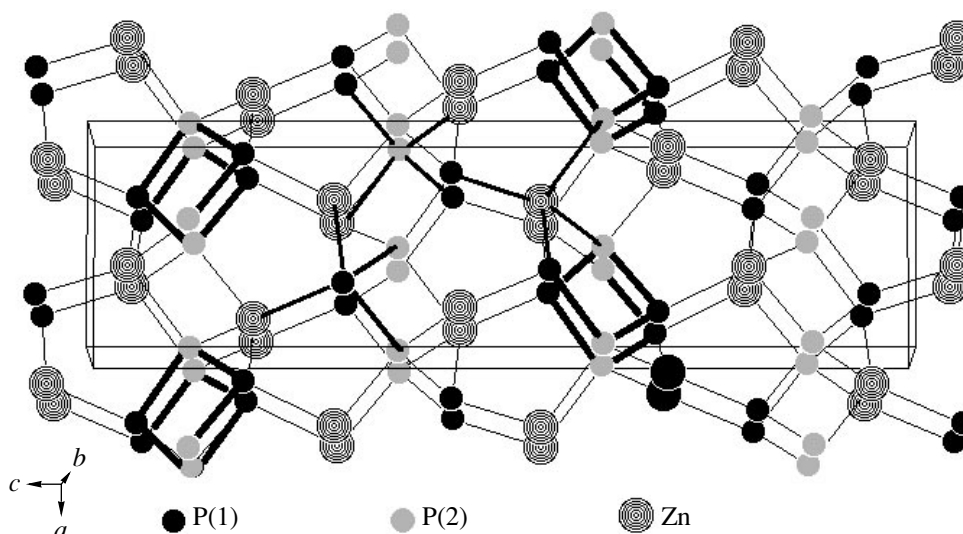
Fig. 2. Scheme of the α-ZnP₂ structure; the phosphorus chains are highlighted.

α-modification. The P(2) atom in **I** is comparable with the P(4) atom in **II**, with the latter being involved in bonding only with the Zn(1)-type atoms. The remaining two independent phosphorus atoms in **II**, namely, P(2) and P(3), are bound to the Zn(1) and Zn(2) atoms. These atoms have no analogs in the structure of **I**, but they can be treated as analogs of one another (Table 4).

In spite of the fact that three of the six independent atoms in the structure of β-ZnP₂ have analogs in the α-ZnP₂ structure, they form no common structural fragments. The phosphorus chains in β-ZnP₂ are less distinct than those in the α modification and are extended only along the *c* axis. When projected, these chains have the shape of an open irregular pentagon. The Zn(2) atom has three bonds with the P atoms of one chain, including the above-mentioned bond, and one bond with the P atom from another chain. The length of the bond with the adjacent chain (2.360 Å) is substantially shorter than the Zn–P bond length within the chain.

The Zn(1) atom is involved in bonds with three phosphorus chains and forms two equal bonds with the P(4) atoms from one chain and bonds of virtually the same lengths with the P(2) and P(3) atoms from two other chains.

The X-ray diffraction data were used to construct DED maps. To obtain maps that give most information on the valence electron distribution at the bonds, we chose the small-angle scattering empirically. In the maps constructed with the use of the reflections with $(\sin\theta)/\lambda > 0.75$ Å^{-1}, the maxima on the bonds are seen rather poorly but the asymmetry of the environment around the zinc atom becomes quite clear. The reduction of $(\sin\theta)/\lambda$ down to 0.4 Å^{-1} leads to a dramatic decrease in the number of reflections and can give rise to the maxima of the termination waves. Chemical

bonding was analyzed using the electron density maps that had no asymmetry of atoms. For the structures under consideration and experimental conditions used, this condition was fulfilled in the $(\sin\theta)/\lambda$ range from 0.65 to 0.7 Å^{-1}.

The DED sections passing through the P–P bonds involving the analogous atoms, namely, P(1) in the α-ZnP₂ phase and P(4) in β-ZnP₂ phase, are shown in Figs. 4 and 5, respectively. The sections are characterized by pronounced maxima located at the midpoints between the phosphorus nuclei, which confirms the pure covalent nature of bonding in the phosphorus
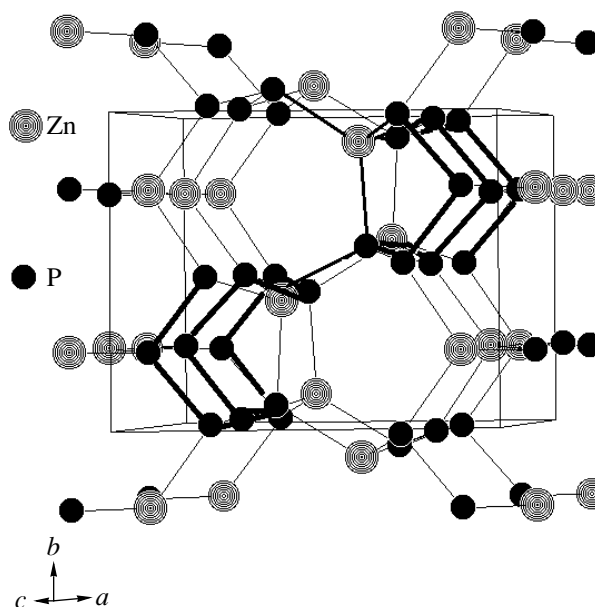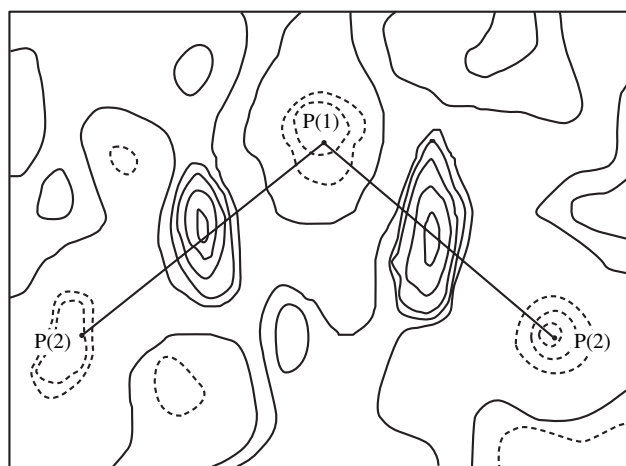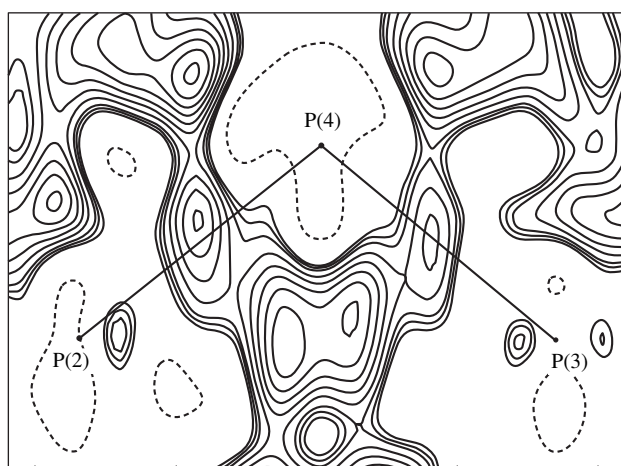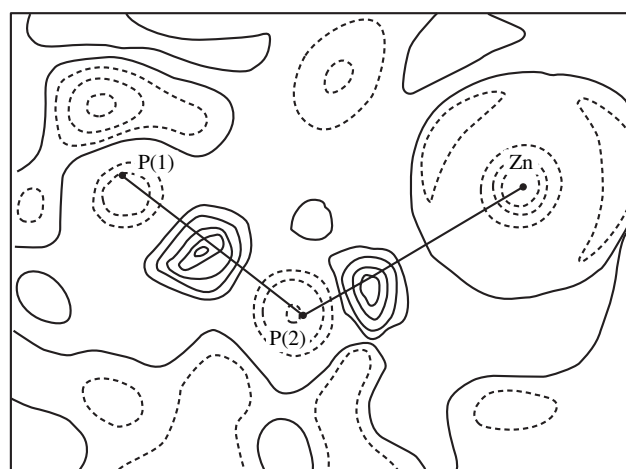

Fig. 3. Scheme of the β-ZnP₂ structure; the phosphorus chains are highlighted.
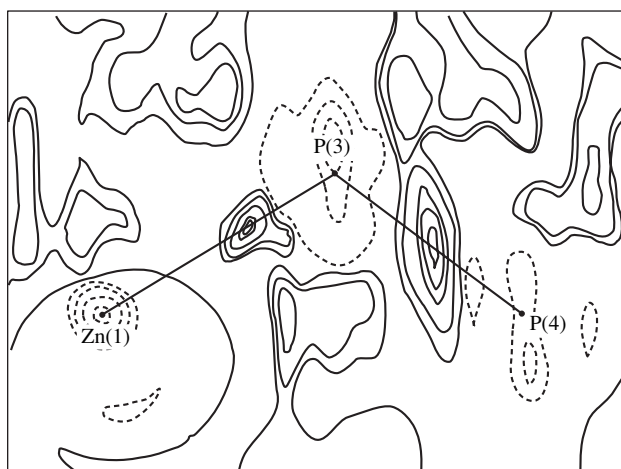
Fig. 4. The DED section through the P–P–P bonds in α-ZnP$_2$.

Fig. 5. The DED section through the P–P–P bonds in β-ZnP$_2$.

Fig. 6. The DED section through the Zn–P–P bonds in α-ZnP$_2$.

Fig. 7. The DED section through the Zn–P–P bonds in β-ZnP$_2$.

chains. In the DED sections of α-ZnP$_2$, the maxima on both bonds have equal heights (0.25 e/Å^3). In the DED sections of β-ZnP$_2$, the maxima in the P(4)–P(2) and P(4)–P(3) bonds have different heights (0.35 and 0.25 e/Å^3, respectively). The maxima are elongated in a direction that is almost perpendicular to the bond line. On the whole, the character of DED distribution at the P–P bonds in α-ZnP$_2$ is analogous to that in β-ZnP$_2$. The main difference comes down to the fact that the β modification is characterized by a high delocalized electron density, which indicates that the metallic component of the bond in this modification is larger than that in the α modification. An increase in the metallic component of the bond leads to equalization of the lattice potential and a decrease in the forbidden gap, which was actually observed.

The DED distributions in the plane passing through the bonds involving the zinc atom are shown in Figs. 6

and 7. The maximum in the P(4)–P(3) bond is virtually equal to the maximum in the DED section passing through the P–P bonds. The difference in the heights is 0.05 e/Å^3, which corresponds to the accuracy of the experimental data and indicates the good reproducibility of the results. The DED maximum in the Zn(1)–P(3) bond (Fig. 6) is shifted to the electronegative phosphorus atom, which is, apparently, evidence for the presence of the ionic component of the bond. The maximum height equals 0.25 e/Å^3. In the red zinc diphosphide modification, the shift of the maximum on the Zn–P bond to the phosphorus atom is somewhat larger than that in the black modification, although the maximum heights are equal within the experimental error. Consequently, the ionicity of the bond in **I** is higher than the ionicity in **II**. An increase in the ionic component of the bond always gives rise to an increase in the

forbidden gap, with the average atomic number in the compounds being the same.

The DED section though the P(1)–P(2) bond (Fig. 6) in α-ZnP$_2$ differs from that shown in Fig. 4. Like the maximum in the Zn–P(2) bond, the maximum in the P(1)–P(2) bond is almost spherical in shape and is localized exactly between two phosphorus atoms. The height of this maximum is 0.25 e/Å^3.

The estimation of the covalent component of the bond from the charge on the bond bridge leads to the conclusion that, on average, the charge on the bonds and, consequently, the degree of covalence are higher in the black modification than in the red one (Figs. 4–7). Since an increase in the ionic component of the bond leads to an increase in the forbidden gap, whereas an increase in the metallic component leads to its decrease, the forbidden gap in the red modification should be more pronounced than in the black modification. This assumption was confirmed experimentally. It should be noted that the DED maps constructed from the X-ray diffraction data correlate quite well with the distributions of valence electrons calculated theoretically by the pseudopotential method [8].

REFERENCES

1. J. G. White, Acta Crystallogr. **18**, 217 (1965).
2. M. E. Fleet and T. A. Mowles, Acta Crystallogr., Sect. A: Found. Crystallogr. **40**, 1778 (1984).
3. N. A. Goryunova, *Compound Diamond-Like Semiconductors* (Sov. Radio, Moscow, 1968), p. 30.
4. B. F. Ormont, *Introduction to Physical Chemistry and Crystal Chemistry of Semiconductors* (Vysshaya Shkola, Moscow, 1982).
5. G. M. Sheldrick, *SHELXTL PLUS. Release 4.2.* (Siemens Analytical Instruments Inc., Madison, Wisconsin, USA, 1991).
6. H. D. Flack, Acta Crystallogr., Sect. A: Found. Crystallogr. **39**, 876 (1983).
7. A. Wells, *Structural Inorganic Chemistry* (Clarendon, Oxford, 1984; Mir, Moscow, 1987).
8. Yu. A. Poplavnoĭ and Yu. N. Polygalov, Zh. Strukt. Khim. **34** (5), 47 (1993).

Translated by T. Safonova

STRUCTURE
OF INORGANIC COMPOUNDS

Structure and Properties of Potassium Titanyl Phosphate Single Crystals with 7 and 11 at. % Nb

O. A. Alekseeva*, N. I. Sorokina*, I. A. Verin*, T. Yu. Losevskaya**, V. I. Voronkova**,
V. K. Yanovskiĭ**, and V. I. Simonov*

* Shubnikov Institute of Crystallography, Russian Academy of Sciences,
Leninskiĭ pr. 59, Moscow, 119333 Russia
e-mail: simonov@ns.crys.ras.ru
** Moscow State University, Vorob'evy gory, Moscow, 119992 Russia
Received July 4, 2002

Abstract—This study is a continuation of research into the atomic structure and physical properties of niobium-doped potassium titanyl phosphate crystals, $KTiOPO_4$ (KTP : Nb). Crystals containing 7 and 11 at. % of niobium were grown and studied. With an increase in niobium content, the number of vacancies and additional potassium positions in the structure also increase. This fact accounts for an increase in both the intensities of relaxation peaks and the conductivity of KTP : Nb crystals. © 2003 MAIK "Nauka/Interperiodica".

INTRODUCTION

Recently, the physical properties and atomic structure of niobium-doped potassium titanyl phosphate crystals, $KTiOPO_4$ (KTP : Nb), have attracted ever increasing attention of researchers [1–7]. KTP crystals possess a unique combination of nonlinear optical, ferroelectric, and superionic properties. Studies of the physical properties of the KTP : Nb crystals have shown that the intensity of the second harmonic generation (SHG) of laser radiation increased in the presence of a small amount of Nb [1] and decreased at an Nb content exceeding 3 at. % [5]. Also, an increase in the Nb content leads to an increase by an order of magnitude of crystal conductivity [3, 5] and a considerable lowering of the phase-transition temperature T_c [5].

The atomic structure of KTP : Nb single crystals with about 3–4 at. % Nb has been studied in sufficient detail by several research groups [1, 4, 7]. It should be noted that the replacement of tetravalent titanium by pentavalent niobium gives rise to the formation of additional vacancies in the K(1) and K(2) positions, with the niobium atoms occupying only the Ti(1) positions [1, 7]. Moorthy *et al.* [4] revealed niobium atoms in two positions, Ti(1) and Ti(2). Additional potassium positions were revealed in [7].

The present study continues our research into the atomic structure and physical properties of KTP : Nb crystals. We grew and studied the crystals doped with 7 and 11 at. % Nb.

EXPERIMENTAL

Single crystals were grown from flux in the quaternary K_2O–TiO_2–Nb_2O_5–P_2O_5 system [5]. Crystals doped with 7 and 11 at. % Nb (determined by chemical analysis) were prepared from melts in which niobium replaced 34 and 46 at. % Ti, respectively. The niobium content in the latter crystal appeared to be close to its maximum content in crystals with a KTP structure, because crystallization from systems in which more than 50% Ti is replaced by niobium yielded monoclinic crystals of another structure type [8, 9].

The chemical composition of the crystals was determined on a Cameca SX-50 X-ray microanalyzer. The temperature dependences of the dielectric constant and electrical conductivity were measured on a Tesla BM-431E bridge at a frequency of 1 MHz in the temperature range from room temperature to 800°C.

The optically homogeneous crystals chosen for X-ray diffraction study were ground to spheres. The samples that were most spherical in shape gave the best X-ray diffraction patterns and therefore were selected for the subsequent investigation. A single crystal with 7 at. % Nb was a sphere 0.10 mm in radius. A single crystal with 11 at. % Nb had the shape of an ellipsoid $(0.25 \times 0.19 \times 0.19$ mm). The details of X-ray data collection are given in Table 1. The parameters of the orthorhombic unit-cell (sp. gr. $Pna2_1$, Table 2) were refined by the least-squares method based on 25 reflections. The complete sets of reflection intensities were collected on a CAD-4F Enraf-Nonius diffractometer equipped with a graphite monochromator.

Both structures were refined by the least-squares method using the JANA 98 program [10]. The atomic coordinates from [7] were used as the starting model in the refinement, in the course of which all the extinction models included in the JANA 98 program were tested. The best results were obtained with the use of the Becker–Coppens extinction correction taking into account misorientation of blocks of mosaic (type I).

Table 1. Details of X-ray data collection and refinement of KTP : Nb single crystals (7 and 11 at. % Nb)

	KTP : Nb (7 at. % Nb)	KTP : Nb (11 at. % Nb)
Chemical composition	$K_{0.93}Ti_{0.93}Nb_{0.07}OPO_4$	$K_{0.89}Ti_{0.89}Nb_{0.11}OPO_4$
Sample radius, mm	$0.10 \times 0.10 \times 0.10$	$0.25 \times 0.19 \times 0.19$
μ, cm^{-1}	32.51	32.84
Diffractometer	"Enraf-Nonius" CAD-4F	
Radiation	MoK_{α}	
Monochromator	graphite	
Scanning technique	$\omega/2\theta$	
θ_{max}, deg	45	
Ranges of h, k, l variation	$-25 \leq h \leq 25$	
	$-12 \leq k \leq 12$	
	$0 \leq l \leq 20$	
Total number of measured reflections and $|F|_{hkl}$	14 193	13 112
Number of independent reflections with $|F|_{hkl} > 3\sigma_{|F|hkl}$	3467	2972
$R_{av}(|F|_{hkl})$, %	1.09	1.80
Structure type	$KTiOPO_4$	
Program for structural computations	JANA 98	
Weighting scheme	$1/\sigma^2$	
Number of parameters in the refinement	220	
Reliability factors R/R_w	1.93/2.21	2.54/3.10

RESULTS AND DISCUSSION

Similar to the structure of KTP crystals containing 4 at. % Nb [7], the structures containing 7 and 11 at. % Nb contain two crystallographically independent titanium positions. All the niobium atoms occupy only one of these positions, Ti(1). Apparently, this is associated with the fact that the cavity occupied by the Ti(1) atom is somewhat larger than that occupied by the Ti(2) atom. The corresponding average distances are (Ti(1)–O)$_{av}$ = 1.974 Å and (Ti(2)–O)$_{av}$ = 1.966 Å for the structure with 7 at. % Nb and (Ti(1)–O)$_{av}$ = 1.972 Å and (Ti(2)–O)$_{av}$ = 1.962 Å for the structure with 11 at. % Nb. Since the ionic radius of Nb^{5+} (0.69 Å) is somewhat larger than that of Ti^{4+} (0.68 Å), the niobium atoms prefer to replace titanium atoms in the Ti(1)-position.
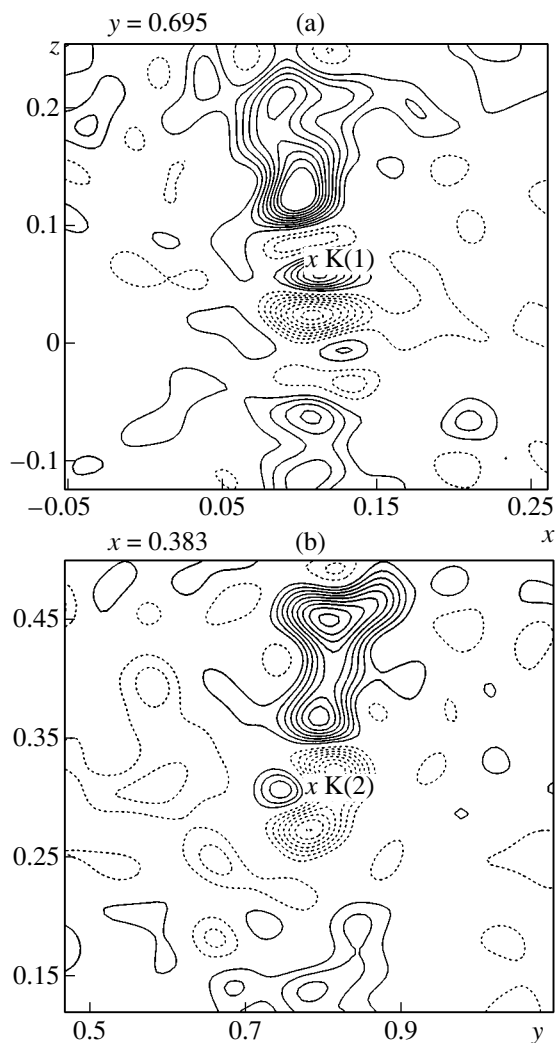
The difference electron-density maps constructed based on this structural model (Figs. 1, 2) revealed residual electron-density peaks in the vicinity of the

Table 2. Unit-cell parameters of the KTP and KTP : Nb (4, 7, and 11 at. % Nb) crystals

	a, Å	b, Å	c, Å	V, Å^3
KTP	12.817(1)	6.403(1)	10.589(1)	868.9(1)
4 at. % Nb	12.814(2)	6.408(1)	10.587(2)	869.5(1)
7 at. % Nb	12.816(1)	6.412(1)	10.595(1)	870.7(1)
11 at. % Nb	12.815(1)	6.415(1)	10.591(1)	870.7(1)

K(1) position (a peak of height 1.65 e/Å^3 at a distance of 0.83 Å and a peak of height 2.03 e/Å^3 at a distance of 0.88 Å in the structures with 7 and 11 at. % Nb, respectively) and K(2) position (a peak of height 2.58 e/Å^3 at a distance of 1.71 Å and a peak of height 3.82 e/Å^3 at a distance of 1.74 Å in the structures with 7 and 11 at. % Nb, respectively). Then the structures were refined within the framework of the models with split K(1) and K(2) positions. The refined parameters were used for constructing difference electron-density maps ($F_{obs} - F_{calcd}$). The sections of these maps passing through the K(1), K(2), K(3), and K(4) atoms for the structures with 7 and 11 at. % Nb are shown in Figs. 3 and 4, respectively. The occupancies of the potassium positions are given in Table 3. Thus, the chemical formulas of the compounds studied can be written as $K_{0.89}Ti_{0.93}Nb_{0.07}OPO_4$ and $K_{0.87}Ti_{0.89}Nb_{0.11}OPO_4$, respectively. The number of K vacancies in these formulas is larger than could be expected under the condition of preservation of electroneutrality without any changes in the valence states of other ions. The sections of the difference electron-density maps ($F_{obs} - F_{calcd}$) show peaks of heights 1.09, 0.93, and 0.80 e/Å^3 (in the structure with 7 at. % Nb) and peaks of heights 0.95, 0.90, and 0.81 e/Å^3 (in the structure with 11 at. % Nb) in the vicinity of the potassium positions (Figs. 3, 4). Apparently, these peaks correspond to the missing potassium atoms necessary for the preservation of electroneutrality. A higher degree of splitting with the for-

Fig. 1. Difference electron-density maps for the starting model of the $K_{0.93}Ti_{0.93}Nb_{0.07}OPO_4$ structure; sections passing through (a) K(1) and (b) K(2) atoms; hereinafter, the contours are spaced by 0.163 e/Å^3.
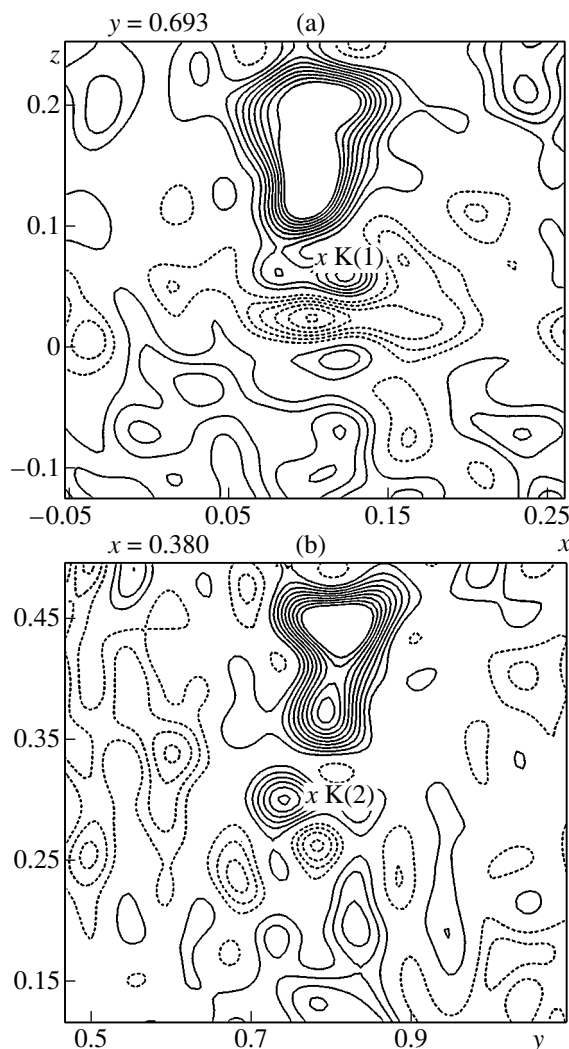
Fig. 2. Difference electron-density maps for the starting model of the $K_{0.89}Ti_{0.89}Nb_{0.11}OPO_4$ structure; sections passing through (a) K(1) and (b) K(2) atoms.

mation of additional positions is also evidenced by the elongation of the electron-density peaks occupied by the K(3) and K(4) atoms (Figs. 1, 2) and their high thermal parameters (Tables 4, 5). However, it was impossible to refine the structural parameters of the new additional potassium positions.

The coordinates of the basis atoms, occupancies q of the crystallographic positions, and equivalent thermal parameters B_{eq} for the crystal structures are given in Tables 4 and 5.

The temperature dependence of the dielectric constant ε_{33} for the KTP single crystal with 11 at. % Nb is presented in Fig. 5. For comparison, this figure also shows the dependences for the corresponding undoped KTP crystal and the crystal with a low (0.2 at. %) niobium content. As can be seen from Fig. 5, the incorporation of a small amount of Nb leads to a shift of T_c to

the low-temperature region and an increase in the relaxation-peak intensity, which has been observed earlier for an undoped KTP crystal [11]. At the maximum Nb content (~11 at. %, Fig. 5, curve *3*), the ferroelectric phase transition occurs at the temperature range of the relaxation peak characterized by several successive anomalies. Therefore, the temperature T_c was determined by the SHG method and is equal to 350°C [5].

Table 3. Occupancies of the potassium positions in the KTP : Nb crystals (4, 7, and 11 at. % Nb)

Structure	K(1)	K(2)	K(3)	K(4)
4 at. % Nb	0.899(1)	0.858(2)	0.108(2)	–
7 at. % Nb	0.702(2)	0.773(1)	0.148(1)	0.168(2)
11 at. % Nb	0.610(1)	0.636(1)	0.275(1)	0.228(2)
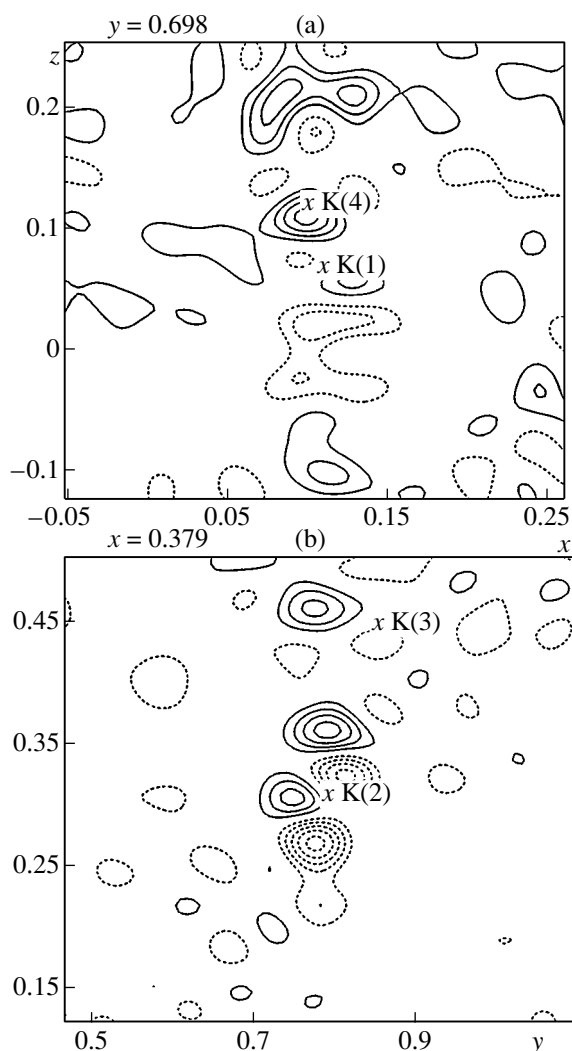
Fig. 3. Difference electron-density maps for the model of the structure of $K_{0.93}Ti_{0.93}Nb_{0.07}OPO_4$ with the statistical distribution of the potassium atoms over the crystallographically independent positions; sections passing through (a) K(1) and K(4) and (b) K(2) and K(3) atoms.

Fig. 4. Difference electron-density maps for the model of the structure of $K_{0.89}Ti_{0.89}Nb_{0.11}OPO_4$ with the statistical distribution of the potassium atoms over independent positions; sections passing through (a) K(1) and K(4) and (b) K(2) and K(3) atoms.

The conductivity σ_{33} of KTP : Nb crystals measured at a frequency of 1 MHz increased with the Nb content (Fig. 6).

The crystals of potassium titanyl phosphate with 7 and 11 at. % Nb are isostructural to undoped KTP crystals and potassium titanyl phosphate crystals with 4 at. % Nb [7]. The unit-cell parameters of all these crystals are given in Table 2. It is seen that the incorporation of Nb into the KTP structure with the accompanying partial replacement of Ti atoms produces no noticeable effect on the unit-cell parameters. Apparently, this is associated with the close ionic radii of Nb^{5+} and Ti^{4+}.

The above crystal structures are composed of $(Ti,Nb)O_6$-octahedra sharing vertices with PO_4-tetrahedra to form three-dimensional frameworks. The chan-

nels in the structures are occupied by potassium ions. As can be seen from Table 3, the change in the niobium content in the crystals leads to substantial changes in the occupancies of all the potassium positions. The occupancies of the main K(1) and K(2) positions decrease, whereas the occupancies of the additional K(3) and K(4) positions increase; in other words, more pronounced splitting of the potassium positions takes place. The formation of additional potassium positions may account for the successive anomalies of the relaxation peak (Fig. 5). These anomalies seem to be associated with hoppings of potassium ions. The lengths of these hoppings were estimated from the dielectric measurements on a KTP crystal with 3 at.% Nb at several frequencies [11]. These distances ranged from 0.34 to 1.52 Å. The results obtained are consistent with data in

Table 4. Atomic coordinates, occupancies of positions (q), and equivalent thermal parameters B_{eq} (Å^2) in the structure of $K_{0.93}Ti_{0.93}Nb_{0.07}OPO_4$

Atom	x/a	y/b	z/c	q	B_{eq}
Ti(1)	0.37230(1)	0.49979(1)	0	0.854(1)	0.55(1)
Nb(1)	0.37230(1)	0.49979(1)	0	0.146	0.55(1)
Ti(2)	0.24764(1)	0.26539(1)	0.24996(2)	1	0.62(1)
P(1)	0.49859(1)	0.33744(2)	0.25715(3)	1	0.52(1)
P(2)	0.18179(1)	0.50138(3)	0.50914(2)	1	0.53(1)
K(1)	0.10498(3)	0.69795(7)	0.06497(4)	0.702(2)	1.64(1)
K(2)	0.37920(2)	0.78162(4)	0.30868(4)	0.773(1)	1.73(1)
K(3)	0.4026(2)	0.8441(5)	0.4434(4)	0.148(1)	5.47(9)
K(4)	0.6067(2)	0.7959(3)	0.1713(6)	0.168(2)	14.7(4)
O(1)	0.48609(6)	0.4841(1)	0.14574(6)	1	0.86(1)
O(2)	0.51020(5)	0.4685(1)	0.37921(6)	1	0.86(1)
O(3)	0.40089(4)	0.1994(1)	0.27664(7)	1	0.73(1)
O(4)	0.59431(4)	0.1956(1)	0.23923(8)	1	0.77(1)
O(5)	0.11234(5)	0.3109(1)	0.53702(7)	1	0.74(1)
O(6)	0.11249(5)	0.6910(1)	0.48371(7)	1	0.91(1)
O(7)	0.25303(6)	0.5400(1)	0.62480(7)	1	0.85(1)
O(8)	0.25343(6)	0.4612(1)	0.39549(7)	1	0.83(1)
O(9)	0.22416(5)	0.0416(1)	0.38601(7)	1	0.76(1)
O(10)	0.22444(5)	−0.0359(1)	0.63911(7)	1	0.76(1)

Table 5. Atomic coordinates, occupancies of positions (q), and equivalent thermal parameters B_{eq} (Å^2) in the structure of $K_{0.89}Ti_{0.89}Nb_{0.11}OPO_4$

Atom	x/a	y/b	z/c	q	B_{eq}
Ti(1)	0.37184(1)	0.49964(1)	0	0.789(1)	0.55(1)
Nb(1)	0.37193(1)	0.49964(3)	0	0.211	0.55(1)
Ti(2)	0.24814(1)	0.25164(2)	0.24968(3)	1	0.72(1)
P(1)	0.49896(1)	0.33776(2)	0.25518(3)	1	0.47(1)
P(2)	0.18206(1)	0.50094(3)	0.50644(2)	1	0.48(1)
K(1)	0.10433(3)	0.69458(7)	0.06393(5)	0.610(1)	1.69(1)
K(2)	0.37969(3)	0.78198(5)	0.30693(4)	0.636(1)	1.64(1)
K(3)	0.3993(1)	0.8313(3)	0.4406(2)	0.275(1)	5.76(7)
K(4)	0.1077(2)	0.7049(3)	0.1713(6)	0.228(2)	8.9(29)
O(1)	0.48672(6)	0.4819(1)	0.14237(6)	1	0.78(1)
O(2)	0.51075(6)	0.4710(1)	0.37632(6)	1	0.88(1)
O(3)	0.40145(4)	0.1983(1)	0.27471(7)	1	0.66(1)
O(4)	0.59508(4)	0.1973(1)	0.23745(7)	1	0.71(1)
O(5)	0.11225(5)	0.31036(1)	0.53424(6)	1	0.68(1)
O(6)	0.11289(5)	0.6904(1)	0.48075(7)	1	0.85(1)
O(7)	0.25335(6)	0.5404(1)	0.62249(7)	1	0.82(1)
O(8)	0.25299(6)	0.4612(1)	0.39258(6)	1	0.77(1)
O(9)	0.22426(5)	0.0409(1)	0.38253(6)	1	0.72(1)
O(10)	0.22445(5)	−0.0376(1)	0.63553(6)	1	0.74(1)

Table 6. Interatomic distances (Å) in the KTP : Nb crystals (4, 7, and 11 at. % Nb)

Distances	$K_{0.96}Ti_{0.96}Nb_{0.04}OPO_4$	$K_{0.93}Ti_{0.93}Nb_{0.07}OPO_4$	$K_{0.89}Ti_{0.89}Nb_{0.11}OPO_4$
Ti(1)–O(9)	1.732(1)	1.750(1)	1.771(1)
O(10)	1.959(1)	1.940(1)	1.908(1)
O(1)	2.139(1)	2.127(1)	2.110(1)
O(2)	1.972(1)	1.987(1)	2.004(1)
O(5)	2.046(1)	2.044(1)	2.036(1)
O(6)	1.990(1)	1.998(1)	2.004(1)
Ti(2)–O(9)	2.077(1)	2.057(1)	2.019(1)
O(10)	1.750(1)	1.770(1)	1.801(1)
O(3)	2.036(1)	2.030(1)	2.024(1)
O(4)	1.981(1)	1.985(1)	1.983(1)
O(7)	1.959(1)	1.962(1)	1.957(1)
O(8)	1.994(1)	1.991(1)	1.985(1)
P(1)–O(1)	1.517(1)	1.518(1)	1.519(1)
O(2)	1.550(1)	1.550(1)	1.549(1)
O(3)	1.543(1)	1.548(1)	1.551(1)
O(4)	1.540(1)	1.540(1)	1.538(1)
P(2)–O(5)	1.538(1)	1.541(1)	1.543(1)
O(6)	1.532(1)	1.531(1)	1.529(1)
O(7)	1.548(1)	1.549(1)	1.552(1)
O(8)	1.537(1)	1.536(1)	1.531(1)
K(1)–O(1)	2.685(1)	2.687(1)	2.700(1)
O(2)	3.002(1)	3.012(1)	3.044(1)
O(3)	3.050(1)	3.056(1)	3.064(1)
O(4)	3.119(1)	3.131(1)	3.116(1)
O(5)	2.802(1)	2.803(1)	2.794(1)
O(7)	2.926(1)	2.922(1)	2.938(1)
O(8)	3.060(1)	3.062(1)	3.093(1)
O(9)	3.062(1)	3.066(1)	3.080(1)
O(10)	2.760(1)	2.767(1)	2.758(1)
K(2)–O(1)	2.908(1)	2.916(1)	2.937(1)
O(2)	2.733(1)	2.723(1)	2.709(1)
O(3)	2.718(1)	2.716(1)	2.707(1)
O(5)	2.874(1)	2.887(1)	2.896(1)
O(7)	3.059(1)	3.070(1)	3.078(1)
O(8)	2.759(1)	2.770(1)	2.772(1)
O(9)	2.717(1)	2.722(1)	2.715(1)
O(10)	3.009(1)	3.024(1)	3.046(1)
K(3)–O(1)		3.327(4)	3.277(2)
O(2)	2.74(1)	2.859(3)	2.801(2)
O(3)	2.73(1)	2.885(4)	2.938(2)
O(4)		3.145(4)	3.150(3)
O(6)	2.80(1)	2.734(3)	2.773(2)
O(7)	–	3.344(4)	3.270(2)
O(8)	3.07(1)	3.155(3)	3.067(2)
O(9)	2.66(1)	2.686(3)	2.687(2)
O(10)	3.45(2)	3.180(4)	3.161(2)
K(4)–O(1)		2.614(4)	2.552(3)
O(2)		3.45(1)	3.229(5)
O(4)		2.72(1)	2.667(3)
O(5)		2.86(1)	3.170(4)
O(6)			3.250(6)
O(7)		2.985(4)	2.861(3)
O(8)			3.363(5)
O(9)		3.47(1)	3.439(5)
O(10)		2.655(4)	2.698(3)
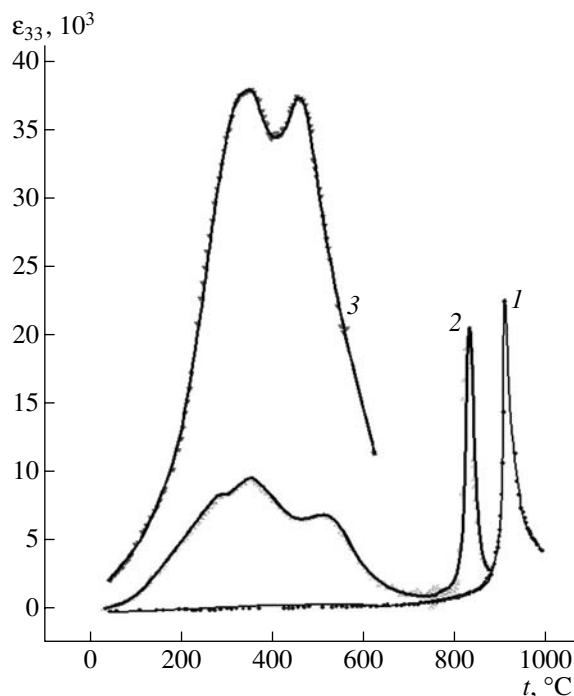
Fig. 5. Temperature dependence of the dielectric constant ε_{33} for $K_{1-x}Ti_{1-x}Nb_xOPO_4$ crystals with different Nb content x: (*1*) 0, (*2*) 0.002, and (*3*) 0.11.
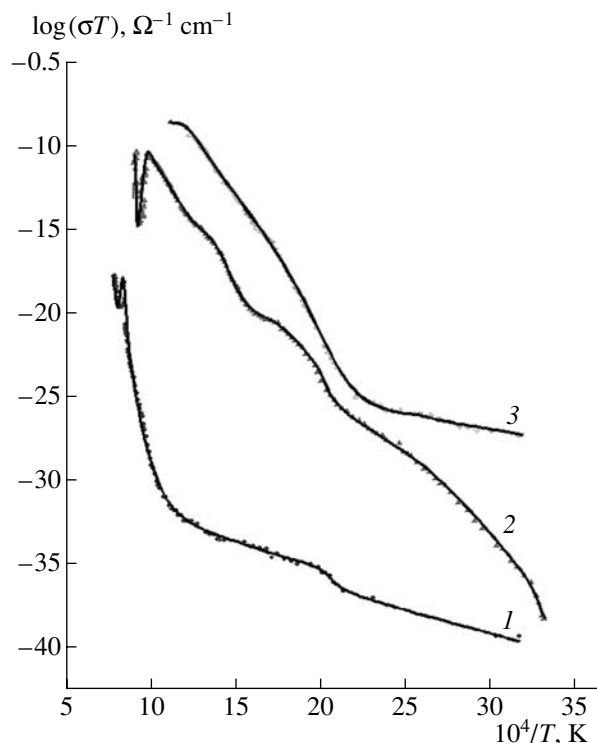
Fig. 6. Temperature dependence of the conductivity σ_{33} of $K_{1-x}Ti_{1-x}Nb_xOPO_4$ crystals with different Nb content x: (*1*) 0, (*2*) 0.002, and (*3*) 0.11.

[7], which also indicate the formation of additional potassium positions.

The replacement of titanium by niobium atoms in potassium titanyl phosphate results in the elongation of short Ti–O distances and the shortening of long Ti–O distances in TiO_6-octahedra, with the average length of the remaining four bonds being unchanged (Table 6). Thus, an increase in the niobium content gives rise to changes in the Ti–O distances such that the TiO_6-octahedra become more symmetric, which may account for the decrease in the SHG intensity in the crystals [5].

The structural studies of single crystals of potassium titanyl phosphate with 4, 7, and 11 at. % Nb demonstrated that the numbers of vacancies and additional potassium positions in the structures increase with niobium content. This fact accounts for the increase in both the relaxation-peak intensities and conductivity of niobium-doped KTP crystals.

ACKNOWLEDGMENTS

REFERENCES

1. P. A. Thomas and B. E. Watts, Solid State Commun. **73** (2), 97 (1990).
2. L. T. Cheng, L. K. Cheng, R. L. Harlow, and J. D. Bierlein, Appl. Phys. Lett. **64** (2), 155 (1994).
3. P. U. M. Sastry, M. S. Somayazulu, and A. Sequiera, Mater. Res. Bull. **27**, 1385 (1992).
4. S. G. Moorthy, F. J. Kumar, C. Subramanian, *et al.*, Mater. Lett. **36**, 266 (1998).
5. T. Yu. Losevskaya, O. A. Alekseeva, V. K. Yanovskiĭ, *et al.*, Kristallografiya **45** (5), 809 (2000) [Crystallogr. Rep. **45**, 739 (2000)].
6. K. B. Hutton, R. C. C. Ward, R. Cameron, *et al.*, Proc. SPIE **3928**, 77 (2000).
7. O. A. Alekseeva, M. K. Blomberg, V. N. Molchanov, *et al.*, Kristallografiya **46** (4), 710 (2001) [Crystallogr. Rep. **46**, 642 (2001)].
8. O. A. Alekseeva, N. I. Sorokina, M. K. Blomberg, *et al.*, Kristallografiya **46** (2), 215 (2001) [Crystallogr. Rep. **46**, 176 (2001)].
9. V. K. Yanovskii and V. I. Voronkova, Phys. Status Solidi A **93**, 665 (1986).
10. V. Petrićek and M. Dusek, *JANA'98: Crystallographic Computing System* (Inst. of Physics, Praha, 1998).
11. S. Yu. Stefanovich and A. V. Mosunov, Izv. Ross. Akad. Nauk, Ser. Fiz. **64**, 1163 (2000).

Translated by T. Safonova

STRUCTURE
OF INORGANIC COMPOUNDS

Crystal Structure of Sr(AsUO$_6$)$_2$ · 8H$_2$O

D. Yu. Pushcharovskiĭ*, E. V. Suleimanov**, M. Pasero***, S. Merlino***,
A. V. Barinova*, and E. V. Alekseev**

* Faculty of Geology, Moscow State University, Vorob'evy gory, Moscow, 119992 Russia
e-mail: dmitp@geol.msu.ru
** Nizhni Novgorod State University, pr. Gagarina 23, Nizhni Novgorod, 603950 Russia
*** University of Pisa, Via S. Maria 53, Pisa, I-56126 Italy
Received August 28, 2002

Abstract—The crystal structure of the compound Sr(AsUO$_6$)$_2$ · 8H$_2$O is determined by X-ray diffraction analysis (monoclinic system, sp. gr. *Pc*, unit-cell parameters $a = 7.154(1)$ Å, $b = 7.101(1)$ Å, $c = 18.901(7)$ Å, $\beta = 92.67(2)°$, $Z = 2$). The structure is built by (001)-parallel [AsUO$_6$]$^-$ layers formed by flattened square UO$_6$ bipyramids and AsO$_4$ tetrahedra. The neighboring layers are connected via SrO$_8$ square antiprisms. The cavities of the polyhedral framework thus formed are occupied by H$_2$O molecules. The displacements of the anion complexes by a half-translation with respect to one another along only one lattice period is a characteristic feature of this polymorphous modification of the uran-mica group. © *2003 MAIK "Nauka/Interperiodica".*

INTRODUCTION

The relatively low content of uranium in the earth's crust does not correspond to the mineralogical and geochemical importance of this chemical element, which is present in the composition of more than 5% of all existing minerals. The study of U–Pb decomposition seems to be extremely important for rock dating. As a source of energy, uranium has attracted the attention of economists for more than sixty years. Recently, interest in the crystal chemistry of uranium has been associated with solving problems of the environment and the rational use of mineral raw materials in the regions where uranium-containing mineral resources are processed and where industrial wastes are buried.

Among natural and synthetic uranium compounds, uranyl-containing arsenates form a group which, at present, comprises more than ten representatives [1]. The conditions of crystallogenesis, composition, specific structural features, and the thermodynamic properties of Sr- and uranyl-containing arsenates synthesized in the Sr(AsUO$_6$)$_2$–nH$_2$O system were considered elsewhere [2]. In this study, the crystal hydrates of the composition Sr(AsUO$_6$)$_2$ · nH$_2$O with different content of H$_2$O (n = 3, 7, 8, and 10) and the nonaqueous phase are identified. Of all these phases, the octahydrate of the composition Sr(AsUO$_6$)$_2$ · 8H$_2$O proved to be stable at atmospheric humidity, whereas the composition of this hydrate indicates its possible similarity to the U-minerals of the uran-mica family [3]. Taking into account these facts and the importance of the structural studies of U-minerals and their synthetic analogues, we synthesized Sr(AsUO$_6$)$_2$ · 8H$_2$O single crystals and studied their crystal structure.

EXPERIMENTAL

The starting materials in the synthesis of Sr(AsUO$_6$)$_2$ · 8H$_2$O single crystals were strontium nitrate and arsenic (V) and uranium (VI) oxides mixed in the atomic ratio As : U = 2 : 1. Nitric acid (1M aqueous solution) was added to the solution up to the complete dissolution of the oxides; then the solution was heated to boiling point and saturated with strontium nitrate. The solution thus obtained was kept for 24 h in a thermostat at 60°C and was then cooled to room temperature. Within two to three days, rather perfect elongated Sr(AsUO$_6$)$_2$ · 8H$_2$O crystals of a greenish-yellow color characteristic of uranyl compounds precipitated. The subsequent X-ray diffraction analysis was performed on a specially selected ~0.18 × 0.03 × 0.03-mm single crystal.

The main parameters of the diffraction experiment and the crystallographic characteristics of the sample are listed in Table 1. The unit-cell parameters were refined using 14 reflections with $11.46° < 2\theta < 17.50°$. The absorption correction was introduced based on ψ-scanning. The regular extinctions for $h0l$ reflections with $l = 2n + 1$ indicated two possible space groups, $P2/c$ and Pc, however the statistics of the normalized structural amplitudes indicated a higher probability of the acentric sp. gr. *Pc*. Finally, this space group was confirmed by the structure determination of the compound by direct methods using the SHELL-93 complex of programs. The drawings of the structure were obtained using the ATOMS program [4]. The concluding atomic coordinates and the local balance of valence strengths at anions calculated based on the data given in [5, 6] are indicated in Tables 2 and 3, respectively.

Table 1. Crystallographic characteristics of the Sr(AsUO$_6$)$_2$ · 8H$_2$O structure

Characteristic	Value
Unit-cell parameters, Å, deg	$a = 7.154(1)$
	$b = 7.101(1)$
	$c = 18.901(7)$
	$\beta = 92.67(2)$
Unit-cell volume V, Å^3	959.14
Sp. gr.	Pc
Number of formula units Z	2
Calculated density ρ, g/cm^3	3.41
Absorption coefficient μ, mm^{-1}	23.1
Molecular weight	1971.3
$F(000)$	864
Diffractometer	Ital structures
Radiation, wavelength	MoK_α, 0.71073
Crystal dimensions, mm	$0.18 \times 0.03 \times 0.03$
Maximum 2θ value, deg	59.95
Scanning mode	$\theta/2\theta$
Ranges of index variations	$-3 < h < 10$
	$-9 < k < 9$
	$-26 < l < 26$
Total number of reflections	4264
Number of independent reflections	2297
Number of reflections with $|F| > 4\sigma(F)$	2086
R_{av}	0.055
Number of parameters to be refined	127
Program for structural computations	SHELXL93
R_{hkl} in the anisotropic approximation	0.051

Table 2. Atomic coordinates in the Sr(AsUO$_6$)$_2$ · 8H$_2$O structure

Atom	x/a	y/b	z/c	$U_{eq} \times 10^2$
U(1)	0.6157(1)	0.2598(2)	0.0648(1)	1.63(4)
U(2)	0.1086(1)	0.2585(2)	0.4650(1)	1.55(4)
As(1)	0.1088(7)	0.2493(5)	0.0146(3)	1.7(1)
As(2)	0.6210(8)	0.7510(6)	0.0132(3)	1.7(1)
Sr	0.3634(15)	0.8307(2)	0.7647(5)	2.61(4)
O(1)	0.609(4)	0.275(3)	−0.032(1)	1.4(4)
O(2)	0.615(5)	0.244(3)	0.160(2)	1.5(6)
O(3)	0.102(5)	0.259(3)	0.557(2)	3.3(8)
O(4)	0.125(7)	0.256(4)	0.370(2)	3.2(10)
O(5)	−0.694(5)	0.292(4)	0.061(2)	2.1(7)
O(6)	−0.059(4)	0.205(3)	0.071(1)	2.3(6)
O(7)	0.141(4)	0.063(4)	−0.041(1)	2.9(6)
O(8)	0.072(3)	0.426(3)	−0.048(1)	1.1(4)
O(9)	0.589(3)	0.949(3)	0.057(1)	1.4(4)
O(10)	0.683(4)	0.578(4)	0.066(1)	3.1(7)
O(11)	0.803(4)	0.769(3)	−0.043(1)	1.5(5)
O(12)	0.430(5)	0.700(4)	−0.039(2)	2.6(8)
H$_2$O(1)	0.491(4)	0.537(4)	0.832(2)	3.2(7)
H$_2$O(2)	0.325(4)	0.120(4)	0.841(1)	4.6(7)
H$_2$O(3)	0.029(4)	0.900(4)	0.713(2)	3.8(7)
H$_2$O(4)	0.707(5)	0.940(4)	0.818(2)	3.9(7)
H$_2$O(5)	0.463(3)	0.143(3)	0.700(1)	2.2(4)
H$_2$O(6)	0.267(5)	0.512(5)	0.692(2)	4.6(9)
H$_2$O(7)	0.814(5)	0.332(4)	0.830(2)	3.9(8)
H$_2$O(8)	0.933(5)	0.302(5)	0.695(2)	4.1(8)

RESULTS AND DISCUSSION

The crystal structure of strontium uranium arsenate consists of mixed anionic [AsUO$_6$]$^-$ layers (Fig. 1) parallel to the (001) plane which are connected by Sr cations and H$_2$O molecules (Fig. 2). The configuration of the uranyl arsenate layers is characteristic of uranmicas. These layers are formed by AsO$_4$ tetrahedra and uranyl groups tetragonally coordinated with oxygen atoms, which play the role of bridge atoms in both coordination polyhedra. The lengths of the U–O bonds in the uranyl groups (1.741–1.830 Å) are noticeably shorter than four other U–O bonds (2.192–2.361 Å). The valence O–U–O angles formed with the participation of oxygen atoms of the uranyl groups in the U(1) and U(2) polyhedra are equal to 178.33° and 177.79°, respectively.

The coordination polyhedron of strontium is a slightly distorted tetragonal antiprism whose six vertices are occupied by H$_2$O molecules located at shorter distances from the central cation (2.533–2.714 Å) and

O(2) and O(4) oxygen atoms (valence angle O(2)–Sr–O(4) = 156.03°) of the uranyl groups of the layers located at longer distances from the central cation (2.756–2.794 Å). Two of the total eight H$_2$O molecules of the formula unit are not included in the coordination polyhedron of strontium and are kept within the structure because of the hydrogen bonds with other H$_2$O molecules and the closest O atoms of the arsenate tetrahedra (Fig. 3). We failed to localize protons in the presence of uranium atoms. At the same time, proceeding from the shortest O···O distances formed with the participation of the H$_2$O molecules, we could guess the directions of possible hydrogen bonds (Fig. 3), which considerably improved the balance of valence strengths at the anions.
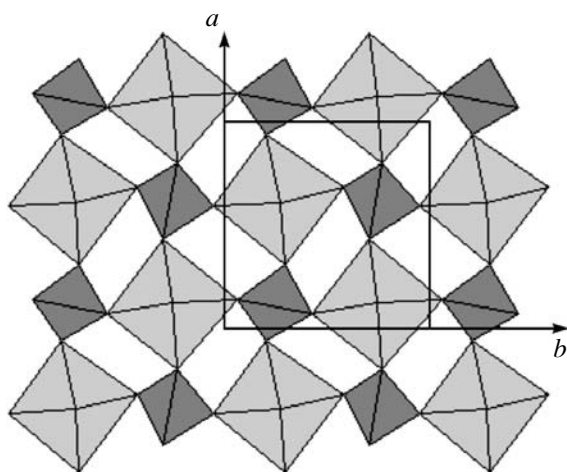
It should be emphasized that the formation of hydrogen bonds with the participation of "free" H$_2$O molecules and O atoms from the arsenate tetrahedra is characteristic of all the compounds of the series $A^{k+}(B^{5+}UO_6)_k \cdot nH_2$O ($B^{5+}$ = P and As), which is indi-

Table 3. Local balance of valences

Atom	U(1)	U(2)	Sr	As(1)	As(2)	Σ	Hydrogen bonds	Σ*
O(1)	1.531					1.531	0.116 + 0.096	1.743
O(2)	1.631		0.161			1.792		1.792
O(3)		1.821				1.821	0.145	1.966
O(4)		1.628	0.178			1.806		1.806
O(5)	0.711			1.383		2.094	0.159	2.253
O(6)	0.550			1.328		1.878	0.145	2.023
O(7)		0.621		1.145		1.766	0.246	2.012
O(8)		0.663		1.081		1.744	0.138	1.882
O(9)	0.719				1.383	2.102	0.135	2.237
O(10)	0.604				1.440	2.044	0.119	2.163
O(11)		0.762			1.138	1.900	0.142	2.042
O(12)		0.594			1.235	1.829	0.203	2.032
$H_2O(1)$			0.278			0.278	−(0.212 + 0.203)	−0.137
$H_2O(2)$			0.326			0.326	−(0.246 + 0.096)	−0.016
$H_2O(3)$			0.278			0.278	−(0.145 + 0.140)	−0.007
$H_2O(4)$			0.193			0.193	−(0.153 + 0.142)	−0.102
$H_2O(5)$			0.241			0.241	−0.135	0.106
$H_2O(6)$			0.200			0.200	−(0.176 + 0.159)	−0.135
$H_2O(7)$						0.000	−(0.116 + 0.138) +(0.212 + 0.153)	0.111
$H_2O(8)$						0.000	−(0.145 + 0.119) +(0.140 + 0.176)	0.052
Σ	5.746	6.089	1.855	4.937	5.196			

* With due regard for hydrogen bonds.

cated by the structural data for $HB^{5+}UO_6 \cdot 4H_2O$, $Mg(PUO_6)_2 \cdot 10H_2O$, $Ba(PUO_6)_2 \cdot 6H_2O$, etc. [7–10]. It is most probable that this fact is associated with the structure stabilization because of such interactions.

The natural representatives of the uran-mica family, autunite and metaautunite, differ in the arrangement of their neighboring layers with respect to one another. In autunite, two neighboring layers along the long period

Fig. 1. Uranyl arsenate $[AsUO_6]^-$ layer projected onto the (001) plane.
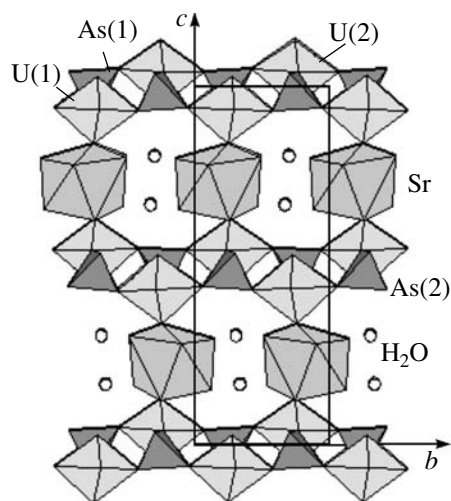
Fig. 2. $Sr(AsUO_6)_2 \cdot 8H_2O$ structure projected onto the (100) plane. Circles indicate free H_2O molecules.
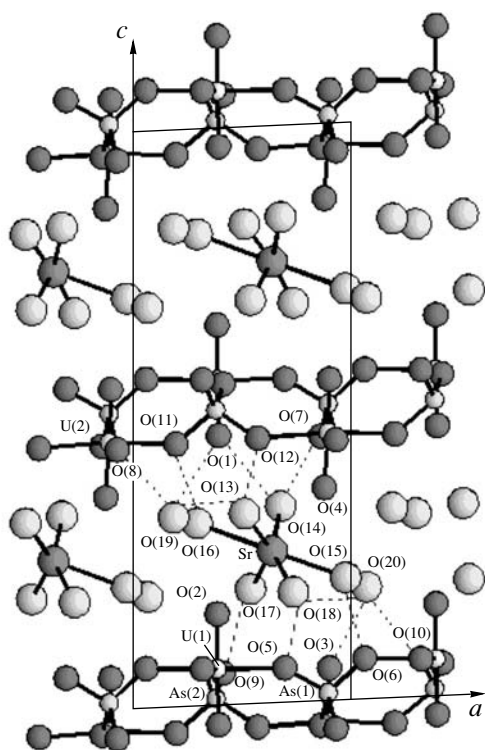
Fig. 3. System of hydrogen bonds in the Sr(AsUO$_6$)$_2$ · 8H$_2$O structure. Large open circles indicate H$_2$O molecules.

the coordination polyhedron of uranium is a pentagonal bipyramid, i.e., differs from the coordination polyhedron of uranium in the strontium uranyl arsenate structure.

The X-ray diffraction and IR-spectroscopy studies of the Sr(PUO$_6$)$_2$ · 8H$_2$O and Sr(AsUO$_6$)$_2$ · 8H$_2$O compounds proved their complete similarity [2]. This allows us to extend the structural information obtained on strontium uranium arsenate to its phosphorus analogue.

c are the mirror reflections of one another, whereas in metaautunite, such layers are displaced by a half-translation along two other axes. A very interesting characteristic of the structural studies, which considerably improved our knowledge about polytipism of uranmicas, is the different layer packing. Considering three neighboring layers in the Sr(AsUO$_6$)$_2$ · 8H$_2$O structure, we see that the first and third layers are related by a translation, whereas the middle layer is displaced relative to both these layers by a half-translation along only one period. As a result, we observe the alternation of arsenic and uranium atoms along the *c* period, unlike autunite and metaautunite structures, where the uranium atoms lie along one line and the phosphorus atoms lie along the other. Thus, the analysis of the related structures shows that autunite, metaautunite, and synthetic uranyl arsenate are, in fact, three different polytype modifications of uran-micas.

On the whole, the configuration of the structure is close to that of Mg[(UO$_2$)(AsO$_4$)]$_2$ · 4H$_2$O, where the uranyl arsenate layers are connected via cationic [Mg(H$_2$O)$_4$]$^{2+}$ complexes [11]. However, in this case,

REFERENCES

1. F. C. Hill, Mineral. Soc. Am. **38**, 653 (1999).
2. N. G. Chernorukov, N. V. Karyakin, E. V. Suleĭmanov, and Yu. S. Belova, Zh. Obshch. Khim. **66** (5), 729 (1996).
3. G. A. Sidorenko, *Crystal Chemistry of Uranium-Containing Minerals* (Atomizdat, Moscow, 1978).
4. E. Dowty, *Atoms 3.2. A Computer Program for Displaying Atomic Structures* (Kingsport, 1995), TN 37663.
5. N. E. Brese and M. O'Keeffe, Acta Crystallogr., Sect. B: Struct. Sci. **47**, 192 (1991).
6. P. C. Burns, R. C. Ewing, and F. C. Hawthorne, Can. Mineral. **35**, 1551 (1997).
7. B. Morosin, Acta Crystallogr., Sect. B: Struct. Crystallogr. Cryst. Chem. **34**, 3732 (1978).
8. A. N. Fitch, L. Bernard, A. T. Howe, *et al.*, Acta Crystallogr., Sect. C: Cryst. Struct. Commun. **39**, 159 (1983).
9. F. Khosrawan-Sazedj, TMPM Tschermaks Mineral. Petrogr. Mitt. **29**, 193 (1982).
10. S. A. Miller and J. C. Taylor, Z. Kristallogr. **177**, 247 (1986).
11. B. Bachet, C. Brassy, and A. Cousson, Acta Crystallogr., Sect. C: Cryst. Struct. Commun. **47**, 2013 (1991).

Translated by L. Man

STRUCTURE
OF INORGANIC COMPOUNDS

Characteristic Structural Features of a Tantalum-Rich Eudialyte Variety from Brazil

R. K. Rastsvetaeva*, N. V. Chukanov**, and S. Möckel***

* Shubnikov Institute of Crystallography, Russian Academy of Sciences,
Leninskiĭ pr. 59, Moscow, 119333 Russia

e-mail: rast@ns.crys.ras.ru

** Institute of Problems of Chemical Physics in Chernogolovka,
Russian Academy of Sciences, Chernogolovka, Moscow oblast, 142432 Russia

*** Alpha-geophysik in Sachsen, Neudorfer Str. 18, D-09629 Burkersdorf, Germany

Received August 1, 2002

Abstract—The crystal structure of a new tantalum-rich variety of the mineral eudialyte discovered in Brazil was established by X-ray diffraction analysis (sp. gr. $R3m$, $R = 0.038$, 1092 independent reflections). The structural characteristic of this mineral is the presence of Ta atoms in the specific positions in the centers of planar "squares" with Ta–O distances ranging from 2.035(7) to 2.116(8) Å. Two additional oxygen atoms located at distances of 2.44 and 2.66 Å can complete these "squares" to strongly distorted octahedra. © *2003 MAIK "Nauka/Interperiodica".*

Minerals of the eudialyte group, trigonal ring silicates with complex variable compositions, are of widespread occurrence in agpaitic rocks. These minerals are considered as zeolite-like compounds. Unlike traditional zeolites (aluminosilicates) and zeolite materials (aluminophosphates, silica gels, etc.) with framework structures composed of elements with the coordination number four (Si, Al, and P), zeolite-like compounds have frameworks that also include elements with the coordination numbers five and six (Ti, Nb, Al, V, Ga, etc.). The densities of the eudialyte frameworks calculated as the number of the Si + (Zr,Ti) atoms per 1000 Å^3 are equal to 15 (Si + Zr) or 18 (Si + Zr + Ca), i.e., are comparable with the densities characteristic of aluminosilicate zeolites (12–22 atoms). Minerals of the eudialyte group attract considerable attention because of their structural diversity, which gives them a broader range of physical and chemical properties and may enable them to be purposefully used in practice.
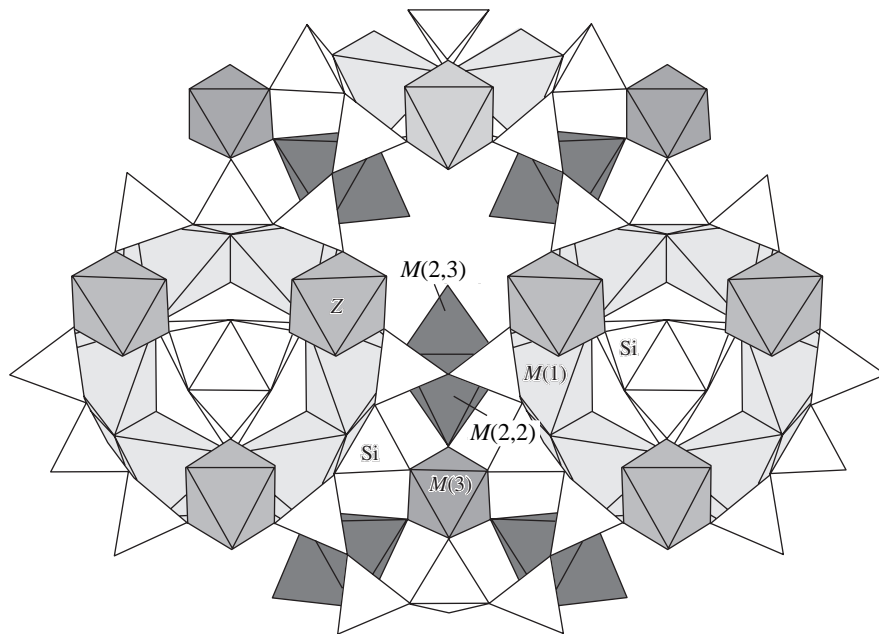

Fig. 1. Framework of the eudialyte structure.

The crystallochemical formula of eudialytes at $Z = 3$ can be written in general form as $A_3M(1)_6[^{IV}M(2,1),$ $^{V}M(2,2),$ $^{V}M(2,3)]_{3-6}[M(3)]_2Z_3$ $[Si_{24}O_{72}](OH)_{2-6}X_{2-4}$, where A = Na, K, Sr, REE, Ba, Mn, or H_3O; $M(1)$ = Ca, Mn, REE, Na, or Fe; $M(2,1)$ = Fe, Na, Zr, or Ta; $M(2,2)$ and $M(2,3)$ = Mn, Zr, Ti, Na, K, Ba, or H_3O; $M(3)$ = Si, Nb, Ti, W, or Na; Z = Zr or Ti; and $X = H_2O$, Cl, F, CO_3, or SO_4.

The eudialyte framework consists of three- and nine-membered Si,O-tetrahedra linked via Z-octahedra and six-membered rings of $M(1)$-octahedra (Fig. 1). The centers of the $[Si_9O_{27}]$-rings, i.e., the $M(3)$-positions, are occupied by additional Si-tetrahedra or octahedra usually filled with Nb. Medium-sized divalent cations (Fe, Mn, etc.) are located in the $M(2,1)$ position, namely, in the center of a planar "square," or in the $M(2,2)$ and $M(2,3)$ positions, namely, in the half-octahedra (octahedra) based on this square. Large (primarily, Na) cations, Cl anions, and water molecules occupy large cavities between these structural elements.

Most eudialytes are characterized by very low Ta and W content (about 0.04 atoms per formula unit). It was assumed that Ta and W atoms replace Nb in the $M(3)$ position, with the W atoms prevailing in this position only in two minerals—khomyakovite and manganokhomyakovite [1, 2]. We studied a specimen found in pegmatites of the Pocos de Caldas alkaline massif (Brazil) in the form of pale pink single-crystal grains with an unusually high tantalum content that had never been observed before in minerals of the eudialyte group. According to microprobe analysis data, the local Ta_2O_5 concentrations are as high as 6.3%. In addition, the mineral also contains tungsten (up to 1.3% of WO_3).

Table 1. Structural data and details of X-ray diffraction study

Characteristic	Data and conditions
Unit-cell parameters, Å	$a = 14.245(4)$,
	$c = 30.163(7)$
Unit-cell volume, V, Å^3	$V = 5300.66$
Density, ρ_{calcd}, g/cm^3	2.83
Sp. gr., Z	$R3m$; 3
Radiation; λ, Å	CuK_α; 1.5418
Crystal dimensions, mm	$0.08 \times 0.2 \times 0.15$
Diffractometer	SYNTEK $P2_1$
Scan technique	$\omega/2\theta$
$\sin\theta/\lambda$, Å^{-1}	<0.59
Ranges of the indices of measured reflections	$-14 < h < 16$,
	$0 < k < -16$,
	$0 < l < -35$
R_{int} for equivalent reflections	0.037
Total number of reflections	3117 I $> 2\sigma$(I)
Number of independent reflections	1092 $|F| > 4\sigma(F)$
Program for structural computations	AREN [4]
Absorption correction	DIFABS [5]
Number of independent positions	51
R factor upon anisotropic refinement	0.038

The chemical composition of the mineral is described by the following empirical formula ($Z = 3$): $(Na_{11.9}K_{0.7}Sr_{0.3}Ba_{0.1}REE_{0.1})_{\Sigma13.1}(Ca_{5.3}Mn_{0.7})_{\Sigma6.0}(Fe_{1.3} \times Mn_{0.6} Zr_{0.6})_{\Sigma2.5}(Zr_{2.7}Ti_{0.2}Hf_{0.1})_{\Sigma3.0}(Ta_{0.8}W_{0.15}Nb_{0.05})_{\Sigma1.0} \times (Si_{24.7}Al_{0.3})_{\Sigma25.0} \times Cl_{1.0}$, where Ce is the prevalent REE.
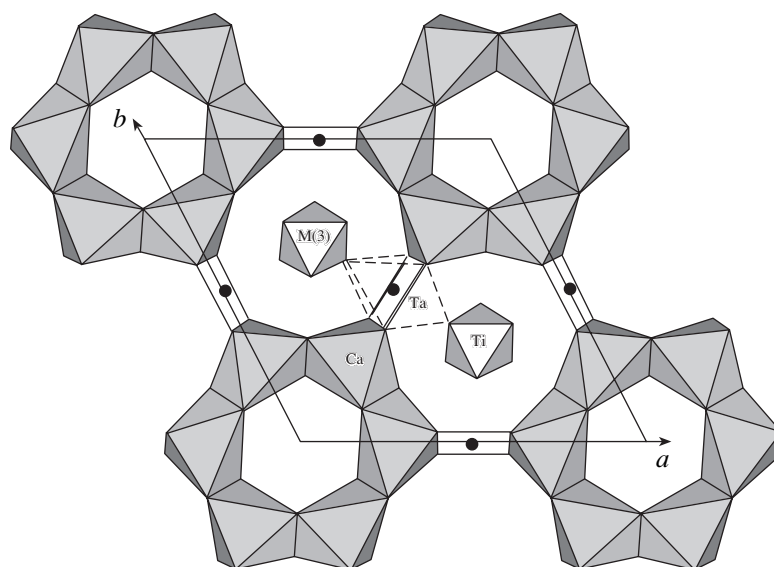
Fig. 2. Fragment of the structure of tantalum-rich eudialyte projected onto the (001) plane. Solid circles represent Ta atoms.

Table 2. Coordinates and equivalent thermal parameters (B_{eq}) of the framework atoms

Atom	x/a	y/b	z/c	B_{eq}, Å^2
Zr	0.3336(1)	0.1668(1)	0.1668(1)	1.50(2)
Ca	−0.0004(2)	0.2604(1)	−0.0001(1)	1.51(4)
Si(1)	0.9945(1)	0.6040(1)	0.0977(1)	1.1(1)
Si(2)	0.0576(1)	0.3268(1)	0.2370(1)	1.2(1)
Si(3)	0.0816(3)	0.5408(2)	0.2587(1)	1.7(2)
Si(4)	0.1406(2)	0.0703(1)	0.0826(1)	1.2(1)
Si(5)	0.2085(1)	0.4170(2)	0.0762(1)	1.7(2)
Si(6)	0.5260(2)	0.2630(1)	0.2518(1)	1.2(2)
O(1)	0.1769(4)	0.3538(6)	0.0296(3)	2.9(6)
O(2)	0.0468(4)	0.3013(4)	0.2890(1)	1.3(3)
O(3)	0.0346(6)	0.5173(4)	0.3067(2)	1.1(3)
O(4)	0.4088(5)	0.3023(5)	0.1268(2)	2.3(4)
O(5)	0.1769(5)	0.3538(8)	0.2193(4)	3.8(6)
O(6)	0.6259(6)	0.0360(5)	0.0456(2)	2.7(4)
O(7)	0.2626(5)	0.0297(5)	0.2077(2)	2.3(3)
O(8)	0.4784(8)	0.2392(5)	0.2018(2)	3.2(6)
O(9)	0.2284(8)	0.1142(5)	0.0439(3)	2.2(5)
O(10)	0.1916(7)	0.0958(5)	0.1304(2)	1.9(4)
O(11)	0.0982(5)	0.3749(5)	0.1066(2)	2.2(4)
O(12)	0.4889(3)	0.5111(3)	0.1144(2)	1.2(4)
O(13)	0.4388(8)	0.2194(5)	0.2892(3)	2.2(5)
O(14)	0.6053(3)	0.3947(3)	0.2595(2)	1.4(4)
O(15)	0.0610(2)	0.1220(4)	0.0822(2)	1.5(4)
O(16)	0.0478(6)	0.6123(5)	0.2277(2)	2.6(5)
O(17)	0.214(1)	0.6071(8)	0.2577(5)	5.2(3)
O(18)	0.2723(3)	0.5446(5)	0.0735(4)	4.0(3)

The aim of the present study was to establish the distribution of these elements over the structural positions.

Taking into account that the new mineral contains Nb, W, and Ta atoms located on threefold axes in the vicinity of the centers of nine-membered rings, we assumed that this mineral is structurally similar to the Fe,Cl-analogue of kentbrooksite [3] and used the coordinates of the basis atoms of the latter as the starting model in the refinement of the new mineral. The isotropic and anisotropic refinement of 33 atoms of the structure reduced the *R* factor from 28 to 10 and 7.8%, respectively. At this stage of the refinement, all the remaining atoms located either in the positions with partial occupancies or in the split positions (in particular, on the threefold axis and in the vicinity of the planar "square") were localized from a series of difference

electron-density maps. Three positions on the threefold axis in the center of one of the nine-membered rings are occupied by *T* atoms (Si + Al) and the OH(1) group. The *T*-tetrahedron is statistically replaced by a Ti-octahedron and three OH(5) groups located around the threefold axis. Five positions were localized in another nine-membered ring. Two of the three cation positions are occupied by the Si(7a) and Si(7b) atoms. The free vertices of the tetrahedra formed around these atoms, namely, OH(4) and OH(3), are oriented along opposite directions. The third position [*M*(3)] has an octahedral environment which involves the OH(3) groups located around the threefold axis. Assuming that the Ta atom occupies the *M*(3)-position, we refined its occupancy and thermal parameter and proved that the thermal parameter corresponds to a lighter atom, with the reduced occupancy of the position. The use of a mixed scattering curve corresponding to (Nb + W) provided a reasonable thermal parameter for this position. Therefore, the compositions of the positions in the centers of both rings are described by the formulas $[Si_{0.5}Al_{0.3}(OH)_{0.8}Ti_{0.2}(OH)_{0.6}]$ and $[Si_{0.78}(OH)_{0.78} \times {}^{VI}Nb_{0.13}{}^{VI}W_{0.09}(O,OH)_{0.66}]$, respectively.

At the same time, the approximation of the position in the center of the "square" by an Fe atom led to a negative thermal parameter, which indicates that this position is occupied by a very heavy atom, i.e., by Ta. This Ta-position is located at a distance of 0.651(5) Å from another position statistically occupied by Fe atoms. The coordination of the latter position is completed with the OH(5) group to a five-vertex polyhedron. As a result, this polyhedron is linked to the Ti-octahedron located on the threefold axis, thus giving rise to a TiFe$_3$ cluster. The refinement of the occupancies of the two subpositions in the "square" and five-vertex polyhedron showed that Fe atoms prevail in both subpositions, whereas Ta atoms are present in smaller amounts so that a vacancy is formed on the opposite side of the square. Thus, the composition of this microregion is described by the formula $[{}^{V}Fe_{1.35}(OH)_{0.7}\square_{1.14}{}^{IV}Ta_{0.51}]$. The amount of Ta determined from the X-ray diffraction data is somewhat smaller than could be expected based on the chemical-analysis data. This fact is explained by sample inhomogeneity, where the composition varies even within a grain.

The crystallochemical formula of the mineral at $Z = 3$ can be written as follows: $[(Na_{1.9}K_{0.6}Mn_{0.3}Ba_{0.1}Ce_{0.1})(Na_{2.7}Sr_{0.3})]Na_8(Ca_{5.28}Mn_{0.72}) \times (Zr_{2.85}Hf_{0.15})[{}^{V}Fe_{1.35}\square_{1.14}{}^{IV}Ta_{0.51}] [Si_{0.78}{}^{VI}Nb_{0.13}{}^{VI}W_{0.09}] [Si_{0.5}Al_{0.3}Ti_{0.2}] [Si_{24}O_{72}] (OH,O)_{3.54}Cl_{0.8} \times 1.2H_2O$, where the compositions of the key positions are indicated in the parentheses and brackets and the coordination numbers of some cations are indicated by Roman numerals. The main characteristics of the mineral and the details of the single-crystal X-ray diffraction study are given in Table 1. The atomic coordinates are listed in Tables 2 and 3. The interatomic distances are given in Table 4.

Table 3. Coordinates, multiplicities of positions (Q), occupancies (q), and equivalent thermal parameters (B_{eq}) of the extraframework atoms

Atom	x/a	y/b	z/c	B_{eq}, Å^2	Q	q
Ta	0.0100(4)	0.5050(2)	0.0011(1)	2.05(6)	9	0.17(1)
Fe	0.5211(2)	0.4789(2)	0.9977(1)	3.4(1)	9	0.45(1)
Ti	0.3333	0.6667	0.2978(6)	3.1(3)	3	0.20(1)
T	0.3333	0.6667	0.2834(2)	1.7(2)	3	0.80(3)
M(3)	0.3333	0.6667	0.0330(2)	1.9(1)	3	0.22(1)
Si(7a)	0.3333	0.6667	0.0888(6)	2.4(3)	3	0.35(2)
Si(7b)	0.3333	0.6667	0.0595(4)	2.5(2)	3	0.43(3)
Na(1)	0.5590(3)	0.4410(3)	0.1794(2)	3.5(4)	9	1
Na(2a)	0.1120(4)	0.2240(5)	0.1545(3)	2.3(2)	9	0.60(2)
Na(2b)	0.0811(7)	0.1622(9)	0.1701(5)	3.0(3)	9	0.40(5)
Na(3a)	0.257(3)	0.514(4)	0.169(2)	7.6(4)*	9	0.20(4)
Na(3b)	0.220(2)	0.610(1)	0.1563(8)	5.0(3)*	9	0.46(2)
Na(4)	0.2020(3)	0.1010(2)	0.2850(1)	2.7(1)	9	1
Na(5)	0.4522(4)	0.2261(3)	0.0524(1)	3.3(1)	9	1
Cl(1)	0.6667	0.3333	0.0973(4)	3.1(3)	3	0.58(3)
Cl(2)	0	0	0.2297(9)	3.2(5)	3	0.43(5)
OH(1)	0.6667	0.3333	0.010(5)	6.3(1)	3	0.80(5)
OH(2)	0	0	0.343(2)	3.1(9)*	3	0.48(5)
OH(3)	0.206(5)	0.603(3)	0.001(2)	3.2(5)	9	0.17(5)
OH(4)	0.3333	0.6667	0.144(3)	7.7(5)	3	0.35(5)
OH(5)	0.604(1)	0.396(1)	0.0012(7)	4.8(4)	9	0.45(5)
H$_2$O(1a)	0	0	0.186(5)	5.1(9)*	3	0.37(8)
H$_2$O(1b)	0	0	0.252(4)	4(2)	3	0.20(5)
H$_2$O(2a)	0.6667	0.3333	0.072(4)	3.8(4)	3	0.22(8)
H$_2$O(2b)	0.586(4)	0.293(3)	0.102(2)	5.6(9)	9	0.20(8)

Note: Cl(2) = 0.5Cl + 0.5H$_2$O; B_{iso} are marked with an asterisk.

The structural characteristic of the mineral studied here is an unusual coordination of Ta atoms. The formal coordination polyhedron around the Ta atom is a strongly distorted octahedron (indicated by dashed lines in Fig. 2), which reflects the directions of the chemical bonds and indicates their nonequivalence. The strongest bonds corresponding to the shortest distances (2.035(7) and 2.116(8) Å) are formed by Ta atoms and four oxygen atoms [two O(2) and two O(6)] that coordinate the Ta atom forming a square. The interactions of the Ta atom with two other ligands, OH(3) and OH(5), are much weaker [2.44(2) and 2.66(1) Å, respectively]. The square coordination formed by the "vertical" edges of the Ca-octahedra of two adjacent six-membered rings can be distorted to a trapezium or rectangle without breaking the structure framework. Such a coordination found earlier for Fe and Na in the

eudialyte structures was also established for some other elements (e.g., Nb) in some synthetic compounds [6]. In eudialytes, we found a square coordination around Zr atoms that were additional to the typical three Zr atoms (per formula unit) [7]. Such a coordination is known for synthetic phases but is unknown for natural minerals.

Thus, four elements (Fe, Na, Zr, and Ta) in eudialytes have a planar square and not tetrahedral coordination. These elements have different valence states and ionic radii, which is seen from the different sizes and shapes of the "squares" (Table 5). The Na-polyhedron is the largest [8], whereas the Fe-polyhedron is the smallest [9], but both are very close to regular squares. The fourfold coordination of Nb in Nb$_4$O$_5$ is provided by a virtually isosceles trapezium [6]. The Zr- and Ta-squares have close dimensions and are rectangles, with

Table 4. Characteristics of the coordination polyhedra

Position	Composition ($Z = 3$)	Coordination number	Cation–anion distance, Å (minimum–maximum)	Position	Composition ($Z = 3$)	Coordination number	Cation–anion distance, Å (minimum–maximum)
Si(1)	Si_6	4	1.615(5)–1.637(5)	Fe	$Fe_{1.35}$	5	2.010(8)–2.153(6)
Si(2)	Si_6	4	1.566(5)–1.646(6)	Ti	$Ti_{0.2}$	6	1.90(1)–1.92(6)
Si(3)	Si_3	4	1.559(8)–1.630(8)	$M(3)$	$Nb_{0.13}W_{0.09}$	6	1.81(2)–1.93(1)
Si(4)	Si_3	4	1.572(9)–1.632(4)	T	$Si_{0.5}Al_{0.3}$	4	1.66(1)–1.81(6)
Si(5)	Si_3	4	1.575(6)–1.651(7)	Na(1)	Na_3	8	2.60(1)–2.81(1)
Si(6)	Si_3	4	1.560(8)–1.651(6)	Na(2a)	$Na_{1.8}$	9	2.51(1)–2.95(5)
Si(7a)	$Si_{0.35}$	4	1.57(1)–1.58(5)	Na(2b)	$Na_{1.2}$	8	2.04(3)–2.80(1)
Si(7b)	$Si_{0.43}$	4	1.51(1)–1.56(2)	Na(3a)	$Na_{0.6}$	5	2.06(6)–2.91(6)
Zr	$Zr_{2.85}Hf_{0.15}$	6	2.065(6)–2.094(6)	Na(3b)	$Na_{1.38}$	4	2.74(2)–3.05(2)
Ca	$Ca_{5.28}Mn_{0.72}$	6	2.314(6)–2.411(7)	Na(4)	$Na_{1.9}K_{0.6}Mn_{0.3}Ba_{0.1}Ce_{0.1}$	11	2.57(1)–3.03(1)
Ta	$Ta_{0.51}$	4	2.035(7)–2.116(9)	Na(5)	$Na_{2.7}Sr_{0.3}$	12	2.19(1)–2.97(1)
		6	2.035(7)–2.657(5)				

Note: Ta atoms can have coordination numbers four or six.

Table 5. Geometric parameters of the "squares" for different $M(2,1)$ elements

Atom	$M(2,1)$–O distances, Å	O–O distances, Å	Reference
Na	2.29(1)–2.29(1)	3.28, 3.28, 3.13 × 2	[8]
Nb	2.078(1)–2.198(1)	2.84, 3.81, 2.50 × 2	[6]
Zr	2.040(6)–2.117(7)	2.78, 2.81, 3.03, 3.08	[7]
Ta	2.035(7)–2.116(9)	2.95, 3.11, 2.85 × 2	Our study
Fe	2.03(1)–2.06(1)	2.95, 2.98, 2.80 × 2	[9]

Table 6. Positions of IR bands for elements in the main positions of the eudialyte structure depending on their valence state and coordination number

Cations	Stretching frequency ν (cm^{-1})
Si(7)	912–935
^{IV}Nb	553
$^{IV}Fe^{2+}$	542–545
$^{IV}Fe^{3+}$	527
$^{IV}Zr^{4+}$	530–531
$^{V}(Mn, Fe^{3+})$	523–526
$^{VI}Fe^{3+}$	473
$^{IV}Ta^{5+}$	534

Note: Roman numerals indicate the coordination numbers.

the Zr-rectangle being elongated in the direction of the long axis of the unit cell, while the Ta-rectangle is elongated in the perpendicular direction.

It is commonly assumed [9] that the iron atoms in a square coordination are divalent, whereas the valence states of Zr and Ta have not been established as yet. According to the local charge balance on the anions forming a square, the central cation tends to have a charge lower than +4, and, thus, it cannot exceed +4. However, no structures containing tantalum in the valence states ranging from 1 to 4 are known in nature (in some rare cases, tantalum is reduced to native tantalum occurring in the zero valence state). In our case, the deviation from the local charge balance is somewhat compensated by its long-range Coulomb interactions with two oxygen atoms (with Ta–O distances being 2.44 and 2.66 Å) formally completing the coordination sphere of the Ta atom to a distorted octahedron.

The relation of Ta to the position in the planar square is supported by the IR spectrum of the sample. Earlier, a structural study of more than 20 eudialyte specimens and more than 100 specimens with a known chemical composition allowed us to bring into correspondence a number of bands of the IR spectra with the presence of various transition metals in this position (Table 6). The spectrum of the new mineral studied here has no absorption band at 543 cm^{-1} due to the stretching vibrations of the Fe atom in the square coordination. At the same time, the spectrum has an unusual band at 534 cm^{-1} assigned to the Ta–O stretching vibrations. The band at 534 cm^{-1} was not observed in the IR spectra of eudialytes with a low Ta content. Thus, the presence of tantalum in an unusual planar-square coordination in the minerals of the eudialyte group can be established by IR spectroscopy without resorting to X-ray diffraction analysis.

ACKNOWLEDGMENTS

REFERENCES

1. O. Johnsen, R. A. Gault, J. D. Grice, and T. S. Ercit, Can. Mineral. **37**, 893 (1999).
2. O. Johnsen, J. D. Grice, and R. A. Gault, Eur. J. Mineral. **10**, 207 (1998).
3. O. Johnsen, J. D. Grice, and R. A. Gault, Can. Mineral. **37**, 1295 (1999).
4. V. I. Andrianov, Kristallografiya **32** (1), 228 (1987) [Sov. Phys. Crystallogr. **32**, 130 (1987)].
5. N. Walker and D. Stuart, Acta Crystallogr., Sect. A: Found. Crystallogr. **39** (2), 158 (1983).
6. A. V. Arakcheeva, Kristallografiya **37** (3), 589 (1992) [Sov. Phys. Crystallogr. **37**, 306 (1992)].
7. R. K. Rastsvetaeva and A. P. Khomyakov, Kristallografiya **45** (2), 251 (2000) [Crystallogr. Rep. **45**, 219 (2000)].
8. R. K. Rastsvetaeva, A. P. Khomyakov, V. I. Andrianov, and A. I. Gusev, Dokl. Akad. Nauk SSSR **312** (6), 1379 (1990) [Sov. Phys. Dokl. **35**, 492 (1990)].
9. R. K. Rastsvetaeva and V. I. Andrianov, Dokl. Akad. Nauk SSSR **293** (5), 1122 (1987) [Sov. Phys. Dokl. **32**, 252 (1987)].

Translated by T. Safonova

STRUCTURE
OF INORGANIC COMPOUNDS

Dedicated to the memory of K. Dornberger-Schiff

OD Family of Ca,Mg-Borates of the Kurchatovite Group

E. L. Belokoneva

Faculty of Geology, Moscow State University, Vorob'evy gory, Moscow, 119992 Russia
e-mail: elbel@geol.msu.ru
Received April 24, 2002

Abstract—A symmetry-topological analysis of Ca,Mg-borates kurchatovites was carried out in the context of the OD theory developed by Dornberger-Schiff. Two types of two-dimensional periodic blocks ("layers") of different symmetry were revealed. According to the fundamental theorem of the OD theory, the number of variations in the layer arrangement equals two and is responsible for the structural diversity. The MDO polytypes and periodic structures are considered. Analysis of these structures shows that the Dornberger-Schiff theory has advantages over the modular approach that takes no account of the fundamental symmetry theorem of the OD theory. © 2003 MAIK "Nauka/Interperiodica".

The mineral kurchatovite $CaMg[B_2O_5]$ was discovered by S.V. Malinko in the Solongo ferrous scarn deposit (Siberia) in 1966. Clinokurchatovite was discovered in the northern Balkhash region and described by A.D. Gorshenin in 1977. The crystal structures of these kurchatovite varieties were first established based on single-crystal X-ray diffraction data in 1976 [1] and 1980 [2]. It was found that these varieties have different symmetries, and their structures belong to the orthorhombic and monoclinic systems, respectively. In study [1], the basic block ("hypothetical protostructure") common to both structures was established, and the unit-cell parameters and symmetry groups were determined. The block size along the *a* axis (~6.2 Å) is equal to half the *a*-parameter of the monoclinic unit sell. Six such blocks form the *a*-parameter of the orthorhombic modification. Both structures are characterized as polytypes derived from the protostructure. In kurchatovite, *c*-pseudoplanes (at four levels along the *a* axis) and pseudocenters of symmetry between them were found. Twinning typical of the crystals of both varieties (in particular, the monoclinic) was explained using those block and pseudosymmetry elements.

Taking into account the polytype relations in the Y-, Nd-, and Gd-borates with a huntite structure established based on the OD theory, it was assumed that monoclinic and orthorhombic kurchatovites are built by two types of layers that include Mg-octahedra and Ca-polyhedra and form an OD family with the MDO polytypes [3].

In spite of the fact that kurchatovite and clinokurchatovite rarely occur in nature, these minerals have attracted the attention of Italian researchers who recently refined the structures of both varieties [4]. For clinokurchatovite, the reliability factor was improved, with the main results being the same. The structure of kurchatovite established in [4] coincides with the structure determined earlier in [1] within the presence of a center of symmetry. Thus, for kurchatovite, the centrosymmetric sp. gr. *Pcab* (*Pbca* in the setting used in [4]) is correct and not the polar sp. gr. *Pc2₁b* used in the refinement in [1]. In [4], not only the kurchatovite structures were refined, but also their crystallochemical analysis was performed with the use of the rather popular modular approach. As earlier in [1], the Italian authors also revealed a structural block but with a different metric: it was two times smaller along the *a* axis (~3.1 Å) [4]. The *c*-pseudoplanes and pseudocenters of symmetry were revealed in both studies [1, 4]. In [4], two symmetry elements were revealed at the block boundary—the center of symmetry ($\bar{1}$), the glide plane (*b* in the setting used in [4]), and the absence of symmetry elements denoted by the noncrystallographic symbol 0. The simplest variant of alternation of the blocks is also described, which corresponds to a structure that has still never been found in synthetic and natural specimens.

Both approaches are reasonable for analysis of pseudosymmetry. However, the modular approach fails to explain the alternation of the symmetry elements and the existence of the structural diversity.

According to the theory of OD structures developed and published by Dornberger-Schiff in 1964 [5], the crystal structures consist of main building units (block) of different dimensionalities which she called "bricks," "rods," and "layers." In other words, she assumed that a structural block can be a structural zero-, one-, or two-dimensionally periodic. The latter case, which actually corresponds to a layer structural element, was analyzed most often, which allowed one to study the polytype

relations in the structures on a new basis. The term "structural block" suggested by Dornberger-Schiff is identical to the more resent term "module." However, unlike arbitrarily separated modules, Dornberger-Schiff suggested not only separating building blocks but also analyzing their symmetry and the symmetry methods of condensation of these blocks. The most important aspect of this symmetry–topological analysis is the consideration of the relationships between the orders of the symmetry groups of individual layers (for a two-dimensional periodic block) and a pair of such layers. If the symmetry-group order N of a layer is higher than the order symmetry-group-order F of a pair of layers, this signifies that the second layer can be located in a number of ways with respect to the first layer of the pair. The number of ways of its location is determined by the ratio $Z = N/F$. According to Dornberger-Schiff, the symmetry of the layer does not characterize the structure as a whole but represents its inherent symmetry or represents a particular symmetry operation. In other words, the elevated symmetry (pseudosymmetry) of the layers compared to the symmetry upon layer combination provides the structural diversity. Consider some clear examples of such an analysis given in [5]. These are close packings (metal structures) in which $Z = 12/6 = 2$, which corresponds to the cubic and hexagonal packings; various ZnS modifications (sphalerite, wurtzite, and their polytype modifications), SiC, etc.

Dornberger-Schiff considered the structures with the maximum degree of order (MDO) and the derivatives with different degrees of periodicity (up to completely disordered ones). One, two, and even three (in kaolinites) different layers were separated as building units. Since [5], this approach has been successfully applied to a large number of structures, and the list of these structures is still being extended. From the viewpoint of the symmetry OD analysis, kurchatovites are similar to calcium silicates, including anhydrous (wollastonite) and hydrated (cement) CSH [6], sapphirine polytypes, and the zoisite–clinozoisite and sursassite–pumpellyite–ardennite OD families [7]. An important point to note is that a separated layer element (two-dimensional periodic block) is not necessarily a layer in the crystallochemical sense.

It is most convenient to analyze kurchatovites by considering the projections of their structures along the common b-parameter (~11.14 Å), which corresponds to the monoclinic axis in the setting used in [4] (see table). Glide pseudoplanes (b planes in the setting used) relating the B(1)-triangles and Mg atoms at several levels along the a axis were revealed in both studies [1, 4]. However, the two-dimensional periodic block chosen ("layer" L_1 in Fig. 1a) is characterized by a higher orthorhombic pseudosymmetry corresponding to the sp. gr. $Pbc2_1$, as follows from analysis of the atomic coordinates of clinokurchatovite at the corresponding level along the a axis. This symmetry is the special

Main crystallographic characteristics of kurchatovites [4]

	Clinokurchatovite	Kurchatovite
a, Å	12.329	36.34
b, Å	11.146	11.135
c, Å	5.519	5.499
β, deg	101.62	
V, Å^3	742.88	2225.09
Z	8	24
Sp. gr.	$P2_1/c$	$Pbca$

symmetry operation, namely, the inherent symmetry of the "layer" that is not obeyed by the structure as a whole. This symmetry is the true symmetry of the structure of orthorhombic kurchatovite only for the layers L_1 located at the levels 1/4 and 3/4 along the a axis (Fig. 1b). The polar group assumes a particular direction of gliding along the 2_1 axis. However, the conjugation of blocks along the a axis can lead to a change in the gliding direction or their "sign," which is characteristic of polytypes. The kurchatovite structures contain the second two-dimensional block ("layer" L_2) alternating with the first block along the a axis. This block includes the B(2) triangles and Ca atoms. Its inherent symmetry is lower and corresponds to the sp. gr. $P12_1/c1$ in the setting used. In this block, the centers of symmetry $\bar{1}$ and axes 2_1 alternate in $c/4$. The ratio of the symmetry-group order of the layer L_1 to the symmetry-group order of the pair of layers L_1L_2 : $Z = N/F = 4/2 = 2$, which corresponds to two variants of the location of the second layer with respect to the first one.

In clinokurchatovite, the direction of the translation component of the 2_1 axis of the sp. gr. $Pbc2_1$ of the layer L_1 is the same for all the layers of the structure, and, therefore, the structure has a high pseudosymmetry. The alternation of the layers along the a axis occurs with a constant shift of the symmetry center of the layer L_2 with respect to the layer L_1 along the c axis. If the pseudoorthorhombic axis (a_{orth} in Fig. 1a) is chosen, the successive shifts of the symmetry center $\bar{1}$ along the c axis are +1/4, +1/4, +1/4, …. This corresponds to the alternation of the symmetry elements $\bar{1}$, 2_1, $\bar{1}$, 2_1, and so on, in the L_2 layers along the pseudoorthorhombic axis. The situation in kurchatovite is different. In this mineral, the "sign" of the shift of the symmetry center is retained within three layers, then the sign of the shift is changed to the opposite one (+1/4, +1/4, +1/4, –1/4, –1/4, –1/4, …) (Fig. 1b). In the orthorhombic unit cell, the symmetry elements $\bar{1}$, 2_1, 2_1, $\bar{1}$, 2_1, 2_1, $\bar{1}$, …, etc., alternate along the a axis. The existence of two varieties of wollastonite (1A and 2M) is provided by the same symmetry principle [7]. However, in the 2M structure, the sign changes in each following layer. It was sug-

(a)

(b)
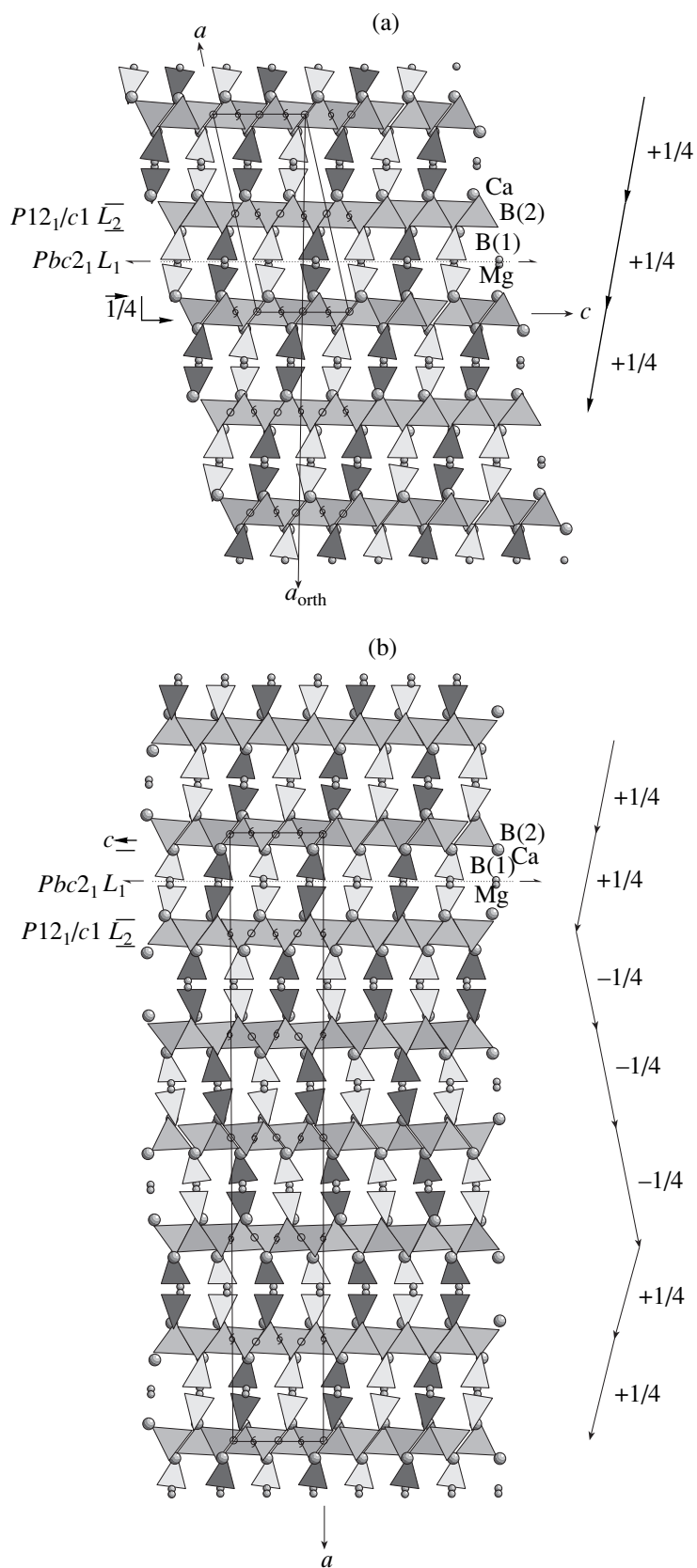
Fig. 1. (a) Clinokurchatovite and (b) kurchatovite structures projected onto the *ac* plane. The B triangles are shown; the triangles located at different heights along the *b* axis are differently shaded. The Mg and Ca atoms are represented by small and large circles, respectively. The layers and symmetry elements are shown. Arrows (on the right-hand side of the figure) indicate the directions of layer shifts (see the text).

gested [5, 7] that such a variable shift be characterized as a derivative of the noncrystallographic symmetry element $2_{\pm1/2}$. However, we believe that it is more appropriate to use the symmetry center and analyze its shifts. This approach was applied to the analysis of the OD family of hexaborates [8].

Clinokurchatovite is the first polytype with a maximum degree of order (or MDO1). The second polytype with a maximum degree of order (MDO2) is a polytype in which the shifts of the symmetry centers alternate as +1/4, –1/4, +1/4, –1/4 .... However, unlike wollastonite $2M$ and lead borate [8], the MDO2 polytype has not been established in the kurchatovite family. The kurchatovite structure is one of the possible periodic structures that can be predicted based on a certain repetition period of the lattice along a. In the absence of periodicity, a disordered structure with an infinite a-parameter would take place.

Dornberger-Schiff developed a method for the general description of all such structures forming the OD family with the use of the symmetry groupoid. A group of partial symmetry operations of the layers is denoted by λ-PO. As is characteristic of the structures containing layers of two types, the position of the layer with a lower symmetry λ-PO is determined by the symmetry of the layer with a higher symmetry λ-PO [3, 5]. Both L_1 and L_2 layers are characterized by the absence of polarity along the direction of the disturbed periodicity (a axis), which is denoted by ρ (or τ for the polar type). Apparently, according to the Dornberger-Schiff nomenclature, these structures belong to the most widespread type, IV [3, 5]. The symmetry groupoid can be written as follows:

$$L_1, \text{MgBO}_{2.5} \quad L_2, \text{CaBO}_{2.5}$$

$$\lambda, \rho\text{-PO} \{P(b)c2_1\} \quad \lambda, \rho\text{-PO} \{P(1)2_1/c1\}$$

$$[(1)\ 1 \pm 1/4\ \bar{1}\ ].$$

The first row of the groupoid presents the formulas of the layers. The second row includes the special symmetry operations characteristic of these layers (the direction corresponding to the direction of the disturbed periodicity is given in parentheses). The possible shifts of the symmetry centers responsible for the structural diversity are given in the third row.

To summarize, the modern modular approach is in fact a somewhat forgotten symmetry-topological analysis of the Dornberger-Schiff OD theory. However, as was demonstrated on kurchatovites, only the combination of the modular and symmetry approaches and the use of the fundamental theorem of the OD theory provides an explanation of the structural diversity and complete description of the OD family, which, as is seen from [4], cannot be done without the invocation of this theorem.

REFERENCES

1. O. V. Yakubovich, M. A. Simonov, E. L. Belokoneva, and Yu. K. Egorov-Tismenko, Dokl. Akad. Nauk SSSR **230** (4), 837 (1976) [Sov. Phys. Dokl. **21**, 542 (1976)].

2. M. A. Simonov, Yu. K. Egorov-Tismenko, N. A. Yamnova, *et al.*, Dokl. Akad. Nauk SSSR **251** (5), 1125 (1980) [Sov. Phys. Dokl. **25**, 228 (1980)].

3. E. L. Belokoneva, T. I. Timchenko, and N. V. Belov, in *Proceedings of XIII Congress on Crystallochemistry of Minerals, Varna, 1982* (Sofia, 1986), p. 781.

4. A. Callegary, F. Mazzi, and C. Tadini, Eur. J. Mineral. (2002) (in press).

5. K. Dornberger-Schiff, Abh. Dtsch. Akad. Wiss. Berlin, No. 3, 1 (1964).

6. *ÉMU Notes in Mineralogy*, Vol. 1: *Modular Aspects of Minerals*, Ed. by S. Merlino (Budapest, 1997), Chap. 1, p. 29.

7. S. Merlino, Per. Mineral. **59**, 69 (1990).

8. E. L. Belokoneva, T. A. Korchemkina, and O. V. Dimitrova, Zh. Neorg. Khim. **44** (6), 889 (1999).

Translated by T. Safonova

STRUCTURE
OF INORGANIC COMPOUNDS

Strontium in the Collinsite Structure: Rietveld Refinement

O. V. Yakubovich*, Yu. K. Kabalov*, P. G. Gavrilenko*,
R. P. Liferovich**, and W. Massa***

* Faculty of Geology, Moscow State University,
Vorob'evy gory, Moscow, 119992 Russia
** Geological Institute, Kola Research Center, Russian Academy of Sciences,
ul. Fersmana 14, Apatity, Murmansk oblast, 184200 Russia
*** Department of Chemistry, Philipps University,
Hans-Meerwein Strasse, D-35032, Marburg, Germany
Received March 12, 2002

Abstract—The crystal structure of a strontium variety of a rare phosphate—mineral collinsite $(Ca_{2-x}Sr_x)_2Mg[PO_4] \cdot 2H_2O$ was solved from powder X-ray diffraction data (λCuK_α radiation, Ni filter, $12.36° \leq 2\theta \leq 100.00°$, scan step $0.02°$, exposure time per step 15 s) by the Rietveld method ($R_{wp} = 4.15\%$, $R_F = 1.03\%$, $R_B = 2.46\%$); $a = 5.8219(1)$ Å, $b = 6.8319(2)$ Å, $c = 5.4713(1)$ Å, $\alpha = 96.965(2)°$, $\beta = 108.846(2)°$, $\gamma = 107.211(2)°$, sp. gr. $P\bar{1}$, $Z = 1$, $\rho_{calcd} = 3.12$ g/cm^3 (at $x = 0.72$). The new mineral was discovered in carbonatites from the Kovdor alkaline-ultrabasic massif. The crystallochemical data for collinsite were analyzed and compared with those for isotypic minerals of the fairfieldite group. Characteristic features of the low-temperature geochemistry of strontium were established. © *2003 MAIK "Nauka/Interperiodica".*

INTRODUCTION

The fairfieldite group of minerals includes hydrated phosphates and arsenates described by the general formula $Ca_2M[TO_4]_2 \cdot 2H_2O$, where M = Mg, Fe, Mn, Zn, Ni, or Co and T = P or As. The crystallographic characteristics of triclinic isostructural members of this mineral group are given in Table 1.

A very unusual Mg,Fe-representative of this mineral group—the mineral collinsite—was discovered in highly hydrothermally altered carbonatites and phoscorites from the Kovdor alkaline-ultrabasic massif, the largest highly differentiated complex in the Paleozoic Kola alkaline-ultrabasic province. This variety contains up to 20.87 wt % of SrO and is mineralogically characterized in [10]. The strontium content in the mineral was found to be four to seven times higher than the values indicated earlier in collinsite from the Kovdor massif [11, 12]. There are indications that the $Ca^{2+} \Longleftrightarrow Sr^{2+}$ diadochy is not typical of collinsite and other known minerals of the fairfieldite group, although the latter are associated with other geological formations (autometasomatically transformed granite pegmatites, ferrous metasedimentary rock masses and erosion crusts [13]).

A preliminary study showed that the powder X-ray diffraction patterns of collinsite samples with practically arbitrary Sr content, which were discovered in the Kovdor massif, differ from the current standard [14] (collinsite from the Milgun Station massif, Western Australia). The most characteristic reflections of these patterns have considerably different intensities. It was found that a gradual increase in the Sr content in the mineral is accompanied by a subsequent increase in its unit-cell parameters (Table 2). The above-mentioned facts and the absence of additional X-ray reflections (compared to the reference collinsite sample) are indicative of probable isomorphous incorporation of Sr atoms into the Ca positions, which can take place because of close ionic radii of these elements ($r_{Ca} = 1.00$ Å and $r_{Sr} = 1.10$ Å [15]).

Below, we describe the study of a strontium variety of collinsite by the Rietveld method. We obtained new structural data for the group of rare natural phosphates and established some characteristic features of the low-temperature strontium geochemistry.

MINERALOGICAL DESCRIPTION

The sample under study was selected from a hydrothermal phosphate association related to a stockwork of late mineralized fractures in serpentinized rocks of the late-stage carbonatite core of the Kovdor massif. Collinsite "lines" the walls of cracks and cavities as radial-axial aggregates and crusts of different brown shadows with a serrated surface (Fig. 1a). These aggregates are formed by wedge-shaped microcrystals of collinsite elongated in the [100] direction (Fig. 1b) whose size does not exceed several micrometers. The habit of the aggregates resembles intergrowths of collinsite crystals from the Yukon Territory (Canada) [16].

The chemical composition of the sample was analyzed on a Cameca MS-46 microanalyzer. The prelimi-

Table 1. Crystallographic and some physical characteristics of minerals of the fairfieldite group (sp. gr. $P\bar{1}$, $Z = 1$)

Mineral, formula	Unit-cell parameters, a, b, c, Å	Angles α, β, γ, deg	Color	Density, g/cm^3	References
Fairfieldite $Ca_2(Mn, Fe)[PO_4]_2 \cdot 2H_2O$	5.79(1)	102.3(2)	White, greenish-white, pale straw-yellow	3.10	[1]
	6.57(1)	108.7(2)			
	5.51(1)	90.3(2)			
Messelite $Ca_2(Fe, Mn)[PO_4]_2 \cdot 2H_2O$	5.95	102.3	From white to greenish-gray	3.16	[2]
	6.52	107.5			
	5.45	90.8			
Cassidyite $Ca_2(Ni, Mg)[PO_4]_2 \cdot 2H_2O$	5.71	96.8	From pale-green to dark-green	3.15	[3]
	6.73	107.4			
	5.41	104.6			
Collinsite $Ca_2(Mg, Fe)[PO_4]_2 \cdot 2H_2O$	5.7344(8)	97.29(1)	White	2.93	[4]
	6.780(1)	108.56(1)			
	5.4413(9)	107.28(1)			
Zinc collinsite $Ca_2(Mg, Zn)[PO_4]_2 \cdot 2H_2O$	5.712(3)	98.63(1)	Gray, white		[5]
	6.830(3)	106.83(1)			
	5.393(2)	103.38(1)			
Strontium collinsite $(Ca, Sr)_2(Mg, Fe)[PO_4]_2 \cdot 2H_2O$	5.8219(1)	96.965(2)	White	3.12	Our data
	6.8319(2)	108.846(2)			
	5.4713(1)	107.211(2)			
Parabrandtite $Ca_2Mn[AsO_4]_2 \cdot 2H_2O$	5.89	96.77	White-pink	3.55	[6]
	7.031	109.32			
	5.64	108.47			
Gaitite $Ca_2(Zn, Mg)[AsO_4]_2 \cdot 2H_2O$	5.90	111.67	White	3.81	[7]
	7.61	70.83			
	5.57	119.42			
Talmessite $Ca_2(Mg, Co)[AsO_4]_2 \cdot 2H_2O$	5.874(7)	97.3(1)	Bright-pink	3.42	[8]
	6.943(11)	108.7(1)			
	5.537(6)	108.1(2)			
β-Roselite $Ca_2(Co, Mg)[AsO_4]_2 \cdot 2H_2O$	5.89	112.63	Dark red-pink	3.60	[9]
	7.69	70.82			
	5.56	119.41			

nary data allowed us to assume that Sr can be an important constituent of some collinsite generations from the Kovdor massif. A thorough examination of all the samples at the maximum magnification of an optical microscope and study in reflected electrons proved the absence of any microscopic inclusions of mineral stron-tium phases. To confirm the characteristic features of the chemical composition of the collinsite crystals from the Kovdor massif, we performed a comparative study of the compositions of collinsites from the Canadian and Australian deposits and of messelite from a holotypic deposit (Messel, Germany) by the same analytical

Table 2. Unit-cell parameters of collinsite from the Kovdor massif with various Sr contents (given in the formula coefficients*)

Sr content	0**	0.12	0.23	0.74
a, Å	5.734	5.738(9)	5.753(9)	5.824(1)
b, Å	6.780	6.772(8)	6.775(8)	6.800(1)
c, Å	5.441	5.444(5)	5.450(6)	5.479(6)
α	97.29	97.3(2)	97.3(2)	97.6(2)
β	108.56	108.7(2)	108.8(2)	108.9(2)
γ	107.28	107.2(2)	107.2(2)	107.3(3)
V, Å^3	185.66	185.61	186.25	189.77

  * According to powder X-ray diffraction data (analyst A.N. Bogdanova).
** Standard ASTM JCPDS no. 26-1063.

methods and under the same conditions. Strontium was not detected in any of the samples. The results of 51 electron microprobe analyses using wavelength dispersive spectrometry (WDS) and two gravimetric chemical analyses of the collinsite crystals from the Kovdor massif are presented in Fig. 2. These results show a rigorous correlation between the total (Sr + Ba) content and the Ca content (no correlation was detected between Sr and Ba and also the elements located in the second structural position in the collinsite crystals). The maximum Sr content revealed in the statistically significant experiments was 37 wt %.

The Sr-enriched collinsite that forms almost chemically homogeneous aggregates (Table 3) was used for further X-ray diffraction analysis.

X-RAY DIFFRACTION EXPERIMENT AND STRUCTURE REFINEMENT

The powder X-ray diffraction pattern of collinsite was obtained on an ADP-2 diffractometer (CuK_α radia-tion, Ni filter) in the angular range $12.36° \leq 2\theta \leq 100.00°$ with a 2θ scan step of $0.02°$ (exposure time at each point was 15 s). All the computations were performed using the WYRIET program (version 3.3 [17]) within the sp. gr. $P\bar{1}$ typical of triclinic fairfieldites.

The structure was refined using the coordinates of the basis atoms of collinsite [4] as the starting model. The unit-cell parameters calculated from the experimental X-ray pattern of collinsite-(Sr) (Table 2, formula coefficient 0.74) were used as the starting values. The peak profiles were approximated by Pearson function VII with 6FWHM, where FWHM is the peak width at the half-height. The peak asymmetry was refined at $2\theta \leq 40°$. At the first stage, the scale factor and counter zero were refined. The subsequent refinement was carried out with the gradual addition of the parameters and automatic modeling of the background until the attainment of constant values of the reliability factors. The crystal structure was refined with anisotropic thermal parameters for the Sr, Ca, P, and Mg atoms and isotropic thermal parameters for the O atoms to $R_{wp} = 4.15\%$,
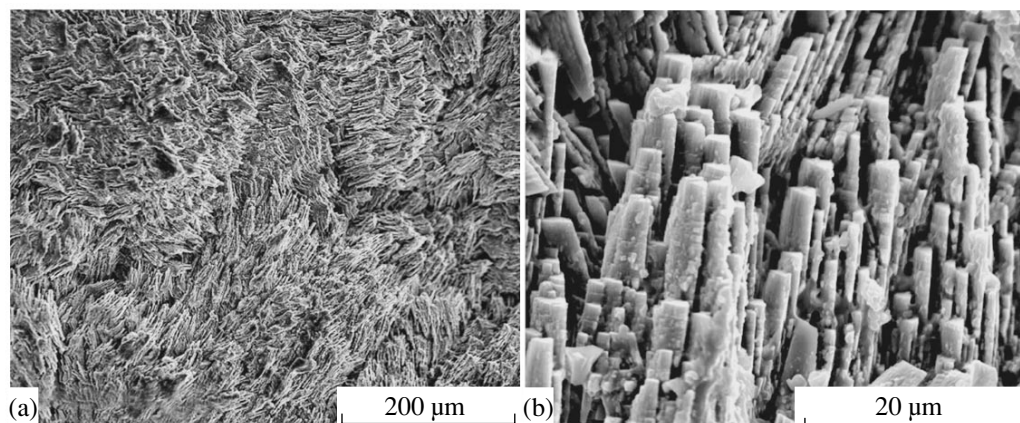

Fig. 1. Morphology of crystals of the strontium variety of collinsite (scanning electron microscropy data).

$R_F = 1.03\%$, and $R_B = 2.46\%$. According to the refined data, the isomorphous substitution of Ca for Sr atoms takes place—these atoms statistically occupy one general position in the ratio 0.64(1) : 0.36(1). The occupancies of the position correspond to $Ca_{1.28}Sr_{0.72}$ per formula unit of the mineral, which coincides with the data of microprobe analysis to within 0.01 (Table 3). The coordinates of the basis atoms of the Sr-containing collinsite variety and the equivalent thermal parameters are listed in Table 4. The interatomic distances are given in Table 5 together with those of other structurally studied minerals of this series. The experimental and calculated X-ray diffraction spectra are shown in Fig. 3.

RESULTS AND DISCUSSION

In the crystal structure of collinsite-(Sr), the Mg–O interatomic distances in centrosymmetric octahedra range within 1.98–2.31 Å (average distance 2.13 Å). The lower accuracy of powder X-ray diffraction experiments compared to single-crystal X-ray experiments did not allow us to perform rigorous analysis of the structural distortions caused by incorporation of strontium atoms into the calcium positions of the conventional collinsite. Nevertheless, the results obtained show the tendency in the changes in collinsite structure caused by the defect nature of one of the cation positions.

In the structure of collinsite-(Sr), the scatter in the interatomic distances in the Mg-octahedron is more pronounced than in collinsite, where the distances vary from 2.00 to 2.14 Å (average distance 2.09 Å). The orthophosphorus tetrahedra are distorted to a larger extent, and the P–O distances range within 1.46–1.58 Å, whereas the corresponding bond lengths in fairfieldite and collinsite range within 1.51–1.56 Å and
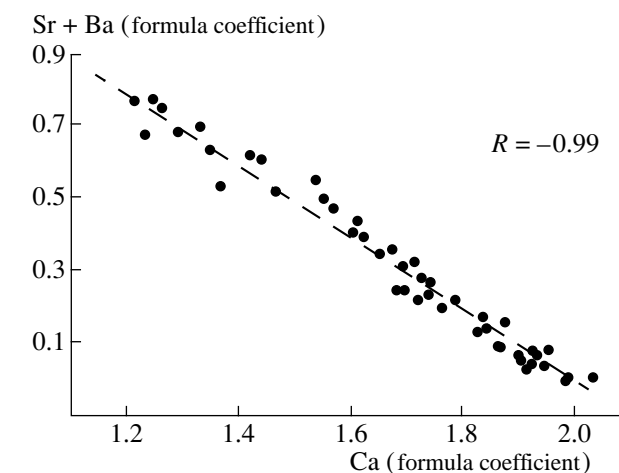
Fig. 2. Chemical composition of collinsite from hydrothermal mineral associations in carbonatites from the Kovdor complex (formula coefficients; per sum of cations equal to three).

1.53–1.56 Å, respectively. The average P–O bond lengths in the three structures are the same (1.54 Å).

The difference in the cation–anion distances in the eight-vertex polyhedron occupied by Ca atoms in the structures of this series seems to be of most interest. In the structures of collinsite, fairfieldite, and talmessite, the Ca–O distances vary from 2.38, 2.34, and 2.36 to 2.70, 2.72, and 2.77 Å, respectively. The isomorphous incorporation of Sr atoms into an eight-vertex polyhedron leads to its further distortion, which is seen from the increase in the cation–oxygen bond lengths (2.27–2.83 Å). Evidently, the incorporation of larger Sr^{2+} cations into eight-vertex polyhedra leads to an increase in the average distance in the polyhedra to 2.57 Å. The corresponding average distances in the structures of

Table 3. Chemical composition (wt %) and formula coefficients for the strontium variety of collinsite (ΣR^{2+} of the cations equals 3)

P_2O_5	39.25	P	2.03
CaO	19.02	Ca	1.24
SrO	20.87	Sr	0.74
BaO	1.60	Ba	0.04
FeO	0.13	Fe^{2+}	0.01
MnO	0.79	Mn	0.04
MgO	10.25	Mg	0.93
H_2O	8.92*	H_2O	1.82
Σ			100.83

* Determined by DTA.

Table 4. Coordinates of the basis atoms and thermal parameters ($Å^2$) in the collinsite-(Sr) structure

Atom	x/a	y/b	z/c	B_{eq}/B_{iso}^*
Mg	0.0	0.0	0.0	1.93(8)
Ca	0.3133(8)	0.7609(8)	0.6576(8)	2.41(4)
Sr	0.3133(8)	0.7609(8)	0.6576(8)	2.41(4)
P	0.312(2)	0.240(1)	0.672(2)	1.60(6)
O(1)	0.377(2)	0.164(2)	0.934(3)	2.1(5)*
O(2)	0.256(2)	0.064(2)	0.409(3)	1.0(4)*
O(3)	0.157(2)	0.372(2)	0.633(3)	1.5(4)*
O(4)	0.605(3)	0.375(2)	0.733(3)	1.0(5)*
O(5)	0.990(3)	0.285(3)	0.099(3)	0.9(4)*

Table 5. Interatomic distances (Å) in the minerals of the fairfieldite group

Mineral	Fairfieldite	Talmessite	Collinsite	Collinsite-(Sr)
Octahedra				
Mg–O(1)		2.14(2)	2.144(5)	2.31(1)
O(2)		2.12(2)	2.107(4)	2.11(1)
O(5)		2.04(2)	1.997(5)	1.98(1)
Mg–O$_{av}$		2.10	2.09	2.13
Tetrahedra				
P–O(1)	1.563(7)		1.549(5)	1.53(1)
O(2)	1.556(6)		1.559(5)	1.57(1)
O(3)	1.514(7)		1.527(6)	1.46(2)
O(4)	1.550(7)		1.538(5)	1.58(1)
P–O$_{av}$	1.55		1.54	1.54
Eight-vertex polyhedra				
Ca(Sr)–O(1)	2.495(9)	2.66(2)	2.594(5)	2.83(1)
O(1')	2.500(7)	2.45(2)	2.523(4)	2.27(1)
O(2)	2.475(8)	2.63(2)	2.589(5)	2.70(1)
O(2')	2.724(9)	2.77(2)	2.702(6)	2.76(1)
O(3)	2.456(8)	2.43(2)	2.468(5)	2.51(1)
O(3')	2.465(8)	2.41(2)	2.403(4)	2.49(1)
O(4)	2.336(9)	2.36(2)	2.384(6)	2.66(1)
O(5)	2.438(7)	2.40(2)	2.385(6)	2.51(1)
Ca(Sr)–O$_{av}$	2.49	2.51	2.50	2.57

collinsite, fairfieldite, and talmessite are 2.50, 2.49, and 2.51 Å, respectively (Table 5).

The crystal structures of the minerals of the fairfieldite group are composed by isolated Mg-octahedra (or Fe-, Mn-, Zn-, Co-, or Ni-octahedra) sharing the oxygen vertices with orthophosphate (orthoarsenate) tetrahedra to form chains parallel to the *c* axis (Fig. 4). In the chain, each tetrahedron shares two vertices with the adjacent octahedra, whereas two "lone" oxygen atoms of each tetrahedron are involved in the coordination of Ca (Sr) atoms only. Four oxygen vertices of each octahedron are shared with tetrahedra, whereas the two remaining vertices are occupied by water molecules. The large Ca^{2+} (Sr^{2+}) cations are located between the chains of the octahedra and tetrahedra, thus forming with these chains a three-dimensional framework; the same function is also performed by hydrogen bonds.

Comparative analysis of our data on collinsite and the known data on all the minerals of the fairfieldite group from all the known deposits in the world [4, 13, 16, 18, 19] leads to the conclusion that the incorporation of Sr atoms into the structures of these hydrated phosphates is determined primarily by the correspond-

ing intensive parameters of the mineral-forming medium. The above-described isomorphism has been established only in hydrothermal mineral associations related to carbonatites from the Kovdor massif.

The parameters of the hydrothermal process that occurred in this carbonatite complex were estimated in the earlier structural studies of yet another hydrated phosphate from the Kovdor massif—bakhchisarait-sevite [20]. This open/partially open moderate-low-temperature hydrothermal system is characterized by high alkalinity, as opposed to the typical manifestations of minerals of the fairfieldite group in granite pegmatites or quartz-enriched ferrous metasediments. The activity of CO_2 was very high compared to other natural hydrothermal systems but still too low compared to the activity of analogous postcarbonatite thermal springs circulated in alkaline and alkaline-ultrabasic complexes of the Kola province.

We believe that the presence of Sr in the structures of chain phosphates of the fairfieldite group is evidence of specific geochemical conditions that rarely occur in nature (they have been revealed only in the Kovdor phoscorite–carbonatite complex). In brief, these condi-
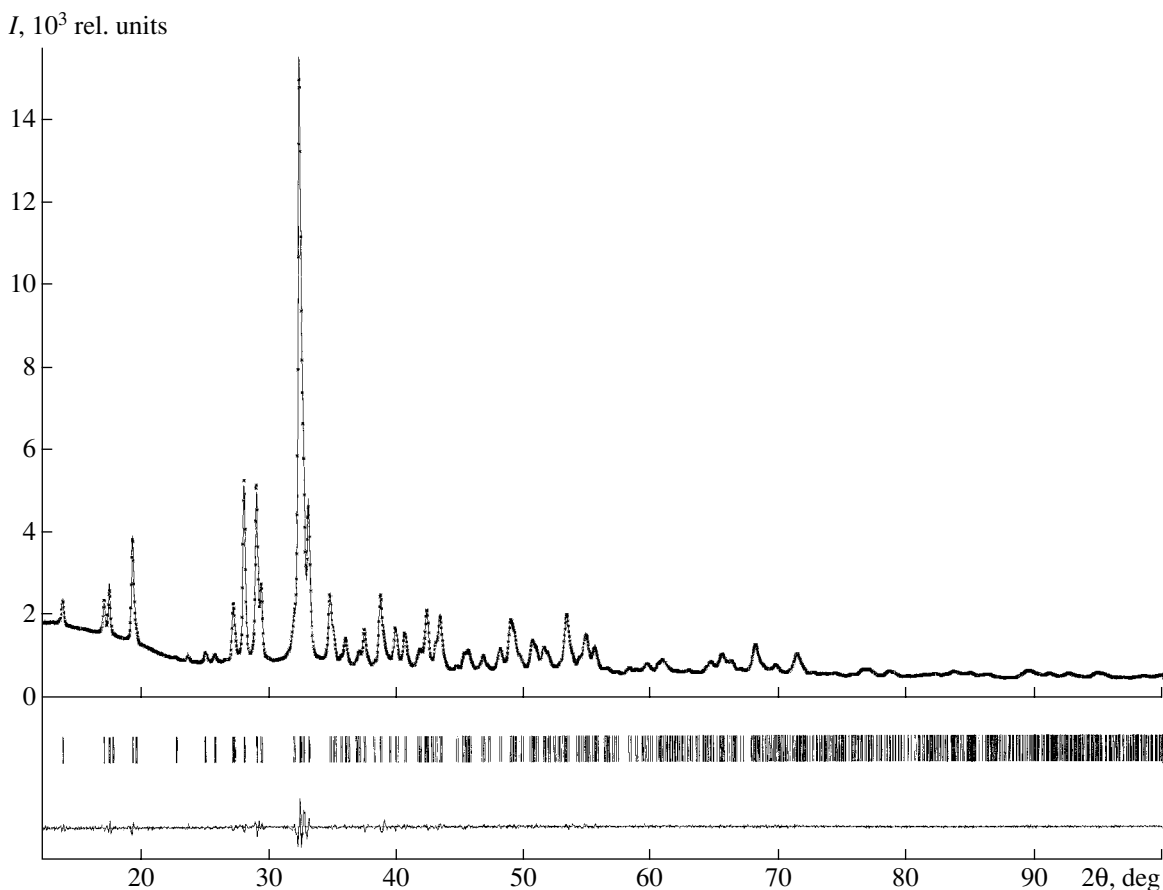
I, 10^3 rel. units

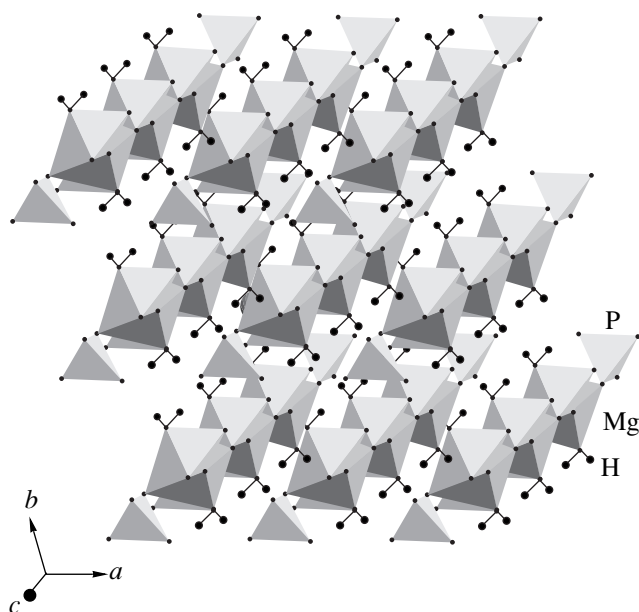**Fig. 3.** Theoretical (points) and experimental spectra of collinsite-(Sr).

Fig. 4. Axonometry of the crystal structure of collinsite-(Sr). Strontium atoms are statistically distributed over Ca-positions.

tions can be considered as the final stage of the evolution of a mantle-derived fluid-saturated carbonate–silicate system in the upper crust (apparently, corresponding to subvolcanic conditions) [10].

REFERENCES

1. L. Fanfani, A. Nunzi, P. F. Zanassi, *et al.*, Acta Crystallogr., Sect. B: Struct. Crystallogr. Cryst. Chem. **26**, 640 (1970).

2. C. Frondel, Am. Mineral. **40**, 828 (1955).

3. E. K. Vasil'ev, G. M. Kashaeva, and Z. F. Ushchapovskaya, *X-ray Index of Minerals (Phosphates)* (Nauka, Moscow, 1974).

4. P. D. Brotherton, E. N. Maslen, M. W. Price, and A. H. White, Aust. J. Chem. **27**, 653 (1974).

5. R. J. Hill and A. R. Milnes, Mineral. Mag. **39**, 684 (1974).

6. P. J. Dunn, D. R. Peacor, Shu-Chun Su, *et al.*, Neues Jahrb. Mineral., Abh., No. 157, 113 (1987).

7. B. Darko Struman and J. Dann Pete, Can. Mineral. **18**, 197 (1980).

8. M. Catti, G. Ferraris, and G. Ivaldi, Bull. Soc. Fr. Mineral. Cristallogr. **100**, 230 (1977).

9. P. Bariand and P. Herpin, Bull. Soc. Fr. Mineral. Cristallogr. **83**, 118 (1960).

10. R. P. Liferovich, Ya. A. Pakhomovsky, A. N. Bogdanova, *et al.*, Can. Mineral. **39**, 1081 (2001).

11. A. A. Kukharernko, M. P. Orlova, A. G. Bulakh, *et al. The Caledonian Complex of the Ultrabasic, Alkaline Rocks, and Carbonatites of the Cola Peninsula and Northern Karelia* (Nedra, Moscow, 1965).

12. S. N. Britvin, Ya. A. Pakhomovksy, A. N. Bogdanova, *et al.,* Can. Mineral. **29**, 87 (1991).

13. F. C. Hawthorne, Mineral. Mag. **62** (2), 141 (1999).

14. ASTM JCPDS, No. 26-1063.

15. R. D. Shannon, Acta Crystallogr., Sect. A: Cryst. Phys., Diffr., Theor. Gen. Crystallogr. **32**, 751 (1976).

16. G. W. Robinson, J. V. Velthuisen, and H. G. Ansell, Mineral. Rec. **23**, 5 (1992).

17. J. Schneider, in *Profile Refinement on IBM-PC: Proceedings of IV Cryst. Int. Workshop on the Rietveld Method* (Petten, 1989), p. 71.

18. P. J. Bridge and M. W. Price, Mineral. Mag. **39**, 577 (1974).

19. P. B. Moore, Mineral. Rec. **4**, 103 (1973).

20. O. V. Yakubovich, W. Massa, R. P. Liferovich, *et al.*, Can. Mineral. **38**, 831 (2000).

Translated by T. Safonova

<center>

STRUCTURE
OF INORGANIC COMPOUNDS

</center>

Molecular and Crystal Structures of Calix[4]arene 1,3-Di-*n*-Propyl Ether

L. G. Kuz'mina*, G. G. Sadikov*, J. A. K. Howard**, É. A. Shokova***, and V. V. Kovalev***

* Kurnakov Institute of General and Inorganic Chemistry, Russian Academy of Sciences,
Leninskiǐ pr. 31, Moscow, 119991 Russia
e-mail: kuzmina@igic.ras.ru
** Department of Chemistry, Durham University, Durham DH1 3LE, England
*** Moscow State University, Vorob'evy gory, Moscow, 119899 Russia
Received May 22, 2002

Abstract—The molecular and crystal structures of calix[4]arene 1,3-di-*n*-propyl ether are determined. The molecule adopts a cone conformation stabilized by a pair of hydrogen bonds of the O–H···O*R* type (*R* is *n*-propyl). The dihedral angles between the planes of the benzene rings and the plane passing through the oxygen atoms are equal to 35.0°, 68.5°, 39.8°, and 71.2°. The larger angles are characteristic of the rings consisting of the ether groups, whereas the smaller angles are observed in the phenol rings. The bond lengths and angles in the molecule have standard values. In the crystal, the molecules form centrosymmetric dimers due to stacking interactions between two benzene rings in each dimer. Each of these rings is enclosed in the cavity of the other molecule in the dimer. The dimers have the shape of an ellipsoid. The packing as a whole can be described as an ellipsoid packing in which all the contacts occur through van der Waals interactions. © *2003 MAIK "Nauka/Interperiodica"*.

INTRODUCTION

Calixarenes belong to the class of macrocyclic compounds. At present, these compounds have been studied extensively [1–8]. The structure of calix[4]arenes involves four phenol groups linked by orthomethylene bridges. The most important feature of these molecular systems is their conformational flexibility, which is responsible for the ability to fulfill the function of a host, i.e., to adapt their shape to include small-sized molecules, molecular fragments, and metal ions of different shape and size. Owing to the presence of aromatic rings and OH functional groups in flexible macrocyclic fragments of calix[4]arenes, they can interact with a guest molecule through stacking and electrostatic mechanisms. This renders calix[4]arenes most suitable for use as model objects in the elucidation of the nature of guest–host interactions that play a crucial role in biochemical processes of molecular recognition [1–8]. The evolution of research in this field necessitates an investigation into the structure of calixarenes with a modified skeleton. The modification consists in introducing different organic substituents either into aromatic rings or instead of protons of OH groups (with the partial or complete removal of active protons). Such a modification can lead to a decrease in the conformational flexibility of the macrocycle, a change in the nature of electrostatic interactions with the guest molecule, and an enhancement of hydrophobic effects. In general, this extends the range of molecular species that can be incorporated as guest molecules into the macrocycle of the host molecule. Moreover, this modification can affect the energy ratio of stable conformers and the ratio between the energies of barriers to conformational transitions. The influence of substituents on the energies of interconversion of the macrocycle and interaction of calix[4]arenes with metal cations was studied in [9–11].

This paper reports on the results of an X-ray structure investigation of calix[4]arene modified by substituting two *n*-propyl groups for two protons of the hydroxyl groups. Details of the chemical experiment performed in this work will be described in a separate paper.

EXPERIMENTAL

The most important parameters of the X-ray diffraction experiment are presented in Table 1. A colorless single crystal in the form of a prism was covered with a perfluorinated oil and placed in a Bruker SMART CCD diffractometer at a temperature of 150.0(2) K. Experimental reflections were measured in the ω scan mode (exposure time per frame, 15 s).

The structure was solved by direct methods and refined using the least-squares procedure for F^2. All the hydrogen atoms were located from the difference synthesis.

The final refinement of the structure was performed by the least-squares method in the full-matrix anisotropic approximation for all the non-hydrogen atoms and in the isotropic approximation for the hydrogen atoms.

Table 1. Crystal data, data collection, and refinement parameters for the crystal structure studied

Empirical formula	$C_{34}H_{36}O_4$
Molecular weight	508.63
Crystal system	Rhombohedral
Space group	$R\bar{3}$
a, Å	35.2039(8)
b, Å	35.2039(8)
c, Å	11.7188(4)
α, deg	90.0
β, deg	90.0
γ, deg	120.0
V, Å^3	12577.5(6)
Z	18
ρ_{calcd}, g/cm^3	1.209
$F(000)$	4896
$\mu(MoK_\alpha)$, mm^{-1}	0.078
Crystal size, mm	$0.42 \times 0.22 \times 0.18$
T, K	150.0(2)
Radiation type (wavelength, Å)	$MoK_\alpha(0.71073)$
Scan mode/θ range, deg	$\omega/1.16-27.51$
Index ranges	$-45 \leq h \leq 45$
	$-41 \leq k \leq 45$
	$-15 \leq l \leq 14$
Number of measured reflections	31619
Number of unique reflections	6426 [$R_{int} = 0.0769$]
Number of reflections with $I > 2\sigma(I)$	5687
Number of refined parameters	488
R factors for reflections with $I > 2\sigma(I)$	$R_1 = 0.0465$, $wR_2 = 0.1008$
R factors for all reflections	$R_1 = 0.0940$, $wR_2 = 0.1174$
Goodness-of-fit on F^2	0.967
Extinction coefficient	0.00126(9)
Residual electron density (min/max), e/Å^3	$-0.294/0.307$

The coordinates of the non-hydrogen atoms and the hydrogen atoms of the hydroxyl groups are listed in Table 2. All the calculations were carried out with the SHELXS86 [12] and SHELXL97 [13] software packages.

MOLECULAR STRUCTURE

The molecular structure is shown in Fig. 1. The geometric parameters of the molecule were obtained with a high accuracy, which makes it possible to discuss in detail the molecular geometry.

It is known [1–9] that 16-membered macrocyclic fragments of calix[4]arenes are characterized by four stable conformations (*cone*, *paco*, 1,2-*alt*, 1,3-*alt*), which differ in the orientation of their benzene rings with respect to each other and to the plane passing through the methylene bridges. Individual conformers only slightly differ in energy (by less than 1 kcal/mol), and the energy barriers to their mutual transformation are not very high (less than 5 kcal/mol) [9–11]. The cone (truncated cone or basket) conformation is additionally stabilized by a cyclic system of hydrogen bonds [14]. The introduction of substituents into the *endo* position (in particular, the substitution of large-sized organic radicals for protons of the OH groups) can substantially affect the energy ratio of the conformers or bring about an increase in the interconversion barriers (to ~13 kcal/mol) [10]. In our case, the substitution of *n*-propyl radicals for two protons in calix[4]arene does not lead to destabilization of the cone conformer. It is this conformation that is revealed in the crystal under investigation. Among the four hydrogen bonds observed in unsubstituted calix[4]arene, the substituted compound retains two hydrogen bonds, namely, O(1)–H⋯O(4) [O⋯O, 2.713 Å; O⋯H, 1.825 Å; and the O–H⋯O angle, 166.7°] and O(2)–H⋯O(3) [O⋯O, 2.679 Å; O⋯H, 1.799 Å; and the O–H⋯O angle, 167.7°]. The distances between the oxygen atoms that are not involved in the hydrogen bonds are as follows: O(1)⋯O(3), 2.804 Å and O(2)⋯O(4), 2.852 Å.

The specific feature of the macrocyclic skeleton of the calix[4]arene ether studied in this work is its flattened structure. Indeed, the oxygen–oxygen diagonal distances differ significantly: O(1)⋯O(2), 3.15 Å and O(3)⋯O(4), 4.46 Å. Apparently, this feature of the macrocyclic skeleton is associated either with the molecular packing effects or with the weak intermolecular interactions.

The dihedral angles between the planes of the C(1)⋯C(6), C(8)⋯C(13), C(15)⋯C(20), and C(22)⋯C(27) benzene rings and the plane passing through the oxygen atoms are equal to 35.0°, 68.5°, 39.8°, and 71.2°, respectively. Most likely, such a systematic distortion of the ideal cone shape is governed primarily by the tendency for hydrogen bonds to reach an optimum geometry. The largest angles are characteristic of the rings consisting of the ether groups, whose oxygen atoms are proton acceptors, whereas the smallest angles are observed in the rings composed of the phenol groups with the participation of protons. The obtained data on the cone geometry, the O(1)⋯O(4)–C(22) and O(1)⋯O(4)–C(32) angles (98.3° and 131.3°, respectively), and the O(2)⋯O(3)–C(8) and O(2)⋯O(3)–C(29) angles (101.1° and 126.7°, respectively) suggest that protons are approximately oriented

Table 2. Coordinates ($\times 10^4$) and equivalent isotropic thermal parameters ($\times 10^3$, Å^2) for non-hydrogen atoms*

Atom	x	y	z	U_{eq}	Atom	x	y	z	U_{eq}
O(1)	508(1)	2001(1)	8713(1)	29(1)	C(16)	1731(1)	2578(1)	5825(1)	23(1)
O(2)	999(1)	2027(1)	6443(1)	31(1)	C(17)	1981(1)	2866(1)	4961(2)	26(1)
O(3)	1306(1)	2012(1)	8523(1)	24(1)	C(18)	1788(1)	2930(1)	4002(2)	30(1)
O(4)	89(1)	1741(1)	6677(1)	28(1)	C(19)	1335(1)	2703(1)	3902(2)	29(1)
C(1)	434(1)	2271(1)	9400(1)	22(1)	C(20)	1070(1)	2406(1)	4734(2)	25(1)
C(2)	80(1)	2343(1)	9238(2)	24(1)	C(21)	573(1)	2149(1)	4613(2)	29(1)
C(3)	9(1)	2590(1)	10051(2)	26(1)	C(22)	131(1)	2142(1)	6352(2)	24(1)
C(4)	286(1)	2771(1)	10980(2)	29(1)	C(23)	352(1)	2341(1)	5342(2)	25(1)
C(5)	639(1)	2704(1)	11111(2)	26(1)	C(24)	380(1)	2736(1)	5030(2)	27(1)
C(6)	721(1)	2454(1)	10336(1)	22(1)	C(25)	204(1)	2931(1)	5723(2)	28(1)
C(7)	1100(1)	2367(1)	10494(2)	24(1)	C(26)	9(1)	2738(1)	6750(2)	26(1)
C(8)	1571(1)	2461(1)	8745(1)	21(1)	C(27)	−30(1)	2341(1)	7088(1)	24(1)
C(9)	1487(1)	2642(1)	9709(1)	22(1)	C(28)	−235(1)	2139(1)	8236(2)	27(1)
C(10)	1761(1)	3091(1)	9904(2)	25(1)	C(29)	1477(1)	1741(1)	8958(2)	30(1)
C(11)	2100(1)	3348(1)	9154(2)	26(1)	C(30)	1185(1)	1279(1)	8547(2)	45(1)
C(12)	2162(1)	3162(1)	8181(2)	25(1)	C(31)	726(1)	1069(1)	9035(3)	66(1)
C(13)	1899(1)	2716(1)	7953(1)	23(1)	C(32)	−311(1)	1362(1)	6284(2)	36(1)
C(14)	1956(1)	2516(1)	6860(2)	26(1)	C(33)	−311(1)	957(1)	6699(2)	51(1)
C(15)	1272(1)	2343(1)	5692(1)	24(1)	C(34)	48(1)	895(1)	6165(3)	71(1)
H(1)*	329(8)	1898(8)	8101(22)	70(8)	H(2)*	1133(9)	2021(9)	7084(25)	88(9)

* The coordinates of the hydrogen atoms of the hydroxyl groups.

toward one of the lone electron pairs of the O(3) and O(4) oxygen atoms.

The O–C(*Ph*) bonds of the hydroxyl groups [1.363(2) and 1.366(2) Å] are shorter than the O–C(*Ph*) bonds of the ether groups [1.400(2) and 1.395(2) Å]. In turn, the latter bonds are shorter than the O–C bonds with the *n*-propyl groups [1.448(2) and 1.448(2) Å]. All these bond lengths have standard values [15].

The C–C bond lengths in the methylene bridges fall in the range 1.522–1.524 Å. The angles at the atoms of the methylene bridges lie in the range 111.9°–113.8°. The benzene rings have a nearly ideal geometry. The geometric parameters given above also correspond to standard values.

CRYSTAL PACKING

The molecular packing in the crystal under investigation is also of considerable interest, because it can provide additional information on the possible nature of the interaction of calixarenes with organic molecules.

In the crystal, two molecules related by the center of symmetry are mutually arranged in such a way that one of the benzene rings of each molecule is located in the cavity of the other molecule (Fig. 2). As a consequence, the mutual arrangement of the molecules ensures the closest packing. Moreover, the enclosed benzene rings

are aligned parallel to each other and their peripheral regions overlap (Fig. 3). The calculations conducted by Müller-Dethlefs and Hobza [16] and Hunter *et al.* [17] demonstrated that only such a displaced mutual arrangement of the benzene rings leads to a stacking interaction. Janiak [18] performed an investigation based on the data available in the Cambridge Structural Database and revealed that the coaxial π–π interaction of aromatic systems without their mutual displacement occurs very rarely. As was shown in [18], the interplanar distances for these interactions, as a rule, lie in the range 3.3–3.8 Å.

Thus, in the studied structure, the interplanar distance (3.45 Å) determined in the dimer is typical of weak interactions of aromatic systems.

In [16], the mutual arrangement described above was referred to as the parallel-displaced arrangement. As follows from the *ab initio* quantum-chemical calculations performed in [17], the parallel-displaced arrangement corresponds to an attractive quadrupole–quadrupole interaction. According to [18], attractive interactions of the C–H···π-system type should be taken into account only in the case when the aromatic systems overlap along their periphery.

It is of interest that, in the dimer, benzene rings of the C(8)···C(13) type are enclosed in the cavities of the other molecule of the dimer along the small diagonal of
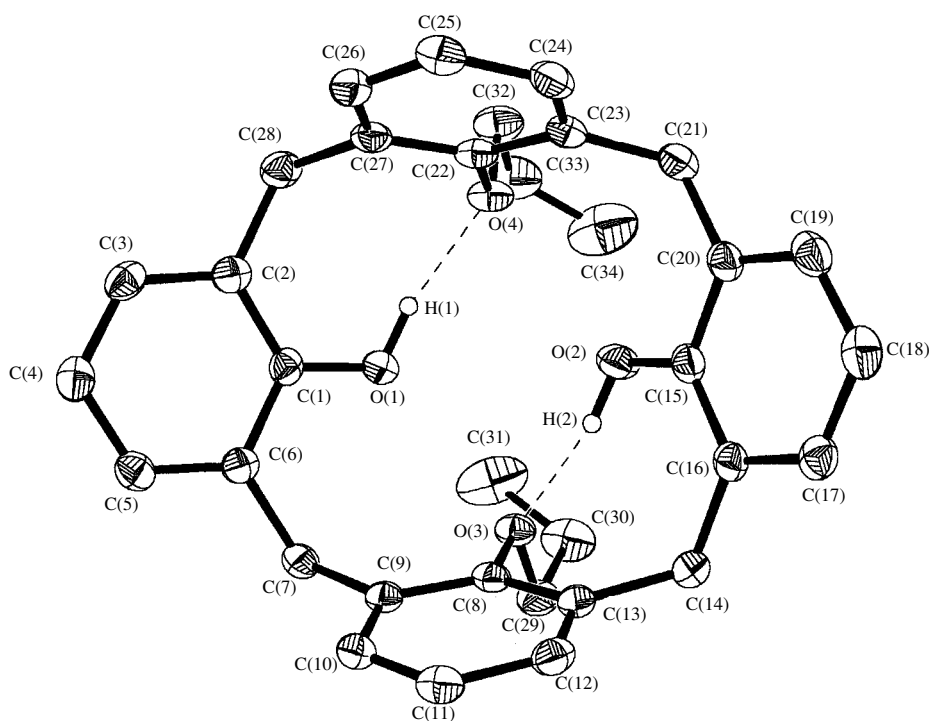
Fig. 1. Molecular structure. Thermal ellipsoids for atoms are drawn at the 30% probability level.
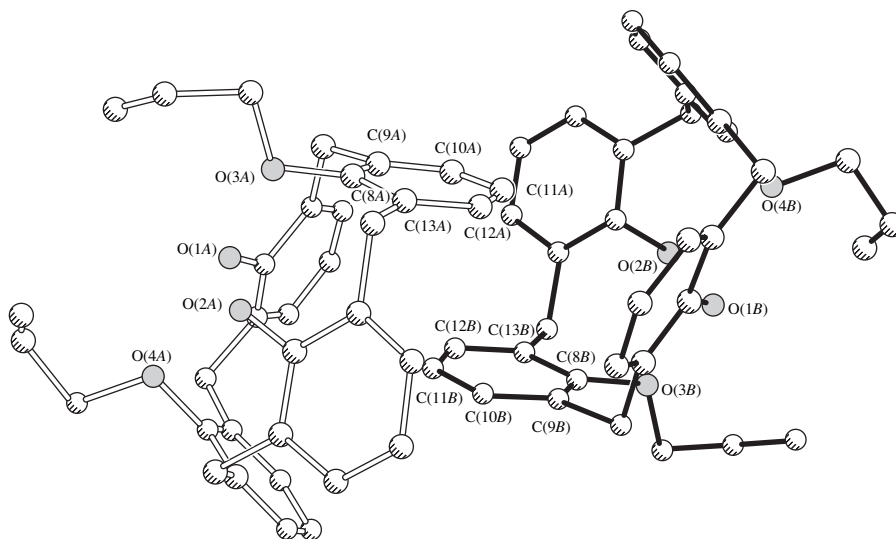
Fig. 2. Structure of the stacking dimer.

the flattened cone. For this geometry of the dimer, the H(10A) and H(12A) hydrogen atoms [as well as the H(10B) and H(12B) hydrogen atoms, which are centrosymmetric with respect to H(10A) and H(12A)] of the benzene rings are arranged almost over the planes of the C(1B)···C(6B) and C(15B)···C(20B) benzene rings [and, correspondingly, the C(1A)···C(6A) and C(15A)···C(20A) benzene rings] of the other half. The distances between the aforementioned hydrogen atoms

and the benzene ring planes are equal to 2.87 and 3.01 Å. This geometry corresponds to a weak interaction of the C–H···π type, which is considered a weak hydrogen bond between the CH group (weak acid) and the π system (weak base) [19]. Analysis of structural information revealed that the distance between the hydrogen atom and the aromatic ring falls in the range from 2.70 to 3.40 Å [19]. Possibly, it is this weak attractive interaction that is responsible for the formation of
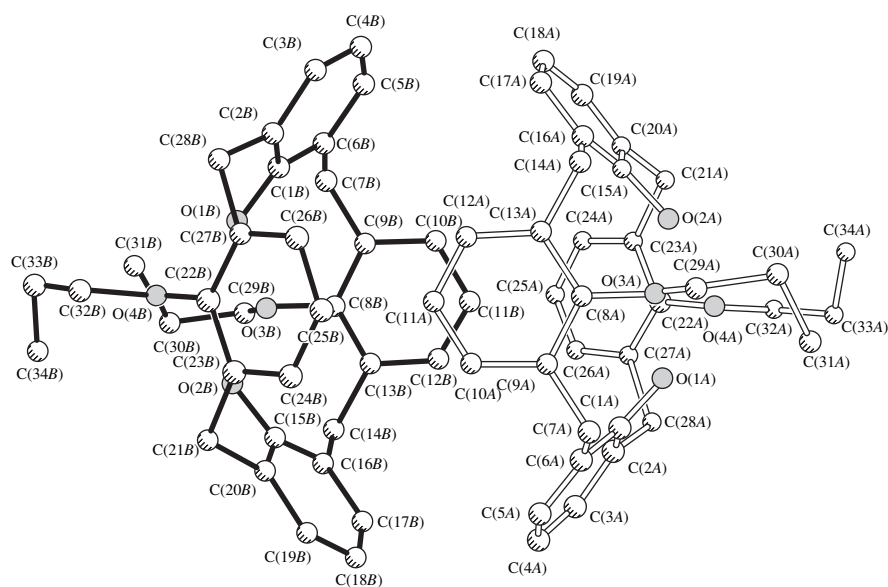
Fig. 3. Structure of the stacking dimer in the projection onto the plane of one of the overlapping benzene rings.
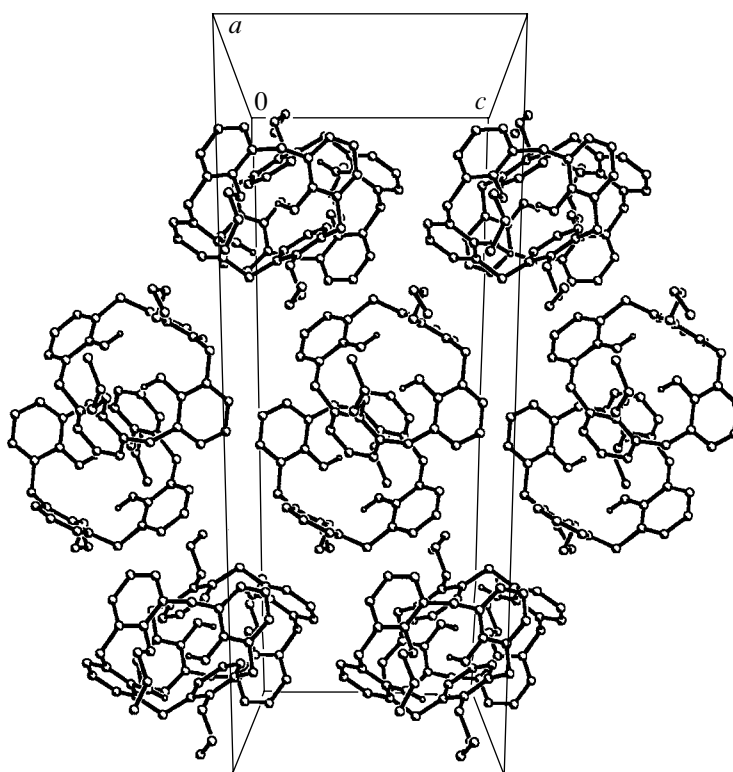

Fig. 4. A fragment of the crystal packing.

the flattened structure of the cone skeleton of the studied compound.

Note that the stacking interaction occurs between the phenyl rings of the ether groups. These rings form large angles with the plane of the basket bottom. It is quite reasonable that the surface energy of the dimer system with this geometry of the interaction should be substantially less than that in the case of the stacking interaction between the phenol groups whose tilt is almost twice as small.

Despite the presence of six benzene rings on the surface of the dimer system, no other stacking interactions are found in the crystal structure. The surface of the dimer system can be approximated by an ellipsoid. The ellipsoids are closely packed in the crystal (Fig. 4). All the interatomic contacts between the dimers occur through van der Waals interactions.

ACKNOWLEDGMENTS

REFERENCES

1. J.-M. Lehn, *Supramolecular Chemistry: Concepts and Perspectives* (VCH, Weinheim, 1995).

2. C. D. Gutsche, *Calixarenes* (Royal Society of Chemistry, Cambridge, 1989).

3. J. L. Atwood, G. W. Orr, K. D. Robinson, and F. Hamada, Supramol. Chem. **2**, 309 (1993).

4. E. van Dienst, W. I. Iwema Bakker, J. F. Engbersen, *et al.*, Pure Appl. Chem. **65**, 387 (1993).

5. C. D. Gutsche, Aldrichim. Acta **28**, 3 (1995).

6. V. Böhmer, Angew. Chem. Int. Ed. Engl. **34**, 713 (1995).

7. C. D. Gutsche, in *Calixarenes*, Ed. by J. F. Stoddart (Royal Society of Chemistry, Cambridge, 1998).

8. A. Ikeda and S. Shinkai, Chem. Rev. **97**, 1713 (1997).

9. B. P. Hay, J. B. Nicholas, and D. Feller, J. Am. Chem. Soc. **122**, 10083 (2000).

10. I. Thondorf, J. Chem. Soc., Perkin Trans. **2**, 1791 (1999).

11. T. Kusano, M. Tabatabai, Y. Okamoto, and V. Bohmer, J. Am. Chem. Soc. **121**, 3789 (1999).

12. G. M. Sheldrick, Acta Crystallogr., Sect. A: Found. Crystallogr. **46**, 467 (1990).

13. G. M. Sheldrick, *SHELXL97: Program for the Refinement of Crystal Structures* (Univ. of Göttingen, Germany, 1997).

14. D. M. Rudkevich, Chem.-Eur. J. **6** (15), 2679 (2000).

15. F. H. Allen, O. Kennard, D. G. Watson, *et al.*, J. Chem. Soc., Perkin Trans. 2, S1 (1987).

16. K. Müller-Dethlefs and P. Hobza, Chem. Rev. **100**, 143 (2000).

17. C. A. Hunter, J. Singh, and J. M. Thornton, J. Mol. Biol. **218**, 837 (1991).

18. C. Janiak, J. Chem. Soc. Dalton Trans. 3885 (2000).

19. H. Takahashi, S. Tsuboyama, Y. Umezawa, *et al.*, Tetrahedron **56**, 6185 (2000).

Translated by O. Borovik-Romanova

Refinement of the Crystal Structure of Lead Titanate with Different Degrees of Imperfection of Cationic and Anionic Sublattices by the Rietveld Method

A. I. Akimov, G. K. Savchuk, V. A. Rubtsov, and A. K. Letko

Institute of Solid-State and Semiconductor Physics, Belarussian National Academy of Sciences,
ul. Brovki 17, Minsk, 220072 Belarus
e-mail: akimov@ifttp.bas-net.by
Received July 23, 2001; in final form, March 28, 2002

Abstract—The parameters of the crystal structure of lead titanate with different degrees of imperfection of the anionic and cationic sublattices are refined by the Rietveld method. The experiments are carried out on a DRON-4 diffractometer (CuK_α radiation; $20° < 2\theta < 70°$; scan step, $0.01°$; exposure time per point, 10 s). All the calculations are performed with the GSAS software package in the space group *P4mm*. The structure parameters are refined in the isotropic approximation to $R_d = 5.0–6.0\%$. © *2003 MAIK "Nauka/Interperiodica"*.

INTRODUCTION

Lead titanate $PbTiO_3$, like barium titanate $BaTiO_3$, is a typical representative of oxygen octahedral ferroelectrics with a perovskite structure. The ferroelectric properties and the crystal structure of lead titanate were determined as far back as 1950. Since that time, there have appeared many works concerned with the determination of the lattice parameters of lead titanate from X-ray diffraction data [1–6].

However, the crystallographic data reported in [1–6] for $PbTiO_3$ and, in particular, the data currently available in the *ASTM Powder Diffraction File* are rather contradictory [1–3]. At room temperature, lead titanate has a tetragonal structure and belongs to the space group *P4mm* ($Z = 1$). According to the published data, the unit cell parameters a and c for $PbTiO_3$ fall in the ranges from 3.895 to 3.94 and from 4.063 to 4.171 Å, respectively. Correspondingly, the ratio c/a varies from 1.0312 to 1.0709. Unfortunately, there has been no discussion of the reasons for such a noticeable scatter of the unit cell parameters.

Koray [7] demonstrated that the aforementioned changes in the lattice parameters of the crystal structure of $PbTiO_3$ can be associated with different sizes of $PbTiO_3$ crystal grains. It was noted that a change in the size of crystal grains from 0.02 to 0.15 μm leads to considerable variations in the unit cell parameters a and c (from 3.915 to 3.905 and from 4.1 to 4.145 Å, respectively). Moreover, it was found that, in the case when the size of crystal grains is larger than 0.15 μm, the unit cell parameters are independent of the grain size [7].

For lack of any adequate explanation of the difference in the lattice parameters of the $PbTiO_3$ crystal structure, we undertook a more detailed investigation of the structural characteristics of lead titanate with different degrees of imperfection of the anionic and cationic sublattices.

EXPERIMENTAL

Lead titanate samples with different degrees of anionic and cationic imperfection were synthesized at temperatures ranging from 860 to 890°C for 2–8 h. Titanium dioxide TiO_2 (OSCh 5-2 grade) and lead oxide PbO (OSCh 5-3 grade) were used as the initial components. The synthesis was performed in closed corundum crucibles in air. Prior to synthesis, the initial components were thoroughly mixed and were then pressed under a pressure of 100 MPa into disks 4 mm thick and 20 mm in diameter. After the synthesis, the samples were crushed to powders, which were examined using X-ray powder diffraction. According to the X-ray powder diffraction data, the $PbTiO_3$ powders synthesized at temperatures of 870–890°C had a single-phase composition and a perovskite structure. The crystal grain size of the studied powders was determined using grain-size analysis on a Fritsch Model 22 instrument and fell in the range 2–8 μm.

The X-ray diffraction patterns of lead titanate were measured on a DRON-4 automated diffractometer (CuK_α monochromatic radiation; silicon internal standard; 2θ scan mode; scan step, $0.01°$; exposure time per point, 10 s). All the calculations were performed with the GSAS program package [8–10]. As in earlier works [1, 4, 5], the structure was refined in the space group *P4mm*. The refinement was carried out first for the background function, scale factor, counter zero, and unit cell parameters and then for the structure and profile parameters. The unit cell parameters and the param-

Table 1. Unit cell parameters of lead titanate with different degrees of cationic and anionic imperfection

Chemical formula	Synthesis time, h	Lattice parameters, Å		Ratio c/a	Unit cell volume, Å^3
		a	c		
870°C					
$Pb_{0.984}Ti_{0.960}O_{2.970}$	2	3.9024(1)	4.1583(1)	1.0656	63.324(1)
$Pb_{0.991}Ti_{0.962}O_{2.985}$	4	3.9005(1)	4.1565(1)	1.0656	63.235(1)
$Pb_{0.992}Ti_{0.984}O_{2.957}$	6	3.8990(3)	4.1552(0)	1.0657	63.169(3)
$Pb_{0.993}Ti_{0.986}O_{2.928}$	8	3.8989(2)	4.1541(1)	1.0655	63.143(2)
880°C					
$Pb_{0.992}Ti_{1.0}O_{2.951}$	2	3.8993(6)	4.1551(1)	1.0656	63.177(1)
$Pb_{0.998}Ti_{1.0}O_{3.000}$	4	3.8993(3)	4.1552(0)	1.0656	63.178(3)
$Pb_{0.983}Ti_{1.0}O_{2.852}$	6	3.8984(5)	4.1543(1)	1.0656	63.137(1)
890°C					
$Pb_{0.998}Ti_{0.964}O_{2.923}$	2	3.9009(5)	4.1574(1)	1.0656	63.263(1)
$Pb_{0.987}Ti_{1.00}O_{2.8965}$	3	3.8988(5)	4.1550(0)	1.0657	63.162(1)
$Pb_{0.963}Ti_{1.00}O_{2.707}$	4	3.9046(4)	4.1597(1)	1.0653	63.419(2)

eters of the theoretical model of the crystal structure were refined by the least-squares method. The structural model was used to calculate the theoretical X-ray diffraction pattern, which was then compared with the experimental X-ray diffraction pattern. When comparing the calculated and experimental diffraction patterns, the background was subtracted.

The peak shape was described with the use of a function proposed by Rietveld with due regard for the asymmetry correction A_s [11]. This function has the form

$$H(\Delta T) = \sum g_i F(\Delta T'),$$

where

$$\Delta T' = \Delta T + f_i A_s / \tan 2\theta + S_s \cos\theta + T_s \sin 2\theta,$$

f_j is the atomic factor, T_s is the absorption coefficient, and S_s is the displacement of the sample. The function $F(\Delta T')$ is a combination of the Lorentzian and Gaussian functions [12], that is,

$$F(\Delta T') = \eta L(\Delta T', \Gamma) + (1 - \eta)G(\Delta T', \Gamma),$$

where $\eta = 1.36606(\gamma/\Gamma) - 0.477719(\gamma/\Gamma)^2 + 0.11116(\gamma/\Gamma)^3$ is the matching coefficient, Γ is the full width at half-maximum, and γ is the Lorentz factor [13].

In this work, we refined 40 parameters. The parameters to be refined were gradually included in the refinement, which was accompanied by geometric simulation of the background. The refinement was terminated when the R factor reached a constant value. The R factor was defined by the formula

$$R_d = (\sum Y_i^{exp} - Y_i^{theor})/\sum Y_i^{exp}.$$

The refinement of the structure parameters was carried out until the final factors R_d characterizing the discrepancy between the experimental and calculated structure amplitudes became equal to 5.0–6.0%.

The results of the structure refinement in the isotropic approximation for $PbTiO_3$ with different degrees of anionic and cationic imperfection are presented in Table 1. The atomic coordinates, site occupancies, and isotropic thermal parameters are listed in Table 2.

The chemical formulas characterizing the degree of anionic and cationic imperfection of the samples under investigations are given in the first column of Table 1. These formulas were obtained as a result of the refinement of the features in the crystal structure by the Rietveld method using the GSAS program package for atomic site occupancies (Table 2).

Analysis revealed that the unit cell parameters (Tables 1, 2) nonlinearly depend on the degree of imperfection of the lead, titanium, and oxygen sites. It should be noted that no imperfection is observed at the O(1) site; moreover, the total number of oxygen atoms ($n_O < 3$) in the unit cell is determined by the degree of imperfection at the O(2) site. The functional dependences of the unit cell parameters a and c on the degree of imperfection of the cationic and anionic sublattices were derived by mathematical modeling of the experiment. For this purpose, the matrix of the experiment (Table 3, columns n_{Pb}, n_O, n_{Ti}, a_{exp}, and c_{exp}) was constructed on the basis of the data obtained in the refinement of the unit cell parameters and the atomic site occupancies. By using the data presented in Table 3 and one of the methods of mathematical modeling of experiments, namely, the method of the group account of arguments [14], we derived the following relationships:
$a = 8.014195 - 2.08275 n_{Pb} - 1.842482 n_{Ti} - 0.791714 n_O +$

Table 2. Positional parameters, site occupancies (q), and root-mean-square atomic displacements (u^2) for lead titanate samples synthesized under different temperature (T, °C) and time conditions

Atom	870				880			890		
	Synthesis time, h									
	2	4	6	8	2	4	6	2	3	4
Pb(0, 0, 0)										
q	0.9844(1)	0.9909(0)	0.9923(2)	0.993(0)	0.9926(3)	0.9982(0)	0.983(1)	0.9981(3)	0.9870(4)	0.9633(3)
u^2	0.0049(1)	0.0058(1)	0.013(1)	0.009(1)	0.0011(1)	0.0116(1)	0.0029(1)	0.0111(1)	0.0043(1)	0.0053(1)
O(1)(0.5, 0.5, z)										
z	0.1266(0)	0.0811(3)	0.0741(1)	0.0716(2)	0.1469(1)	0.0907(0)	0.0741(4)	0.1362(3)	0.0679(1)	0.0103(0)
q	1	1	1	1	1	1	1	1	1	1
u^2	0.059(1)	0.020(1)	0.053(5)	0.045(7)	0.033(1)	0.020(3)	0.053(1)	0.0098(1)	0.0569(4)	0.3045(8)
Ti(0.5, 0.5, z)										
z	0.5537(1)	0.5333(1)	0.5300(1)	0.4701(4)	0.5243(1)	0.5291(3)	0.4819(1)	0.5691(4)	0.5424(1)	0.5580(1)
q	0.960(1)	0.962(3)	0.984(1)	0.986(1)	1	1	1	0.964(1)	1	1
u^2	0.024(2)	0.024(1)	0.018(0)	0.018(0)	0.003(1)	0.012(1)	0.002(1)	0.0001(0)	0.0002(6)	0.0004(1)
O(2)(0.5, 0, z)										
z	0.5838(2)	0.6143(4)	0.6409(4)	0.6458(3)	0.6042(1)	0.5907(0)	0.5315(1)	0.5868(1)	0.5975(1)	0.6090(1)
q	0.980(1)	0.9897(0)	0.9713(0)	0.9522(1)	0.9671(2)	1	0.9010(1)	0.9486(3)	0.9795(2)	0.8049(3)
u^2	0.012(1)	0.0023(5)	0.0039(1)	0.0058(2)	0.005(1)	0.025(1)	0.096(3)	0.0098(1)	0.0014(4)	0.0688(1)

$0.623518 n_O n_{Pb} n_{Ti} + 0.034965 n_O^2$; $c = -1.207632 - 1.960091 n_{Pb} - 0.677579 n_{Ti} + 2.63785 n_O + 0.578774 n_O n_{Pb} n_{Ti} - 0.412336 n_O^2 + 0.994991/n_{Ti} + 9.595909/n_O^2$. The dependences of the unit cell parameters a and c on the degree of imperfection of the anionic and cationic sublattices of lead titanate are described by the above relationships with a high accuracy (Table 3, columns a_{theor} and c_{theor}). The validity of these relationships was checked against the F criterion, and their applicability was judged by the coefficient of determination. In our case, the coefficients of determination were equal to 0.96 and 0.97 for the formulas representing the parameters a and c, respectively, at the following atomic site occupancies in the crystal lattice: $g_{Pb} = (0.963–1.0)$; $g_{Ti} = (0.954–1.0)$; $g_{O(2)} = (0.963–0.998)$; and $g_{O(1)} = 1.0$.

DISCUSSION

In the crystal structure of lead titanate, the sizes of lead and titanium cations are less than those of the holes occupied by these cations. The interrelation of hole sizes leads to a displacement of the titanium ion from the center of the oxygen tetrahedron. It should be noted that, in a perfect crystal structure of lead titanate, the ionic displacements in all unit cells should be identical in magnitude and direction.

The results obtained in the refinement of the structure parameters of lead titanate powders (synthesized under different temperature–time conditions) with different degrees of anionic and cationic imperfections indicate that the lead titanate prepared at 880°C for 4 h has a more perfect crystal structure. Under these conditions, the TiO_6 oxygen octahedra are distorted to a smaller extent. The angles in these octahedra are as follows: O(1)–Ti–O(1) = 180°, O(1)–Ti–O(2) ~ 90°,

Table 3. Matrix of the experiment and results of mathematical modeling

n_{Pb}	n_O	n_{Ti}	a_{exp}	c_{exp}	a_{theor}	c_{theor}
0.963	2.707	1.00	3.9046	4.1597	3.9045	4.1596
0.983	2.852	1.00	3.8984	4.1543	3.8989	4.1546
0.987	2.897	1.00	3.8989	4.1550	3.8987	4.1547
0.992	2.951	1.00	3.8993	4.1551	3.8991	4.1551
0.998	3.00	1.00	3.8993	4.1551	3.8995	4.1552
0.984	2.97	0.96	3.9024	4.1583	3.9024	4.1585
0.989	2.599	0.97	3.9003	4.1565	3.9003	4.1565
0.991	2.985	0.962	3.9005	4.1565	3.9004	4.1563
0.992	2.957	0.984	3.8990	4.1552	3.8995	4.1551
0.993	2.928	0.986	3.8989	4.1541	3.8985	4.1541
0.9885	2.923	0.954	3.9009	4.1574	3.9009	4.1573

Note: n_{Pb}, n_{Ti}, and n_O are the numbers of Pb, Ti, and O atoms in the unit cell, respectively.
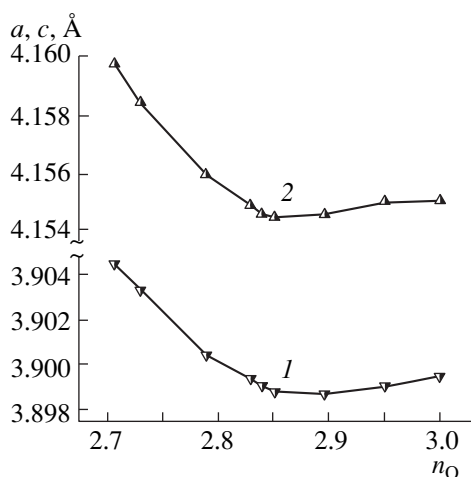
Fig. 1. Dependences of the lattice parameters (*1*) *a* and (*2*) *c* on the total number n_O of oxygen atoms in the unit cell.
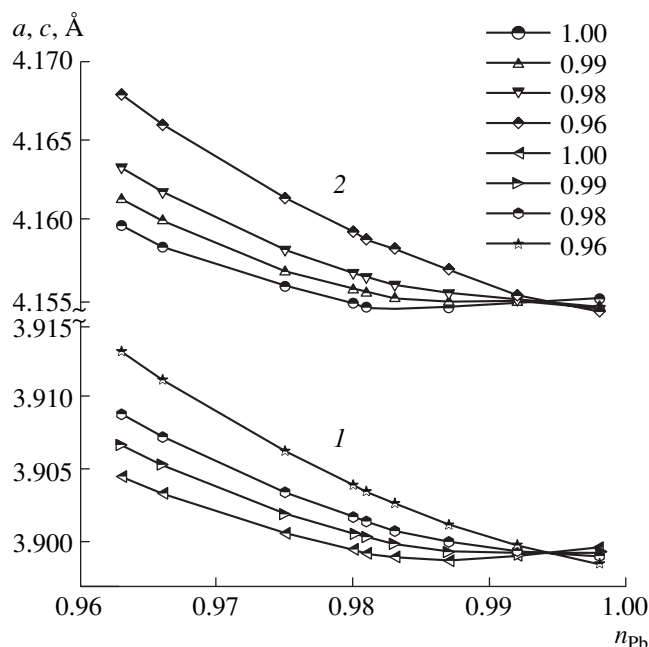
Fig. 2. Dependences of the lattice parameters (*1*) *a* and (*2*) *c* on the number n_{Pb} of lead atoms in the unit cell at different site occupancies of titanium atoms (site occupancies are given in the legend).

O(2)–Ti–O(2) = 89.365°, and O(2)–Ti–O(2) = 167.91°. The site occupancies of the Ti and O(1) atoms are equal to unity. The maximum site occupancies are observed for the Pb (0.9982) and O(2) (0.9997) atoms. The positional parameters (in terms of fractional coordinates) for the O(1) and O(2) atoms along the *z* axis are identical and equal to 0.0907.

A comparison of the structural characteristics (the lattice parameters, positional and thermal parameters of the basis atoms, and site occupancies) for lead titanate powders with different degrees of imperfection allowed us to make the following inferences.

(i) The lattice parameters *a* and *c* only slightly increase with a decrease in the degree of imperfection at the Pb, Ti, and O(2) sites.

(ii) The unit cell volume decreases with an increase in the degree of imperfection at the Pb and O sites in the case when the Ti sites are completely filled. The unit cell volume decreases by 0.4% as the site occupancies of the Pb and O(2) atoms increase by 0.02 and 0.145, respectively.

(iii) The displacement of the O(1) and O(2) atoms along the *z* axis decreases with an increase in the synthesis time at a given temperature.

(iv) A decrease in the degree of imperfection at the Ti sites is accompanied by a decrease in the displacement of the Ti atom along the *z* axis.

(v) The occupancy of the O(2) site decreases when the synthesis time exceeds 4 h at a given temperature.

The data presented in Tables 1–3 clearly demonstrate that the changes in the unit cell parameters are associated with the presence of defects at the Pb, O(2), and Ti sites. The functional relationships derived for the unit cell parameters *a* and *c* contain a term accounting for the product of all the three quantities. We examined the dependence of the total number n_O of oxygen atoms in the unit cell on the number of lead atoms n_{Pb} under the conditions when the Ti sites are completely occupied ($n_{Ti} = 1$) (Table 3). This analysis revealed that, within the accuracy of the determination, the increase in the degree of imperfection at the Pb sites is attended by a proportional increase in the degree of imperfection at the O sites. The functional relationships obtained for the unit cell parameters *a* and *c* make it possible to calculate these parameters as a function of the degree of anionic and cationic imperfection, provided the numbers of atoms in the unit cell fall in the following ranges: $0.95 \le n_{Ti} \le 1$, $2.6 \le n_O \le 3$, and $0.96 \le n_{Pb} \le 1$. The dependences of the unit cell parameters on the total number of oxygen atoms (at $n_{Ti} = 1$) are depicted in Fig. 1. Since the number of lead atoms in the unit cell varies in proportion to the total number of oxygen atoms, the dependences of the unit cell parameters *a* and *c* on the lead content show a similar behavior. It follows from analyzing the dependences displayed in Fig. 1 that the unit cell parameters are minimum at $n_{Pb} = 0.98$ and $n_O = 2.85$. An increase in the degree of imperfection at the Pb and O sites ($T = 890°C$; time, 4 h) results in a considerable increase in the unit cell parameters. The dependences of the parameters *a* and *c* on the degree of imperfection at the Ti sites are shown in Fig. 2. These dependences indicate that the unit cell parameters $a = 3.915$ Å and $c = 4.17$ Å can be observed only in the case when, apart from the imperfection at the Pb and O sites, the degree of imperfection at the Ti sites in lead titanate is of the order of 3–4%.

The results of the above investigation demonstrated that the TiO_6 oxygen octahedra can undergo relatively small but characteristic changes depending on the

degree of imperfection. A decrease in the displacement of the titanium and oxygen atoms along the z axis and an increase in the occupancy of the O(2) site bring about an increase in the Ti–O bond length in the (001) plane from 1.95 to 1.98 Å. In the situation where the occupancy of the Ti site is close to unity, the Ti–O interatomic distances along the polar axis decrease with a decrease in the displacement of the Ti and O(1) atoms and fall in the ranges 1.89–1.41 and 2.58–2.33 Å, respectively.

The electronic structure of Pb^{2+} is responsible for the formation of four shorter (2.61–2.43 Å) and eight longer (2.82–2.71 Å) Pb–O bonds. The Pb–O(1) bond lengths decrease with a decrease in the degree of imperfection at the Pb sites and a decrease in the displacement of the O(1) atom along the z axis. The length of the shorter Pb–O(2) bonds depends on both the occupancy of the O(2) site and the displacement of the O(2) atom along the z axis.

CONCLUSIONS

The structure of lead titanate powders with 2- to 8-μm grains and different degrees of anionic and cationic imperfection was refined by the Rietveld method using X-ray diffraction data. It was demonstrated that the formation of defects at the Pb, Ti, and O(2) sites in the crystal lattice is responsible for the change in the structural characteristics of lead titanate.

The analysis of the structural data obtained revealed a correlation between the unit cell parameters, the interplanar distances, and the degree of anionic and cationic imperfection.

REFERENCES

1. Yu. Ya. Tomashpol'skiĭ, Yu. N. Venevtsev, and G. S. Zhdanov, Kristallografiya **13** (3), 521 (1968) [Sov. Phys. Crystallogr. **13**, 425 (1968)].
2. R. J. Nelmes and W. F. Kuhs, Solid State Commun. **54**, 721 (1985).
3. A. M. Glazer and S. A. Mabud, Acta Crystallogr., Sect. B: Struct. Crystallogr. Cryst. Chem. **34**, 1065 (1978).
4. S. A. Mabud and A. M. Glazer, J. Appl. Crystallogr. **12**, 49 (1979).
5. M. Kupriyanov, D. Kovtun, A. Zakharov, *et al.*, Phase Transit. **64**, 145 (1998).
6. J. Joseph, T. M. Vimala, V. Sivasubramanian, and V. R. K. Murthy, J. Mater. Sci. **35**, 1571 (2000).
7. E. Koray, *Structure-Property Relations in Mesoscopic BaTiO₃ and PbTiO₃*, Thesis Dissertation (1998), p. 13.
8. A. C. Larson and R. B. von Dreele, *Los Alamos National Laboratory Report LAUR* (2000), p. 86.
9. ftp://ftp.lanl.gov/public/gsas.
10. A. I. Akimov, A. L. Karpeĭ, G. K. Savchuk, *et al.*, in *Proceedings of the 3rd International Scientific and Technical Conference "Modern Technology of Hybrid Integrated Circuits Including Elements of Superconductor Electronics," Naroch', 1994*, p. 139.
11. H. M. Rietveld, J. Appl. Crystallogr. **2**, 65 (1969).
12. H. M. Rietveld and J. Thomas, J. Appl. Crystallogr. **10**, 12 (1977).
13. C. J. Howard, J. Appl. Crystallogr. **15**, 615 (1982).
14. *Algorithms and Programs for Reconstruction of Dependences* (Nauka, Moscow, 1984).

Translated by O. Borovik-Romanova

STRUCTURE
OF ORGANIC COMPOUNDS

Palladium (II) Compounds with Diaminocarboxylic Acids: Crystal Structures of [Pd(H$_2$*Cdta*)] · H$_2$O, [Pd(H$_3$*Edtp*)Cl] · 2H$_2$O, and (H$_6$*Edtp*)[PdCl$_4$] · 4H$_2$O

I. N. Polyakova*, A. L. Poznyak**, and V. S. Sergienko*

* Kurnakov Institute of General and Inorganic Chemistry, Russian Academy of Sciences,
Leninskiĭ pr. 31, Moscow, GSP-1, 119991 Russia
e-mail: sokol@igic.ras.ru
** Institute of Molecular and Atomic Physics, Belarussian Academy of Sciences,
pr. F. Skoriny 70, Minsk, 220072 Belarus
Received June 11, 2002

Abstract—The crystal structures of three Pd(II) compounds with diamine tetracarboxylates in different protonation states are determined, namely, [Pd(H$_2$*Cdta*)] · H$_2$O (**I**), [Pd(H$_3$*Edtp*)Cl] · 2H$_2$O (**II**), and (H$_6$*Edtp*)[PdCl$_4$] · 4H$_2$O (**III**) (R_1 = 0.0230, 0.0313, and 0.0277 for 3040, 3377, and 3809 reflections with $I > 2\sigma(I)$ for **I–III**, respectively). Crystals **I** and **II** are built of neutral complexes [Pd(H$_2$*Cdta*)] and [Pd(H$_3$*Edtp*)Cl], respectively, and crystallization water molecules. Crystal **III** consists of [PdCl$_4$]$^{2-}$ anionic complexes, H$_6$*Edtp*$^{2+}$ cations, and water molecules. In **I**, one of the protonated acetate groups of the H$_2$*Cdta*$^{2-}$ ligand forms a very weak additional Pd–O bond [2.968(2) Å] over the 2N + 2O coordination square. In **II** and **III**, the protonated propionate groups of the H$_3$*Edtp*$^-$ ligand and the H$_6$*Edtp*$^{2+}$ cation are not involved in Pd coordination and the coordination squares consist of the 2N + O + Cl and 4Cl atoms, respectively. © *2003 MAIK "Nauka/Interperiodica".*

INTRODUCTION

Compounds of bivalent Pd occupy a modest place among the large number of structurally characterized metal compounds with diaminocarboxylic acids (H$_4$*Edta* and its analogues). The crystal structures of [Pd(H$_4$*Edta*)Cl$_2$] · 5H$_2$O [1, 2], Ba$_2$[Pd(*Edta*)]$_2$ · 10H$_2$O [3], and (H$_6$*Cdta*)[PdCl$_4$] · 5H$_2$O [4], where H$_4$*Cdta* is cyclohexanediaminetetraacetic acid, are known from the literature. We obtained new acid complexes of Pd(II) with diamine ligands in different protonation states, namely, the [Pd(H$_2$*Cdta*)] · H$_2$O (**I**) and [Pd(H$_3$*Edtp*)Cl] · 2H$_2$O (**II**) complexes, and the (H$_6$*Edtp*)[PdCl$_4$] · 4H$_2$O (**III**) salt, where H$_4$*Edtp* is ethylenediaminetetrapropionic acid. In this paper, the results of X-ray diffraction studies of **I–III** are reported.

EXPERIMENTAL

Synthesis. Compound **I** was synthesized according to the procedure described in [5]. Single crystals were obtained by slow evaporation of an aqueous solution at room temperature.

Compounds **II** and **III** were isolated sequentially from the same reaction mixture. The H$_4$*Edtp* acid was synthesized beforehand. For this purpose, a mixture of ethylenediamine (En) and acrylamide in the mole ratio 1 : 4 was heated at 60°C for a few hours, hydrolyzed with NaOH on a water bath until the ammonia evolution was complete, and acidified with HCl in order to precipitate H$_4$*Edtp*. No less than four moles of NaOH and HCl each were used per mole of En.

The H$_4$*Edtp* acid obtained was dissolved in water and partially neutralized with NaOH (two moles per mole of the acid). The equimolar amount of PdCl$_2$ was added to the solution, and the solution was heated gently at 50°C until it completely dissolved. The resultant yellow solution was evaporated under vacuum. In order to obtain single crystals of **II**, the yellow precipitate was recrystallized by slow evaporation of an aqueous solution.

After crystals **II** were separated, HCl was added to the mother liquor to a concentration of 0.1 mol/l. This solution was allowed to evaporate in air. First, orange crystals (probably, [Pd(H$_4$*Edtp*)Cl$_2$]) precipitated but dissolved with time, and then, brownish yellow crystals **III** of the X-ray quality were formed.

X-ray diffraction study. The main crystal data and parameters of data collection and structure refinement for compounds **I–III** are summarized in Table 1.

The sets of intensities for crystals **I–III** were obtained on an Enraf–Nonius CAD4 automated diffractometer (λMoK_α, graphite monochromator, ω scan mode). For all crystals, correction for absorption was introduced using the azimuthal scan method.

Table 1. Main crystal data and parameters of data collection and structure refinement for **I–III**

Parameter	I	II	III
Empirical formula	$C_{14}H_{20}N_2O_9Pd$	$C_{14}H_{27}ClN_2O_{10}Pd$	$C_{14}H_{34}ClN_2O_{12}Pd$
M	466.72	525.23	670.63
Space group	$P2_1/n$	$P2_1/n$	$P\bar{1}$
a, Å	9.165(3)	7.242(2)	6.968(1)
b, Å	13.299(4)	12.896(4)	9.086(2)
c, Å	14.178(4)	21.523(5)	10.947(2)
α, deg	90	90	74.70(3)
β, deg	100.69(2)	93.32(2)	72.87(3)
γ, deg	90	90	79.63(3)
V, Å^3	1698.1(9)	2007(1)	634.9(2)
Z	4	4	1
ρ_{calcd}, g/cm^3	1.826	1.738	1.754
Crystal size, mm	$0.09 \times 0.15 \times 0.30$	$0.03 \times 0.21 \times 0.24$	$0.09 \times 0.24 \times 0.30$
μ_{Mo}, mm^{-1}	1.146	1.112	1.210
θ_{max}, deg	28	28	32
Number of measured reflections	3981	4411	4458
Number of unique reflections (N_1) [R_{int}]	3775 [0.0288]	4317 [0.0284]	4251 [0.0275]
Number of reflections with $I > 2\sigma(I)$ (N_2)	3040	3377	3809
R_1, wR_2 for N_1	0.0391, 0.0624	0.0519, 0.0874	0.0343, 0.0775
R_1, wR_2 for N_2	0.0230, 0.0585	0.0313, 0.0807	0.0277, 0.0750
GOOF	1.062	1.062	1.059
$\Delta\rho_{min}$ and $\Delta\rho_{max}$, e/Å^3	−0.459 and 0.582	−0.513 and 0.915	−0.608 and 0.410

The structures were solved by the direct method (SHELXS86 [6]). The non-hydrogen atoms were refined in the anisotropic approximation. All the hydrogen atoms were located from the difference Fourier syntheses. The hydrogen atoms attached to the C(6) and C(7) atoms in structure **II** and the hydrogen atoms of water molecules in structure **III** were refined within a riding model with the isotropic thermal parameters larger than the U_{eq} values of the corresponding non-hydrogen atoms by a factor of 1.2. The remaining hydrogen atoms in all the structures were refined in the isotropic approximation. The refinement was performed with the SHELXL97 program [7].

The atomic coordinates and thermal parameters for structures **I–III** are listed in Table 2.

RESULTS AND DISCUSSION

Crystals **I** are built of [Pd(H$_2$*Cdta*)] complexes (Fig. 1) and crystallization water molecules. The environment of the Pd(1) atom includes two nitrogen atoms and the O(1) and O(5) oxygen atoms of the deprotonated acetate groups of the H$_2$*Cdta*$^{2-}$ ligand. The N(1), N(2), O(1), and O(5) atoms are approximately copla-

nar; the mean atomic deviation from this plane is 0.008 Å. The Pd(1) atom deviates from this plane by 0.184 Å. The H$_2$*Cdta*$^{2-}$ ligand closes three five-membered chelate rings. All the rings are corrugated and lie on one side of the plane of the coordination square. The uncoordinated acetate arms are situated on the opposite side of this plane, and one of them hangs over the coordination square and forms a very weak additional bond Pd(1)···O(8) [2.968(2) Å], which deviates from the normal to the plane of the square by 30.2°. Similarly, two additional Pd···O bonds (3.04 Å) complement the Pd polyhedron (2N + 2O) to the elongated bipyramid in the structure of [Pd(H$_4$*Edta*)Cl$_2$] · 5H$_2$O (**IV**) [1, 2].

Crystals **II** are built of [Pd(H$_3$*Edtp*)Cl] complexes (Fig. 2) and water molecules. The coordination square of the Pd(1) atom consists of the O(1) oxygen atom of the deprotonated propionate group, the N(1) and N(2) nitrogen atoms of the H$_3$*Edtp*$^-$ ligand, and the Cl(1) atom in the *trans* position to N(1). The mean deviation of the four atoms of the environment from their plane is 0.017 Å. The Pd(1) atom deviates from this plane by 0.056 Å. The protonated alanine groups are turned away from the plane of the coordination square and do not form additional bonds with the metal.

Table 2. Atomic coordinates and parameters of thermal vibrations U_{eq} (for H atoms, U_{iso}) in structures **I**–**III**

Atom	x	y	z	U_{eq}/U_{iso}, Å^2	Atom	x	y	z	U_{eq}/U_{iso}, Å^2
			I					**II**	
Pd(1)	0.15929(2)	0.38191(1)	0.66302(1)	0.02199(7)	Pd(1)	0.26129(3)	0.22876(2)	0.17777(1)	0.02121(8)
O(1)	0.1358(2)	0.5152(1)	0.5957(1)	0.0284(4)	Cl(1)	0.0341(1)	0.15079(7)	0.23332(4)	0.0344(2)
O(2)	0.2200(2)	0.5969(1)	0.4806(1)	0.0371(4)	O(1)	0.1375(4)	0.1684(2)	0.0993(1)	0.0359(6)
O(3)	0.6516(2)	0.4556(2)	0.7273(2)	0.0376(4)	O(2)	0.1238(4)	0.1004(3)	0.0063(1)	0.0525(8)
O(4)	0.4539(2)	0.5314(2)	0.6504(2)	0.0457(5)	O(3)	0.2385(6)	0.6385(3)	0.0897(1)	0.060(1)
O(5)	−0.0189(2)	0.3884(1)	0.7306(1)	0.0307(4)	O(4)	0.2635(5)	0.5383(2)	0.0084(1)	0.0541(8)
O(6)	−0.2073(2)	0.2858(2)	0.7396(1)	0.0384(4)	O(5)	−0.1255(4)	0.4836(2)	0.3116(1)	0.0349(6)
O(7)	0.3989(2)	0.2501(2)	0.9500(1)	0.0389(5)	O(6)	0.0668(5)	0.4262(3)	0.3866(1)	0.061(1)
O(8)	0.4114(2)	0.3413(2)	0.8227(1)	0.0427(5)	O(7)	0.7526(6)	0.1293(3)	0.4316(2)	0.063(1)
N(1)	0.3112(2)	0.3496(2)	0.5803(1)	0.0237(4)	O(8)	0.6295(6)	0.0262(2)	0.3581(2)	0.062(1)
N(2)	0.1652(2)	0.2379(2)	0.7072(1)	0.0231(4)	N(1)	0.4652(4)	0.2921(2)	0.1285(1)	0.0266(6)
C(1)	0.2716(3)	0.4207(2)	0.4964(2)	0.0310(5)	N(2)	0.4049(4)	0.2829(2)	0.2567(1)	0.0211(5)
C(2)	0.2075(3)	0.5185(2)	0.5261(2)	0.0289(5)	C(1)	0.6188(5)	0.3230(3)	0.1751(2)	0.0290(7)
C(3)	0.4725(3)	0.3552(2)	0.6237(2)	0.0280(5)	C(2)	0.5390(5)	0.3608(3)	0.2343(2)	0.0282(7)
C(4)	0.5222(3)	0.4546(2)	0.6690(2)	0.0292(5)	C(3)	0.5419(6)	0.2037(3)	0.0912(2)	0.0375(9)
C(5)	0.0018(3)	0.2156(2)	0.6862(2)	0.0264(5)	C(4)	0.4150(6)	0.1626(4)	0.0399(2)	0.0399(9)
C(6)	−0.0817(3)	0.3022(2)	0.7221(2)	0.0280(5)	C(5)	0.2148(5)	0.1423(3)	0.0496(2)	0.0322(8)
C(7)	0.2193(3)	0.2161(2)	0.8108(2)	0.0283(5)	C(6)	0.4075(6)	0.3759(3)	0.0852(2)	0.0413(9)
C(8)	0.3531(3)	0.2754(2)	0.8587(2)	0.0299(5)	C(7)	0.3374(7)	0.4696(4)	0.1134(2)	0.049(1)
C(9)	0.2653(3)	0.2412(2)	0.5537(2)	0.0265(5)	C(8)	0.2745(7)	0.5511(3)	0.0643(2)	0.045(1)
C(10)	0.2564(3)	0.1804(2)	0.6446(2)	0.0268(5)	C(9)	0.2932(5)	0.3316(3)	0.3052(2)	0.0259(7)
C(11)	0.1986(3)	0.0747(2)	0.6185(2)	0.0378(6)	C(10)	0.1520(5)	0.4096(3)	0.2812(2)	0.0306(7)
C(12)	0.2949(4)	0.0216(2)	0.5567(2)	0.0461(7)	C(11)	0.0283(5)	0.4396(3)	0.3323(2)	0.0286(7)
C(13)	0.3011(4)	0.0825(3)	0.4661(2)	0.0448(7)	C(12)	0.5009(5)	0.1886(3)	0.2844(2)	0.0255(7)
C(14)	0.3629(3)	0.1872(2)	0.4924(2)	0.0379(6)	C(13)	0.6380(6)	0.2094(3)	0.3396(2)	0.0328(8)
O(1w)	0.5912(4)	0.1208(3)	0.7599(4)	0.081(1)	C(14)	0.6719(6)	0.1116(3)	0.3764(2)	0.0372(9)
H(1A)	0.201(4)	0.396(2)	0.449(3)	0.047(9)	O(1w)	0.2966(5)	0.3090(3)	0.4688(2)	0.0440(7)
H(1B)	0.352(4)	0.433(2)	0.470(2)	0.042(8)	O(2w)	0.8658(5)	0.0015(3)	0.1068(2)	0.0506(9)
H(3A)	0.529(3)	0.342(2)	0.575(2)	0.033(7)	H(3)	0.211(6)	0.685(4)	0.060(2)	0.04(1)
H(3B)	0.491(3)	0.310(2)	0.665(2)	0.028(7)	H(5)	−0.196(7)	0.487(4)	0.343(2)	0.05(1)
H(5A)	−0.024(3)	0.155(2)	0.713(2)	0.019(6)	H(7)	0.755(7)	0.082(4)	0.448(2)	0.05(2)
H(5B)	−0.032(3)	0.213(2)	0.616(2)	0.019(6)	H(1A)	0.696(5)	0.266(3)	0.184(2)	0.021(9)
H(7A)	0.240(3)	0.152(3)	0.820(2)	0.038(8)	H(1B)	0.693(6)	0.375(4)	0.159(2)	0.04(1)
H(7B)	0.147(3)	0.233(2)	0.845(2)	0.036(8)	H(2A)	0.472(6)	0.429(3)	0.227(2)	0.04(1)
H(9)	0.162(3)	0.245(2)	0.515(2)	0.029(7)	H(2B)	0.628(6)	0.367(3)	0.264(2)	0.04(1)
H(10)	0.350(3)	0.174(2)	0.684(2)	0.032(7)	H(3A)	0.656(6)	0.232(3)	0.072(2)	0.04(1)
H(11A)	0.094(4)	0.084(3)	0.585(2)	0.051(9)	H(3B)	0.578(7)	0.139(4)	0.120(2)	0.06(2)
H(11B)	0.197(4)	0.038(3)	0.672(2)	0.050(9)	H(4A)	0.465(6)	0.103(4)	0.020(2)	0.04(1)
H(12A)	0.258(4)	−0.042(3)	0.540(2)	0.048(9)	H(4B)	0.418(7)	0.215(4)	0.009(2)	0.05(1)
H(12B)	0.398(4)	0.012(2)	0.594(2)	0.037(8)	H(6A)	0.5155(0)	0.3920(0)	0.0573(0)	0.05
H(13A)	0.202(4)	0.082(2)	0.429(2)	0.035(7)	H(6B)	0.3149(0)	0.3426(0)	0.0508(0)	0.05
H(13B)	0.370(3)	0.050(2)	0.428(2)	0.042(8)	H(7A)	0.2323(0)	0.4512(0)	0.1363(0)	0.06
H(14A)	0.462(3)	0.177(2)	0.532(2)	0.035(7)	H(7B)	0.4386(0)	0.5026(0)	0.1443(0)	0.06
H(14B)	0.361(4)	0.230(2)	0.438(2)	0.046(9)	H(9A)	0.240(6)	0.281(3)	0.325(2)	0.03(1)
H(3)	0.688(4)	0.398(3)	0.736(3)	0.05(1)	H(9B)	0.376(6)	0.360(3)	0.331(2)	0.03(1)
H(7)	0.368(4)	0.200(3)	0.969(2)	0.042(9)	H(10A)	0.072(6)	0.386(3)	0.252(2)	0.03(1)
H(1w)	0.631(6)	0.127(3)	0.710(4)	0.07(2)	H(10B)	0.197(5)	0.473(3)	0.268(2)	0.03(1)
H(2w)	0.596(6)	0.076(4)	0.770(4)	0.10(2)	H(12A)	0.409(5)	0.140(3)	0.298(2)	0.021(9)

Table 2. (Contd.)

Atom	x	y	z	U_{eq}/U_{iso}, Å^2	Atom	x	y	z	U_{eq}/U_{iso}, Å^2
H(12B)	0.570(6)	0.156(3)	0.256(2)	0.04(1)	C(6)	0.8159(3)	0.6120(2)	0.1907(2)	0.0269(3)
H(13A)	0.768(7)	0.235(4)	0.327(2)	0.05(1)	C(7)	0.9949(3)	0.6511(2)	0.0765(2)	0.0272(3)
H(13B)	0.592(6)	0.256(3)	0.367(2)	0.04(1)	O(1w)	0.3404(4)	0.0354(3)	0.9259(3)	0.0896(9)
H(1w1)	0.379(7)	0.331(4)	0.479(3)	0.05(2)	O(2w)	1.1530(5)	−0.2256(4)	0.2446(3)	0.0860(8)
H(2w1)	0.252(9)	0.365(6)	0.441(3)	0.10(2)	H(1)	1.093(4)	0.484(3)	0.301(3)	0.042(7)
H(1w2)	0.923(8)	0.049(5)	0.102(3)	0.07(2)	H(2)	1.608(5)	0.344(4)	0.044(3)	0.06(1)
H(2w2)	0.842(7)	−0.025(4)	0.067(3)	0.07(2)	H(4)	0.875(7)	0.842(5)	0.023(4)	0.09(1)
III					H(1A)	0.830(4)	0.417(3)	0.528(3)	0.038(7)
Pd(1)	0.5	0	0.5	0.02595(6)	H(1B)	0.844(4)	0.586(3)	0.449(2)	0.029(6)
Cl(1)	0.22223(9)	−0.03724(8)	0.67667(6)	0.0481(1)	H(2A)	0.996(4)	0.205(3)	0.413(3)	0.040(7)
Cl(2)	0.44742(9)	−0.20507(7)	0.43183(6)	0.0440(1)	H(2B)	1.178(4)	0.261(3)	0.434(3)	0.044(7)
O(1)	1.4357(2)	0.4272(2)	0.2297(2)	0.0382(3)	H(3A)	1.172(4)	0.227(3)	0.189(3)	0.033(6)
O(2)	1.5233(3)	0.2907(2)	0.0747(2)	0.0444(4)	H(3B)	1.300(4)	0.128(3)	0.273(3)	0.040(7)
O(3)	1.1472(2)	0.5615(2)	0.0548(1)	0.0352(3)	H(5A)	0.723(4)	0.429(3)	0.338(3)	0.037(7)
O(4)	0.9839(3)	0.7869(2)	−0.0027(2)	0.0418(4)	H(5B)	0.888(4)	0.382(3)	0.220(3)	0.039(7)
N(1)	1.0069(2)	0.4350(2)	0.3461(1)	0.0227(2)	H(6A)	0.785(4)	0.689(3)	0.240(2)	0.030(6)
C(1)	0.9174(3)	0.4918(2)	0.4704(2)	0.0280(3)	H(6B)	0.696(4)	0.616(3)	0.160(2)	0.029(6)
C(2)	1.1022(3)	0.2711(2)	0.3731(2)	0.0282(3)	H(1w1)	0.327	−0.013	1.002	0.108
C(3)	1.2406(3)	0.2262(2)	0.2501(2)	0.0288(3)	H(2w1)	0.316	−0.028	0.880	0.108
C(4)	1.4096(3)	0.3261(2)	0.1855(2)	0.0295(3)	H(1w2)	1.259	−0.219	0.275	0.103
C(5)	0.8457(3)	0.4524(2)	0.2738(2)	0.0261(3)	H(2w2)	1.062	−0.160	0.280	0.103

In complexes **I** and **II**, the Pd–N bonds are slightly shorter than those in **IV**, in which the H$_4$*Edta* molecule coordinates the metal atom only by two N atoms, thus closing the ethylenediamine ring (2.026(2) and 2.012(2) Å in **I**, 2.039(3) and 2.061(3) Å in **II**, and 2.087 Å in **IV** [2]). In the dimeric complex
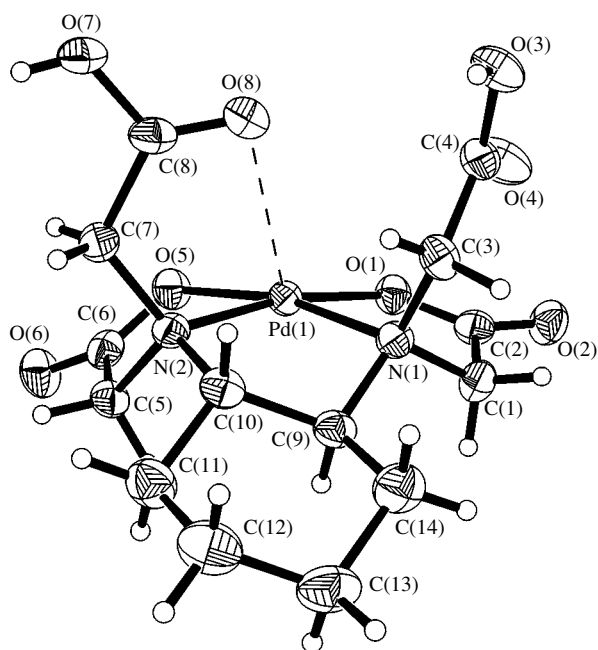
Fig. 1. Structure of the [Pd(H$_2$*Cdta*)] complex in **I**.
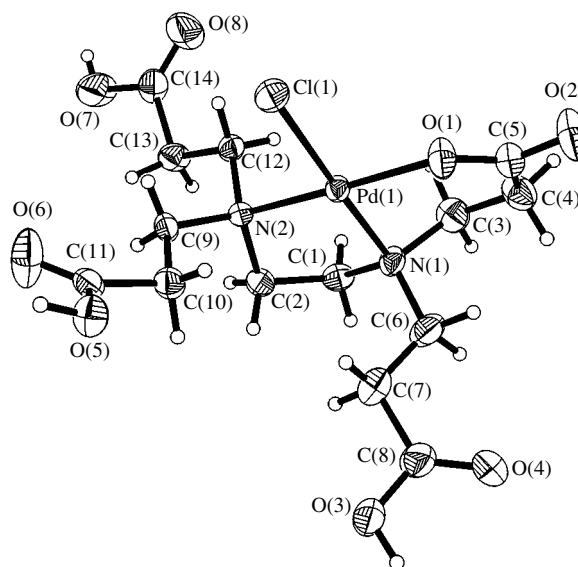
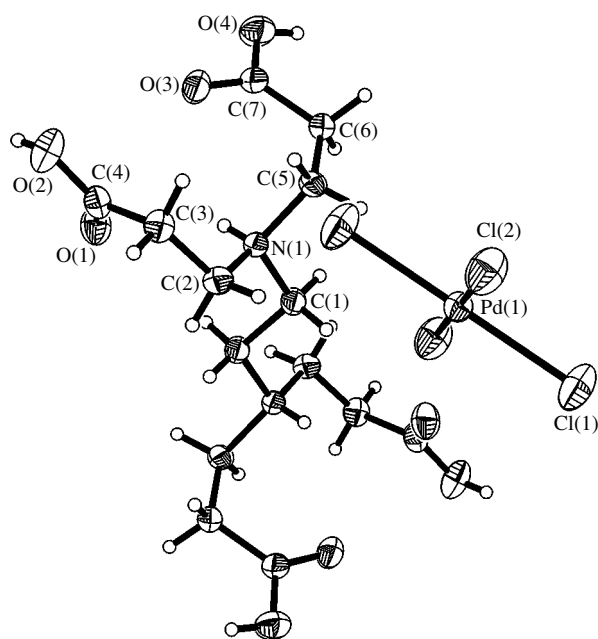**Fig. 2.** Structure of the [Pd(H$_3$*Edtp*)Cl] complex in **II**.

Fig. 3. Fragment of structure **III**.

[Pd(*Edta*)]$_2^{4-}$ (**V**) [3], each of the independent *Edta*$^{4-}$ ligands forms two glycinate rings, in which the mean Pd–N bond length [2.08(1) Å] is larger than that in **I** and **II**. The Pd–O bond lengths in **I** [2.006(2) and 2.043(2) Å] and **II** [2.022(2) Å] are close to the corresponding values in the dimeric complex **V** [3] [1.996(8)–2.020(8) Å], and the Pd–Cl bond length in **II** [2.319(1) Å] is comparable to the length of the symmetrically equivalent Pd–Cl bonds in **IV** (2.299 Å [2]).

Crystals **III** are built of H$_6$*Edtp*$^{2+}$ cations, [PdCl$_4$]$^{2-}$ anionic complexes, and crystallization water molecules. A fragment of structure **III** is shown in Fig. 3. The cations and anions occupy centrosymmetric positions. The [PdCl$_4$]$^{2-}$ anion has a planar-square structure. The Pd(1)–Cl bond lengths are 2.299(1) and 2.303(1) Å, and the Cl(1)Pd(1)Cl(2) angle is 91.08(4)°. In the H$_6$*Edtp*$^{2+}$ cation, all carboxyl groups and nitrogen atoms are protonated and do not participate in the coordination of the Pd(1) atom.

All the acid protons in structures **I**–**III** form hydrogen bonds. In structure **I**, strong hydrogen bonds O(3)–H(3)···O(6) $(1 + x, y, z)$ and O(7)–H(7)···O(2) $(0.5 - x, y - 0.5, 1.5 - z)$ [O···O, 2.592(3) and 2.589(3) Å, respectively] link complexes into layers parallel to the *xy* plane. The water molecule forms weak hydrogen bonds O(1*w*)–H(1*w*1)···O(6) $(1 + x, y, z)$ and O(1*w*)–H(2*w*1)···O(5) $(0.5 - x, y - 0.5, 1.5 - z)$ [O···O, 2.918(5) and 3.169(5) Å, respectively] inside the layer.

In structure **II**, the O(7)–H(7)···O(4) $(0.5 + x, 0.5 - y, 0.5 + z)$ hydrogen bond [O···O, 2.719(5) Å] links the [Pd(H$_3$*Edtp*)Cl] complexes into chains. Two other acid protons are bound to water molecules: O(3)–H(3)···O(1*w*) $(0.5 - x, 0.5 + y, 0.5 - z)$ [O···O, 2.538(4) Å] and O(5)–H(5)···O(2*w*) $(0.5 - x, 0.5 + y, 0.5 - z)$ [O···O, 2.553(4) Å]. In turn, the water molecules donate protons in the hydrogen bonds with the oxygen atoms of the ligands: O(1*w*)–H(1*w*1)···O(2) $(0.5 + x, 0.5 - y, 0.5 + z)$, O(1*w*)–H(2*w*1)···O(6) (x, y, z), O(2*w*)–H(1*w*2)···O(1) $(1 + x, y, z)$, and O(2*w*)–H(2*w*2)···O(2) $(1 - x, -y, -z)$ [O···O, 2.722(4), 2.800(4), 2.926(4), and 2.771(4) Å, respectively]. Water molecules link the complexes into a three-dimensional framework.

In structure **III**, the H$_6$*Edtp*$^{2+}$ cations and the [PdCl$_4$]$^{2-}$ anions are separately packed into layers parallel to the *xz* plane. Inside both layers, chains are distinguished. The cations are interlinked by hydrogen bonds O(2)–H(2)···O(3) $(3 - x, 1 - y, -z)$ [O···O, 2.697(2) Å], and the anions are bound through the *w*(2) water molecules, which form hydrogen bonds with the Cl(1) $(1 - x, -y, 1 - z)$ and Cl(2) $(1 + x, y, z)$ atoms [O···Cl, 3.285(3) and 3.355(3) Å, respectively]. The second water molecule is attached to the cation by the O(4)–H(4)···O(1*w*) $(1 - x, 1 - y, 1 - z)$ hydrogen bond [O···O, 2.589(4) Å]. The H(2*w*1) atom forms a bifurcated bond with the Cl(1) (x, y, z) and O(2) $(2 - x, -y, 1 - z)$ atoms [O···Cl, 3.321(3) Å; O···O, 2.946(3) Å], and the H(1*w*1) atom probably forms a weak hydrogen bond with the O(1*w*) $(1 - x, -y, 2 - z)$ atom [O···O, 3.008(5) Å]. Thus, the *w*(1) water molecule links two neighboring cationic layers and the anionic layer situated between them. In addition, intramolecular N(1)–H(1)···O(1) hydrogen bonds [N···O, 2.878(2) Å] are formed in the H$_6$*Edtp*$^{2+}$ cation.

REFERENCES

1. D. J. Robinson and C. H. L. Kennard, J. Chem. Soc. A **1008** (1970).

2. X.-M. Luo, X.-H. Chen, S. Sh. S. Rai, *et al.*, Acta Crystallogr., Sect. C: Cryst. Struct. Commun. **55**, 1220 (1999).

3. A. L. Poznyak, A. B. Ilyukhin, and V. S. Sergienko, Zh. Neorg. Khim. **42** (10), 1660 (1997).

4. E. N. Duesler, R. E. Tapscott, M. Garcia-Basallote, and F. Gonzales-Vilches, Acta Crystallogr., Sect. C: Cryst. Struct. Commun. **41**, 678 (1985).

5. N. A. Ezerskaya, T. P. Solovykh, and L. K. Shubochkin, Koord. Khim. **6** (7), 1064 (1980).

6. G. M. Sheldrick, Acta Crystallogr., Sect. A: Found. Crystallogr. **46**, 467 (1990).

7. G. M. Sheldrick, *SHELXL97. Program for the Refinement of Crystal Structures* (Univ. of Göttingen, Germany, 1997).

Translated by I. Polyakova

STRUCTURE
OF ORGANIC COMPOUNDS

Molecular and Crystal Structures of Decamethylruthenocene (η^5-C$_5$*Me$_5$*)$_2$Ru in the Temperature Range 153–300 K: Thermal Motion in a Crystal According to X-ray Diffraction Data

I. E. Zanin* and M. Yu. Antipin**

* Voronezh State University, Universitetskaya pl. 1, Voronezh, 394006 Russia
e-mail: zie@main.ru
** Nesmeyanov Institute of Organoelement Compounds, Russian Academy of Sciences,
ul. Vavilova 28, Moscow, 119991 Russia
Received January 15, 2002; in final form, May 7, 2002

Abstract—The crystal structure of decamethylruthenocene (η^5-C$_5$*Me$_5$*)$_2$Ru (**I**) is investigated by X-ray diffraction. It is demonstrated that the compound studied crystallizes in two polymorphic modifications, namely, modification **Ia** with space group $P2_1/m$ ($Z = 2$) in the temperature range 153–300 K and modification **Ib** with space group $P2_1/n$ ($Z = 4$) at 203 K. No temperature phase transition between the modifications is found. In crystal **Ia**, the molecule occupies a special position in the mirror plane. In crystal **Ib**, the molecule is located in the general position. The cyclic ligands η^5-C$_5$*Me$_5$*, (Cp*) are aligned parallel to each other and adopt an eclipsed conformation. The bond lengths in compounds **Ia** and **Ib** are identical. Analysis of the anisotropic displacement parameters of the atoms indicates that molecules **Ia** and **Ib** are not structurally rigid and that the Cp* rings involved in these molecules can execute independent librations. In the temperature range 153–300 K, the Cp*(1) ligand in molecule **Ia** is statically disordered over two positions. The barrier heights B_5 for rotation of the Cp* ligands are estimated both from the root-mean-square amplitudes of librations $\langle\varphi^2\rangle$ and with the use of the atom–atom potential method. © 2003 MAIK "Nauka/Interperiodica".

INTRODUCTION

Decamethylruthenocene (η^5-C$_5$*Me$_5$*)$_2$Ru (**I**) belongs to the series of substituted metallocenes $Cp_2^* M$, where Cp* is the pentamethylcyclopentadienyl ligand and M is a 3d, 4d, or 5d transition metal. Earlier investigations revealed that, in metallocene crystals, ligands can execute torsional vibrations about the "metal–ring center" axis [1–4]. Moreover, these compounds are characterized by a wide variety of crystalline phases (modifications). In particular, reversible phase transitions occur in nickelocene, ferrocene, decamethylosmocene, and acetylruthenocene [5–8]. It should also be noted that ligands in metallocene compounds can be disordered in different ways [9]. The disordering can exhibit a dynamic [1–4] or static nature [5, 6]. The data available in the literature on the nature of mechanisms of disordering and phase transitions in molecular crystals are very scarce. With the aim of obtaining additional information on the structure and properties of molecular crystals, we continued our systematic X-ray diffraction investigations into the intramolecular motion in crystals of metallocene derivatives. In this work, we performed X-ray structure analysis of decamethylruthenocene (η^5-C$_5$*Me$_5$*)$_2$Ru and examined the intramolecular thermal motion in this crystal as a function of the temperature.

EXPERIMENTAL

Single crystals **I** were grown by slow evaporation of a solvent from a solution in acetone. The X-ray diffraction experiments were performed using two approximately isometric, prismatic crystals (~0.3 × 0.3 × 0.4 mm in size). The X-ray diffraction data were collected on a Siemens P3/PC four-circle automated diffractometer (λMoK_α, graphite monochromator, $\theta/2\theta$ scan mode, $\theta \le 30°$) equipped with an LT-2 low-temperature attachment. X-ray diffraction investigations revealed that compound **I** crystallizes in two polymorphic modifications. Modification **Ia** crystallizes in the space group $P2_1/m$, $Z = 2$ (the molecule occupies a special position in the mirror plane). For a single crystal of this modification, the diffraction data were obtained at temperatures of 153, 203, 223, 263, and 300 K. The second modification (**Ib**), which was separated from the same solvent together with crystals **Ia**, is described by the space group $P2_1/n$, $Z = 4$ at 203 K. We failed to examined the crystal of modification **Ib** at other temperatures.

Crystals **I** are monoclinic. The unit cell parameters of crystal **Ia** at temperatures of 153 and 300 K are as follows: $a = 7.625(2)$ and $7.735(2)$ Å, $b = 14.536(3)$ and $14.664(3)$ Å, $c = 8.547(2)$ and $8.628(2)$ Å, $\beta = 106.93(3)°$ and $106.51(3)°$, and $V = 906.2(4)$ and
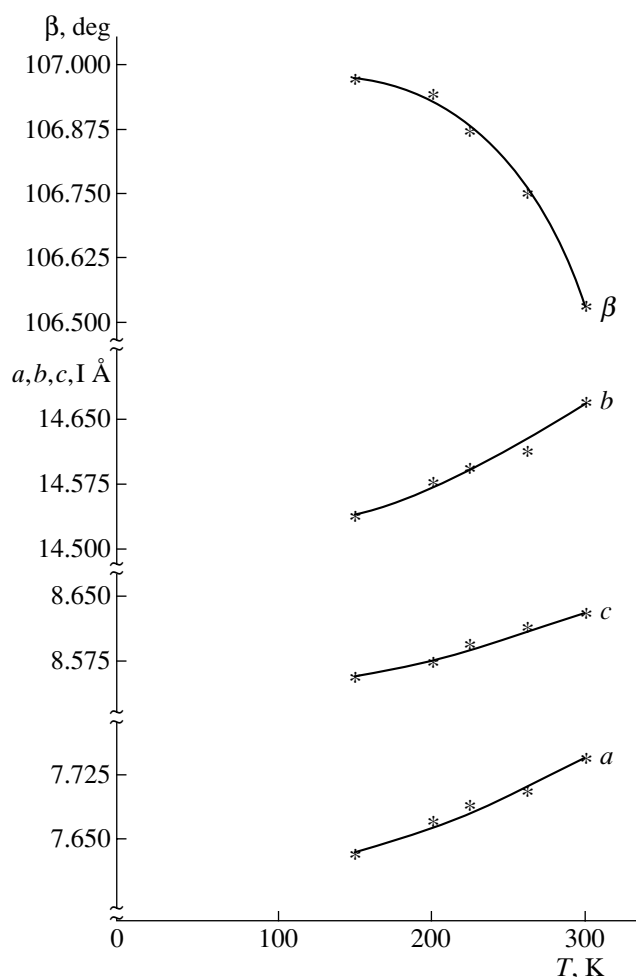
Fig. 1. Temperature dependences of the unit cell parameters for crystal **Ia**.

938.3(4) $Å^3$, respectively. The temperature dependences of the unit cell parameters exhibit a nearly linear behavior (Fig. 1).

The unit cell parameters of crystal **Ib** at 203 K are as follows: $a = 7.676(2)$ Å, $b = 14.576(3)$ Å, $c = 16.630(3)$ Å, $\beta = 99.26(3)°$, and $V = 1836.3(7)$ $Å^3$.

It is interesting to note that, as was shown in our previous work [7], the decamethylosmocene crystal

$(\eta^5\text{-}C_5Me_5)_2Os$ (**II**) undergoes an order–disorder reversible structural phase transition $(P2_1/m \longrightarrow P2_1/n)$ with a decrease in the temperature in the range from 213 to 183 K; however, the sample remains in the single-crystal state. Crystals **II** are isostructural to crystals **Ib** in the temperature range 153–183 K [for **II** at 153 K, space group $P2_1/n$, $Z = 4$, $a = 7.669(2)$ Å, $b = 14.546(3)$ Å, $c = 16.607(3)$ Å, $\beta = 99.16(3)°$, and $V = 1828.9(7)$ $Å^3$] and to crystals **Ia** in the range 213–293 K [for **II** at 293 K, space group $P2_1/m$, $Z = 2$, $a = 7.757(1)$ Å, $b = 14.654(2)$ Å, $c = 8.636(1)$ Å, $\beta = 106.47(2)°$, and $V = 941.3(3)$ $Å^3$].

Therefore, both decamethylruthenocene (**Ia** and **Ib**) and decamethylosmocene (**IIa** and **IIb**) have two polymorphic modifications. However, no phase transition between these modifications is found in the case of decamethylruthenocene (**Ia** and **Ib**).

Structures **Ia** and **Ib** were solved by the heavy-atom method and refined by the least-squares procedure in the anisotropic (isotropic for H atoms) full-matrix approximation. The hydrogen atoms were located from the difference Fourier synthesis. Details of data collection and refinement parameters are summarized in Table 1. The coordinates and anisotropic thermal parameters for the non-hydrogen atoms in structure **Ia** at temperatures of 153 and 300 K and in structure **Ib** at 203 K are presented in Tables 2 and 3, respectively. All the calculations were performed according to the SHELXTL PLUS 4.2 PC software package [10].

Structure **Ia** at room temperature was solved earlier by Albers *et al.* [11]. However, the molecular structure was not analyzed in detail. In [11], the authors only noted that anomalously large anisotropic thermal parameters of the carbon atoms in the methyl groups (up to $U = 0.275$ $Å^2$) can indicate their disordering.

In some cases, the particular (static or dynamic) nature of disordering can be judged from multitemperature X-ray diffraction investigations [12]. For the static disordering, the cooling of a crystal to certain temperatures should not result in a regular decrease in the thermal parameters of the atoms, because these parameters reflect only the presence of molecules with different orientations in the crystal. At the same time, since the dynamic disordering is associated with large-

Table 1. Data collection and refinement parameters for structure **Ia** in the temperature range 153–300 K and structure **Ib** at 203 K

Modification	Ia					Ib
T, K	153	203	223	263	300	203
Number of observed reflections	1801	1863	2997	3563	2395	3332
Number of reflections with $F > 8\sigma(F)$	1479	1471	2411	2743	1818	2814
R, %	2.21	2.01	1.97	2.11	2.35	2.11
Rw, %	3.02	2.70	2.81	2.87	3.02	2.40
$GOOF$	1.07	0.83	0.80	0.76	0.78	0.96

Table 2. Coordinates ($\times 10^4$) and anisotropic thermal parameters ($\text{Å}^2 \times 10^2$) as components of the tensor $T = -2\pi^2(h^2 a^{*2} U_{11} + \ldots + 2hka^*b^*U_{12})$ for non-hydrogen atoms in crystal **Ia** at temperatures of 300 K (first row) and 203 K (second row)

Atom	x	y	z	U_{11}	U_{22}	U_{33}	U_{23}	U_{13}	U_{12}
Ru	797(1)	1/4	2921(1)	36(1)	45(1)	34(1)	0	10(1)	0
	800(1)	1/4	2963(1)	25(1)	15(1)	46(1)	15(1)	7(1)	6(1)
C(1)	−1657(5)	1/4	939(5)	35(2)	164(6)	41(2)	0	4(1)	0
	−1705(8)	1/4	930(8)	85(4)	11(2)	226(2)	20(3)	0	6(2)
C(2)	−1647(4)	1702(3)	1912(4)	45(1)	95(2)	66(2)	−7(1)	−16(1)	−29(2)
	−1678(5)	1700(5)	1921(6)	70(2)	19(2)	154(6)	40(2)	−30(3)	16(2)
C(3)	−1628(3)	2013(2)	3476(3)	41(1)	62(1)	55(1)	−8(1)	18(1)	−5(1)
	−1640(5)	2014(3)	3525(4)	34(1)	17(1)	54(2)	32(2)	−10(1)	10(1)
C(4)	3241(6)	1/4	2139(6)	32(2)	17(2)	55(4)	26(2)	7(9)	11(2)
	3231(5)	1/4	2120(5)	39(2)	114(4)	45(2)	0	15(1)	0
C(5)	3230(4)	1710(2)	3095(4)	45(1)	62(2)	61(1)	7(1)	11(1)	−15(1)
	3258(4)	1709(3)	3112(4)	30(1)	19(1)	40(2)	32(2)	−5(1)	10(1)
C(6)	3251(3)	2016(2)	4664(3)	42(1)	43(1)	50(1)	3(1)	6(1)	1(1)
	3294(4)	2006(2)	4719(4)	22(1)	18(1)	23(2)	26(2)	−1(1)	7(1)
C(7)	−1788(12)	1/4	−832(9)	68(4)	261(28)	40(3)	0	4(3)	0
	−1854(11)	1/4	−837(9)	149(11)	26(4)	200(9)	19(3)	35(40)	6(3)
C(8)	−1749(9)	721(6)	1398(12)	91(3)	139(6)	162(6)	−53(4)	55(4)	−98(5)
	−1779(9)	719(7)	1388(10)	119(4)	62(3)	188(9)	131(6)	−81(5)	66(4)
C(9)	−1696(6)	1434(3)	4894(6)	72(2)	83(2)	88(2)	−15(2)	37(2)	15(2)
	−1683(6)	1418(3)	4950(6)	42(1)	40(2)	37(2)	59(2)	−12(2)	31(2)
C(10)	3305(9)	1/4	411(7)	66(3)	243(11)	50(3)	0	29(2)	0
	3286(8)	1/4	397(7)	56(3)	30(3)	119(8)	25(3)	−1(15)	18(2)
C(11)	3316(8)	729(4)	2616(9)	84(3)	87(3)	131(4)	18(2)	17(3)	−54(3)
	3352(7)	723(3)	2611(7)	57(2)	56(3)	47(2)	78(3)	−13(2)	36(2)
C(12)	3363(6)	1425(3)	6108(5)	76(2)	68(2)	72(2)	4(2)	6(2)	26(2)
	3410(5)	1409(2)	6169(5)	37(1)	40(2)	29(2)	42(2)	3(1)	13(2)

amplitude low-frequency molecular motions, which are readily frozen, we can expect a sharp decrease in the thermal parameters with a decrease in the temperature.

An examination of crystals **Ia** at different temperature revealed that this modification exhibits a complex character of disordering. Analysis of the thermal ellipsoids at the 50% probability level for the carbon atoms in the Cp^* ligands at temperatures of 153 and 300 K (Fig. 2) demonstrated that, most probably, the $Cp^*(1)$ ligand [with the C(1), C(2), C(3), C(7), C(8), and C(9) independent atoms] undergoes a substantially static disordering. Actually, the major axes of the ellipsoids for almost all the carbon atoms remain virtually unchanged as the temperature decreases by a factor of two. This suggests the occurrence of two possible orientations of the $Cp^*(1)$ ligand. In this case, the C(1) and C(7) atoms lying in the mirror plane are disordered to the greatest extent. In contrast, the change in the thermal ellipsoids of atoms of the second ligand $Cp^*(2)$ [the C(4), C(5), C(6), C(10), C(11), and C(12) independent atoms] with variations in the temperature indicates usual (dynamic) torsional vibrations.

In order to resolve two possible orientations of the $Cp^*(1)$ ring, structure **Ia** was solved and refined in the space group $P2_1$. The least-squares refinement in the anisotropic (isotropic for the H atoms) full-matrix approximation led to discrepancy factors $R = 0.019–0.030$ (at different temperatures). It was established that only the C(1) atom in the $Cp^*(1)$ ring is disordered over two equally occupied positions separated by a distance of 0.5 Å and that the character of disordering does not depend on the temperature. Note that the positions of the other carbon atoms [including the C(7) methyl atom] remain unresolved. However, as a whole, the data obtained can be interpreted as follows. In the crystal, the $Cp^*(1)$ ligand has two orientations that are rotated through an angle of 10° with respect to each other and an angle of 5° with respect to the $Cp^*(2)$ ligand. Certainly, these disordered positions of the carbon atoms

Table 3. Coordinates ($\times 10^4$) and anisotropic thermal parameters ($\text{Å}^2 \times 10^2$) as components of the tensor $T = -2\pi^2(h^2a^{*2}U_{11} + \ldots + 2hka^*b^*U_{12})$ for non-hydrogen atoms in crystal **Ib** at a temperature of 203 K

Atom	x	y	z	U_{11}	U_{22}	U_{33}	U_{23}	U_{13}	U_{12}
Ru	683(1)	2414(1)	1479(1)	21(1)	23(1)	21(1)	1(1)	3(1)	1(1)
C(1)	3399(3)	2908(2)	1724(1)	23(1)	39(1)	37(1)	−3(1)	7(1)	0(1)
C(2)	3396(3)	1929(1)	1791(1)	23(1)	36(1)	33(1)	4(1)	4(1)	−4(1)
C(3)	2630(3)	1559(2)	1014(2)	25(1)	47(1)	35(1)	8(1)	5(1)	11(1)
C(4)	2161(3)	2315(2)	471(1)	25(1)	69(2)	28(1)	3(1)	8(1)	0(1)
C(5)	2639(3)	3147(2)	911(2)	29(1)	52(1)	40(1)	0(1)	11(1)	14(1)
C(6)	−910(3)	2971(1)	2336(1)	29(1)	23(1)	35(1)	1(1)	11(1)	−1(1)
C(7)	−934(3)	1988(1)	2379(1)	29(1)	24(1)	30(1)	−2(1)	9(1)	0(1)
C(8)	−1711(3)	1650(1)	1595(1)	27(1)	34(1)	34(1)	−7(1)	8(1)	−7(1)
C(9)	−2162(3)	2416(2)	1069(1)	22(1)	51(1)	30(1)	2(1)	4(1)	1(1)
C(10)	−1662(3)	3232(2)	1528(2)	26(1)	33(1)	42(1)	6(1)	10(1)	8(1)
C(11)	4166(4)	3553(2)	2392(2)	36(1)	45(1)	56(2)	−12(1)	5(1)	−12(1)
C(12)	4148(4)	1391(2)	2532(2)	33(1)	47(1)	42(1)	12(1)	−4(1)	4(1)
C(13)	2445(4)	563(2)	800(2)	46(2)	57(2)	63(2)	13(1)	−1(1)	−33(1)
C(14)	1397(5)	2237(4)	−412(2)	45(2)	127(3)	28(1)	7(2)	7(1)	0(2)
C(15)	2479(5)	4094(3)	558(3)	54(2)	67(2)	82(3)	−5(2)	18(2)	42(2)
C(16)	−266(4)	3604(2)	3033(2)	52(2)	33(1)	48(2)	−5(1)	17(1)	−15(1)
C(17)	−352(4)	1425(2)	3123(2)	50(2)	39(1)	37(1)	1(1)	13(1)	10(1)
C(18)	−2077(4)	661(2)	1382(2)	56(2)	41(1)	62(2)	−19(1)	17(1)	−19(1)
C(19)	−3095(4)	2377(3)	209(2)	31(1)	107(3)	37(1)	0(2)	−5(1)	1(2)
C(20)	−1980(5)	4200(2)	1229(3)	58(2)	46(2)	77(2)	24(1)	23(2)	29(1)

cannot be resolved when the structure is refined in the space group $P2_1/m$.

The distance between two unresolved positions of the C(1) atom was determined to be 0.45 Å from the relationship $B_{iso} = 1/3 \times 8\pi^2(\Delta x/2)^2 = 6.58(\Delta x)^2$ Å. This distance only slightly depends on the temperature in view of the static disordering of the $Cp^*(1)$ ligand. Therefore, in crystal **Ia**, the mirror plane m can occur only statistically and the $\text{Ru}(Cp^*)_2$ molecules actually adopt a conformation that differs from an ideal eclipsed conformation by the rotation of one ligand through an angle of 5°. It should be noted that the $Cp^*(1)$ ligand is disordered over the entire temperature range under consideration. No similar disordering is observed in the $Cp^*(2)$ ligand. This suggests that the $Cp^*(1)$ ligand undergoes a substantially static disordering, whereas the $Cp^*(2)$ ligand exhibits a typical dynamic temperature behavior.

In structure **Ia**, the bond lengths obtained in the refinement in the space group $P2_1$ are close to those determined in the space group $P2_1/m$. However, the

errors in calculating the former bond lengths are larger (up to 0.02 Å) due to the high correlation between the parameters in the least-squares refinement of the structure. For this reason, further analysis of the molecular geometry will be performed using the results refined in the space group $P2_1/m$.

The anisotropic thermal parameters derived in the least-squares refinement of structure **Ib** are characteristic of ordered structures.

MOLECULAR GEOMETRY

The general view of molecules **I** is given in Fig. 3. The bond lengths in molecule **Ia** are listed in Table 4.

In crystal **Ia**, the molecule lies in the mirror plane passing through the Ru, C(1), C(4), C(7), and C(10) atoms. The crystallographically independent ligands Cp^* adopt an eclipsed conformation. The molecule has a proper symmetry similar to D_{5h}. In crystal **Ib**, the molecule occupies the general position and the Cp^* ligands also exhibit an eclipsed conformation [the deviation

$T = 153$ K $T = 300$ K
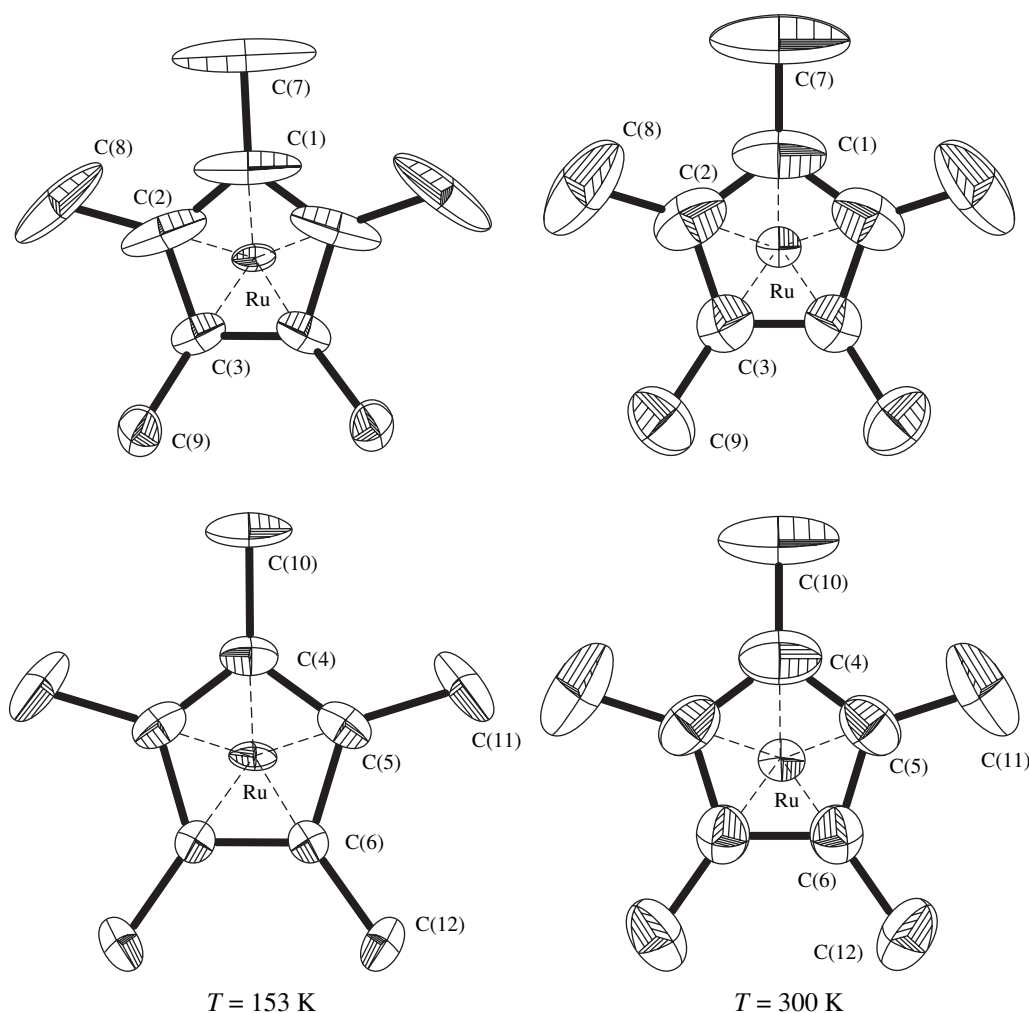
Fig. 2. Structures of the *Cp** ligands in molecule **Ia** (space group $P2_1/m$) at temperatures of 153 and 300 K. The atoms are represented as thermal ellipsoids at the 50% probability level.

from an ideal eclipsed conformation is equal to 1.6(1)°]. In both modifications, the cyclopentadienyl rings are nearly regular pentagons: the difference between the bond angles and their ideal value (108°) does not exceed 0.5° for **Ia** and 0.2° for **Ib**, and the deviations of the C atoms from the root-mean-square planes of the rings fall in the range 0.0001–0.0021 Å [the mean value is 0.0008(2) Å for **Ia** and 0.005 Å for **Ib**, irrespective of the temperature]. The rings are aligned parallel to each other: the angle between the normals to the root-mean-square planes of the rings is no greater than 0.2°. The carbon atoms of the methyl groups deviate from the planes of the *Cp** rings by 0.064–0.072 Å [on average, by 0.067(3) Å] toward the side opposite to the Ru atom for both molecules **Ia** and **Ib**, irrespective of the temperature. The mean deviations of the carbon atoms of the *Me* groups in crystals of pentamethylruthenocene (**III**) [1] and decamethylosmocene (**II**) [7], also regardless of the temperature and the space group, are equal to 0.073(6) and 0.08(3) Å, respectively.

It should be noted that the bond lengths in molecules of both modifications at the same temperature (203 K) coincide with each other: Ru–C, 2.167–2.182 Å [on average, 2.178(3) Å] and 2.171–2.183 Å [on average, 2.179(3) Å]; C–C(*Cp*), 1.420–1.436 Å [on average, 1.429(6) Å] and 1.426–1.435 Å [on average, 1.431(3) Å]; and C–C(*Me*), 1.491–1.506 Å [on average, 1.499(5) Å] and 1.494–1.503 Å [on average, 1.498(4) Å] for **Ia** and **Ib**, respectively. In molecule **Ia** (unlike the metallocene derivatives studied earlier in [1–4, 7, 8]), a change in the temperature from 153 to 300 K does not lead to a variation in the bond lengths. These bond lengths are as follows: Ru–C, 2.171–2.176 Å [on average, 2.173(3) Å] and 2.164–2.183 Å [on average, 2.179(3) Å]; C–C(*Cp*), 1.416–1.437 Å [on average, 1.428(9) Å] and 1.420–1.439 Å [on average, 1.429(7) Å]; and C–C(*Me*), 1.481–1.503 Å [on average, 1.495(7) Å] and 1.492–1.504 Å [on average, 1.501(4) Å] at temperatures of 153 and 300 K, respectively. In structure **Ia**, the sole geometric parameter, which depends on the temperature, is the distance

Ia   **Ib**
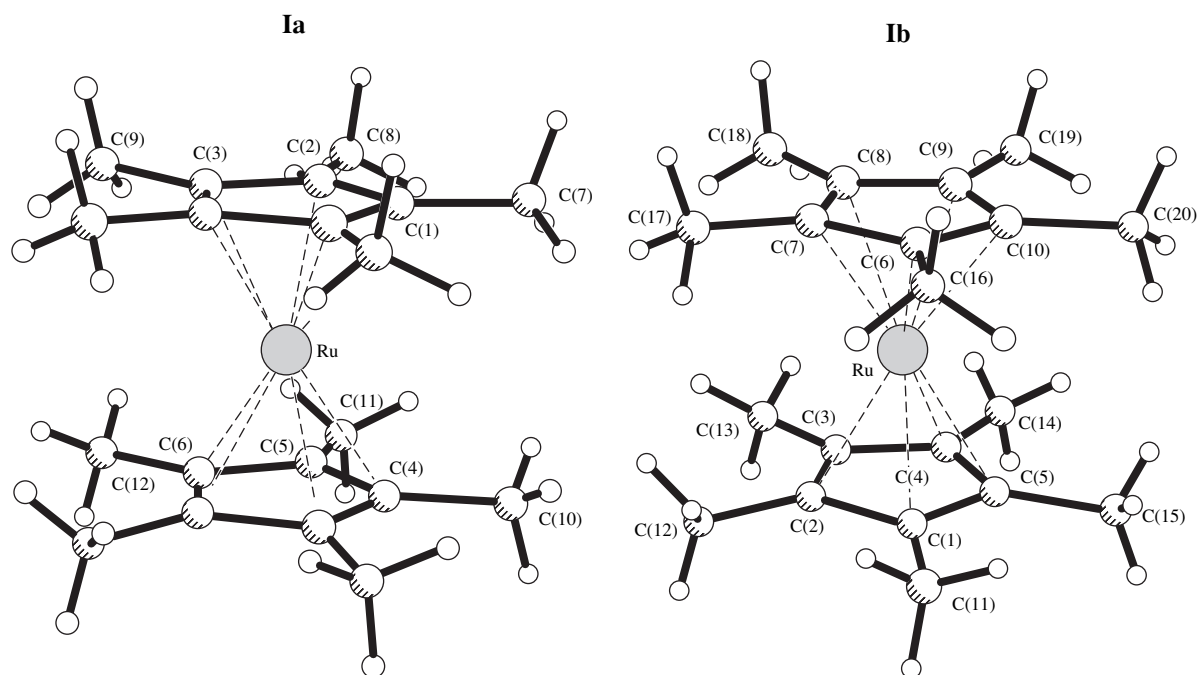
Fig. 3. A general view of molecules **I** with the atomic numbering.

between the centroids of the *Cp** ligands. This distance increases from 3.602(5) to 3.620(6) Å with an increase in the temperature from 153 to 300 K. At a temperature of 203 K, the distance between the centroids in structure **Ib** is equal to 3.615(5) Å. The inclusion of atomic thermal

motion in the framework of the TLS model [13, 14] results in an increase in the bond lengths by 0.005–0.01 Å.

The bond lengths obtained for molecules **I** are close to those determined for molecules **II** and **III**. In the

Table 4. Bond lengths (Å) in molecule **Ia** at temperatures of 153 K (first row) and 300 K (second row) with correction (*d*') and without correction (*d*) for thermal motion

Bond	d	d'	Bond	d	d'
Ru–C(1)	2.175(5)	2.181	C(4)–C(5)	1.416(5)	1.425
	2.164(4)	2.178		1.431(4)	1.440
Ru–C(2)	2.176(5)	2.182	C(5)–C(8)	1.432(5)	1.440
	2.183(3)	2.187		1.422(4)	1.435
Ru–C(3)	2.171(4)	2.177	C(1)–C(7)	1.481(9)	1.409
	2.183(3)	2.186		1.502(9)	1.516
Ru–C(4)	2.173(6)	2.177	C(2)–C(8)	1.492(10)	1.503
	2.182(5)	2.187		1.502(10)	1.517
Ru–C(5)	2.171(4)	2.179	C(3)–C(9)	1.502(6)	1.511
	2.178(3)	2.185		1.503(6)	1.517
Ru–C(6)	2.173(3)	2.180	C(4)–C(10)	1.499(8)	1.507
	2.179(2)	2.187		1.492(8)	1.505
C(1)–C(2)	1.435(8)	1.440	C(5)–C(11)	1.503(6)	1.514
	1.439(5)	1.443		1.504(7)	1.517
C(2)–C(3)	1.437(7)	1.441	C(6)–C(12)	1.494(5)	1.504
	1.420(5)	1.433		1.500(5)	1.514

L_{ij}, deg^2
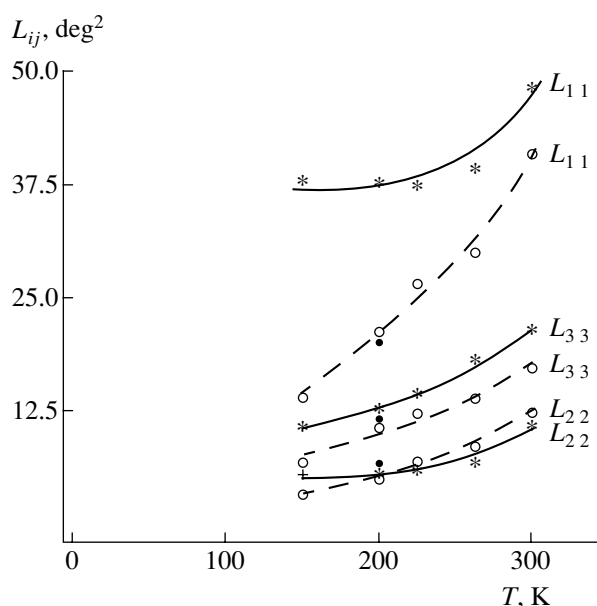
Fig. 4. Temperature dependences of the diagonal components of the libration tensor L_{ij}. The results obtained in the structure refinement in the space groups $P2_1/m$ and $P2_1$ are shown by the solid and dashed lines, respectively.

$\langle\varphi^2\rangle$, deg^2
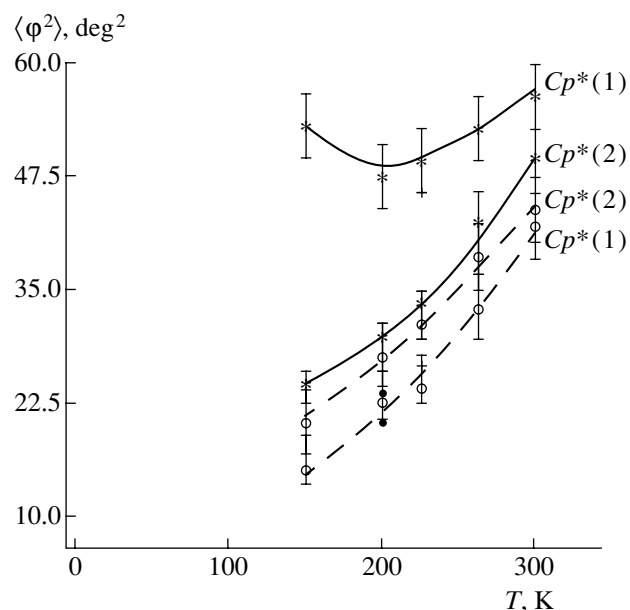
Fig. 5. Temperature dependences of the root-mean-square libration amplitudes for the Cp^* ligands. The results obtained in the structure refinement in the space groups $P2_1/m$ and $P2_1$ are shown by the solid and dashed lines, respectively.

crystal, each molecule **Ia** or **Ib** is in contact with 12 adjacent molecules and the packing is characterized by the presence of a number of H···H intermolecular contacts.

ANALYSIS OF THE THERMAL MOTION

The refined coordinates and anisotropic thermal parameters for atoms in structures **Ia** and **Ib** (at each temperature) were used to calculate the root-mean-square amplitudes of librations and the barrier heights

for rotation of the Cp^* ligands in terms of the TLS rigid-body model [13, 14] and the Dunitz–White one-parameter model [15]. The calculations were carried out according to the THMA-11 program package [16], in which both models were implemented. The data obtained are presented in Figs. 4 and 5 and in Table 5.

In crystal **Ia**, the molecule as a whole executes anisotropic librations. The maximum amplitude of librations is observed around the L_1 axis, which corresponds to the minimum moment of inertia and is actually aligned with the fivefold symmetry axis of the mol-

Table 5. Eigenvalues (first row) and eigenvectors (second row) of the tensors L and T for molecule **Ia** in the Cartesian coordinate system of the crystal

T, K	153	203	223	263	300
L_1	41.5	38.0	36.5	42.2	49.5
	0.944 0.0 −0.331	0.986 0.0 −0.167	0.999 0.0 −0.052	0.989 0.0 0.031	0.990 0.0 0.144
L_2	7.5	13.0	14.8	17.5	21.0
	−0.331 0.0 −0.944	−0.167 0.0 −0.986	−0.052 0.0 −0.999	0.052 0.0 −0.989	0.144 0.0 −0.990
L_3	5.8	5.9	6.7	7.4	10.3
	0.0 1.0 0.0	0.0 1.0 0.0	0.0 1.0 0.0	0.0 1.0 0.0	0.0 1.0 0.0
T_1	0.0601	0.0540	0.0497	0.0520	0.0580
	0.0 −1.0 0.0	0.0 −1.0 0.0	0.0 −1.0 0.0	0.0 −1.0 0.0	0.0 −1.0 0.0
T_2	0.0153	0.0199	0.0233	0.0281	0.0354
	−0.573 0.0 −0.819	−0.540 0.0 −0.842	0.793 0.0 0.610	0.814 0.0 0.415	0.996 0.0 0.089
T_3	0.0137	0.0190	0.0215	0.0273	0.0336
	0.819 0.0 −0.573	0.842 0.0 −0.540	−0.610 0.0 0.793	−0.415 0.0 0.814	−0.089 0.0 0.996

ecule (as for the previously studied metallocene derivatives). A distinguishing feature of the motion of molecule **Ia** is that the temperature dependence of the amplitude of librations about the L_1 axis differs from the quadratic dependence observed earlier in [1–4], whereas the dependences of the amplitude of librations around the L_2 and L_3 axes exhibit a quadratic behavior (see Fig. 4). This is possibly associated with the fact that the disordering of the molecule in our case manifests itself in the anomalously large anisotropic thermal parameters, which, in turn, result in large libration amplitudes. Moreover, the temperature dependence $L_{11} = f(T)$ permits us to make the inference that the disordering at low temperatures is predominantly static in nature, whereas the dynamic contribution appears in addition to the static disordering at temperatures above 223 K.

The root-mean-square amplitudes of librations of molecule **Ia** were also calculated from the structural data refined in the space group $P2_1$ [with the resolved positions of the disordered atom C(1)]. It is found that, in this case, the temperature dependence of the amplitude of librations about the L_1 axis turns out to be similar to the quadratic dependence (Fig. 4). At 300 K, the amplitude of librations about the L_1 axis is close to that calculated using the results of the refinement in the space group $P2_1/m$. This also confirms the inference regarding the predominantly dynamic nature of disordering at 300 K. Note that the root-mean-square amplitude of librations of molecule **Ia** in the crystal at 300 K is close to that of the Cp_2^*Os molecule (42 deg^2) [7] but is somewhat less than the root-mean-square amplitude of librations of the CpRuCp^* (71 deg^2). This supports the conclusion drawn in our previous works [1, 2] that the nearest nonbonded environment in the crystal has a decisive effect on the molecular motion in metallocene crystals. Indeed, the CpRuCp^* molecule in crystal **III** interacts with eight adjacent molecules, whereas the Cp_2^*Ru molecule in crystal **I** and the Cp_2^*Os molecule in crystal **II** interact with twelve adjacent molecules.

The translational motion in crystal **Ia** is also anisotropic. The maximum amplitude of translations is observed along the T_1 axis and remains nearly constant with a variation in the temperature. Most likely, this is also associated with the disordering of the molecule. The amplitudes of translational vibrations along the T_2 and T_3 axes are close to each other and increase by a factor of two as the temperature increases from 153 to 300 K.

Research into the intramolecular thermal motion in crystals of metallocene derivatives revealed that ligands can independently librate in molecules of these compounds [1–4]. In order to evaluate the possibility of these motions occurring in crystal **Ia**, the *L*, *T*, and *S* tensors were calculated separately for each Cp^* ring. With the aim of eliminating the singularity arising from

a regular structure of the ligands, the Ru atom was included in the calculations [14]. As a result, the experimental and calculated values of U_{ij} appeared to be in better agreement as compared to the TLS calculations for molecule **Ia** as a whole. Actually, we obtained the following characteristics of the TLS model: Ru = 0.02–0.06, $\langle\Delta U^2\rangle^{1/2} = 0.0005$–0.004 Å^2, and $\langle\sigma^2(u)\rangle^{1/2} = 0.0004$–0.003 Å^2 in the case of the separate calculations for each Cp^* ring and Ru = 0.04–0.09, $\langle\Delta U^2\rangle^{1/2} = 0.002$–0.006 Å^2, and $\langle\sigma^2(u)\rangle^{1/2} = 0.001$–0.004 Å^2 in the calculations for the molecule as a whole. Consequently, molecule **Ia** is not structurally rigid and their Cp^* ligands can execute independent librations. This is supported by the calculated root-mean-square amplitudes of librations of the rings (see Fig. 5).

An interesting feature of crystal **Ia** is that the root-mean-square amplitude of librations of the $Cp^*(1)$ ring remains nearly constant with a change in the temperature [53(6) and 57(6) deg^2 at 153 and 300 K, respectively], whereas the root-mean-square amplitude of librations of the $Cp^*(2)$ ring increases from 27(4) to 49(6) deg^2 with an increase in the temperature from 153 to 300 K. This behavior can be explained by the aforementioned static disordering of the $Cp^*(1)$ ligand. At the same time, this can be treated as if the quantitative corroboration of the static disordering of the $Cp^*(1)$ ring and the dynamic disordering of the $Cp^*(2)$ ring. The root-mean-square amplitudes of librations of each Cp^* ring were calculated from the data obtained by refining structure **Ia** in the space group $P2_1$ [with the resolved positions of the disordered atom C(1)]. According to these calculations, the dependences of $\langle\varphi^2\rangle$ on T exhibit a nearly quadratic behavior for both rings (Fig. 5) and can be described by the equations

$$\langle\varphi^2\rangle = 7.4 - 0.032T + 0.0005T^2, \qquad (1)$$

$$\langle\varphi^2\rangle = 10.8 - 0.216T - 0.0001T^2. \qquad (2)$$

Thus, in this case, it is as if we separate the contributions of the static and dynamic disordering to the anisotropic thermal parameters. Then, we take into account the static contribution and determine the amplitude of librations of the $Cp^*(1)$ ring in one of the orientations.

The motion of the $Cp^*(1)$ ring with respect to the $Cp^*(2)$ ring in the structure refined in the space group $P2_1/m$ was analyzed using the Dunitz–White one-parameter model [15]. At 153 K, the root-mean-square amplitude of librations of the $Cp^*(1)$ ring with respect to the $Cp^*(2)$ ring is equal to 16 deg^2 and the total amplitude of librations is 51 deg^2. At 300 K, the difference between the amplitudes of librations of the rings decreases to 5 deg^2 (which is close to the error in calculating $\langle\varphi^2\rangle$) and the total amplitude of librations of the $Cp^*(1)$ ring is equal to 55 deg^2. The calculated root-mean-square amplitudes $\langle\varphi^2\rangle$ of librations of the Cp^* ligands were used for estimating the barrier heights B_5 for rotation about the fivefold symmetry axis in crystal

Ia in the harmonic approximation [17, 18]. In the structure refined in the space group $P2_1/m$, the barriers heights B_5 estimated at 153 K differ significantly [8(1) kJ/mol for the $Cp^*(1)$ ring and 18(2) kJ/mol for the $Cp^*(2)$ ring]. By contrast, at 300 K, the barrier heights B_5 are almost identical [13(1) and 15(2) kJ/mol]. The low barrier height for rotation of the $Cp^*(1)$ ring at 153 K and the fact that the barrier height for this ligand does not decrease with an increase in the temperature (due to the thermal expansion of the crystal) are explained by ignoring the disordering. Indeed, the thermal parameters and the root-mean-square amplitudes of librations are anomalously large owing to unresolved positions of the C atoms.

For the space group $P2_1$, the estimated barrier heights for rotation of the Cp^* ligands are approximately identical (within the limits of computational error) for both ligands and decrease, on average, from 21(2) to 16(2) kJ/mol as the temperature increases from 153 to 300 K.

Similar calculations performed for crystal **Ib** demonstrated that the root-mean-square amplitudes of librations and the barrier heights for rotation of the Cp^* ligands at 203 K are the same for both ligands (on average, $\langle \varphi^2 \rangle = 22(3)$ deg^2 and $B_5 = 21(3)$ kJ/mol). These parameters are close to those calculated for the $Cp^*(2)$ ordered ligand in crystal **Ia** at this temperature.

The barrier heights obtained for rotation of the Cp^* ligands are close to the barrier height [28(2) kJ/mol] determined for compound **I** by Narankevich [19] from the NMR data and also to the barrier heights estimated for the Cp^* ligands in crystal **II** [25(6) and 21(4) kJ/mol at 153 and 293 K] with the use of a similar technique. The barrier heights B_5 for rotation of the Cp^* ligand in crystal **III** at 123 and 293 K are equal to 20(5) and 11(1) kJ/mol, respectively.

In a number of cases, valuable information on the nature of disordering can be obtained by calculating the energy of crystal packing with the use of the atom–atom potential method [20, 21]. On the basis of this method, the barrier heights for rotation of the Cp^* ligands in crystals **Ia** and **Ib** with due regard for relaxation of the nearest environment (in the range up to 5 Å) were calculated (from the dependence of the crystal lattice energy on the rotation angle for one of the ligands) according to the OPEC program package [20]. The atomic coordinates for structure **Ia** (space group $P2_1/m$) at 153 and 300 K and structure **Ib** at 203 K were used as the initial data.

As follows from the calculations, the potential energy of crystal **Ia** over the entire temperature range studied is characterized by two minima when the rotation angles for the $Cp^*(1)$ ring are equal to –6° and 6°, 66° and 78°, etc. (i.e., in 72-degree intervals). Thus, there are two ligand orientations rotated through an angle of ~6° from the mirror plane. This indicates the static character of disordering. The differences in the

energies upon transition between two minima at 153 and 300 K are equal to 1.0 and 0.7 kJ/mol, respectively. According to the calculations performed for the $Cp^*(2)$ ligand in crystal **Ia**, only one energy minimum is observed at $\varphi = 0°$, 72°, etc. This suggests the absence of static disordering. The alternation of the energy minima in 72-degree intervals implies that the eclipsed conformation of the ligands in structure **I** is energetically favorable, which agrees with the X-ray diffraction data.

The calculated barrier heights B_5 for rotation at 153 and 293 K are equal to 15(2) and 13(2) kJ/mol for the $Cp^*(1)$ ring and 25(2) and 23(2) kJ/mol for the $Cp^*(2)$ ring, respectively. Note that the largest contribution to the barrier height is made by the intermolecular interactions (the intramolecular interactions are virtually independent of the rotation angle of the ligands, and the energy of these interactions varies from 0.1 to 0.3 kJ/mol).

CONCLUSION

Thus, the results obtained in the above investigation demonstrated that compound **I** crystallizes in two polymorphic modifications. It was revealed that one Cp^* ligand in modification **Ia** (space group $P2_1/m$) is disordered. The barrier heights were estimated for rotation of the Cp^* ligands.

ACKNOWLEDGMENTS

REFERENCES

1. I. E. Zanin, M. Yu. Antipin, and Yu. T. Struchkov, Kristallografiya **36** (2), 420 (1991) [Sov. Phys. Crystallogr. **36**, 225 (1991)].

2. I. E. Zanin, M. Yu. Antipin, Yu. T. Struchkov, *et al.*, Metallorg. Khim. **5** (3), 579 (1992).

3. I. E. Zanin, M. Yu. Antipin, and Yu. T. Struchkov, in *Abstracts of XV Congress of the International Union of Crystallography* (Bordeaux, France, 1990), p. C-299.

4. I. E. Zanin, M. Yu. Antipin, and Yu. T. Struchkov, in *Abstracts of XIII European Crystallographic Meeting* (Trieste, 1991), p. 207.

5. P. Seiler and J. D. Dunitz, Acta Crystallogr., Sect. B: Struct. Crystallogr. Cryst. Chem. **36**, 1068 (1980).

6. P. Seiler and J. D. Dunitz, Acta Crystallogr., Sect. B: Struct. Crystallogr. Cryst. Chem. **38**, 1741 (1982).

7. I. I. Vorontsov, K. A. Potekhin, M. Yu. Antipin, and I. E. Zanin, Kristallografiya **45** (2), 266 (2000) [Crystallogr. Rep. **45**, 234 (2000)].

8. I. E. Zanin, Candidate's Dissertation in Physics and Mathematics (Nesmeyanov Inst. of Organoelement Compounds, Russ. Acad. Sci., Moscow, 1991).

9. M. Yu. Antipin and R. Boese, Acta Crystallogr., Sect. B: Struct. Sci. **52**, 314 (1996).

10. G. M. Sheldrick, *SHELXTL PLUS: Release 4.2* (Siemens Analytical Instruments, Madison, Wisconsin, USA, 1991).

11. M. O. Albers, D. C. Liles, D. S. Robinson, *et al.*, Organometallics, No. 5, 2321 (1986).

12. I. E. Zanin, M. Yu. Antipin, and Yu. T. Struchkov, in *Problems in Crystal Chemistry* (Nauka, Moscow, 1991), p. 56.

13. V. Shomaker and K. N. Trueblood, Acta Crystallogr., Sect. B: Struct. Crystallogr. Cryst. Chem. **24**, 63 (1968).

14. K. N. Trueblood, Acta Crystallogr., Sect. A: Cryst. Phys., Diffr., Theor. Gen. Crystallogr. **34**, 950 (1978).

15. J. D. Dunitz and D. White, Acta Crystallogr., Sect. A: Cryst. Phys., Diffr., Theor. Gen. Crystallogr. **29**, 93 (1973).

16. E. Maverick and K. N. Trueblood, *Program THMA-11*.

17. E. Maverick and J. D. Dunitz, Mol. Phys. **62** (2), 451 (1987).

18. J. D. Dunitz, V. Shomaker, and K. N. Trueblood, J. Phys. Chem. **92**, 856 (1988).

19. Z. Narankevich, Candidate's Dissertation in Chemistry (Nesmeyanov Inst. of Organoelement Compounds, Russ. Acad. Sci., Moscow, 1991).

20. A. Gavezzotti, J. Am. Chem. Soc. **105**, 5220 (1983).

21. A. J. Campbell, C. A. Fybe, D. Harold-Smith, and K. Jeffrey, Mol. Cryst. Liq. Cryst., No. 36, 1 (1984).

Translated by O. Borovik-Romanova

General Structural Features of Centric and Acentric Polymorphic Pairs of Organic Molecular Crystals: II. Polymorphic Pairs $P2_1/c$–$P2_1$, $P2_1/c$–Pc, and $P2_1/c$–$Pna2_1$

L. N. Kuleshova and M. Yu. Antipin

Nesmeyanov Institute of Organoelement Compounds, Russian Academy of Sciences,
ul. Vavilova 28, Moscow, 119991 Russia
e-mail: lukul@xrlab.ineos.ac.ru
Received February 13, 2002

Abstract—A systematic investigation into the general structural features of centric and acentric polymorphic pairs of organic molecular crystals is performed using the data available in the Cambridge Structural Database. The structural aspects of the $P2_1/c$–$P2_1$, $P2_1/c$–Pc, and $P2_1/c$–$Pna2_1$ polymorphic pairs are considered. The most important inferences made in this study are as follows: (i) the centric and acentric modifications rather frequently (~50% of all the cases) crystallize simultaneously under the same conditions (concomitant polymorphism); (ii) the unit cell parameters of these modifications are found to be either close in magnitude or multiples; (iii) in the centric and acentric modifications, identical or very similar types of chiral or acentric stable molecular associates are formed through hydrogen bonds or other specific intermolecular interactions; and (iv) the centric and acentric modifications more often than other compounds are characterized by polysystem unit cells (Z' > 1). © 2003 MAIK "Nauka/Interperiodica".

INTRODUCTION

Systematic investigations into the general structural features of centric and acentric polymorphic pairs of crystalline materials are of considerable importance in the understanding of the mechanisms of formation of the crystal structure. The results obtained in these studies provide a better insight into the mechanisms of crystallization processes and can be useful in solving many problems of crystal engineering, including important problems concerning the design of acentric crystalline modifications with nonlinear optical properties. In our previous work [1], we formulated the problem, described the procedure of choosing the objects of investigation, and examined the structural regularities of the $P2_1/c$–$P2_12_12_1$ polymorphic pair, which is most frequently encountered in centric and acentric modifications. The analysis was performed with due regard for the crystallization conditions, unit cell parameters, densities of crystals, types of associates formed by molecules, specific physical properties, and the occurrence of phase transitions. The present work continues our investigation into the general structural features of other commonly encountered polymorphic pairs of centric and acentric modifications, namely, the $P2_1/c$–$P2_1$, $P2_1/c$–Pc, and $P2_1/c$–$Pna2_1$ polymorphic pairs. Uncommon and rarely occurring pairs will be considered in a separate paper.

THE $P2_1/c$–$P2_1$ POLYMORPHIC PAIRS

The $P2_1/c$–$P2_1$ pair (17 compounds) is the second most frequently encountered polymorphic pair of centric and acentric modifications (Table 1). After rejecting the compounds with incomplete data, we obtained 13 pairs. The greater part of modifications (11 compounds) belong to the group of unresolved (or rapidly inverted) enantiomers. The $P2_1$ group is one of the most commonly encountered space groups in nonlinear optical crystals. Consequently, the chosen pairs involve both typical nonlinear optical materials (HAMNEO and FOVYOE) and compounds with a similar structure (BANGON, MOPBZA, MBZYAN, and ATCPEN). The unit cell parameters for polymorphs of this pair rather frequently (eight out of thirteen cases) are multiples. More exactly, two unit cell parameters are close to each other, whereas the third parameter (in the centric modification) is doubled. This becomes clear because the space group $P2_1$ is the subgroup of the centrosymmetric space group $P2_1/c$ and the volume of the relevant unit cell is smaller by a factor of two. In the group of resolved enantiomers (represented by two compounds, namely, LAVMOK and HPTHEL), the unit cell parameters of the modifications are different and the modifications themselves are concomitant.[1] In the group of unresolved enantiomers, only the ATCPEN and ZEBFAB concomitant modifications and the FOVYOE modifications obtained under different conditions are

---

[1] The modifications prepared simultaneously under the same conditions are referred to as concomitant modifications.
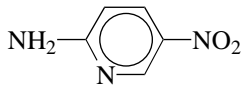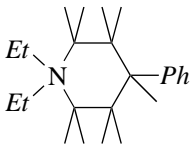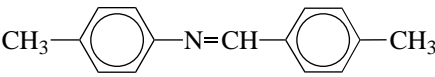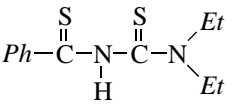
Table 1. Polymorphic pairs $P2_1/c$–$P2_1$
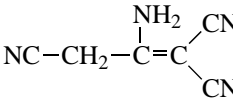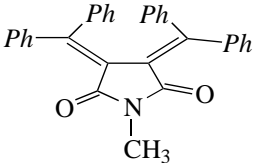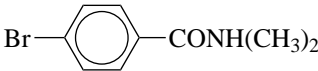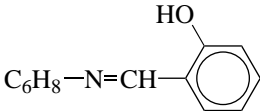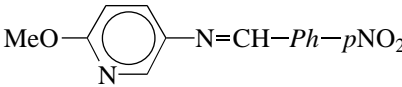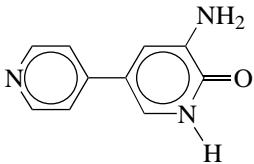
Compound	REFCODE (Δd)	Space group	Z'	V, Å³	d, g/cm³	Unit cell parameters	Packing fragments	Molecular geometry	Solvent	Comments
						Concomitant modifications of unresolved enantiomers				
NH_2–⟨ring, Br, NO_2, N⟩	HAMNEO	$P2_1/a$	1	778.2	1.877	Multiple	Similar	Similar	Both from the water–acetone mixture	$a = a$, $b = b$, $c = 2c$
	(−0.099)	$P2$	1	387.3	1.886					Nonlinear optical activity
NH_3^-–CH_2—COO^-	CLYCIN	$P2_1/n$	1	309.7	1.609	Multiple	Similar	Similar	Both by cooling the saturated aqueous solution	$a = a$, $b = 2b$, $c = c$
	(0.025)	$P2_1$	1	157.4	1.584					Similar systems of hydrogen bonds
⟨piperidine ring, Cl, Et, Et, N, Ph⟩	EMPIPP	$P2_1/c$	1	1547.1	1.304	Multiple	Similar	Similar	Both from an aqueous solution	$a = a$, $b = b$, $c = 2c$
	(0.048)	$P2_1$	1	802.7	1.256					
CH_3–⟨ring⟩–$N=CH$–⟨ring⟩–CH_3	MBZYAN	$P2_1/c$	1	1230.1	1.130	Multiple	Identical	Similar	Both from the ethanol solution	$a = a$, $b = b$, $c = 2c$
	(−0.017)	$P2_1$	1	605.9	1.147					
Ph–$\overset{S}{\overset{\|}{C}}$–$\overset{H}{N}$–$\overset{S}{\overset{\|}{C}}$–$N\overset{Et}{\underset{Et}{}}$	FAJTIT	$P2_1/n$	1	1344.9	1.246	Multiple	Similar	Similar	Both from the 2-propanol solution	$a = a$, $b = 2b$, $c = 2c$
	(0.030)	$P2_1$	2	1378.0	1.216					Dimers with different symmetries
NC–CH_2–$\overset{NH_2}{C}$=$C\overset{CN}{\underset{CN}{}}$	ATSPEN	$P2_1/c$	1	661.4	1.326	Different	Similar	Similar	Both from solutions in ethanol, benzene, and petroleum ether	
	(−0.007)	$P2_1$	1	329.1	1.333					
Ph–$\overset{Ph}{C}$=⟨ring⟩=$\overset{Ph}{C}$–Ph, O, N, O, CH_3	ZEPFAB	$P2_1/n$	1	2369.9	1.237	Different	Different	Different	Both from the acetone solution	Phase transition $P2_1 \xrightarrow{533\ K} P2_1/n$
	(−0.001)	$P2_1$	1	1183.6	1.238					

Table 1. (Contd.)

Compound	REFCODE (Δd)	Space group	Z	V, Å³	d, g/cm³	Unit cell parameters	Packing fragments	Molecular geometry	Solvent	Comments
Modifications prepared from the same solvent under different conditions									
Br—⟨⟩—CONH(CH₃)₂	MOPBZA	$P2_1/c$	1	1565.9	1.477	Multiple	Identical	Similar	From saturated and diluted ethanol solutions	$a = 2c$, $b = b$, $c = a$
	(0.003)	$P2_1$	1	784.4	1.474					Identical systems of hydrogen bonds
Modifications of unresolved enantiomers, prepared from different solvents									
C₆H₈—N=CH—(phenol)	BANGOM	$P2_1/c$	1	1143.9	1.667	Multiple	Identical	Similar	From the ethanol solution	Charge-transfer complex
	(−0.004)	$P2_1$	1	570.6	1.671				From the pentane solution	$a = a$, $b = b$, $c = 2c$
MeO—(pyridine)—N=CH—Ph—pNO₂	FOVYOE	$P2_1/n$	1	1231.0	1.387	Different	Different	Similar	From the ethanol solution	Charge-transfer complex
	(−0.018)	$P2_1$	1	607.8	1.405				From the ethanol–chloroform solution	Nonlinear optical activity
(aminopyridinone structure)	DUVZOJ	$P2_1/c$	4	3563.9	1.396	Multiple	Different	Similar	From the ethanol solution	$a = a$, $b = b$, $c = 2c$
	(−0.047)	$P2_1$	6	2584.6	1.443					$a = a$, $b = b$, $c = 3c$
	(−0.033)		2	870.23	1.429					
Modifications of resolved enantiomers									
Di-*Me*-9-chloromethyl-dibenzobar-relene-11,12-dicarboxylate	LAVMOK	$P2_1/c$	1	1750.0	1.400	Different	Different	Similar	Both from the hexane–acetone solution	
	(0.023)	$P2_1/c$	2	3657.7	1.339					
	(−0.038)	$P2_1$	1	889.3	1.377					
Heptahelicene	HPTHEL	$P2_1/c$	1	1933.9	1.299	Different	Different	Different		
	(0.011)	$P2_1$	2	1948.6	1.288					

(a)   (b)
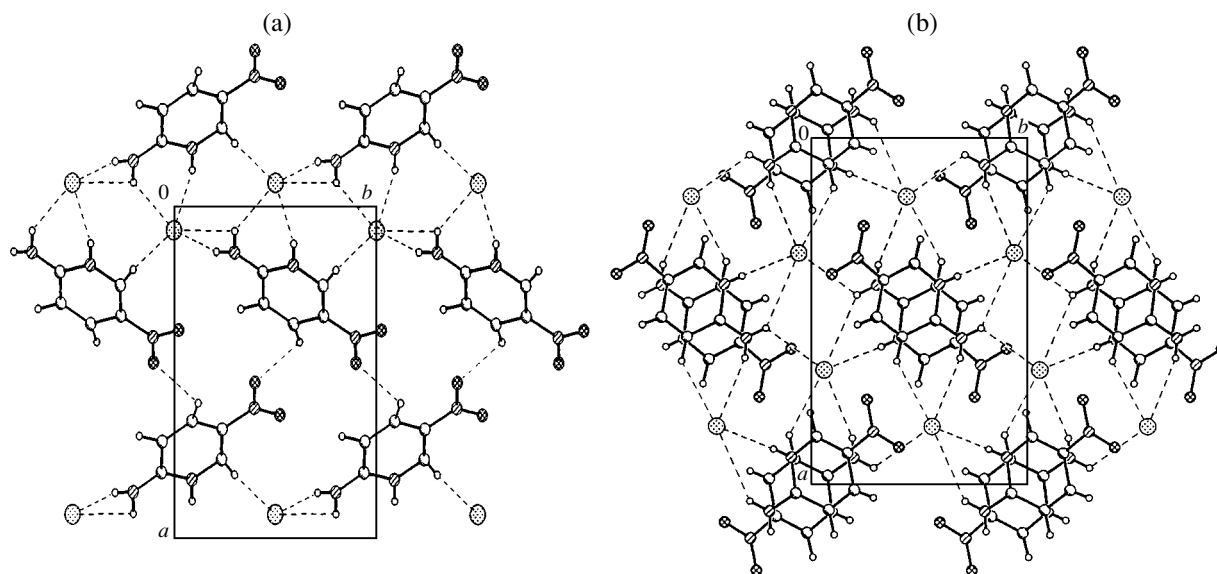
Fig. 1. (a) Structure of a chiral layer in the $P2_1$ modification and (b) superposition of antiparallel layers in the $P2_1/c$ modification of HAMNEO.

characterized by different unit cell parameters. The densities of centric and acentric crystalline modifications are close in magnitude. However, unlike the $P2_1/c$–$P2_12_12_1$ pair [1], the aforementioned polymorths do not exhibit a tendency to form denser acentric modifications.

The concomitant polymorphism is observed in nine out of thirteen compounds, i.e., more often than in the $P2_1/c$–$P2_12_12_1$ pair. The polymorphic modifications of each of the ATCPEN, EMPIPP, FAJTIT, HAMNEO, GLYCIN, MBZYAN, ZEPFAB, LAVMOK, and HPTHEL compounds were prepared under the same conditions. The MOPBZA modifications are also formally concomitant; however, the acentric enantiomer was formed only after the centric crystals initially precipitated from a saturated solution were removed from the mother solution. Therefore, in the strict sense, these modifications were obtained from the same solvent but with different concentrations: the $P2_1/c$ modification was produced from a saturated solution, whereas the $P2_1$ modification was synthesized from a diluted ethanol solution. The BANGOM, FOVYOE, and DUVZOJ modifications were prepared from solutions of different solvents.

Concomitant polymorphic modifications. In the group of unresolved enantiomers, the unit cell parameters for almost all the modifications synthesized under the same conditions are multiples. For example, the structure of the HAMNEO acentric modification with a substantial nonlinear activity [2] is composed of chiral layers that are formed by molecular cations and Br⁻ anions linked via the system of contacts (Fig. 1a). The layers are aligned parallel to the *XY*0 coordinate plane. In the crystal, these layers are joined together by the

NH···Br hydrogen bonds along the *c* axis. The structure of the centric modification involves similar chiral layers aligned parallel to the above coordinate plane. However, in the crystal, layers with different chiralities and antiparallel orientation (Fig. 1b) are joined in pairs to form a centrosymmetric double layer (stack). The stacking along the *c* axis leads to doubling of the parameter *c* of the $P2_1/c$ modification. The same structural type is characteristic of centric and acentric modifications of GLYCIN, whose molecules, like the HAMNEO molecules, form an extended system of intermolecular hydrogen bonds. In both modifications, the chiral layers (Fig. 2a), which have p_l1 symmetry and are aligned parallel to the *X*0*Z* plane, are formed by molecules through the NH···O strong hydrogen bonds. In the $P2_1$ crystal, the layers of the same chirality are joined together by hydrogen bonds. In the $P2_1/c$ crystal, the layers with different chiralities and antiparallel orientation are linked by hydrogen bonds to form double layers, i.e., stacks (Fig. 2c). The congruent stacking results in the formation of the structure with a doubled parameter *b*. Identical chiral layers are also formed in the EMPIPP modification. The MBZYAN modifications whose molecules do not form hydrogen bonds are geometrically characterized by topologically identical layers (Fig. 3). The layers are located in the *X*0*Z* plane, and the parameter *c* is doubled in the same plane. This structure differs from that of the aforementioned modifications in which the unit cell parameters are doubled in the plane of the molecular associate. This can be explained by the difference in the layer symmetry: $p_l\bar{1}$ for the $P2_1$ modification and p_lc for the $P2_1/c$ modification. The molecular geometry in the acentric modifications is also somewhat different; specifically, the ben-

zene rings are twisted in a different manner with respect to the central bond of the molecule.

For the FAJTIT polymorphic modifications, the unit cell parameters are multiples; however, the unit cell volumes are close in magnitude. This can be associated with the fact that the unit cell of the acentric modification involves two independent molecules. A comparison of the geometries of the independent molecules according to the OFIT procedure of the XP program package demonstrated that, first, these molecules are very similar in geometry and, second, both molecules have the same chirality; i.e., they are brought into coincidence without inversion (Fig. 4). A closer examination revealed that two independent molecules are related by the twofold pseudoaxis, which makes an angle of ~30° with the crystallographic direction 0b. The two independent molecules are linked into a stable dimer $D2$ by the NH···S hydrogen bonds. These bonds are responsible for the formation of a centrosymmetric dimer $D\bar{1}$ in the centric modification. Most probably, dimers of these types exist already in a solution and serve as building blocks for different modifications. In the centric modification, the $D\bar{1}$ dimer has the crystallographic symmetry $\bar{1}$. At the same time, the crystallographic axis 2 cannot be realized in the acentric modification, which results in the formation of a pseudosymmetric crystal. It is of interest that, although the molecular layers composed of these dimers in the crystals differ in symmetry, they are closely similar in topology, which eventually reflects in close unit-cell parameters.

As was noted above, concomitant modifications of the group of unresolved enantiomers are characterized by different unit-cell parameters only for the ATCPEN and ZEPFAB modifications. Small-sized molecules of ATCPEN form an extended system of strong hydrogen bonds. The structures of both modifications contain chiral layers with p_l2_1 symmetry. However, the structures of these layers differ radically. In the $P2_1/c$ modification, the molecular plane lies in the layer plane (Fig. 5a). In the $P2_1$ modification, the layer is a three-dimensional stack formed by cross-linking of chains involving the strongest hydrogen bonds NH···N≡ (Fig. 5b). In this case, the molecular planes are perpendicular to the stack plane. A noticeable difference in the unit cell parameters of the modifications stems from different molecular packings. In the ZEPFAB modifications, the geometries of molecules, their packings, and, correspondingly, the unit cell parameters are different. The phase transition $P2_1 \xrightarrow{533\ K} P2_1/n$ accompanied by the racemization of molecules was revealed between the modifications.

The structures of the MOPBZA modifications *prepared from the same solvent but at different initial concentrations* are composed of identical chains. In both forms, chains lie along the b axis. However, the pack-
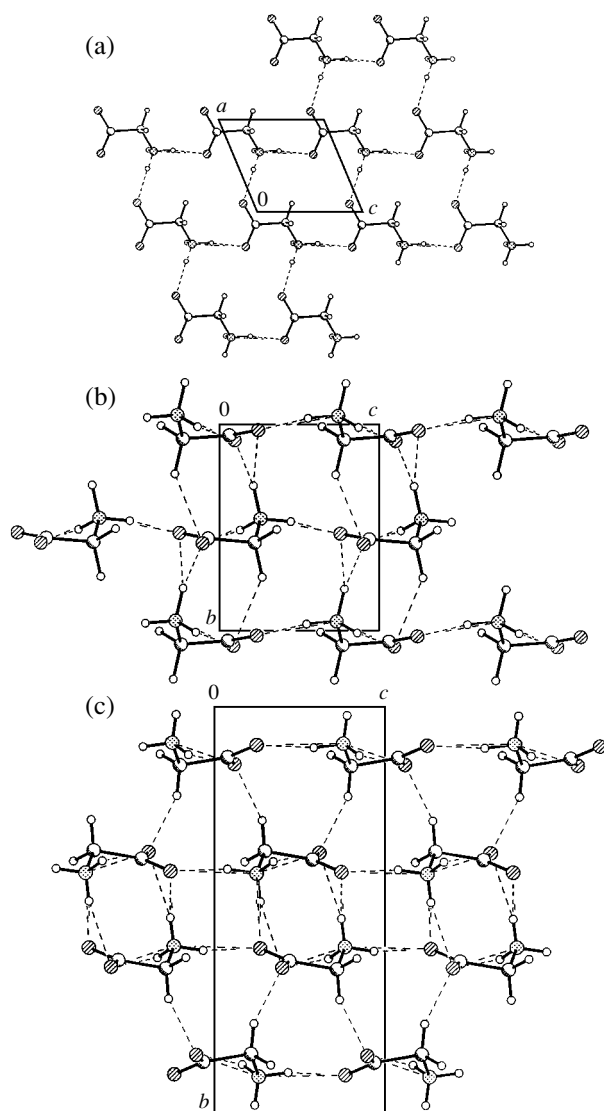
Fig. 2. Modifications of GLYCIN: (a) structure of a chiral molecular layer and packings of layers in the (b) $P2_1$ and (c) $P2_1/c$ modifications.

ings of these chains are different in the crystals. The doubling of the parameter a in the centric modification is caused by joining chains comprised of molecules with different chirality into layers owing to the CH···O shortened contacts.

Polymorphic modifications synthesized under different conditions. Both the BANGOM polymorphic modifications are charge-transfer complexes, and stacks of antiparallel molecules are formed in the centric and acentric structures (Fig. 6). Apparently, it is these fragments that are the most stable molecular associates occurring in polar ethanol and nonpolar pentane. The interplanar distance is relatively short (3.34 Å) in both modifications. The stacks are differently joined into the crystal structure. In the $P2_1$ modification, the CH···F shortened contacts are responsible for the for-

(a)

(b)
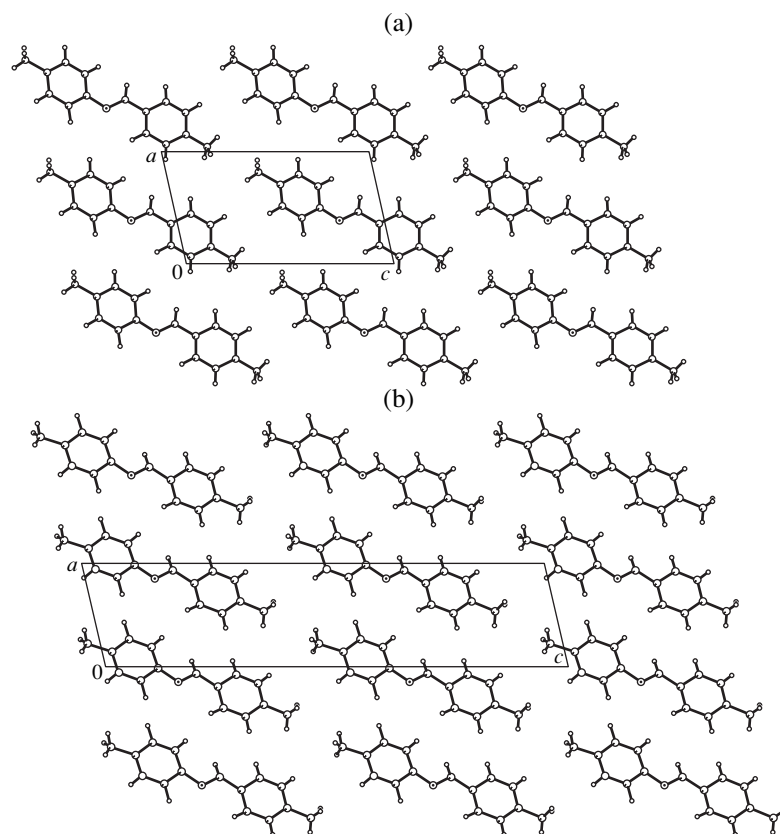
Fig. 3. Structures of molecular layers with (a) $p_l 2_1$ symmetry in the $P2_1$ modification and (b) $p_l c$ symmetry in the $P2_1/c$ modification of MBZYAN.

mation of chains along the $0y$ axis. In the $P2_1/c$ modification, layers are formed along the $0z$ axis, which results in a doubling of the parameter c. An unusual feature of the polymorphic structures is the absence of the intermolecular hydrogen bonds involving the hydroxyl groups of the molecules. In both modifications, the rotation angle of the benzene ring planes with respect to the C=N central bond falls in the range 40°–45°. Consequently, the OH···N intermolecular contacts are not too short: 1.89 Å in the $P2_1$ enantiomer and 1.98 Å in the $P2_1/c$ enantiomer. Possibly, this is explained by the intermolecular charge transfer in stable associates of this strongly polar molecule; as a result, hydrogen of the hydroxyl group ceases to be a donor of the hydrogen bond.

The structures of the FOVYOE polymorphic modifications whose molecules are characterized by a high molecular hyperpolarizability differ radically. The molecular geometries are also different: the angles between the planar rings in the centric and acentric modifications are equal to 19.5° and 35.7°, respectively. This is favorable to intramolecular charge transfer in the former case and, most likely, excludes charge transfer in the latter case. The FOVYOE molecules cannot form intermolecular hydrogen bonds, and strong intermolecular contacts can be produced only due to stack-

ing interaction [3]. It is this situation that is observed in the acentric modification whose structure consists of stacks of parallel molecules (Fig. 7a). This packing is typical of nonlinear optical crystals. Moreover, an angle of 52° between the molecular dipole direction and the polar axis is close to an optimum angle [4]. In the centric modification, layers are formed by the antiparallel molecules, which superpose on each other with a considerable shift (Fig. 7b).

All the known modifications of DUVZOJ possess an antitubercular activity and belong to polysystem crystals. Both acentric modifications have a pseudosymmetry, and their structures involve pseudocentrosymmetric dimers formed through the NH···O intermolecular hydrogen bonds. The modification with $P2_1$ and $Z' = 6$ is a disordered analog of the modification with $P2_1$ and $Z' = 2$, which can be reduced to the hypothetical pseudosymmetric group $P2_1/c$ [5]: $(P2_1, Z' = 6 + c/3) \longrightarrow (P2_1, Z' = 2) + \bar{1} (000) \longrightarrow (P2_1/c, Z' = 1)$. However, the real structure of the DUVZOJ centric modification prepared from different solution contains no centrosymmetric dimers, and the crystal is built up of molecular chains formed by hydrogen bonds NH···N.

Analysis of the structures of all the aforementioned modifications confirms our assumption that one of the
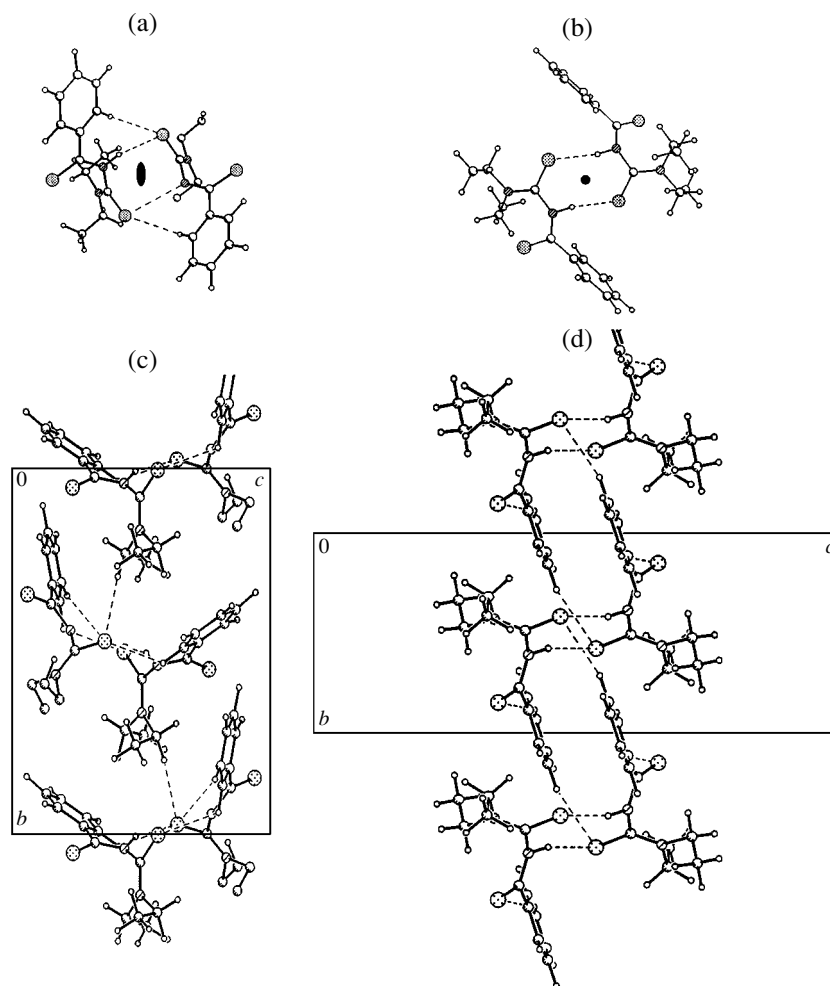
Fig. 4. (a, c) Structures of dimers formed by independent molecules and (b, d) chains formed by dimers in the (a, b) $P2_1$ and (c, d) $P2_1/c$ modifications of FAJTIT.

necessary conditions for the formation of centric and acentric modifications of a particular compound is the occurrence of a stable chiral packing fragment identical for all structures. Furthermore, when the structures of the modifications consist of large-sized stable molecular fragments, their unit cell parameters are most frequently close in magnitude.

THE $P2_1/c$–Pc POLYMORPHIC PAIRS

We revealed 11 pairs of $P2_1/c$–Pc polymorphic modifications. The complete set of crystal structure data are available for ten compounds (Table 2). It should be noted that the smaller the number of representatives in the pair of polymorphs, the stronger the influence of a specific set of compounds on the results of the analysis. Moreover, information regarding the methods of preparing crystals, their physical properties, and the occurrence of phase transitions has been rarely updated in the Cambridge Structural Database, and the journals required (especially those published in recent years) are

often absent in libraries. Certainly, this leads to a decrease in the degree of correctness of generalizations for the given polymorphic pair. However, it is evident that the $P2_1/c$–Pc pair has a number of distinguishing features as compared to the pairs described earlier.

First, the group Pc, as well as the group $P2_1$, is the subgroup of the space group $P2_1/c$; however, unlike the two previously considered pairs, both groups in the pair under investigation are racemic. Note that a larger number of centric and acentric crystals of these compounds were synthesized from different solvents, whereas the concomitant polymorphism was reliably established only in SILXUG and FAHVOZ (in the case of four more pairs in Table 2, information on the crystal preparation is incomplete). Close unit-cell parameters are more rarely observed (for DGLYCN, DHNAPH, and SLFNMF) as compared to the two preceding pairs. Furthermore, the unit cell parameters of the compounds in the $P2_1/c$–$P2_1$ pairs are often multiples, whereas multiple parameters for polymorphs in the $P2_1/c$–Pc pairs are observed only for the BESKAL, PYRZIN, and

(a) (b)
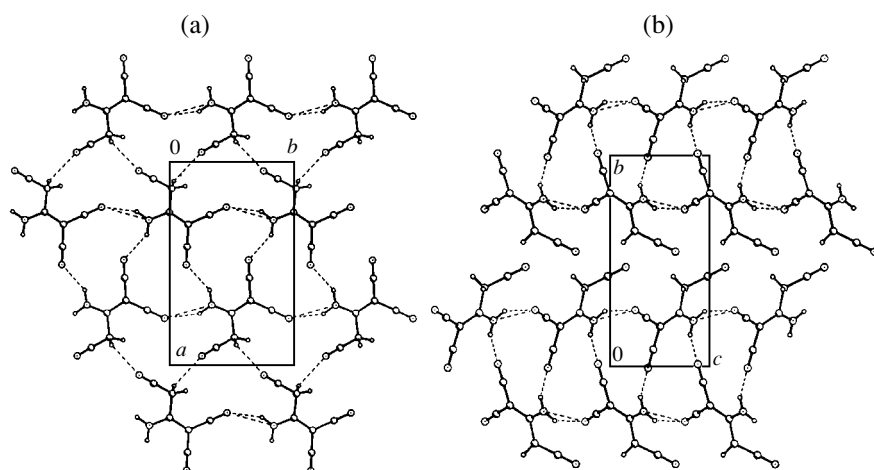
Fig. 5. Structures of chiral layers in the (a) $P2_1$ and (b) $P2_1/c$ modifications of ATCPEN.

(a) (c)

(b) (d)
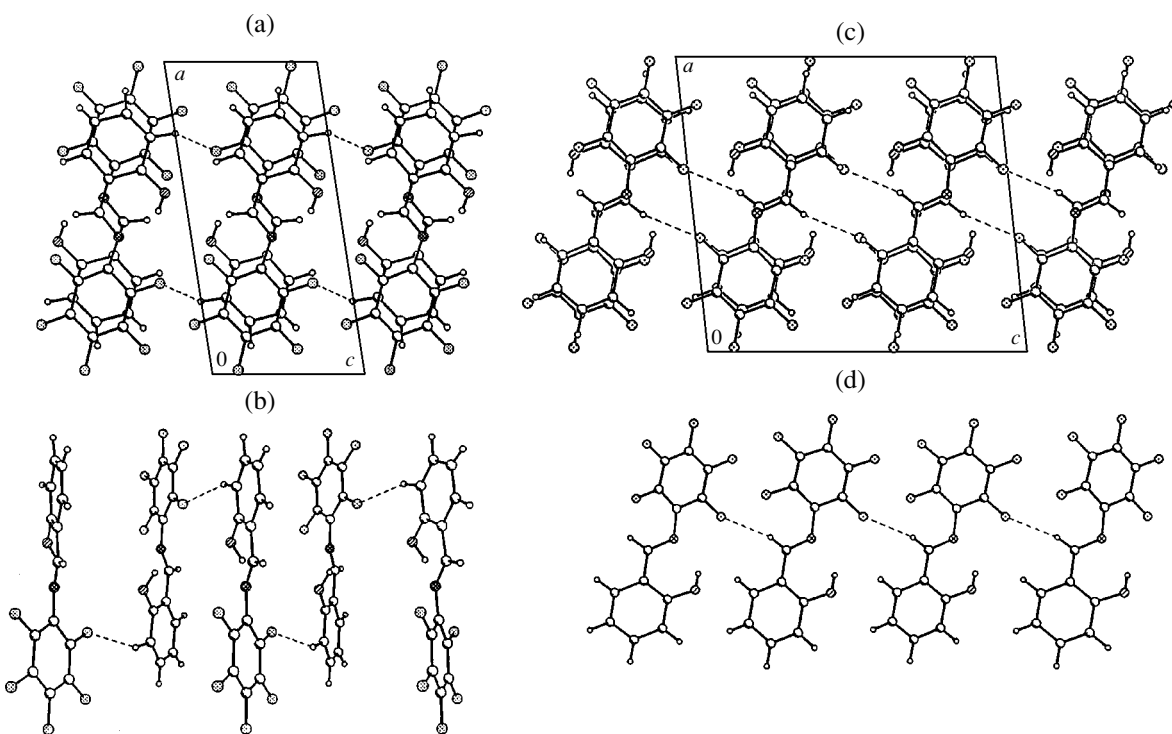
Fig. 6. (a, c) Molecular packings and (b, d) structures of chains in the (a, b) $P2_1$ and (c, d) $P2_1/c$ modifications of BANGOM.

SILXUG modifications. In this case, the volume of the acentric cell is not necessarily smaller than that of the centrosymmetric cell. This is associated with the *second* structural feature of these polymorphic pairs, namely, a very large number of polysystem crystals. Indeed, seven (out of ten) compounds are characterized by $Z' > 1$. The *third* distinctive feature of this group is the occurrence of a relatively large number of polymorphic phase transitions. It is worth noting that all the four known transitions in the modifications of the pair under consideration are accompanied by the lowering of the

$P2_1/c \longrightarrow Pc$ symmetry, irrespective of whether they occur with a decrease or an increase in the temperature.

The *fourth* specific feature is that the $P2_1/c$–Pc polymorphic pairs are represented by the most chemically homogeneous molecules. The molecules of six out of ten compounds (the corresponding data are presented in the first part of Table 2) have an achiral, planar, usually aromatic structure (containing benzo, naphtha, or anthraquinone rings) with hydroxy, carboxy, and other functional substituents that are capable of transferring

(a)

(b)
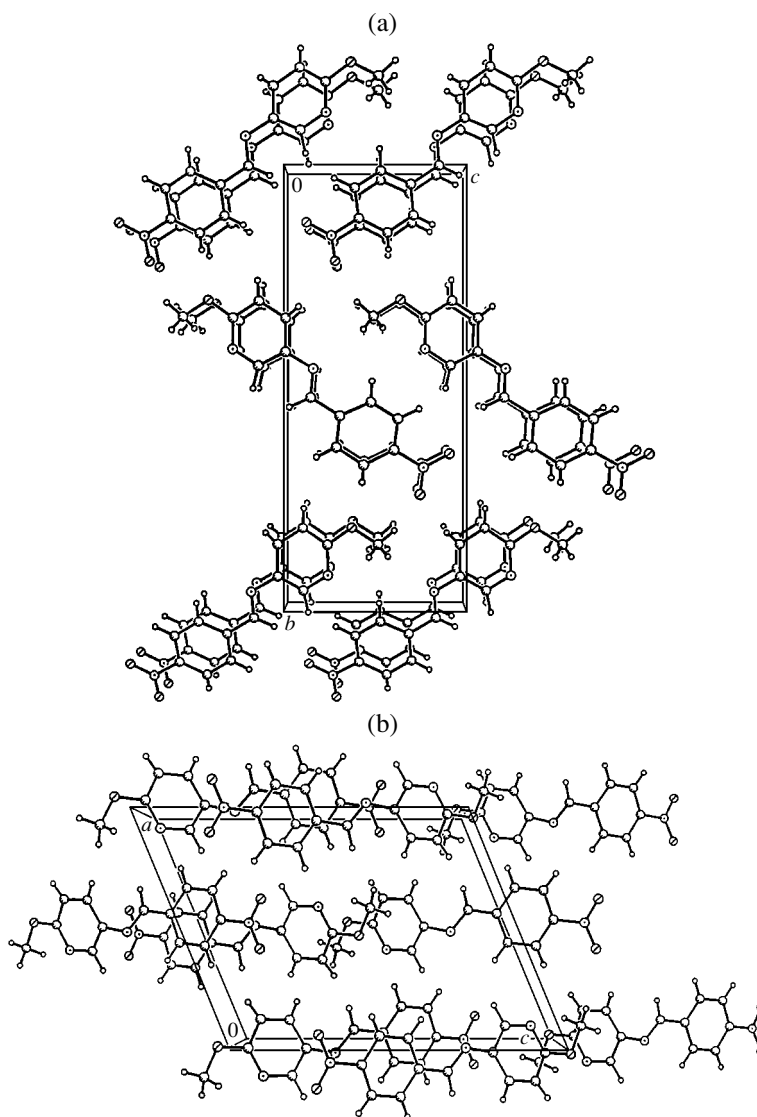
Fig. 7. Molecular packings in the (a) $P2_1$ and (b) $P2_1/c$ modifications of FOVYOE.

protons and forming strong intermolecular bonds. It is not improbable that the last circumstance is responsible for the large number of polysystem crystals observed in the polymorphic pairs under consideration. The role played by the molecular association in the manifestation of a pseudosymmetry in crystals was discussed in detail in our earlier work [5]. In [5], we proposed a simple scheme for the crystal chemical analysis of pseudosymmetric crystals. This scheme is based on the search for a higher symmetry group G, which is related to the initial pseudosymmetric group H by the operation $G = H + (g/t)H$. Here, g and t are the rotational and translational components of the pseudoelement. Moreover, the applicability of this operation was illustrated using crystals of particular compounds as examples. It should be noted that the majority of examples (BESKAl,

DGLYCN, SILXUG, and SLFNMF) were found among the $P2_1/c$–Pc polymorphic pairs.

Despite the above features, modifications of this polymorphic pair exhibit a tendency for the unit cell parameters to retain close (or multiple) values, provided that the sufficiently large-sized stable packing fragments remain unchanged irrespective of crystallization conditions. However, in this case, the formation of chiral associates is not a necessary condition. Acentric and even pseudocentrosymmetric packing fragments are frequently formed in polymorphs of the $P2_1/c$–Pc pair. In particular, both modifications of glycine nitrate (DGLYCN) have virtually identical structures (Fig. 8) and, correspondingly, close unit-cell parameters. In the $P2_1/c$ denser modification, two glycine molecules are linked together by a symmetric hydrogen bond into a stable molecular centrosymmet-

KULESHOVA, ANTIPIN

Table 2. Polymorphic pairs $P2_1/c$–Pc
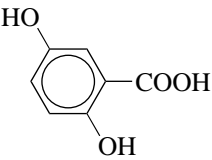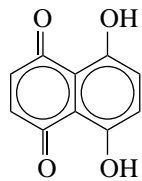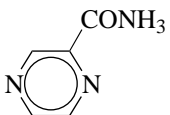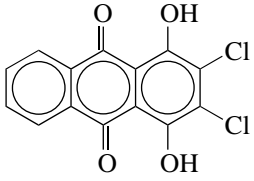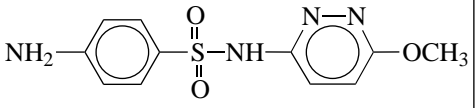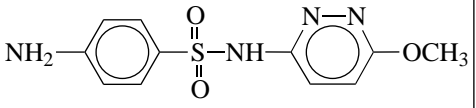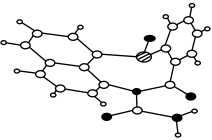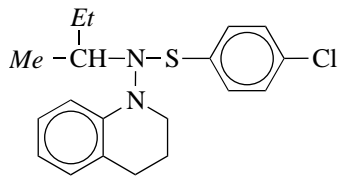
Compound	REFCODE (Δd)	Space group	Z'	V, Å^3	d, g/cm^3	Unit cell parameters	Packing fragments	Molecular geometry	Solvent	Comments
NH_3–CH_2–COOH1/2NO_3^-	DGLYCN	$P2_1/a$	1	443.9	1.595	Close	Similar	Similar	?	Paraelectric
	(−0.016)	Pa	2	438.2	1.611				?	Ferroelectric
Cl—⟨⟩—CN	CLBZNT	$P2_1/c$	1	639.3	1.429	Different	Different	Similar	Sublimation	Phase transition $P2_1/c \longrightarrow Pc$
	(−0.012)	Pc	1	317.0	1.441				From the ethanol solution	Weak nonlinear optical activity
HO—⟨⟩—COOH (OH)	BESKAL	$P2_1/a$	1	648.5	1.578	Multiple	Similar	Similar	From the aqueous solution	T_m = 481–483 K
	(0.036)	Pa	2	663.8	1.542				From the chloroform–acetone mixture	T_m = 488–490 K $a = 2a$, $2b = c$, $c = b$
(naphthoquinone structure)	DHNAPH	$P2_1/c$	1/2, 1/2	808.2	1.562	Close	Similar	Similar	From benzene and chloroform solutions	Phase transition $P2_1/c \longrightarrow Pc$
	(−0.065)	Pc	2	771.6	1.637				?	T_{exp} = 60 K
$CONH_3$ (pyrazine)	PYRZIN	$P2_1/c$	1	559.7	1.460	Multiple	Similar	Similar	From pyrazinecarboxamide	
	(−0.025)	Pa	1	275.1	1.485				From the melt	$a = c$, $b = b$, $c = 2a$

Table 2. (Contd.)

Compound	REFCODE (Δd)	Space group	Z'	V, Å³	d, g/cm³	Unit cell parameters	Packing fragments	Molecular geometry	Solvent	Comments
(anthraquinone: O, OH, Cl, Cl, OH, O)	GAXLEW	$P2_1/c$	1	1198.3	1.718	Different	Different	Similar	From the chloroform solution	Phase transition $P2_1/c \longrightarrow Pc$
	(−0.018)	Pc	1	591.5	1.736				From hot toluene	Weak nonlinear optical activity
(Ph–COO–Ph–COOCH$_2$–)$_2$	SILXUG	$P2_1/c$	1/2	1332.9	1.341	Multiple	Similar	Similar	Both the toluene solution	Phase transition $P2_1/c \longrightarrow Pc$
	(−0.001)	Pn	2	2664.9	1.342					Liquid crystal $a = 4c$, $b = b$, $2c = a$
NH$_2$–(C$_6$H$_4$)–SO$_2$–NH–(N–N pyridazine)–OCH$_3$	SLFNMF	$P2_1/c$	2	2621.2	1.421	Close	Similar	Similar	?	Rotamer with inversion
	(0.058)	Pc	4	2731.4	1.363				?	
(polycyclic structure)	FAHVOZ	$P2_1/c$	2	3166.4	1.407	Different	Different	Similar	Both from the benzene–methanol solution	T_m = 198–213°C
	(0.004)	Pc	2	1587.2	1.403					
Me –CH(Et)–N–S–(C$_6$H$_4$)–Cl with tetrahydroquinoline	HOQABS	$P2_1/c$	2	3644.2	1.300	Different	Different	Similar	?	
	(−0.047)	Pc	1	879.7	1.347				?	

(a)

(b)
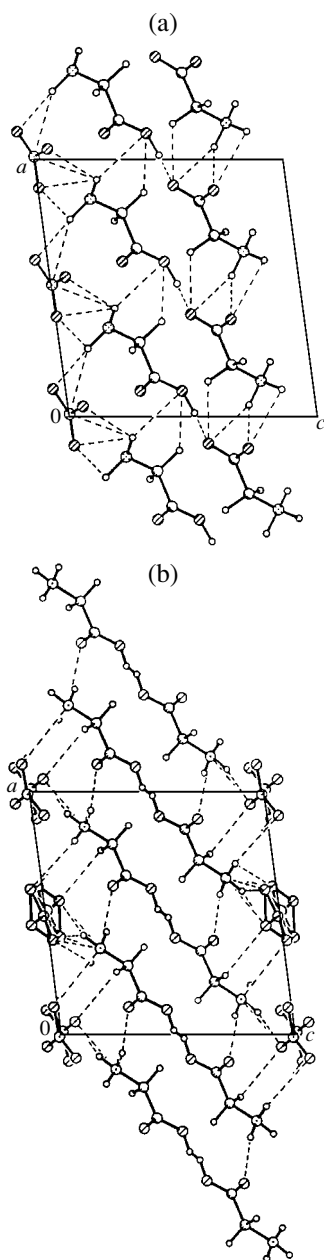
Fig. 8. Molecular packings in the (a) *Pc* and (b) *P*2$_1$/*c* modifications of DGLYCN.

ric dimer. In the *Pc* modification, owing to intermolecular proton transfer, the independent glycine molecules related by a pseudocenter occur in the form of a neutral molecule and a zwitterion. However, the molecular topology remains almost the same. The pseudocenter is located in the vicinity of the (1/2, 1/2, 1/2) crystallographic point. The displacement of the pseudocenter with respect to the crystallographic position does not exceed 0.4 Å. The space groups of the modifications are related by the operation $(P2_1/c, Z' = 1) = (Pa, Z' = 2) + \bar{1} (1/2, 1/2, 1/2)$. According to the Abrahams concepts [6] and the results of our previous work [5], we can

assume that a paramagnetic–ferromagnetic phase transition between these polymorphs is quite probable.

The structures and the unit cell parameters of centric and acentric CLBZNT crystals obtained by different techniques differ significantly. The acentric modification prepared from an ethanol solution possesses weakly pronounced nonlinear optical properties. Although both polymorphs have a layered structure, these layers substantially differ in topology (Fig. 9). The phase transformation **I** $(P2_1/c, Z' = 1) \longrightarrow$ **II** $(Pc, Z' = 1)$ between partially disordered modification **I** and completely ordered modification **II** is observed at room temperature. The transition is attended by the cooperative rotation of molecules about the centers of gravity and the corresponding change in the crystal axes.

The same structural fragments are also observed in the modifications of each of the BESKAL, DHNAPH, and PYRZIN compounds. Molecules of these compounds form systems of strong intermolecular hydrogen bonds whose fragments are retained irrespective of crystallization conditions. For example, the BESKAL acentric modification with a lower density but a higher melting point was obtained from a mixture of aprotic solvents. The centric modification was synthesized from an aqueous solution. However, both modifications are composed of topologically identical layers, which are centrosymmetric in the *P*2$_1$/*c* modification and pseudocentrosymmetric in the *Pc* modification. In the crystal of the *Pc* modification, the layers are linked together only through van der Waals interactions and one hydroxyl group in each independent molecule remains free (Fig. 10). In the *P*2$_1$/*c* crystal, the layers are displaced with respect to each other so that hydrogen bonds are formed between these hydroxyl groups. The independent molecules of the acentric modification are related by the pseudocenter of symmetry, which is noticeably displaced (by ~2 Å) from the crystallographic position. Most likely, this excludes the occurrence of a phase transition between the modifications. The symmetry relationship between the groups can be written in the form $(P2_1/c, Z' = 1) = (Pa, Z' = 2) + \bar{1} (1/2, 1/2, 1/2)$.

Both modifications of naphthazarin DHNAPH belong to polysystem crystals. In both crystals, similar systems of intermolecular contacts bring about the formation of typical pseudohexagonal layers, which were already noted in other donor–acceptor aromatic systems (HAMNEO). With a decrease in the temperature to 110 K, the centric modification undergoes the reversible transition $(P2_1/c, Z' = 1/2, 1/2) \xrightarrow{110\,\text{K}} (Pc, Z' = 2)$ to the denser acentric form. The transition is accompanied by the intramolecular proton migration and a small displacement of layers with respect to each other. This leads to loss of the proper center of the molecular symmetry; therefore, independent molecules in the *Pc* crystal are not related by a pseudoelement. Although the DHNAPH molecules do not possess high molecular hyperpolarizability, the phase transition was judged
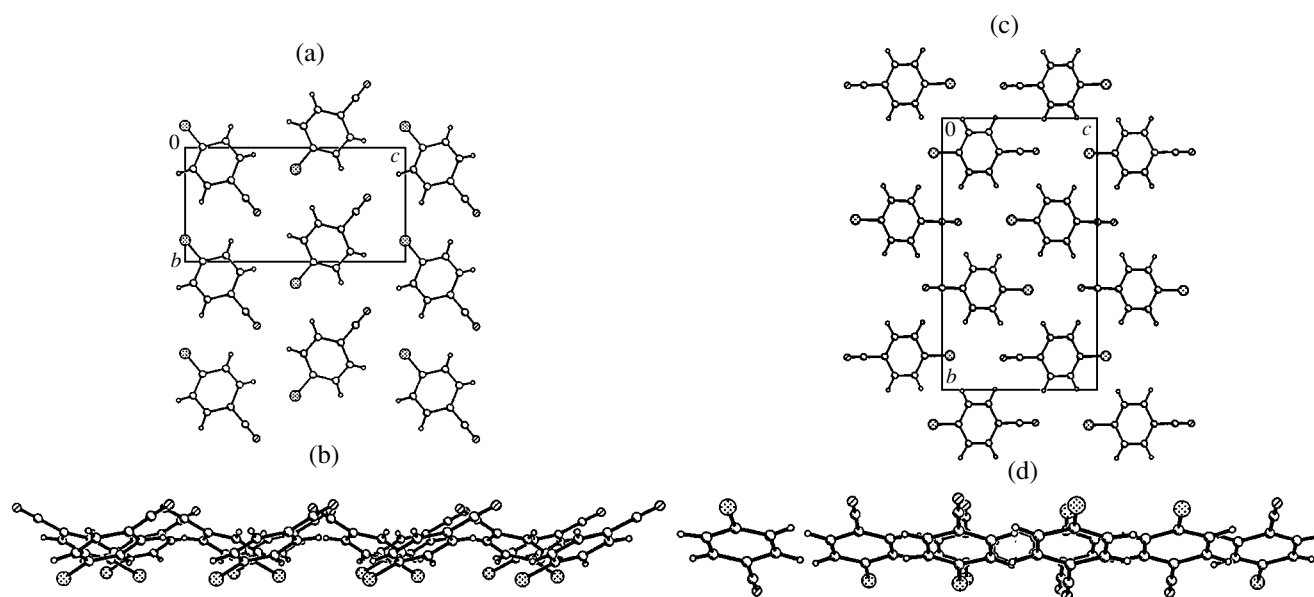
Fig. 9. Molecular packings in the (a, b) *Pc* and (c, d) *P*2₁/*c* modifications of CLBZNT in the projections (a, c) parallel and (b, d) perpendicular to the plane of the molecular layer.
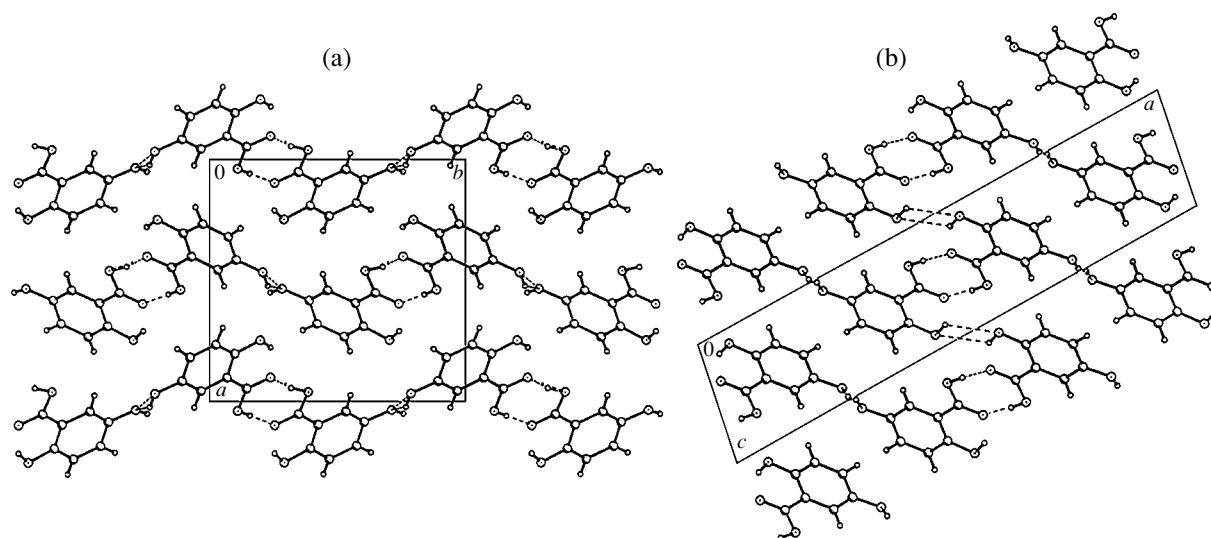
Fig. 10. Packings of (a) pseudocentrosymmetric layers in the *Pc* modification and (b) centrosymmetric layers in the *P*2₁/*c* modification of BESKAL in the projection perpendicular to the layer plane.

from the second harmonic generation, which is characteristic of the acentric modification [7]. Note that the related compound GAXLEW forms the same polymorphic modifications. In this case, the high-temperature acentric modification crystallizes from hot toluene. For this reason, the phase transition from the centric modification to the acentric modification ($P2_1/c$, $Z' = 1$) $\xrightarrow{130°C}$ (Pc, $Z' = 1$) occurs upon heating to 130°C with the destruction of the sample. The PYRZIN modifications, which possess an antitubercular activity, were prepared from different solvents. However, their packings

involve identical acentric molecular chains (Fig. 11). These chains are repetitive from modification to modification and are responsible for multiple values of the unit cell parameters.

The concomitant modifications of SILXUG were obtained by slow evaporation of a toluene solution at room temperature. This compound possesses liquid-crystal properties. The transition to the liquid-crystal state is described by the scheme $\alpha(P2_1/c$, $Z' = 1/2)$ $\xrightarrow{110°C}$ $\beta(Pn$, $Z' = 2)$ $\xrightarrow{185°C}$ LC. The transition between the modifications is characterized by the reten-

(a)   (b)
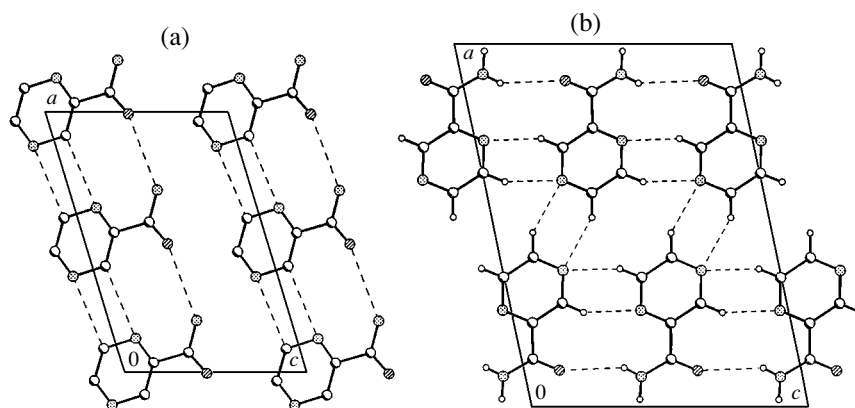
Fig. 11. Packings of acentric chains in the (a) *Pc* and (b) *P*2$_1$/*c* modifications of PYRZIN.

tion of three-dimensional molecular stacks and a change in the molecular conformation, namely, the twisting of central benzene rings and the loss of the proper center of inversion in the molecule. In addition, the crystallographic symmetry is lowered owing to loss of the center of symmetry [which transforms into a pseudocenter with the coordinates (0.8, 0.26, 0.8)] and the symmetry relationship is represented as ($P2_1/c$, $Z' =$ 1/2) = (Pn, $Z' = 2$) + $\bar{1}$ (0, 1/2, 0). These transformations upon phase transition result in a doubling of the unit cell volume without a change in the columnar structure of the crystal. One more example of crystal packings, which can differ by either the presence or the absence of the symmetry center and can be treated as a pair made up of a centrosymmetric group and a subgroup with the pseudocenter [($P2_1/c$, $Z' = 2$) = (Pc, $Z' = 4$) + $\bar{1}$ (0, 1/2, 0)], is provided by the SLFNMF modifications. Molecules of this compound form stable noncentrosymmetric dimers in the structures of all the modifications.

It should be emphasized once again that, although the modifications of the polymorphic pair under investigation exhibit a tendency for the unit cell parameters to retain close (or multiple) values, provided that sufficiently large-sized stable packing fragments remain unchanged, the formation of chiral associates is not a necessary condition. The acentric and pseudocentrosymmetric packing fragments are frequently observed in the $P2_1/c$–Pc pairs considered above.

THE $P2_1/c$–$Pna2_1$ POLYMORPHIC PAIRS

We revealed 16 pairs of $P2_1/c$–$Pna2_1$ polymorphic modifications. The complete set of crystal structure data are available for 15 compounds. Note that the $P2_1/c$–$Pca2_1$ and $Pbca$–$Pna2_1$ pairs are encountered considerably more rarely. Although the space groups $P2_1/c$ and $Pna2_1$ are isomorphic, they are not symmetrically subordinate and belong to different symmetry classes,

namely, to the classes $2/m$ and $mm2$. Therefore, in this case, the unit cells should be compared using the reduced unit-cell parameters. The main crystal parameters of these modifications are presented in Table 3. The distinctive structural feature of polymorphic modifications of this pair is that the unit cells are characterized primarily by different parameters. In rare cases, when the unit cell parameters appear to be close to each other (the ACTOLD, PEGVAY, PEZBOL, and TOLSAM modifications), the differences between them are relatively large and sometimes exceed 10%. Almost all the compounds listed in Table 3 belong to the group of unresolved (or rapidly inverted) enantiomers. The data for concomitant modifications (for the most part, with nonconjugate, conformationally nonrigid molecules) are given in the first part of the table. Modifications characterized by conjugate molecules with donor–acceptor substituents were prepared from different solvents. The data for these compounds are presented in the second part of Table 3. The densities of the modifications, as for the preceding pairs, are close in magnitude. The rare exceptions are provided by the modifications of PEGVAY (the experimental data were obtained at different temperatures) and CAXMOD (whose centric modification has a denser packing).

Concomitant polymorphic modifications. These modifications are relatively rare in occurrence among the $P2_1/c$–$Pna2_1$ pairs. Only the modifications of each of the CAXMOD, FAHNOR, BAAANL, PEGVAY, and PEZBOL compounds were synthesized under the same conditions. Among them, three compounds have nonconjugate (saturated), conformationally nonrigid molecules. Possibly, this is the reason why the tendency noted in [1] that the modifications prepared under the same conditions are more frequently characterized by close unit-cell parameters as compared to the modifications obtained from different solvents manifests itself to a smaller extent for the pairs under consideration. Actually, the unit cell parameters are close to each other in two out of five pairs synthesized under the same conditions and in one out of nine pairs produced from dif-
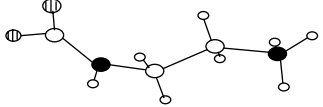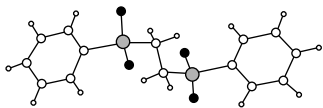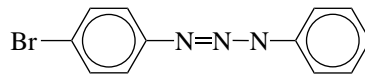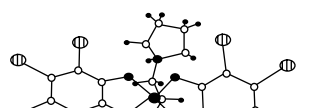
Table 3. Polymorphic pairs $P2_1/c$–$Pna2_1$
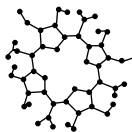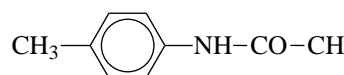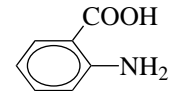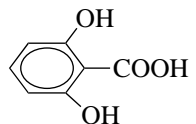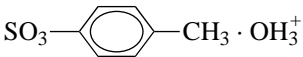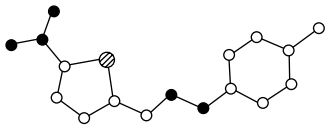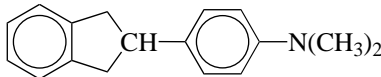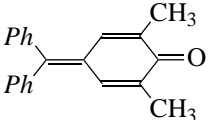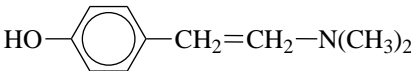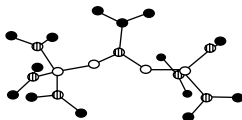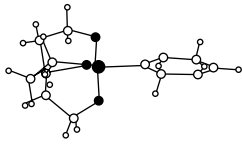
Compound	REFCODE (Δd)	Space group	Z'	V, Å³	d, g/cm³	Unit cell parameters	Packing fragments	Molecular geometry	Solvent	Comments
				From the same solvent						
(structure)	CAXMOD (+0.096)	$P2_1/a$	1	479.6	1.441	Different	Different	Different	Both from a solution in absolute ethanol	Rotamers
		$Pna2_1$	1	513.8	1.345					
(structure)	FAHNOR (−0.004)	$P2_1/n$	1/2	708.5	1.455	Different	Different	Different	Both (slowly) from the acetone solution	Rotamers
		$Pna2_1$	1	1412.3	1.459					
Br—⬡—N=N—N—⬡	BAAANL (0.000)	$P2_1/c$	1	1160.2	1.580	Different	Different	Similar	Both upon cocrystallization	
		$Pna2_1$	2	2320.3	1.580					
(structure)	PEGVAY (−0.112)	$P2_1/n$	1	2658.6	2.434	Close	Similar	Similar	Both from the reaction mixture in acetonitrile	$T_m = 297°C$, $T_{exp} = 233$ K
		$Pna2_1$	1	2543.0	2.546					$T_m = 249°C$, $T_{exp} = 173$ K
(structure)	PEZBOL (−0.001)	$P2_1/n$	1	3577.2	1.327	Close	Similar	Similar	Both through diffusion of hexane in the CH_2Cl_2 solution	$T_{exp} = 130$ K
		$Pna2_1$	1	3572.6	1.328					
				From the same solvent at different concentrations						
CH₃—⬡—NH—CO—CH₃	ACTOLD (−0.010)	$P2_1/c$	1	812.1	1.221	Close	Similar	Similar	Slowly from the saturated ethanol solution	$T_m = 147.5°C$
		$Pna2_1$	1	838.9	1.231				From the diluted ethanol solution	$T_m = 151.5°C$
				From different solvents						
COOH / —NH₂	AMBACO (−0.022)	$P2_1/a$	1	656.3	1.387	Different	Similar	Similar	From the melt	Phase transition
		$Pna2_1$	2	1292.8	1.409				Slowly from an aqueous solution	Triboluminescence activity
		$Pbca$	1	1330.9	1.368				From the aniline solution	
OH / —COOH / OH	LEZJAB (−0.026)	$P2_1/c$	1	647.3	1.581	Different	Different	Similar	From the pyridine solution	Different orientations of OH groups
		$Pna2_1$	1	658.3	1.555				From the chloroform solution	

Table 3. (Contd.)

Compound	REFCODE (Δd)	Space group	Z'	V, Å³	d, g/cm³	Unit cell parameters	Packing fragments	Molecular geometry	Solvent	Comments
SO_3—⟨⟩—$CH_3 \cdot OH_3^+$	TOLSAM	$P2_1/c$	1	869.4	1.453	Close	Similar	Similar	From the ethanol–water solution	$T_m = 104°C$
	(+0.056)	$Pna2_1$	1	904.0	1.397				From an aqueous solution	–
	NOJHEZ	$P2_1/n$	1	1249.4	1.389	Different	Different	Different	Rapid cooling of the ethanol solution	$T_m = 156°C$
	(+0.027)	$P2_1/n$	2	2511.9	1.382				Slowly from the chloroform solution	$T_m = 157°C$
		$Pna2_1$	1	1273.9	1.362				Rapid cooling of the chloroform solution	Nonlinear optical activity
⟨⟩CH—⟨⟩—$N(CH_3)_2$	MBYINO	$P2_1/c$	2	2760.1	1.334	Different	Different	Identical	From the methyl ethyl ketone–ethanol mixture	Charge-transfer complex
	(0.003)	$P2_1/c$	1	1396.9	1.318				Rapidly from the methyl ethyl ketone solution	Charge-transfer complex
		$Pna2_1$	1	1382.9	1.331				Rapidly from the ethanol solution	Charge-transfer complex
Ph, Ph C= with CH_3, O, CH_3	DMFUSC	$P2_1/c$	1	1596.5	1.191	Different	Different	Similar	Slowly from the toluene solution	
	(−0.006)	$Pna2_1$	1	1588.2	1.197				From the saturated cyclohexane solution	
		$P2_12_12_1$	1	1587.5	1.198				Slowly from the benzene solution	
HO—⟨⟩—$CH_2=CH_2$—$N(CH_3)_2$	TALIZ	$P2_1/n$	1	1001.2	1.096	Different	Similar	Different	From the diethyl ether solution	
	(−0.031)	$Pna2_1$	1	973.5	1.127				Slowly from the methanol solution	
	NOETNA	$P2_1/c$	1	1318.9	1.954	Different	Different	Similar	From the CCl_4 solution	
	(+0.036)	$Pna2_1$	1	1343.7	1.918				From the reaction mixture	$T_m = 95°C$
	PNEOSI	$P2_1/n$	1	1220.4	1.367	Different	Different	Similar		$T_m = 207°C$
	(0.006)	$Pna2_1$	1	1226.4	1.361					$T_m = 208°C$

ferent solvents. Moreover, in the pairs discussed earlier, the closeness of the parameters was explained by the retention of identical (sufficiently large-sized) structural fragments in different modifications (whose molecules have a similar geometry). At the same time, the opposite structural correlation is observed for the $P2_1/c$–$Pna2_1$ pairs: different geometries of molecules lead to the formation of different structural fragments that, in turn, are responsible for different unit-cell parameters.

For example, in different CAXMOD modifications, molecular zwitterions are in the form of different rotamers, which probably can exist even in solutions. Therefore, different conformers form different molecular associates (Fig. 12) through sufficiently strong intermolecular hydrogen bonds. In turn, these associates most likely stabilize a particular geometry of the molecules in the crystal. More "compact" conformers are joined together into centrosymmetric dimers. The dimers are linked into three-dimensional layers (stacks) with $p_l 2_1/a$ symmetry, which form the $P2_1/a$ crystal. Linear conformers are responsible for the formation of a considerably looser noncentrosymmetric framework with $Pna2_1$ symmetry. The FAHNOR molecules in different modifications also occur in the form of different rotamers. These molecules do not form strong intermolecular hydrogen bonds. However, compact conformers are joined through the CH···O short contacts into achiral molecular layers with $p_l n$ symmetry, which form the $P2_1/n$ structure. As in the preceding case, linear conformers form a molecular diamond-like framework with $Pna2_1$ symmetry. The densities of both packings are close in magnitude. The BAAANL molecules have similar geometries but differ in packing. The centric modification is composed of chiral helixes aligned parallel to the screw axes (Fig. 13). The $Pna2_1$ modification is built up of chains formed by pseudocentrosymmetric dimers, which involve pairs of independent molecules joined by the NH···N intermolecular hydrogen bonds. In both modifications, the chains lie along the polar direction (the 2_1 axis). However, different chain structures are responsible for different unit-cell parameters. Note that the orthorhombic form dominates in both crystals obtained by cocrystallization. Consequently, we can assume that a larger number of molecules are linked into dimers even in the mother solution. In the PEGVAY modifications, molecules exhibit similar geometries. In the crystals of different modifications, molecules form chains along the polar direction. These chains are similar in topology (Fig. 14) but differ in symmetry ($p_c \bar{1}$ in the $P2_1/c$ modification and $p_c 2_1$ in the $Pna2_1$ modification). The reduced unit-cell parameters are close in magnitude. A similar situation is observed for the PEZBOL modifications. In the crystals of both modifications, molecules form layers that are similar in topology but different in symmetry (chiral layers with $p_l 2_1$ symmetry in the $P2_1/c$ modifi-
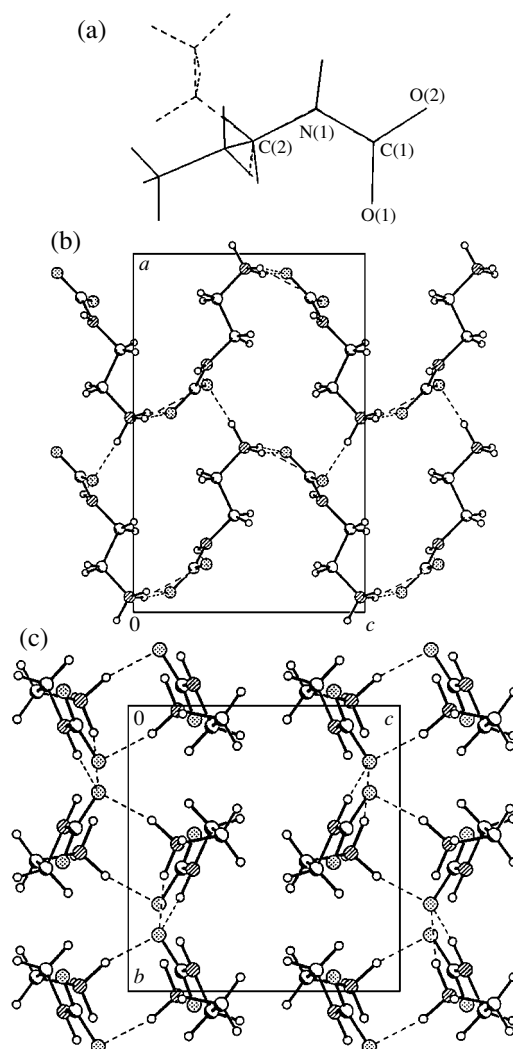

Fig. 12. Modifications of CAXMOD: (a) molecular geometries and molecular packings in the (b) $Pna2_1$ and (c) $P2_1/c$ modifications.

cation and racemic layers with $p_l a$ symmetry in the $Pna2_1$ modification). The packing of these layers leads to close values of the reduced unit-cell parameters.

Only for one compound (ACTOLD), the polymorphic modifications were synthesized *from the same solvent but at different concentrations of the mother solution.* The structures of both modifications contain identical chiral chains of molecules linked by the NH···O intermolecular hydrogen bonds.[2] In the modifications, molecules have the same geometry, but the mutual arrangements of molecules in the chains are different. However, this circumstance does not affect the unit cell parameters, which turn out to be close to each other.

Polymorphic modifications prepared from different solvents. Pairs of $P2_1/c$–$Pna2_1$ polymorphic

---

[2] The $P2_12_12_1$ modification of this compound is also included in the Cambridge Structural Database; unfortunately, only the data on the unit cell parameters are available for this modification.
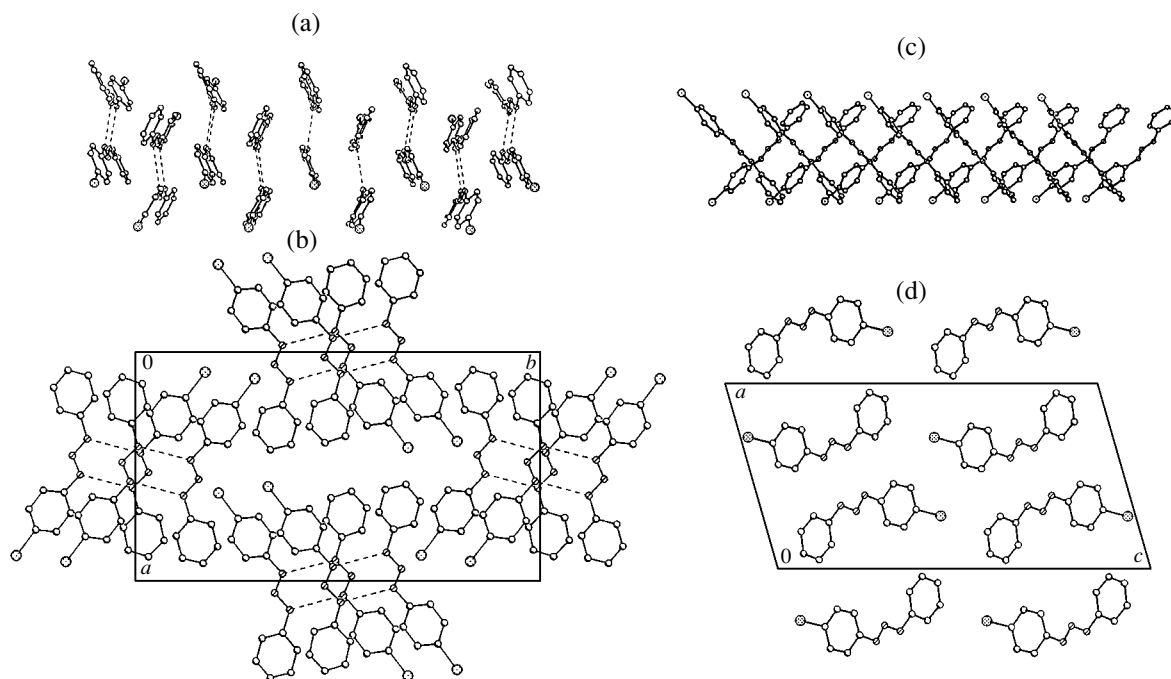
Fig. 13. (a, c) Structures of molecular chains and (b, d) projections of chain packings in the (a, b) $Pna2_1$ and (c, d) $P2_1/c$ modifications of BAAANL.
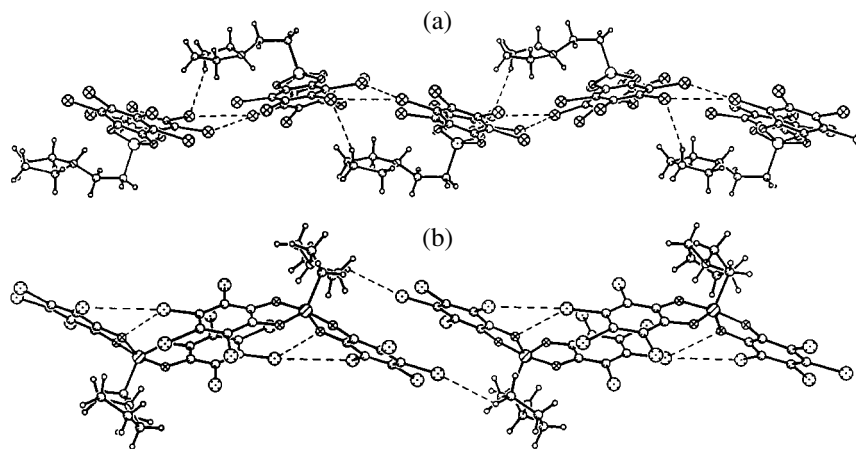
Fig. 14. Structures of molecular chains in the (a) $Pna2_1$ and (b) $P2_1/c$ modifications of PEGVAY.

modifications with conjugate rigid molecules were predominantly obtained from different solvents. The solvent nature (polarity or protonation ability) especially strongly affects the crystallization of compounds that contain active acid protons, for example, carboxylic acids. In particular, three polymorphic modifications were found for *o*-aminobenzoic acid AMBACO (see Table 3). The acentric modification ($Pna2_1$, $Z' = 2$) synthesized from the aqueous solution possesses tribolu-minescent activity, i.e., the capability of luminescing under friction. Apart from the $P2_1/c$ centric modification (prepared from the melt), there exists the centric

orthorhombic modification ($Pbca$, $Z' = 1$) produced from the aniline solution. The structures of all the modifications involve centrosymmetric dimers (Fig. 15). However, in the $Pna2_1$ modification, these dimers are pseudocentrosymmetric due to different structures of the independent molecules, which occur in the form of a neutral molecule and a zwitterion (water used for preparing this modification transfers protons). In all the modifications, dimers are involved in the formation of two-dimensional layers, which, in turn, form the crystal structure. In the $Pna2_1$ and $Pbca$ polymorphs, the crystal structures are strengthened by additional hydrogen
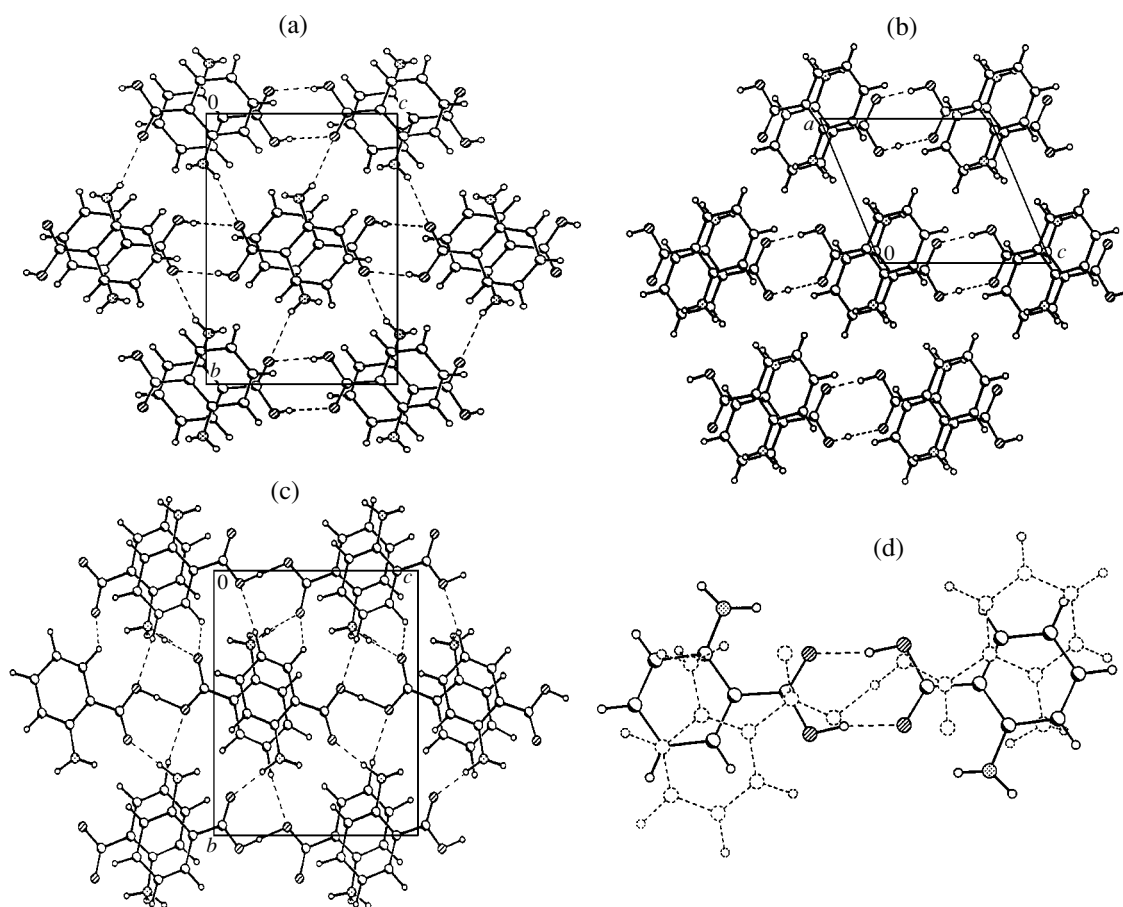
Fig. 15. Molecular packings in the (a) $Pna2_1$, (b) $P2_1/c$, and (c) $Pbca$ modifications and (d) structures of molecular dimers in the $Pna2_1$ (dashed lines) and $Pbca$ modifications of AMBACO.

bonds between layers (see Fig. 15). Furthermore, the $Pna2_1$ modification undergoes the phase transition $(Pna2_1, Z' = 2) \xrightarrow{81°C} (Pbca, Z' = 1)$. The phase transition occurs upon heating and is attended by proton migration, the displacement of the pseudocenter by $\Delta r = 0.2$ Å, and the rotation of crystallographically independent molecules with respect to each other by approximately 30° (Fig. 7). The unit cell parameters of the $Pbca$ modification are close to those of the $P2_1/a$ ($Z' = 1$) modification (in this modification, one parameter is doubled). The highest density is observed for the $Pna2_1$ modification.

In modifications of dihydroxybenzoic acid LEZ-JAB, molecules differ only in the orientation of one hydroxyl group. In the crystals precipitated from a nonpolar solvent (chloroform), the carboxyl group of dihydroxybenzoic acid is involved in the intramolecular hydrogen bond, which prevents the formation of centrosymmetric dimers typical of carboxylic acids. As a result, there arises a three-dimensional framework with $Pna2_1$ symmetry. In the crystals synthesized in polar pyridine, both hydroxyl groups of the molecule participate in the formation of intramolecular hydrogen

bonds. Hydrogen atoms of free carboxyl groups form stable centrosymmetric dimers through strong (nearly symmetric) hydrogen bonds. The CH···O weaker contacts are responsible for the formation of planar ribbons with $p_c\bar{1}$ symmetry (Fig. 16). The sole example of the same unit-cell parameters for the modifications produced from different, even if related, solvents is provided by crystals of oxonium salt of 4-methylsulfonium acid TOLSAM. In this case, salt molecules have the same structure and form layers with similar structures but different symmetries through identical systems of contacts. The packing of these layers results in the formation of crystals with different symmetries but close unit-cell parameters. At the same time, it should be noted that the modification synthesized from the water–alcohol solution is characterized by a substantially denser packing.

However, investigation into the crystallization of 5-nitro-2-thiophenecarboxaldehyde-4-methylphenylhydrazone NOJHEZ [7] revealed that the symmetry of the crystal structure depends on the crystallization kinetics rather than on the solvent polarity. It was found that a slow crystallization (through evaporation or upon con-
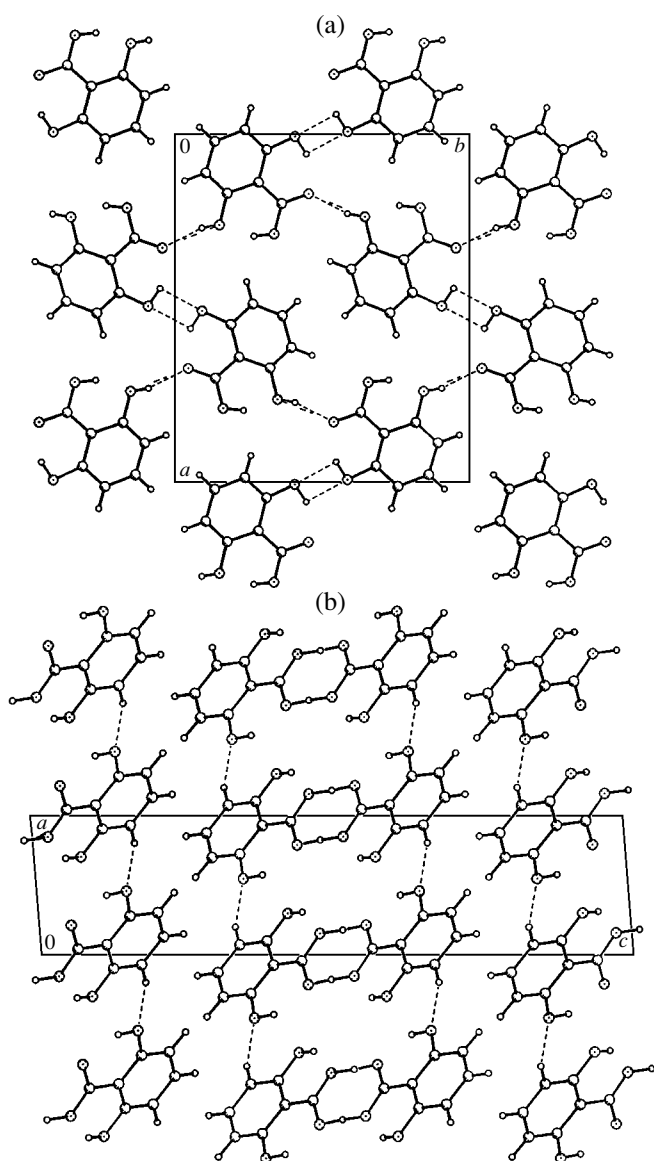
Fig. 16. Molecular packings in the (a) $Pna2_1$ and (b) $P2_1/c$ modifications of LEZJAB.

example of a systematic investigation into the polymorphism and the search for acentric modifications of hydrazone derivatives. In [7], it was also demonstrated that hydrazones rather easily form polymorphic modifications owing to the high conformational flexibility of molecules (the torsion angle between two planar molecular fragments varies from 0° to 60° in different modifications). Furthermore, it was shown that hydrazones are a very promising class of compounds due to, first, the high molecular hyperpolarizability of donor–acceptor derivatives and, second, the high probability of forming noncentrosymmetric structures (~40%). The molecular conformations in the modifications predominantly differ in the angle between the planes of the phenyl and thiophene rings: 8° in **I**, 3° in **II**, and 16° in **III**. The largest differences between the molecular geometries are observed for modifications **II** and **III**, which are produced by rapid cocrystallization. Most likely, similar differences in the geometry occur even in the solution, which is responsible for the formation of different crystal structures. It is of interest that, in the modifications prepared by rapid crystallization, molecules probably have not managed to form intermolecular hydrogen bonds. The opposite situation is observed for modification **I** prepared by slow evaporation of the solution. In this modification, chiral molecular chains are formed through the NH···N hydrogen bonds between crystallographically independent molecules. No obvious relation between the symmetry of the crystal structure and the solvent nature was revealed for the other compounds of this group.

All the three MBYINO modifications obtained under different conditions from different solvents are organic photoelectron semiconductors, irrespective of the lattice symmetry. These properties are attributed by researchers to intramolecular and intermolecular (in the case of centric modifications) charge transfer. The unit cell parameters of all the polymorphs are different, even though all the modifications have a layered packing. In the centric modifications, layers are formed by stacking contacts between antiparallel molecules, which is typical of charge-transfer organic complexes. The structure of the acentric modification is formed through stacking contacts between translational molecules. The DMFUSC compound is characterized by three modifications, namely, one monoclinic and two orthorhombic modifications. As was already noted in our earlier work [1], the modifications α($P2_1/c$, $Z' = 1$) and β($P2_12_12_1$, $Z' = 1$) were prepared by slow evaporation from the solutions in benzene and toluene. The γ($Pna2_1$, $Z' = 1$) was synthesized from a saturated cyclohexane solution. The molecular conformations are similar in all the three modifications, whereas the packing and the unit cell parameters of the γ modification differ from those of the α and β modifications. In the TALJIZ modifications (Fig. 17), despite identical systems of intermolecular hydrogen bonds, local fragments (chains) exhibit different symmetries. The structure of the centric modification is characterized by the antiparallel packing of
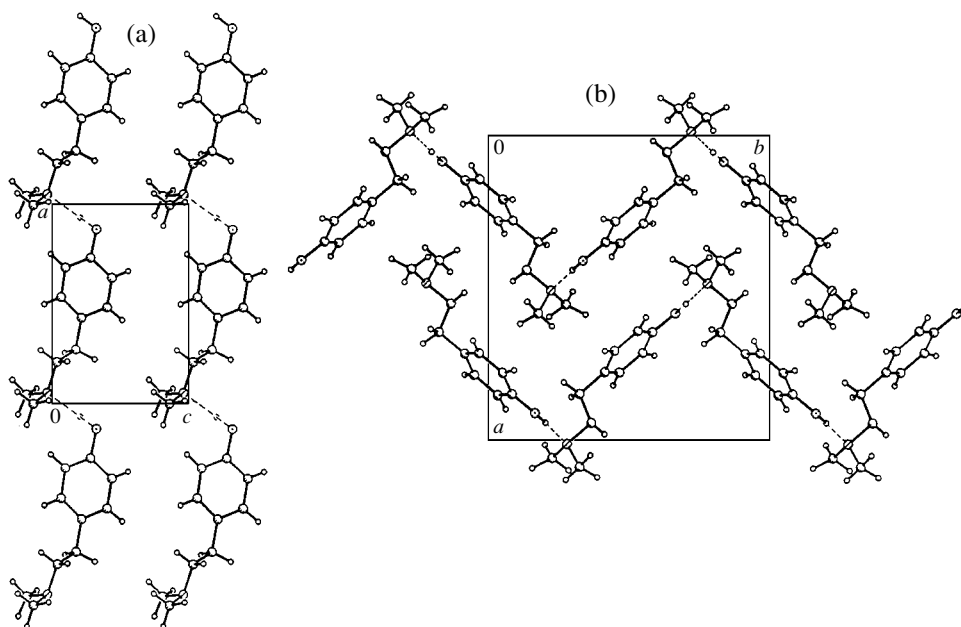
trolled cooling) from solutions in any one of the seven solvents studied leads to the growth of the $P2_1/n$ modification ($Z' = 2$) (**I**).[3] A rapid cooling of the supersaturated solutions in the same solvents results in the cocrystallization of the $Pna2_1$ modification ($Z' = 1$) (**II**) and $P2_1/n$ modification ($Z' = 1$) (**III**), which have a higher thermodynamic stability. Moreover, the crystallization in protic and aprotic solvents is accompanied by the predominant formation of modifications **III** and **II**, respectively. It should be noted that NOJHEZ is the sole compound that possesses the nonlinear optical activity in the pair of polymorphic modifications under consideration. The work performed by Pan *et al.* [7] is a rare

---

[3] The solutions used were prepared in toluene, chloroform, methanol, ethanol, ethyl formate, acetone, and acetonitrile.

Fig. 17. Packings of chains in the (a) $Pna2_1$ and (b) $P2_1/c$ modifications of TALJIZ.

chains (p_c2_1) of different chiralities. These chains are formed by the OH···N hydrogen bonds. The structure of the acentric modification is composed of chains with p_cc symmetry.

Therefore, irrespective of the method used for preparing the crystals, identical molecular associates occur in the pair of $P2_1/c–Pna2_1$ polymorphic modifications considerably more rarely as compared to those in all the pairs considered above.

CONCLUSIONS

The results of analyzing the structures of pairs of centric and acentric polymorphic modifications allowed us to make the following inferences. Although each of the studied pairs of polymorphic modifications exhibits its own specific features, these pairs, according to their basic characteristics, can be divided into two groups, namely, the centric–chiral and centric–racemic groups. In the former group (the $P2_1/c–P2_12_12_1$ and $P2_1/c–P2_1$ pairs), more than one half of the pairs are concomitant modifications and the revealed regularities manifest themselves most clearly. In this group, the most important condition for the occurrence of a pair of centric and acentric polymorphic modifications is the formation of stable chiral molecular associates with identical or very similar structures. In the cases when molecules in the polymorphs form sufficiently large-sized supramolecular fragments (layers or chains), the unit cell parameters either are close in magnitude or are multiples. In the latter group (the $P2_1/c–Pc$ and $P2_1/c–Pna2_1$ pairs), the stable molecular associates found in the polymorphs do not necessarily exhibit a chiral structure. Racemic and even pseudocentrosymmetric molecular fragments are rather commonly encountered in the acentric phase. Moreover, close unit-cell parameters are observed more rarely (especially in the $P2_1/c–Pna2_1$ pair), and the concomitant polymorphic modifications are also rare in occurrence.

REFERENCES

1. L. N. Kuleshova and M. Yu. Antipin, Kristallografiya **47** (2), 303 (2002) [Crystallogr. Rep. **47**, 268 (2002)].
2. J. Pecaut, J. P. Levi, and R. Masse, J. Mater. Chem. **3** (10), 999 (1993).
3. I. Moustakali-Mavridis and E. Hadjoudis, Mol. Cryst. Liq. Cryst. **156**, 35 (1988).
4. *Nonlinear Optical Properties of Organic Molecules and Crystals*, Ed. by D. S. Chemla and J. Zyss (Academic, New York, 1987), Vols. 1 and 2.
5. L. N. Kuleshova, V. N. Khrustalev, and M. Yu. Antipin, Kristallografiya **45** (6), 1034 (2000) [Crystallogr. Rep. **45**, 953 (2000)].
6. S. C. Abrahams, Acta Crystallogr., Sect. B: Struct. Sci. **45**, 228 (1989).
7. F. Pan, C. Bosshard, M. S. Wong, *et al.*, Chem. Mater. **9**, 1328 (1997).

Translated by O. Borovik-Romanova

STRUCTURE
OF ORGANIC COMPOUNDS

X-ray Mapping in Heterocyclic Design:
X. X-ray Diffraction Study
of 4-Methyl-6,7,8,9-Tetrahydro-2-Quinolone

D. V. Al'bov, V. B. Rybakov, E. V. Babaev, and L. A. Aslanov

Faculty of Chemistry, Moscow State University, Vorob'evy gory, Moscow, 119899 Russia
*e-mail: albov@biocryst.phys.msu.su*
Received November 18, 2002

Abstract—The structure of 4-methyl-6,7,8,9-tetrahydro-2-quinolone is studied by the single-crystal X-ray diffraction technique ($a = 6.6890(17)$ Å, $b = 7.926(2)$ Å, $c = 8.993(3)$ Å, $\alpha = 85.50(2)°$, $\beta = 68.22(2)°$, $\gamma = 82.89(2)°$, $Z = 2$, and space group $P\bar{1}$). The structure is solved by direct methods and refined to $R_1 = 0.0592$ and $wR_2 = 0.1206$. In the crystal, intermolecular hydrogen bonds link molecules into centrosymmetric dimers. © 2003 MAIK "Nauka/Interperiodica".

INTRODUCTION

This work continues our structural investigations of the heterocyclic compounds that are able to undergo various rearrangements, in particular, cyclization reactions [1–10]. As in our previous papers, we step-by-step perform the X-ray diffraction studies of all the intermediates and final products of multistage cyclization reactions and rearrangements. Substituted pyridones are interesting objects for these investigations, because they are characterized by a high reactivity. In this study, we determined the structure of 4-methyl-6,7,8,9-tetrahydro-2-quinolone. At present, data on its molecular and crystal structures are not available in the Cambridge Structural Database (Version 04.02) [11].

EXPERIMENTAL

4-Methyl-6,7,8,9-tetrahydro-2-quinolone (**I**) was synthesized according to the procedure described in [12]:

I
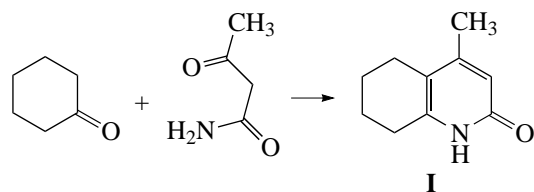
The ^{1}H NMR spectrum was recorded on a Bruker AM-360 spectrometer (field strength, 8.46 T; operating frequency, 360.14 MHz for protons; DMSO-d_6; internal standard, TMS). Based on the available data, the NMR signals were assigned as follows (δ, ppm): 11.50 (s) H(1); 5.90 (s) H(3); 2.48 (t) H(9A), H(9B); 2.34 (t) H(6A), H(6B); 2.03 (s) H(1A), H(1B), H(1C); 1.72 (m) H(7A), H (7B), H(8A), H(8B).

The intensities of diffraction reflections were measured on a CAD4 diffractometer [13] (MoK_α radiation,

graphite monochromator, ω scan mode) at room temperature. The unit cell parameters were determined and refined using 25 reflections in the θ range 13°–15°. Selected experimental parameters and crystal data are included in Table 1.

Since the crystals of the compound studied are small in size and have small linear absorption coefficients, the data were not corrected for absorption. The primary

Table 1. Crystal data and details of the X-ray diffraction experiment and refinement of structure **I**

Compound	$C_{10}H_{13}NO$
Molecular weight	163.21
Crystal system	Triclinic
Space group	$P\bar{1}$
a, Å	6.6890(17)
b, Å	7.926(2)
c, Å	8.993(3)
α, deg	85.50(2)
β, deg	68.22(2)
γ, deg	82.89(2)
V, Å^3	439.1(2)
Z	2
ρ_{calcd}, g/cm^3	1.235
$\mu(MoK_\alpha)$, cm^{-1}	0.080
Crystal size, mm	$0.30 \times 0.30 \times 0.30$
θ_{max}, deg	26
Number of reflections with $I \geq 2\sigma(I)$/number of parameters	1618/162
R_1/wR_2	0.0592/0.1206
$\Delta\rho_{max}/\Delta\rho_{min}$, e/Å^3	0.203/–0.141

Table 2. Bond lengths d (Å) for non-hydrogen atoms in structure **I**

Bond	d
N(1)–C(2)	1.3541(16)
N(1)–C(10)	1.3830(18)
C(2)–O(2)	1.2578(17)
C(2)–C(3)	1.4107(18)
C(3)–C(4)	1.374(2)
C(4)–C(5)	1.4172(18)
C(4)–C(11)	1.5122(18)
C(5)–C(10)	1.3541(17)
C(5)–C(6)	1.514(2)
C(6)–C(7)	1.503(2)
C(7)–C(8)	1.451(2)
C(8)–C(9)	1.509(2)
C(9)–C(10)	1.4754(18)

Table 3. Bond angles ω (deg) for non-hydrogen atoms in structure **I**

Angle	ω
C(2)–N(1)–C(10)	125.10(10)
O(2)–C(2)–N(1)	120.04(11)
O(2)–C(2)–C(3)	124.34(12)
N(1)–C(2)–C(3)	115.61(13)
C(4)–C(3)–C(2)	121.00(12)
C(3)–C(4)–C(5)	120.58(11)
C(3)–C(4)–C(11)	118.99(12)
C(5)–C(4)–C(11)	120.43(13)
C(10)–C(5)–C(4)	118.52(13)
C(10)–C(5)–C(6)	119.81(11)
C(4)–C(5)–C(6)	121.65(11)
C(7)–C(6)–C(5)	113.50(12)
C(8)–C(7)–C(6)	114.38(16)
C(7)–C(8)–C(9)	112.60(13)
C(10)–C(9)–C(8)	111.96(12)
C(5)–C(10)–N(1)	119.14(11)
C(5)–C(10)–C(9)	125.08(13)
N(1)–C(10)–C(9)	115.78(11)

**Table 4.** Parameters of interatomic contacts in structure **I**

| D–H	$d(D–H)$	$d(D{\cdots}A)$	$d(H{\cdots}A)$	ωDHA	A	Symmetry operation
N(1)–H(1)	0.82(1)	2.772(1)	1.96(1)	174(1)	O(2)	(2–x; 1–y; 1–z)
C(7)–H(7A)	1.07(2)	3.515(2)	2.66(2)	137(1)	O(2)	(1–x; 1–y; 1–z)
C(8)–H(8B)	0.99(2)	3.536(2)	2.58(2)	163(1)	O(2)	(x; y; z–1)
C(11)–H(11C)	0.89(2)	3.547(2)	2.81(2)	141(2)	O(2)	(x–1; y; z)

Note: D is a donor, A is an acceptor, and H is a hydrogen atom; the d distances and ω angles are given in angstroms and degrees, respectively.

processing of the experimental data was performed with the WinGX98 program package [14], and all further calculations were performed with the SHELX97 program package [15]. The crystal structure was solved by direct methods. The positional and thermal parameters were refined in the anisotropic approximation for all the non-hydrogen atoms. The hydrogen atoms were located from the difference Fourier synthesis and refined in the isotropic approximation. The interatomic distances and bond angles are listed in Tables 2 and 3, respectively. The parameters of the interatomic contacts involving the hydrogen atoms are given in Table 4. The crystal data for compound **I** are deposited in the Cambridge Structural Database (deposit no. 198666). The molecular structure of **I** and the atomic numbering are shown in the figure, which was drawn with the use of the PLUTON96 program [16].

RESULTS AND DISCUSSION

In molecule **I**, the N(1)C(2)C(3)C(4)C(5)C(10) six-membered ring is planar within 0.014 Å. The O(2), C(6), C(9), and C(11) atoms lie in the plane of this ring. The C(7) and C(8) atoms deviate from this plane by −0.236 and 0.425 Å, respectively. In crystal **I**, intermolecular hydrogen bonds link molecules into centrosymmetric dimers (figure, Table 4). In the Cambridge Structural Database (Version 04.02) [11], we found a compound with a similar structure, namely, 7,8-dihydro-7-methyl-2,5(1H,6H)-quinoline-2,5-dione (**II**) [17]

II
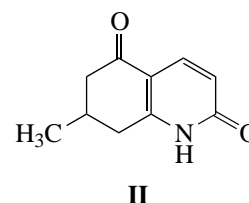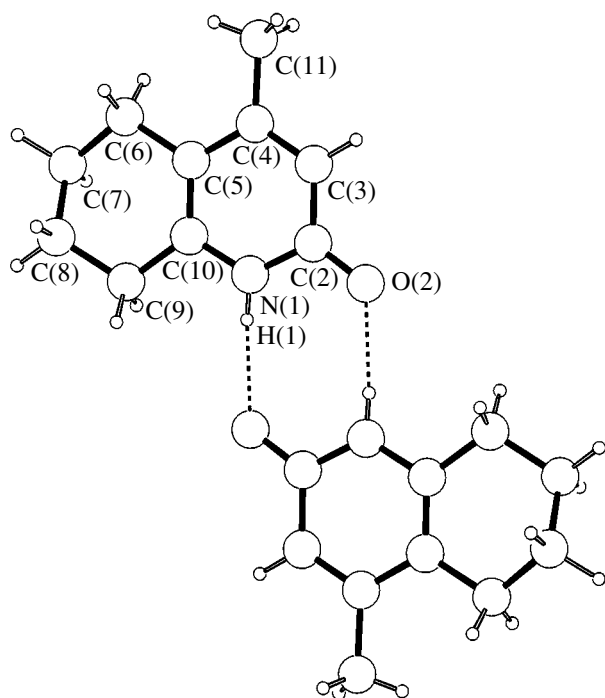
Molecular structure with the atomic numbering and formation of the centrosymmetric dimer in structure **I**.

In both structures, the ellipsoids of thermal vibrations of the C(7) and C(8) atoms (the numberings are identical; see figure) are elongated almost perpendicular to the plane of the heterocyclic system. As a consequence, the distance between the C(7) and C(8) atoms is significantly shorter [1.451(2) Å] than the C(5)–C(6), C(6)–C(7), C(8)–C(9), and C(9)–C(10) distances (Table 2). However, with allowance made for strong anisotropy of the thermal parameters [18], the C(7)–C(8) distance is 1.58 Å, which is consistent with the *sp*^{3} hybridization. The structure of the heterocyclic fragment of the bicycle in molecules **I** and **II** corresponds to the pyridone, rather than pyridol, tautomer.

The fusion of the cyclohexene and pyridone fragments in molecule **I** along the C(5)–C(10) double bond results in a slight shortening of this bond (1.354 Å) in comparison with the other double bond, namely, C(3)–C(4) (1.374 Å); that is, the carbocyclic fragment slightly contracts the bond in the adjacent heterocycle. Note that the environment of the C(5)–C(10) double bond in the bicycle includes the C(4), C(6), C(9), and N(1) atoms and has an asymmetric configuration: the C(6)–C(5)–C(4) exocyclic angle is 121.7°, whereas the C(9)–C(10)–N(1) angle is only 115.8°. This leads to a close spacing between the C(9)H$_2$ methylene fragment and the nitrogen atom, which should be considered in the analysis of the reactivity of molecule **I**. For example, in the alkylation reactions, the N(1) nitrogen atom can be considerably shielded by the C(9) methylene link.

In the coming months, we are going to study the reactivity of compound **I** and to perform X-ray structure analysis of the products obtained.

REFERENCES

1. V. B. Rybakov, S. G. Zhukov, E. V. Babaev, *et al.*, Kristallografiya **44** (6), 1067 (1999) [Crystallogr. Rep. **44**, 997 (1999)].
2. V. B. Rybakov, S. G. Zhukov, E. V. Babaev, *et al.*, Kristallografiya **45** (1), 108 (2000) [Crystallogr. Rep. **45**, 103 (2000)].
3. V. B. Rybakov, S. G. Zhukov, E. V. Babaev, *et al.*, Kristallografiya **45** (2), 292 (2000) [Crystallogr. Rep. **45**, 261 (2000)].
4. V. B. Rybakov, S. G. Zhukov, K. Yu. Pasichnichenko, and E. V. Babaev, Koord. Khim. **26** (9), 714 (2000).
5. V. B. Rybakov, S. G. Zhukov, E. V. Babaev, and E. J. Sonneveld, Kristallografiya **46** (3), 435 (2001) [Crystallogr. Rep. **46**, 385 (2001)].
6. V. B. Rybakov, S. I. Troyanov, E. V. Babaev, *et al.*, Kristallografiya **46** (5), 1069 (2001) [Crystallogr. Rep. **46**, 986 (2001)].
7. V. B. Rybakov, E. V. Babaev, K. Yu. Pasichnichenko, and E. J. Sonneveld, Kristallografiya **47** (1), 76 (2002) [Crystallogr. Rep. **47**, 69 (2002)].
8. V. B. Rybakov, E. V. Babaev, and V. V. Chernyshev, Kristallografiya **47** (3), 473 (2002) [Crystallogr. Rep. **47**, 428 (2002)].
9. V. B. Rybakov, E. V. Babaev, and K. Yu. Pasichnichenko, Kristallografiya **47** (4), 678 (2002) [Crystallogr. Rep. **47**, 622 (2002)].
10. V. B. Rybakov, E. V. Babaev, A. A. Tsisevich, *et al.*, Kristallografiya **47** (6), 1042 (2002) [Crystallogr. Rep. **47**, 973 (2002)].
11. F. H. Allen and O. Kennard, Chem. Design Autom. News **8** (1), 589 (1993).
12. T. Kato, M. Sato, M. Noda, and T. Itoh, Chem. Pharm. Bull. (Tokyo) **28**, 2244 (1980).
13. *Enraf–Nonius CAD4 Software: Version 5.0* (Enraf–Nonius, Delft, Netherlands, 1989).
14. L. J. Farrugia, *WinGX98: X-Ray Crystallographic Programs for Windows* (Univ. of Glasgow, UK, 1998).
15. G. M. Sheldrick, *SHELX97: Program for the Solution and Refinement of Crystal Structures* (Univ. of Göttingen, Germany, 1997).
16. A. L. Spek, *PLUTON96: Molecular Graphics Program* (Univ. of Utrecht, Netherlands, 1996).
17. P. Dorigo, R. M. Gaion, D. Fraccarollo, *et al.*, J. Med. Chem. **36**, 2475 (1993).
18. W. R. Busing and H. A. Levy, Acta Crystallogr. **17**, 142 (1964).

Translated by I. Polyakova

Crystal Structure of *L*-Alanine Phosphate

Yu. I. Smolin*, A. E. Lapshin*, and G. A. Pankova**

* Grebenshchikov Institute of Silicate Chemistry, Russian Academy of Sciences,
ul. Odoevskogo 24/2, St. Petersburg, 199155 Russia
e-mail: smolin@isc.nw.ru
** Institute of Macromolecular Compounds, Russian Academy of Sciences,
*Bol'shoĭ pr. 31, St. Petersburg, 199004 Russia*
Received March 13, 2002

Abstract—The crystal structure of *L*-alanine phosphate ($C_3O_2NH_7 \cdot H_3PO_4$) is determined by the single-crystal diffraction technique; $a = 11.918(1)$ Å, $b = 9.117(1)$ Å, $c = 7.285(1)$ Å, $\gamma = 104.7(1)°$, space group $P2_1$, and $Z = 4$. The amino group of the alanine is protonated by the hydrogen atom of the phosphoric acid. Pairs of $H_2PO_4^-$ hydrogen-bonded ions are packed into layers alternating with layers of alanine molecules in the crystal. No hydrogen bonds are formed immediately between the alanine molecules. © *2003 MAIK "Nauka/Interperiodica".*

The structures of β-alanine, *DL*-alanine, and sarcosine phosphates were investigated earlier in [1]. This study concentrates on the determination of the crystal structure of *L*-alanine phosphate [2], which has not yet been studied. This compound exhibits piezoelectric properties [3]. The crystals for this study were obtained by slow cooling a saturated aqueous solution of alanine and H_3PO_4 at pH < 2 in an LKB-Brommo thermostat, which operated in the temperature range between –10 and +40°C with an error of 0.5 K.

The temperature of the solution was lowered from 25 to 8°C at a rate of 1 K per day. The unit cell param-
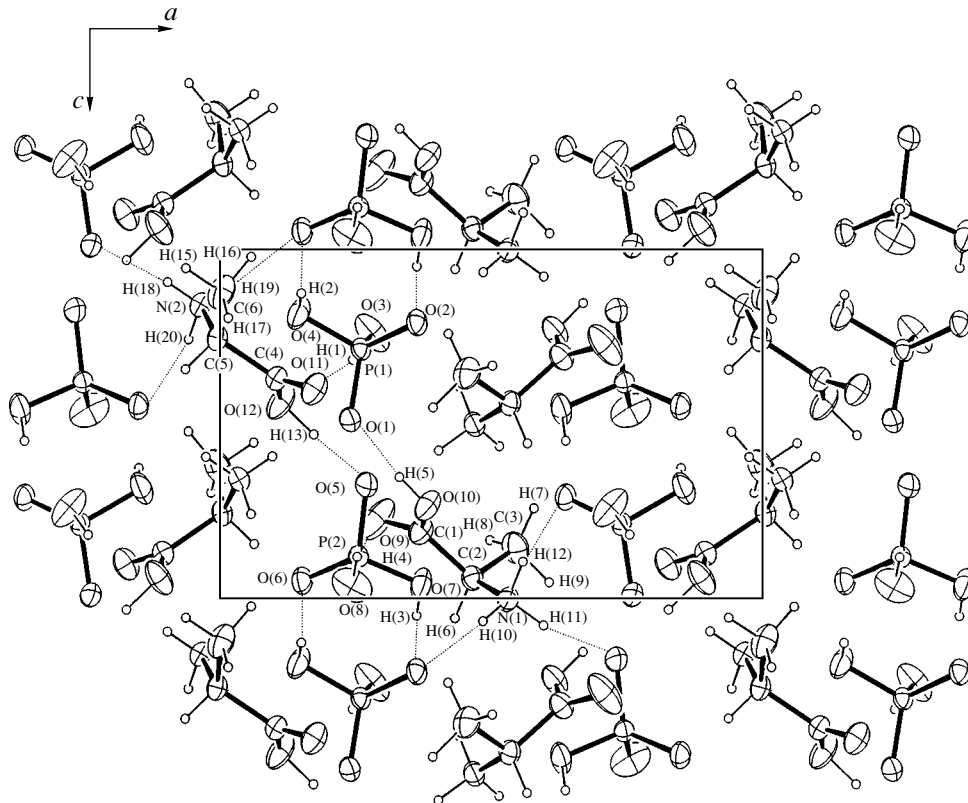
Projection of the structure along the *b* axis.

Table 1. Bond lengths d (Å) and angles ω (deg) in *L*-alanine molecules and $H_2PO_4^-$ ions

Bond	d	Angle	ω
		$H_2PO_4^-$	
P(1)–O(1)	1.497(1)	O(1)–P(1)–O(2)	115.4(1)
P(1)–O(2)	1.507(1)	O(1)–P(1)–O(3)	107.9(1)
P(1)–O(3)	1.561(1)	O(1)–P(1)–O(4)	110.3(1)
P(1)–O(4)	1.566(1)	O(2)–P(1)–O(3)	111.2(1)
		O(2)–P(1)–O(4)	105.8(1)
		O(3)–P(1)–O(4)	105.6(1)
P(2)–O(5)	1.501(1)	O(5)–P(2)–O(6)	116.1(1)
P(2)–O(6)	1.510(1)	O(5)–P(2)–O(7)	106.3(1)
P(2)–O(7)	1.562(1)	O(5)–P(2)–O(8)	110.5(1)
P(2)–O(8)	1.564(1)	O(6)–P(2)–O(7)	111.4(1)
		O(6)–P(2)–O(8)	106.4(1)
		O(7)–P(2)–O(8)	105.6(1)
		L-alanine-1	
C(1)–O(9)	1.217(1)	O(9)–C(1)–O(10)	124.4(1)
C(1)–O(10)	1.293(2)	O(9)–C(1)–C(2)	120.9(2)
C(1)–C(2)	1.522(2)	O(10)–C(1)–C(2)	114.5(1)
C(2)–N(1)	1.490(1)	C(1)–C(2)–C(3)	110.6(1)
C(2)–C(3)	1.521(2)	N(1)–C(2)–C(1)	110.6(1)
		N(1)–C(2)–C(3)	111.0(1)
		L-alanine-2	
C(4)–O(11)	1.210(1)	O(11)–C(4)–O(12)	124.2(1)
C(4)–O(12)	1.307(2)	O(11)–C(4)–C(5)	122.6(2)
C(4)–C(5)	1.524(2)	O(12)–C(4)–C(5)	113.0(1)
C(5)–N(2)	1.494(1)	C(4)–C(5)–C(6)	114.0(1)
C(5)–C(6)	1.507(2)	N(2)–C(5)–C(4)	109.6(2)
		N(2)–C(5)–C(6)	111.7(1)

eters of the crystal studied are as follows: $a = 11.918(1)$ Å, $b = 9.117(1)$ Å, $c = 7.285(1)$ Å, $\gamma = 104.7(1)°$, space group $P2_1$, and $Z = 4$. The intensities of X-ray reflections were measured on an automated single-crystal diffractometer operating in a perpendicular beam geometry with layer-by-layer recording of reflections (MoK_α radiation, pyrolytic graphite monochromator). In the index ranges $-18 \le h \le 18$, $0 \le k \le 15$, and $0 \le l \le 7$ ($2\theta_{max} = 80.27°$), 2749 nonzero unique reflections were measured, of which 2593 reflections with $I > 3\sigma(I)$ were used in further calculations.

The estimation of the integrated intensities and correction for the background were performed using an algorithm of the profile analysis [4]. The crystal stability was controlled by periodic measurements of the intensity of the reference reflection. The coordinates of the non-hydrogen atoms were determined by direct methods with the AREN program package [5]. All the hydrogen atoms were located in a series of difference Fourier syntheses alternating with the least-squares refinement of the positional and thermal parameters of the atoms with the use of the modified ORFLS program [6] and the weighting function $w = [\sigma^2(F_0) + 0.001 F_0^2]^-$. The scattering factors of the neutral atoms were used in the refinement. The thermal parameters of the non-hydrogen and hydrogen atoms were refined in the anisotropic and isotropic approximations, respectively. The final R factors have the following values: $R = 0.027$ and $wR = 0.030$ for 2593 reflections with $I > 3\sigma(I)$ and $R = wR = 0.039$ for the complete set of diffraction data. The number of the parameters refined in the structure is 286. The projection of the structure of *L*-alanine phosphate along the b axis is shown in the figure, which is drawn with the ORTEP III program [7].

The crystal data are deposited in the Cambridge Crystallographic Database (CCDC deposit no. 196194).

Table 2. Parameters of hydrogen bonds

D–H⋯A	$d(D–H)$	$d(D⋯A)$	$d(H⋯A)$	$\omega(DHA)$
O(3)–H(1)⋯O(11)[i]	.91(4)	2.658(1)	1.78(3)	161(3)
O(4)–H(2)⋯O(6)[ii]	.83(3)	2.604(2)	1.79(3)	163(2)
O(7)–H(3)⋯O(2)[iii]	.91(4)	2.592(2)	1.67(4)	173(5)
O(8)–H(4)⋯O(9)[iv]	.90(4)	2.628(2)	1.74(4)	164(3)
O(10)–H(5)⋯O(1)	.84(3)	2.512(2)	1.70(3)	159(5)
O(12)–H(13)⋯O(5)	.97(3)	2.507(2)	1.53(3)	175(5)
N(1)–H(10)⋯O(2)[iii]	.87(3)	2.911(1)	2.04(3)	173(3)
N(1)–H(11)⋯O(5)[v]	.99(4)	2.782(1)	1.80(3)	169(2)
N(1)–H(12)⋯O(2)[v]	.99(3)	2.904(1)	1.91(3)	170(2)
N(2)–H(18)⋯O(1)[vi]	.86(3)	2.756(1)	1.90(3)	168(3)
N(2)–H(19)⋯O(6)[ii]	.91(3)	2.918(1)	2.00(3)	176(3)
N(2)–H(20)⋯O(6)[vi]	.99(3)	2.883(1)	1.93(3)	157(4)

Note: D is a donor, A is an acceptor, and H is a hydrogen atom (distances d and angles ω are expressed in angstroms and degrees, respectively). The symmetry codes are as follows: [i] x, $y - 1$, z; [ii] x, y, $z - 1$; [iii] x, y, $1 + z$; [iv] x, $1 + y$, z; [v] $1 - x$, $1 - y$, $1/2 + z$; [vi] $-x$, $1 - y$, $z - 1/2$.

As is obvious from the figure, the amino group of the alanine is protonated by the hydrogen atom of the phosphoric acid. The $H_2PO_4^-$ ions are linked by two strong hydrogen bonds in pairs and form layers parallel to the *bc* plane. These negatively charged layers alternate with layers formed of the protonated alanine molecules. The interatomic distances and angles in the alanine molecules and $H_2PO_4^-$ ions are included in Table 1. The $H_2PO_4^-$ ion has a distorted tetrahedral structure, because the P–OH bonds are significantly longer than the P–O bonds. Note that, although two alanine molecules and two $H_2PO_4^-$ ions are symmetrically independent, the corresponding bond lengths and angles have very close values. A noticeable difference is observed only in the torsion angles of two molecules. For example, the O(9)–C(1)–C(2)–C(3) and O(11)–C(4)–C(5)–C(6) torsion angles are 73.5(2)° and 23.7(2)°, respectively. These angles are apparently determined by the interactions between the methyl group and its environment, which is different for the two molecules. The Flack parameter, which is equal to –0.0415, confirms the validity of the configuration described above.

The bond lengths and angles in the alanine molecules agree well with the values reported earlier in [8].

Three hydrogen atoms of the NH_3 group are bound to three oxygen atoms of three different phosphate groups situated in the neighboring layers. The hydroxyl groups of the alanine molecules are also included in the hydrogen-bond system. Thus, in addition to the electrostatic interactions, the structural units are linked by the extended hydrogen-bond system. The geometry of the hydrogen bonds is represented in Table 2. Note that there are no hydrogen bonds immediately between the alanine molecules.

ACKNOWLEDGMENTS

REFERENCES

1. M. T. Averbuch-Pouchot, A. Durif, and J. C. Guite, Acta Crystallogr., Sect. C: Cryst. Struct. Commun. **44**, 1968 (1988).
2. F. H. Allen and O. Kennard, Chem. Design Automat. News **8** (1), 589 (1993) (Version 5.23).
3. V. V. Lemanov, S. N. Popov, and G. A. Pankova, Fiz. Tverd. Tela (St. Petersburg) **44** (2002) [Phys. Solid State **44** (2002)] (in press).
4. S. Oatley and S. French, Acta Crystallogr., Sect. A: Cryst. Phys., Diffr., Theor. Gen. Crystallogr. **38**, 537 (1982).
5. V. N. Andrianov, Kristallografiya **32** (1), 228 (1987) [Sov. Phys. Crystallogr. **32**, 130 (1987)].
6. W. R. Busing, K. O. Martin, and H. A. Levy, *Report ORNL-TM-305* (Oak Ridge Natl. Lab., 1962).
7. M. N. Burnett and C. K. Johnson, *ORTEP III: Report ORNL-6895* (Oak Ridge Natl. Lab., Tennessee, 1996).
8. H. J. Simpson and R. E. Marsh, Acta Crystallogr. **20** (4), 550 (1966).

Translated by I. Polyakova

STRUCTURE
OF ORGANIC COMPOUNDS

X-ray Structure Analysis
of 4-Cyano-4'-*n*-Undecyloxybiphenyl[1]

Rajnikant*, V. K. Gupta*, Dinesh*, A. Kumar*, and B. Varghese**

* Crystallography Laboratory, Post-Graduate Department of Physics,
University of Jammu, Jammu Tawi, 180006 India
e-mail: rajni_kant_verma@hotmail.com
** Regional Sophisticated Instrumentation Center, Indian Institute of Technology,
Chennai, 600036 India
Received April 17, 2001; in final form, September 3, 2001

Abstract—The structure of a liquid crystal of 4-cyano-4'-*n*-undecyloxybiphenyl ($C_{24}H_{31}NO$) is determined by X-ray diffraction. The compound crystallizes in the monoclinic crystal system (space group $C2/c$) with the unit cell parameters $a = 84.108(7)$ Å, $b = 7.159(2)$ Å, $c = 6.922(2)$ Å, and $\beta = 91.6(4)°$. The structure has been solved by direct methods and refined to the residual index $R_1 = 0.067$. Both phenyl rings are almost planar, and the dihedral angle between these rings is $31.5(6)°$. © 2003 MAIK "Nauka/Interperiodica".

INTRODUCTION

Biphenyl and its derivatives have been studied extensively in the past because of the difference found in the exocyclic torsion angles in the solid state [1–3] and in the gas phase [4, 5]. This has entailed extended studies of the molecular geometry, crystal packing, and thermal motion effects [6–9]. In continuation of our work on crystallization and preparation of biphenyl single crystals of X-ray diffraction quality with the use of solvent-loss and vapor diffusion techniques [10–18], the present paper reports the three-dimensional molecular and crystal structures of 4–cyano-4'-*n*-undecyloxybiphenyl determined by X-ray diffraction.

EXPERIMENTAL

Single crystals of 4-cyano-4'-*n*-undecyloxybiphenyl of X-ray diffraction quality were obtained by the vapor-precipitation technique using dimethylformamide and cyclohexane as solvent systems.

A three-dimensional set of X-ray diffraction data for a pale yellow platelike crystal ($0.40 \times 0.25 \times 0.15$ mm) were collected on an Enraf–Nonius CAD4 diffractometer (CuK_α radiation). The accurate unit-cell dimensions and orientation matrix were obtained by a least-squares fit to the setting angles for 25 reflections. The $\omega/2\theta$ scan mode was employed for intensity data collection. A total of 3509 reflections were collected ($-99 \le h \le 100$, $-4 \le k \le 8$, $-4 \le l \le 8$). One standard reflection measured every hour showed no variation in the intensity data. The reflection data were corrected for Lorentz and polarization effects. Absorption and extinction corrections were not applied.

The crystal structure has been solved by direct methods with the SHELXS97 software package [19] and refined by using the SHELXL97 software package [20]. The atomic scattering factors were taken from the *International Tables for Crystallography* [21]. All the

Table 1. Crystal data and details of X-ray diffraction experiment and structure refinement

Chemical formula	$C_{24}H_{31}NO$
Molecular weight	349.5
Crystal system	Monoclinic
Space group	$C2/c$
a, α (Å, deg)	84.11(7), 90.0
b, β (Å, deg)	7.159(2), 91.63(4)
c, γ (Å, deg)	6.9223(19), 90.0
V (Å^3)	4166(4)
Z	8
ρ_{calcd}, g/cm^3	1.114
μ(CuK_α), cm^{-1}	0.510
Crystal size, mm	$0.15 \times 0.25 \times 0.40$
θ_{max}, deg	68.00
Number of unique reflections	3510 ($R_{int} = 0.0435$)
Number of reflections in L.S. with $I \ge 2\sigma(I)$	3510/360
$GOOF$ (F^2)	0.977
R_1/wR_2	0.0672/0.1929
Extinction	0.00021(11)
$\Delta\rho_{max}/\Delta\rho_{min}$, e/Å^3	0.270/−0.270

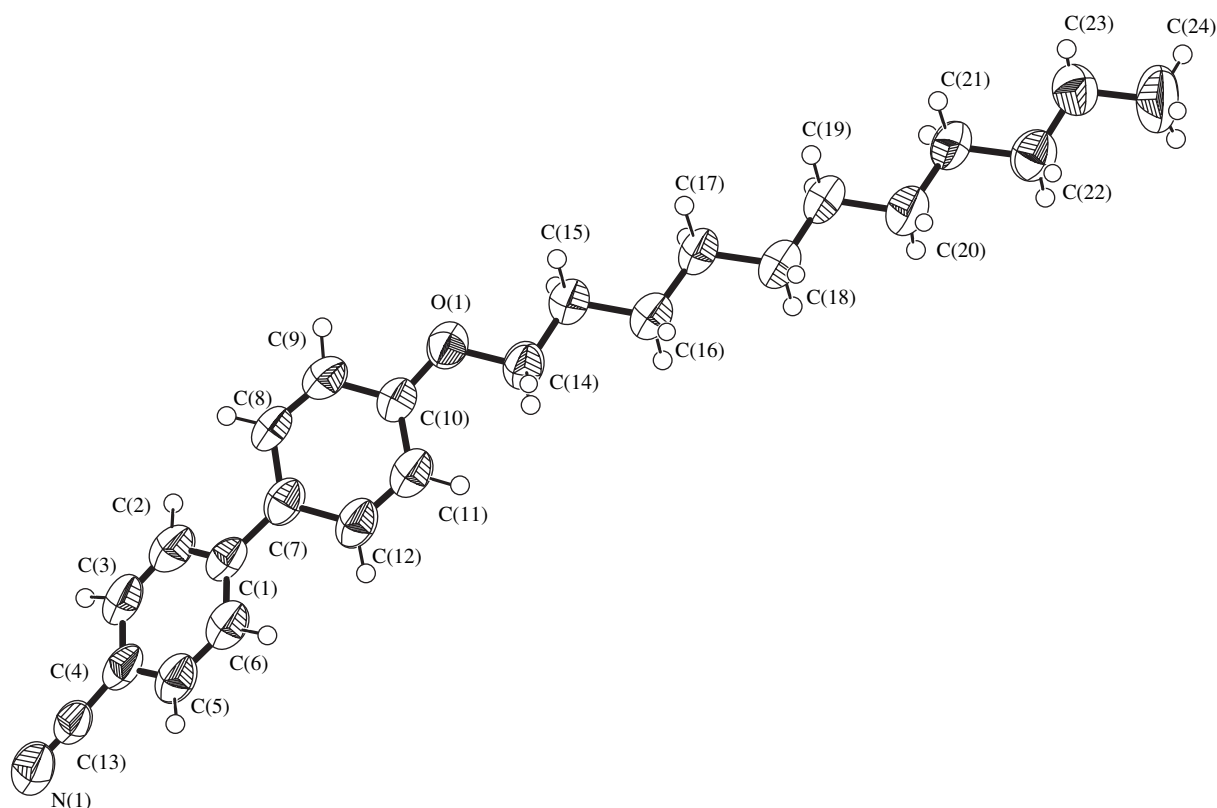[1] This article was submitted by authors in English.

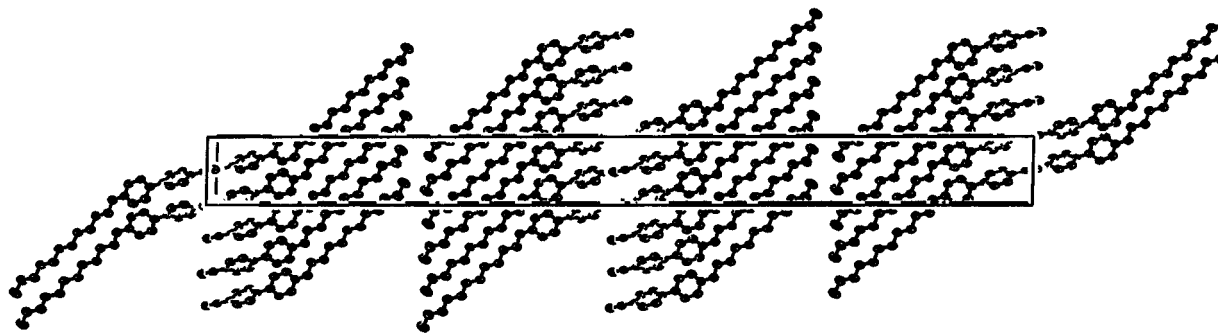**Fig. 1.** A general view of the molecule and the atomic numbering.

Fig. 2. Packing of the molecule.

hydrogen atoms were located from the difference Fourier map, and their positions and isotropic temperature factors were refined. The crystal data are presented in Table 1. Information on this crystal structure (CIF) has been deposited (CCDC [22], deposit no. 196013). The general view of the molecule with the atomic numbering is shown in Fig. 1. The molecular packing is shown in Fig. 2 and designed using the ORTEP-3 program [23]. Bond lengths and angles are listed in Tables 2 and 3, respectively. The geometrical calculations were performed using the PARST program [24].

RESULTS AND DISCUSSION

The average bond lengths for both phenyl rings are in good agreement with those obtained in analogous structures [10–17, 25, 26]. The $C(13) \equiv N(1)$ bond length [1.143(1) Å] is slightly less than its standard value [27]. The four endocyclic angles at the C(1), C(4), C(7), and C(10) atoms are significantly smaller than ideal angle of 120.0° [117.4(2)°, 117.4(1)°, 116.0(1)°, and 118.9(1)°] but similar to those found in related compounds [10–17, 25, 26]. The length of the C(1)–C(7) bond between two phenyl rings [1.479(2) Å]

Table 2. Interatomic distances d (Å) in the structure studied

Bond	d	Bond	d
O(1)–C(10)	1.351(3)	C(9)–C(10)	1.411(3)
O(1)–C(14)	1.436(3)	C(10)–C(11)	1.377(4)
N(1)–C(13)	1.142(3)	C(11)–C(12)	1.358(4)
C(1)–C(6)	1.390(3)	C(14)–C(15)	1.484(4)
C(1)–C(2)	1.403(3)	C(15)–C(16)	1.522(4)
C(1)–C(7)	1.477(4)	C(16)–C(17)	1.517(4)
C(2)–C(3)	1.362(4)	C(17)–C(18)	1.522(3)
C(3)–C(4)	1.399(4)	C(18)–C(19)	1.506(5)
C(4)–C(5)	1.399(3)	C(19)–C(20)	1.528(4)
C(4)–C(13)	1.419(4)	C(20)–C(21)	1.515(5)
C(5)–C(6)	1.359(4)	C(21)–C(22)	1.516(4)
C(7)–C(8)	1.397(4)	C(22)–C(23)	1.508(6)
C(7)–C(12)	1.406(3)	C(23)–C(24)	1.509(5)
C(8)–C(9)	1.353(4)		

Table 3. Bond angles ω (deg) in the structure studied

Angle	ω	Angle	ω
C(10)–O(1)–C(14)	117.6(2)	C(6)–C(1)–C(2)	116.9(3)
C(6)–C(1)–C(7)	121.9(2)	C(2)–C(1)–C(7)	121.1(2)
C(3)–C(2)–C(1)	121.4(3)	C(2)–C(3)–C(4)	121.3(2)
C(5)–C(4)–C(3)	117.2(3)	C(5)–C(4)–C(13)	120.4(2)
C(3)–C(4)–C(13)	122.4(2)	C(6)–C(5)–C(4)	121.1(2)
C(5)–C(6)–C(1)	122.0(2)	C(8)–C(7)–C(12)	116.0(3)
C(8)–C(7)–C(1)	123.3(2)	C(12)–C(7)–C(1)	120.7(2)
C(9)–C(8)–C(7)	122.5(2)	C(8)–C(9)–C(10)	120.0(2)
C(1)–C(10)–C(11)	125.7(2)	O(1)–C(10)–C(19)	115.5(2)
C(11)–C(10)–C(9)	118.8(3)	C(12)–C(11)–C(10)	120.3(2)
C(11)–C(12)–C(7)	122.4(3)	N(1)–C(13)–C(4)	178.9(2)
O(1)–C(14)–C(15)	108.3(2)	C(14)–C(15)–C(16)	112.6(2)
C(17)–C(16)–C(15)	113.2(2)	C(16)–C(17)–C(18)	114.3(2)
C(19)–C(18)–C(17)	113.5(2)	C(18)–C(19)–C(20)	113.8(2)
C(21)–C(20)–C(19)	113.3(3)	C(20)–C(21)–C(22)	113.8(3)
C(23)–C(22)–C(21)	112.8(2)	C(22)–C(23)–C(24)	112.7(4)

is quite close to the standard value for a single bond between the trigonally linked carbon atoms [28]. The bond angles in both phenyl rings have normal values. The dihedral angle between the two phenyl rings is 31.5(6)°. In view of the *a* parameter having an exceptionally large value, the molecular packing along the *b* axis shows the manner in which molecules have lined themselves up and appear to be extending diagonally across the *ac* plane. The molecules are stacked in reversed orientations.

ACKNOWLEDGMENTS

REFERENCES

1. A. Hargreaves and S. H. Rizvi, Acta Crystallogr. **15**, 365 (1962).
2. G. P. Charbonneau and Y. Delugeard, Acta Crystallogr., Sect. B: Struct. Crystallogr. Cryst. Chem. **32**, 1420 (1976).
3. G. P. Charbonneau and Y. Delugeard, Acta Crystallogr., Sect. C: Cryst. Struct. Commun **33**, 1586 (1977).
4. A. Almenningen and O. Bastianssen, K. Nor. Vidensk. Selsk. Skr. **4**, 1 (1958).
5. O. Bastianssen and M. Traetteberg, Tetrahedron **17**, 147 (1962).
6. C. P. Brock and K. L. Haller, J. Phys. Chem. **88**, 3570 (1984).
7. C. P. Brock and K. L. Haller, Acta Crystallogr., Sect. C: Cryst. Struct. Commun. **40**, 1387 (1984).
8. C. P. Brock and G. L. Morelan, J. Phys. Chem. **90**, 5631 (1986).
9. C. P. Brock and R. P. Minton, J. Am. Chem. Soc. **111**, 4586 (1989).
10. Rajnikant, D. Watkin, and G. Tranter, Acta Crystallogr., Sect. C: Cryst. Struct. Commun. **51**, 2388 (1995).
11. Rajnikant, D. Watkin, and G. Tranter, Acta Crystallogr., Sect. C: Cryst. Struct. Commun. **51**, 1452 (1995).
12. Rajnikant, D. Watkin, and G. Tranter, Acta Crystallogr., Sect. C: Cryst. Struct. Commun. **51**, 2071 (1995).
13. Rajnikant, D. Watkin, and G. Tranter, Acta Crystallogr., Sect. C: Cryst. Struct. Commun. **51**, 2161 (1995).
14. Rajnikant, V. K. Gupta, R. Gupta, *et al.*, Mol. Mater. **11**, 165 (1999).
15. Rajnikant, V. K. Gupta, A. Kumar, *et al.*, Mol. Cryst. Liq. Cryst. **333**, 237 (1999).
16. Rajnikant, V. K. Gupta, R. Gupta, and A. Kumar, Asian J. Phys. **8**, 89 (1999).
17. Rajnikant, V. K. Gupta, R. Gupta, *et al.*, Kristallografiya **45** (1), 98 (2000) [Crystallogr. Rep. **45**, 98 (2000)].
18. Rajnikant, V. K. Gupta, Dinesh, *et al.*, Mol. Cryst. Liq. Cryst. Commun. (2002) (in press).

19. G. M. Sheldrick, *SHELXS97. Program for the Solution of Crystal Structure* (Univ. of Göttingen, Germany, 1997).

20. G. M. Sheldrick, *SHELXL97. Program for the Refinement of Crystal Structures* (Univ. of Göttingen, Germany, 1997).

21. *International Tables for Crystallography* (1992), Vol. C, Tables 4.2.6.8 and 6.1.1.4.

22. F. H. Allen and O. Kennard, Chem. Design Autom. News **8** (1), 31 (1993).

23. L. J. Farrugia, J. Appl. Crystallogr. **30**, 565 (1997).

24. M. Nardelli, Comput. Chem. **7**, 95 (1993).

25. M. Nieger, H. Hupper, and M. Bolte, Acta Crystallogr., Sect. C: Cryst. Struct. Commun. **54**, 656 (1998).

26. A. Sekine and Y. Ohashi, Acta Crystallogr., Sect. C: Cryst. Struct. Commun. **50**, 1101 (1994).

27. H. H. Sutherland and M. J. Mottram, Acta Crystallogr., Sect. B: Struct. Crystallogr. Cryst. Chem. **28**, 2212 (1972).

28. D. W. J. Cruckshank and R. A. Sparks, Proc. R. Soc. London, Ser. A **258**, 270 (1960).

LATTICE DYNAMICS
AND PHASE TRANSITIONS

Interlayer for Matching Crystal Lattices in the Domain Walls of Ferroelastic Lead Orthophosphate

V. A. Nepochatenko

Bila Tserkva State Agrarian University, Ukraine
e-mail: aaa@btsau.kiev.ua
Received March 4, 2002

Abstract—The possible existence of an interlayer with the symmetry of the paraphase in the W and W' domain walls of lead orthophosphate has been checked from the condition of matching the crystal lattices of adjacent domains. It is shown that two types of interlayers are possible, which possess different symmetries, strain tensors, matrices of the rotation of the coordinate system, thicknesses, and elastic energies. It is shown that the domain-wall energy is proportional to the squared spontaneous deformation. © *2003 MAIK "Nauka/Interperiodica".*

INTRODUCTION

The domain structure of crystals undergoing phase transitions is considered in numerous experimental and theoretical studies. However, the acting twinning mechanism is not clear. In this connection, the "pure" ferroelastics are the simplest objects for studying the structural changes associated with the formation of domain walls.

Below, we consider a model of an equilibrium domain wall for crystals possessing a ferroelastic monoclinic phase using lead orthophosphate as an example.

Lead orthophosphate $Pb_3(PO_4)_2$ belongs to the class of pure improper ferroelastics [1]. This crystal undergoes a first-order ferroelactic phase transition from the rhombohedral β-phase to the monoclinic α-phase at 180°C [2, 3]. In the ferroelastic phase, three types of domains and two types of domain walls, W and W', are formed [4, 5]. The W domain wall is almost normal to the (100) plane of the monoclinic phase, and W' forms an angle of ~73° with it. The orientation of the domain walls is consistent (within 1°) with the equations obtained from the condition of consistency of spontaneous deformation in a domain wall [6].

It is well known that the temperature variation gives rise to the rotation of the crystallographic axes in adjacent domains in ferroelastics with the rotation angle being dependent on the spontaneous deformation [7–9]. Such a behavior of the crystallographic axes cannot be explained in the frameworks of continuous approach [6].

The equations of the phase boundaries are obtained from the condition of matching the crystal lattices of both phases of $Pb_3(PO_4)_2$ [10]. It is also shown that in the first-order phase transition, the rotation of the crystallographic axes is proportional to the change in the parameters of one phase relative to the other.

Since the crystal lattices of the adjacent domains show no matching, then, taking into account the aforesaid, we can assume the existence of an induced phase (interlayer) that should promote lattice matching and also of adjacent domains between the interlayer and the α phase, i.e., the occurrence of a first-order phase transition.

Consider this model in two stages: first, determine the parameters and symmetry of the interlayer in the W' and W domain walls at room temperature ($t = 20$°C), and then perform analogous calculations in the vicinity of the phase transition in order to establish the temperature dependence of the domain-wall energy.

Since the lattice can be matched only if certain symmetry elements of the paraphase are present, the interlayer symmetry is no lower than monoclinic. Therefore, we describe all the phases using the parameters of the monoclinic system. Denote the parameters of the β-phase near the phase transition by a_0, b_0, c_0, and $β_0$; those of the α-phase, by a_1, b_1, c_1, and $β_1$; the parameters of the interlayer, by a_2, b_2, c_2, and $β_2$; and those of the orientational states, by C_1, C_2, C_3. The X axis of the chosen orthogonal coordinate system is parallel to c, the Y axis is parallel to b, and the Z axis forms the angle $φ = β - 90$° with a.

STRUCTURE OF THE DOMAIN WALL W'

Since a domain wall is the reversible first-order phase transition, the interlayer "matches" the adjacent orientation states with the aid of two phase boundaries that have the orientation of the domain wall. According to [10], the equation of the phase boundary matching two monoclinic unit-cells with the parameters a_1, b_1, c_1, $φ_1 = β_1 - 90$° and a_2, b_2, c_2, $φ_2 = β_2 - 90$° in the coordi-

nate system of the first phase has the following form:

$$A_{11}x_1^2 + A_{22}y_1^2 + A_{33}z_1^2 + 2A_{13}x_1z_1 = 0, \qquad (1)$$

where $A_{11} = 1 - \left(\dfrac{c_2}{c_1}\right)^2$, $A_{22} = 1 - \left(\dfrac{b_2}{b_1}\right)^2$, $A_{13} =$

$-\dfrac{c_2}{c_1\cos\varphi_1}\left(\dfrac{c_2}{c_1}\sin\varphi_1 - \dfrac{a_2}{a_1}\sin\varphi_2\right)$, $A_{33} = 1 -$

$\dfrac{1}{\cos^2\varphi_1}\left(\left(\dfrac{a_2}{a_1}\right)^2\cos^2\varphi_2 + \left(\dfrac{c_2}{c_1}\sin\varphi_1 - \dfrac{a_2}{a_1}\sin\varphi_2\right)^2\right)$; in the

coordinate system of the second phase, it is

$$B_{11}x_2^2 + B_{22}y_2^2 + B_{33}z_2^2 + 2B_{13}x_2z_2 = 0, \qquad (2)$$

where $B_{11} = 1 - \left(\dfrac{c_1}{c_2}\right)^2$, $B_{22} = 1 - \left(\dfrac{b_1}{b_2}\right)^2$, $B_{13} =$

$-\dfrac{c_1}{c_2\cos\varphi_2}\left(\dfrac{c_1}{c_2}\sin\varphi_2 - \dfrac{a_1}{a_2}\sin\varphi_1\right)$, $B_{33} = 1 -$

$\dfrac{1}{\cos^2\varphi_2}\left(\left(\dfrac{a_1}{a_2}\right)^2\cos^2\varphi_1 + \left(\dfrac{c_1}{c_2}\sin\varphi_2 - \dfrac{a_1}{a_2}\sin\varphi_1\right)^2\right)$.

Under the condition

$$\det\|A_{ij}\| = 0. \qquad (3)$$

Equation (1) corresponds to the equation of two intersecting planes [10]

$$(x + By + Cz)(x - By + Cz) = 0, \qquad (4)$$

where $B = \sqrt{-D_{22}}$; $D_{22} = A_{22}/A_{11}$; $C = D_{13} = A_{13}/A_{11}$. From the experimental data [7, 8], one can obtain the equation of the W' domain wall separating C_1 and C_2 in the coordinate system of the α-phase:

$$x_1 + A_2y_1 + A_3z_1 = 0, \qquad (5)$$

where $A_2 = 1.6643$; $A_3 = -0.59355$.

Since the phase boundary possesses the orientation of the domain wall, one of two possible conditions (4) coincides with (5), i.e.,

$$\sqrt{-D_{22}} = A_2, \qquad (6)$$

$$D_{13} = A_3. \qquad (7)$$

Equations (3), (6), and (7) form a system of three equations with four unknowns. It can be shown that it has numerous solutions. Impose an additional constraint: the interlayer has the symmetry of the paraphase. In the chosen coordinate system, the tensor of spontaneous deformation has the form [11]

$$e^s = \begin{pmatrix} e_{11}^s & 0 & e_{13}^s \\ & -e_{11}^s & 0 \\ & & 0 \end{pmatrix},$$

where $e_{11}^s = 0.5(e_{11} - e_{22})$, $e_{11} = (c_2 - c_0)/c_0$, $e_{22} = (b_2 - b_0)/b_0$, $e_{13}^s = (c_2 + 3a_2\cos\beta_2)/(6a_2\sin\beta_2)$. Hence,

$$e_{11}^s = 0, \qquad (8)$$

$$e_{13}^s = 0. \qquad (9)$$

Since the unambiguous solution of the system requires one more equation, we search for an interlayer satisfying condition (8). We arrive at the following system of equations:

$$\begin{cases} \sqrt{-D_{22}} = A_2 \\ D_{13} = A_3 \\ \det\|A_{ij}\| = 0 \\ e_{11} = e_{22}. \end{cases} \qquad (10)$$

Solving this system, we obtain

$$b_2 = b_1\sqrt{(1 + A_2^2)/(1 + A_2^2F^2)}, \qquad (11)$$

$$c_2 = c_1b_2F/b_1, \qquad (12)$$

$$\tan\varphi_2 = (A_3(1 - c^2) + c^2\tan\varphi_1)/c\sqrt{P}, \qquad (13)$$

$$a_2 = a_1\cos\varphi_1\sqrt{P}/\cos\varphi_2, \qquad (14)$$

where $F = \dfrac{b_1c_0}{b_0c_1}$, $c = \dfrac{c_2}{c_1}$, $P = 1 - \dfrac{A_3^2(1 - c^2)}{c^2}$.

Substituting the corresponding crystal-lattice parameters of the α- and β-phases from [12] into the solution, we obtain the interlayer parameters; then, using these data we obtain the deformation tensors P_1' in the coordinate system of the α-phase and D_1' in the coordinate system of the β-phase (see table). As is seen from P_1', $e_{13} = -1.66 \times 10^{-4}$. Since this value lies within the experimental error, condition (9) should be fulfilled, and the interlayer has the symmetry of the paraphase.

Substituting the interlayer parameters into (2), we obtain the equation of the domain wall in the coordinate system of the interlayer:

$$x_2 + 1.73832y_2 - 0.58141z_2 = 0. \qquad (15)$$

Within the accuracy 0.08°, this equation corresponds to the orientation of W' along the twofold axis of the β-phase lost in the phase transition, which is consistent with [1].

Since the equations of the domain-wall plane are known in two coordinate systems, [(5) and (15)], we can determine the rotation matrix T_1' in the transition from the β- to the α-phase [13] (see table).

Solving the analogous problem for the adjacent orientation state C_2, we obtain an interlayer similar to the

Parameters of interlayers in the domain walls W' и W

t, °C		Domain wall W'		Domain wall W
20	a_2, Å	13.8973	a_2, Å	13.824
	b_2, Å	5.5128	b_2, Å	5.6341
	c_2, Å	9.5482	c_2, Å	9.7583
	β_2, deg	103.2582	β_2, deg	102.9034
	P', 10^{-3}	$\begin{pmatrix} -5.8126 & 0 & -0.166 \\ & -5.8126 & 0 \\ & & -1.1 \end{pmatrix}$	P, 10^{-3}	$\begin{pmatrix} 16.066 & 0 & 6.153 \\ & 16.066 & 0 \\ & & -4.96 \end{pmatrix}$
	D', 10^{-3}	$\begin{pmatrix} 11.245 & 0 & -6.565 \\ & -31.828 & 0 \\ & & 3.889 \end{pmatrix}$	D, 10^{-3}	$\begin{pmatrix} 33.499 & 0 & -0.246 \\ & -10.523 & 0 \\ & & 0.006 \end{pmatrix}$
	T'_1	$\begin{pmatrix} 0.9998 & -0.0175 & -0.002 \\ 0.0174 & 0.9997 & -0.014 \\ 0.0022 & 0.0138 & 0.9999 \end{pmatrix}$	T_1	$\begin{pmatrix} 0.9998 & 0.0187 & -0.0105 \\ -0.0186 & 0.9998 & 0.0062 \\ 0.0106 & -0.006 & 0.99992 \end{pmatrix}$
	T'_2	$\begin{pmatrix} 0.9998 & 0.0175 & -0.002 \\ -0.0174 & 0.9997 & 0.014 \\ 0.0022 & -0.0138 & 0.9999 \end{pmatrix}$	T_2	$\begin{pmatrix} 0.9998 & -0.0187 & -0.0105 \\ 0.0186 & 0.9998 & -0.0062 \\ 0.0106 & 0.006 & 0.99992 \end{pmatrix}$
	E', J/m^2	3.7596	E', J/m^2	13.3205
	E'_s, J/m^2	7861	E_s, J/m^2	27 851
180	E', J/m^2	0.09029	E', J/m^2	0.3018
	E'_s, J/m^2	7917	E_s, J/m^2	26464

previous one but rotated via an angle of 120° around the Z axis of the β-phase.

Thus, with due regard for the symmetry, these interlayers are similar and one common interlayer matches the crystal lattices of the adjacent domains: so-called P-twinning.

Consider the criterion of choosing the domain-wall thickness. Since the energy of the ferroelastic domain walls increases with an increase in the interlayer thickness, the thickness d was taken to be the shortest distance between two parallel phase boundaries that limit, with due regard for the orientation, one unit cell ($d \approx$ 20 Å).

The surface density of the elastic energy was evaluated by the formula

$$E = \frac{d}{2}c_{ijkl}e_{ij}e_{kl}, \tag{16}$$

where d is the wall thickness, e_{ij} are the components of the deformation tensor D'_1, and c_{ijkl} are the elastic constants [14, 15]. As is seen, this value is comparable (by

an order of magnitude) to the value obtained for the Kittel model [16].

Now, return to Eq. (4). The equation of the second-phase boundary is

$$x - By + Cz = 0, \tag{17}$$

where $B = A_2$, $C = A_3$. The above equation coincides with the equation of the domain wall W' separating C_1 and C_3. To this domain wall there corresponds the interlayer that differs from the first one only by the rotation matrix T'_2 (see table).

Thus, each orientational state in the formation of W' can have two orientations with the matrices T'_1 and T'_2.

STRUCTURE OF THE DOMAIN WALL W

The equation of the domain wall W in the coordinate system of the α-phase has the form [1, 2]

$$x_1 - 0.554363y_1 - 0.0139635z_1 = 0. \tag{18}$$

Performing the calculations by Eqs. (11)–(14), we obtain the interlayer parameters for W and, based on these data, the deformation tensors P_1 and D_1 (see table). It is seen from the deformation tensor that $e_{13} = 6.15 \times 10^{-3}$, i.e., $e_{13}^{s} \neq 0$, and, thus, the interlayer has monoclinic symmetry. The equation of this domain wall in the coordinate system of the interlayer differs from the equation of a straight wall

$$x_2 - 0.579026y_2 - 0.013505z_2 = 0. \qquad (19)$$

Such an interlayer can be considered as pseudotrigonal, but rotated by an angle of $\alpha = 2\arctan(e_{13})$ in the XZ plane. A similar situation takes place in the adjacent domain. To match these two interlayers, it is necessary to rotate each of them about their Y axes by the angle $-\alpha$. Performing this operation, we arrive at the following equation:

$$x_3 - 0.57897y_3 - 0.0012z_3 = 0, \qquad (20)$$

which corresponds, within $0.07°$, to the lost symmetry plane of the β-phase.

Since two equations of the domain wall (16) and (20) are known, we can determine the matrix of rotation from the β to the α phase, T_1 (see table).

From the analysis of the structure of the wall W separating C_1 and C_2 and also C_1 and C_3, we obtain that each orientational state arising in the formation of the domain wall W can take two orientations, to which the rotation matrices T_1 and T_2 from the β- to the α-phase correspond (table). A similar "splitting" of each orientation state into close four orientations was observed in a polydomain $BaTiO_3$ crystal [17].

Consider the thickness of the domain wall W. Unlike W', where the reversible phase transition to one interlayer is observed, in W, an additional rotation of each interlayer by an angle $-\alpha$ is observed. Hence, W consists of two interlayers, and its thickness equals twice the thickness of W'. With due regard for the latter fact, we obtain an essential increase in the elastic energy in this domain wall.

Thus, in the formation of W, a more complex twinning process is observed, which we will call F-twinning.

It is expedient to study the variation of the domain-wall energy with a change of temperature within the framework of this model. In [18], the equations of W and W' in the vicinity of the phase transition are obtained. Performing analogous calculations, we established a considerable decrease (by about 40 times) of the domain-wall energy in comparison with the decrease observed at room temperature (see table).

Now, introduce a new quantity E_s equal to the ratio of the surface density of the elastic energy E to a squared component of the spontaneous deformation.

$$E_s = E/(e_{11}^{s})^{2}. \qquad (21)$$

This quantity will be referred to as a relative surface density of the elastic energy of a domain wall. As is seen from the table, E_s is almost independent of temperature.

DISCUSSION AND CONCLUSIONS

It is seen from the given calculations that two different mechanisms of twinning are possible in lead orthophosphate. In P-twinning, all the components of spontaneous deformation of the induced interlayer are equal to zero. In F-twinning, only the main components of spontaneous deformation of the matching interlayer are zeroes. The existence of a nonzero shear component complicates the twinning mechanism and increases the thickness and energy of the twinning boundary (domain wall).

In [19], a motion of the domain walls W and W' was studied during overheating (ΔT) of the α-phase associated with a certain orientation of the temperature gradient. It was obtained that ΔT depends linearly on the domain-wall length, whereas the $\Delta T_{W'}/\Delta T_W$ ratio was equal to 0.3 for infinitesimal domain walls. This ratio was interpreted as the ratio of the energies of the corresponding domain walls in the vicinity of the phase transition. Dividing the first energy density into the second energy density, we obtain 0.282 at $t = 20°C$ and 0.299 at $t = 180°C$, which is in a good agreement with the experiment.

Thus, it follows from the above model of the domain wall that various types of domain walls in lead orthophosphate have different symmetries of interlayers, thicknesses, energies, and mechanisms of twinning. The thickness of the domain wall W is twice as great as W', whereas its energy is higher (by a factor of 3.5) than the energy of W'. The domain walls are formed along the corresponding symmetry elements of the paraphase lost in the phase transition in those cases, where one or several parallel domain walls of the same type are formed in a crystal. Each orientation state can have four close orientations depending on the type of the domain wall and the orientation of the adjacent domain. The domain-wall energy is proportional to a squared spontaneous deformation. The relative density of the surface energy E_s is the temperature-independent energy characteristic of each type of the domain walls in a crystal.

REFERENCES

1. L. A. Shuvalov, Izv. Akad. Nauk SSSR, Ser. Fiz. **43** (8), 1554 (1979).

2. K. Aizu, J. Phys. Soc. Jpn. **27**, 387 (1969).

3. V. Keppler, Z. Kristallogr. **132**, 228 (1970).

4. L. H. Brixner, P. E. Bierstedt, W. F. Jaep, and J. R. Barkley, Mater. Res. Bull. **8**, 497 (1973).

5. E. F. Dudnik, E. V. Sinyakov, V. V. Gene, and S. V. Vagin, Fiz. Tverd. Tela (Leningrad) **17**, 1212 (1975) [Sov. Phys. Solid State **17**, 785 (1975)].

6. J. Sapriel, Ferroelectrics **13** (1–4), 459 (1976).

7. M. Chabin, J. P. Ildefonse, and F. Gilletta, Ferroelectrics **13**, 333 (1976).

8. M. Chabin and F. Gilletta, J. Appl. Crystallogr. **10**, 247 (1977).

9. L. S. Wainer and R. F. Bagio, Ferroelectrics **31**, 121 (1981).

10. E. F. Dudnik and V. A. Nepochatenko, Kristallografiya **25**, 984 (1980) [Sov. Phys. Crystallogr. **25**, 564 (1980)].

11. J. C. Toledano, L. Pateau, J. Primot, *et al.*, Mater. Res. Bull. **10**, 103 (1975).

12. C. Joffren, J. P. Benoit, L. Deschamps, and M. Lambert, J. Phys. (Paris) **38** (2), 205 (1977).

13. G. A. Korn and T. M. Korn, *Mathematical Handbook for Scientists and Engineers* (McGraw-Hill, New York, 1968; Nauka, Moscow, 1974).

14. An. Cao-Xuan, G. Hauret, and J. P. Chapelle, CR Seances Acad. Sci., Ser. B **280** (5), 543 (1975).

15. J. Torres, J. Primot, A. M. Pougnet, and J. Aubree, Ferroelectrics **26** (1–4), 689 (1980).

16. C. S. Kittel, Solid State Commun. **10**, 119 (1972).

17. L. G. Shabel'nikov, V. Sh. Shekhtman, and O. M. Tsarev, Fiz. Tverd. Tela (Leningrad) **18** (6), 1529 (1976) [Sov. Phys. Solid State **18**, 889 (1976)].

18. V. A. Nepochatenko, Kristallografiya **47** (3), 514 (2002) [Crystallogr. Rep. **47**, 467 (2002)].

19. E. F. Dudnik and V. A. Nepochatenko, *Physics of Active Dielectrics* (Dnepropetrovsk. Gos. Univ., Dnepropetrovsk, 1980), p. 94.

Translated by T. Dmitrieva

PHYSICAL PROPERTIES
OF CRYSTALS

Stimulated Raman Scattering
by $C_{12}H_{22}O_{11}$ Sugar (Sucrose)[1]

A. A. Kaminskii

Shubnikov Institute of Crystallography, Russian Academy of Sciences,
Leninskiĭ pr. 59, Moscow, 117333 Russia

e-mail: kaminalex@mail.ru

Received November 4, 2002

Abstract—The efficient Stokes and anti-Stokes laser emissions with Raman frequency shift at about 2960 cm^{-1} are excited in a food $C_{12}H_{22}O_{11}$ sugar (sucrose) single crystal under pulsed pumping. Other $(\chi^{(2)} + \chi^{(3)})$ effects of the parametric Raman generation are also detected. © *2003 MAIK "Nauka/Interperiodica".*

In recent years, the necessity of creating efficient sources of high-quality laser radiation with specific wavelengths in the visible, near IR, and medium IR ranges has increased interest in laser converters based on stimulated Raman scattering (SRS) by $\chi^{(3)}$-nonlinear crystals [1–3]. Among the well-known solid-state SRS-$\chi^{(3)}$-media [4, 5], the most attractive ones are several organic crystals and one organometallic crystal [6]. The pronounced Raman frequency shift of their SRS-active vibrational modes (ω_{SRS} up to ~3150 cm^{-1}, Table 1) allows one to transform the pump (fundamental radiation) into laser emission with the required wavelength rather efficiently without using higher Stokes orders (unlike the case of inorganic $\chi^{(3)}$ crystals with a nonextended phonon spectrum). It is obvious that this advantage inherent in organic crystals can substantially simplify the development of a number of practically important SRS-converters, SRS-lasers, and SRS-amplifiers. Realizing the importance of the search for new organic SRS-crystals, the author focused on the commonly used food (sweet) $C_{12}H_{22}O_{11}$ sugar (sucrose or β-*D*-fructofuranosyl-α-*D*-glucopyranoside), which has an acentric crystalline nature and, therefore, a nonlinear $(\chi^{(2)} + \chi^{(3)})$ material. Numerous applications and the availability and low cost of sucrose are obvious—the sugar industry has existed in many countries for quite a long time; there are numerous institutes and museums studying sugar as well as related scientific journals. Moreover, there exist numerous international scientific and industrial societies and unions dealing with sugar.

Below, we briefly report the first results on excitation of the high-order pulsed SRS in the visible range (Fig. 1) in $C_{12}H_{22}O_{11}$ single crystals. In this mode of $\chi^{(3)}$-generation, some additional manifestations of nonlinear self-frequency $(\chi^{(2)} + \chi^{(3)})$-conversion of the SRS-components were also observed in the UV range. The preliminary data on these effects are also considered.

Sugar is crystallized in the acentric monoclinic sp. gr. C_2^2 with two formula units in the unit cell; the structure contains no crystallization water. The hardness of $C_{12}H_{22}O_{11}$ crystals is somewhat higher than the hardness of nonlinear $[NH_4]H_2PO_4$ (ADP) and KH_2PO_4 (KDP) crystals widely used in quantum electronics [11]. Compared to the latter crystals, $C_{12}H_{22}O_{11}$ crystals are also more resistant against atmospheric moisture. Pulsed second-harmonic generation of 1-μm radiation from a $Nd^{3+} : Y_3Al_5O_{12}$ laser was first obtained in $C_{12}H_{22}O_{11}$ crystals many years ago [12]. Dispersion of the refractive indices of this crystal was also measured in [12]. The crystals showed piezoelectricity and triboluminescence and are optically active, so they can be assigned to the class of UV-nonlinear materials.

SRS-spectroscopy experiments were performed on specially prepared 6 to 8-mm-thick samples cut out from rather large single crystals of food sugar.[2] No protective or blooming coatings were applied to polished plane-parallel surfaces of the samples. Some physical characteristics of the $C_{12}H_{22}O_{11}$ crystals studied are presented in Table 2.

In the SRS-experiments, a single-pass cavity-free scheme was used. The excitation was produced by frequency-doubled ($\lambda_P = 0.53207$ μm) pulses from pico- ($\tau_P \approx 80$ ps) and nanosecond ($\tau_P \approx 20$ ns) $Nd^{3+} : Y_3Al_5O_{12}$ lasers with an emission energy of up to 2 mJ. This pump radiation with the Gaussian intensity distribution over the cross-section was directed by a lens onto $C_{12}H_{22}O_{11}$ samples. The focal length of the lens

---

[1] The results of this study were presented at the 201st meeting of the monthly Moscow Seminar on Physics and Spectroscopy of Lasing Crystals on September 26, 2002.

[2] The sugar, produced by Pfeifer & Lamp Co., was bought in a Berlin supermarket.

Table 1. Organic and organometallic SRS-active crystals

Crystal	Sp. gr.	Nonlinearity	SRS-active vibrational modes, cm^{-1}	Nonlinear-laser effects	Reference
Organic crystals					
$C_{12}H_{22}O_{11}$(sugar)	C_2^2	$\chi^{(2)} + \chi^{(3)}$	~2960	SHG*, SRS, self-SHG (SRS)**, self-SFM***	Present study
$C_{13}H_{10}O$ (benzophenone)	D_2^4	$\chi^{(2)} + \chi^{(3)}$	3070, 1650, 998, ~103	SHG, SRS	[7]
$C_{13}H_{10}O_3$ (salol)	D_{2h}^{16}	$\chi^{(2)} + \chi^{(3)}$	~3150	SRS	[7]
$C_{14}H_{10}O_2$ (benzyl)	$D_3^4 (D_3^6)$	$\chi^{(2)} + \chi^{(3)}$	~1000	SRS	[7]
α-$C_{14}H_{12}O$	C_{2h}^5	$\chi^{(3)}$	3065	SRS	[7]
$C_{15}H_{19}N_3O_2$ (AANP)	C_{2v}^9	$\chi^{(2)} + \chi^{(3)}$	~1280	SHG, SRS, self-SFM***	[8]
$C_{16}H_{15}N_3O_4$ (MNBA)	C_s^4	$\chi^{(2)} + \chi^{(3)}$	~1587	SHG, SRS, self-SFM***	[9]
Organometallic crystal					
$C_{14}H_{26}N_8O_{13}Zr$ (GuZN-III)	D_2^5	$\chi^{(2)} + \chi^{(3)}$	~2940, ~1008	SHG, SRS	[10]

   * Second-harmonic generation.
  ** Self-frequency doubling of the first Stokes component of the generation excited in the crystal.
*** Self-sum-frequency mixing of the parametric Raman generation and the laser pump.

was chosen so as to achieve the highest possible efficiency of the SRS-conversion without causing crystal destruction. The experimental conditions ensured the steady-state SRS mode ($\tau_P \gg T_2 = 1/\pi\Delta\nu_R \approx 2$ ps, where T_2 is the time of phonon relaxation and $\Delta\nu_R \approx 7$ cm^{-1} is the linewidth of the SRS-active vibrational mode in the spectrum of spontaneous Raman scattering (inset in Fig. 2)). The spectral composition of the parametric Raman generation in sugar crystals was measured by a technique described elsewhere [7–10]. The recorded lines of the $\chi^{(3)}$-conversion and ($\chi^{(2)} + \chi^{(3)}$)-self-conversion of the laser pump radiation and the components of the parametric Raman generation in $C_{12}H_{22}O_{11}$ are summarized in Table 3 and partly illustrated in Fig. 1.

Using the approximate expression for the increment in the steady-state Raman amplification $g_{ssR}I_{th}l_R \approx 30$ [13] (I_{th} and l_R are the threshold pump power and the SRS-active length of the crystal, respectively), the gain g_{ssR} in the first Stokes component ($\lambda_{St1} = 0.5315$ μm) of the generation in the $C_{12}H_{22}O_{11}$ crystals was estimated from the comparative measurements involving well-known $\chi^{(3)}$-active NaCl and α-KY(WO$_4$)$_2$ crystals. Its lower limit proved to be $g_{ssR} \approx 6.5$ cm GW^{-1}. Under picosecond pumping (pulse energy ~1.5 mJ) under experimental conditions that were far from optimal (the quality of the crystals, optical treatment of their "work-

ing" surfaces, and low values $l_R = 6$–8 mm), the total efficiency of the nonlinear $\chi^{(3)}$-conversion into the Stokes and anti-Stokes components in $C_{12}H_{22}O_{11}$ was about 35%. Under nanosecond excitation (with the energy of the pump pulses being the same), the efficiency was two times lower.

Because of the low symmetry of a $C_{12}H_{22}O_{11}$ crystal and, hence, the large number of the vibrational modes in the spectra of spontaneous Raman scattering (see Fig. 2) and IR absorption (3NZ = 270; Γ_N = 133A + 137B, of which (A + 2B) are acoustic modes and (129A + 129B) are internal modes), it is quite difficult at this stage of the research to establish the relation of the observed SRS-mode ω_{SRS} = 2960 cm^{-1} to the specific C–H vibrational bond (ν[CH] or ν[CH$_2$]). It is planned to establish such a relation after a detailed study of all the vibrational spectra of a $C_{12}H_{22}O_{11}$ crystal and the performance of necessary quantum chemical calculations of its vibrational levels.

Thus, the experiments performed showed that $C_{12}H_{22}O_{11}$ single crystals can be considered as a rather efficient $\chi^{(2)}$ and $\chi^{(3)}$ optical material. Its SRS-potential, availability, low cost, and various structural modifications make this crystal quite attractive for application in laser physics and nonlinear optics.
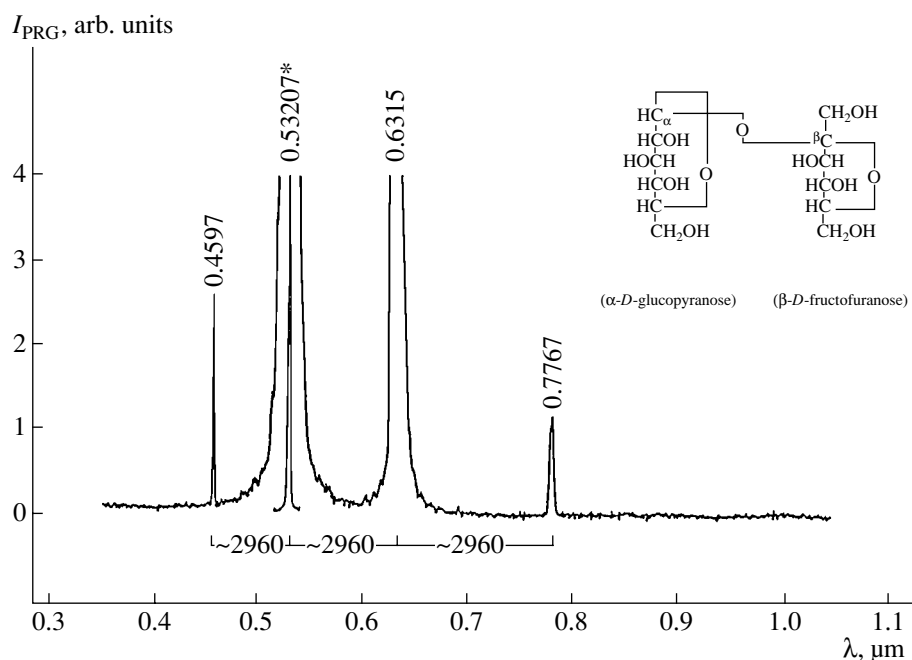
Fig. 1. Spectrum of parametric Raman generation in a $C_{12}H_{22}O_{11}$ crystal obtained at picosecond pumping with $\lambda_P = 0.53207$ μm (marked with an asterisk) at 300 K. The generation wavelengths are indicated in micrometers; their intensities were not corrected for the spectral sensitivity of the recording system based on an Si-CCD matrix. Brackets show the relation between the Stokes and anti-Stokes lines of the $\chi^{(3)}$-generation and the SRS-active vibrational mode $\omega_{SRS} = 2060$ cm^{-1} of the crystal. The inset shows a sugar molecule and its two constituents.
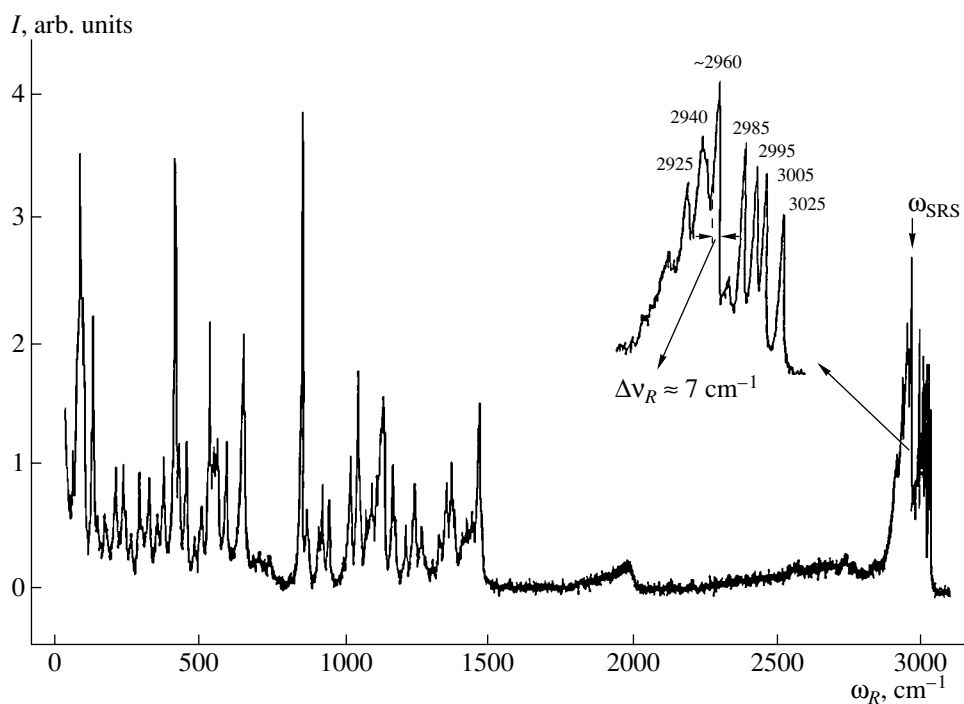
Fig. 2. Fragment of the spectrum of spontaneous Raman scattering of a $C_{12}H_{22}O_{11}$ crystal obtained under excitation by Ar-laser radiation with $\lambda = 0.5145$ μm at 300 K. The line intensities were not corrected for photodetector sensitivity (the sensitivity in the long-wavelength range of the spectrum is about twice as low as the sensitivity in the excitation region). The inset shows the lines of the long-wavelength fragment of the spectrum, of which the most intense one (with $\omega_{SRS} = 2060$ cm^{-1}) is associated with the SRS-active vibrational mode of the crystal.

Table 2. Some physical characteristics of a monoclinic $C_{12}H_{22}O_{11}$ crystal at ~300 K

Characteristic	
Sp. gr.	$C_2^2 - P2_1$ (no. 4)
Class	Polar
Unit-cell parameters, Å, deg	$a = 10.86$
	$b = 8.7$
	$c = 7.75$
	$\beta \approx 103.5$
The number of formula units in the unit cell	$Z = 2$
Local symmetry of atoms	C, H, and O in the C_1-positions
Density, g cm^{-3}	$d \approx 1.59$
Melting point, $t°$, C	~186
Vickers microhardness, N mm^2	~600*
Thermal conductivity, W m^{-1} K^{-1}	~0.5
Thermal expansion**, K^{-1}	8.2×10^{-5}
Linear optical classification	Negative, biaxial
Optical transparency***, μm	~0.19…~1.35
Dispersion formula for refractive indices [12]****, λ, μm	$n^2 = A + \dfrac{B\lambda^2}{\lambda^2 - C} - D\lambda^2$
Effective nonlinear SHG coefficient at λ = 1.064 μm [12]	$d_{\text{eff}}^2 = 0.2 d_{\text{eff(ADP)}}^2$
Threshold of optical damage [12]*****, MW cm^{-2}	~500
Extension of phonon spectrum******, cm^{-1}	~3600
Raman frequency shift of the $\chi^{(3)}$-active vibration*******, cm^{-1}	~2960

* Mohs hardness >2.5.
** The value averaged over the temperature range from –20 to 50°C.
*** For a ~1-mm-thick plate.
**** Sellmeier coefficients.

n	A	B	C	D
n_x	1.8719	0.4660	0.0214	0.0113
n_y	1.9703	0.4502	0.0238	0.0101
n_z	2.0526	0.3909	0.0252	0.0187

***** For 1.064-μm laser pulses with a duration of ~10 ns.
****** From spectra of spontaneous Raman scattering and IR absorption.
******* From picosecond SRS spectra (Fig. 1).

Table 3. Spectral composition of the $\chi^{(3)}$ and $(\chi^{(2)} + \chi^{(3)})$ parametric Raman generation in $C_{12}H_{22}O_{11}$ single crystals under pumping by the second harmonic of pulsed $Nd^{3+} : Y_3Al_5O_{12}$ lasers at 300 K

Wavelength*, μm	Line**	Line identification	Experimental and measurement conditions
0.7767***	St_2	$\omega_P - 2\omega_{SRS}$	Along ~a axis
0.6315***	St_1	$\omega_P - \omega_{SRS}$	Along ~a axis; the SRS-conversion efficiency exceeds 30%
0.53207***	λ_P	ω_P	
0.4597***	ASt_1	$\omega_P + 2\omega_{SRS}$	Along ~a axis
0.3158****	SHG	$2\omega_{St1}$	*****
0.2887****	$\Sigma\lambda_P, \lambda_{St1}$	$\omega_P + \omega_{SRS}$	******

    * Measurement accuracy is not lower than ±0.0005 μm.

    ** The symbol Σ indicates the process of parametric self-sum-frequency mixing.

    *** Recording by an Si-CCD matrix (Hamamatsu S3429-1024Q) and McPherson-218 grating monochromator.

    **** Recording with a photomultiplier with an antimony–cesium cathode and a MDR grating monochromator supplied with UV optics.

    ***** Excitation conditions close to phase matching.

    ****** Excitation geometry should be refined.

REFERENCES

1. J. T. Murray, W. L. Austin, and R. C. Powell, *Advanced Solid-State Lasers* (Opt. Soc. Am., Washington, D.C., 1998), p. 129.
2. Special Issue on Solid State Raman Lasers, Opt. Mater. **11** (3) (1999).
3. G. A. Pasmnik, Laser Focus World **35** (11), 138 (1999).
4. A. A. Kaminskiĭ, *Raman Scattering: 70 Years of Research* (Fiz. Inst. Ross. Akad. Nauk, Moscow, 1998), p. 206.
5. T. T. Basiev, A. A. Sobol, P. G. Zverev, *et al.*, Appl. Opt. **38** (3), 594 (1999).
6. J. Hulliger, A. A. Kaminskii, and H. J. Eichler, Adv. Funct. Mater. **11** (4), 243 (2001).
7. A. A. Kaminskii, H. Klapper, J. Hulliger, *et al.*, Laser Phys. **12** (7), 1041 (2002).
8. A. A. Kaminskii, T. Kaino, T. Taima, *et al.*, Jpn. J. Appl. Phys. A, Part 2 **41** (6), L603 (2002).
9. A. A. Kaminskii, J. Hulliger, and H. J. Eichler, Phys. Status Solidi A **186** (3), R19 (2001).
10. A. A. Kaminskii, E. Haussuhl, J. Hulliger, *et al.*, Phys. Status Solidi A **193** (1), 167 (2002).
11. V. G. Dmitriev, G. G. Gurzadyan, and D. N. Nikogasyan, *Handbook of Nonlinear Optical Crystals* (Springer, Berlin, 1999).
12. J. M. Halbout and C. L. Tang, IEEE J. Quantum Electron. **18** (3), 410 (1982).
13. Y. R. Shen, *The Principles of Nonlinear Optics* (Wiley, New York, 1984; Nauka, Moscow, 1989).

Translated by A. Zolot'ko

PHYSICAL PROPERTIES
OF CRYSTALS

Conoscopic Figures of Optically Active Uniaxial Crystals

K. A. Rudoĭ*, B. V. Nabatov**, V. I. Stroganov*, A. F. Konstantinova**,
L. V. Alekseeva*, E. A. Evdishchenko**, and B. I. Kidyarov***

* Far Eastern State Transport University,
ul. Serysheva 47, Khabarovsk, 680000 Russia
** Shubnikov Institute of Crystallography, Russian Academy of Sciences,
Leninskiĭ pr. 59, Moscow, 119333 Russia
e-mail: afkonst@ns.crys.ras.ru
*** Institute of Physics of Semiconductors, Siberian Division, Russian Academy of Sciences,
pr. Akademika Lavrent'eva 13, Novosibirsk, 630090 Russia
Received September 19, 2002

Abstract—Conoscopic figures of optically active crystals are described by the formulas for the intensity of light transmitted by a plate located between arbitrarily oriented polarizer and analyzer. The differences in the behavior of optically active and inactive crystals and also of right- and left-handed crystals are established. The corresponding computations and the simulation of conoscopic figures are performed using the Mathematica-4.1 package of computer programs. © 2003 MAIK "Nauka/Interperiodica".

INTRODUCTION

Interference patterns formed during transmission of a convergent light beam through crystalline plates placed between a polarizer and analyzer provide rich information about the plate properties. The information extracted from conoscopic figures allows one to determine the orientation and character of the optical indicatrix, the angle formed by the optical axes of a biaxial crystal, the optical sign, the dispersion of the optical axes, and the qualitative and quantitative changes in the optical indicatrix under the action of various external factors. It is also well known that the optical activity (or gyroscopy) gives rise to certain changes in conoscopic figures in comparison with the conoscopic figures of inactive crystals during light beam propagation along the optic axis.

A typical conoscopic figure of an optically inactive uniaxial plate cut out normally to the optic axis of the crystal is a black Maltese cross consisting of two isogyres and a series of concentric rings (isochromes). The conoscopic figure of an optically active crystal consists of a well pronounced system of isochromes. In this case, the black Maltese cross does not occupy the whole figure—its center is not black and may be colored.

Conoscopic figures of uni- and biaxial crystals are considered in various monographs [1–4], which also describe the formation of conoscopic figures of optically inactive crystals. As far as we know, no analogous consideration has yet been made for optically active crystals. Therefore, the present article aimed to fill this gap.

INTENSITY OF LIGHT TRANSMITTED
BY AN OPTICALLY ACTIVE PLATE

To describe conoscopic figures of optically active crystals theoretically, we used the following formula for the intensity of light transmitted by a plate cut out from an optically active crystal which is located between arbitrarily oriented polarizer and analyzer [5]:

$$
\begin{aligned}
J = \ & [\cos^2(\alpha - \beta) - \sin 2\alpha \sin 2\beta \sin^2(\Delta_{el}/2)] \\
& - \cos 2\alpha \cos 2\beta \sin^2 2\gamma \sin^2(\Delta_{el}/2) \\
\pm \ & [\sin 2(\alpha - \beta)\sin 2\gamma \sin \Delta_{el}]/2 = J_1 - J_2 \pm J_3,
\end{aligned}
\tag{1}
$$

where $J = I/I_0$, I is the intensity of the transmitted light, I_0 is the intensity of the incident light, α is the angle of rotation of the polarizer from its initial position, β is the angle of rotation of the analyzer from its initial position, Δ_{el} is the phase difference introduced by the crystalline plate, and γ is the quantity which describes the optical activity ($k = \tan\gamma$ is the ellipticity of the eigenwaves in the crystal, $\sin 2\gamma = 2k/(1 + k^2)$).

As usual (see, e.g., [1]), we assume that the conoscopic figures of optically inactive crystals are described by the term J_1 (in brackets) in Eq. (1). The additional terms J_2 and J_3 describe the contribution of the optical activity to the total intensity with a plus sign before the latter term for a right-handed crystal and a minus sign, for a left-handed one.

One has to bear in mind that the quantity Δ_{el} depends not only on birefringence but also on the parameters of the optical activity. In the general case, Δ_{el} is calculated

by the formula

$$\Delta_{el} = 2\pi d(n_2 - n_1)/(\lambda \cos \phi_s), \qquad (2)$$

where d is the plate thickness, n_1 and n_2 are the refractive indices of the waves propagating in optically active crystals, λ is the wavelength of the incident light, ϕ_s is the average value of the angles formed by the waves refracted by the crystal. The angle ϕ_s is determined by the well-known Snell's law, $\sin \phi_s = \sin \phi_i / n_s$, where ϕ_i is the angle of incidence and $n_s = (n_1 + n_2)/2$.

In optically active crystals, the quantity $\Delta n_{el} = (n_2 - n_1)$ (so-called elliptical birefringence) is calculated from the rigorous equation of normals [6]. However, since the conoscopic figures are determined from the approximate relationship for angles of light refraction, one can calculate Δn_{el} using the principle of birefringence superposition [7]

$$\Delta n_{el}^2 = \Delta n_1^2 + \Delta n_c^2, \qquad (3)$$

where $\Delta n_l = (n_{02} - n_{01})$ is the linear birefringence, $\Delta n_c = G/\sqrt{n_{01} n_{02}}$ is the circular birefringence, n_{02} and n_{01} are the refractive indices of eigenwaves propagating along the given direction of the wave normal in the absence of optical activity, and G is the scalar parameter of gyration.

All the above formulas are applicable to optically active uni- and biaxial crystals.

Now, consider in more detail the uniaxial crystals for which the refractive index n_{02} of the extraordinary wave is calculated by the formula [4]

$$n_{02}^2 = n_o^2 n_e^2 / [n_o^2 n_e^2 + (n_e^2 - n_o^2)(\mathbf{n}_{av}\mathbf{c})^2], \qquad (4)$$

where n_o and n_e are the principal refractive indices of the ordinary and extraordinary waves, respectively; $\mathbf{n}_{av}$ is the unit vector along the average direction of the wave normals of the refracted waves; $\mathbf{c}$ is the unit vector along the optical axis; $(\mathbf{n}_{av}\mathbf{c}) = \cos \theta$; and θ is the angle formed by the optic axis and the wave normal $\mathbf{n}_{av}$.

The ellipticity of eigenwaves, $k = \tan \gamma$, is calculated by the relationship given in [4]:

$$k = [(n_{02}^2 - n_{01}^2) - \sqrt{(n_{02}^2 - n_{01}^2)^2 + 4G^2}]/(2G), \qquad (5)$$

where $G = g_{33}\cos^2\theta + g_{11}\sin^2\theta$ for uniaxial crystals and g_{33} and g_{11} are the components of the gyration pseudotensor [5, 7]. As was shown in [8], the components of the gyration pseudotensor in the approximate and the rigorous theories (g_{ij}) and (α_{ij}) are related as

$$g_{33} = 2\alpha_{11}n_{01}, \quad g_{11} = (\alpha_{11} + \alpha_{33})(n_{01} + n_{02})/2. \quad (6)$$

DESCRIPTION OF CONOSCOPIC FIGURES OF CRYSTALS

Now, demonstrate how one can interpret the well-known difference between the conoscopic figures of optically inactive and active crystals in the case of light propagation along the optic axis ($\theta = 0°$) using Eq. (1). With this aim, one has to consider the conoscopic figures obtained for real crystals. We observed conoscopic figures of plates cut out normally to the optic axis of an optically active quartz, lithium iodate, and paratellurite crystals, optically inactive lithium niobate, and many other crystals. We consider here simulated conoscopic figures that coincide with the experimentally observed ones.

As was indicated earlier [9], the possibilities provided by the systems of computer mathematics are still insufficiently used for solving the problems of crystal optics. In the present study, all the curves and figures were simulated using the Mathematica-4.1 package of programs.

Normally Located Polarizer and Analyzer

It is usually assumed that the clockwise rotation of the electric vector of a light wave is a right-handed rotation if the observer is looking toward the incident beam [1–5]. Then the corresponding component of the gyration tensor is given a negative sign. In accordance with this, the sign of g_{33} in a right-handed quartz crystal is negative and the sign of g_{11} is positive (which contradicts the Nye definition [7]). In this case, one has to assume that, for a right-handed crystal, the ellipticity of a faster wave propagating along the optic axis is $k = -1$. In an optically active crystal, the rotation of the polarization plane of the incident light Δ_{el} is determined by the relationship

$$\Delta_{el} = \rho d = g_{33}\pi d/(n_o\lambda), \qquad (7)$$

where ρ is the specific rotation.

To interpret the conoscopic figures of optically active crystals, consider first the case of the crossed polarizer and analyzer ($\alpha - \beta = 90°$). Then, using Eq. (1), we have

$$J = [\sin^2 2\alpha \sin^2(\Delta_{el}/2)] \qquad (8)$$
$$+ [\cos^2 2\alpha \sin^2 2\gamma \sin^2(\Delta_{el}/2)].$$

It is seen that, in comparison with the case of optically inactive crystals, Eq. (8) has an additional term J_2 proportional to $\sin^2 2\gamma$ and, moreover, the quantities Δ_{el} and γ have nonzero values along the optic axis. Now, it should be indicated that the conoscopic figures observed at such an orientation of the polarizer and analyzer for right- and left-handed crystals are the same, because the additional term J_2 associated with the optical activity always has the same sign.

(a)

(b)

(c)

J, arb. units
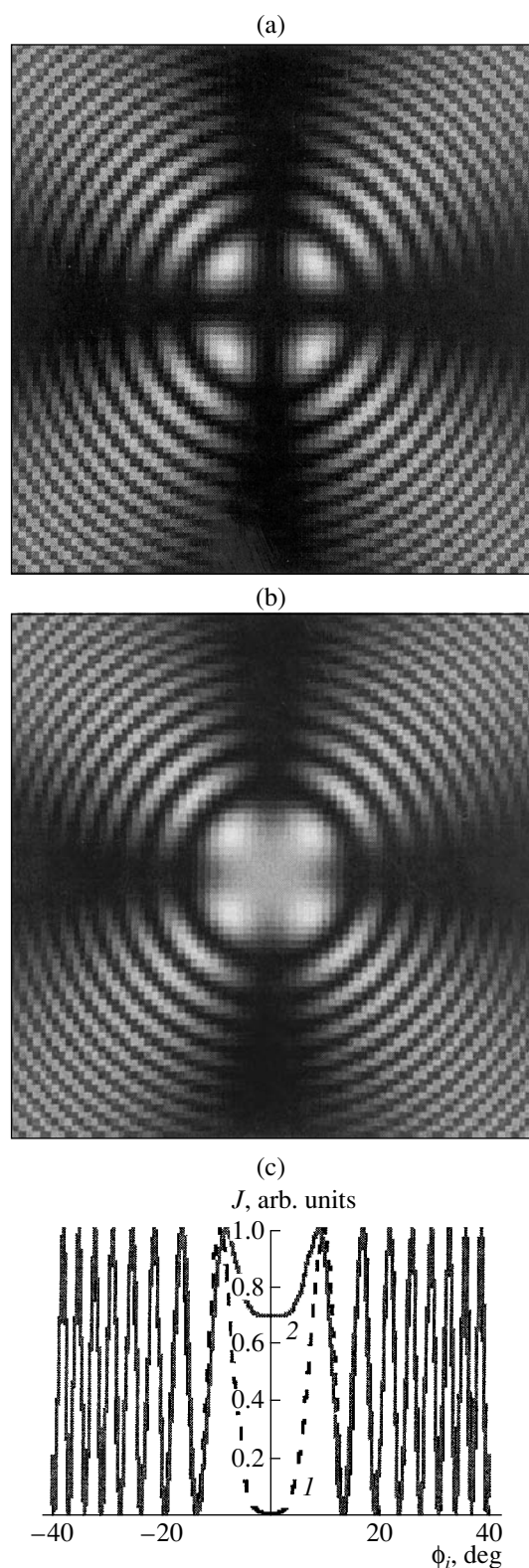
Fig. 1. Conoscopic figures of crystalline plates cut out normally to the optic axis of a crystal. (a) Optically inactive crystal, (b) optically active left- or right-handed quartz crystal, (c) section of the conoscopic figures at angle $\alpha = 45°$ corresponding to the direction of the diagonals of the squares in (a, b); (*1*) optically inactive and (*2*) optically active crystals.

Figures 1a and 1b show the conoscopic figures in a monochromatic light simulated for an optically inactive and active crystal, respectively. The simulation was performed for a plate cut out from a right- (or left-) handed quartz crystal with a thickness of $d = 3$ mm and the refractive indices $n_o = 1.54263$, $n_e = 1.55169$ and $g_{33} = \mp 10.258 \times 10^{-5}$, $g_{11} = \pm 5.539 \times 10^{-5}$ ($\alpha_{11} = \mp 3.315 \times 10^{-5}$ and $\alpha_{33} = \pm 6.895 \times 10^{-5}$) at the wavelength $\lambda = 632.8$ nm [4]. For more convenient comparison, we also used the same parameters for an optically inactive crystal with due regard for the fact that $g_{33} = g_{11} = 0$.

Since the conoscopic figures are observed if the incident light is emitted by a far extended source, one has to consider the transmission by the plate of the waves propagating along different directions and, therefore, incident onto the plate at different angles. Using Eq. (8), we consider the intensity of the transmitted light at $\alpha = 45°$ as a function of the angle of incidence (Fig. 1c). Curves *1* and *2* correspond to the "section" of the conoscopic figures along the diagonals of the squares shown in Figs. 1a and 1b.

It is clearly seen from Eq. (8) and Fig. 1 that if the light propagates along the optic axis, the intensity of the transmitted light in an optically inactive crystal equals zero (Fig. 1c, curve *1*), whereas in an optically inactive crystal, it considerably differs from zero because $\Delta_{el} \neq 0$ (Fig. 1c, curve *2*). It is seen that at the given parameters, the effect of the optical activity is important in the angular range close to the direction of the optic axis. It is clear that this angular range depends on the relationship between birefringence and the parameters of the optical activity of the crystal.

Polarizer and Analyzer Located at an Arbitrary Angle

Now consider the case where the polarizer and analyzer are located at an arbitrary angle to one another. It is clear that, with a gradual rotation of the analyzer from the initial crossed position, the conoscopic figures change. It is usually assumed that the negative change of the rotation angle of the polarizer corresponds to its clockwise rotation and the positive change of this angle, to the anticlockwise rotation. It follows from Eq. (1) that, depending on whether the crystal is right- or left-handed, the term $J_3 = \pm(\sin 2(\alpha - \beta)\sin 2\gamma \sin \Delta_{el})/2$ can make different contributions to the total intensity of the transmitted light during rotation of the analyzer for the same angle φ from the crossed position. Since in the vicinity of the optic axis of a right-handed crystal, $g_{33} < 0$ and $k < 0$, and in the left-handed crystal, $g_{33} > 0$ and $k > 0$, the sign of the product $(\sin 2\gamma \sin \Delta_{el})$ is the same for the right- and left-handed crystals. It is positive if $\Delta_{el} < 180°$ and negative if $\Delta_{el} > 180°$. Thus, at the same angle of the analyzer rotation from the crossed position, the signs of J_3 would be different for the right-

and left-handed crystals. Therefore, the conoscopic figures of these crystals would also be different. This provides the possibility of distinguishing between right- and left-handed crystals.

The above is illustrated by Fig. 2. Figures 2a and 2b show the conoscopic figures calculated for the right- and left-handed quartz crystals at $\beta = -90° + 30°$, which corresponds to the clockwise rotation of the analyzer by an angle $\varphi = 30°$ from the crossed position. The optical parameters here are the same as in Fig. 1. One can clearly see the difference between the conoscopic figures of the right- and left-handed crystals: the bright region looks like a small diffuse cross in the center in Fig. 2a, whereas the corresponding region in Fig. 2b has a dark cross. Figure 2c shows the corresponding sections of the conoscopic figures calculated by Eq. (1) at $\alpha = 45°$ (along the diagonals of the squares in Figs. 2a and 2b). The obvious difference in the vicinity of the direction of the optic axis is explained by different signs of the term J_3 for the right- (curve 1) and left-handed (curve 2) crystals. If the analyzer is rotated from the crossed position ($\beta = -90°-30°$) in the opposite direction, the conoscopic figures for the right- and left-handed crystals change places. This is explained by the behavior of the term J_3, which describes the optical activity and changes its sign with the change of the sign of $\sin 2(\alpha - \beta)$. For optically inactive crystals, these changes are independent of the rotation angle β of the analyzer ($\beta = -90° \pm \varphi$) (Fig. 3a).

DETERMINATION OF THE SIGN AND MAGNITUDE OF THE ROTATION OF THE POLARIZATION PLANE

Rotating the analyzer, one can determine the sign and magnitude of the rotation of the polarization plane and also its dispersion with the variation of the wavelength of the incident light. The angle of rotation of the analyzer from the crossed position to the position corresponding to the extinction of the central part of the conoscopic figure ($J = 0$) equals $\pm \varphi = \Delta_{el} = \rho d$, whence one can determine the specific rotation ρ. The minus sign of the angle φ defining the right-handed crystal corresponds to the clockwise rotation of the analyzer, whereas the plus sign defining the left-handed crystal, to the rotation in the anticlockwise direction. This is clearly demonstrated by Figs. 3b and 3c, which show the dependence of the light intensity J transmitted at certain wavelengths for the right- and left-handed crystals. It is seen that the rotation of the analyzer from the crossed position by certain angles determining the sign, magnitude, and dispersion of the polarization-plane rotation gives rise to extinction. Thus, it is seen from Fig. 3b (curve 1) that if the rotation of the analyzer by an angle $\varphi \approx -57°$ from the crossed position in the clockwise direction results in the extinction of a quartz crystal in the red light, this quartz crystal is right-handed.

(a)

(b)

(c)
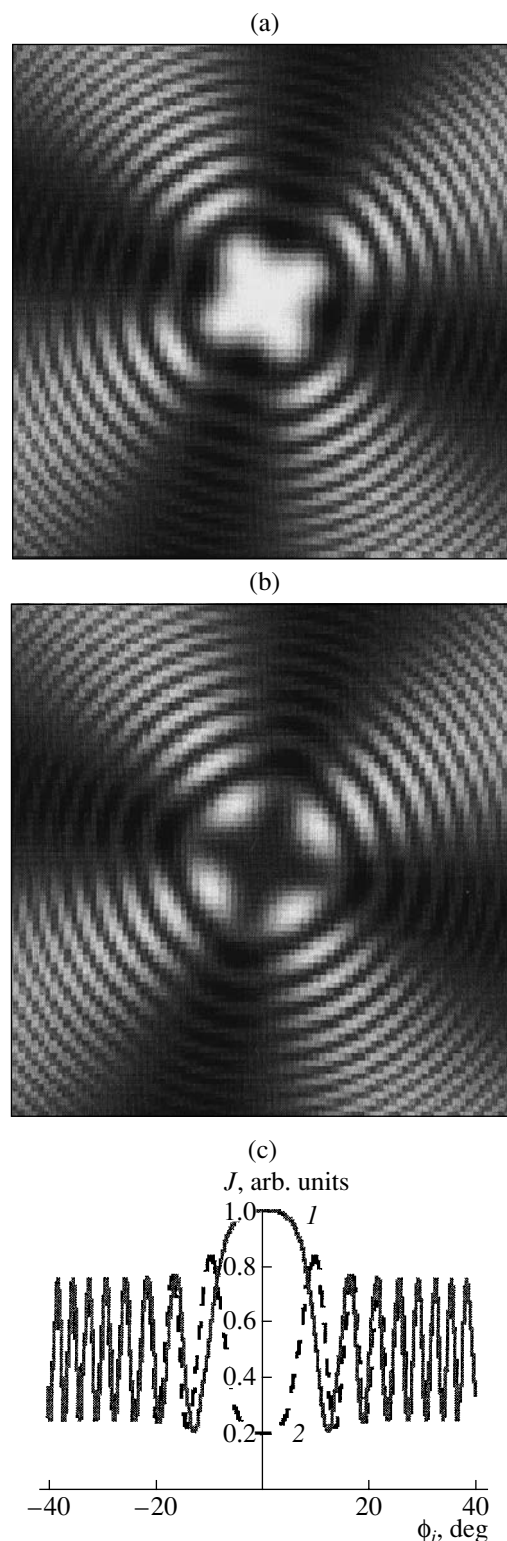
Fig. 2. Conoscopic figures of the crystalline quartz plates cut out normally to the optic axis of a crystal with the analyzer being rotated by an angle $\varphi = 30°$ from the crossed position with the polarizer; (a) right- and (b) left-handed crystals and (c) section of the conoscopic figures at $\alpha = 45°$, which corresponds to the direction of the diagonals of the squares in (a, b); (1) right-handed and (2) left-handed crystals.

(a)

J, arb. units

(b)

(c)
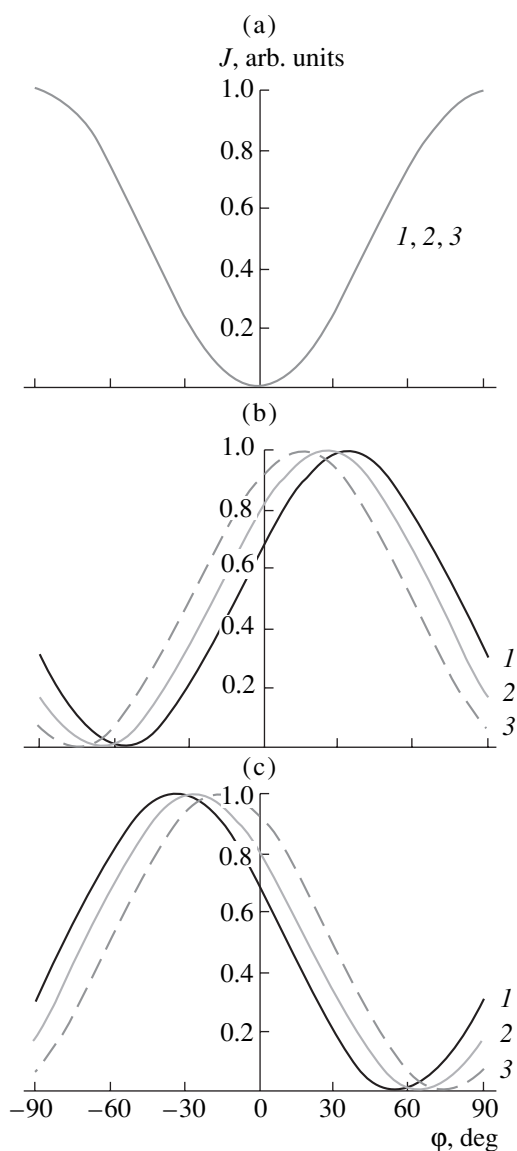
Fig. 3. Variation in the intensity *J* of the light transmitted by the crystalline plate in the center of the conoscopic figure at the rotation of the analyzer by an angle φ from the crossed position with the polarizer at several wavelengths λ of the incident light: (*1*) 633, (*2*) 589, and (*3*) 546 nm. (a) Optically inactive crystal, (b) right-, and (c) left-handed crystals.

To determine the sign of the polarization-plane rotation, one has to compare the conoscopic figures obtained in the monochromatic light with the use of two filters, e.g., first with a red filter and then with a green one [2]. In this case, the direction of the necessary rotation of the analyzer from the position of extinction with the use of a red filter (φ ≈ –57°) to the position of extinction with a green filter (φ ≈ –75°) coincides with the direction of the polarization-plane rotation of a right-handed crystal (Fig. 3b). For a left-handed crystal, the angle φ has the opposite sign, although the absolute values Δ_{el} remain unchanged (Fig. 3c).

It is the term J_3 that explains the determination of the sign of the polarization-plane rotation described in [2, 3], which is necessary for the observation of conoscopic figures in both monochromatic and white light. If the rotation of the analyzer in the clockwise direction (which corresponds to the negative angle φ) results in a "decrease" in the interference color of the central part of the conoscopic figure (in the sequence of the spectrum colors—from red to violet), the crystal is right-handed; if it results in an "increase" in the color, the crystal is left-handed. Moreover, if the clockwise rotation of the analyzer results in the "repulsion" of the isochromatic rings from one another, the crystal is right-handed; if the these rings are "attracted" to one another, i.e., become closer, the crystal is left-handed. One has to take into account that the above speculations are valid only if $\Delta_{el} < 180°$. If $\Delta_{el} > 180°$, the opposite occurs. At a considerable rotation, one has to use light filters possessing closer transmission ranges [2].

Thus, the above analysis of the light transmitted by a plate cut out from a uniaxial crystal and placed between the arbitrarily oriented polarizer and analyzer explains the differences in the conoscopic figures of optically active and optically inactive crystals. The above relationships show how one can distinguish between right- and left-handed crystals and evaluate the dispersion in the specific-rotation values in these crystals.

REFERENCES

1. M. Born and E. Wolf, *Principles of Optics*, 4th ed. (Pergamon, Oxford, 1969; Nauka, Moscow, 1970).

2. N. M. Melankholin and S. V. Grum-Grzhimaĭlo, *Methods of Studying the Optical Properties of Crystals* (Akad. Nauk SSSR, Moscow, 1954).

3. A. V. Shubnikov, *Principles of Optical Crystallography* (Akad. Nauk SSSR, Moscow, 1958; Consultants Bureau, New York, 1960).

4. B. N. Grechushnikov, in *Modern Crystallography*, Vol. 4: *Physical Properties of Crystals*, Ed. by B. K. Vaĭnshteĭn, A. A. Chernov, and L. A. Shuvalov (Nauka, Moscow, 1981; Springer, Berlin, 1988).

5. A. F. Konstantinova, B. N. Grechushnikov, B. V. Bokut', and E. G. Valyashko, *Optical Properties of Crystals* (Nauka i Tekhnika, Minsk, 1995).

6. F. I. Fedorov, *Theory of Gyrotropy* (Nauka i Tekhnika, Minsk, 1976).

7. J. F. Nye, *Physical Properties of Crystals: Their Representation by Tensors and Matrices* (Clarendon Press, Oxford, 1957; Inostrannaya Literatura, Moscow, 1960).

8. A. F. Konstantinova, B. V. Nabatov, E. A. Evdishchenko, and K. K. Konstantinov, Kristallografiya **47** (5), 879 (2002) [Crystallogr. Rep. **47**, 815 (2002)].

9. A. F. Konstantinova, K. K. Konstantinov, B. V. Nabatov, and E. A. Evdishchenko, Kristallografiya **47** (4), 702 (2002) [Crystallogr. Rep. **47**, 645 (2002)].

Translated by L. Man

Light Reflection at the Interface
between a Transparent Insulator and Magnet
with an Arbitrary Orientation of Magnetization

I. F. Gismyatov and D. I. Sementsov

Ul'yanovsk State University, ul. Tolstogo 42, Ul'yanovsk, 432700 Russia

Received March 15, 2001; in final form, May 31, 2002

Abstract—The boundary problem for a semi-infinite magnetic medium with an arbitrary orientation of the magnetization vector has been solved. The polarization and intensity characteristics of the reflected light wave are analyzed. It is shown that the variations of the incidence angle, magnetization orientation, and polarization plane substantially affect the polarization characteristics and give rise to typical features in the dependences studied. © 2003 MAIK "Nauka/Interperiodica".

INTRODUCTION

It is well known that magnetooptical Kerr effects are widely used in fundamental studies, namely, in spectroscopy of magnetically ordered media. A great number of publications [1–6] deal with the parameters of the light reflected from a planar interface between a nonmagnetic insulator and a uniformly magnetized medium. However, the majority of the studies are devoted to the limiting cases of the magnetic-moment orientation in a medium corresponding to the polar, meridional, and equatorial geometry in the Kerr effect. At the same time, the reflection effects can be most pronounced at magnetization orientations that differ from those mentioned above. It is in these situations that new features of magnetooptical reflection can be revealed.

In the present study, we analyze the polarization and energy characteristics of a light wave reflected from a nonabsorbing magnetic medium with an arbitrary orientation of the magnetization vector in the linear approximation with respect to the magnetooptical parameter. The linear approximation is chosen because in this case the form of the dielectric constant tensor $\hat{\varepsilon}$ for cubic crystals (such as garnet ferrites), the most typical representatives of magnetic dielectrics, does not depend on the orientation of the crystallographic axes on the crystal surface [7, 8].

FORMULATION OF THE PROBLEM

Let a linearly polarized laser radiation be incident on the interface (*xy* plane) between a transparent isotropic dielectric with the dielectric constant ε_0 and a cubic magnet at the angle φ_0 to the normal (*z* axis). The *yz* plane coincides with the incidence plane of the light wave. The dielectric-constant tensor for a magnetic medium in a uniformly magnetized state with the magnetic moment being oriented at an angle γ with respect to the *z* axis in the *yz* plane in the linear magnetooptical coupling approximation has the form [8]

$$\hat{\varepsilon} = \begin{pmatrix} \varepsilon & if\cos\gamma & -if\sin\gamma \\ -if\cos\gamma & \varepsilon & 0 \\ if\sin\gamma & 0 & \varepsilon \end{pmatrix}, \qquad (1)$$

where *f* is the magnetooptical parameter. In the optical range, the magnetic permeability of the medium is equal, within a high accuracy, to unity, $\mu = 1$, and, hence, the wave equation for the electric field in this medium has the form

$$\mathrm{curl\,curl}\mathbf{E} + \frac{\hat{\varepsilon}}{c^2}\frac{\partial^2 \mathbf{E}}{\partial t^2} = 0, \qquad (2)$$

where *c* is the light velocity in vacuum. The solution of Eq. (2) is sought as a plane wave,

$$\mathbf{E}(\mathbf{r}, t) = \mathbf{E}\exp[i(\omega t - \mathbf{kr})], \qquad (3)$$

where ω is the radiation frequency, $\mathbf{k}$ is the wave vector, which, in general, is a complex quantity. Substituting Eqs. (1) and (3) into the wave equation, one obtains the electric-field amplitude of the light wave,

$$k^2\mathbf{E} - \mathbf{k}(\mathbf{kE}) = k_0^2\hat{\varepsilon}\mathbf{E}, \qquad (4)$$

where $k_0 = \omega/c$ is the wave number in vacuum. Let ψ be the refraction angle, i.e., the angle between the direction of the light propagation in the medium and the surface normal. The medium is considered to be nonabsorbing, which is quite justified for the transparency windows in magnetic crystals. For garnet-type ferrites, this interval corresponds to the near IR-range. In this

case, the parameters ε and f are real quantities, which makes the wave number and the refraction angle also real quantities. In the geometry considered here, the wave vector $\mathbf{k}$ has the components $(0, k\sin\psi, k\cos\psi)$. With due regard for this fact, Eq. (4) can be represented in the form

$$
\begin{pmatrix}
k^2 - \varepsilon k_0^2 & -if k_0^2 \cos\gamma & if k_0^2 \sin\gamma \\
if k_0^2 \cos\gamma & k^2\cos^2\psi - \varepsilon k_0^2 & -(k^2/2)\sin 2\psi \\
-if k_0^2 \sin\gamma & -(k^2/2)\sin 2\psi & k^2\sin^2\psi - \varepsilon k_0^2
\end{pmatrix}
\begin{pmatrix}
E_x \\
E_y \\
E_z
\end{pmatrix} = 0. \quad (5)
$$

System (5) has a nontrivial solution if its determinant is equal to zero, whence we obtain the following characteristic equation:

$$
k^4 - 2k^2 k_0^2 [\varepsilon - f^2 \sin^2(\gamma - \psi)/2\varepsilon] + k_0^4(\varepsilon^2 - f^2) = 0. \quad (6)
$$

The solution of the above equation is the wave numbers k_j of two pairs of eigenwaves ($j = 1, 2$) propagating in opposite directions:

$$
k_j = \pm k_0 \left[\varepsilon - \frac{f^2 \sin^2(\gamma - \psi)}{2\varepsilon} \right.
$$

$$
\left. + (-1)^j \sqrt{\frac{f^4 \sin^4(\gamma - \psi)}{4\varepsilon^2} + f^2 \cos^2(\gamma - \psi)} \right]^{1/2}. \quad (7)
$$

From Eq. (7), we obtain the well-known relations of the wave numbers of the light waves propagating in the longitudinal direction, where $\gamma - \psi = 0, \pi$ and the eigenwaves are the circularly polarized waves with $k_j = k_0\sqrt{\varepsilon \pm f}$, and the transverse direction, where $\gamma - \psi = \pm\pi/2$ and the eigenwaves are two waves with orthogonal polarization planes and the wave numbers $k_1 = k_0\sqrt{\varepsilon}$ and $k_2 = k_0\sqrt{\varepsilon - f^2/\varepsilon}$.

In the general case, the eigenwaves in a medium uniformly magnetized along the arbitrary direction are two elliptically polarized waves with the wave vectors determined by Eq. (7).

Denote the electric-field amplitudes of the incident, reflected, and transmitted waves as $\mathbf{E}_i$, $\mathbf{E}_r$, and $\mathbf{E}_t$, respectively; and the magnetic-field amplitudes, as $\mathbf{H}_i$, $\mathbf{H}_r$, and $\mathbf{H}_t$, respectively. The wave vectors of these waves are $\mathbf{k}_\alpha = (0, k_{\alpha y}, k_{\alpha z})$, where $\alpha = i, r, t$. The continuity condition for the tangential components of the electric and magnetic fields at the interface between the two media ($z = 0$) valid for any interface point yields the relation for the y-components of the wave vectors of the waves in question, $k_{iy} = k_{ry} = k_{ty}$, whence we obtain the equation for the determination of angles at which the eigenwaves propagate in the magnetic medium:

$$
k_j \sin\psi_j = k_0 \sin\varphi_0, \quad (8)
$$

where k_j is determined from Eq. (7).

REFLECTION MATRIX

In the experiments on reflection of light from a magnetogyrotropic medium, a linearly polarized radiation is commonly used [3–5]. Therefore, in what follows, we analyze the p- and s-components of the electric field of a wave either parallel or perpendicular to the incidence plane. Their relation to the Cartesian components of the field in the incident wave is given by the expression

$$
E_{ix} = E_{is}, \quad E_{iy} = E_{ip}\cos\varphi_0, \quad E_{iz} = E_{ip}\sin\varphi_0.
$$

Now, introduce the reflection matrix $\hat{r}$ relating the incident and the reflected waves:

$$
\begin{pmatrix} E_{rp} \\ E_{rs} \end{pmatrix} = \begin{pmatrix} r_{pp} & r_{ps} \\ r_{sp} & r_{ss} \end{pmatrix} \begin{pmatrix} E_{ip} \\ E_{is} \end{pmatrix}, \quad (9)
$$

where the corresponding elements $\hat{r}$ are determined as

$$
r_{pp} = 2\frac{A_1 U_2 - A_2 U_1}{A_1 B_2 - A_2 B_1} - 1, \quad r_{ss} = 2\frac{B_2 - B_1}{A_1 B_2 - A_2 B_1} - 1,
$$

$$
r_{ps} = \frac{2}{\cos\varphi_0}\frac{B_2 U_1 - B_1 U_2}{A_1 B_2 - A_2 B_1}, \quad (10)
$$

$$
r_{sp} = 2\cos\varphi_0\frac{A_1 - A_2}{A_1 B_2 - A_2 B_1}.
$$

Here, the following notation is used:

$$
A_j = 1 + \tan\varphi_0/\tan\psi_j,
$$

$$
B_j = -if\cos\gamma\frac{\tan\psi_j}{\tan\varphi_0} + U_j\left(1 + \varepsilon\frac{\tan\psi_j}{\tan\varphi_0}\right),
$$

$$
U_j = \frac{i}{f}\frac{[(k_j/k_0)^2 - \varepsilon]\sin 2\psi_j - (k_0/k_j)^2 f^2 \sin 2\gamma}{2[\cos^2\psi_j - \varepsilon(k_0/k_j)^2]\sin\gamma - \sin 2\psi_j\cos\gamma}.
$$

Let the polarization plane in an incident beam be determined by the angle β of the beam deviation from the incidence plane. Then, the components of the electric field of the incident wave are determined as $E_{ip} = E_i\cos\beta$ and $E_{is} = E_i\sin\beta$, whereas the components of the reflected wave are

$$
E_{rp} = (r_{pp}\cos\beta + r_{ps}\sin\beta)E_i,
$$
$$
E_{rs} = (r_{sp}\cos\beta + r_{ss}\sin\beta)E_i. \quad (11)
$$

The energy reflection coefficients, which determine the part of the energy of the incident wave for the corresponding polarization component of the reflected wave in the case of an arbitrary orientation of the polar-

ization plane of the incident radiation, can be introduced as follows:

$$R_p = \frac{|E_{rp}|^2}{|E_i|^2} = |r_{pp}\cos\beta + r_{ps}\sin\beta|^2,$$

$$R_s = \frac{|E_{rs}|^2}{|E_i|^2} = |r_{sp}\cos\beta + r_{ss}\sin\beta|^2. \qquad (12)$$

In this case, the total reflection coefficient, which determines the total reflected energy, is given by the expression $R = R_p + R_s$. The reflection coefficients defined as

$$R'_p = \frac{|E_{rp}|^2}{|E_{ip}|^2}, \quad R'_s = \frac{|E_{rs}|^2}{|E_{is}|^2} \qquad (13)$$

should be introduced, if the incident wave is either p- or s-polarized. In the general case, the coefficients given by (13) are less convenient for the analysis than those given by (12). The relation between these coefficients can readily be established and has the form

$$R'_p = R_p/\cos^2\beta, \quad R'_s = R_s/\sin^2\beta.$$

If the incident wave is p- or z-polarized, i.e., if $\beta = 0$ or $\beta = \pi/2$, respectively, the above coefficients coincide:

$$R'_p(0) = R'_p(0) = |r_{pp}|^2, \quad R_s(\pi/2) = R'_s(\pi/2) = |r_{ss}|^2.$$

However, in this case, $R_p(\pi/2) = |r_{ps}|^2$ and $R_s(0) = |r_{sp}|^2$, whereas the coefficients $R'_p(\pi/2)$ and $R'_s(0)$ lose their meaning since they acquire infinitely high values.

The polarization characteristics of the reflected radiation are determined by the relation $E_{rs}/E_{rp} = \tan(\theta - i\eta)$, where θ is the angle determining the orientation of the major axis of the polarization ellipse with respect to the incident plane and the angle η determines the ratio of semi-axes of the polarization ellipse, i.e., the ellipticity.

NUMERICAL ANALYSIS

For the convenient representation of the graphical data characterizing the polarization state of the reflected wave, it is advisable to introduce an auxiliary quantity, $\chi = \tan\eta$. Below, we present the results of the numerical analysis of the relations obtained above for χ, θ, and $R_{p,s}$ as their dependences on the magnetization orientation determined by the angle γ, the angle of incidence φ_0, and the orientation of the polarization plane of the incident wave determined by the angle β. In the calculations, we used the following values of parameters: $\varepsilon = 5$, $f = 5 \times 10^{-3}$ for a magnetic medium and $\varepsilon_0 = 1$ for a nonmagnetic dielectric medium.
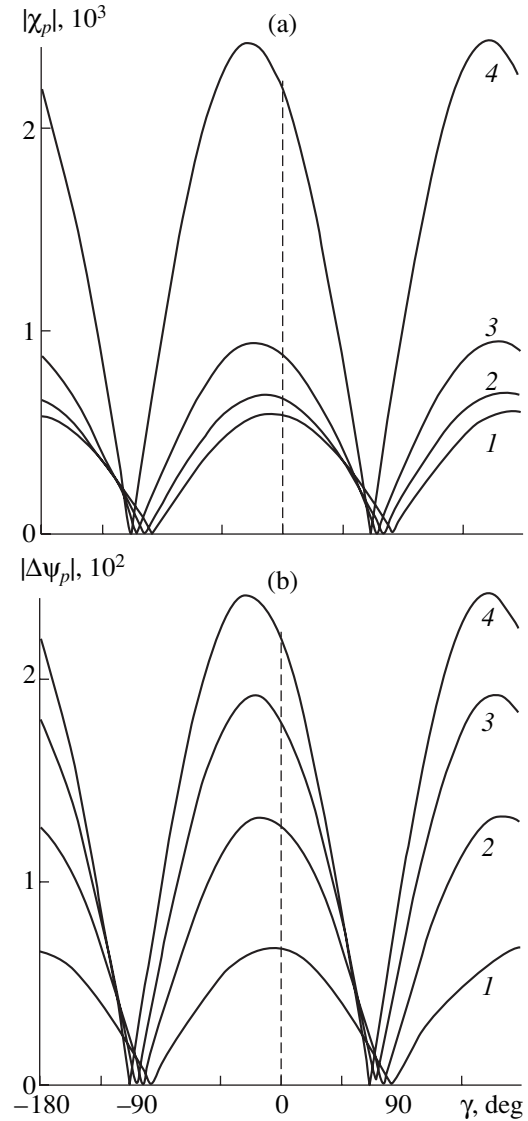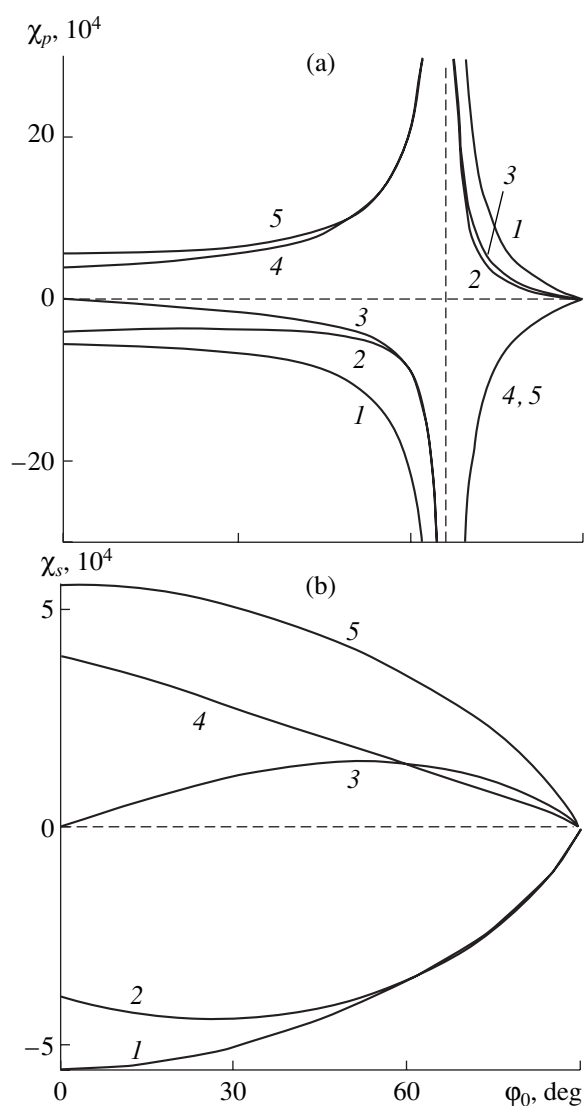

Fig. 1. (a) Moduli of ellipticity of the reflected wave and (b) the difference between the refraction angles of eigenwaves as functions of the orientation of the magnetization vector at various angles of incidence of the p-type wave: $\varphi_0 = 15°$, $30°$, $45°$, $60°$ (curves 1–4).

It is shown that the ellipticity of the reflected wave χ and the difference of the refraction angles of the eigenwaves $\Delta\psi = \psi_1 - \psi_2$ are the most sensitive to changes in the magnetization orientation. Figure 1 shows the moduli of the above quantities as functions of the angle γ obtained for the p-type incident wave and the angles of incidence $\varphi_0 = 15°$, $30°$, $45°$, $60°$ (curves 1–4). Both dependences look similar, they have the same period, and the values of the amplitudes increase with the angle of incidence in the same way. However, if the angles φ_0 are equidistant, the amplitudes $|\Delta\psi_p|$ are also equidistant, whereas the amplitudes of $|\chi_p|$ considerably increase with the approach of the

Fig. 2. Ellipticity of the reflected wave as a function of the angle of incidence at various magnetization orientations γ for the (a) p- and (b) s-polarizations of the incident wave: $\gamma = 0°$, $45°$, $90°$, $135°$, and $180°$ (curves *1–5*).
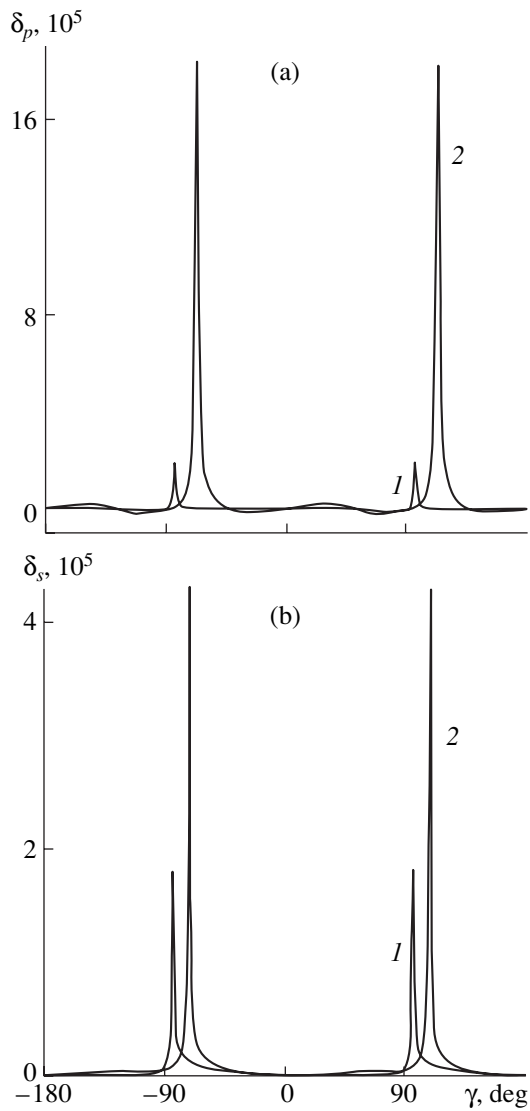
angle of incidence to the Brewster angle. The change in the sign of χ_p, which determines the direction of the rotation of the light vector over the polarization ellipse, occurs at the angle γ corresponding to the orthogonal orientation of the magnetization vector with respect to the direction of the wave propagation in the medium.

The dependence $\chi_s(\gamma)$ has a similar character; however, the amplitudes in this case are essentially less than at χ_p. Moreover, in the vicinity of the angles $\gamma = \pm 90°$, the quantity χ_s, in the linear approximation, has some singularities, which disappear if the quadratic magnetooptic coupling is taken into account.

Figure 2 shows the dependences of the ellipticity of the reflected wave on the angle of incidence at various magnetization orientations, $\gamma = 0°$, $45°$, $90°$, $135°$, and
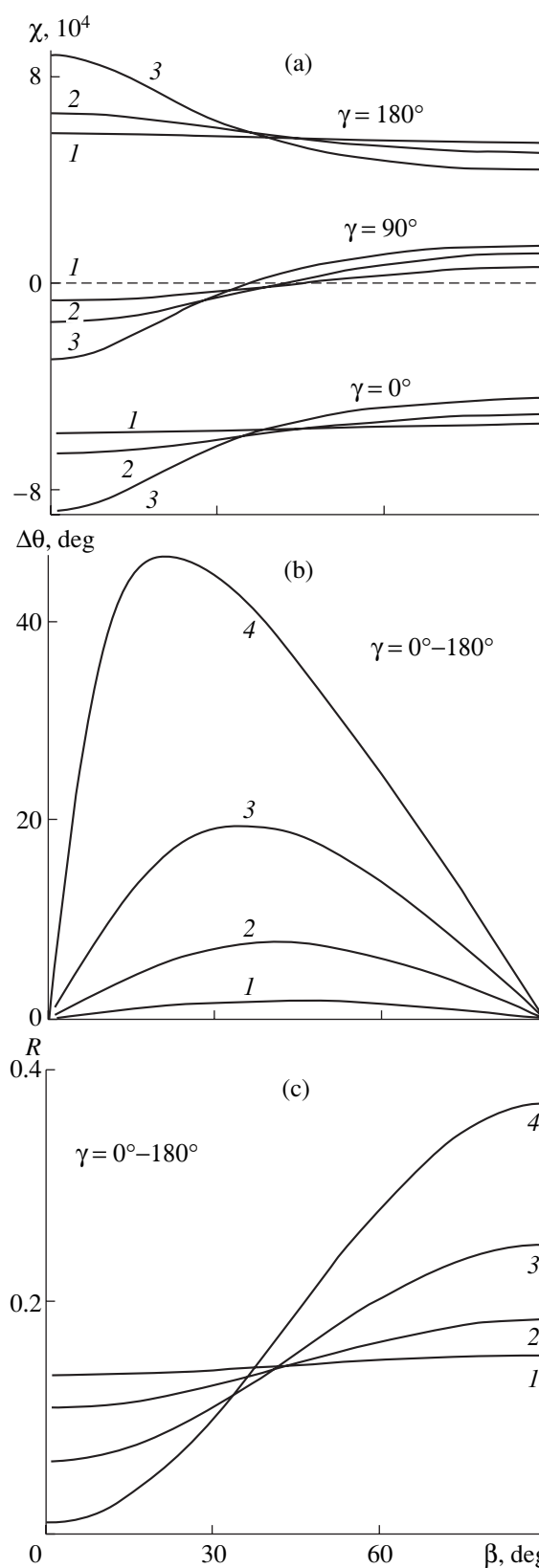
Fig. 3. (a) Ellipticity, (b) the angle or rotation of the major axis of the polarization ellipse, and (c) the reflection coefficient as functions of the orientation of the polarization plane at various angles of incidence: $\varphi_0 = 15°$, $30°$, $45°$, and $60°$ (curves *1–4*).

Fig. 4. Dependence of δ on the angle between the magnetization vector and the z axis for the (a) p- and (b) s-polarizations of the incident waves and the angles of incidence $\varphi_0 = 15°$ and $45°$ (curves $1, 2$).

angles of incidence $\varphi_0 = 15°$, $30°$, $45°$, and $60°$ (curves 1–4). Of all the dependences analyzed, only the dependence $\chi(\beta)$ is strongly dependent on the orientation of the magnetic moment, whereas $\Delta\theta(\beta)$ and $R(\beta)$ are independent of γ within the graphical accuracy. It is also seen that the ellipticity of the reflected wave at any angle β and the polar orientation ($\gamma = 0°$, $180°$) has a higher absolute value than that at meridional orientation ($\gamma = 90°$). In the latter case, with an increase in the angle β, the ellipticity goes through zero. The dependence $\Delta\theta(\beta)$ has characteristic zero values of the p- and s-polarizations at any angle of incidence, and also the maximum whose value increases with an increase in the incidence angle. At $\varphi_0 = 0°$, the maximum at $\beta = \pi/4$ is displaced towards lower β-values. The intensity of the reflected wave increases monotonically with β; the range of R variation increases with an increase in the angle of incidence within the whole range of β variation.

Figure 4 shows the $\delta = (R_0 - R)/R_0$ as a function of the magnetization orientation; here R and R_0 are the reflection coefficients at an arbitrary γ and at $\gamma = 0$. These dependences are shown for p- and s-polarized incident waves at the angles of incidence $\varphi_0 = 15°$ and $45°$ (curves 1, 2). It is seen that there are two sharp peaks for both types of polarization at two γ values corresponding to two mutually orthogonal orientations of the magnetic moment and the direction of the wave propagation. Their intensities of these peaks indicate the quadratic character of these effects with respect to the magnetooptic parameter f. This effect increases with an increase in the angle of incidence. The effect is much more pronounced for the p-polarization than for the s-polarization.

CONCLUSIONS

The main result of this study is the solution of the boundary problem for a semi-infinite magnetic medium in a saturated state with an arbitrary orientation of magnetization along the incidence plane. As a result of the numerical analysis, the intensity and the polarization parameters of the reflected wave (intensity R, the rotation angle θ of the principal axis of the polarization ellipse, and the ellipticity χ) are represented in graphical form. It is shown that the change of the angle of incidence, magnetization orientation, and the polarization plane substantially influence the polarization characteristics of the reflected wave and result in the formation of some singularities in the dependences studied. These singularities can be detected experimentally by making precise ellipsometric measurements in the windows of optical transparency of single crystal samples of garnet ferrites.

$180°$ (curves 1–5), for the p- and s-polarized incident wave. It is seen that in the vicinity of the Brewster angle, χ_p essentially depends on the angle of incidence, where a pronounced increase of ellipticity takes place. The angle ($\varphi_0 \approx 66°$) is almost independent of the magnetization orientation. At the Brewster angle, the ellipticity sign changes irrespective of the angle γ. The quantity χ_s is either a monotonic function of the angle φ_0 or has a weakly marked extremum at different values of the angle γ.

Figure 3 shows the ellipticity χ, angle of rotation of the principal axis of the polarization ellipse $\Delta\theta = \theta - \beta$, and the reflection coefficient R as functions of the orientation of the polarization plane, β, recorded at various

REFERENCES

1. G. J. Sprokel, Appl. Opt. **23** (22), 3983 (1984).

2. I. A. Andronova, E. A. Kuvatova, Yu. A. Mamaev, *et al.*, Opt. Spektrosk. **57** (2), 292 (1984) [Opt. Spectrosc. **57**, 176 (1984)].

3. G. S. Krinchik, V. L. Gribkov, V. E. Zubov, *et al.*, Opt. Spektrosk. **56** (3), 468 (1984) [Opt. Spectrosc. **56**, 287 (1984)].

4. V. E. Zubov, G. S. Krinchik, and A. S. Tablin, Opt. Spektrosk. **59** (4), 821 (1985) [Opt. Spectrosc. **59**, 496 (1985)].

5. G. S. Krinchik, E. E. Chepurova, and T. I. Kraeva, Pis'ma Zh. Tekh. Fiz. **11** (16), 1014 (1985) [Sov. Tech. Phys. Lett. **11**, 420 (1985)].

6. S. Visnovsky, Czech. J. Phys., Sect. B **36**, 834 (1986).

7. F. V. Lisovskiĭ, O. S. Markelova, and V. I. Shapovalov, Fiz. Tverd. Tela (Leningrad) **16** (12), 3570 (1974) [Sov. Phys. Solid State **16**, 2323 (1974)].

8. O. V. Ivanov and D. I. Sementsov, Kristallografiya **41** (5), 791 (1996) [Crystallogr. Rep. **41**, 749 (1996)].

Translated by A. Zalesskiĭ

Optical Phenomena in Planar AgBr Microcrystals

I. K. Azizov, A. Kh. Liev, and Kh. B. Khokonov

Kabardino-Balkar State University, ul. Chernyshevskogo 173, Nalchik, 360004 Russia
e-mail: karmokov@rambler.ru

Abstract—The formation and subsequent changes of a fringe pattern of the surface and the bulk of planar AgBr microcrystals were observed for the first time as well as their light-induced deformation in the course of a microscopic study. © *2003 MAIK "Nauka/Interperiodica"*.

Large AgBr crystals were grown from a saturated solution by two methods. The first one was a somewhat modified version of the procedure proposed in [1]. The second one, proposed by us, is based on the use of planar 1–15 μm-long microcrystals in order to grow larger AgBr crystals. Both methods for growth of microcrystals were based on the use of aqueous solutions of the starting materials.

The first method reduced to the following: 50 ml of the AgNO$_3$ solution was poured for 3 min into 50 ml of 1.0 N KBr solution at $t = 35°C$. Upon decantation (separation of the solid precipitate and the solution), the vessel with the precipitate was filled with 300 ml of 15% ammonia solution, closed tightly with a stopper, and was left to settle for 24–48 h at room temperature. Then a thin layer of the settled solution was applied onto an object plate. One to two minutes later, crystals 20–100 μm in diameter appeared on the glass surface. To prevent settlement of smaller crystals, the excessive solution was removed with the aid of the filter paper. The preparations thus obtained were washed with distilled water to remove soluble salts.

The second method for growing large silver bromide microcrystals reduces to the use of preliminarily prepared planar microcrystals synthesized by two-stream emulsification (simultaneous filling of the vessel with a vigorously stirred aqueous medium with two solutions). Upon precipitation of planar microcrystals, the vessel was filled with 15% ammonia solution, was tightly closed, and the solution thus obtained was brought to boiling point and then slowly cooled for 2–4 h in darkness. With an increase in temperature, the solubility of AgBr microcrystals in the silver medium dramatically increases, and, thus, smaller crystals are dissolved. Slow cooling results in a lower solubility and slow precipitation of AgBr from the solution. This method gives the possibility growing larger AgBr crystals (40–500 μm in diameter). The model were studied using the second method; AgBr crystals were applied to the glass surface.

The X-ray diffraction analysis of the photographic emulsions containing the planar crystals showed the presence of a certain texture oriented along the [111] direction. At the same time, during coating of the substrate with the photographic emulsion, AgBr microcrystals precipitated with larger faces onto the substrate.

Since an X-ray counter records the faces parallel to the sample surfaces, then, comparing the experimental data obtained, one can draw the conclusion that the upper and lower surfaces of a planar microcrystal are faceted with {111} faces.

The averaged thickness of planar microcrystals was determined by two methods: (1) from the broadening of the X-ray reflections from the {111} planes of AgBr microcrystals and (2) from the interference colors described by the formula for a normally incident light wave:

$$L = \frac{\lambda}{4n},$$

where L is the thickness of the microcrystal, λ is the wavelength of coloring, and n is the refractive index.

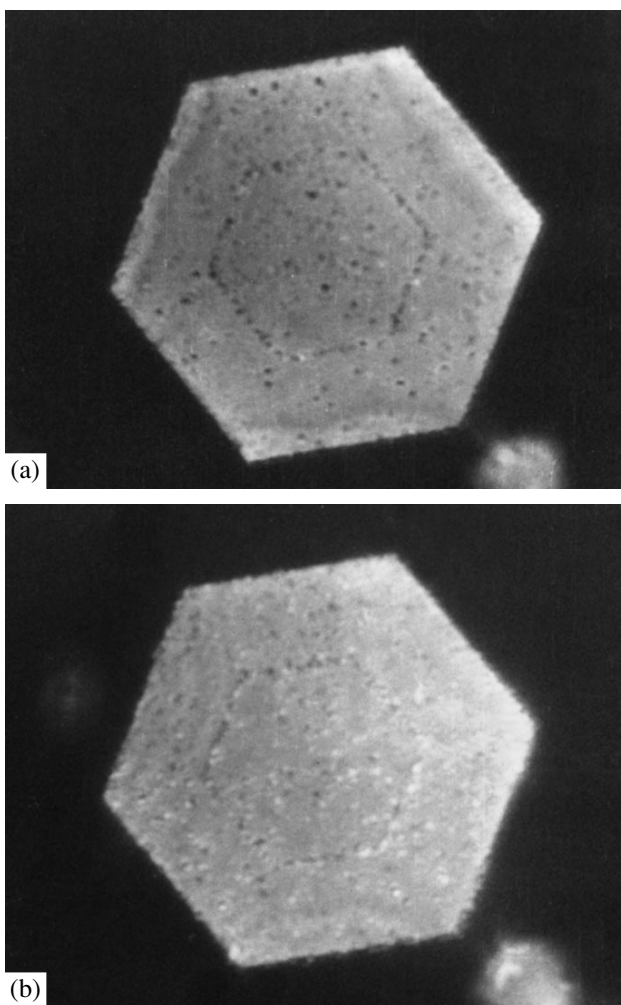The thickness of the synthesized AgBr crystals ranged from 44 to 82 nm.

The optical microscopy study of the AgBr microcrystals by the above methods showed that the microcrystal coloring "embraces" the entire visible range of the spectrum (Fig. 1). The microcrystals were also colored if a microscope objective was focused on the surface. This phenomenon should be attributed to the localized interference of light in the plane-parallel plates.

If light is absorbed by microcrystals, the excited photoelectrons reduce the interstitial Ag ions. This process is accompanied by a change in the refractive index of these microcrystals. Photolytic Ag is aggregated at certain sites of the surface (bulk) of a microcrystal, which results in the change of the fringe pattern at the sites of separation of photolytic Ag. This allows one to reconstruct the history of microcrystal growth and trace
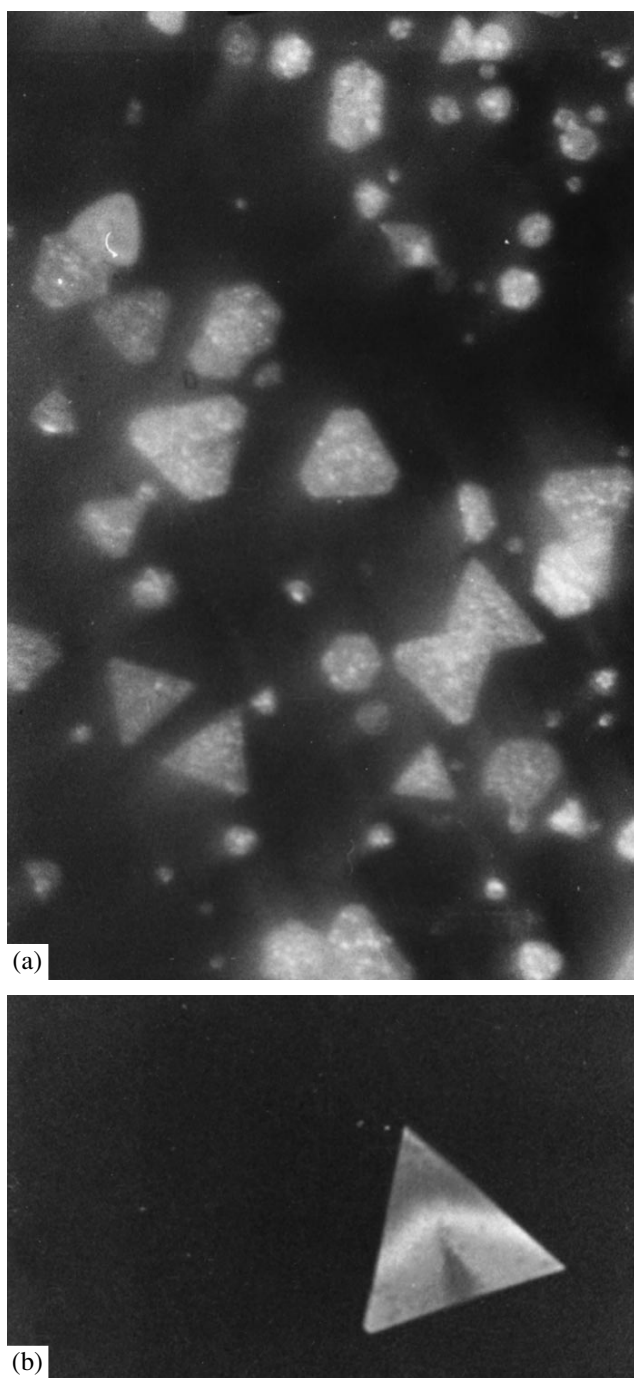
Fig. 1. (a) General view of planar AgBr microcrystals in a light microscope; (b) an individual microcrystal.

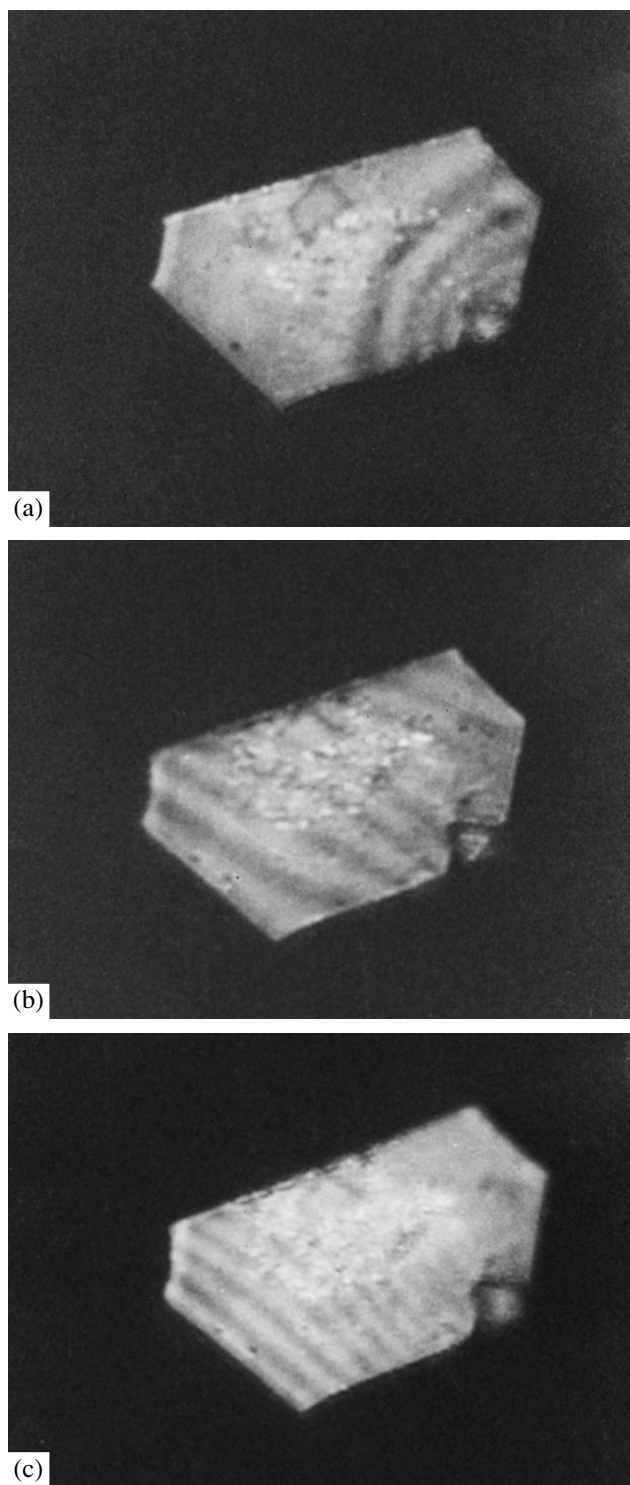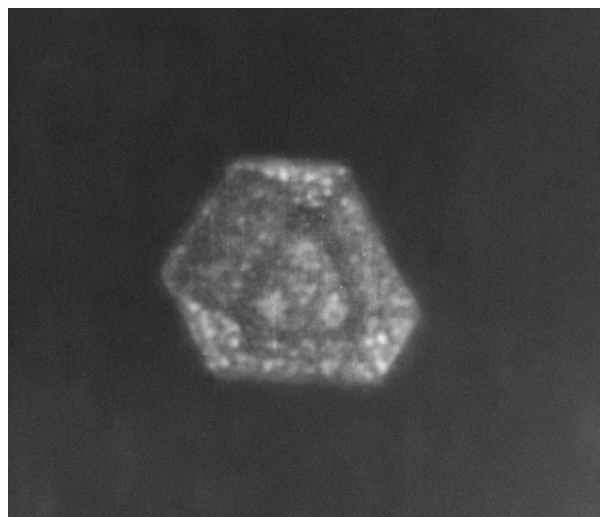**Fig. 2.** Light-induced autodecoding: (a) the initial view of a microcrystal and (b) the same view 12 s later.

the evolution of formation of silver aggregate at the microcrystal surface (autodecoding) (Fig. 2). Figure 2a is transformed into Fig. 2b within the time of 12 s. These photographs show planar microcrystals exposed to white light. Evidently, the zones of separation of photolytic silver formed under the action of light on the microcrystal surface have regular geometric shape. Silver particles are deposited on growth steps of the crystal. The photographs show alternating light and dark fringes parallel to the microcrystal faces and associated with pAg pulsation during formation of the AgBr crystal.

Thus, we observed for the first time a new phenomenon: the appearance and propagation of interference fringes at the surface (bulk) of silver bromide microcrystals synthesized by the second method under the action of white light. The "sources" of interference fringes are the sites of the highest defect concentration in microcrystals. Similar to waves, fringes propagate through microcrystals. The direction and the shape of the wave change, and the wavelength becomes shorter. The hemispherical shape of the fringes is transformed into planar (Fig. 3). Within 3 s, Fig. 3a is transformed into Fig. 3b. The samples were placed on an STN-1 table where the temperature was kept constant within ± 0.1–$0.05°C$. The effects observed do not depend on temperature, which is confirmed by the fact that the wave effects are observed only on some microcrystals of the same color (thickness).

Fig. 4. Pattern of light-induced deformation in an AgBr microcrystal.


Fig. 3. (a) Formation and (b, c) propagation of interference fringes over the surface (in the bulk) of AgBr microcrystals illuminated with white light. Fig. 3b is obtained three seconds later than Fig. 3a.

The generation of propagating waves and the change in the refractive index seem to be associated with the formation of photolytic Ag during excitation from the 4P level onto the free 5S level of silver:

$$(Ag^+ + Br^-) + h\nu \longrightarrow Ag_s + Br.$$
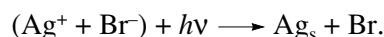
The reduction of a silver ion occurs directly at the site of the AgBr lattice. In fact, the AgBr lattice is face-centered, $a = 4.077$ Å, which is equal to the distance between the nearest Ag ions along the [111] direction in the AgBr lattice. Thus, the formation of the Ag crystal lattice requires only the deformation of the AgBr lattice accompanied by the formation of the microstress zones. On the other hand, the mobility of these zones shows the instability of the silver formed in the sites of the AgBr microcrystals, while the photoelectron motion in the conduction band of 5S silver along a certain [110] direction provides the aggregation of photolytic Ag on the "defect sites" of the lattice.

Thus, under the action of white light, the defects in the crystal lattice become the sources of propagating microstresses. Photolytic Ag concentrates at the imperfections of AgBr microcrystals. The interference phenomena on the surface of the platelike microcrystals can also be of great importance because of the unique property of AgBr to evolve photolytic silver under the action of a light quantum. The combination of these two phenomena can produce a qualitative effect on the parameters characterizing the photosensitivity of AgBr microcrystals.

In the course of the study of the optical properties of AgBr microcrystals, we discovered the phenomenon of the light-induced deformation of microcrystals. Figure 4 shows the microdeformation of a triangular silver bromide microcrystal. An electromagnetic wave from the visible range incident onto the microcrystal surface normally gives rise to a 0.5 to 1-s-long deformation that consists in bending the triangle vertices, whereas the middle part of the microcrystal is not deformed. Under the action of normally incident light, all the crystals are

deformed either in the direction of light incidence or in the opposite direction. This effect can be explained on the assumption that the larger surfaces of the microcrystals are characterized by the {111} faceting. The study of the distribution of photolytic silver over the thickness [2] showed that the crystal bulk has no visible Ag particles. These particles are concentrated in a subsurface layer several micrometers thick. The surface of an AgBr microcrystal is formed by the network of Br⁻ ions, which leave the crystal under the action of light. In turn, this may give rise to deformation of planar AgBr crystals.

Thus, new optical phenomena were found in 40 to 85-nm-thick AgBr microcrystals with a diameter of 40–500 μm. These phenomena require further investigation.

REFERENCES

1. I. M. Ratner, Zh. Nauchn. Prikl. Fotogr. Kinematogr. **11** (5), 326 (1966).
2. W. West and V. I. Saunders, J. Phys. Chem. **63**, 45 (1959).

Translated by A. Zolot'ko

PHYSICAL PROPERTIES
OF CRYSTALS

Characteristic of Spontaneous Polarization in $Li_2Ge_7O_{15}$ Crystals

Yu. V. Shaldin*, S. Matyjasik**, and M. Kh. Rabadanov*

* Shubnikov Institute of Crystallography, Russian Academy of Sciences,
Leninskiĭ pr. 59, Moscow, 119333 Russia
e-mail: graimo@aha.ru
** International Laboratory of High Magnetic Fields and Low Temperatures, Wroclaw, Poland
Received March 28, 2002

Abstract—The temperature dependence of spontaneous polarization in $Li_2Ge_7O_{15}$, a ferroelectric with one polarization axis, is studied in the temperature range from 4.2 K to T_C. An unusual character of spontaneous polarization associated with the change of the crystal behavior from the Ising to multipole type is revealed in the vicinity of T_C. The low value of spontaneous polarization is explained not by the relation between certain physical quantities, but rather by the interaction of the components of higher order ($n > 2$) electric moments which, by definition, have rather low values. The $Li_2Ge_7O_{15}$ structure is built by macrofragments consisting of two types of mesotetrahedra whose distortion results in the appearance of pseudopolarization of the nonvector type. © 2003 MAIK "Nauka/Interperiodica".

INTRODUCTION

It is obvious that, in the broad sense, spontaneous polarization is the central problem for all pyroelectrics, including so-called pseudoproper ferroelectrics. It seems that $Li_2Ge_7O_{15}$ (LGO) crystals, in which the phase transition is characterized by low values of the spontaneous polarization and Curie–Weiss constant, should be assigned to pseudoproper ferroelectrics as well.

An LGO ferroelectric with one polarization axis undergoes a phase transition from the polar ($Pbc2_1$) to the high-temperature ($Pbcn$) phase at $T_C = 238.5$ K [1–3]. The Curie–Weiss constants are rather low, 0.82 ($T < T_C$) and 3.2 K ($T > T_C$) [4]. The known data on the spontaneous polarization P_s show a considerable scatter, from 2.2×10^{-4} to 3.8×10^{-4} C/m² ($T = 248$ K) [4, 5]. There is no detailed information on the behavior of $P_s(T)$ in the vicinity of T_C. The data on spontaneous polarization obtained in the temperature range from 15 to 300 K [5] indicate its rather unusual behavior, in particular, the change of its sign at $T = 135$ K. Similar behavior was also established for sodium biphthalate single crystals [6]. The pyroelectric studies [4] revealed a slight anomaly in the pyroelectric constant $\gamma(T)$ in the vicinity of 220 K and a change in the sign of this constant at $T = 248$ K, which corresponds to the maximum spontaneous polarization. It was also established that a 1%-level of LGO doping (e.g., with Ni) considerably changes the behavior of spontaneous polarization and the phase-transition temperature [7].

The dynamics of the vibration spectrum of the LGO lattice studied by the Raman scattering [8] and submillimeter spectroscopy [9] revealed the soft mode on both left- and right-hand sides of T_C responsible for the displacive-type phase transition. Thus, LGO crystals are reminiscent of $(CH_3NHCH_2COOH)_3CaCl_2$ crystals [10]: the authors believe that the dipole–dipole interaction is rather weak and gives a pronounced contribution to spontaneous polarization only in the vicinity of T_C. Therefore, there are grounds to believe that with an approach to T_C, the typical Ising behavior of LGO crystals changes to pseudodipole behavior. At first sight, this assumption is consistent with the data of more recent studies [11]. The key role is assumed to be played by the ordering of the orientations of GeO_4 tetrahedra, which, together with GeO_6 octahedra, form continuous $GeO_6–GeO_4–GeO_4–GeO_4–GeO_6–\dots$ chains along the $\langle 001 \rangle$ directions (Fig. 1). With an approach to T_C from the side of the polar phase, the disorder in tetrahedron orientations induces a displacive-type phase transition in the sublattice formed by the tetrahedra. On the other hand, the diffraction experiments show the existence of two nonequivalent lithium positions in the structure, Li(1) and Li(2). The NMR ⁷Li data [12] allowed one to establish that the sublattice of Li(1) atoms at $T > T_C$ is more ordered than the lattice of Li(2) atoms. Further NMR experiments showed that the geometry of the nearest environment of a Li(1) atom undergoes considerable changes in the transition to the low-temperature phase [13]. The pronounced deformations of the nearest environment arising in this case compensate the distortion of the medium along the crystallographic $\langle 001 \rangle$ directions and, thus, determine a low value of P_s. The possible contribution of multipole interactions was ignored.
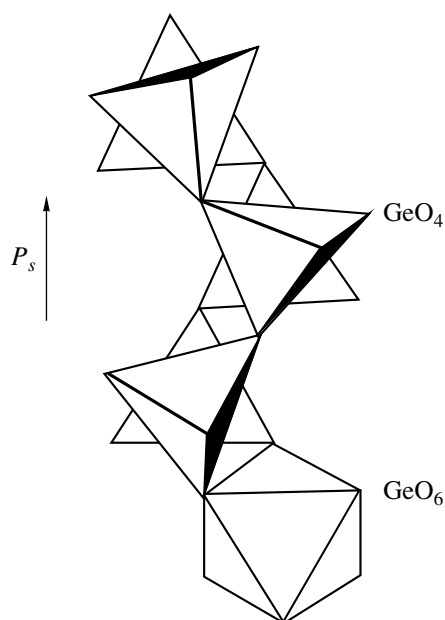
Fig. 1. Fragment of the LGO structure where ordering of the tetrahedron orientations determines the order–disorder phase transition. P_s is the direction of the spontaneous polarization.

Despite the unambiguous structural data, the specific features of the phase transition were interpreted in [5, 11] as a result of the presence in the structure of two strongly interacting antiparallel polarized sublattices. However, a similar situation should be characteristic not only of LGO crystals but also of all pyroelectrics. This was confirmed within the framework of the crystallophysical approach [14]. Moreover, in the structure of some crystals such as $LiTaO_3$ [15], $KTiOPO_4$ [16], $LiBO_3$ [17], etc., two antiparallel-polarized sublattices formed by two types of mesotetrahedra possessing dipole moments with different magnitudes and signs were singled out. Thus, the existence of two sublattices cannot be explained by low spontaneous polarization P_s in LGO crystals. We believe that it is very interesting to establish the cause of such a low effective charge of the soft-mode branch. The latter can be established by comparing the data on the temperature dependence of the order parameters (which are not necessarily the components of the first-rank tensor) with the results of structural studies.

Thus, to better understand the nature of the phase transitions, in general, and in LGO, in particular, it is important to establish the nature of the order parameters in LGO, a weak ferroelectric. With this aim, we undertook a detailed study of spontaneous polarization everywhere including the region of the phase transition. The data obtained are analyzed with due regard for the structural characteristics of LGO crystals determining the character of multipole interactions.

EXPERIMENTAL

To measure the spontaneous polarization of LGO crystals, we used the conventional pyroelectric method, which allows one to reproduce the behavior of $P_s(T)$ in the whole range of existence of the low-temperature phase with a sufficient accuracy under the condition that the phase-transition temperature can be attained under real experimental conditions.
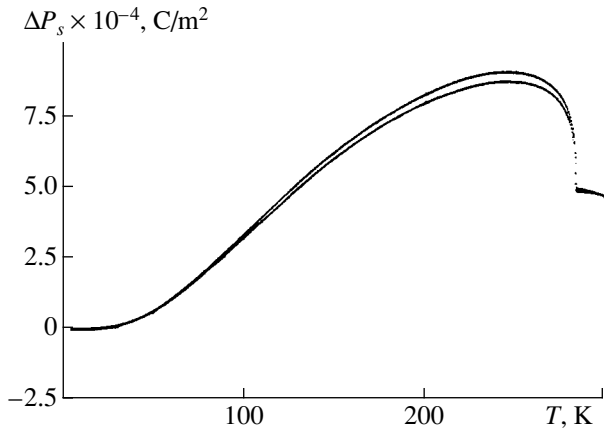
LGO Crystals

The studies were performed on single crystals grown at the Institute of Crystallography of the Russian Academy of Sciences. The faceting of the crystals grown corresponded to the inherent symmetry elements. The crystals had a cleavage plane, which indicated a high perfection of the grown boule; chromium impurity attained a level of $10^{-2}\%$. The study of the absorption spectra showed that chromium ions, Cr^{+4} and Cr^{+3}, are located in the germanium positions in the octahedra and tetrahedra, respectively [18]. Different intensities of the two absorption bands allow one to assume that the probability of chromium being located in octahedra is higher by an order of magnitude than the probability of their being located in tetrahedra, i.e., that the concentration of Cr^{+3} is at a level of noncontrollable impurities. This is a very important result, because, as will be shown later, the tetrahedra directly participate in the formation of the polar LGO phase.

We selected a boule elongated in the $\langle 100 \rangle$ direction and cut out of it two rectangular z-cut plates with surface areas of 0.49 and 0.89 mm^2 and a thickness of 2.3 mm. The electrodes were prepared from a silver paste applied to preliminarily cleaned (001) surfaces. A monodomain state of the sample was attained in a ± 500-V/cm electric field.

Preliminary measurements showed that the incorporation of chromium into the sample composition does not change the temperature of the ferroelectric phase transition.

Experimental Technique

The electric charge arising on the surface of LGO samples with a change in temperature of ΔT was measured by an electrometer of series 617 produced by Keithly. The sample was suspended on a thin wire in a crystal holder placed into a helium cryostat. The temperature was measured by a Cemox-1050CD thermometer. The sample temperature was varied with a programmed thermoregulator of series 222 produced by the same company. The samples were mounted in correspondence with the conditions necessary for measuring spontaneous polarization and the pyroelectric constant of the sample in the mechanically free state. All the measurements were made during sample heating from 4.2 K to the temperatures $T > T_C$. The measurements were repeated in the fields of different polarity

$\Delta P_s \times 10^{-4}$, C/m^2

Fig. 2. Effective values of the changes in spontaneous polarization in LGO crystals in the temperature range from 4.2 to 300 K. The curves correspond to two cycles of ΔP_s measurements.

$P_s \times 10^{-4}$, C/m^2
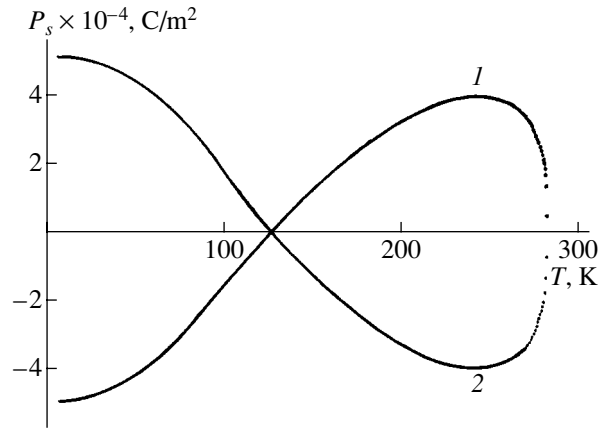
Fig. 3. Temperature dependence of spontaneous polarization of LGO crystals. (*1*) $E = 500$, (*2*) $E = -500$ V/cm.

with the subsequent cooling of the sample to helium temperature. Then, the sample was kept for a certain time under these conditions, and then the measurements were taken again. The drift of the zero of the measuring system within the three-hour-long experiment determined the main experimental error, which did not exceed ±5%.

The experimental curves of the change in ΔP_s with an increase in the sample temperature were recorded within two cycles of measurements. The difference between these curves is caused only by the zero drift in the measuring system. No noticeable anomalies were recorded either in the low-temperature range or in the range of the phase transition. The experimental $\Delta P_s(T)$ curves thus obtained were normalized with due regard for the fact that spontaneous polarization tends to zero at $T > T_C$.

RESULTS AND DISCUSSION

The results of the processing of the experimental data that describe the temperature dependence $P_s(T)$ in LGO crystals are shown in Fig. 3. As was to be expected, the maximum P_s value is obtained in the low-temperature range. The difference between the data obtained in [5] and our results seems to be caused by different fixation of the sample in the crystal holder and, therefore, are of minor importance. The change in the sign of spontaneous polarization is observed at $T = 125$ K. No anomalies in the low-temperature range that could indicate the presence of impurities were observed.

The study of the behavior of P_s in the vicinity of the phase transition showed its nonmonotonic dependence on temperature (Figs. 4a, 4b), which indicates some specific features of the phase transition in LGO. The anomaly is also characteristic of the temperature dependence of the pyroelectric constant (Fig. 4c). The

well pronounced transition to the high-temperature phase indicates the infinitesimal contribution of the substitutional-type defects to the change of the transition temperature. The $P_s(T)$ dependence in the logarithmic coordinates (Fig. 4b) confirms the change in the
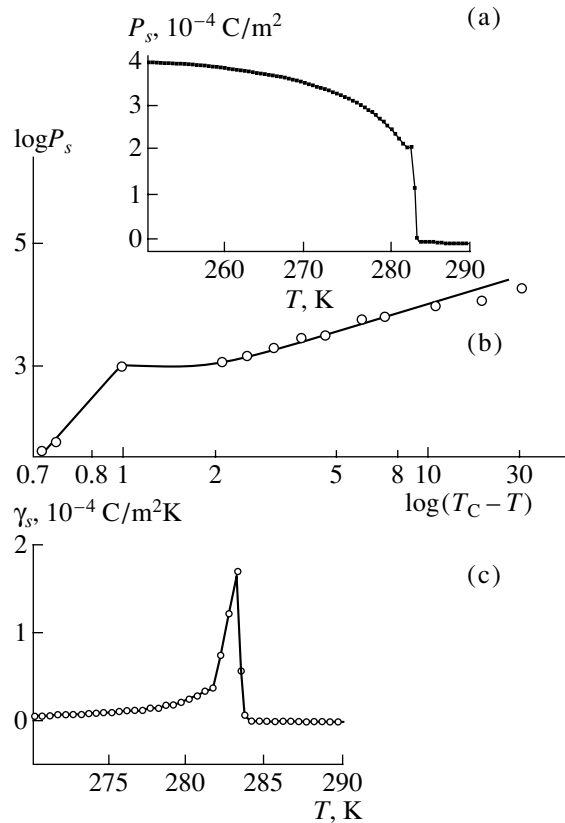
Fig. 4. Temperature dependence of (a, b) spontaneous polarization P_s and (c) pyroelectric constant γ_s in the vicinity of the phase transition; (a, c) on the conventional scale, (b) on the logarithmic scale.
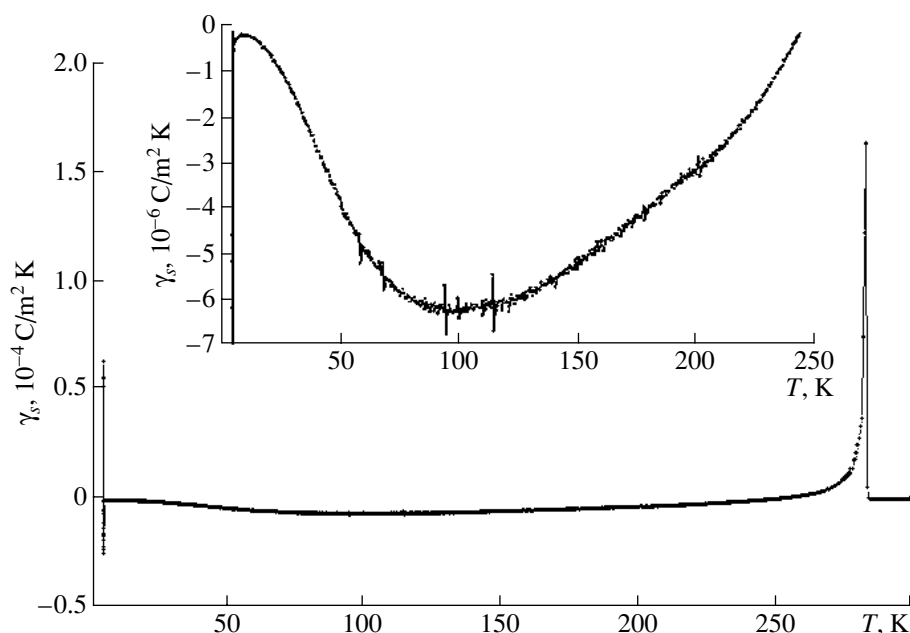
Fig. 5. Temperature dependence of the pyroelectric constant in the range from 4.2 to 300 K.

character of the phase transition, namely, in the temperature range from $(T_C–2$ K$)$ to $(T_C–30$ K$)$, polarization obeys the law $P_s \sim (T_C–T)^{0.3}$ at $T_C = 284$ K, whereas in the temperature range from 283 to 283.5 K, it obeys the law $P_s \sim (T_C–T)^{1.25}$. In the first case, the exponent is close to the critical one, 5/16 [19], which correspond to the three-dimensional Ising model. In the range from $T_C–2$ K to 283 K, $\partial P_s/\partial T$ goes to zero.

Additional information on the characteristics of the phase transition can be obtained from the detailed analysis of the data on the pyroelectric constant measured over a wide temperature range (Fig. 5). Figure 5 also shows the dependence $\gamma_s(T)$ in the temperature range from 4.2 K to T_C. The maximum value of γ_s equal to 1.7×10^{-4} C/m^2 K corresponds to $(283.1 \pm 0.5$ K$)$ and exceeds the result obtained in [4] by an order of magnitude.

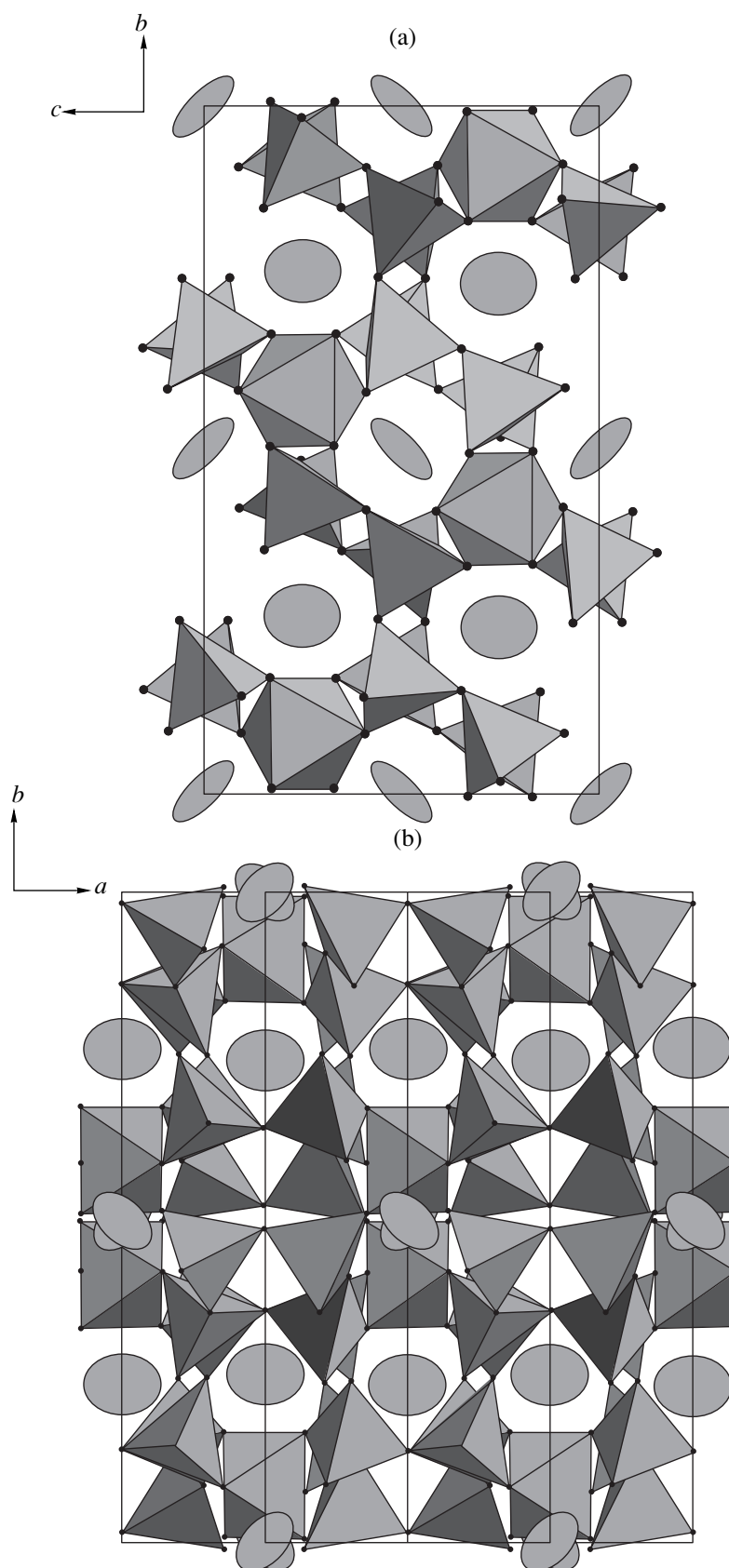It is well known that within the Born–Einstein model, the temperature dependence $\gamma_s(T)$ can be approximated by the following expression [20]:

$$\gamma_s(T) = A_d D(\theta_d/T) + \sum_{i=1}^{3} A_{ei} E(\theta_{ei}/T), \qquad (1)$$

where $D(\theta_d/T)$ and $E(\theta_{ei}/T)$ are the Debye and Einstein functions and A_d and A_{ei} are the corresponding coefficients. Such an approximation is valid only for linear pyroelectrics. In ferroelectrics, the situation is quite different. At temperatures lower than 4 K, the main contribution comes from the acoustic vibrations and $\gamma_s \sim T^3$ [21]; with an increase in the temperature, the more pronounced optical vibrations "catch" weak acoustic vibrations. This phenomenon is well known in the theory of vibrations. For LGO, the condition $A_d \neq 0$ (see table) should be considered as a result of the weak efficiency of the interactions between the acoustic and optical lattice vibrations. It seems that it is this fact that constitutes the difference between conventional ferroelectrics and their pseudoanalogues.

The above data on spontaneous polarization in LGO are inconsistent with the conventional concepts of the nature of ferroelectric ordering in crystals [19]. Therefore, we shall try here to take into account not only the dipole–dipole interactions but also the multipole interactions within the phenomenological approach described in [22]. Thus, the transition into the polar LGO phase can be described by a set of noncentrosymmetric parameters that can be transformed like tensor quantities such as vectors, pseudodeviators, and septors [23]. According to the symmetry of crystals described by the point group *mm*2, the components of the tensors

Parameters of the approximation of the temperature dependence of the pyroelectric constant of an LGO crystal calculated by Eq. (1) ($A_j \times 10^{-6}$ C/m^2 K and θ_j, K)

A_d	A_{e1}	A_{e2}	A_{e3}
2.05	7.77	–3.67	–1.43
θ_d	θ_{e1}	θ_{e2}	θ_{e3}
125	200	360	880

Fig. 6. LGO structure projected onto the (a) (001) and (b) (100) planes of the paraelectric phase.
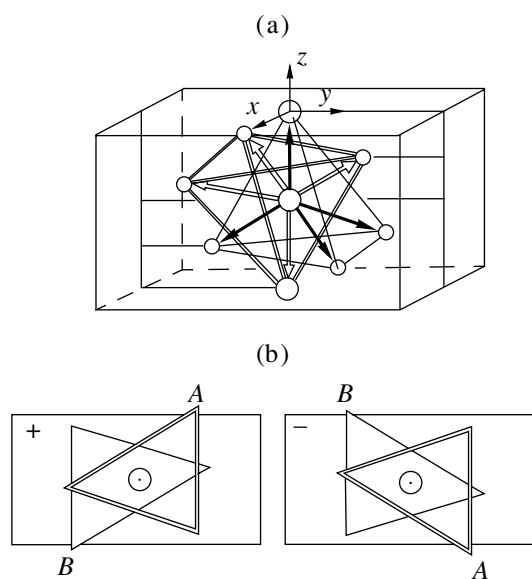
Fig. 7. (a) The main motif of the LGO structure represented by two mesotetrahedra, $A(1)$ and $B(2)$, connected by the GeO_4–GeO_4–GeO_4–GeO_6 chains and (b) their projections onto the (001) plane with the change of the sign of the field that gives rise to the formation of the monodomain state of the sample. Large circles represent Li(1) atoms; small circles represent Li (2) atoms.

P_3', $-P_3''$, Q_{12}^*, S_{131}, and S_{232} have nonzero values. The quantities thus introduced characterize the dipole, pseudoquadrupole, and octupole moments of the LGO structure.

On the other hand, the loss of the center of inversion by the medium can be depicted in graphical form by representing the structure by a set of mesotetrahedra connecting individual fragments of the structure. Analyzing the data in [11], we can single out two types of mesotetrahedra formed by two lithium atoms, Li(1) and Li(2), located in crystallographically different positions (Fig. 6). The charge states of these atoms are not equivalent and are determined by their nearest environment. Two mesotetrahedra in Fig. 7a form infinite chains along the $\langle 001 \rangle$ directions. The local symmetry of the chain elements corresponds to the point group $mm2$. The orientation of the mesotetrahedra with respect to one another corresponds to a sphalerite-type structure with the zero dipole moment dictated by the symmetry. Thus, in the first approximation, the intrinsic dipole moment of the LGO structure should be infinitesimal.

The Li(1) and Li(2) atoms are bound by the structural fragments obeying the symmetry conditions (Fig. 1). In turn, the central atoms of the Li(1) mesotetrahedra are bound to the periphery Li(2) atoms via GeO_4 tetrahedra. The tetrahedra are strongly deformed [11] and, therefore, possess dipole moments. Unlike the KH_2PO_4 structure, where the mesotetrahedra are bound by hydrogen atoms [23], in the LGO structure, the situation is much more complicated. The existence of the

intermediate element (GeO_6 octahedron possessing no dipole moment in the first approximation) in the infinite chain (Fig. 1) makes multipole interactions less efficient. Thus, this model is reminiscent of the situation with the structurally simplest NH_4Cl compound, where the ordering of hydrogen atoms over the bonds is described sufficiently well within the Ising model [24]. The temperature dependence of the octupole moment (which seems to play the role of the order parameter) obeys the law of 1/8. In the case of LGO, the critical index calculated based on the experimental data is close to 5/16, which corresponds to a three-dimensional analogue of the Ising model [19]. Therefore, there are grounds to believe that, in the LGO structure, the orientations of GeO_4 tetrahedra are ordered along all the three crystallographic directions. In other words, the transition to the polar phase is accompanied by the appearance of the octupole moment of the structure.

The experimentally measured spontaneous polarization is related to the components of the octupole moment by the formula

$$P_s' = g_{3311}S_{311} + g_{3322}S_{322}, \qquad (2)$$

where g_{33ii} are the coefficients of a tensor of rank four symmetric with respect to the permutation of the three latter indices. Thus, in the case of LGO, one has to consider the order–disorder phase transition of the sublattice of GeO_4 positions, which is accompanied by the appearance of an octupole moment of mesotetrahedra forming the noncentrosymmetric motif of the LGO structure.

The appearance of octupole moments is accompanied by the change in the nearest environment of the Li(1) atoms [13], whereas the Li(2) atoms (statistically distributed over two equilibrium positions) are ordered in the (001) plane (Fig. 7b). Depending on the sign of the applied field, the bases of the mesotetrahedra are rotated in two opposite directions. Such a distortion of the LGO structure is accompanied by the appearance of the pseudoquadrupole moment whose magnitude, as in the case of KH_2PO_4, can be either measured directly [23] or calculated measuring the total pseudopolarization of the LGO sample:

$$P_s = P_s' + P_s'' = g_{3311}S_{311} + g_{3322}S_{322} + g_{123}^*Q_{12}^*. \quad (3)$$

Here g_{123}^* is the nonzero component of the pseudotensor of rank three in the low-temperature phase. From the condition of the free-energy minimum, it follows that the signs of the quantities P_s' and P_s'' should be opposite, which decreases the total polarization, whereas its change in the range from 4.2 to 300 K acquires the form shown in Fig. 3. This is confirmed by the approximated temperature dependence of the pyroelectric constant (see table) which indicates different contributions (both in magnitude and sign) of the optical vibrations of the LGO lattice. Therefore, the tem-

perature dependence of the pseudopolarization of LGO is the consequence of a number of facts. First, it is quite obvious that the octupole moment is the quantity of the next order of smallness in comparison with Q_{12}^*; i.e., $P_s'' > P_s'$. Second, the temperature dependence of P_s' far from T_C should be more pronounced than P_s''. Third, at a temperature of 283.5 K, a displacive-type phase transition takes place, since the value of P_s changes almost in a jumpwise manner. Fourth, the phase-transition temperatures of the GeO sublattice GeO_4 and $Li(2)$ positions should be different. To show this, one has to develop direct methods for measuring multipole moments in noncentrosymmetric crystals.

CONCLUSIONS

The situation in LGO is reminiscent of the situation in improper ferroelectrics of the gadolinium molybdate type [25], in which the role of the transition parameter is played by spontaneous deformation and the spontaneous polarization attaining the values of 10^{-3} C/m² is only a consequence of this fact. In LGO crystals, the problem of the existence of multipole interactions has not been formulated even theoretically as yet, although the low spontaneous polarization is the consequence of the existence of nonzero multipole moments. In conventional ferroelectrics such as KH_2PO_4, the contribution of multipole moments is infinitesimal [21].

ACKNOWLEDGMENTS

REFERENCES

1. V. Wada, A. Sawada, and Y. Ishibashi, J. Phys. Soc. Jpn. **50** (6), 1811 (1981).

2. P. Preu and S. Hausuhl, Solid State Commun. **41** (8), 627 (1982).

3. M. Wada and Y. Ishibashi, J. Phys. Soc. Jpn. **52** (1), 193 (1983).

4. A. A. Bush and Yu. N. Venevtsev, Fiz. Tverd. Tela (Leningrad) **28** (7), 1970 (1986) [Sov. Phys. Solid State **28**, 1101 (1986)].

5. F. Sawada and M. Njvfnsu, Ferroelectrics **137**, 297 (1992).

6. R. Poprawski, S. Matyjasik, and Yu. Shaldin, Mat. Sci. XIII **1–2**, 203 (1987).

7. A. Yu. Kudzin, M. D. Volnyanskiĭ, M. P. Trubitsyn, and I. A. Busoul, Fiz. Tverd. Tela (St. Petersburg) **12**, 2198 (1998) [Phys. Solid State **40**, 1994 (1998)].

8. H. Orihara, V. Wada, and Y. Ishibashi, J. Phys. Soc. Jpn. **52** (4), 1478 (1983).

9. A. Volkov, G. Kozlov, Yu. Goncharov, *et al.*, J. Phys. Soc. Jpn. **54** (1), 818 (1985).

10. G. A. Smolenskiĭ, I. G. Siniĭ, A. K. Tagantsev, *et al.*, Zh. Éksp. Teor. Fiz. **88**, 1020 (1985) [Sov. Phys. JETP **61**, 599 (1985)].

11. Y. Iwata, J. Shibyja, M. Wada, *et al.*, J. Phys. Soc. Jpn. **56** (7), 2420 (1987).

12. A. A. Vashman, Yu. B. Muravlev, A. M. Vilyanskiĭ, *et al.*, Zh. Neorg. Khim. **44** (11), 1894 (1999).

13. E. G. Il'in, A. A. Vashman, Yu. B. Muravlev, *et al.*, Dokl. Akad. Nauk **380** (4), 501 (2001).

14. Yu. V. Shaldin, Fiz. Tverd. Tela (Leningrad) **19** (6), 1580 (1977) [Sov. Phys. Solid State **19**, 922 (1977)].

15. Yu. V. Shaldin and V. A. Maslov, Opt. Spektrosk. **72** (4), 913 (1992) [Opt. Spectrosc. **72**, 492 (1992)].

16. Yu. V. Shaldin, R. Popravskiĭ, and S. Matyyasik, Fiz. Tverd. Tela (St. Petersburg) **34** (4), 1160 (1995) [Phys. Solid State **37**, 630 (1995)].

17. S. Matyyasik and Yu. V. Shaldin, Fiz. Tverd. Tela (St. Petersburg) **43** (8), 1405 (2001) [Phys. Solid State **43**, 1464 (2001)].

18. Z. B. Perekalina, V. P. Orekhova, K. A. Kaldybaev, *et al.*, Kristallografiya **46** (5), 900 (2001) [Crystallogr. Rep. **46**, 826 (2001)].

19. M. E. Lines and A. M. Glass, *Principles and Application of Ferroelectrics and Related Materials* (Clarendon Press, Oxford, 1977; Mir, Moscow, 1981).

20. N. D. Gavrilova, E. G. Maksimov, V. K. Novik, and S. P. Drozhdin, Fiz. Tverd. Tela (St. Petersburg) **27** (9), 2597 (1985) [Sov. Phys. Solid State **27**, 1559 (1985)].

21. J. Magnin and A. Handi, Phys. Rev. B **27** (12), 7730 (1983).

22. J. A. Schouten, *Tensor Analysis for Physicists*, 2nd ed. (Clarendon Press, Oxford, 1954; Nauka, Moscow, 1965).

23. Yu. V. Shaldin, Dokl. Akad. Nauk **364** (1), 49 (1999) [Dokl. Phys. **44**, 14 (1999)].

24. J. Pique, G. Dolino, and V. Vallade, J. Phys. (Paris) **39**, 1003 (1978).

25. A. P. Levanyuk and D. G. Sannikov, Usp. Fiz. Nauk **112**, 561 (1974) [Sov. Phys. Usp. **17**, 199 (1974)].

Translated by L. Man

PHYSICAL PROPERTIES
OF CRYSTALS

Dielectric Properties of Rapidly Grown KDP Crystals

S. V. Grabovskiĭ, I. V. Shnaĭdshteĭn, and B. A. Strukov

Moscow State University, Vorob'evy gory, Moscow, 119992 Russia
e-mail: serg1979@mtu-net.ru
Received March 28, 2002

Abstract—The dielectric properties of rapidly grown potassium dihydrogen phosphate KH_2PO_4 (KDP) crystals have been studied over a wide temperature range and compared with the properties of traditionally grown KDP crystals. It was found that the contribution of domains to permittivity in rapidly grown crystals is considerably less than in conventionally grown ones. The dielectric properties in various growth sectors of KDP crystals are determined. © *2003 MAIK "Nauka/Interperiodica".*

INTRODUCTION

It is well known that the polar phase of ferroelectric KDP crystals exhibits an anomalous behavior of dielectric properties [1, 2]: permittivity does not decrease (as is expected according to the phenomenological theory) but has anomalously high values and remains almost constant over a wide temperature range. Such a behavior of permittivity of a KDP crystal is explained by an anomalous contribution of domains to permittivity in the ferroelectric phase [3, 4].

The nature of the anomalous contribution of domains to permittivity was studied in many works, in particular, the effect of various external factors, defects, and impurities [5, 6], as well as the measurement conditions [7]. However, the physical nature of the anomalous behavior of the dielectric properties has not been established as yet [8]. Below we describe our study of the dielectric properties of KDP crystals grown by different methods.

KDP crystals are a model object for studying the basic problems of ferroelectricity and phase transitions and are of great interest because of the practical use of their nonlinear optical properties. The use of large KDP crystals in laser optics stimulated the development of a rapid growth method with [9] a growth rate of up to 10 mm/day, which is higher by more than an order of magnitude than in the traditional method of growth in KPD crystals. Usually, an increase in the growth rate results in a deterioration of the crystal quality. However, the optical properties of rapidly grown KDP crystals proved to be sufficient for their use in nonlinear optical devices [10]. Since no data on the dielectric properties of these crystals are available, the present study was undertaken with the aim of comparing the dielectric properties of rapidly grown KDP crystals with the properties of KDP crystals grown by the traditional method and, thus, establishing the influence of the growth method on the quality of KDP crystals.

Rapidly grown KDP crystals are characterized by the well-developed prismatic sector that is practically not observed in crystals grown by the traditional method [11, 12], which allows one to compare the dielectric properties in different sectors of rapidly grows KDP crystals (in the studies of the "traditional" KDP crystals, only the data for the pyramidal sector are reported).

EXPERIMENTAL

The KDP crystals under study were grown on a point seed using the rapid-growth technique described in [12, 13]. The dimensions of the crystals grown were $\sim 8 \times 8 \times 9$ cm. The crystals had well-developed {101} pyramidal and {100} prismatic growth sectors.

The samples were cut out from both sectors of the crystal in the shape of plates with the surface plane being normal to the polar axis. The average surface area was 5×8 mm^2; the thickness was 1 mm. The sample faces normal to the c axis were coated with a thin layer of silver paste.

For the comparative analysis of the dielectric properties, we also used a KDP crystal grown by the traditional slow growth method, in which growth of the prismatic sector was practically blocked. Samples of the same dimensions were also prepared from the pyramidal sector of this crystal.

The temperature dependences of permittivity were measured during the cooling of samples from room to liquid-nitrogen temperature. The cooling rate was 0.5–1 K/min in the paraphase that is far from T_C and 0.2 K/min in the vicinity of the transition point. In recording the temperature hysteresis in the close vicinity of the phase transition, both the cooling and heating rates were 0.1 K/min.

All the measurements were performed by the bridge method using an E7-14 immitance meter at a frequency

of 10 kHz; the level of the measuring signal applied to the sample was 0.04 or 2 V.

RESULTS

Figure 1 shows the temperature dependences of permittivity and the tangent of dielectric losses for a rapidly grown KDP crystal and a traditionally grown KDP crystal.

In the paraelectric phase, the temperature dependences of permittivity were the same for all the crystals studied; the Curie point was measured at 121.8 K.

The temperature dependence for the traditional ("classical") crystal (Fig. 1a, curve *1*) coincides with data [14, 15]. Below the Curie point, a region of anomalous values of permittivity is observed ("plateau" region). Close to 80 K, the ε_C value drops, while $\tan\delta$ approaches the maximum (the phenomenon of domain freezing; the maximum of $\tan\delta$ is observed at the freezing temperature T_F).

As is seen from Fig. 1a, the dielectric properties of the polar phase of rapidly grown crystals are characterized by the suppression of the ε_C maximum at the Curie point. The permittivity value in the plateau region of a rapidly grown crystal is much lower than the value in the "classical" crystal.

The temperature dependences of the dielectric-loss tangent (Fig. 1b) are typical of KDP crystals—a jump at the Curie point and the maximum in the region of domain freezing [16]. For "rapid crystals," the values of the maxima at T_F are lower than for a traditional crystals. In addition, the character of the $\tan\delta$ curve is changed below T_C in the plateau region—with a decrease in the temperature below the transition point, $\tan\delta$ starts increasing instead of decreasing (as in the pyramidal sectors). In the plateau region, the values of $\tan\delta$ in the prismatic sector are higher by a factor of 2–3 than in the pyramidal sector (Fig. 1b, curve *3*).

Figures 2 and 3 show the temperature dependences of the inverse permittivity in the vicinity of the phase transition during cooling and heating. For all the crystals, the hysteresis characteristic of the point of the first-order phase transition is observed. For a traditional crystal (Fig. 2), a continuous transition is observed during cooling and a jumplike transition, during heating. The hysteresis reproduces the dependence first reported in [17]. In both pyramidal and prismatic sectors of the rapid crystal (Fig. 3), the jumps in permittivity were observed during heating and cooling. In this case, noticeable hysteresis of ε_C in the polar phase was observed in the pyramidal sector of a rapid crystal; the results of its study will be considered elsewhere.

DISCUSSION

Figure 1a shows that permittivity in the plateau region of the rapidly grown KDP crystals is much lower than the permittivity of traditional crystals. High per-
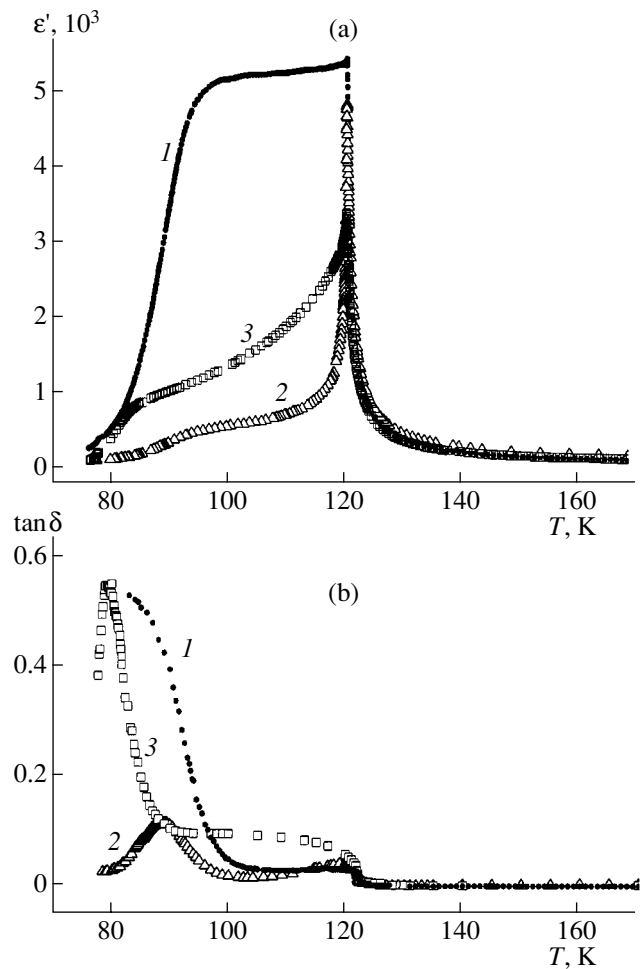
Fig. 1. Temperature dependences of (a) permittivity and (b) the tangent of dielectric losses for (*1*) the pyramidal sector of a traditionally grown KDP crystal and the (*2*) pyramidal and (*3*) prismatic sectors of a rapidly grown KDP crystal.
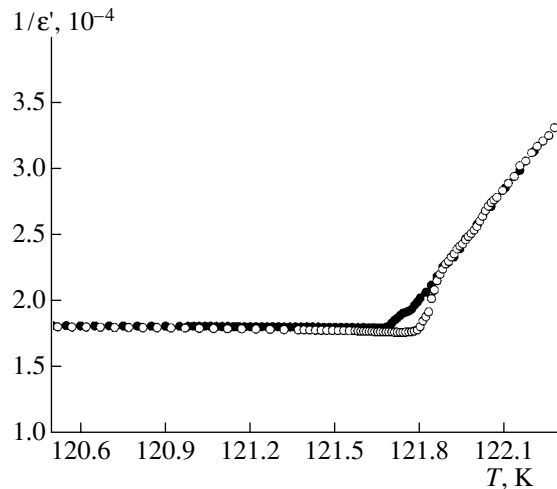
Fig. 2. Temperature hysteresis of permittivity in the vicinity of the phase transition for a "traditional" KDP crystal during (●) cooling and (○) heating.
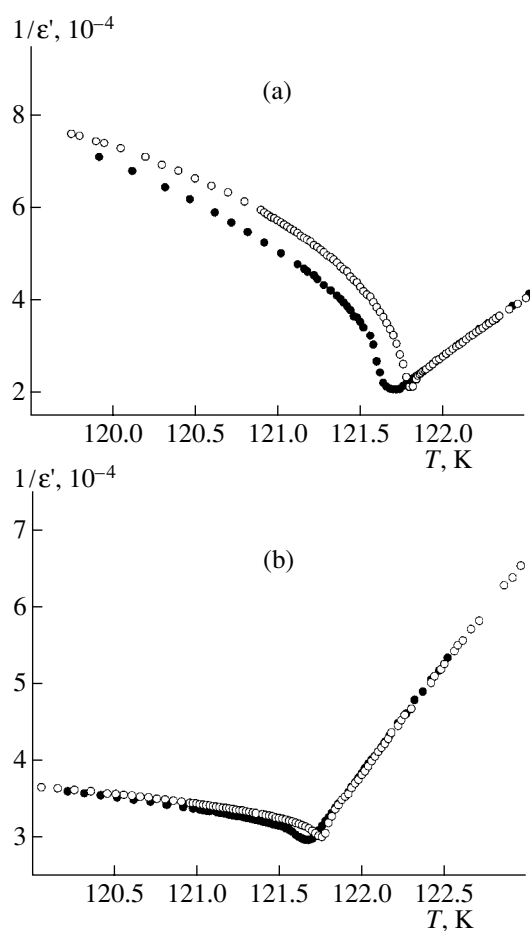
Fig. 3. Temperature hysteresis of permittivity for the (a) pyramidal and (b) prismatic sectors of the rapidly grown KDP crystal during (●) cooling and (○) heating.

mittivity in this region seems to be associated with an anomalously high mobility of domain walls [4]. The studies of the influence of various defects and impurities on the dielectric properties of KDP crystals showed that the contribution of domains to ε_C decreases in the presence of the defects because of pinning of domain walls at these defects [5, 6].

The suppression of the "domain contribution" detected in rapidly grown KDP crystals seems to be caused by "background impurities" (cations of trivalent metals), which are almost always present in KDP single crystals [18]. It seems that the incorporation of the background impurities at concentrations higher than their concentration in traditional crystals results in the formation of certain structure defects ("stoppers") that hinder the motion of domain walls.

A reduced domain contribution can be observed not only in the wide temperature range of the plateau region but also in the close vicinity of the phase transition temperature. This is clearly seen in the temperature dependence of ε_C^{-1} (Figs. 2, 3): in the traditional crystal (with an enormous domain contribution), the jump in ε_C is

observed only during heating, while in the rapid crystal (suppressed domain contribution), the jumps in ε_C are observed during both heating and cooling. Thus, one can assume that the absence of a jump in ε_C in the classical KDP crystal during cooling is explained by a considerable domain contribution (which can exceed ε_C in a single-domain crystal). With a decrease in the domain contribution (as in the rapidly grown crystals), this sign of a first-order phase transition is also observed during cooling.

Figure 1 shows that the dielectric properties in the prismatic and pyramidal sectors of rapidly grown crystals are different. The most noticeable difference is observed in the domain contributions, which indicates different quantities of growth defects and background impurities in different growth sectors. The domain contribution in the prismatic sector is rather high, and a well-defined maximum of tanδ is observed in the region of domain freezing. In the pyramidal sector, the domain contribution is suppressed, and the tanδ has much a lower maximum at T_F.

Close to T_C, the temperature dependences of the inverse permittivity in the pyramidal and prismatic sectors are also different. In the prismatic sector, the hysteresis value is lower, and the dependence resembles the dependence of a classical crystal. In the pyramidal sector (where the domain contribution is considerably suppressed), the slope of the temperature dependence of $1/\varepsilon_C$ in the polar phase increases, and $1/\varepsilon_C$ deviates from an approximately linear dependence. This may indicate a different mechanism of the formation of the temperature dependence of the domain contribution to permittivity (Fig. 3a).

Different defect structures in different sectors of a crystal are also confirmed by the dielectric-loss data. Figure 4 shows a portion of the temperature dependence of tanδ in the vicinity of room temperature. At room temperature, the value of tanδ is 85×10^{-3} in the pyramidal sector of a rapidly grown crystal, whereas in the prismatic sector of a rapidly grown and a traditional crystal, it is 3×10^{-3} and 1×10^{-3}, respectively. This result shows that electrical conductivity in the pyramidal sector of a rapid crystal exceeds the value in the pyramidal sector of a traditional crystal by more than an order of magnitude. Nominally pure KDP crystals have low dielectric losses at room temperature, while in doped KDP crystals, the value of tanδ is substantially higher [19]. In this case, the losses due to conductivity are especially high in the high-temperature region of the paraphase [6]. This was really observed in the pyramidal sector of a rapidly grown crystal, which showed the high concentration of defects in this crystal.

The data on domain contribution, dielectric losses in the vicinity of room temperature, and the formation of a hysteresis in the vicinity of the phase-transition point indicate the fact that the characteristics of the prismatic sector in a rapid crystal are closer to the classical crystal than the characteristics of the pyramidal one. This leads
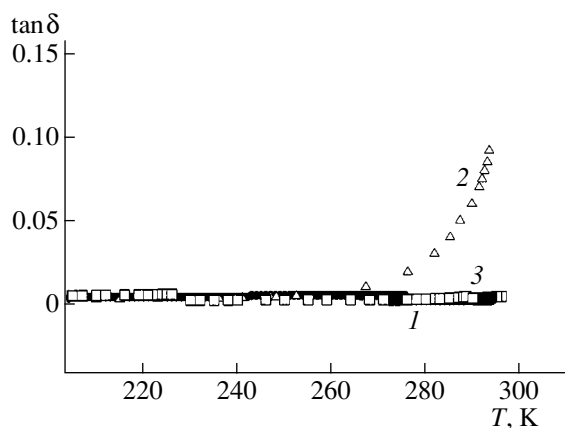
Fig. 4. Temperature dependence of the tangent of dielectric losses for (*1*) the pyramidal sector of a traditionally grown paraelectric KDP crystal and the (*2*) pyramidal and (*3*) prismatic sectors of a rapidly grown paraelectric KDP crystal at the temperature close to room temperature.

to the conclusion that the prismatic sector of a rapid crystal has a lower concentration of defects than the pyramidal one.

We mean here, first and foremost, those defects that interact with domain walls and influence their mobility, because the dielectric measurements allow one to extract the data on those defects that affect the domain contribution to permittivity.

It is also interesting to compare the results obtained with a classical crystal, in which the weakly developed prismatic sector has a higher defect concentration than the pyramidal one [20]. Our dielectric measurements showed that, in a rapidly grown KDP crystal, the pyramidal sector has more defects than the prismatic one. In the traditional growth method, the background impurities are absorbed mainly by the prism, thus forming numerous defects and blocking its growth [11]. In the rapid growth method, background impurities are distributed more uniformly over both sectors, thus increasing the defect concentration in the pyramid and decreasing it in the prism. It is the incorporation of the smaller amount of background impurities into the prism that results in the efficient development of this sector in rapidly grown crystals.

CONCLUSIONS

Dielectric measurements show that the rapid growth method gives rise to a certain increase in the concentration of structural defects in KDP crystals, which reduces the mobility of domain walls and, hence, influences the suppression of the domain contribution to permittivity. The value and form of the domain contribution can serve as a measure of the "purity" of KDP crystals containing growth and impurity defects.

It is shown that the dielectric properties in different sectors of a KDP single crystal are different. Unlike in a classical KDP crystal, the prismatic sector in rapidly

grown KDP crystals has a lower concentration of defects than the pyramidal one.

REFERENCES

1. H. M. Barcla and D. M. Finlayson, Philos. Mag. **44**, 109 (1953).
2. L. A. Shuvalov and A. V. Mnatsakanyan, Izv. Akad. Nauk SSSR, Ser. Fiz. **29**, 1974 (1965).
3. P. Bornarel, A. Fouskova, P. Guyon, and J. Lajzerowicz, in *Proceedings of the International Meeting on Ferroelectricity, Prague, 1966*, Vol. 2, p. 81.
4. Z. Malek, L. A. Shuvalov, I. Fiala, and Ya. Shtraïblova, Kristallografiya **13** (5), 825 (1968) [Sov. Phys. Crystallogr. **13**, 713 (1968)].
5. L. N. Kamysheva, N. A. Burdanina, O. K. Zhukov, *et al.*, Kristallografiya **14** (5), 941 (1969) [Sov. Phys. Crystallogr. **14**, 816 (1969)].
6. E. Nakamura, Ferroelectrics **135**, 237 (1992).
7. E. V. Peshikov and L. A. Shuvalov, Kristallografiya **26** (5), 855 (1981) [Sov. Phys. Crystallogr. **26**, 484 (1981)].
8. A. S. Sidorkin, *Domain Structure in Ferroelectrics and Related Materials* (Fizmatlit, Moscow, 2000).
9. L. N. Rashkovich, Vestn. Akad. Nauk SSSR, No. 9, 15 (1984).
10. N. Zaitseva, L. Carman, and I. Smolsky, J. Cryst. Growth **204**, 512 (1999).
11. L. N. Rashkovich, *KDP-Family Single Crystals* (Adam Hilger, Bristol, 1991).
12. N. Zaitseva and L. Carman, Prog. Cryst. Growth Charact. Mater. **43**, 1 (2001).
13. N. P. Zaitseva, J. J. Yoreo, M. R. Dehaven, *et al.*, J. Cryst. Growth **180**, 255 (1997).
14. M. Tsukamoto, E. Nakamura, and T. Ozaki, J. Phys. Soc. Jpn. **42**, 190 (1977).
15. L. N. Kamysheva, O. K. Zhukov, N. A. Burdanina, *et al.*, Izv. Akad. Nauk SSSR, Ser. Fiz. **31**, 1180 (1967).
16. A. S. Sidorkin, N. A. Burdanina, and A. P. Lazarev, Fiz. Tverd. Tela (Leningrad) **26**, 1419 (1984) [Sov. Phys. Solid State **26**, 861 (1984)].
17. B. A. Strukov, M. A. Korzhuev, and V. A. Koptsik, Izv. Akad. Nauk SSSR, Ser. Fiz. **25**, 1846 (1971).
18. E. P. Efremova, N. P. Zaïtseva, A. Yu. Klimova, *et al.*, Neorg. Mater. **27**, 2600 (1991).
19. E. D. Yakushkin, E. P. Efremova, and A. I. Baranov, Kristallografiya **46** (5), 904 (2001) [Crystallogr. Rep. **46**, 830 (2001)].
20. C. Belouet, E. Dunia, and J. F. Petroff, J. Cryst. Growth **23**, 243 (1974).

Translated by A. Zolot'ko

<center>
SURFACE, THIN FILMS,
AND NANOMATERIALS
</center>

Characterization of the Structure of Porous Germanium Layers by High-Resolution X-ray Diffractometry

A. A. Lomov*, V. A. Bushuev**, V. A. Karavanskiĭ***, and S. Bayliss****

* Shubnikov Institute of Crystallography, Russian Academy of Sciences,
Leninskiĭ pr. 59, Moscow, 119333 Russia

e-mail: a.lomov@ns.crys.ras.ru

** Faculty of Physics, Moscow State University, Vorob'evy gory, Moscow, 119992 Russia

*** Institute of General Physics, Russian Academy of Sciences, ul. Vavilova 38, Moscow, 117942 Russia

**** Solid State Research Center, Faculty of Applied Sciences, De Monfort University, Leicester, UK

Received April 23, 2002

Abstract—The surface morphology and the structure of porous germanium layers obtained by chemical etching of *n*-type single-crystal Ge(111) substrates with their subsequent annealing in hydrogen atmosphere are studied by high-resolution X-ray diffractometry. It is established that upon etching a 1.5 to 2.0-μm-thick porous germanium layer is formed, which contains quasi-ordered microinhomogeneities in the form of elongated pits with characteristic dimensions of 1 μm and an average distance between them of 3–4 μm. The layer bulk has pores with radii ranging within 25–30 nm and nanocrystallites with an average size of 10 nm, with the average porosity being 56%. © *2003 MAIK "Nauka/Interperiodica".*

INTRODUCTION

High-resolution X-ray diffractometry (HRXRD) is widely used for studying the real structure of crystals, thin subsurface layers, multilayer heterosystems, etc. [1, 2]. Traditionally, the analysis of rough surfaces is performed by X-ray reflectometry [2]. The possibility of determining the relief and roughness of the surfaces of perfect single crystals by the method of triple-crystal X-ray diffractometry (TCXRD) was first studied theoretically in [3] and used experimentally in [4]. However, the rapid development of various technologies of surface treatment, the use of electron microscopy, X-ray reflectometry, and atomic force microscopy to some extent postponed the study of the surface morphology by X-ray diffraction methods.

The great interest in newly synthesized porous materials in recent decades is associated, first and foremost, with the discovery of photoluminescence in the visible range of the spectrum of silicon containing pores of nanometer dimensions (nanopores), which gave new impetus to the development of X-ray diffraction methods for studying the structure of porous films and surface microrelief [5–11]. It should be indicated that the possibilities provided by X-ray reflectometry at the grazing angles of the radiation incidence onto the sample surface become rather limited for surfaces with roughness of micron dimensions because of the spreading and weakening of the reflected beam. In the Bragg scattering of the X-ray radiation, the incident beam forms angles with the surface equal to several tens of degrees, which is sufficient for the solution of the above

problem. It was established [10] that the primary beam used for studying porous silicon layers of the thicknesses of the order of several microns is rather spread, which can be used for characterization of pores with a size of several nanometers. The possibility of using high-resolution X-ray diffractometry for characterization of porous structures with pores having dimensions of the order of several microns has not been studied as yet. In recent years, such structures have been obtained by various technologies [11–13]. Thus, it was shown [11] that the formation of porous germanium layers by chemical (stain) etching was accompanied by the appearance of a large-scale relief responsible for the formation of rocking curves with nontraditional shapes.

Porous germanium layers attract the considerable attention of numerous researchers [12, 13] because they provide the formation of nanocrystals. Since the effective masses of the carriers in germanium are rather small, the quantum-dimensional effects in germanium nanocrystals should manifest themselves at considerably larger crystallite dimensions than in nanocrystals of other semiconductors [13]. Moreover, the technology of obtaining nanocrystals of elemental semiconductors is considerably simpler than that of multicomponent ones. It should also be indicated that, in this case, chemical etching has a number of advantages; namely, it allows one to use the initial germanium of a given quality, orientation, and conductivity type and also provides the formation of layers with controllable thickness and porosity. This method also agrees well with the modern technologies used in microelectronics.

The present article considers the possible use of high-resolution X-ray diffractometry for characterization of the microrelief and structure of porous layers and also the specific features of the rocking and triple-crystal XRD curves observed in [11]. The experiments were made on chemically etched (stain etching) and thermally annealed Ge(111) single crystals. The results obtained are compared with the scanning electron and atomic force microscopy data.

SAMPLES AND METHODS OF STUDY

Porous layers were obtained by using chemical (stain) etching of samples in the $HF : H_3PO_4 : H_2O$ mixture (in the proportion 34 : 17 : 1) [11]. The initial substrates were n-type (111)-oriented single-crystal germanium wafers with a conductivity of 4.6 Ω cm. The porous layers to be studied were formed upon 3-h-etching under illumination with an incandescent lamp. The samples thus obtained were broken into two parts, of which one was subjected to 30-min thermal annealing in a hydrogen atmosphere at 600°C, whereas the other was left intact in order to be used as a standard for the comparison with the treated part. Annealing was used for passivation of dangling bonds and removing possible stresses at the interface with the porous surface. According to the already published data, our estimates, and the scanning electron microscopy data, the temperature of 600°C (the optimum temperature for stress relaxation) still cannot give rise to any structural changes of the pores (their collapse and the aggregation of nanocrystals accompanied by considerable changes in their dimensions). Being illuminated with natural light, a porous layer thus formed on the sample surface was, in fact, a slightly scattering but specularly reflecting transparent film whose color changed from brownish to silver upon annealing.

X-ray diffraction experiments were performed on a TRS-1 triple-crystal X-ray diffractometer controlled by a personal computer via a programmed MATEX controller. The radiation source was a linear projection of the focal point of a 1.1-kW X-ray tube with a copper anode. The X-ray beam was formed by a slit single-crystal silicon monochromator with a triple 111 reflection and 2.0- and 0.3-mm-wide exit collimating slits in the vertical and horizontal directions, respectively. To study the Ge(111) reflection, we used a quasi-dispersionless arrangement of the crystals $(n, -m)$ and $(n, -m, n)$ in a double- and triple-crystal configuration for recording the rocking and triple-crystal XRD curves, respectively. The rocking curves were measured at the open slit placed before the detector by a $\theta/2\theta$ scan. The triple-crystal XRD curves were recorded with the aid of a plane Si(111) crystal analyzer. The scattered-intensity distribution in the vicinity of the reciprocal-lattice point Ge(111) was recorded in the ω-scan mode.

EXPERIMENTAL RESULTS AND DISCUSSION

Rocking Curves

Figure 1 shows the double-crystal rocking curves $R(\alpha)$ from porous germanium samples prior to (curve 1) and upon (curve 2) annealing in a hydrogen atmosphere and also the curve for the initial substrate (curve 3), where $\alpha = \vartheta - \vartheta_B$ is the angle of the sample rotation with respect to the Bragg angle $\vartheta_B = 13.64°$. The width of the rocking curve from the sample with the porous germanium layer was 19″ prior to annealing, and 17.8″ after it. The latter value was practically equal to the half-widths of the rocking curves obtained for the initial substrate and calculated for an ideal Ge(111) single crystal, 17.5″ and 17.3″, respectively. The calculations were performed based on the dynamical theory of scattering with due regard for dispersion and the convolution of the rocking curves of the sample and the crystal monochromator. The rocking curves from the sample prior to and upon annealing have two symmetrically located (with respect to the angle $\alpha = 0$) regions of additional diffraction scattering in the vicinity of the angles $\alpha_0 \approx \pm 20″$ and $\alpha_0 \approx \pm 28″$. Upon annealing (curve 2), the scattered intensity was almost two times lower than that of curve 1 obtained prior to annealing in the vicinity of the exact Bragg angle and slightly increased at angles $|\alpha| \geq 50″$.

Comparing the data obtained and those indicated in [5, 6], we see that a porous-germanium film is formed
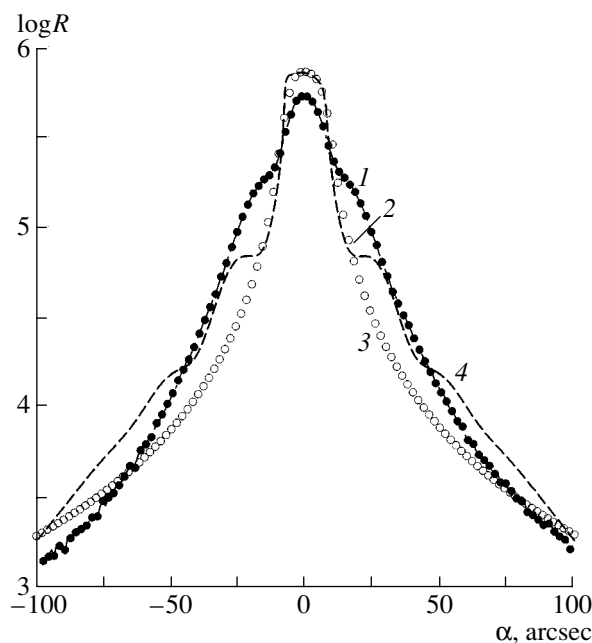
Fig. 1. Double-crystal rocking curves for a Ge(111) sample with the porous surface layer (1) prior to and (2) upon annealing, (3) a Ge(111) sample prior to etching, and (4) the rocking curve calculated with due regard for the correlation in defect location.

q_z[111], µm^{-1}
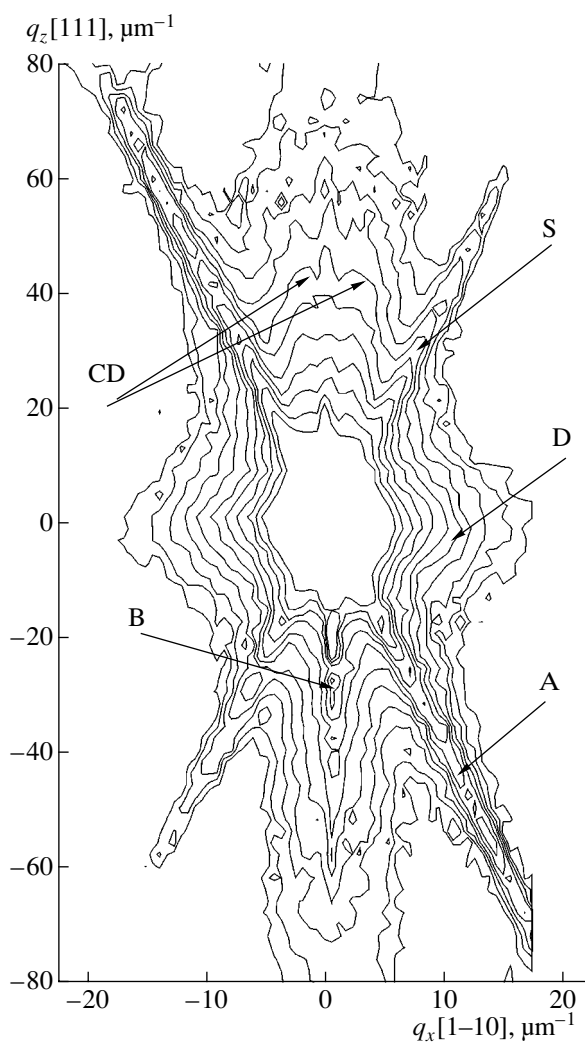
Fig. 2. Map of the scattered intensity distribution in the vicinity of the 111 reciprocal-lattice point for porous germanium upon annealing.

on the surface, but the pore parameters and the crystallite dimensions and their deformation differ from those in porous silicon films. Diffuse scattering in the porous structure in our case is much stronger and is localized in the vicinity of the exact Bragg angle. This indicates that the major scattering objects are rather large and have the characteristic dimensions $r \approx \lambda/2|\alpha_0|\cos\theta_B$, which are approximately of the order of a micron. The absence of a noticeable diffraction maximum from the film and the broadening of the rocking-curve maximum shows that the scattering objects are only partly coherent with respect to one another and the substrate. This is confirmed by the fact that the diffraction reflection from the crystals with the porous-germanium layer is lower by about 10–15% than the diffraction reflection from the nonetched sample. This indicates the formation of a layer that is amorphous with respect to X-ray radiation (hereafter referred to as an X-ray-amorphous layer). Earlier, X-ray reflectometry data showed [11]

that the average density of the porous germanium layers is about 40% of the substrate density, whereas its thickness is about 1.5–2.0 µm. However the data obtained are too scarce to construct the model of surface morphology.

Triple-Crystal X-ray Diffractometry

To obtain more detailed information on the structure of porous germanium layers, we measured the intensity distribution of diffraction scattering in the vicinity of the 111 reciprocal-lattice point by triple-crystal X-ray diffractometry. The two-dimensional distribution of the $I(q_x, q_z)$ intensities was obtained by recording a series of triple-crystal XRD curves measured in the angular ranges of the sample and analyzer rotation ±450″ in the ω-scan mode. Figure 2 shows the 111 reflection for the annealed sample, where $q_x = k_0(2\alpha - \Delta\theta)\sin\theta_B$, $q_z = k_0\Delta\theta\cos\theta_B$, and $k_0 = 2\pi/\lambda$, where λ is the radiation wavelength. One can clearly see the dynamical bands in the narrow regions in the vicinity of the lines $q_z = -q_x\cot\theta_B$ (the apparatus band A associated with the use of the crystal analyzer with a single reflection) and $q_x = 0$ (the Bragg scattering B localized along the surface normal of the crystal). It should be indicated that the intense small-angle scattering S along the $q_z = q_x\cot\theta_B$ line could not be detected if, at the given setting of the crystals, one uses a triple-reflection slit monochromator and a highly perfect single crystal as a sample. In the general case of such scattering, it is associated with both defects in the crystal lattice [14] and the structure of the sample surface [10]. The contours of equal intensities in the form of concentric circumferences around a reciprocal-lattice point indicate diffuse scattering D from small defects. It was discovered [11] that such defects in these samples are the pores with an average radius of 30 nm at the layer porosity $P = 56\%$. The distinctive feature of this intensity distribution is the presence of rather narrow weak coherent diffuse (CD) bands symmetric with respect to the line $q_x = 0$. On the whole, the map of the intensity distribution obtained upon etching is analogous to the map shown in Fig. 2, and, therefore, it is not given here.

Thus, the porous germanium layers studied have a rather complicated structure and contain two types of defects—microinhomogeneities and nanopores. These defects give rise to diffuse scattering represented in Fig. 2. To construct the model of subsurface porous germanium layers, we analyze the intensity distribution in several sections of a reciprocal-lattice point.

The triple-crystal XRD curves in the section of the reciprocal-lattice point along q_x for a porous germanium layer prior to annealing (curve *1*) and after it (curve *2*) and for the initial substrate (curve *3*) are shown in Fig. 3a (analyzer angle $\Delta\theta = 0$, ω-scan mode). Since the angular resolution of a triple-crystal X-ray diffractometer is much higher than that of a double-

crystal one, the diffuse scattering on the tails of the diffraction maximum in the ω-scan mode (Fig. 3a) is more distinct than in Fig. 1. This partly coherent diffuse scattering manifests itself as two humps that are symmetric with respect to the central Bragg maximum at the deviation angles of the sample $\alpha_0 \approx \pm 16''$ prior to annealing (curve 1) and $\alpha_0 \approx \pm 23''$ after it (curve 2). The additional maxima are also observed on the ω-scan curves at other nonzero positions of the analyzer (Fig. 4). It should be indicated that similar features are also observed in systems possessing a short-range order in the arrangement of the scattering objects along the crystal surface characterized by the average distance L between these objects and a certain length of the longitudinal correlation [5, 7, 11, 15].

The quantitative characterization of the morphology and the surface structure requires the establishment of the causes that give rise to the appearance of diffuse scattering. First, it is small-angle scattering associated with a certain order in the arrangement of the pores and microinhomogeneities along the sample surface. Second, it is the contribution to scattering that comes from crystallites that are incoherently related to the substrate matrix. Therefore, one has to take into account the shape and mosaic distribution of such crystallites. One more cause of diffuse scattering is the deformation in the subsurface layers of crystallites associated with the surface-tension forces at the oxide–crystallite and second-phase–crystallite interfaces and also the existence of elastically stressed regions at the porous-germanium–germanium substrate interface. The appearance of diffuse scattering by the latter mechanism is demonstrated by Fig. 3a. Upon thermal annealing, the occurrence of reduction reactions results in stress relaxation and their more uniform distribution along the surface. As a result, one observes a reduced intensity and an increased angular distance $|\alpha_0| \sim \lambda/L$ between the diffuse-scattering maxima (cf. curves 1 and 2 in Fig. 3a), which confirms the conclusions drawn from the rocking curve data.

Measuring the pure Bragg scattering along q_z, one can determine the slightest deformations in the subsurface layer of the sample and extract information on the crystalline objects coherently related to the sample matrix. The triple-crystal XRD curves were recorded in the $\theta/2\theta$ scan mode and are shown in Fig. 3b. In fact, this scan mode provides a measurement of only the coherent component of the total scattering from the chosen samples, whereas the contribution of diffuse scattering is negligible. It is seen from Fig. 3b that the widths of all the Bragg maxima are almost the same and are equal to $17.7''$, the value corresponding to the value calculated in the geometry chosen for the experiment. However, the deviation from the exact Bragg angle results in some characteristic features in curves 1 and 2: the diffraction-reflection intensities in the region of the negative α values are higher than at $\alpha > 0$. Moreover, the scattering intensities at the tails of curves 1 and 2
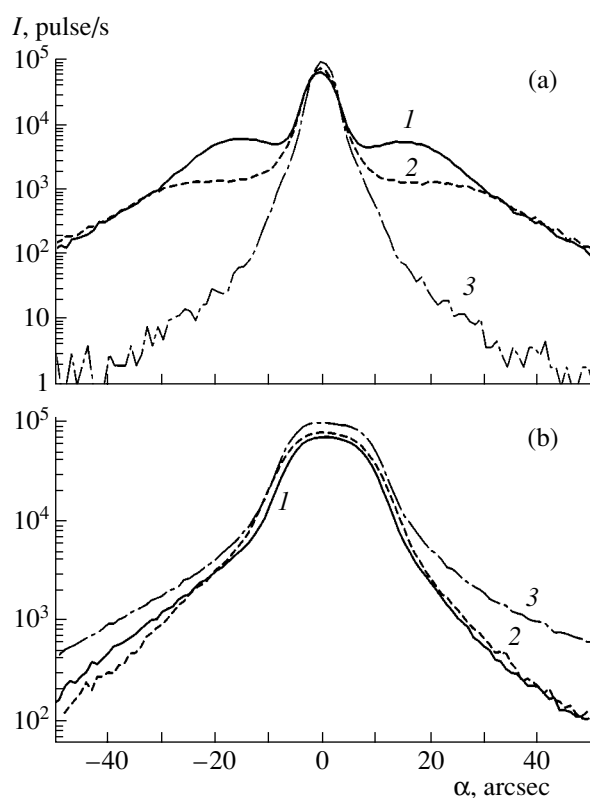

Fig. 3. Triple-crystal XRD curves for the section of the 111 reciprocal-lattice point of a Ge(111) sample at (a) $q_z = 0$ and (b) $q_x = 0$: (1) upon etching, (2) upon etching and subsequent thermal annealing, and (3) prior to etching.
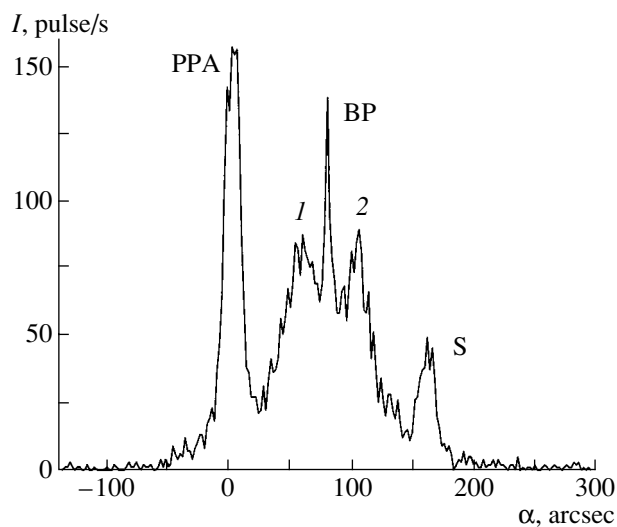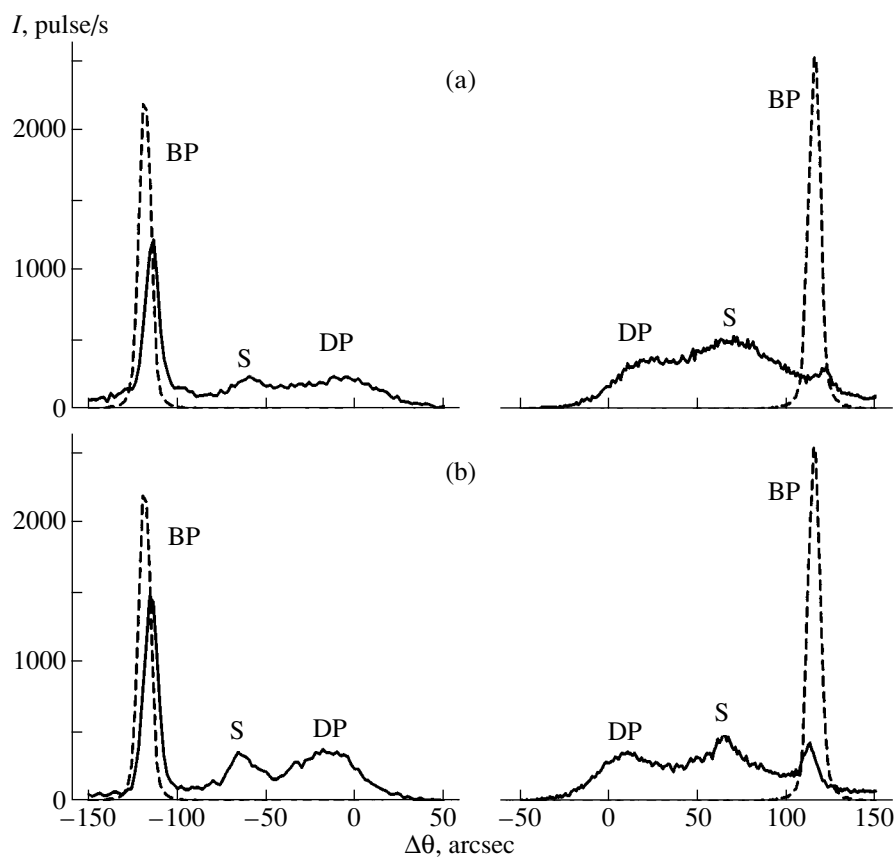

Fig. 4. Triple-crystal XRD curve from a Ge(111) sample with the porous surface layer prior to annealing obtained in the ω-scan mode at a fixed position of the crystal analyzer $\Delta\theta = 160''$. BP denotes the Bragg peak, PPA denotes the pseudopeak of the analyzer, and S denotes the small-angle scattering recorded at the position of the monochromator pseudopeak. Partly coherent diffuse scattering from microinhomogeneities is recorded as two satellites (1 and 2) on both sides of the Bragg peak BP.

Fig. 5. Triple-crystal XRD curves from a Ge(111) sample with the layer of porous germanium recorded in the θ-scan mode (a) prior to and (b) upon annealing in a hydrogen atmosphere. Dash lines show scattering from a Ge(111) sample prior to etching. On the left, scattering at the deviation angle $\alpha = -60''$ is shown; on the right, scattering at $\alpha = 60''$.

from the samples with porous germanium layers are much lower than the corresponding values on the curve from the initial substrate (cf. with curve *3* in Fig. 3b). Thus, in porous germanium layers, only some crystallites are coherently related to the substrate matrix. A considerable part of the porous germanium layers do not participate in the Bragg scattering because they have no scattering atoms, i.e., because of the formation of pores at the sites of scattering atoms. A similar result was also obtained in the study of porous silicon films [6] despite the fact that they had different morphology and a more perfect structure of nanocrystallites.

The intensity measurements in the vicinity of the reciprocal-lattice point in θ-scan allow one to compare the contributions of various components to the total scattering. Figure 5 shows the corresponding triple-crystal XRD curves $I(\Delta\theta)$ at the angles α of the sample deviation from the exact Bragg angle equal to $\alpha = \pm 60''$. Each of the curve sections has three maxima: a Bragg peak at $\Delta\theta = 2\alpha$, a pseudopeak at $\Delta\theta = \alpha$, and a diffuse-scattering peak whose shape, angular position, and intensity are determined by the type and number of defects. It is seen that, in this scan mode, the triple-crystal XRD curve for the initial Ge(111) substrate (curve *3*) has only one Bragg maximum, whereas no noticeable

diffuse-scattering peak and pseudopeak are observed. In this case, the X-ray scattering corresponds to scattering from a perfect crystal. At the same time, for the sample with a porous germanium layer, the intensity of the Bragg peaks in the vicinity of the negative $\Delta\theta$ angles exceeds by a factor of 3–4 the intensity of the Bragg peaks on the side of the positive angles (Figs. 5a, 5b). This confirms the results shown in Fig. 3b and proves that the porous germanium layer formed upon chemical etching has a lattice parameter exceeding that of the substrate. The average deformation obtained from the angular dependence of the reduced intensity function $\alpha^2 I(2\alpha)$ [1] is $\Delta d/d \approx 4 \times 10^{-4}$. This deformation is determined by the capillary phenomena and surface-tension forces in various substances, which are either the products of the chemical reactions or are adsorbed from the atmosphere upon sample preparation.

It is seen from Fig. 5 that, both prior to and upon annealing, the triple-crystal XRD curve from porous germanium possesses a rather intense diffuse-scattering peak in the vicinity of the angle $\Delta\vartheta \approx 2\alpha \sin^2\theta_B$, which corresponds to the scattering from randomly distributed spherical defects [1]. As a result of annealing, the θ-scan curves show the following considerable

changes: the Bragg scattering peak becomes less asymmetric; the pseudopeaks become more pronounced, whereas their intensities simultaneously increase (especially in the range of positive angles); and the diffuse scattering in the vicinity of the reciprocal-lattice point is symmetrized and slightly increases. All these facts indicate that annealing results in the partial removal of the stresses, an increase in the number of coherently scattering nanocrystallites or their scattering power, and also in the formation of more pronounced interfaces between the pores and crystallites. Since the diffuse peak remained almost unchanged, we can assume that it is associated with scattering by the objects located in the layer and not with the stresses at the crystallite surface.

Another feature that distinguishes the triple-crystal XRD curves (Fig. 5) from those of porous germanium layers is the existence of the maximum at the position of the monochromator pseudopeak, which is practically absent on the curve from the initial substrate (note the noticeable intensity distribution along $q_z = q_x \cot\theta_B$ in Fig. 2). As was shown in [10], this results from the small-angle scattering of the X-ray beam with an almost Π-like angular profile in a medium with pronounced local density variations. The magnitude of this effect is proportional to the density gradient in the neighboring regions and the number of such regions. Assuming that chemical etching results in the formation of microinhomogeneities on the surface, we obtain that modeling of the angular dependence of the small-angle scattering intensity (peak S) yields the following value of the average dimension of microinhomogeneities $D \approx 0.8\ \mu m$ (see Figs. 6, 7b).

The above results show that the main characteristic feature of scattering from the samples with porous germanium layers is the formation of pronounced additional maxima on the rocking curves (Fig. 1) and two narrow bands parallel to the Bragg-scattering band $q_x = 0$ on the map (Fig. 2) and also of the maxima on the corresponding sections (Figs. 3a, 4). These features are associated with diffuse X-ray scattering from partly ordered noncrystalline regions located along the surface which are, in fact, the pores in the bulk, cracks, or etch pits on the sample surface. Therefore, this effect can be used for studying surface morphology.

Diffuse Scattering from the Blocks on the Sample Surface Which Are Amorphous for X-rays

In the kinematical approximation, the scattering amplitude of such a structure is represented by the sum of the scattering amplitudes of the crystalline part of the sample and the defects located in it:

$$A(\mathbf{S}) = \sum_{V_c - V_d} f_c \exp(i\mathbf{S}\mathbf{R}_n) + \sum_{V_d} f_d \exp(i\mathbf{S}\mathbf{r}_n), \quad (1)$$

where $\mathbf{S} = \mathbf{k}_1 - \mathbf{k}_0$ is the scattering vector, V_c is the sample volume, V_d is the sum of the defect volumes, f_c and
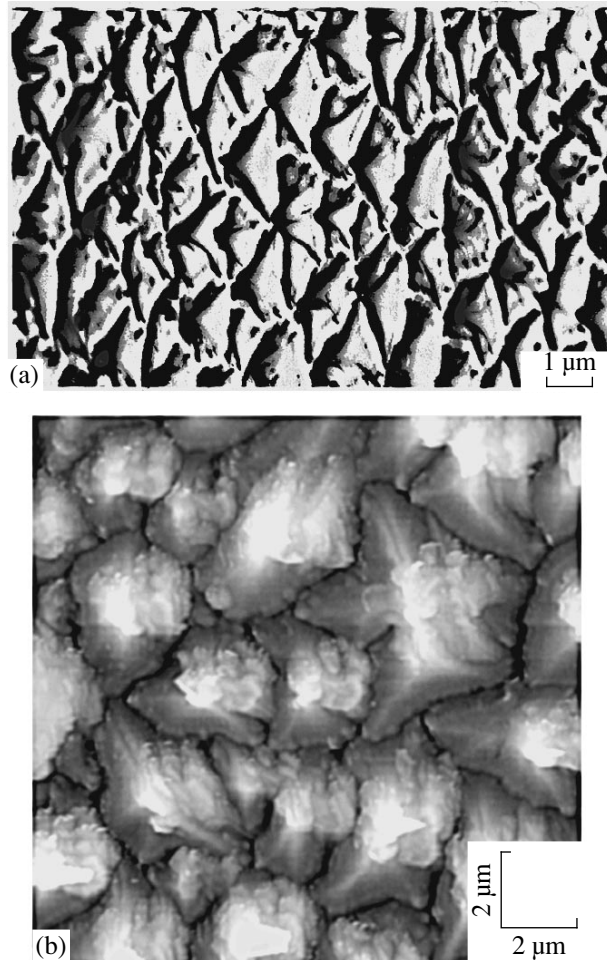
Fig. 6. Images of the surface of a Ge(111) sample upon etching and subsequent thermal annealing in a hydrogen atmosphere: (a) electron microscopy image at the incidence angle 30°, (b) atomic force microscopy image from a 14 × 14 μm surface region.

f_d are the scattering factors of atoms and defects in the crystal, and $\mathbf{R}_n$ and $\mathbf{r}_n$ are the atomic coordinates of the crystalline part of the sample and the part with defects, respectively. Now, adding to and subtracting from Eq. (1) the term equal to the scattering amplitude from the crystalline regions with the total volume V_d [16], we obtain
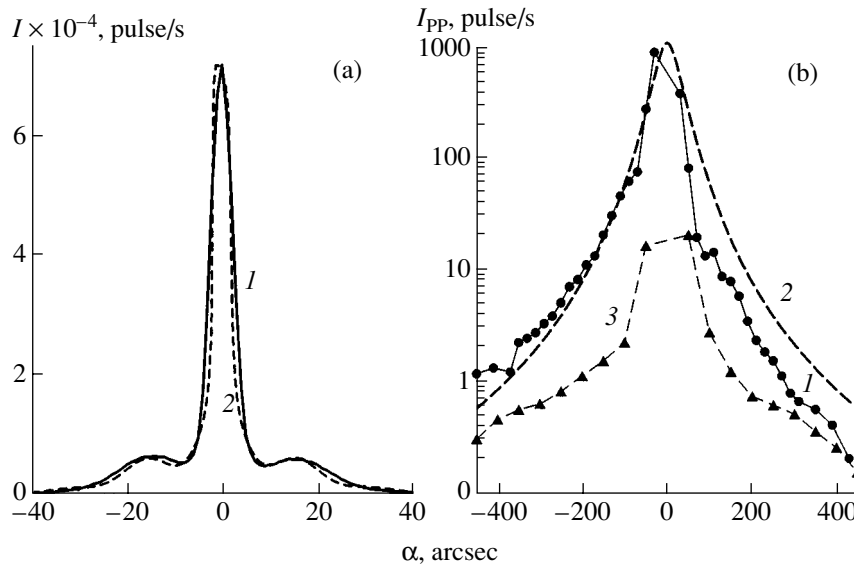
$$A(\mathbf{S}) = A_B(\mathbf{S}) + A_d(\mathbf{S}), \quad (2)$$

where

$$A_B(\mathbf{S}) = \sum_{V_c} f_c \exp(i\mathbf{S}\mathbf{R}_n),$$

$$A_d(\mathbf{S}) = \sum_{V_d} [f_d \exp(i\mathbf{S}\mathbf{r}_n) - f_c \exp(i\mathbf{S}\mathbf{R}_n)].$$

Here, A_B is the amplitude of the Bragg scattering from the defect-free crystal, which has a nonzero value only in the small vicinity of the reciprocal-lattice points, and

Fig. 7. (a) Section of the scattered intensity along $q_z = 0$ in the vicinity of the 111 reciprocal-lattice point for a porous germanium sample upon etching and (b) the pseudopeak intensity as a function of the rotation angle of an annealed porous germanium sample; (*1*) experiment, (a) calculation with due regard for the partial correlation in the defect location (*2*), (b) calculation with due regard for diffuse scattering in the vicinity of the zeroth reciprocal-lattice point (*2*), and (*3*) pseudopeak intensity for the initial substrate.

A_d is the amplitude of diffuse scattering from defects. It is assumed that the defects do not distort the crystal lattice. If the defects are either empty pores or etch pits on the surface, the scattering factors in Eqs. (1) and (2) are zeroes, $f_d = 0$.

Now, assume that all the defects have the same shape and volume. Then $\mathbf{R}_n = \boldsymbol{\rho}_m + \mathbf{r}_n'$, where $\boldsymbol{\rho}_m$ is the position of the mth defect with respect to the origin and $\mathbf{r}_n'$ are the positions of the atoms with respect to the defect center. The intensity of diffuse scattering due to the presence of etched regions in the porous layer is determined by the expression

$$I(q_x, q_z) = C\int F(\mathbf{S})|G(\mathbf{q})|^2 dq_y, \qquad (3)$$

where C is a constant, $\mathbf{S} = \mathbf{h} + \mathbf{q}$, $\mathbf{h}$ is the reciprocal-lattice vector, and $G(\mathbf{q})$ is the Fourier transform of the formfactor of an individual defect. The function

$$F(\mathbf{S}) = \left\langle \sum_m \sum_n \exp[i\mathbf{S}(\boldsymbol{\rho}_m - \boldsymbol{\rho}_n)] \right\rangle \qquad (4)$$

is determined by the defect distribution over the crystal. Now, assume that pores are spheres of radii r and that the formfactor is $G(q) = 3(\sin\beta - \beta\cos\beta)/\beta^3$, where $\beta = qr$. For the regions that have a parallelepiped shape with the characteristic dimensions a_x, a_y, and a_z, it is convenient to use the representation that takes into account the possible scatter in the dimensions and spreading of the interfaces:

$$|G(\mathbf{q})|^2 = g(q_x)g(q_y)g(q_z), \qquad (5)$$

where $g(q_i) = 1/[1 + (0.36a_iq_i)^2]$.

If the defects are distributed randomly, $F(\mathbf{S}) = N$, where N is the total number of such defects in the illuminated volume of the sample. In this case, the angular dependence of the diffusely scattered intensity (3) is determined only by the pore nature. However, at high porosity ($P \geq 50\%$) and an average distance between the pores, L, comparable with their dimensions, the formation of a certain short-range order in the pore distribution is possible. A similar situation also takes place if chemical etching along certain highly symmetric directions results in the formation of macroscopic elongated etched regions of submicron dimensions (Fig. 6). In this case as well, it is possible to single out a system of parallel pits on the surface arranged almost periodically (with a certain interval) along the surface. If the defects are periodically arranged along the x axis, then

$$F(q_x) = N_0[\sin(N_c\xi)/\sin(\xi)]^2, \qquad (6)$$

where $\xi = (1/2)q_xL$, N_c is the number of defects in the surface region where the periodicity is observed, and N_0 is the number of such regions. It is also assumed that these regions do not correlate with one another.

In the general case, one has to perform statistical averaging in Eq. (4) with due regard for the mutual correlation function in the pore distribution, C_{mn}, and pore orientation. For the Gaussian distribution, we have

$$C_{mn} = \exp[-(\boldsymbol{\rho}_m - \boldsymbol{\rho}_n)_\parallel^2/L_\parallel^2]\exp[-(z_m - z_n)^2/L_\perp^2],$$

where $L_\parallel$ and $L_\perp$ are the longitudinal and transverse correlation lengths. As a result, some additional symmetrically located weak broad maxima are formed on diffuse-scattering curve *3*. Their angular position at

q_z = const is determined by Eq. (6) under the condition $q_x L = 2\pi j$, where L is the average distance between the centers of the neighboring pores along the surface and j are the integers ($jL \le L_{\parallel, \perp}$). If α_1 is the angular position of the first maximum with respect to the Bragg peak, the average distance between the defects is $L \approx \lambda/2\alpha_1 \sin\vartheta_B$.

The intensities of the additional maxima on partly correlated components of the total diffuse scattering are proportional to the squared $L_{\parallel}/L$ ratio, whereas their widths are inversely proportional to this ratio. The formation of these maxima is most pronounced at such dimensions a_x and a_z at which the angular half-width of the scattering function $|G(\mathbf{q})|^2$ at a defect approximately coincides with the position of the first maximum, i.e., at $L \approx 2.3 a_x$.

Figure 7a shows (on a linear scale) the experimental section of the scattered intensity along the chemically etched Ge(111) surface in the vicinity of the reciprocal-lattice point (solid curve *1*) and the data calculated by Eq. (3) at $q_z = 0$ with due regard for the correlation between the defects in the form of rectangular etched regions on the surface (dash curve *2*). The Bragg reflection from the substrate was calculated within the theory of dynamical diffraction with due regard for absorption in the porous germanium layer. The best fitting of the calculated and experimental curves is attained at the following parameters: $a_x \approx 1$ μm, the etching depth $a_z \approx 0.6 a_x$, the average distance between these regions $L \approx 3.8$ μm, and the longitudinal correlation length $L_{\parallel} \approx 7.6$ μm.

In the double-crystal scheme, the diffuse-scattering intensity is determined by summing up the intensities over all the scattering angles at each fixed position of the crystal

$$I_{ds}(\alpha) = \int I(q_x, q_z) d\Delta\vartheta. \tag{7}$$

Figure 1 shows the rocking curve for a sample of porous germanium upon annealing (curve *4*) calculated by Eqs. (3)–(7) for the defects in the form of elongated pits on the surface at the model parameters $a_x \approx 0.8$ μm, $a_z \approx 0.6 a_x$ and the average distances between the defects $L \approx 2.6$ μm and $L_{\parallel} \approx 5$ μm. Despite the simplicity of the model used, the values obtained from the analysis of the rocking curve (Fig. 1, curve *4*) and the section along q_x (Fig. 7a, curve *2*) are close to the data obtained from the analysis of the electron microscopy image of the porous germanium surface shown in Fig. 6a.

Some decrease in a_x upon annealing is explained by the restoration of the crystal structure in the amorphized walls of etched pits on the porous germanium surface.

As was indicated above, the existence of a porous-germanium layer results in a dramatic (by almost two orders of magnitude) increase in the pseudopeak intensities on triple-crystal XRD curves in comparison with those on the curves obtained from the initial substrate (Fig. 7b). This increase is associated with the angular spread of the X-ray beam during its passage through the layer of amorphous germanium and caused by diffuse scattering from the defects and its subsequent reflection from the perfect region of the sample. Figure 7b shows the angular dependence of the peak intensity provided by diffuse scattering in the direction toward the zeroth reciprocal-lattice point [see Eq. (5) at $\mathbf{h} = 0$]. The calculations were performed at the model parameters obtained above for the annealed porous germanium layer. It is seen that the angular behavior of curves *1* and *2* and their widths (68″ and 74″) are practically the same, which confirms the validity of the assumption made. In this case, the contribution from nanopores to the scattering intensity is much less than the contribution from the etched regions of micron dimensions and, therefore, is ignored. The intensity of the pseudopeak from the initial highly perfect Ge(111) substrate (curve *3*) is low. This proves that the mechanism of such scattering resulting from the X-ray diffraction from the exit slit of the collimator considered in [10] is much less probable than the small-angle diffuse scattering from the large-scale roughness of the porous germanium surface. The roughness is formed by the etched regions of micron dimensions separated by hillocks at the germanium surface.

In the model used, the contribution of diffuse scattering that comes to the inner structure of microblocks to the total diffuse-scattering intensity is insignificant despite the pronounced thickness (1.5–2.0 μm) of the porous germanium layer. This is explained, first and foremost, by the number, shape, and dimensions of the scattering objects. Based on the rocking and triple-crystal XRD curves, it is natural to assume that the microblocks revealed consist of nanopores and nanocrystals with the average dimensions $r \approx L(3P/4\pi)^{1/3}$ and $d_c \approx 2r[K(L/r) - 1]$, respectively, where P is porosity. The coefficient K is determined by the symmetry of the pore environment ($K \approx 0.87$ and 0.57 for the cubic and hexagonal close packings of pores). The bulk porosity in the porous germanium layer is determined by the relationship $P \approx (4\pi/3)(r/L)^3$, where $L \ge 2r$. With due regard for the angular position ($\alpha \approx \pm 1000″$) of weak humps on the experimental rocking curves obtained from the annealed porous germanium [11], we have $L \approx 65$ nm, whereas the average pore radius and the characteristic dimension of nanocrystallites are 25–30 and ~10 nm, respectively. The porosity of the porous germanium layer was determined by the reflectometry method and equals 56%. These X-ray diffraction data are consistent with the Raman scattering data (for details see [11]).

CONCLUSIONS

Thus, our experiments showed that high-resolution X-ray diffractometry allows one to study such structural characteristics of a porous germanium layer as the presence of micro- and nanoinhomogeneities, the

degree of their deformation and coherence with the substrate matrix, etc. The analysis of the results obtained lead to the following conclusions. Chemical (stain) etching of the Ge(111) surface results in the formation of a 1.5 to 2.0-µm-thick porous germanium layer. The surface of this layer has a system of elongated etch pits with a width of ~1 µm, depth of ~0.6 µm, and average distance between the parallel pits of ~3–4 µm. The distribution and orientation of these pits show certain short-range order with a correlation length of ~5–8 µm. The pits are separated by hillocklike ledges, which, being projected onto the (111) surface, have a shape close to regular triangles. The bulk of hillocklike ledges of porous germanium contains pores with characteristic dimensions of ~25–30 nm and a distance between the pore centers of ~65 nm. The average porosity equals 56%.

ACKNOWLEDGMENTS

REFERENCES

1. A. M. Afanas'ev, P. A. Aleksandrov, and R. M. Imamov, *X-Ray Diffraction Diagnostics of Submicron Layers* (Nauka, Moscow, 1989).

2. V. Holy, U. Pietsch, and T. Baumbach, *High-Resolution X-Ray Scattering from Thin Films and Multilayers* (Springer, Berlin, 1999).

3. P. A. Aleksandrov, A. M. Afanas'ev, and M. K. Melkonyan, Kristallografiya **26** (6), 1275 (1981) [Sov. Phys. Crystallogr. **26**, 725 (1981)].

4. P. A. Aleksandrov, A. A. Zav'yalova, and A. A. Lomov, Kristallografiya **29** (4), 652 (1984) [Sov. Phys. Crystallogr. **29**, 386 (1984)].

5. D. Bellet, G. Dolino, M. Ligeon, *et al.*, J. Appl. Phys. **71** (1), 145 (1992).

6. A. A. Lomov, D. Bellet, and G. Dolino, Phys. Status Solidi B **190** (2), 219 (1995).

7. M. Binder, T. Edelmann, T. H. Metzger, and J. Peisl, Solid State Commun. **100** (1), 13 (1996).

8. D. Buttard, G. Dolino, D. Bellet, and T. Baumbach, Mater. Res. Soc. Symp. Proc. **452**, 437 (1997).

9. V. A. Karavanskiĭ, A. A. Lomov, E. V. Rakova, *et al.*, Poverkhnost, No. 12, 32 (1999).

10. A. A. Lomov, V. A. Bushuev, and V. A. Karavanskiĭ, Kristallografiya **45** (5), 915 (2000) [Crystallogr. Rep. **45**, 842 (2000)].

11. V. A. Karavanskii, A. A. Lomov, V. A. Bushuev, *et al.*, Phys. Status Solidi B (2003) (in press).

12. J. R. Heath, J. J. Shiang, and A. P. Alivisatos, J. Chem. Phys. **101** (6), 1607 (1994).

13. Y. M. Niquet, G. Allan, C. Delerue, and M. Lannoo, Appl. Phys. Lett. **77** (8), 1182 (2000).

14. A. E. Voloshin, A. A. Lomov, T. Nishinaga, *et al.*, J. Cryst. Growth **236** (3), 501 (2002).

15. A. A. Darhuber, J. Stangl, V. Holy, *et al.*, Thin Solid Films **306** (2), 198 (1997).

16. V. I. Iveronova and G. P. Revkevich, *Theory of X-Ray Scattering* (Mosk. Gos. Univ., Moscow, 1978).

Translated by L. Man

Growth of Filamentary KDP Crystals from Solution with the Addition of Al(NO₃)₃ · 9H₂O

D. A. Vorontsov, E. L. Kim, V. N. Portnov, and E. V. Chuprunov

Nizhni Novgorod State University, pr. Gagarina 23, Nizhni Novgorod, 630600 Russia

e-mail: Chuprun@phys.unn.runnet.ru

Received August 2, 2001; in final form, February 8, 2002

Abstract—To elucidate the mechanism of nucleation and growth of filamentary crystals on the bipyramid faces of KH_2PO_4 (KDP) crystals from solution with the addition of $Al(NO_3)_3 \cdot 9H_2O$, the growth rates and transverse dimensions of the crystals were measured at various supersaturations, temperatures, and impurity concentrations. The dependences obtained can be interpreted with due regard for the competition between the intrinsic and impurity particles in the presence of Cabrera–Vermilyea stoppers. © *2003 MAIK "Nauka/Interperiodica".*

INTRODUCTION

At a certain critical supercooling of the solution with the addition of $Al(NO_3)_3 \cdot 9H_2O$, one observes nucleation and growth of filamentary KDP crystals on the bipyramid faces [1]. Below we report the results of a detailed study of the influence of impurity on the growth of filamentary KDP crystals at high impurity concentration and supersaturations in the solution. The effect of low impurity concentrations at low supersaturations was thoroughly studied by measuring the velocity of step motion [2]. The dependence of the velocity of the step motion over the {100} KDP faces on supersaturation in the presence of Cr^{3+} ions can be attributed to the action of the impurity unreliably adsorbed at the terraces and kinks. The effect of an impurity on the growth of KDP crystals was also studied using scanning atomic force microscopy [3]. We observed the step motion at a constant supersaturation and the change in the step shape upon the addition of Fe^{3+} ions during the growth process. As a consequence, the step profile acquired a wavy profile and the surface ceased to grow, which may be caused by the Cabrera–Vermilyea mechanism.

The filamentary KDP crystals are convenient objects for studying the effect of impurity on crystal growth from solution, because the impurities produce practically no effect on the solution state during growth and have a very small growing surface and high growth rates. The measurements of the growth rate and the transverse dimensions of filamentary crystals allow one to elucidate the mechanisms of crystal formation and the action of the impurity effect and impurity trapping.

EXPERIMENTAL

The measurements were performed in a glass cell in which the temperature was kept constant with the aid of an ultrathermostat with an accuracy of ±0.1 K. A cylinder with transparent base (window) can be screwed into the cell cover in such a way that the window is located in the solution. A ~$5 \times 2 \times 2$-mm³ seed crystal was fixed at a distance of 2–3 mm from the plane of the cylinder bottom, with the z axis of the crystal being horizontal. The solutions were prepared from distilled water and analytically-pure-grade materials. First the impurity and then the basic substance were dissolved in a certain weight of water. Upon filtration, the overheated solution was poured into the cell, which was then closed with the cover containing the seed. The latter was submerged into the solution during its cooling to the necessary temperature.

In several minutes, tapered ledges were formed at the faces of the seed bipyramid. Then, filamentary crystals grew from these ledges along the z axis. Using a microscope with an ocular micrometer, we measured the displacement of the vertex of a chosen filamentary crystal with the cross section size 20–50 μm per one minute and calculated the growth rate. Such measurements were performed for 20–30 min on each crystal. The growth rates were different, but no monotonous change was observed during crystal growth. Therefore, we determined the average growth rate of the filamentary crystal during the whole observation time. Then, the confidence interval was calculated. The transverse dimensions were measured on several tens of grown filamentary crystals in each experiment and were then averaged.

RESULTS

Three types of experiments were made: (1) those at a constant temperature and impurity content but at different supersaturations, (2) those at a constant temperature and supersaturation but at different contents of
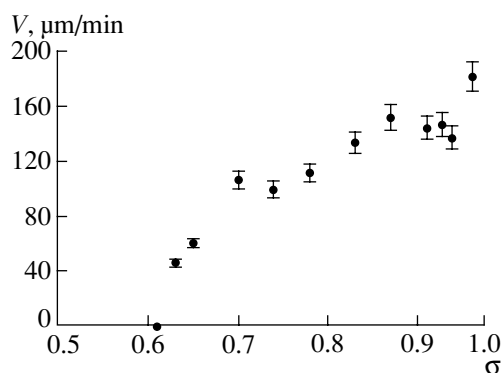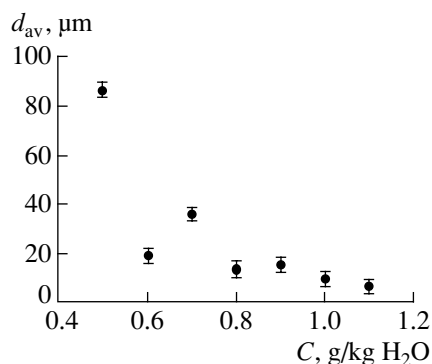
Fig. 1. Growth rate of filamentary KDP crystals as a function of relative supersaturation.
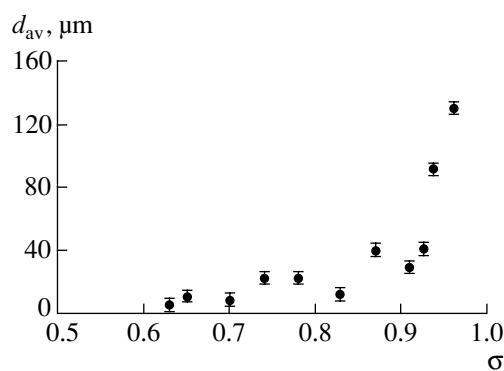
Fig. 2. Average transverse dimension of filamentary KDP crystals as a function of relative supersaturation.
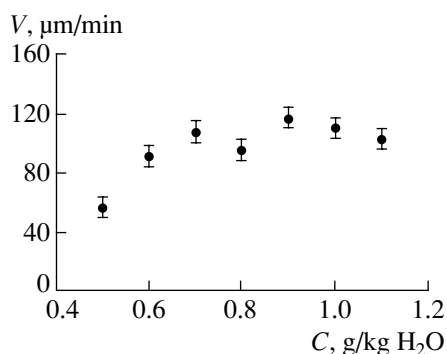
Fig. 3. Growth rate of filamentary KDP crystals as a function of impurity concentration in the solution.

Fig. 4. Average transverse dimension of filamentary KDP crystals as a function of impurity concentration in the solution.

$Al(NO_3)_3 \cdot 9H_2O$ in the solution, and (3) those at a constant content of aluminum nitrate but at different temperatures and supersaturations. The growth rates of the filamentary KDP crystals along the z axis were measured in all the experiments, whereas their transverse dimensions, in the experiments of the first two types only.

Figure 1 shows the results of the measurements made at a constant temperature, 21°C, and impurity content, 0.7 g $Al(NO_3)_3 \cdot 9H_2O$ per kg of water, but at different supersaturations. No filamentary crystals were formed up to a relative supersaturation of $\sigma \approx 0.6$. At $\sigma > 0.6$, crystals start growing with their growth rate increasing with an increase in σ.

The average transverse dimension of the filamentary crystals increases with an increase in σ, all the other factors being the same (Fig. 2). The minimum transverse dimensions of the filamentary crystals were in the range 2–10 μm; the maximum dimensions, in the range 60–150 μm.

Figure 3 shows the experimental results obtained at the constant temperature, 18°C, and the constant supersaturation, $\sigma = 0.85$, but at different contents of $Al(NO_3)_3 \cdot 9H_2O$. For the given σ, the growth of the fil-

amentary KDP crystals begins only at an $Al(NO_3)_3 \cdot 9H_2O$ concentration of 0.5 g/kg H_2O (only thick tapering ledges grow at lower concentrations). With an increase in impurity content, the growth rate also increases, then remains constant, and, finally, drops to zero at an $Al(NO_3)_3 \cdot 9H_2O$ content of 1.2 g/kg H_2O. At concentrations higher than 0.6 g/kg H_2O, no substantial effect of the transverse dimensions of the filamentary crystals on their growth rate was observed. With an increase in the $Al(NO_3)_3 \cdot 9H_2O$ content, the average transverse dimension of the crystals decreases (Fig. 4).

Finally, the measurements were also performed with a stepwise change of the temperature. The solution saturated at 50°C was prepared by addition of $Al(NO_3)_3 \cdot 9H_2O$ (0.7 g/1 kg H_2O); then the solution was cooled to 21°C, and a seed was introduced. The measurements were made on an isolated filamentary crystal with a transverse dimension of about 30 μm. The results are shown in Fig. 5. The points were obtained by averaging the growth rate over a 5-min interval. The error was 15%. The temperature 21°C corresponds to $\sigma_1 = 0.70$. A decrease in the supersaturation at higher temperatures results in a decrease in the growth rate. At 26.5°C ($\sigma_2 = 0.54$), the filamentary crystal is tapered and stops

growing (like all the other crystals). With a decrease in σ, some thick filamentary crystals split into several thinner ones. The repeated decrease in the temperature down to 12°C ($\sigma_3 = 1.1$) gave no rise to crystal growth. Below 12°C, the crystals start expanding rapidly either along their length or only in the individual segments, and new filamentary crystals (as a rule, isolated and oriented along the z axis) are formed. After some time, some of these crystals also expand, whereas some other continue growing as thin crystals. There were also some filamentary crystals that grew without seeds. An increase in the temperature up to 25.5°C stops the growth of all the crystals. The cessation of growth at a temperature lower than 26.5°C is associated with the formation of a certain amount of a crystalline precipitate in the course of experiment, i.e., with the absence of supersaturation.

DISCUSSION AND CONCLUSIONS

Considering the experimental results, we can suggest causes of formation and growth of the filamentary KDP crystals on a seed crystal in the presence of $Al(NO_3)_3 \cdot 9H_2O$ in the solution.

Since the dislocation-free growth of the faces of the KDP bipyramid in a "pure" solution takes place at a rather low supersaturation, $\sigma = 0.29$ [4], the face growth via the formation of two-dimensional (2D) nuclei in the range 0.5–0.95 becomes even more probable. The 2D nucleation at the faces of the KDP bipyramid significantly contributes to the total step density at values as low as $\sigma = 0.1$ [5]. At $\sigma = 0.6$–0.95, this contribution should be dominant.

This assumption is confirmed by the fact that the surface density on the bipyramid face of the filamentary crystals is higher than the density of the dislocation etch pits on the z-cuts of the crystal [6]. In addition, we made a special experiment. Using selective etching, we first determined the etching-pit density on the seed, (25 ± 4) cm^{-2}. Then the filamentary crystals were grown on the same seed; their density was ~600 cm^{-3}. Nevertheless, only direct methods of dislocation observation can give the answer to the question about the nature of step sources.

Upon introduction of a seed into the solution, numerous 2D nuclei appear on the bipyramid faces. The steps formed by these nuclei propagate over the face. Simultaneously, the impurity molecules arrive at the crystal surface. Their flux is proportional to the impurity concentration in the solution. According to the Paneth rule [7], compounds whose formation involves Al^{3+} ions should be adsorbed at the KDP crystal. One can assume that impurity islets (probably, based on phosphate complexes) of colloidal size are formed in front of the steps. These islets are Cabrera–Vermilyea stoppers [8]. An expanding step encounters on its way an ever denser row of such stoppers. The velocity of the
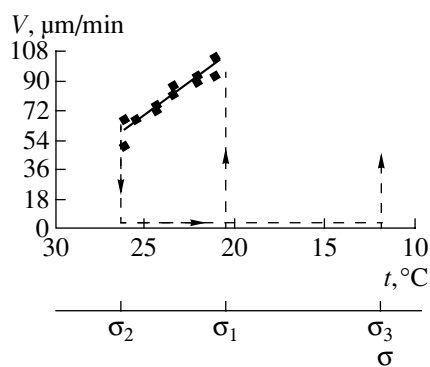

Fig. 5. Growth-rate hysteresis in filamentary KDP crystals.

growth-step motion over the face is determined by the expression

$$v = v_0(1 - 2r_c/l)^{1/2},$$

where v_0 is the velocity of a rectilinear step in the absence of an impurity, l is the average interstopper distance, and r_c is the radius of the critical nucleus. It follows from the above expression that a growth step ceases to move if $l \approx 2r_c$. The longer the initially clean surface of the face–solution contact (that is, the lower σ) and the higher the impurity concentration, the shorter the distance passed by the step and the smaller the transverse dimensions of the bases of filamentary crystals (Figs. 2, 4). If new 2D nuclei appear on the underlying layer, the following layer is formed whose dimensions are limited by the area of the basic layer. The ends of these successive layers are the side faces of a filamentary crystal—the prism faces, which practically do not grow at high impurity concentration [9]. Thus, the bipyramid faces are divided into a set of the individual growing regions (filamentary crystals of various thicknesses). Thicker crystals are formed due to merging of the steps from several nuclei or due to the nonuniform distribution of the impurity aggregates over the surface. At the whisker top, the impurity aggregates are formed less intensely because of the small area of the top and the intense inflow of intrinsic particles. The independence of the growth rate of the filamentary crystals (Fig. 3) from the impurity concentration (for a dopant content ranging from 0.7 to 1.0 g/kg of water at $\sigma = 0.85$) indicates an insignificant effect of the impurity on the rate of nucleation on the vertices of filamentary crystals and, what is more important, on the step velocity. This results from the fact that the growth rate is not limited by the step velocity at high σ. Upon the addition to the solution of $Al(NO_3)_3 \cdot 9H_2O$ (1.2 g/kg H$_2$O), no filamentary crystals grow, because the step motion from all the step sources ceases. The curve in Fig. 1 fits the above pattern well. Up to $\sigma = 0.6$, no step motion is observed and, hence, no face growth is observed either. In the range $\sigma = 0.6$–0.8, the step velocity increases for two reasons. First, with an increase in supersaturation

the number of stoppers decreases because of the competition between the intrinsic and impurity particles. It is not improbable that their dimensions and the strength of their attachment to the face also change. Second, the dimension of the critical nucleus decreases, and, in conformity with the Cabrera–Vermilyea formula, the step velocity increases. The portion of the curve at even higher σ corresponds to the maximum step velocity (in this case, the face becomes kinetically rough, and the effect of stoppers becomes insignificant). Thus, the impurity determines the nonlinear character of the changes in the step velocity with variation of supersaturation and, hence, also the normal growth rate of the filamentary crystals.

Thus, the explanation of the growth process of filamentary KDP crystals from solution with the addition of $Al(NO_3)_3 \cdot 9H_2O$ requires the use of the concept of the finite time of the formation of impurity aggregates on the faces [10]. The competition between the intrinsic and impurity particles is confirmed by the splitting (and sharpening and tapering before growth cessation) of the filamentary crystals with a decrease in the supersaturation. This is explained by an increase in the stopper density and the larger dimensions of the critical nucleus.

As was indicated in [11], local growth occurs under conditions of strong adsorption of the impurity according to the Cabrera–Vermilyea mechanism and the temporal dependence of adsorption. The slow adsorption is indicated by the hysteresis of the growth rate, which was actually observed for filamentary crystals (see Fig. 5). Earlier, the hysteresis of the growth rate of the faces of the KDP prism was revealed in solution with the addition of Fe^{3+}. The hysteresis was explained by slow adsorption of the impurity in accordance with the Cabrera–Vermilyea mechanism [12].

As follows from the results obtained, the following model of the formation and growth of filamentary KDP crystals in the presence of an active impurity seems to be probable. A high supersaturation provides the formation of a 2D nucleus. The step velocity increases with an increase in the supersaturation and, along with the impurity concentration, controls the stage of the adsorption development on the surface in front of the step of this impurity. Here, there exists a certain characteristic time either of the impurity arrival from the solution [10] or of the formation of the aggregates of certain active dimensions that become the step stoppers. The suggested mechanism is consistent with the experimental results obtained in this study.

REFERENCES

1. V. N. Portnov, G. N. Sazontova, T. M. Ryzhkova, *et al.*, Izv. Akad. Nauk SSSR, Neorg. Mater. **7** (2), 336 (1971).
2. A. A. Chernov, L. N. Rashkovich, I. L. Smol'skiǐ, *et al.*, in *Crystal Growth* (Nauka, Moscow, 1986), Vol. 15, p. 43.
3. T. A. Land, J. J. De Yoreo, T. L. Martin, and G. T. Palmore, Kristallografiya **44** (4), 704 (1999) [Crystallogr. Rep. **44**, 655 (1999)].
4. A. V. Belyustin and N. S. Stepanova, in *Extended Abstracts of the International Conference on Crystal Growth, Moscow, 1980*, Vol. IV, p. 8.
5. J. J. De Yoreo, T. A. Land, and B. Dair, Phys. Rev. Lett. **73**, 838 (1994).
6. E. A. Kuleva, *Structure and Properties of Solids* (Nizhnenovgor. Gos. Univ., Nizhni Novgorod, 1998), p. 35.
7. G. G. Lemmlein, *Morphology and Genesis of Crystals* (Nauka, Moscow, 1973), p. 114.
8. N. Cabrera and D. A. Vermilyea, *Growth and Perfection of Crystals* (Wiley, New York, 1958), p. 393.
9. V. N. Portnov, Kristallografiya **12** (3), 530 (1967) [Sov. Phys. Crystallogr. **12**, 463 (1967)].
10. A. A. Chernov, *Physicochemical Problems of Crystallization* (Kazakhskiǐ Univ., Alma-Ata, 1969).
11. V. D. Franke and Yu. O. Punin, in *Proceedings of National Conference on Crystal Growth (NKRK-2000), Moscow, 2000*, p. 151.
12. Yu. O. Punin and O. I. Artamonova, Kristallografiya **34** (5), 1262 (1989) [Sov. Phys. Crystallogr. **34**, 760 (1989)].

Translated by A. Zolot'ko

CRYSTAL
GROWTH

Statistical Method of Image Analysis of Heterogeneities in $Ba_{1-x}R_xF_{2+x}$ Crystals

M. O. Marychev*, E. V. Chuprunov*, P. Herrero**, and B. P. Sobolev***

* Nizhni Novgorod State University, Nizhni Novgorod, 603600 Russia
e-mail: marychev@yandex.ru
** Instituto de Ciencia de Materiales, Madrid, 28049 Spain
*** Shubnikov Institute of Crystallography, Russian Academy of Sciences,
Leninskiĭ pr. 59, Moscow, 119333 Russia
Received July 19, 2002

Abstract—A statistical method for image analysis of smooth heterogeneities (with comparatively large luminance grade) is suggested. The method allows one to determine the average dimensions of image heterogeneities and characterize the anisotropy of their dimensions and heterogeneity of image luminance by constructing the corresponding pointer curves. The algorithms suggested for the image analysis are tested on two types of heterogeneities in $Ba_{1-x}R_xF_{2+x}$ crystals grown from melts by the Stockbarger method—the cellular substructure and heterogeneity on a nanometer scale. These heterogeneities are characteristic of the whole family of nonstoichiometric fluorite $M_{1-x}R_xF_{2+x}$ phases. The analysis of the typical images proves the high efficiency of the method of extraction of quantitative information on heterogeneities in $M_{1-x}R_xF_{2+x}$ crystals on various scales. © *2003 MAIK "Nauka/Interperiodica".*

INTRODUCTION

Recently, the computer image analysis of objects obtained by various methods has begun to play an important part in various branches of science and, in particular, in crystal physics. Crystals often contain heterogeneities of various origins that can be observed on different scales. Depending on the dimensions and origin of these heterogeneities, they can be revealed and studied by different methods—from optical (in particular, polarization) microscopy, X-ray topography, and high-resolution electron microscopy to intensely developing scanning probe microscopy, which allows one to study the images of solid surfaces at a resolution close to atomic.

Once the image of the object under study containing the information on various types of heterogeneities is obtained, one has to analyze it with the aim of extracting information on the heterogeneity dimensions (average dimension and its scatter), the morphology of heterogeneities and their mutual arrangement, the presence or absence of boundaries, the degree of homogeneity (heterogeneity) of the sample as a whole, image symmetry, etc. [1].

Over recent decades, the theory of the analysis and processing of images (and, in general, signals) has been well developed. The corresponding methods are used in modern program packages. Suffice it to mention here the Image-Pro Plus program developed by Media Cybernetics.

The automatic methods for measuring the dimensions of the image details are especially well developed

for images which can readily be reduced to a binary form (two luminance levels) or images characterized by a small luminance range. As an example, we mention here the images of a series of single erythrocytes, eutectic structures formed by regular intergrowth of various phases, etc.

The problem becomes even more complicated if the image heterogeneities are smooth, i.e., if the number of the luminance grades is comparatively large. In these cases, it is rather difficult to develop a universal method for evaluating even such a simple characteristic as the average dimension of heterogeneities. Therefore, one has to develop several methods applicable to the analysis of various groups of image heterogeneities.

We studied the crystals of a large practically important family of nonstoichiometric $M_{1-x}R_xF_{2+x}$ phases with a defect fluorite-type structure in the $MF_2 - RF_3$ systems (M = Ca, Sr, Ba and R are rare earth elements) [2–5]. Therefore, the algorithms developed were tested on two types of heterogeneities in $Ba_{1-x}R_xF_{2+x}$ crystals grown from melt by the Stockbarger method. These types of heterogeneities determine numerous important properties of the crystals and are also characteristic of the whole family of nonstoichiometric fluorite phases.

The scale of the first type of heterogeneities (cellular substructure) ranges from fractions of a millimeter to several millimeters, i.e., is a macroscopic scale. A cellular substructure is formed as a result of the concentration supercooling of a multicomponent melt characterized by incongruent melting (i.e., melting occurring with melt decomposition) [6–9]. This type of heteroge-

neity is observed in transmitted light because of the concentration gradient of the second component in the crystal bulk and the corresponding gradient of the refractive index.

An example of the second type of heterogeneities observed in $M_{1-x}R_xF_{2+x}$ crystals is the images of atomic planes and moiré fringes observed in a high-resolution electron microscope [9–11]. The scale of these heterogeneities is close to atomic.

The present study aims to design algorithms that would provide the determination of the average dimensions of heterogeneities and the characterization of the anisotropy in their dimensions and luminance of the image as a whole by constructing the corresponding pointer curves.

The experimental images are digitized and input into the computer. The corresponding information is represented as a certain numerical matrix. Each number of the matrix corresponds to the minimum image unit (pixel) defining its luminance. Thus, if the luminance is given by eight bytes of information, it is an integer from the interval from 0 to 255, where 0 corresponds to the zero intensity and 255, to the maximum intensity. The algorithms for the analysis of the image heterogeneities are based on certain operations with such numerical matrices.

The general idea underlying the suggested algorithms reduces to an analysis of the estimates of the statistical characteristics of the arrays of mean square deviations of luminance for a sufficiently large number of regions of a given shape and arbitrary dimensions and orientations singled out from the image in a random way.

DETERMINATION OF THE AVERAGE DIMENSION OF HETEROGENEITIES IN $Ba_{1-x}R_xF_{2+x}$ CRYSTALS

The simplest measure of the heterogeneity of the image as a whole or its arbitrary portion is the mean square deviation of the pixel luminance from the corresponding average luminance. However, this characteristic provides no information either on the dimensions or other characteristics of heterogeneities. Therefore, the average dimension of heterogeneities is determined in the following way.

Consider a gray-level array and single out a rather large number N of square regions having the same pixel size, $j \times j$. The position of each of these regions is chosen in a random way using a generator of uniformly distributed pseudorandom numbers. Now calculate the mean square deviation of the pixel luminance $S_i(j)$ ($i = 1, …, N$) for each region. Hereafter, the $S_i(j)$ values are called local heterogeneities. Then, calculate the average value $M(j) = \langle S_i(j) \rangle$ and the mean square (standard) deviation $D(j)$ of the local heterogeneities $S_i(j)$.

Let the dimension of the above regions increase at a step of unity in the range from unity up to a certain

value j_{max}. This value is set in a way to exceed *a priori* the average heterogeneity dimension. Thus, first, we single out a series of N regions of the same dimensions and then a series of N regions of different dimensions, etc. For each of the series of N regions of the dimension j, the $M(j)$ and $D(j)$ values are calculated.

Thus, we obtain j_{max} pairs of $M(j)$ and $D(j)$ values for the given image. Then, construct the curves $M(j)$ and $D(j)$ ($1 \le j \le j_{max}$).

Figure 1 shows the image of the region of the crystal of the solid solution of the composition $Ba_{0.95}Yb_{0.05}F_{2.05}$ (5 mol % YbF_3). This crystal melts incongruently (with decomposition). In the course of the directed crystallization, the conditions are created (concentration supercooling) under which the growth front stops being planar and a cellular substructure is formed. In the bulk of the solid-solution crystal, the concentration of the impurity component (in this case, Yb) varies from point to point. This process is accompanied by changes in the refractive index and other crystal properties, which can be observed visually. Figure 1a shows the image of the cellular substructure of a 1-mm-thick plane-parallel plate cut out from this crystal obtained by the shadow method.

It is seen from Fig. 1b that $M(j)$ increases monotonically from the zero value and shows a tendency to saturation. Indeed, if the regions are small, they are all almost homogeneous and the mean square deviation of the pixel luminance in each region (local heterogeneity) is rather small. Therefore, the average value of the local heterogeneities is also small (close to zero).

With an increase in the area of the singled-out regions, one encounters an ever increasing number of regions with noticeable heterogeneities. Therefore, the average value of the local heterogeneities also increases. With a further increase in the dimension j, the singled-out regions would contain several heterogeneities simultaneously. Therefore, the local heterogeneity in each of these regions would attain a considerable but approximately the same value. As a consequence, the average value of the local heterogeneities also becomes large. The curve shows a tendency to saturation if the dimension j becomes comparable with the average dimension of heterogeneities.

The area under the curve $M(j)$ can be calculated as

$$\Sigma = \sum_{j=1}^{w} M_j. \tag{1}$$

The above formula can be used as the integral estimate of the heterogeneity of the image as a whole. Since the dimension of the singled-out regions cannot be larger than the shorter side of the image, the variable j should vary from unity to the length of the shorter side of the image denoted as w.

It is expedient to consider the plot $D(j)$ with the maximum (Fig. 1c), which can be interpreted as fol-
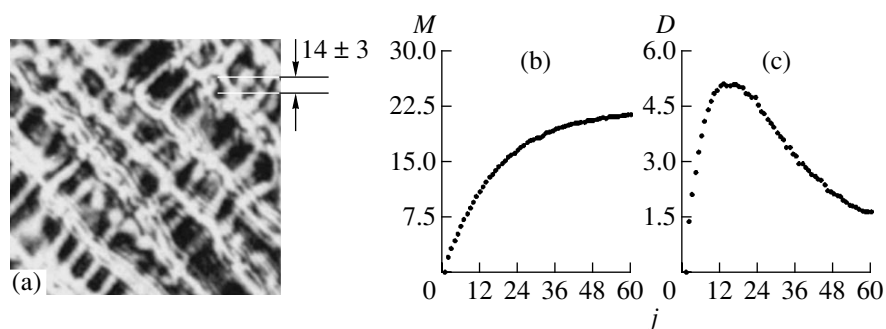
Fig. 1. (a) Image of the portion of a $Ba_{0.95}Yb_{0.05}F_{2.05}$ crystal obtained in transmitted light (shadow method); (b) the average local heterogeneity M as a function of the region dimension j; (c) the mean square deviation of the local heterogeneities, D, as a function of region dimension j. The average heterogeneity dimension and its error in pixels is indicated in the upper right-hand corner. The parameter $N = 3000$. The image dimensions are 375×354 pixels (4.28×4.04 mm^2).

lows. If the dimensions of the singled-out regions are small (low j value), the local heterogeneities of each region are small and approximately equal. Therefore, the mean square deviation $D(j)$ of the local heterogeneities $S_i(j)$ ($i = 1, ..., N$) is also small. With an increase in the dimensions of the singled-out regions, this value increases, because along with the homogeneous regions there are also inhomogeneous ones, which makes the scatter in the values of local heterogeneities more pronounced.

With a still further increase in the region dimensions, most of the singled-out regions would contain several heterogeneities simultaneously. The local heterogeneities in all the large regions tend to have a certain average value and, therefore, the mean square deviation $D(j)$ of the local heterogeneities would decrease. Therefore, at a certain intermediate dimension j comparable with the average heterogeneity dimension, the curve $D(j)$ should acquire a maximum.

Approximating the portion of the plot $D(j)$ containing the region around the maximum by a certain smooth curve $f(x)$ (usually a polynomial of degree three or four), we can determine the value of j at the maximum, which is denoted here as R_{av}. Hereafter, the R_{av} value is called the average dimension of image heterogeneities. To calculate the error in R_{av}, one has to expand the approximating function $f(x)$ into a Taylor series in the neighborhood of the maximum and take into account the terms up to the third one (one has to calculate its second derivative $f''(x)$). The increment in the function in this expansion is taken to be the mean square deviation of the residual vector; thus, we arrive at the corresponding increment in the argument which is considered to be the error in the average heterogeneity dimension (ΔR_{av}).

Of course, in the conventional sense of the theory of measurement processing, this quantity is not an error. The $\Delta R_{av}/R_{av}$ ratio has a higher value if the image contains both small and large heterogeneities and is lower if all the heterogeneities are of approximately the same dimensions. However, this ratio can be considered as a measure of scatter in the heterogeneity dimensions with respect to their average value only conditionally, because $\Delta R_{av}/R_{av}$ decreases with an increase in N.

Within this algorithm, the average dimension of heterogeneities and its error for the image shown in Fig. 1a equals $R_{av} = 14 \pm 3$ pixels. The corresponding heterogeneity dimension in the studied $Ba_{0.95}Yb_{0.05}F_{2.05}$ crystal equals 0.16 ± 0.04 mm.

The image considered above is rather simple and consists of the elements that have close shapes and dimensions. The electron microscopy image of a $Ba_{0.8}Lu_{0.2}F_{2.2}$ crystal (20 mol % LuF_3) at an atomic resolution is much more complicated (Fig. 2a) [10]. This image is formed by several systems of atomic planes having different orientations, extensions, and interatomic spacings. It is also complicated by several systems of moiré fringes having different orientations and periods. Such a complicated crystal structure reflects crystal microheterogeneity on the nanometer scale [11].

The average dimension of image heterogeneities in Fig. 2a determined from the $D(j)$ plot (Fig. 2b) is $R_{av} = 22 \pm 4$ pixels, which corresponds to 52 nm. It should be indicated that, unlike the image shown in Fig. 1a, the calculation of the average heterogeneity dimension of the complicated images, e.g., of that shown in Fig. 2a, can give a rather unexpected result. However, even the approximate quantitative estimate of the heterogeneity dimension can turn out to be rather useful.

ANISOTROPY OF LUMINANCE OF HETEROGENEITIES AND THEIR DIMENSIONS

Introduce some definitions. Moving along a certain straight line of the image, we encounter pixels having different luminance. If pronounced luminance differences along a given direction are encountered more often than along some other direction, we state that the luminance heterogeneity along the former direction is more pronounced than along other directions, and this phenomenon is called the anisotropy of the luminance
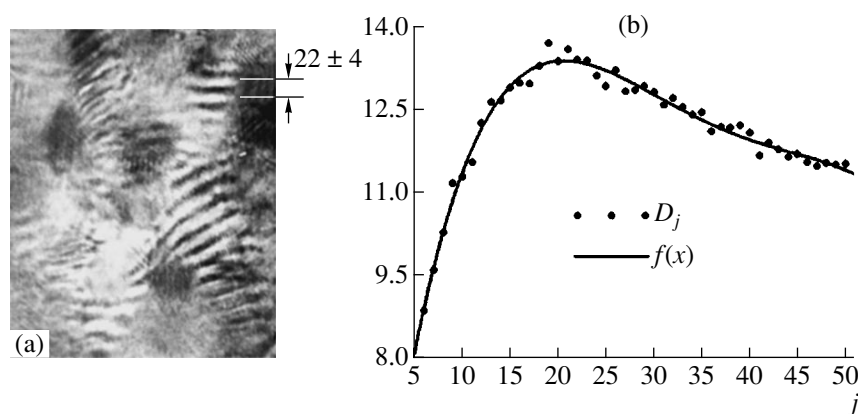
Fig. 2. (a) Electron microscopy image of a $Ba_{0.8}Lu_{0.2}F_{2.2}$ crystal (20 mol % LuF_3) at an atomic resolution; (b) mean square deviation of the local heterogeneities, D, as a function of the region dimension j. The average heterogeneity dimension and its error in pixels is indicated in the upper right-hand corner. The parameter $N = 3000$. The image dimensions are 372×462 pixels (890×1100 nm^2).

heterogeneity. An example of the structure with such an anisotropy is a system of alternating parallel dark and light fringes. Often, heterogeneities are of an elongated shape and arranged more or less orderly. In such instances, one can consider anisotropy of heterogeneity dimensions.

To characterize these characteristics of the image quantitatively, the following method can be used. One singles out on the image a series of N regions in the shape of straight parallel strips of length ρ and a thickness of one pixel. The origin of each strip is chosen arbitrarily. This series of strips can also be characterized by the angle φ formed by the strips and the positive direction of the X axis. The X axis originates at the left upper angle of the image and goes to the right (Fig. 3b). The angle φ can vary from $0°$ to $180°$.

Now, calculate the average value of $M(\rho, \varphi)$ and the mean square deviation $D(\rho, \varphi)$ for N mean square deviations of the luminance of the strips of this series. Since the variables ρ and φ vary in a discrete manner, then, for each direction φ, we obtain the arrays of the functions $M(\rho, \varphi)$ and $D(\rho, \varphi)$ corresponding to the series that differ only in the length ρ of the strips.

We shall use the sum Σ_φ calculated in a way similar to Eq. (1) as the absolute characteristic of luminance heterogeneity along the given direction. The number of such sums is determined by the number of the values of the variable φ for which the average values of $M(\rho, \varphi)$ were calculated.

It is more convenient to use the following relative characteristic of the luminance heterogeneity:

$$A(\varphi) = \frac{\Sigma_\varphi}{\Sigma_{\varphi \max}} \times 100\%, \qquad (2)$$

where $\Sigma_{\varphi \max}$ is the maximum value of all the Σ_φ sums.

The set of $A(\varphi)$ values can conveniently be represented as a plot in the polar coordinates, the so-called

pointer curve of luminance heterogeneity. If no anisotropy of luminance is observed, the plot has the form of a circumference arc of the 100% radius.

Approximating the portions of the maxima of the dependences $D(\rho, \varphi)$ which, irrespective of the angle φ, are considered as functions of one variable, ρ, we can determine the average heterogeneity and its error along each direction. Thus, we can construct the curve of the average heterogeneity dimension as a function of direction in the polar coordinates, the so-called pointer curve of the heterogeneity dimension.

The $A(\varphi)$ and $R(\varphi)$ curves for the image shown in Fig. 3a (similar to the image in Fig. 1a with the only difference—the heterogeneity dimension is averaged over the plot shown in Fig. 3d) are given in Figs. 3c and 3d.

At the angle $\varphi = 45°$, the global minimum of the relative heterogeneity luminance has the form shown in Fig. 3c. This corresponds to the presence on the image of a system of quasiparallel bright fringes alternating with relatively dark fringes and forming an angle of $45°$ with the positive direction of the X axis. It should also be indicated that, on the whole, Fig. 3a shows no obvious anisotropy of the heterogeneity dimensions, although some individual heterogeneities show such anisotropy. This is confirmed by the plot $R(\varphi)$ (Fig. 3d). However, a certain tendency for $R(\varphi)$ values to increase in the angular range $120°–150°$ indicates that heterogeneity dimensions along these directions are somewhat larger.

It is important to indicate that the heterogeneity dimensions averaged over the plot $R(\varphi)$ are equal to 26 ± 5 pixels (which corresponds to 0.30 ± 0.05 mm) and differ from the average heterogeneity dimension of the same image obtained by the first algorithm. It is explained by different shapes of the singled-out regions, so that one should not expect their complete correspondence. If necessary, this difference can be

$A(\varphi)$

26 ± 5

(a)

(b)

X

φ

ρ

Y

(c)

(d)

$R(\varphi)$
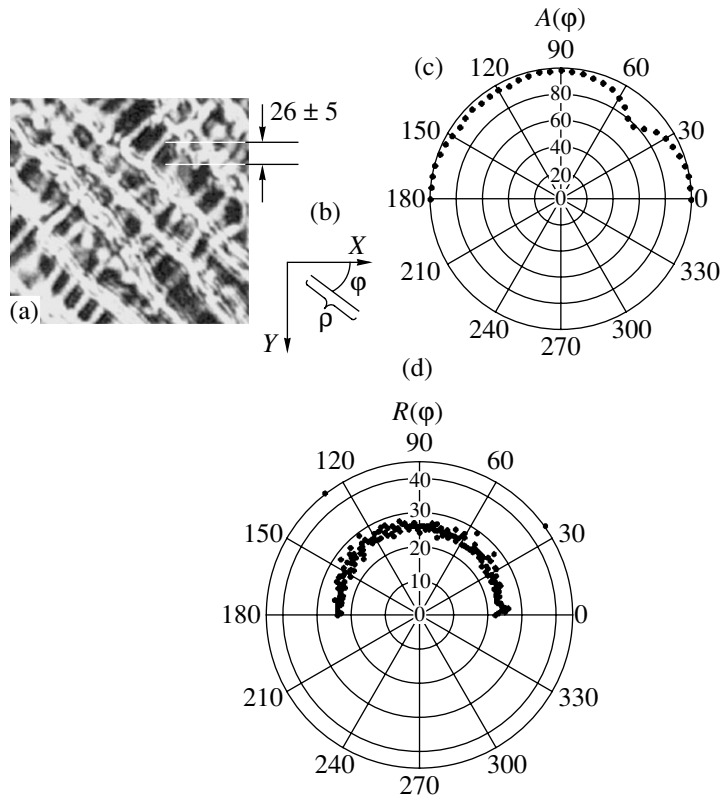
Fig. 3. (a) Image of a $Ba_{0.95}Yb_{0.05}F_{2.05}$ crystal (analogous to that shown in Fig. 1a); (b) the reference system and the parameters of the singled-out strip; (c) pointer curve of the relative heterogeneity of image luminance (parameter $N = 100$, step in ρ equals 5 pixels, step in φ equals 5°); (d) the pointer curve of the heterogeneity dimensions of the image (parameter $N = 3000$, a step in ρ equals 1 pixel, a step in φ equals 1°); the average heterogeneity dimension and its error in pixels (calculated by averaging the data in Fig. 3d) are indicated in the upper right-hand corner. The image dimensions are 375×354 pixels.

"balanced" by the introduction of a certain factor into one of the algorithms.

It is interesting to compare the pointer curves for some other crystals studied. Thus, Fig. 4 shows the $A(\varphi)$ and $R(\varphi)$ pointer curves for the electron microscopy image shown in Fig. 2a.

The pointer curve of the relative luminance heterogeneity in Fig. 4a shows that this characteristic is maximal in the angular range $\varphi = 30°-60°$; in Fig. 2, this corresponds to the directions transverse to the series of tilted moiré fringes in the right-hand part of the image. In addition to this system of fringes, one can see the contrast horizontal mooiré fringes in the upper right-hand angle of the image. It seems that these features give rise to the formation of a broad minimum in the angular range $\varphi = 30°-90°$ of the pointer curve of the heterogeneity dimension shown in Fig. 4b.

Consider also an example of the image of the cellular substructure of the portion of a $Ba_{0.9}Pr_{0.1}F_{2.1}$ crystal (10 mol % PrF_3) (Fig. 5). The pointer curves $A(\varphi)$ and $R(\varphi)$ for this crystal are shown in Fig. 6. It is seen that the image of this substructure is characterized by the almost complete absence of anisotropy of the luminance heterogeneity and heterogeneity dimensions,

which satisfactorily agrees with the qualitative conclusions drawn from Fig. 5.

Sometimes, an image has two characteristic directions along which the image properties differ more significantly. In these cases, it is possible to introduce certain quantities defining the relative difference in the

(a) $A(\varphi)$

(b) $R(\varphi)$
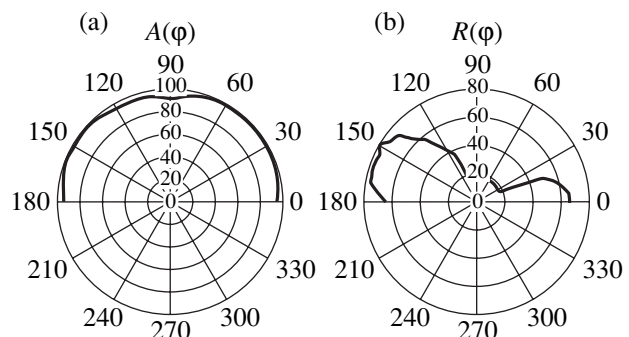
Fig. 4. (a) Pointer curve of the relative heterogeneity of relative luminance heterogeneity on the image shown in Fig. 2a (parameter $N = 500$; the step in ρ equals 2 pixels, the step in φ equals 5°); (b) pointer curve of the heterogeneity dimensions on the image shown in Fig. 2a (parameter $N = 3000$, the step in ρ equals 1 pixel, the step in φ equals 5°).
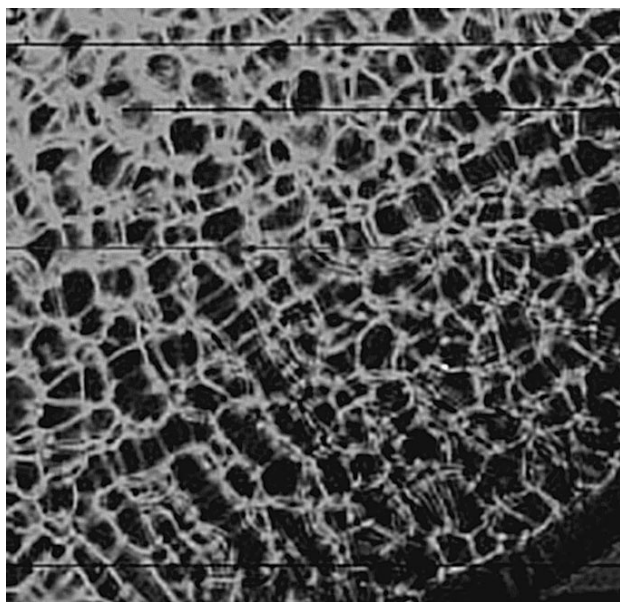
Fig. 5. Image of the portion of the solid-solution crystal of the composition $Ba_{0.9}Pr_{0.1}F_{2.1}$ (10 mol % PrF_3) in transmitted light (shadow method).
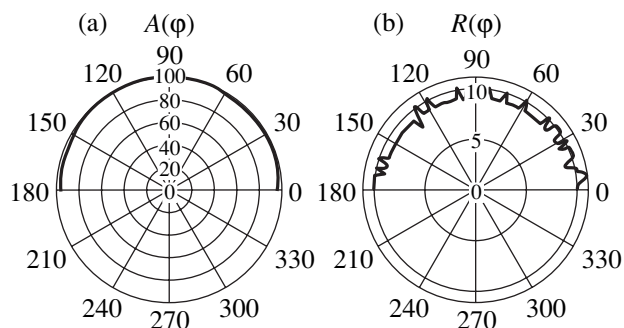
Fig. 6. (a) Pointer curve of the relative luminance heterogeneity on the image shown in Fig. 5 (parameter $N = 200$, the step in ρ equals 2 pixels, the step in φ equals 5°); (b) pointer curve of the heterogeneity dimensions on the image shown in Fig. 5 (parameter $N = 15\,000$, the step in ρ equals 1 pixel, the step in φ equals 2°).

above image characteristics along these two directions. For simplicity, we assume that these are the horizontal and vertical directions.

Let the series of N horizontal and N vertical straight strips of the same length j and the width of one pixel be singled out in a random way. For each strip, we can calculate the mean square deviation of the pixel luminance—the value of the local heterogeneity. Then, we can calculate the average value of the local heterogeneities $M_G(j)$ and $M_V(j)$ and the mean square deviations $D_G(j)$ and $D_V(j)$ of the local heterogeneities for the series of vertical and horizontal strips, where the subscripts G and V indicate the horizontal and vertical directions, respectively. The lengths of the vertical

strips can vary in a discrete manner within a step of one pixel in the range from unity to r (r is the number of rows in the image matrix), whereas the lengths of the horizontal strips vary from unity to c (c is the number of columns in the image matrix). Let the above procedure of singling-out the series of horizontal and vertical strips of pixels on the image and the subsequent calculation of $M_G(j)$, $M_V(j)$, $D_G(j)$, and $D_V(j)$ values be repeated for all the possible j values. Then, for the horizontal direction, we obtain c pairs of the $M_G(j)$ and $D_G(j)$ values, whereas for the vertical one, r pairs of the $M_V(j)$ and $D_V(j)$ values. These sets of the values can conveniently be represented in graphical form. Figure 7b shows the $M_G(j)$ and $M_V(j)$ curves for the image shown in Fig. 1a (Fig. 3a) rotated by an angle of 45°.

Now, limiting the variable j from above by the length w of the shorter side of the image, we can calculate, similar to Eq. (1), the areas Σ_G and Σ_V under the curves $M_G(j)$ and $M_V(j)$. We suggest using the ratio of the difference between their areas to their average value as the estimate of the luminance anisotropy along the vertical and horizontal directions:

$$\varepsilon_{Br} = \frac{2(\Sigma_G - \Sigma_V)}{\Sigma_G + \Sigma_V} 100\%. \tag{3}$$

The sign of ε_{Br} depends on the fringe directions on the image: the plus sign corresponds to the vertical or near vertical direction of the fringes, whereas the minus sign corresponds to the horizontal or near horizontal direction (the latter situation is illustrated by Fig. 7).

Figure 8a shows the curves $D_G(j)$ and $D_V(j)$ for the image identical to that shown in Fig. 7a, and Fig. 8b shows the curves $D_G(j)$ and $D_V(j)$ for the image obtained by its 25%-extension along the vertical (increase of the scale by 25%).

Using the curves $D_G(j)$ and $D_V(j)$, we can calculate the average heterogeneity dimensions along the horizontal and vertical directions (the method of processing these curves is the same as in the calculation of the average heterogeneity dimensions in the first algorithm). We suggest using the ratio of these dimensions to their average value as an estimate of the anisotropy degree of heterogeneity in dimensions along the vertical and horizontal directions:

$$\varepsilon_{RVG} = \frac{2(R_G - R_V)}{R_G + R_V} 100\%. \tag{4}$$

The sign of the ε_{RVG} value contains information on the direction of "elongation" of the image heterogeneities. It should be noted that ε_{RVG} and ε_{Br} can have opposite signs.

It is seen from Fig. 8b that the 25%-image extension in the vertical direction resulted in the equivalent changes in the heterogeneity dimensions along the horizontal and vertical directions and the estimate of the
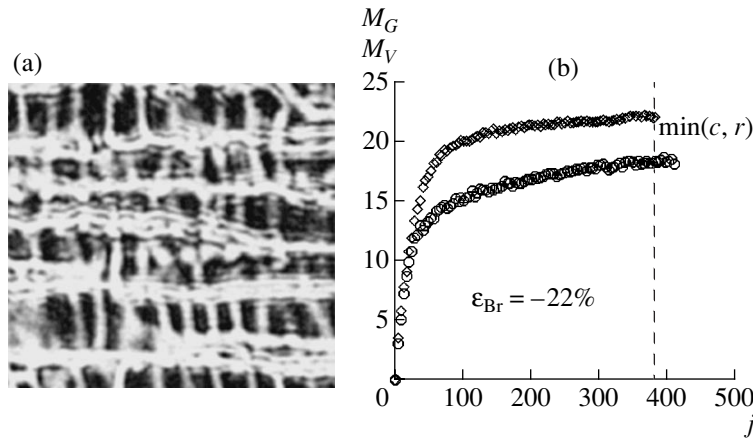
Fig. 7. (a) Image of a crystal of the solid solution of the composition $Ba_{0.95}Yb_{0.05}F_{2.05}$ rotated by 45° with respect to the image shown in Figs. 1a and 3a; (b) the average values of the local heterogeneities in the series of thin strips of pixels oriented along the horizontal (M_G is the lower curve) and vertical (M_V is the upper curve) directions as functions of the strip lengths j. The quantitative estimate of the anisotropy of the luminance heterogeneity is indicated. Parameter $N = 1000$. Image dimensions are 410×383 pixels.
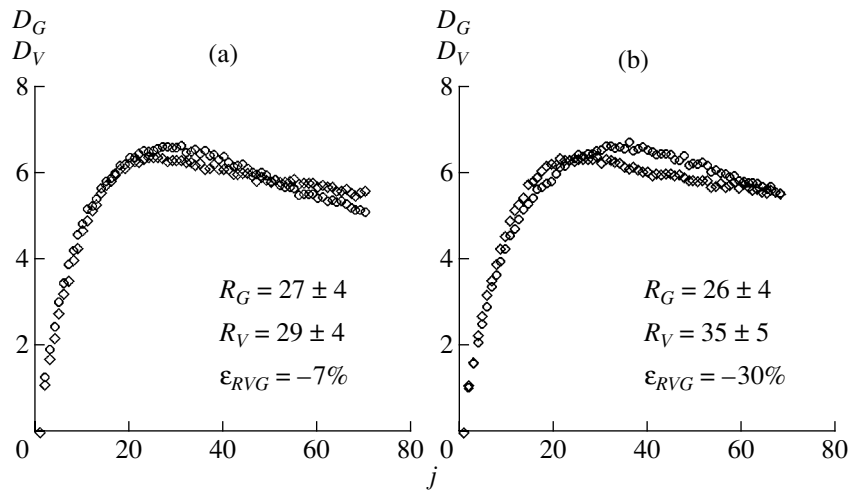
Fig. 8. (a) Mean square deviations of the local heterogeneities in the series of thin strips of pixels oriented along the horizontal D_G and the vertical D_V dimensions as functions of strip length j on the image shown in Fig. 7a; (b) mean square deviation of the local heterogeneities in the series of thin strips of pixels oriented along the horizontal D_G and vertical D_V directions as functions of the strip length j upon the 25%-extension of the image along the vertical direction (new dimensions 410×478 pixels) illustrated by Fig. 7a. The values of the average dimensions of heterogeneities along the horizontal and vertical directions are indicated together with the estimate of the degree of anisotropy of these dimensions. Parameter $N = 5000$.

degree of anisotropy of the heterogeneity dimensions introduced above.

CONCLUSIONS

All the algorithms suggested above are based on the analysis of a rather large but finite number of the regions of various dimensions and shapes singled out from the image in a random way. Therefore, the results obtained are somewhat dependent on the input parameters, e.g., the number N of the regions of the given dimensions singled out from the image (one passage) and also on the degree of the approximating polynomials used to refine the form of the experimental dependences. One has also to take into account the statistical nature of the results obtained and evaluate the corresponding errors.

If the characteristic heterogeneity dimension is about 5–10 pixels, one also observes the noticeable effect of low image resolution. This is especially clearly seen in the algorithm used to calculate the pointer curves of heterogeneities in luminance and dimensions, especially of the pointer curve of heterogeneity dimensions. We recommend digitizing the image at such a resolution that the characteristic dimension of the heterogeneities would not exceed 30–50 pixels. This advice also seems to be useful for analysis of images by any other method.

In addition to the formal description of the statistical method of the analysis of the image heterogeneity, one also has to consider those specific characteristics of the image that are necessary for the reasonable application of the method. This condition requires the presence on the image of a sufficiently large number of heterogeneities that are approximately uniformly distributed over the whole image area. For example, in this case, the value of the average heterogeneity dimension will be the closest to the dimension that is determined visually.

The algorithms suggested here are not universal and should be considered only as one of the possible approaches to the analysis of the heterogeneity of images. The efficiency of the use of these algorithms should be determined for each set of the images studied.

The above method was tested when analyzing the growth heterogeneities in crystals of fluorite-type solid solutions. We believe that, in general, this method can be rather efficient for analysis of the images of physical objects obtained by various methods.

ACKNOWLEDGMENTS

REFERENCES

1. W. K. Pratt, *Digital Image Processing* (Wiley, New York, 1978; Mir, Moscow, 1982).
2. B. P. Sobolev, in *Crystal Growth* (Nauka, Moscow, 1990), Vol. 18, p. 233.
3. B. P. Sobolev, *The Rare Earth Trifluorides* (Inst. d'Estudis Catalans, Barcelona, 2000), Part 1.
4. B. P. Sobolev, Buttl. Soc. Catalana Cien. Fis. Quim. Mat. **12** (2), 275 (1991).
5. M. O. Marychev, E. V. Chuprunov, E. A. Krivandina, *et al.*, Vestn. Nizhegorod. Univ. im. N. I. Lobachevskogo, Fiz. Tverd. Tela, No. 1, 111 (2001).
6. B. Chalmers, *Principles of Solidification* (Wiley, New York, 1964; Metallurgiya, Moscow, 1968).
7. T. M. Turkina, P. P. Fedorov, and B. P. Sobolev, Kristallografiya **31** (1), 146 (1986) [Sov. Phys. Crystallogr. **31**, 83 (1986)].
8. P. P. Fedorov, T. M. Turkina, V. A. Meleshina, and B. P. Sobolev, in *Growth of Crystals* (Consultants Bureau, New York, 1988), Vol. 17, p. 165.
9. B. P. Sobolev, A. M. Golubev, E. A. Krivandina, *et al.*, Kristallografiya **47** (2), 237 (2002) [Crystallogr. Rep. **47**, 201 (2002)].
10. R. Muñoz, R. Rojas, B. P. Sobolev, and P. Herrero, in *Proceedings of 19th Reunion Bienal Sociedad Española de Microscopia Electronica* (Murcia, Spain, 1999), p. 317.
11. B. P. Sobolev, A. M. Golubev, and P. Errero, Kristallografiya **48** (1) (2003) [Crystallogr. Rep. **48** (2003)].

Translated by L. Man